



AFRL-RX-WP-TR-2012-0472



**PASSIVE, HIGHLY-SENSITIVE, ROOM-TEMPERATURE
MAGNETIC FIELD SENSORS AND ARRAYS FOR
DETECTION AND IMAGING OF HIDDEN THREATS IN
URBAN ENVIRONMENTS**

Dwight Viehland

Virginia Tech

**JULY 2012
Final Report**

Approved for public release; distribution unlimited.

See additional restrictions described on inside pages

STINFO COPY

**AIR FORCE RESEARCH LABORATORY
MATERIALS AND MANUFACTURING DIRECTORATE
WRIGHT-PATTERSON AIR FORCE BASE, OH 45433-7750
AIR FORCE MATERIEL COMMAND
UNITED STATES AIR FORCE**

NOTICE AND SIGNATURE PAGE

Using Government drawings, specifications, or other data included in this document for any purpose other than Government procurement does not in any way obligate the U.S. Government. The fact that the Government formulated or supplied the drawings, specifications, or other data does not license the holder or any other person or corporation; or convey any rights or permission to manufacture, use, or sell any patented invention that may relate to them.

This report was cleared for public release by the Air Force Research Laboratory 88ABW Public Affairs Office and is available to the general public, including foreign nationals. Copies may be obtained from the Defense Technical Information Center (DTIC) (<http://www.dtic.mil>).

AFRL-RX-WP-TR-2012-0427 HAS BEEN REVIEWED AND IS APPROVED FOR PUBLICATION IN ACCORDANCE WITH ASSIGNED DISTRIBUTION STATEMENT.

//SIGNATURE//

KENT L. AVERETT, Program Manager
Photonic Materials Branch

//SIGNATURE//

DANIEL J. BREWER, Chief
Photonic Materials Branch
Functional Materials Division

//SIGNATURE//

KAREN R. OLSON, Deputy Chief
Functional Materials Division
Materials & Manufacturing Directorate

This report is published in the interest of scientific and technical information exchange and its publication does not constitute the Government's approval or disapproval of its ideas or findings.

REPORT DOCUMENTATION PAGE

*Form Approved
OMB No. 0704-0188*

The public reporting burden for this collection of information is estimated to average 1 hour per response, including the time for reviewing instructions, searching existing data sources, gathering and maintaining the data needed, and completing and reviewing the collection of information. Send comments regarding this burden estimate or any other aspect of this collection of information, including suggestions for reducing this burden, to Department of Defense, Washington Headquarters Services, Directorate for Information Operations and Reports (0704-0188), 1215 Jefferson Davis Highway, Suite 1204, Arlington, VA 22202-4302. Respondents should be aware that notwithstanding any other provision of law, no person shall be subject to any penalty for failing to comply with a collection of information if it does not display a currently valid OMB control number. PLEASE DO NOT RETURN YOUR FORM TO THE ABOVE ADDRESS.

1. REPORT DATE (DD-MM-YY) July 2012			2. REPORT TYPE Final		3. DATES COVERED (From - To) 25 September 2009 – 30 June 2012	
4. TITLE AND SUBTITLE PASSIVE, HIGHLY-SENSITIVE, ROOM-TEMPERATURE MAGNETIC FIELD SENSORS AND ARRAYS FOR DETECTION AND IMAGING OF HIDDEN THREATS IN URBAN ENVIRONMENTS			5a. CONTRACT NUMBER FA8650-09-1-7945 5b. GRANT NUMBER 5c. PROGRAM ELEMENT NUMBER 61101E			
6. AUTHOR(S) Dwight Viehland			5d. PROJECT NUMBER 1000 5e. TASK NUMBER 5f. WORK UNIT NUMBER X0A3 (PS105402)			
7. PERFORMING ORGANIZATION NAME(S) AND ADDRESS(ES) Virginia Polytechnic Institute & State University Virginia Tech 1880 Pratt Dr Suite 2006 Blacksburg, VA 24060			8. PERFORMING ORGANIZATION REPORT NUMBER Defense Advanced Research Projects Agency 3701 North Fairfax Drive Arlington, VA 22203-1714			
9. SPONSORING/MONITORING AGENCY NAME(S) AND ADDRESS(ES) Air Force Research Laboratory Materials and Manufacturing Directorate Wright-Patterson Air Force Base, OH 45433-7750 Air Force Materiel Command United States Air Force			10. SPONSORING/MONITORING AGENCY ACRONYM(S) AFRL/RXAP 11. SPONSORING/MONITORING AGENCY REPORT NUMBER(S) AFRL-RX-WP-TR-2012-0472			
12. DISTRIBUTION/AVAILABILITY STATEMENT Approved for public release; distribution unlimited.						
13. SUPPLEMENTARY NOTES Approved by 88ABW Public Affairs Office: 88ABW-2012-5285 on 11Oct2012. Report contains color.						
14. ABSTRACT This material is based on research sponsored by the Defense Advanced Research Projects Agency (DARPA) under agreement number FA8650-09-1-7945. The U.S. Government is authorized to reproduce and distribute reprints for Governmental purposes notwithstanding any copyright notation thereon. Virginia Tech has achieved noise floors of about $1\text{pT}/\sqrt{\text{Hz}}$ at $f=1\text{Hz}$ in passive sensors operated at room temperature that consisted of magnetostrictive Metglas layers bonded to piezoelectric PMN-PT single crystal fiber ones. These noise floors were benchmarked by our international team members at the University of Caen. Furthermore, Passive Sensors has developed 3×3 arrays of ME sensors, also achieving noise floors on the order of $1\text{pT}/\sqrt{\text{Hz}}$ at $f=1\text{Hz}$. Working together Virginia Tech and University of Caen have developed gradiometers with high common mode rejection efficiencies, enabling real world applications. Overall the investigations have clearly identified Metglas/PMN-PT tri-layer laminates as the superior technology.						
15. SUBJECT TERMS Magnetoelectric (ME), Longitudinal-longitudinal (L-L), Longitudinal-transverse (L-T), Multi-push-pull (M-P-P), DC magnetic bias field (H_{dc}), AC magnetic bias field (H_{ac}), Temperature in Kelvin (T), Capacitance of a sensor (C), DC resistance of a sensor (R_{dc})						
16. SECURITY CLASSIFICATION OF:		17. LIMITATION OF ABSTRACT: SAR		18. NUMBER OF PAGES 338	19a. NAME OF RESPONSIBLE PERSON (Monitor) Kent L. Averett 19b. TELEPHONE NUMBER (Include Area Code) (937) 255-9779	
a. REPORT Unclassified	b. ABSTRACT Unclassified	c. THIS PAGE Unclassified				

Table of Contents

<u>Section</u>	<u>Page</u>
List of Figures	iv
List of Tables	xx
1. Summary	1
2. Introduction	14
2.1. Program Objectives	14
2.2. Program Team	15
3. Results and discussion.....	16
A. Dwight Viehland, Virginia Tech.....	16
A.3.1. ME modeling	16
A.3.1.1. M-P-P mode sensors.....	16
A.3.1.2. Geometry-dependent ME coefficient	27
A.3.1.3. Bending mode sensors.....	32
A.3.2. Noise contribution modeling.....	51
A.3.3. ME coefficient enhancement	52
A.3.3.1. Constitute components	52
A.3.3.2. Operation modes.....	55
A.3.3.3. Dumbbell shaped sensor.....	62
A.3.3.4. Self-stressed sensor	67
A.3.3.5. Geometry-induced ME enhancement	68
A.3.3.6. Electric-field tuning effect.....	70
A.3.4. Dielectric loss noise reduction	74
A.3.4.1. Interfacial bonding optimization	74
A.3.4.2. Poling optimization	76
A.3.4.3. Single crystal sensors	79
A.3.5. Sensor stacking for noise floor reduction	80
A.3.5.1. Effect of mutual inductance	80
A.3.5.2. Sensor array	82
A.3.6. ME sensor gradiometer	84
A.3.6.1. Gradiometer for AC magnetic dipole localization	84
A.3.6.2. Gradiometer for external noise rejection.....	90
B. Christophe Dolabdjian, Universite de Caen.....	96
B.3.1. Sensor noise modeling	96
B.3.2. Measurement.....	130
B.3.3. Magnetometer development.....	134
B.3.4. Gradiometer development.....	138
B.3.5. Magnetic source localization	144
C. Keith McLaughlin, SAIC.....	147
C.3.1. Applications and System Concepts.....	147
C.3.2. Array Design.....	147
C.3.2.1. Overview	147
C.3.2.2. ME Technology Trade-Space.....	147
C.3.2.3. Potential Applications	149
C.3.2.4. Persistent Perimeter Monitoring.....	149
C.3.2.5. Target Localization and Tracking	150

<u>Section</u>	<u>Page</u>
C.3.2.6. Packaging and Integration	151
C.3.3. Signal and Image Processing	151
C.3.3.1. SigProc Subsystem	152
C.3.3.2. Algorithms	153
C.3.3.3. Data Set	153
C.3.3.4. Vibration Noise Cancelation	154
C.3.3.5. Transfer Response Estimation	159
C.3.3.6. A Strawman Adaptive Beamformer and Gradiometer	161
C3.4. Low-Noise Electronics.....	165
C.3.4.1. Opamp-Based Low-Noise Charge Amplifier.....	165
C.3.4.2. FET-Based Low-Noise Charge Amplifier	167
C.3.4.3. Miniaturized FET-Based Low-Noise Charge Amplifier.....	173
D. Jiefang Li, Passive Sensors	175
D.3.1. Materials Issues and Characterization	175
D.3.1.1. Metglas and Metglas/Epoxy Characterization:	175
D.3.1.2. Core Epoxy.....	179
D.3.1.3. Kapton and interdigit vs ME response of sensors	184
D.3.1.4. Piezoelectric Phase: Loss Analysis	193
D.3.2. Fabrication	200
D.3.3. Study of ME sensor nonlinearity	204
D.3.3.1. Signal distortion at maximum α_E :	204
D.3.3.2. Harmonics as function of f and ac drive amplitude.....	205
D.3.3.3. Comparison of nonlinearities of various sensors	207
D.3.3.4. Cross-modulation effect at different f , H_{dc} and H_{ac}	208
D.3.4. Sensor arrays.....	211
D.3.4.1. Initial Design	211
D.3.4.2. Revised Design.....	217
D.3.4.3. Sensor Stacking	229
E. Shashank Priya, Virginia Tech	231
E.3.1. Synthesis of Ferroelectric PZT Fibers using Sol–gel Technique.....	231
E.3.2. [001] Textured PMN-PT Ceramics.....	233
E.3.3. [001] Textured PMN-PZT Ceramics	237
E.3.4. Mn doped [001] Textured PMN-PZT Ceramics	239
E.3.5. Fiber Fabrication Using Dicing	244
E.3.6. Co-fired Textured Magnetoelectric Composite	244
E.3.7. Effect of Loss Factors on the Dynamic ME Response	245
E.3.8. Direct and Converse ME effect.....	247
F. Gopalan Srinivasan, Oakland University.....	249
F.3.1. Sample synthesis	249
F.3.2. Low-frequency ME effects	249
F.3.3. ME response at bending resonance	251
F.3.4. Magnetic noise measurements	252
F.3.5. Noise reduction strategies	253
F.3.5.1. q- and d- graded Sensors	253
F.3.5.2. Sensors with annealed Metglas	253
G. Vince Harris, Northeastern University	254

<u>Section</u>	<u>Page</u>
G.3.1. Modulation sensing method vs. DC biasing method	254
G.3.2. Magnetic Spectral Density Response Comparison	262
G.3.3. On-resonance vs. off-resonance modulation.....	266
G.3.4. PZT Tube sensor sensitivity and noise floor measurements.....	269
G.3.5. PZT/FN (Iron/Nickel) ME Tube Sensors.	271
G.3.6. Galfenol-based PZT tube sensors.	274
G.3.6.1. Comparison in sensitivity for 1D-tube sensor.....	274
G.3.6.2. Length dependence of sensitivity for 1D-tube sensor	275
G.3.7. Thin film PZT/Metglas composites	277
G.3.7.1. Experiment	277
G.3.7.2. Result and discussion	278
H. Alan Edelstein, Army Research Lab.....	283
H.3.1. Modeling and Experimental Results on Flux concentrators	283
H.3.2. Modulating the field with Rotations	287
H.3.3. Shifting the resonant frequency of magnetoelectric sensors.....	288
H.3.4. Increasing the sensitivity of magnetoelectric sensors by field modulation	291
H.3.5. Field Test Results.....	293
H.3.6. Conclusions and Recommendations	297
I. Edmund Nowak, University of Delaware.....	298
I.3.1. Noise Statistics of Magnetoelectric Laminate Composite Sensors.....	298
4. Conclusions	306
5. References	307
APPENDIX.....	308
List of Publications and Presentations	308
List of Acronyms, Abbreviations, and Symbols	313

List of Figures

<u>Figure</u>	<u>Page</u>
1. Schematic diagram of the Metglas/piezofiber multi-push-pull mode configuration	16
2. Estimated and measured α_E for multi-push-pull configuration.....	19
3. (a) Estimated and measured α_Q for multi-push-pull configuration Metglas/PZT-fiber composite as a function of volume fraction v for PZT-fibers phase. (b) Estimated and measured maximum α_Q at optimal v dependence on the s of Kapton® over the range of $0.5\text{mm} < s < 5 \text{ mm}$	21
4. (a) Estimated and measured charge noise density of the Metglas/PZT-fiber sensor units, including constituent dielectric loss and DC resistance loss, over the frequency range of $0.125 \text{ Hz} < f < 100 \text{ Hz}$ for $s=1\text{mm}$. (b) Theoretical charge noise density as a function of s and the experimental data for the Metglas/PZT-fiber sensor.....	23
5. Theoretical modeling equivalent magnetic noise over the frequency range of $0.125 \text{ Hz} < f < 100 \text{ Hz}$	25
6. (a) Predicted dependence of α_E on thickness fraction v under various length fractions ξ and width fractions $\omega = 0.5$ (i.e. $w_p=w_m$) for the piezoelectric phase in the Metglas/PMN-PT multilayer composite. (b) Variation with ξ of maximum $\alpha_{E,\max}$ and the corresponding v_{\max} under $\omega = 0.5$	29
7. (a) Predicted dependence of α_E on thickness fraction v under various width fractions ω and length fractions $\xi=0.5$ (i.e. $l_p=l_m$) for the piezoelectric phase in the Metglas/PMN-PT multilayer composite. (b) Variation with ω of maximum $\alpha_{E,\max}$ and the corresponding v_{\max} under $\xi=0.5$	30
8. Experimental α_E as a function of Hdc for various widths and lengths of Metglas.....	31
9. Comparison of theoretical (solid line) and experimental (line and symbol) α_E as function of: (a) width fraction ω under a length fraction $\xi=0.2$ and a thickness fraction $v=0.86$; (b) length fraction ξ under a width fraction $\omega = 0.5$ and a thickness fraction $v=0.86$	31
10. Magneto electric multilayer laminated composite.....	32
11. (a) Low-frequency ME voltage coefficient as a function of bilayer (Metglas and PZT) volume fraction. (b) Low-frequency ME voltage coefficient as a function of a bilayer thickness ratio. (c) Low-frequency ME voltage coefficient as a function of a bilayer volume fraction. (d) Low-frequency ME voltage coefficient as a function of a bilayer thickness ratio. (e) Low-frequency ME voltage coefficient as a function of bilayer (NFO-PZT) volume fraction.	47
12. (a) ME voltage coefficient as a function of $f = \omega/2\pi$ for different values of \mathbf{h}_M/\mathbf{L} . (b) ME voltage coefficient as a function of $f = 2\pi/\omega$. (c) ME voltage coefficient as a function of $f = \omega/2\pi$ for different values of \mathbf{h}_P/\mathbf{L}	48

<u>Figure</u>	<u>Page</u>
13. (a) ME voltage coefficient as a function of a \mathbf{h}_M/L for different $f = 2\pi/\omega$ frequency values. (b) ME voltage coefficient as a function of bilayer (Metglas and PZT) volume fraction for different $f = 2\pi/\omega$ frequency values. (c) ME voltage coefficient as a function of a \mathbf{h}_P/L for different $f = 2\pi/\omega$ frequency values.	49
14. (a) Nondimensional bend as a function of $f = \omega/2\pi$ for different values of $x = x_1/L$. (b) Nondimensional bend as a function of x for different values of frequency f . (c) Nondimensional strain as a function of $x = x_1/L$ for different values of frequency f	50
15. Schematic diagram and photograph of charge amplifier, showing the interface to the sensor and battery box.	51
16. Predicted equivalent magnetic noise and the noise contributions for a normal Metglas/PZT sensor with a spacing of 1 mm.....	52
17. Comparison of (a) ME response and (b) noise floors for Metglas-PZT, Metglas-PZN-PT, and Metglas-PMN-PT laminates.....	53
18. (a) Schematic diagram of the Metglas/piezofiber configuration consisting of an ID electrodes/PMN-PT fibers core composite, and symmetric 3-layer Metglas actuators on the bottom and top of the core composite. (b) Illustration of the numerous alternating push-pull mode units. (c) Optical micrograph of a longitudinally poled push-pull element in the core composite. (d) and (e) Photographs of the ID electrode/piezofiber core composite and the complete Metglas/piezofiber ME sensor.	53
19. The magnetic field dependence of (a) the longitudinal magnetostrictive strain λ and (b) the ME voltage coefficient and ME charge coefficient of the Metglas/piezofiber sensor. (c) ME charge coefficient shows a flat response over the quasi-static frequency range.	54
20. (a) Measured and estimated charge noise density of the proposed sensor unit, including constituent dielectric loss and DC resistance loss, over the frequency range of $0.125 \text{ Hz} < f < 100 \text{ Hz}$	55
21. (a) Schematic diagram of the proposed shear mode three-phase magnetostrictive/piezoelectric/brass heterostructure. (b) The coordinate system shows the crystalline directions of the PMN-PT single crystal. (c) and (d) illustrate the motion of the PMN-PT single crystal under shear extensional and longitudinal extensional stresses, respectively.	57
22. ME coefficient α_E as a function of dc magnetic bias H_{dc} for a shear-mode Terfenol-D/PMN-PT laminate composite.	57
23. Time-domain waveforms of (a) applied ac magnetic field H_{ac} and ME output voltage V_{ME} for (b) the shear mode Terfenol-D/PMN-PT laminates and (c) a one-sided longitudinal-extensional laminate.	58
24. Schematic diagram and photograph of the proposed Metglas/Mn-doped PMN-PT bimorph heterostructure.	59
25. ME coefficient α_E as a function of dc magnetic bias field H_{dc} for various layers of Metglas.	60

<u>Figure</u>	<u>Page</u>
26. (a) Measured and estimated noise charge density and (b) equivalent magnetic noise for the multi-push-pull mode Metglas/PMN-PT sensor unit (Ref. ⁹) and the proposed one over the frequency range of $0.125 \text{ Hz} < f < 100 \text{ Hz}$	62
27. (a) Schematic diagram of dumbbell-shaped Metglas/piezofiber ME laminate with magnetic field amplification effect, (b) exploded view photo of constituent components: six-layers of magnetostrictive Metglas and a piezoelectric core composite consisting of two PZT fibers interrogated by a pair of Kapton® interdigitated (ID) electrodes. (c) Cross-sectional schematic diagram of the ID electrodes in a multi-push-pull configuration (d) and geometry of Metglas layers in barbell configuration showing width and length of end-flange. The magnetic field was applied along the length direction of the laminate, i.e. axially.....	63
28. (a) 1 kHz ME coefficient of the dumbbell-shaped Metglas/piezofiber ME laminate as a function of DC magnetic field for various flange widths. (b) Dependence of optimal DC magnetic field and the maximum ME coefficient under optimal DC magnetic field on width of Metglas flange.	64
29. (a) Magnetic flux density distribution under a uniform external field of 1 Oe in free space obtained by numerical simulations using Maxwell 3D. (b) Line trace of magnetic flux density within Metglas sheets with dumbbell-/rectangle-shapes ($W=18\text{mm}$, 12mm and 4mm) along axially centerline. The origin is the center of Metglas sheet (see Figure 27 (d)). (c) The relative magnetic field gain (as compared to rectangular-shape, $W=4\text{mm}$) for the dumbbell-shaped designs ($W=18\text{mm}$ and 12mm), calculated by normalizing axial flux density trace to that of rectangular Metglas.....	66
30. Schematic of the self-stress in the longitudinal section of a ME laminate configured in M-P-P mode.....	67
31. (a) The values of the α_E as a function of H_{dc} for Metglas/PZT/Metglas laminates epoxied together under various H_{bias} . (b) Maximum values of α_E as a function of H_{bias} . (c) Maximum values of α_{ME} as a function of E_{bias} . The data were measured at an ac magnetic field of $H_{ac} = 0.1 \text{ Oe}$ and at a frequency of $f=1 \text{ kHz}$	68
32. Equivalent magnetic noise floors of self-stress Metglas/PZT/Metglas laminates epoxied together under $H_{bias} = 20 \text{ Oe}$, and laminate without self-stress.....	68
33. (a) Three-dimensional and (c) cross-sectional schematic illustration of the multi-push-pull mode Metglas/piezofiber heterostructure. (b) Photograph for the PZT-fiber core composites with $N=3$ and 5	69
34. Measured ME coefficient α_E as a function of dc magnetic bias H_{dc} for various piezofiber width fraction ω	70

<u>Figure</u>	<u>Page</u>
35. (a) Schematic diagram of the multi-push-pull configuration Metglas/PZT-fiber ME composite; (b) enlarged view of the constituent components: six-layers of magnetostrictive Metglas and a piezoelectric core composite consisting of five PZT fibers interrogated by a pair of Kapton® interdigitated (ID) electrodes; and (c) the electric field tuning effect measurement set-up.	71
36. The capacitance and dielectric loss of a Metglas/PZT-fiber sensor as a function of applied E ; (b) dependence of α_E on H_{dc} under various applied E ; and (c) the maximum values of α_E and α_Q as a function of applied E	71
37. (a) Estimated noise charge densities of the proposed sensor unit under applied E of 0 V/mm and 300 V/mm and the measured values for $E = 0$ V/mm, over the frequency range of $0.125 \text{ Hz} < f < 100 \text{ Hz}$. (b) Measured equivalent magnetic noise of the sensor unit under applied E of 0 V/mm, 300 V/mm and 600 V/mm.	73
38. Images of the PZT-patterned electrode-Kapton tape structures after (a) previous process, (b) and (c) vacuum bag process, and (d) vacuum bag and spin coating process. The epoxy thicknesses are as indicated.	75
39. Equivalent magnetic noise spectrum of manual lay-up and spin-coat/vacuum bag technique.	76
40. Computer display showing Labview interface ramping voltage to poling setup	77
41. (a) ME voltage coefficient as a function of magnetic bias field for the Metglas/PMN-PT fiber heterostructures poled by different procedures: denoted as sensor #1 and sensor #2, respectively. (b) Theoretical and experimental equivalent magnetic noise spectra for the two sensor units.	78
42. (a) Schematic representation of a pair of Metglas/PZT L-L mode ME laminates separated by a distance d . (b) Magnetic flux density of the Metglas foils along the x-axis at $y=0$, $z=0$ when another identical foil was placed at various distances from it.....	81
43. (a) the value of α_E as a function of H_{dc} for one Metglas/PZT laminate when another one was placed at different distance from it. (b) The maximum value of α_E as a function of distance between two Metglas/PZT laminates.	82
44. Schematic representation of the ME sensor arrays of four units.	83
45. (a) Equivalent magnetic noise spectra for four ME sensor units over the frequency range of $0.125\text{Hz} < f < 100\text{Hz}$. (b) Background voltage noise of single unit and calculated noise of the sensor array.....	83
46. (a) Schematic illustration of test layout, where the tensor ME sensors are constructed in three linear orthogonal directions. (b) Block diagram of signal collection model.....	86
47. Power spectral density of applied AC magnetic dipole at $f=7 \text{ Hz}$ on (a) sensor i, (b) sensor j and (c) sensor k in x-axis (blue curve), y-axis (red curve) and z-axis (cyan curve).....	88

<u>Figure</u>	<u>Page</u>
48. Estimation for dipole position (green cross) based on SRR (blue line and star head) by three tensor ME sensors (blue open circles) responding to solenoid dipole (red open circle) with moment direction (red line and star head) with different dipole moment directions as in (a), (b) and (d), and with different distance in y as in (a), (d) and (e).....	89
49. (a) Diagram of experimental layout as the coil position is rotated from 0 to 180 degree for our two biaxial ME magnetometers. (b) Power spectral density curves of the background noise for sensors G_{1x} and G_{2x} (blue and red curves respectively), sensors G_{1y} and G_{2y} (cyan and pink curves respectively), and gradiometric noise floor signals diff (G_x) and diff (G_y) (green and black curves respectively).....	91
50. (a) Coherence value, (b) relative amplitude difference and (c) phase shift for G_{1x} and G_{2x}	92
51. (a) Coherence value, (b) relative amplitude difference and (c) phase shift for G_{1y} and G_{2y}	93
52. Power spectral density curves at (a) $\theta_1=0^\circ$, (b) $\theta_1=30^\circ$, (c) $\theta_1=90^\circ$ for sensor G_{1x} and G_{2x} (blue and red curves respectively), sensors G_{1y} and G_{2y} (cyan and pink curves respectively), and gradiometric noise floor signals diff (G_x) and diff (G_y) (green and black curves respectively).....	94
53. Piezoelectric layer with associated parameters.....	96
54. Presents the equivalent electric scheme of piezoelectric layer.....	100
55. Sketch view of the magnetostrictive layer with associated parameters.....	101
56. Sketch view of the ME laminated sensor with associated parameters.....	104
57. Sketch view of the electrical 1-D L-T mode equivalent circuit of a magnetoelectric laminated sensor.....	106
58. Simplified equivalent circuit under free boundary conditions and at low frequency. Z_{mech} ($= Z_I // Z_1 + Z_2$) is the mechanical impedance.....	107
59. Sketch view of the equivalent circuit under free boundary conditions and at the resonance frequency. Z_{mech} ($= R_{mech} + j \omega L_{mech} + 1/j \omega C_{mech}$) is the mechanical impedance at the resonance frequency.....	109
60. Sketch view of the current charge preamplifier electronics.....	112
61. Sketch view of the voltage preamplifier electronics.....	115
62. Sketch-view of the sensor.....	119
63. Associated axes for LT mode.	119
64. Sketch-view of a push-pull sensor.	121
65. Electric equivalent circuits (Models A& B) of a ME sensor by using 1-D Mason Model.	122
66. Laminate model with associated mechanical noise source.....	126
67. Simplified laminate model.....	126

<u>Figure</u>	<u>Page</u>
68. Expected equivalent magnetic noise behavior versus the frequency and given by the model, a) including the full model, b) including the ideal model.....	130
69. Setup of sensor characterization	131
70. View of a) theD.U.T.& b) GREYC Shielding room.....	131
71. Expected equivalent magnetic noise behavior given by the model.	132
72. Output voltage noise for laminates F21 (black) and F22 (red) with the use of the charge FCL-2 amplifier.....	132
73. Equivalent input magnetic noise level for the laminates F21 (black) and F22 (red).	133
74. Zoom around the resonance of the output voltage noise level for the F22 laminate.	133
75. Zoom around the resonance of the equivalent input magnetic noise level for the F22 laminate.	134
76. View of the feedback loop design.....	134
77. Magnetic field transfer function of sensor F20 and GREYC classical electronics (Black) without feedback system, (Red) with feedback system.....	135
78. Phase of sensor F20 and GREYC classical electronics (Black) without feedback system, (Red) with feedback system.	136
79. Experimental set-up with the magnetometer and dipole moment used as a magnetic source.	136
80. Black dots, red dots and line give the experimental measurement, measurement uncertainties, for the given interval errors $\Delta\alpha \in [-5^\circ, 5^\circ]$, $\Delta\theta \in [-5^\circ, 5^\circ]$, $\Delta\alpha \in [-2 \text{ cm}, 2 \text{ cm}]$, and the theoretical response of the magnetometer, respectively.	137
81. Experimental set-up.	138
82. Equivalent input magnetic noise of V_1 , V_2 , V_3 , V_4 (red, green, yellow and black curves respectively).....	139
83. Set-up (d is the gradiometer base line and z the distance between the sensors to the magnetic moment).	139
84. Theoretical (black curve) and experimental (red curve) CMRR evaluation corresponding to the measurement a) and b) given in figures 15 and 16, respectively.	140
85. Spatial transfer function of the gradiometer V_3/V_2 in Log-Log scale.z and d are the distance of the source to the gradiometer and gradiometer base-line, respectively.	140

<u>Figure</u>	<u>Page</u>
86. Effect of the tilt between the two magnetometers on the spatial transfer function of the gradiometer.....	143
87. Sketch view of a source localization. \vec{r} and \vec{p} are the 3D spatial position and orientation of the magnetic moment, respectively.....	144
88. Example of a source localization in 2D versus sensor performances.....	146
89. Phase 1 ME sensors in the context of available Commercial Off The Shelf (COTS) magnetic sensors.	148
90. Low-noise magnetometers may be placed further apart and further back from the perimeter.....	150
91. The concept for detection of CW magnetic sources with a gradiometer (upper left), performance projections as a function of sensor noise, stand-off, aperture, and number of sensors (lower-left), and a Phase 1 2x2 gradiometer.....	151
92. Subsystems for a HUMS array include the sensors, charge amplifiers, power for the charge amplifiers, cabling, test gear, a multi-channel digitizer, a data archivist and signal processing.	152
93. Sensors were mounted on cinder blocks. Note locations and orientations of VT #6 (VT6) and Bartington 1 (B1) and Bartington 2 (B2).	154
94. (Top) Time history of the vertical accelerometers, A1 (blue), A2 (red). (Bottom) An upper estimate of the equivalent magnetic noise due to the rocking motion of the cinder block from A1 (blue) and A2 (red) assuming all accelerations are caused by rocking around the worst possible axis.	155
95. The adaptive Widrow-Hoff LMS algorithm estimates a filter, A, to transform Y to X.	156
96. LMS stripping algorithm applied to VT3 using accelerometer A1.	156
97. LMS stripping algorithm applied to VT6 using accelerometer A2.	157
98. LMS stripping algorithm applied to VT8 using accelerometer A2.	158
99. VT3 time series before and after adaptive removal of the 180 Hz tone.	159
100. Relative response with respect to Bartington mag03 for VT3, VT6, and VT8.	160
101. A repeat of the response response determination with respect to a Bartington mag03 fluxgate for VT03, VT6, and VT8 for a longer time period and a higher clutter level.	161
102. A simple 3-element adaptive beamformer and gradiometer array extendable to $N > 2$ channels.	162
103. The top panel shows the time domain signal for the conventional beamformer (CBF blue) and the adaptive beamformer (ABF red). The bottom panel shows the median spectra of each.	163

<u>Figure</u>	<u>Page</u>
104. The median CBF and ABF spectra are compared to the median VT3, VT6, and VT8 spectra	164
105. Spectrogram of the CBF (upper left) is compared with the spectrogram of the ABF (upper right). The gain is shown as a function of time and	164
106. The differences between the VT6 and VT8 sensors (the quietest of the sensors) and the ABF are good estimates of the gradient spectra.....	165
107. Predicted Charge Noise Density	166
108. Charge noise spectra for the new charge amplifier compared to the current amplifier provided by Virginia Tech.	166
109. Schematic of prototype low-noise charge amplifier.	167
110. Current and voltage noise for a selection of FETs that might be used in the first stage of the charge amplifier.	168
111. Schematic of the JFET-based charge amplifier.	169
112. Combined noise model for a JFET-based charge amplifier and laminate ME sensor.	170
113. Photo of JFET-based charge amplifier board: a side view (top), and inside the enclosure (bottom).	171
114. Measured charge noise of four JFET-based charge amplifiers.....	171
115. Noise model for sensor plus charge amplifier showing improvements achievable by stacking.	172
116. Noise model for a notional next generation of sensor plus charge amplifier showing improvements from enhanced charge coefficient and reduced dielectric loss.	172
117. Miniaturized JFET-based charge amplifier, bare and packaged in protective box with clear lid.	173
118. Distributions of noise and other characteristics of the miniaturized charge amplifiers, after removing rejected units.	174
119. Illustration of three layers of Metglas with two bonding layers of epoxy.....	175
120. Metglas press for controlling curing pressure.....	178
121. Sensor with one additional 9 cm piece of Metglas attached to top.....	178
122. Schematic of calculated condition with ideal electrode connection.	181
123. Equivalent circuit for ideal bonding electrode bonding condition.....	181
124. Illustration of actual electrode interface to piezoelectric fibers.....	182
125. Equivalent circuit for the non-ideal bonding of electrodes to piezoelectric fibers simplified from top to bottom.....	183
126. Copper electrodes after coating with liquid tinning solution.....	184
127. Noise floor comparison of sensors fabricated with various interdigit geometries and Kapton® thicknesses.	185

<u>Figure</u>	<u>Page</u>
128. Comparison of current PZT sensors characteristics to previously modeled values based on previous obtained empirical data.....	186
129. Comparison of most often used electrode spacing, labeled Normal Electrode, and new modeled geometry.....	187
130. Equivalent noise floor with increasing charge due to larger poling voltage assuming electrical noise pattern stays the same.	188
131. Measured capacitance data for a single batch of samples made with different electrodes.	190
132. Measured dielectric loss data for a single batch of samples made with different electrodes.....	191
133. Measured ME voltage output for a single batch of samples made with different electrodes.....	192
134. New improved large footprint electrode layout.	192
135. Gold sputtered PZT fibers used for dielectric loss tests.	193
136. Unpoled capacitance and loss values for PMN-PT showing loss >4% at low frequency.....	193
137. PMN-PT capacitance and loss data after poling showing loss of 1.42 to 1.68% from 1 to 10 kHz.....	194
138. Equivalent circuit for dielectric materials for conduction loss (a) and rotation loss (b).	195
139. Equivalent circuit to model the dielectric loss in our piezoelectric material.	195
140. Schematic illustrating wiring used to measure and monitor sample poling currents.....	197
141. Computer display showing Labview interface ramping voltage to poling setup	198
142. Impedance angle measurement for PMN-PT samples poled	199
143. Noise floor comparison of sensors fabricated with various interdigit geometries and Kapton® thicknesses.	200
144. Diagram outlining screen printing process.	201
145. Screen printing mesh characteristics.....	201
146. Capacitance curves of two samples manufactured using Stycast epoxy applied with a 325 screen printing mesh.....	201
147. Increase to eight sensors produced simultaneously through a screen printing process of epoxy application.....	202
148. Test setup for determining signal distortion (second harmonic, third harmonic...)	204
149. Experimental α_E versus bias field for a Metglas/PZT composites.....	204
150. ME voltage as a function of frequency for (a) 1st harmonic, and (b) 2nd harmonic.	205
151. ME voltage as a function of ac drive amplitude at various frequencies for (a) 1st harmonic, and (b) 2nd harmonic.	206

<u>Figure</u>	<u>Page</u>
152. ME voltage as a function of frequency for (a) 1st harmonic, and (b) 2nd harmonic; and the ME voltage as a function of ac magnetic drive at various frequencies for (c) 1st harmonic, and (d) 2nd harmonic.....	206
153. ME voltage as a function of ac drive amplutde at various frequencies for (a) 1st harmonic, and (b) 2nd harmonic.	207
154. Calibrated αE vs. H_{dc} curves of PZT sensor and single crystal sensor.....	207
155. Calibrated αE vs. H_{ac} curves (a) for Metglas/PZT sensor, and (b) Metglas / single crystal fiber sensor.....	208
156. (a) Nonlinear ME response with respect to bias field and (b) verification of modulation of incident field resulting in sideband signals.	209
157. Magnitude of modulated side-band as a function of H_{dc}	209
158. ME response to bias field strength at resonance for PMN-PT sensor.	210
159. ME response to AC drive field strength at resonance for PMN-PT sensor.	210
160. 2 by 2 array prototype.	211
161. Example of possible orientation changes available using symmetric package.....	211
162. Photo of fabricated assembly with one attached sensor for illustration.....	212
163. Drawing of single sensor with individual charge amplifier mounted above.	212
164. Single module with new thin charge amplifier and SMA fitting attached.	213
165. (a) Real voltage noise of parallel (red trace), single (black trace) and series (blue trace) sensor configurations. (b) equivalent magnetic noise of arrays showing that shift in voltage noise due to impedance change is offset by increased output charge.....	214
166. Noise floor measurements for three sensors in parallel.	216
167. (a) Four parallel sensor sensitivity measurement showing SNR>2, Pk-Pk: 23.2mV@ 0.09nT @ 1Hz and (b) noise floor measurement of approximately 10pT using SAIC charge amplifier.	217
168. Virginia Tech constructed low frequency charge amplifiers for each module in the 2 by 2 array.	217
169. Low frequency charge amplifiers mounted to individual sensor modules.	218
170. (a) Modules oriented with charge amplifiers close together (b) modules oriented out of plane in an effort to increase flux capture.	218
171. PSU array modules with individual charge amps and batteries ready for configuration experiments	219
172. Noise floor tests of four sensors connected in parallel using VT constructed wide band charge amplifier.....	220
173. Noise floor tests of four sensors connected in parallel using charge amplifier constructed by SAIC.	220
174. Noise floor tests of four sensors connected in series and measured using VT constructed made wide band charge amplifier.....	221
175. Noise floor tests of four sensors connected in series using JFET charge amplifier constructed by SAIC.	221

<u>Figure</u>	<u>Page</u>
176. (a) sensors packaged with individual bias in the same plane. (b) Sensors packaged with individual bias magnets oriented in different planes.....	221
177. (a) parallel ME voltage output as a function of in-plane center-to-center separation distance. (b) ME charge output as a function of in plane separation distance.....	222
178. (a) parallel ME voltage output as a function of out-of-plane center-to-center separation distance. (b) ME charge output as a function of out of plane separation distance.....	223
179. PSU array modules with individual charge amps and batteries ready for configuration experiments.....	223
180. New PSU array module design with SAIC charge amplifier.....	224
181. Electrical Configuration used in sensor stacking experiments.....	225
182. Noise floor for four stacked PZT sensors using serial/parallel configuration	225
183. Noise floor for four stacked PMN-PT sensors using serial/parallel configuration.....	226
184. Noise floor of four stacked PMN-PT sensors in serial/parallel configuration.....	227
185. MATLAB model of predicted equivalent magnetic noise utilizing four PMN-PT sensors in parallel configuration.....	228
186. MATLAB model of equivalent magnetic noise using four PMN-PT sensors in parallel configuration.....	228
187. Measured noise floor of four PMN-PT using a parallel connection.....	229
188. Testing protocol and pattern established for sensor stacking tests.....	230
189. (a) Schematic diagram of drawing process of PZT gel fibers and (b) optical microscopy image of PZT gel fibers drawn from #5.0 solution.....	231
190. Picture of PZT ceramic fibers sintered at 950 °C for 10 h: (a) from #2.5 solution, (b) from #5.0 solution, and (c)– (f) from #5.0-2 .4 M solution.....	231
191. (a) Polarization vs. electric field curve measured at 0.1 Hz and (b) dielectric constant and loss factor at various frequencies for 1–3 composite.....	232
192. (a) XRD patterns of PMN-PT-xBT ceramics; (b) Texture degree of PMN-PT ceramics as a function of BT concentration; cross-sectional SEM image of (c) PMN-PT-1BT and (d) PMN-PT-0BT ceramic.....	233
193. (a,b) Dielectric and piezoelectric properties of PMN-PT- x BT ceramics; (c) Dielectric permittivity as a function of temperature for PMN-PT- x BT ceramics; (d) Polarization (P) vs. electric field (E) hysteresis loops of PMN-PT- x BT ceramics; and (e) XRD patterns of PMN-PT- x BT ceramics.....	234

<u>Figure</u>	<u>Page</u>
194. (a) Schematic illustration of grains of textured ceramic (left: [100] or [010] view, and right: [001] view). (b) Required growth distance (x) of matrix crystal (solid line) and specific interface area (A_i/V) (dashed line) as a function of the volume fraction and dimensions of template. (c) Schematic illustration of single templated grain. (d) Calculated relative permittivity of fully textured PMN-PT ceramic as a function of the volume fraction and dimensions of BT template.	235
195. Theoretical prediction of dielectric and piezoelectric properties of textured PMN-PT ceramics as a function of BT template volume fraction.....	237
196. (a) Comparison of g_{33} and d_{33} values of various piezoelectric ceramics. (b) Comparison of $d_{33(T)}/d_{33(R)}$ ratio vs. $d_{33(T)}$ of various textured piezoelectric ceramics.	238
197. Photo image of textured PMN-PZT fibers.....	239
198. (a) XRD patterns of randomly oriented and textured MnO_2 doped PMN-PZT ceramics with 5 vol% BT template (abbreviated as R and T-5BT, respectively); SEM images of (b) T-5BT and (c) R ceramic; (d) line scanning element analysis of EDS across BT and PMN-PZT matrix.	240
199. (a) Dielectric constant ($\epsilon_{33}^T/\epsilon_0$) and (b) electromechanical coupling coefficient (k_{31}) of R and T-5BT ceramic as a function of temperature.	241
200. Pyroelectric current vs. temperature curves.....	242
201. (a) k_{31} vs. temperature characteristics of randomly oriented and textured MnO_2 doped PMN-PZT ceramics with 1, 3 and 5 vol% BT template poled at 140 °C (abbreviated as R, T-1BT140, T-3BT140 and T-5BT140, respectively); (b) Lotgering factor (f), degradation temperature (T_{de}), d_{33} and k_{31} of textured MnO_2 doped PMN-PZT ceramics as a function of BT template content.	243
202. Optical image of texture fiber set.....	244
203. ME voltage coefficients (α_E) of co-fired NCZF/T-PMN-PT/NCZF (C-N/T/N), NCZF/R-PMN-PT/NCZF (C-N/R/N), and epoxy bonded Metglas/R-PMN-PT/Metglas (B-M/R/M) laminate	245
204. The rate of capacitance change, dielectric loss and piezoelectric loss of PMS, MPZN and PZN piezoelectric compositions measured in the frequency range of 20 Hz ~ 1 kHz.	246
205. Magnetoelectric voltage coefficient of PMS / Metglas, MPZN / Metglas and PZN / Metglas laminates measured in H_{AC} frequency range of 20 Hz ~ 1 kHz under H_{DC} of 21 Oe.	247

<u>Figure</u>	<u>Page</u>
206. (a) Impedance versus frequency of the P-layer, (b) capacitance versus frequency of the P-layer, (c) $\alpha_{E,31}$ versus $H_{1,ac}$ frequency, and (d) $\alpha_{H,31}$ versus $E_{3,ac}$ frequency characteristic of the MP laminate.....	248
207. Magnetoelectric voltage coefficient (MEVC) as a function of the bias field H_0 for samples of PZT and ferromagnetic layers with Ni and Metglas.....	249
208. The zero-bias ME voltage as a function of frequency f of the ac field H_1 measured for a sample of PZT-Ni and 75 μm thick Metglas.....	250
209. Zero-bias MEVC obtained from data as in Figure 209 as a function of number of Metglas layers L for magnetization graded samples.....	251
210. Magnetoelectric voltage coefficient for $H_0 = 0$ as a function of frequency f of the ac magnetic field H_1 for a sample of PZT-Ni-25 μm thick Metglas.....	251
211. The resonance value of zero-bias MEVC versus number of Metglas layers in the magnetization graded samples. The solid and dashed lines are theoretical values	252
212. Magnetic noises at low-frequency and at bending resonance at zero-bias for PZT-Ni Metglas sensors.	252
213. (a) MEVC vs H and (b) Noise vs f for q- and d- graded sensors.....	253
214. (a) MEVC vs H and (b) N vs f with bias and zero bias condition. for q- and d- graded sensors with annealed Metglas	253
215. New dual Helmholtz coil exhibiting ~9 cm uniform magnetic field capability.....	254
216. Block diagram of the DC biasing method.....	255
217. Block diagram of the modulation sensing technique.....	255
218. SNR, Sensitivity, and 0-Hz noise floor of Northeastern's ME sensor (Sensor 1) and VT's sensor (Sensor 2) using the DC biasing method (left column) and the modulation sensing technique (right column).	256
219. MSD measurements of Sensor 1 for the DC biasing method.	257
220. MSD measurements of Sensor 1 for the modulated sensing technique.....	258
221. MSD measurements of Sensor 2 for the DC biasing method.	258
222. MSD measurements of Sensor 2 for the modulated sensing technique.....	259
223. VTn sensor (Top) provided by Virginia Tech and NU sensor (lower right) provided by Carmine Carosella.	260
224. Magnetic spectral density plots of NU (upper), VTn (middle), and VTo (lower) compare the conventional DC biasing method (red) response with the modulated sensing technique (blue) response for a 25 Hz 0.001 Oe RMS test H-field.	261
225. 1) CC Sensor. 2) VT Old Sensor. 3) VT New Sensor. 4) PZT Tube Sensor.....	263

<u>Figure</u>	<u>Page</u>
226. Magnetic spectral density comparison of DC vs. modulation technique for CC sensor.....	264
227. Magnetic spectral density comparison of DC vs. modulation technique for VT old	264
228. Magnetic spectral density comparison of DC vs. modulation technique for VT new.....	265
229. Magnetic spectral density comparison of DC vs. modulation technique for PZT tube.....	265
230. Experimental test setup.....	267
231. Magnetic spectral density plots of 5cm PZT FN tube sensor for modulation frequencies of 36 KHz, 35 KHz, and 37 KHz	269
232. Magnetic noise of WBFN 8cm sensor captured at Northeastern (blue) and at SAIC (black) and of the WB21 7.5cm sensor captured at Northeastern (green) and at SAIC (red). Shown with log scale x axis.....	270
233. Magnetic noise of WBFN 8cm sensor captured at Northeastern (blue) and at SAIC (black) and of the WB21 7.5cm sensor captured at Northeastern (green) and at SAIC (red).	271
234. 10 Hz sensitivity of two 5cm PZT/FN magnetoelectric tube sensors.....	272
235. 10 Hz sensitivity of two 5cm PZT/FN magnetoelectric tube sensors.....	272
236. 10 Hz sensitivity of two 5cm PZT/FN magnetoelectric tube sensors.....	273
237. 10 Hz sensitivity of two 5cm PZT/FN magnetoelectric tube sensors.....	273
238. (a) Magnetic hysteresis loops and (b) magnetostriction measurements of GaFe wires used in this patented invention.	274
239. A Bias field dependence of sensitivity for 1D GaFe/PZT sensor with bending and free standing mode. ($f=100$ Hz, $H_{ac}=1$ Oe)	275
240. Bias field dependence of sensitivity for 1D GaFe/PZT sensor with different PZT tube lengths ($H_{DC}=0$, 10 and 20 Oe). ($f=100$ Hz, $H_{ac}=1$ Oe)	276
241. PZT tube length dependence of sensitivity for 1D GaFe/PZT sensor with different bias fields ($H_{DC}=0$, 10 and 20 Oe). ($f=100$ Hz, $H_{ac}=1$ Oe).	276
242. XRD pattern of PZT thin film on Pt (a) and Au (b) buffer layer.....	278
243. SEM images of Pt or Au buffered PZT thin films under different oxygen pressures.....	279
244. Ferroelectric measurements for PZT thin films on an Metglas substrate with a Au or Pt buffer layer.	281
245. Piezoelectric coefficient d_{33} measurements for the PZT thin film on a Metglas substrate with a Pt or Au buffer layer.	282

<u>Figure</u>	<u>Page</u>
246. Enhancement as a function of the relative permeability of the magnetostrictive material in ME sensors.....	283
247. (a) Additional enhancement achieved by including flux concentrators symmetrically place around the sensor as a function of the length of each flux concentrators. (b) The magnitude of the field as a function the longitudinal position along the length of the sensor.	284
248. (a) Additional enhancement as a function of overlap and vertical gap between the sensor and flux concentrators of similar dimensions. Additional enhancement from tapered flux concentrators as a function of (b) width/length and (c) width/thickness.	285
249. (a) Optimal sensor setup with solenoid for magnetic DC bias and flux concentrators for enhancement of the measurement field. (b) The PSD enhancement with DC bias using Conetic AA mu metal as both the inner and outer flux concentrators.....	286
250. Rotating flux concentrator system	287
251. Power spectrum showing the 10 Hz sidebands from a modulating field created by a rotating disc containing flux concentrators.	287
252. (a) Diagram of the setup in which θ is the small angle away from the vertical direction. (b) Resonance peaks of sensor in an oscillating field of 0.0162 Oe with different in-plane tensile forces.	289
253. The change in resonance frequency and peak amplitude in the power spectrum at this frequency measured in an AC field of 0.0162 Oe as a function of the in-plane tensile force.	289
254. (a) Signal vs. applied field at and above the unshifted resonant frequency of 132.2 Hz. (b) Signal vs. applied field at the shifted resonant frequency $f_r=$ 146.5 Hz and at the unshifted $f_r=132.2$ Hz Hz in the presence of a 1.96 N tensile force.....	290
255. Power spectra from the symmetric sensor detecting a 1.019 Hz, 0.0162 Oe field while modulating the sensor with a 0.72 Oe field either off resonance at 140 Hz (dashed curve) or on resonance at 28.9 k Hz (solid curve, top x-scale).	292
256. Comparison of the direct signal (squares) and the demodulated sideband signal (triangles) from the symmetric ME sensor at resonance as a function of signal field.	293
257. The PSD enhancement with DC bias from stockroom mu metal flux concentrators	294
258. The PSD enhancement with DC bias and mu metal outer flux concentrators	296

<u>Figure</u>	<u>Page</u>
259. Setup to achieve a signal field within 10% across each sensor/flux concentrator setup in the direction of the long axis of the sensor.....	297
260. The response of the PZT with long metglas sensor to a 20 Hz, 20 nT excitation field.	298
261. The noise equivalent magnetic field spectra of the PZT with long Metglas sensor at the point of maximum magnetic field response (point A in Figure 260).	298
262. Time average noise power spectrum of an ME long Metglas sensor and the octave frequency bands used for studying statistical properties of the noise.	299
263. Representative octave time series for the ME long Metglas sensor. Octave 3 and 4 are offset for clarity.....	300
264. Measured and predicted octave noise power distributions.	301
265. Measured and predicted octave noise power distributions for a PZT device and the long Metglas ME sensor device. Significant deviations from the Chi-square distribution are evident.....	301
266. Second spectra for octaves 2, 3, and 4 that were computed from the corresponding octave time series.	303
267. Several second spectra for a given device that were measure successively in time.	304
268. Plots the variation from successive runs of the mean (average) octave noise power and its variance.	304

List of Tables

<u>Table</u>	<u>Page</u>
1. Team members	15
2. Materials parameter for magnetostrictive and piezoelectric components in the multi-push-pull configuration.....	18
3. Material parameters Metglas, and PMN-PT used for theoretical modeling.....	28
4. Material parameters for lead zirconate titanate (PZT), nickel ferrite (NFO) and Metglas.	46
5. Model Equations for Charge noise density in C/ $\sqrt{\text{Hz}}$	52
6. Constituent material parameters of PMN-PT for transverse-extensional, longitudinal-extensional, and shear modes.	56
7. Comparison of dielectric loss, ME responses with and without aluminum box, and with plastic box for a Metglas-PZT sensor.....	75
8. Poling procedures for PMN-PT fibers, and the their properites poled under various procedures.....	78
9. Property parameters for multi-push-pull mode Metglas/PMN-PT and L-T mode Metglas/Mn-doped PMN-PT sensors and the related pure single crystals.....	79
10. Properties of PZN-PT, PMN-PT and Mn-doped PMN-PT sensors.	80
11. Target dipole localization as a function of (α , β , γ) and y.....	90
12. Calibrated observed data for sensors of magnetic field as a function of θ_1	95
13. Comparison of different magnetic sensor energy resolution.....	114
14. Calculations Synthesis Associated to the Four Main Modes and, also for the LL Push-Pull Mode.	120
15. Calculations Synthesis Associated to the Four Main Modes and, also for the LL Push-Pull Mode.	121
16. Calculations Synthesis Associated to the Four Main Modes and, also for the LL Push-Pull Mode.	123
17. Calculations Synthesis Associated to the Four Main Modes and, also for the LL Push-Pull Mode.	124
18. Calculations Synthesis Associated to the Four Main Modes and, also for the LL Push-Pull Mode.	124
19. Calculations Synthesis Associated to the Four Main Modes and, also for the LL Push-Pull Mode.	125
20. Three Passive ME Sensor Classes.....	149
21. Sensor channels and calibration	154
22. Average characteristics of the miniaturized charge amplifiers, excluding rejected units.....	174

<u>Table</u>	<u>Page</u>
23. Comparison of average characteristics of miniaturized charge amplifiers using a 2SK369GR JFET (top) and 2SK369BL JFET (bottom).....	174
24. This table shows an increase in properties with change in Metglas attachment improvements for PZT cores with similiar electrical properties.....	176
25. Experimental results for pressure dependence cure on Metglas properties.	177
26. ME Voltage output and Hdc bias for three conditions of Metglas.....	179
27. ME properties with changing Metglas thickness	179
28. Core electrical property deviations with different interior epoxy.	180
29. Summary of ME response of sensors fabricated with different thickness electrode and differently spaced interdigit.....	185
30. Mn doped PMNPT used with two differing electrode spacings showing loss reduction of larger spacing.....	188
31. Properties of four PMN-PT sensor using different electrode trace width and interdigit spacings.....	189
32. Electrodes available for experiments to determine optimum characteristics.	190
33. Loss characteristics of several different varieties of piezoelectric core material available for manufacturing.	195
34. Comparison of poling effects on current PZT cores versus previously poled PZT cores.	198
35. Comparison of datasheet and experimentally observed loss values.....	199
36. Single batch property distributions of PZT sensors using screen printing epoxy application.	203
37. Measured properties of PMN-PT sensors made with similar 2.5mm ID electrodes as a comparison of property repeatability.	203
38. Matching sensors manufactured for array testing.	215
39. Changes in ME charge and voltage as a function of spacing.	215
40. Change in ME properties with series additions.....	215
41. Comparison of parallel and series sensor combinations and their effect on loss characteristics.	216
42. Comparison of individual sensor properties to properties of stacked sensors in serial/parallel combination.	225
43. Comparison of individual PMN-PT sensors to four PMN-PT sensors stacked in serial/parallel configuration.....	226
44. Sensors fabricated for stacking experiments and recorded ME properties.	230
45. Properties of stacked sensors utilizing only one JFET charge amplifier for set.....	230
46. Piezoelectric and dielectric properties of PMN-PZT piezoelectrics: randomly oriented ceramic (R-ceramic), <001> textured ceramic (T-ceramic) and <001> single crystal (S-crystal).	238

<u>Table</u>	<u>Page</u>
47. Dielectric and piezoelectric properties of randomly oriented pure PMN-PZT, randomly oriented and textured MnO ₂ doped PMN-PZT ceramics (abbreviated as R-pure, R and T-5BT, respectively).....	240
48. Material parameters of piezoelectric compositions used in this study.....	246
49. Comparison of DC biasing method with modulated sensing technique for both magnetoelectric heterostructural magnetic field sensors.	257
50. Comparison of magnetic field sensitivity and noise floor.....	262
51. Comparison of magnetic field sensitivity and noise floor.....	266
52. Comparison of sensitivity, SNR and noise floor with respect to modulation frequency for several ME sensors.	268
53. Comparison of PZT lattice constant between Pt and Au buffered samples by using XRD analysis	280
54. The diagonal elements of the covariance matrix are shown for octaves 2, 3, and 4.	302

1. Summary

Virginia Tech HUMS program has made important progress with regards to their Phase I goals of lowering noise. Virginia Tech has achieved noise floors of about $1\text{pT}/\sqrt{\text{Hz}}$ at $f=1\text{Hz}$ in passive sensors operated at room temperature that consisted of magnetostrictive Metglas layers bonded to piezoelectric PMN-PT single crystal fiber ones. We note that this was done without incorporating signal modulation, flux concentration, or signal condition/analysis: which offer the opportunity to lower the noise floor by an order of magnitude further. These noise floors were benchmarked by our international team members at the University of Caen. Furthermore, Passive Sensors has developed 3x3 arrays of ME sensors, also achieving noise floors on the order of $1\text{pT}/\sqrt{\text{Hz}}$ at $f=1\text{Hz}$. Working together Virginia Tech and University of Caen have developed gradiometers with high common mode rejection efficiencies, enabling real world applications. Issues that remained unresolved included an internal supply of grain oriented PMN-PT fibers, and incorporation of the signal/flux modulation methodologies. Overall the investigations have clearly identified Metglas/PMN-PT tri-layer laminates as the superior technology.

We now provide a summary of progress, listed by quarter.

Quarter 9 (no-cost extension)

(1) Virginia Tech focused on the development of a theoretical model by which to design future generations of ME resonators with optimal ME gain. This was going to be a critical aspect to Phase II. We invested our time and effort into laying the conceptual groundwork for this approach.

(2) In addition, they found that applied dc electrical biases can make a significant increase in the ME coefficient, offering a means to enhance the gain coefficient of the transfer function. Furthermore, Virginia Tech made progress in fabricating ME laminates with high mechanical quality factors and low dielectric losses, by incorporating Mn-doped PMN-PT single crystals.

(3) Passive Sensors theoretically and experimentally studied the geometry-dependent ME coefficient in L-T mode sensor. A significant enhancement in ME coefficient was found, in turn, a great reduction in noise floors, if wider and longer Metglas layers were used in the laminate composites.

(4) CNRS-Caen has completed their project.

(5) SAIC has completed their project.

(6) Oakland University developed bilayers and trilayers of piezoelectric single-crystal lanthanum gallium tantalate (LGT) and magnetostrictive permendur (P). The ME voltage coefficient ranges from 2.3 V/cm Oe at 20 Hz to 720 V/cm Oe at bending resonance. The low-frequency magnetic noise for P-LGT-P was also investigated. Langatate is free of ferroelectric hysteresis, pyroelectric effects and phase transitions up to 1450°C and is of interest for ultrasensitive, high temperature magnetic sensors. These findings have not been benchmarked either by Virginia Tech or CNRS-CAEN.

(7) Virginia Tech (Priya) investigated the piezoelectric properties of textured MnO₂ doped PMN-PZT ceramics. The combination of texturing and hardening effect confirmed to be suitable for developing piezoelectric materials possessing excellent “hard and soft” combinatory characteristics. The effect of template content on temperature stability of piezoelectric properties was investigated. Mn-doped PMN-PZT textured ceramics containing 3 vol% BT exhibited excellent piezoelectric properties $d_{33} = 720 \text{ pC/N}$, $k_{31} = 0.53$, $Q_m = 403$, $\tan \delta = 0.3\%$ along with good temperature stability.

(8) NEU has finished their project.

(9) The Army Research Lab has finished their project.

Quarter 8.

(10) Virginia Tech and Passive sensors focused on decreasing the noise floor by reduction of $\tan \delta$ and by stacking of laminates. Multi-sensor stacks consisting of 4 sensors were studied in both series and parallel. Noise floor reductions were achieved by a factor of $N^{1/2}$, as predicted. Noise floor levels of $4\text{pT}/\text{Hz}^{1/2}$ and $2\text{pT}/\text{Hz}^{1/2}$ at $f=1\text{Hz}$ were found for Metglas/PZT and Metglas/PMN-PT laminate stacks. Analysis of the noise floor for these stacks by theoretical models demonstrated that the dominate noise sources are $\tan \delta$ and that of the detection electronics: which are nearly equivalent at this noise level. Furthermore, they improved the noise model for the multi-push pull mode configuration.

(11) Passive Sensors and Virginia Tech have optimized the Kapton® electrode for the ME laminate. They developed ID electrode distances which give rise to lower capacitances, and lower equivalent magnetic noise floors. In addition, they investigated the effect of sensor spacing in a gradiometer array on the ME voltage coefficient. They showed that an optimum sensor spacing of about 4cm is better, with regards to prevent mutual inductance effects between sensors. They also begun investigations of applications of gradiometers with regard to detection of targets.

(12) CNRS-Caen pursued investigations of sensors from Virginia Tech and Northeastern in a vacuum. The results provided insights into understanding the origins of sensed external vibrational noise sources. Such vibrational noise studies have been performed inside a magnetically shielded room.

Work focused on determining the intrinsic noise floor of the sensor. Studies at resonance have possibly revealed magnetic noise floors on the order of $\text{fT}/\sqrt{\text{Hz}}$ for the Metglas/PMN-PT crystal fiber laminates. This would have been an important step towards the focus of Phase II goals: it demonstrates feasibility. In addition, CNRS has continued benchmarking the ME laminate sensors from various group members. The results clearly demonstrated that the Metglas/PMN-PT single crystal laminates are far superior (10-100x) in terms of lower noise floor. Agreement in values has been achieved between the various partners.

In addition, CNRS developed a new model for the ME equivalent magnetic white noise. The model fits very well with all experiments. Also, it completed the previous description and gave the elements to evaluate the expected ME sensor magnetic noise floor level in the full frequency

range and at the ME resonance also. Finally, an improvement to theoretical modeling was made, with regards to pseudo-2D cases.

(13) SAIC focused on signal analysis and algorithm development, working in conjunction with students at Virginia Tech. They demonstrated the ability by signal analysis to lower the equivalent magnetic noise floor. Such analysis and algorithms were developed for applications to arrays. Arrays were constructed by Passive Sensors, and the investigations completed by SAIC and Virginia Tech. The results showed significant promise with regards to developing array and gradiometer applications. Furthermore, SAIC has worked with ARL on field tests and advancements towards incorporating flux concentrators with ME sensors.

(14) Passive Sensors and Virginia Tech made progress on the potential to manufacture. Passive Sensors has demonstrated the potential to make ME laminates in lots of eight with good repeatability (+/- 10%) and good yield. Some progress has been made to incorporating piezoelectric single crystal fibers (purchased from China), but however due to the lack of internal availability of textured fibers within the team such studies were limited. Progress was made by Passive Sensors in the development of ME arrays. The optimum geometry, stacking dimensions, spacings, and element interactions were investigated. Arrays of dimensions 2x2 were studied both in the field and in an environmentally shielded chamber.

(15) Oakland University made significant progress on lowering the values of the equivalent magnetic noise floor of their graded laminate structures, and trilayer Permendur/PZT ones. The values obtained were in agreement with benchmark measurements made at CNRS-Caen. The noise floor of these structures was on the order of $200\text{pT}/\text{Hz}^{1/2}$ at $f=1\text{Hz}$, and of $30\text{pT}/\text{Hz}^{1/2}$ at the fundamental bending mode. Oakland made progress of incorporating PMN-PT single crystal fibers into Permendur-based sensors. Due to a limited fiber length, they found lower sensitivities and higher magnetic noise floors compared to sensors with 5cm long PZT fibers.

(16) Virginia Tech (Priya) made progress on the development of longer textured piezoelectric fibers. Two approaches were studied: (i) seeding of PMN-PT ceramics with BaTiO_3 (BT) crystals which has been found to be an effective manner in which to achieve chemically stable nonreactive solid state conversion; and (ii) addition of Mn. Enhancements in the degree of grain orientation to 95.5% have been achieved for fibers up to 7cm long. These compositions could serve as base compositions by which to achieve high d_{33} and low $\tan\delta$ in single crystal fibers. Efforts focused on trying to enhance the degree of texture for these long fibers, as the remaining 5% of texture can make big differences in d_{33} and $\tan\delta$. Grain oriented fiber with piezoelectric d_{33} coefficients of about 1000pC/N were fabricated.

(17) Northeastern made progress on their investigations of modulation, studying both on-resonance and off-resonance conditions. They showed that the noise floor can be notably reduced by modulation for the sensors they investigated. In addition, NEU completed investigations of PZT-tube based ME sensors. They found equivalent magnetic noise floors of $1\text{nT}/\sqrt{\text{Hz}}$ at $f=1\text{Hz}$. These investigations confirmed by CNRS-CAEN. Such studies of tubes were done in bending and free-standing modes.

(18) The Army Research Lab focused on field testing of ME sensor setups in less noisy and more spacious environments than in the lab. Fortunately, ARL has a custom-built facility for such studies. Testing was done in an environment which allowed 50ft movement in either x or y directions. Noise reductions were found, and the greater spaced allowed for ease of measurement, for the study of both sensors and gradiometers, and for incorporation of flux concentrators. In particular, ARL demonstrated significant flux concentration enhancements, which had promise to lower the noise floor of the ME sensors.

Quarter 7.

(19) Passive Sensors and Virginia Tech explored the use of alternative materials in the ME laminates. Comparative investigations of Metglas/PMN-PT crystal and Metgals/PZN-PT crystal laminates were performed, using crystals from various sources. Investigations of various epoxies in the core composites have been studied. These results represent an on-going struggle to find the optimum materials combination for high d_{33} (and stress transfer) which represent the gain in the sensor transfer function, and a low $\tan\delta$ which represents one of the important noise sources.

In addition, we studied the effect of poling on the ME laminate sensor gain and equivalent magnetic noise floor. Poling is important with regards to achieving the optimum d_{33} values. We took into account the importance of the spacing between the digits in the ID electrodes, in order to reduce variations in performance and in electrical breakdown. We measured the noise floors for various ME laminates with different ID electrode geometries, and compared the measured values to theoretical ones calculated using our noise model.

Furthermore, we began to think about how the optimum design of the ME laminates maybe different between low and high frequencies. The design we currently are pursuing is for the optimization the quasi-static or passive mode. However, in Phase II of this program, we will be transferring our approach to the near resonance frequency range, in order to take advantage of the high ME resonance gain. Our initial findings suggested that the high Q factor need to achieve the highest resonance gain may require slightly different ME laminate design optimizations.

(20) CNRS-Caen made important progress on gradiometer development and characterization. They studied the performance of gradiometers with regards to source localization. Theoretical development of source localization and error was achieved. Such studies are important to evaluate performances in the real world.

Work focused on determining the intrinsic noise floor of the sensor. Studies at resonance have possibly revealed magnetic noise floors on the order of fT/\sqrt{Hz} for the Metglas/PMN-PT crystal fiber laminates. This was an important step towards the focus of Phase II goals: it demonstrates feasibility. In addition, CNRS continued benchmarking the ME laminate sensors from various group members. The results clearly demonstrate that the Metglas/PMN-PT single crystal laminates are far superior (10-100x) in terms of lower noise floor, than the graded structures. Agreement in values was achieved between the various partners.

In addition, CNRS performed detailed investigations of the dominate sources of noise. They determined the importance of vibration, acoustic, and barometric noise sources. Means to reduce acoustic and barometric noise sources were studied by vacuum encapsulation. The results were

used to improve the noise source model. The experimental and theoretical findings demonstrated that the dominant ultra-low frequency noise sources are acoustic and barometric.

(21) SAIC focused on low-noise electronics, to design, fabricate and test a set of miniaturized JFET-based charge amplifiers that can be flexibly integrated with ME sensors in the array structure developed by VT and Passive Sensors. Thirty two (32) of these charge amplifiers were successfully tested and delivered to Passive Sensors and the Army Research Lab, along with supporting battery boxes and charges.

(22) Better epoxy control and electrode design enabled Passive Sensors to be able to make multiple sensors with reduced property variations. They investigated means to better control epoxy application with a method that is more conducive to mass production. In the last quarter, passive sensors began investigations of processing of epoxy by screen printing. Studies demonstrated the ability to easily increase sensor production to eight simultaneous units, and they believe that it offers a means to significantly higher through-put. Furthermore, array modules were developed, fabricated, and characterized.

(23) Oakland University made progress on reducing the resonance frequency of the fundamental bending mode, by active tip-mass loading. They successfully measured noise floors of $5\text{pT}/\text{Hz}^{1/2}$ at fundamental bending mode resonance of $f_{\text{bend}}=1\text{Hz}$.

These noise floor measurements were in agreement with Benchmarks performed at CNRS. One limitation to the graded bending mode structures is the extremely small bandwidth for sensor detection units.

(24) Virginia Tech (Priya) made progress on the development of longer textured piezoelectric fibers. Seeding of PMN-PT ceramics with BaTiO₃ (BT) crystals was found to be an effective manner in which to achieve chemically stable nonreactive solid state conversion. Enhancements in the degree of grain orientation to 90% have been achieved for fibers up to 7cm long. These compositions could serve as base compositions by which to achieve high d_{33} and low $\tan\delta$ in single crystal fibers. Efforts focused on trying to enhance the degree of texture for these long fibers, as the remaining 10% of texture can make big differences in d_{33} and $\tan\delta$.

One limitation had been, and remains to be, the availability of sufficiently large grain oriented samples from Priya to Passive Sensors. We hope that this will be rectified soon, and remain optimistic that there will be an internal source of highly textured fibers, whose base composition can be modified to achieve special needs required for Phase II success.

(25) Northeastern reported significant improvements in a modulation sensing technique. The goal of these experiments was to see if any improvement in noise floor could be achieved if the amplitude of the test and modulation H -fields were reduced. In addition, measurements were taken inside of an earth-grounded dual-walled Gauss chamber to reduce the effects of environmental electric and magnetic noise. A small dual-nesting Helmholtz coil was characterized to generate small-amplitude test and modulation magnetic fields on the order of 100 nT and 1000 nT, respectively. This crucial step ensured dynamic range compatibility with the instruments and relieved the dynamic range limiting effects that caused higher noise floor

values in previous HUMS reports. They reported up to a 40x increase in 0-Hz noise floor values since last month and, when compared to the conventional DC biasing method, the modulation sensing technique exhibits up to 3-orders-of-magnitude improvement in 0-Hz noise floor, while simultaneously enhancing SNR and sensitivity. As previously demonstrated, the modulation technique continues to offer superior spurious noise mitigating than the conventional DC biasing method.

(26) The Army Research Lab demonstrated reduced noise floors by flux concentration. They developed flux concentrating units to employ in field tests to demonstrate the concept of noise floor reduction by this means. Designs were finished, and components for the field tests obtained.

Quarter 6.

(27) Virginia Tech and Passive sensors focused on decreasing the noise floor by design of the electrode geometry and by lowering the $\tan\delta$. We took into consideration the finite size of the electrode geometry in our Metglas / piezoelectric fiber laminated layers. We found that a minimum required spacing is necessary in order to achieve the full piezoelectric voltage coefficient. These findings had importance to the magnetoelectric coefficient of the laminated layers, as the ME coefficient is linearly proportional to the piezoelectric d_{33} one. We were able to achieve a significant increase in the sensor transfer function following this approach.

We systematically studied the effect of $\tan\delta$ of the piezoelectric layer on the equivalent magnetic noise floor of the ME laminates. We firmly believe that in ideal piezofiber layers that the value of $\tan\delta$ of the layer should be equal to that of the individual fibers. However, in practice, we found a significant difference: in particular, we found it difficult to reduce $\tan\delta$ below a value of 0.01, even if the $\tan\delta$ of the fiber was 0.001. Our modeling indicated that small amounts of residual epoxy between the ID electrode and the fiber significantly increase the value of $\tan\delta$, even though the volume fraction is very small. Through our investigations, we achieved significant decreases in $\tan\delta$ to values of 0.005, but have yet to achieve the full potential of reducing $\tan\delta$ to reduce the equivalent magnetic noise floor.

Together, the redesign of the electrode geometry and decrease in $\tan\delta$ allowed us to reduce the equivalent magnetic noise floor to values of $5\text{pT}/\text{Hz}^{1/2}$ at $f=1\text{Hz}$. We believe that by achieving the full potential of the low $\tan\delta$ and high d_{33} of modified piezoelectric single crystal fibers that we can further reduce the noise floor by a factor of 2-3x.

(28) Passive Sensors and Virginia Tech investigated the influence of sensor stacking on reducing the equivalent magnetic noise floor. Investigations focused not only on the number of sensors stacked, but also the geometry in which they are stacked. We found that the sensors must be stacked with respect to each other in a manner such they do not steal magnetic flux from each other. This requires critical sensor spacing, and preferential geometrical arrangements of sensors.

Following these investigations, we demonstrated that the equivalent magnetic noise floor of Metglas / PMN-PT ME laminate sensors can be reduced by a factor of $N^{1/2}$. Our investigations showed that noise floors on the order of $3\text{-}4\text{pT}/\text{Hz}^{1/2}$ at $f=1\text{Hz}$ can be achieved for $N=4$. We believe that we can do better than this value, by use of fibers with lower values of $\tan\delta$ and

improved electrode design. Modeling of the equivalent noise floor for stacking of such improved ME laminates indicates that we should be able to achieve equivalent magnetic noise floors on the order of $<1\text{pT}/\text{Hz}^{1/2}$ at $f=1\text{Hz}$, without flux concentration and or electronic modulation.

(29) CNRS-Caen made important progress on magnetometer and gradiometer development and characterization. Such studies are important to evaluate performances in the real world. The magnetometers were made with a magnetic feedback field, in order to improve the linearity of the gain in the bandwidth and to reduce the phase shift effect. Both magnetometers (with and without feedback field) were tested in a gradiometric or differentiator mode. Measurements were made in an open laboratory environment. Simultaneously, the total harmonic distortion of the magnetometer and the spatial transfer function of the gradiometer for a given baseline with or without tilt effect and started to evaluate the associated limit of source localization.

In addition, CNRS-Caen and Oakland worked together to benchmark the equivalent magnetic noise floors of the ME sensors fabricated by Oakland. Agreement in values was achieved between the various partners.

(30) SAIC worked on system design. In particular, they have considered the trade-off space of the ME sensor SWaP space. These studies have clearly demonstrated the advantage of ME laminates in the trade-space of volume and power. They offer unique approaches in these important application spaces.

In addition, SAIC proceeded with the prototyping of array fixtures. Integration issues were considered – including mechanical, charge amplifiers, power supplies and sensor stacking. The plans were to deliver to Virginia Tech and Passive Sensors 50 prototype JFET charge amplifier circuits.

(31) Oakland University made significant progress on lowering the values of the equivalent magnetic noise floor of their graded laminate structures, and trilayer Permendur/PZT ones. The values obtained were in agreement with benchmark measurements made at CNRS-Caen. The noise floor of these structures is on the order of $200\text{pT}/\text{Hz}^{1/2}$ at $f=1\text{Hz}$, and of $<100\text{pT}/\text{Hz}^{1/2}$ at the fundamental bending mode.

Oakland also made progress on reducing the resonance frequency of the fundamental bending mode, by active tip-mass loading. They successfully measured noise floors of $<100\text{pT}/\text{Hz}^{1/2}$ at fundamental bending mode resonance of $f_{\text{bend}}=1\text{Hz}$.

(32) Virginia Tech (Priya) made progress on the development of textured piezoelectric fibers. Seeding of PMN-PT ceramics with BaTiO₃ (BT) crystals was found to be an effective manner in which to achieve chemically stable nonreactive solid state conversion. Enhancements in the degree of grain orientation to 98.5% were achieved. This is a significant advancement, as the piezoelectric charge coefficient was found to be notably enhanced by increasing the grain orientation from 90% to 98.5%.

One limitation has been, and remains to be the availability of sufficiently large grain oriented samples from Virginia Tech to Passive Sensors. Virginia Tech has finished setting up furnaces

for large piezoelectric fibers of length 8cm. This requires much more sophisticated furnace controls, in order to keep the temperature sufficiently uniform to favor homogeneous nucleation rather than heterogenous during the grain growth process. We are optimistic that by end of Phase I that there will be an internal source of highly textured fibers, whose base composition can be modified to achieve are special needs required for Phase II success.

(33) Northeastern showed through a comparison of peak parameter values capturing using a DC bias method and a modulation sensing technique that the modulation sensing technique exhibits SNR, sensitivity, and 0-Hz noise floor enhances for ME laminate sensors. It was found that the degree of enhancement provided by the modulation sensing method is nonuniform between sensors. Their findings demonstrate that the magnetic spectral density is lowered by the modulation at frequencies above 0-Hz noise floor.

Northeastern grew PZT films at low temperatures on Metglas. They continued to focus on deposition and characterization of PZT films grown on Metglas with buffers such as Au or Pt to improve film quality. They found that high crystallographic texture can be realized and controlled by the choice of deposition conditions which are showed to correspond to the specific buffer layer. The PZT films were characterized by XRD, SEM and EDX. Ferroelectric measurements verified that the PZT films buffered with Pt were ferroelectric with high piezoelectric constants of $d_{33}=45\text{pm/V}$. Magnetoelectric measurements and equivalent magnetic noise floor studies are currently being tested.

(34) The Army Research Lab was involved in three activities on the HUMS program. These activities were: (i) estimating and measuring how large an enhancement of the performance of magnetoelectric (ME) magnetic sensors one can get using flux concentrators, (ii) measuring the increase in the resonant frequency of asymmetric ME sensors due to an in-plane tensile force, and (iii) using an AC magnetic modulation field to increase the signal frequency of ME sensors.

Quarter 5.

(35) Passive Sensors and Virginia Tech investigated the influence of the dielectric loss factor on the equivalent magnetic noise floor. Results indicate that a significant lowering of the magnetic noise floor can be achieved by using materials with lower $\tan\delta$ values: that is if the piezoelectric constant is not decreased, which is directly proportional to the magnetoelectric voltage coefficient or gain in the transfer function between voltage and equivalent magnetic noises. Investigations, and hope, have focused on Mn-doped PMN-PT single crystal fibers provided by the Shanghai Institute of Ceramics. Measurements demonstrated that ME laminates of these fibers with Metglas can achieve noise floors of $6\text{-}7\text{pT/Hz}^{1/2}$ at $f=1\text{Hz}$. Furthermore, we have not yet realized the full reduction in the noise floor offered by the approach, as the value of $\tan\delta$ of the laminate containing the fibers is notably higher than those of the fibers. These developments are recent and on-going.

To understand why the laminates have higher values of $\tan\delta$ than that for individual fibers, we employed modeling of $\tan\delta$. We believe that small amounts of epoxy between the fiber and the Kapton ID electrodes may significantly enhance the effective $\tan\delta$ of the fiber.

(36) Virginia Tech and Oakland University demonstrated the potential to reduce the equivalent magnetic noise floor by use of a bending mode resonance. Investigations of Metglas/PZT-fiber laminates showed that asymmetric bilayers have ME voltage coefficients equal to that of symmetric trilayers. This indicated that the dominate contribution to the piezoelectric coefficient in the L-L symmetric mode may in fact come from a flexural or shear contribution. Using these Metglas/PZT-fiber bilayer structures, equivalent magnetic noise floors of $0.3\text{pT/Hz}^{1/2}$ were achieved at $f=240\text{Hz}$. Corresponding investigations of asymmetric trilayers of Ni/PZT/Metglas yielded equivalent magnetic noise floors of $45\text{pT/Hz}^{1/2}$ at $f=242\text{Hz}$.

(37) CNRS-Caen and Oakland University made progress on standardizing noise floor measurements. Presently, Virginia Tech, CNRS-Caen and Oakland University can achieve similar values of the equivalent magnetic noise floor spectra for the various types of ME laminates made in the program.

(38) CNRS-Caen pursued analysis of the noise model of ME sensors which can help to predict the full theoretical equivalent mechanical/ vibrational/magnetic sensor noises. The model was based on their previous development and Mason's model. Results give the theoretical ME laminated sensor noise in the one Dimension and All modes "1D" ($l \gg w$ & $l \gg t_{lam}$).

They improved their noise model of the ME sensor, developed a first magnetometer with feedback loop and made magnetometer characterization in order to give and to compare its performances to those of the single ME device as a magnetic sensor.

They have made noise measurements and noise level analysis in order to test the new sensors (With the help of a coherence method, we achieved to reach the expected noise limit in measurement range frequency lower than 1 Hz) and new SAIC electronics. In addition, they have pursued the testing of the Oakland sensors with a bias magnet. Also, we have studied the low frequency excess noise and the effect of different associations of several piezoelectric (3 or 5) segments on the output sensor noise. Experimental results showed the influence of the number of segments on the noise floor as predicted by the theory.

In addition, they also made cross-modulation technic and evaluated the environmental rejection efficiency in a differentiator configuration of around 100.

(39) Virginia Tech and Passive Sensors have shown that Metglas/PZT-fiber laminates can be stacked to result in a decrease in the equivalent magnetic noise floor by a factor of $N^{1/2}$, where N is the number of elements in the stacked. They were able to achieve for arrays of Metglas/PZT/Metglas symmetric trilayer structures a noise floor of $12\text{pT/Hz}^{1/2}$ at $f=1\text{Hz}$, and for arrays of Metglas/PMN-PT/Metglas symmetric structures a noise floor of $6\text{pT/Hz}^{1/2}$ at $f=1\text{Hz}$. The goal was to make stacked structures of Metglas/Mn:PMN-PT/Metglas laminates, combining the enhancement from the lower $\tan\delta$ with that of increasing N. This has yet to be tried, but analysis using the models developed by SAIC indicate that the electronic noise floor of the JFET detection circuit with these laminates should be around $1-2\text{pT/Hz}^{1/2}$ at $f=1\text{Hz}$.

Corresponding investigations of arrays of asymmetric Ni/PZT/Metglas structures are currently under investigation by Oakland University. These structures have been fabricated and their ME

coefficients shown to have enhanced gain, however noise floor measurements have yet to be performed.

Asymmetric Metglas/PZT stacked structures have not yet been fabricated or tested. If the benefits of resonance enhancement of the single layer ($0.3\text{pT}/\text{Hz}^{1/2}$) can be combined with that of stacking, then equivalent magnetic noise floors of $<0.1\text{pT}/\text{Hz}^{1/2}$ should be feasible. Even lower noise floors should be possible in asymmetric structures of Metglas/PMN-PT and Metglas/Mn:PMN-PT.

(40) Passive Sensors and SAIC worked together on applications concepts, and made progress together on ME array designs. They developed a concept for 3x3 arrays, which can be adapted to higher dimensions, and whose spatial distribution of sensors and their baselines can be adjusted. One of the important design issues was to avoid “mutual inductance”, which can serve to lower the advantages of stacking. Investigations focused on array designs that avoid this effect. SAIC has provided to Virginia Tech and Passive Sensors additional JFET circuits, designed for the higher capacitances and unique electrical parameters, of stacked ME laminates.

(41) Virginia Tech (Priya) made some progress on the development of textured piezoelectric fibers. Seeding of PMN-PT ceramics with BaTiO_3 (BT) crystals was found to be an effective manner in which to achieve chemically stable nonreactive solid state conversion. Enhancements in the degree of grain orientation were achieved, but progress on developing larger samples to incorporate into the ME laminates remained to be finished. Investigations of compositional modifications that lower $\tan\delta$ continued but have yet (in ceramic form) been able to render materials with high d_{33} and low $\tan\delta$.

One limitation has been, and remains to be, the availability of grain oriented samples from Virginia Tech (Priya) to Passive Sensors for investigations of the potential to manufacture. This was the main purpose of Virginia Tech (Priya) in the program. Presently, Passive Sensors is focusing on demonstrating the ability to fabricate Metglas/PZT-fiber laminates in batches of four (4), where they have demonstrated properties repeatable within +/-10%.

(42) Northeastern performed a proof of concept of their modulation detection technique on a relatively low sensitivity ME sensor where the noise floor of the electronics used in the experimental setup was below that of the ME sensor. In collaboration with Virginia Tech (Viehland), they extended these studies to a highly sensitive magnetoelectric magnetic field sensor to test with their modulation technique. Initial results suggested that the modulation technique showed no improvement over the conventional DC biasing method. Further investigation indicated that the noise floor of VT's highly sensitive ME sensor was below that of the instrument's electronic noise floor in the modulated technique's experimental setup causing SNR, sensitivity, and noise floor measurements to be incorrect. Next, a gain stage prior to the modulated sensing technique's experimental setup was used to amplify the noise floor of each sensor to a level above that of the instrument's electronic noise floor: investigations are still ongoing.

Northeastern grew PZT films at low temperatures on magnetostrictive Hyperco substrates. They have been able to deposit and crystallize PZT on Hyperco, shown the ability to obtain good P-E

curves typical of well-crystallized PZT, and have also demonstrated that the magnetostrictive properties of Hyperco are not degraded by annealing. Recent investigations demonstrated a controlled and uniform grain size for the PZT: the approach looks promising.

(43) The Army Research Lab optimized an air turbine and air bearing rotation system for flux concentrators that did not increase the noise. In the last quarter, they developed a method by which to shield the step up from stray fields. They began investigations of flux concentration for asymmetric structure with Oakland University, which showed promise of lowering the background noise.

In addition, they developed a method by which to shift the resonant frequency of ME sensors in this rotation flux concentration system. If they can extract the increased signal from the background, it should be possible to use this new approach to make a sensor with increased sensitivity over a range of frequencies by changing the resonant frequency. This sensor would include a method for sweeping the resonant frequency by changing the force continuously.

Quarter 4.

(44) Passive Sensors, Virginia Tech and CNRS-Caen finished their benchmark studies of the latest generation of ME sensor units. The sensors were three layer Metglas / PZT-fiber / Metglas laminates that had Metglas layers 8cm long and 1 cm wide, and one PZT layer consisting of 5 fibers 4cm long and 0.2cm wide. These studies confirmed noise floors of $2\text{-}3 \times 10^{-11}\text{ T/Hz}^{\frac{1}{2}}$ at $f=1\text{Hz}$. Now, we move forward together to further reduce the noise levels.

(45) Virginia Tech worked on an audit of possible noise sources that limit sensor performance, both external and internal ones. The =worked on designs for cancellation of thermal, acoustic/vibration, and magnetic noises. There was promise to remove low frequency acoustic/vibration noise using either double sided symmetric ME sensors or active cancellation using a separate accelerometer. Gradiometric configurations of ME sensors were designed and fabricated, and shown capable of cancelling magnetic noise.

(46) CNRS-Caen developed a model for analyzing noise sources of ME sensors. The showed the importance of three types of noise sources. (i) A thermal polarization noise that is proportional to the dielectric loss factor ($\tan\delta$), which scales with frequency as $1/f^{\frac{1}{2}}$; (ii) a resistive noise that is proportional to the DC resistance of the ME sensor, which scales with frequency, as $1/f$; and (iii) an acoustic / vibrational noise, which scales as $1/f^2$. Experimental noise power spectra support this noise theory, as we can identify regions with the respective slopes.

(47) SAIC developed a noise model tool-kit. This tool-kit includes was used to model the performance of various ME detection units, including amplifier noise and internal sensor noise. Simulations demonstrate that our laminate sensor noise floor is close to that of the detection units. Furthermore, SAIC performed a comprehensive investigation of various low noise op-amp detection systems, and recommended a suite of ones best suitable for use with our ME laminate sensors.

(48) Virginia Tech, CNRS-Caen and SAIC are currently working together to enhance the resistivity of the ME laminate through improved electrode design and better polymer processing. In particular, we are focusing on packaging, in order to control moisture absorption that can reduce the leakage resistance, and thus increase the noise floor. Furthermore, we are working towards incorporating piezoelectric fibers with lower values of $\tan\delta$.

(49) Passive Sensors investigated the nonlinear ME effect. Such information was deemed important by SAIC and CNRS in order to begin to understand modulation methods by which to reduce noise. Passive Sensors mapped out the amplitude, DC bias, and frequency dependence of the nonlinear ME voltage and charge coefficients for three layer Metglas/PZT-fiber/Metglas and Metglas/PMN-PT crystal fiber /Metglas ME laminates. They identified the optimum operational points.

(50) Based on these nonlinear results, CNRS-Caen developed modulation techniques that can transfer low frequency signals to higher frequency ones. Theory predicted that the transfer ability depends mainly on the amplitude of the carrier signal and the sensor nonlinearity. This was confirmed by our experiments. The equivalent magnetic noise was analyzed, and shown to be dominated only by the signal transfer ability and the output electrical noise level around the carrier frequency. In this case, low frequency signals do not suffer from low frequency interferences – such as noise vibration! In the future, enhancement of the nonlinear transfer ability is an important goal for this modulation method, as it would foster the ability to reject low frequency environmental noises and thus to lower the equivalent magnetic noise floor. Passive Sensors and Virginia Tech are looking into the approach to achieve this enhancement.

(51) Investigations by Oakland University showed the ability to lower the electromechanical resonance to frequencies lower than 30Hz, by using asymmetric laminated structures. In consideration that there is a large gain in the ME coefficient at the EMR, a notable lowering of the noise floor can be expected. In collaboration with Virginia Tech studying two layer Metglas/PZT-fiber asymmetric structures, noise floors on the order of $10^{-12} \text{ T/Hz}^{1/2}$ were obtained at low frequency bending modes.

Oakland University took the important step to attempt to remove the dc magnetic bias that has so far been required of ME sensors. Using a method of self-bias through functionally graded elements they developed laminates with ME voltage coefficients of $\alpha_{ME}=1 \text{ V/cm-Oe}$. Furthermore, a comprehensive investigations of the noise floor of various types of ME laminate sensors was begun by Oakland University, Virginia Tech, and CNRS. We were not yet in agreement with the ‘most honest’ method by which to compare the performance of detection units made from the various sensors. This was because the different types of ME laminates have different electrical properties (resistance and capacitance), which can affect the noise levels of the detection electronics.

(52) Virginia Tech (Priya) made notable progress on the development of textured piezoelectric fibers. Seeding of PMN-PT ceramics with BaTiO_3 (BT) crystals was found to be an effective manner in which to achieve chemically stable nonreactive solid state conversion. Calculations were performed to identify the dependence of growth distance and rate on the volume fraction of seeds. Some increase in the d_{33} coefficient of the PMN-PT fibers was already demonstrated using

their approach. We are hopeful that important barriers to fiber fabrication has breeched, and that we may be on to a means by which to manufacture such textured fibers in a cost effective manner.

Furthermore, investigations of compositional modifications that optimize properties has begun. In particular, lower loss materials are beginning developed and studied. Such advancements could be important to lower the $1/f^{1/2}$ thermal polarization noise source, if that is the piezoelectric d_{33} constant is not lowered. We are hopeful that an optimum composition can be chosen, developed and textured.

(53) Northeastern grew PZT films at low temperatures on magnetostrictive Metglas substrate has been systematically investigated, including buffer layers, deposition conditions, target fabrications, etc. An optimized processing was successfully resulted in the PZT films demonstrating pronounced ferroelectric hysteresis behavior and high remnant polarization, 30 $\mu\text{C}/\text{cm}^2$.

(54) Additionally, a new modulated sensing technique exhibiting preferred SNR (12.47 dB higher), sensitivity (47.3x higher), and noise floor (4.2x lower) over the conventional DC biasing method, was proposed. The modulated sensing technique also had the ability to reject spurious environmental noise. It was demonstrated that the modulated sensing technique was advantageous to the DC biasing technique.

(55) The Army Research Lab developed an air turbine and air bearing rotation system for flux concentrators that did not increase the noise. This was an important step forward in lowering the overall noise floor of ME sensors, without introducing new noise sources from the flux enhancement. Investigations are focused now on increasing the torque of the rotation, and longitudinal distance along the axis of rotation. In addition, investigations of feedback control systems to match the EMR resonance frequency of the ME laminate have begun.

2. Introduction

2.1. Program Objectives

The ME sensor has the potential to meet the demands for future generations of magnetic sensors, arrays, and imaging systems. Building on our group's prior successes our program goals are (i) develop small ME sensors that have sub pico-Tesla resolution over the bandwidth of $10^{-3} < f < 10^4$ Hz, which operate in a passive mode and are integrated with detection circuitry enabling autonomy, and which are appropriate encapsulated and have optimized signal-noise (S/N) ratios; and (ii) explore development of future generations of arrays of ME sensors and imaging systems.

Phase I

PI.1 Characterize and model the intrinsic noise of the sensors and detection schemes, and advance methods for measuring noise spectra with precision.

PI.2 Enhance the sensitivity of ME magnetic sensors by ONE order of magnitude to range of 10^{-13} Tesla/ $\sqrt{\text{Hz}}$ @ 1Hz. This will be done by developing (i) new heterostructural configurations that restrain non-magnetic environmental noise; (ii) reduction of magnetic background noise by flux compensators and gradiometers; and (iii) developing filter techniques.

PI.3 Develop a 3×3 array of ME magnetic sensors based on laminated and co-fired composites, with enhanced SNR. The goal is a sensitivity of 5×10^{-12} Tesla/ $\sqrt{\text{Hz}}$ @ 1Hz.

PI.4 Develop ME heterostructural materials and individual compositions, synthesize them by various deposition methods, and develop process to miniaturize them.

PI.5 Demonstrate the ability to fabricate ME laminate composite sensors in lots of 10 units, with a 50% yield, within a 10% variability in properties.

PI.6 Develop low-noise readout electronics, and perform system designs aimed at a Phase II demonstration of an imaging system.

Phase II

PII.1 Further enhance the sensitivity of ME magnetic sensors to the range of 10^{-16} Tesla/ $\sqrt{\text{Hz}}$ using the advancements made in Phase I approaches and by use of a resonance gain enhancement.

PII.2 Mature and forward transition new generations of miniature heterostructures developed by various deposition methods into magnetic field sensors and arrays.

PII.3 Develop readout and electronics for magnetic imaging arrays.

PII.4 Characterize and model the intrinsic and environmental sources of noise that influences array and imaging systems.

PII.5 Forward transition new generations of magnetic sensors and arrays into fielded magnetic imaging systems.

2.2. Program Team

For convenience, our Team Members are summarized in Table 1.

Table 1. Team members

Purpose	Lead PI
A. Noise characterization and modeling	Nowak, Dolabdjian [Linked PI's - Li Priya, Viehland]
B. Noise reduction	Edelstein, Li, Priya, Viehland [Linked PI – Dolabdjian]
C. Signal gain (new materials, geometries, and constructions)	Li, Priya, Srinivasan, Viehland [Linked PIs – Nowak, Beall, McLaughlin]
D. Potential to manufacture	Li, Viehland [Linked PIs – Beall, McLaughlin, Priya, Srinivasan]
E. Minaturization	Harris [Linked – Priya, Srinivasan, Viehland]
F. Devices and imaging systems	Beall and McLaughlin [Linked – Li, Priya, Viehland]

3. Results and discussion

A. Dwight Viehland, Virginia Tech

A.3.1. ME modeling

A.3.1.1. M-P-P mode sensors

We have obtained approximate theoretical models for both ME effect and equivalent magnetic noise in the magnetostriuctive/piezofiber M-P-P configuration. The ME coefficient model was obtained based on the field-averaging method under assumption of piezoelectric uniform polarization direction. After the derivation of ME coefficient, the dielectric properties of the multi-push-pull configuration was expressed, then the equivalent magnetic noise in proposed structure was determined.

Figure 1 (a) shows the schematic diagram of multi-push-pull configuration Metglas/piezofiber laminate composites, in which the core composite was composed of a pair of insulation Kapton/interdigitated electrodes (Kapton®) with center-to-center space of s , and was sandwiched by n -layers Metglas with thickness of t_m , each with thickness of $25\mu\text{m}$. The polarization direction of piezofibers between the adjacent ID-electrodes was also illustrated in Figure 1 (a). For sake of clarity, we consider the thickness (t_p) of the core composite was totally contributed by the piezofiber because the thickness of the bonding epoxy and the Kapton® is negligible compared to the piezofiber of $200\mu\text{m}$. The analysis assumes the polarization of piezofibers was arranged in longitudinal direction (3-axis) between the adjacent ID-electrodes. In turn the multi-push-pull configuration was idealized to a multi-L-L mode, as shown in Figure 1 (b). Correspondingly, the simplified configuration was consisted of numerous alternating symmetric L-L mode units in electrically-parallel-connection that each has length of s . While the derivation is specific to this layout, the approach is valid for any multi-push-pull configuration ME laminate composite.

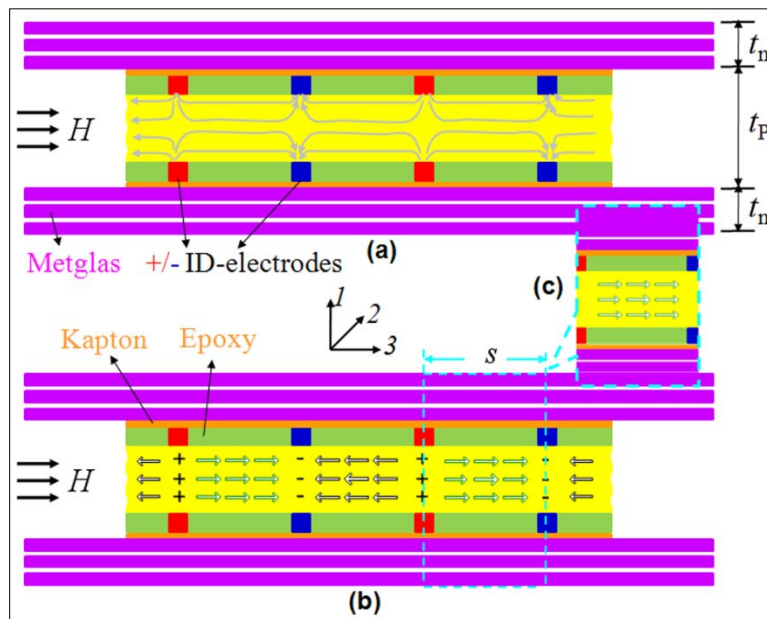


Figure 1. Schematic diagram of the Metglas/piezofiber multi-push-pull mode configuration

The configuration consists of Kapton®/piezofibers core composite, and symmetric n -layer Metglas actuators on the bottom and top of the core composite, where the polarization of

piezoelectric and the “dead zone” were illustrated. The Kapton® consists of interdigitated electrodes and insulating polymer Kapton, which was bonded with piezofiber by epoxy resin. (b) Schematic diagram of the simplified multi-L-L mode structure, in which the polarization of piezofibers was idealized to arrange in longitudinal direction over the whole center-to-center distance (s) of adjacent ID-electrodes. (c) The simplified structure has numerous alternating symmetric longitudinal poled L-L mode units in electrically-parallel-connection that each has length of s .

For a poled piezoelectric phase with the symmetry ∞m , the constitutive equations for the piezoelectric phase can be written for the strain and electric displacement:

$$\begin{aligned} {}^p S_i &= {}^p s_{ij} {}^p T_j + {}^p d_{ki} {}^p E_k \\ {}^p D_k &= {}^p d_{ki} {}^p T_i + {}^p \epsilon_{kn} {}^p E_n \end{aligned} \quad (1)$$

where ${}^p S_i$ and ${}^p T_j$ are strain and stress tensor components of the piezoelectric phase. ${}^p E_k$, ${}^p E_n$ and ${}^p D_k$ are the vector components of the electric field and electric displacement. ${}^p s_{ij}$ and ${}^p d_{ki}$ are compliance and piezoelectric coefficient, and ${}^p \epsilon_{kn}$ is the permittivity matrix of the piezoelectric phase.

The magnetostrictive phase was assumed to have a cubic symmetry and is described by the following constitutive equations:

$$\begin{aligned} {}^m S_i &= {}^m s_{ij} {}^m T_j + {}^m q_{ki} {}^m H_k \\ {}^m B_k &= {}^m q_{ki} {}^m T_i + {}^m \mu_{kn} {}^m H_n \end{aligned} \quad (2)$$

where ${}^m S_i$ and ${}^m T_j$ are strain and stress tensor components of the piezoelectric phase. ${}^m H_k$, ${}^m H_n$ and ${}^m B_k$ are the vector components of the magnetic field and magnetic flux induction. ${}^m s_{ij}$ and ${}^m q_{ki}$ are compliance and piezomagnetic coefficients, and ${}^m \mu_{kn}$ is the permittivity matrix of the magnetostrictive phase.

The analysis assumes small deformations, linear materials performance, perfect interfacial bonding, open-circuit condition. For the solution of the set of Equations (1) and (2), the following boundary conditions, including the traction free boundary conditions, plane stress in the cross-sectional directions, equivalence of in-plane strains and equilibrium conditions are used :

$$\begin{aligned} {}^m S_i &= {}^p S_i \quad (i = 2, 3), \\ {}^m T_1 &= {}^p T_1 = 0, \\ 2 {}^m T_i t_m + {}^p T_i t_p &= 0 \quad (i = 2, 3), \\ {}^p D_3 &= 0, \end{aligned} \quad (3)$$

where $v_p = \frac{t_p}{t_p + 2t_m}$ denotes the thickness ratio of piezoelectric and magnetostrictive phase, respectively.

The constitutive equations can be solved to predict the uniform (or far-field) ME coefficient for an applied magnetic field as shown in Equation (4).

$$\alpha_{E,33} = \frac{E_3}{H_3} = \frac{\{[{}^m q_{31}({}^p d_{33} {}^p s_{11} - {}^p d_{31} {}^p s_{13}) + {}^m q_{31}({}^p d_{31} {}^p s_{33} - {}^p d_{33} {}^p s_{13})](1-v) + [{}^m q_{31}({}^p d_{33} {}^m s_{33} - {}^p d_{31} {}^m s_{12}) + {}^m q_{31}({}^p d_{31} {}^m s_{33} - {}^p d_{33} {}^m s_{12})]v\}(1-v)}{{}^p \epsilon_{33} \{[(1-v)^2({}^p s_{13}^2 - {}^p s_{33} {}^p s_{11}) + (1-v)v(2 {}^m s_{12} {}^p s_{13} - {}^m s_{33} {}^p s_{11} - {}^m s_{33} {}^p s_{13})] + v^2({}^m s_{12}^2 - {}^m s_{33}^2)\} + [(1-v)^2({}^p d_{33}^2 {}^p s_{11} - 2 {}^p d_{31} {}^p d_{33} {}^p s_{13} + {}^p d_{31}^2 {}^p s_{33}) + v(1-v)({}^p d_{33}^2 {}^m s_{33} - 2 {}^p d_{31} {}^p d_{33} {}^m s_{12} + {}^p d_{31}^2 {}^m s_{33})\}} \quad (4)$$

Table 2. Materials parameter for magnetostrictive and piezoelectric components in the multi-push-pull configuration.

Parameter (units)		Metglas ^(a)	PZT ^(b)
Piezoelectric constant (10^{-12} pC/N)	d_{31}		-185
	d_{33}		440
Piezomagnetic coefficient ^(c) (10^{-9} m/A)	q_{31}	-21.3	
	q_{33}	50.3	
Dielectric constant	${}^p \epsilon_{33} / \epsilon_0$		1750
Elastic compliance (10^{-12} m 2 /N)	${}^p s_{11}$		15.3
	${}^p s_{13}$		-5
	${}^p s_{33}$		17.3
	${}^m s_{12}$	-5.2	
	${}^m s_{33}$	10	
Dielectric loss	$\tan\delta$		0.012
DC resistivity ^(c) (10^8 Ω m)	ρ		30

(a) Data sheet form Metglas®

(b) Data sheet from smart materials

(c) Measured values

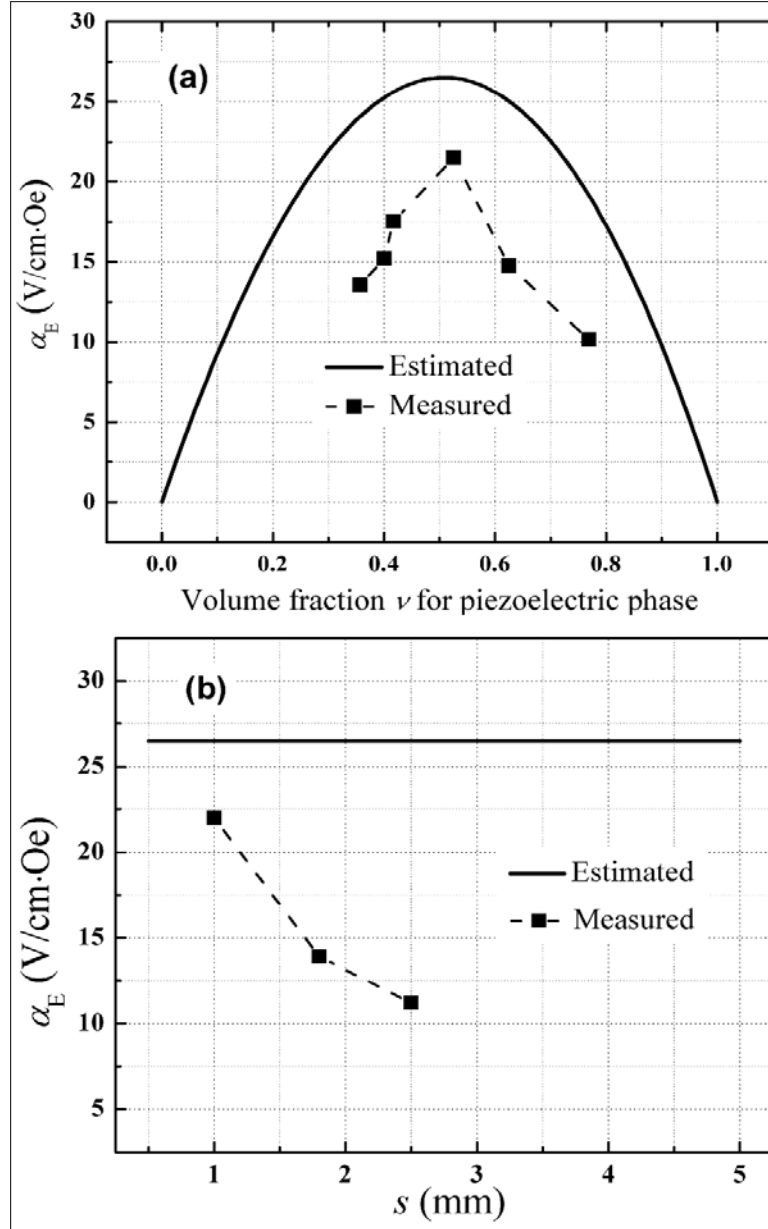


Figure 2. Estimated and measured α_E for multi-push-pull configuration

The configuration contains Metglas/PZT-fiber composite as a function of volume fraction v for PZT-fibers phase. (b) Estimated and measured maximum α_E at optimal v dependence on the s of the Kapton® over the range of $0.5\text{mm} < s < 5 \text{ mm}$.

The theoretical model allows for detailed analysis of the ME effect in the composite components. Analysis was first done on influence of thickness fraction v of the piezoelectric component to the ME coefficients. The theoretical ME voltage coefficient α_E for Metglas/PZT-fiber composite in Figure 2 (a) were obtained assuming non-demagnetization, non-shear lag effects and for the materials parameters given in Table 2. The ME coupling is absent in the individual phase of Metglas ($v=0$) or PZT-fibers ($v=1$). As v was increased from 0, α_E increased to maximum value

of 26.5 V/cm·Oe for $v=0.51$, which was due to the continuous increase in the elastic interaction between the piezoelectric and magnetostrictive phases. The coupling then weakens with a further increase in v . These results are consistent with the other ME theoretical modeling and composite system. The experimental α_E was first measured on dependence of various numbers N of Metglas layers stacked on both sides of PZT-fibers in a Metglas/PZT-fibers composite with $s=1\text{mm}$, and then directly calculated as a function of piezoelectric phase thickness fraction v (i.e. $t_p=0.2\text{ mm}$, $t_m=0.03n\text{ mm}$). We observed similar trends between the theoretically modeled ME coefficients and the experimentally measured ones. The maximum experimental α_E was 21.5 V/cmOe at $v_m=0.53$, which was due to the over-assumption of non-demagnetization, non-shear lag effects, and perfect coupling between the magnetostrictive and piezoelectric phases. Also, the experimental maximum α_E shifted to piezoelectric-rich composites compared with the theoretical trends, which was resulted in the non-continues alteration of Metglas thickness and the less than perfect coupling in experiment. Consider the space of ID-electrodes was a significant merit to the Metglas/piezofiber sensors, the vibrations in theoretical and experimental α_E with s were presented in Figure 2 (b). It can see that the estimated α_E was no response to s , which was determined by the instinct parameters of components. However, the measured α_E for $s=1\text{mm}$, 1.8mm and 2.5mm are 21.5 V/cm·Oe, 13.9V/ cm·Oe and 11.2 V/cm·Oe, which was $1.23\times$, $1.90\times$ and $2.37\times$ smaller than the corresponding estimated values. It is importantly noted that the poling voltage for the three composites was 1600V, 2000V and 2400V, respectively. It would be dielectric breakdown if we applied a high voltage for the composites with $s=2.5\text{ mm}$ partly because of the residual bubbles in the composite during bonding Kapton® and PZT-fibers. Due to the relatively low poling voltage for high s composites, the PZT-fibers exhibited lower piezoelectric properties, which directly determined α_E decreased with the s increase.

The ME voltage coefficient α_V in a unit can be determined by α_E and space s of ID-electrodes (i.e., $\alpha_V=s\alpha_E$). Because the laminate composite was consisted of n (i.e., $n=L/s$, L is the length of the piezofiber) units in electrical polarization in parallel connection, the ME charge coefficient α_Q for the multi-push-pull mode laminate composite can be determined by both α_V and the capacitance of the composite as:

$$\alpha_Q = \frac{s \epsilon_{33} \alpha_E V}{L} \quad , \quad (5)$$

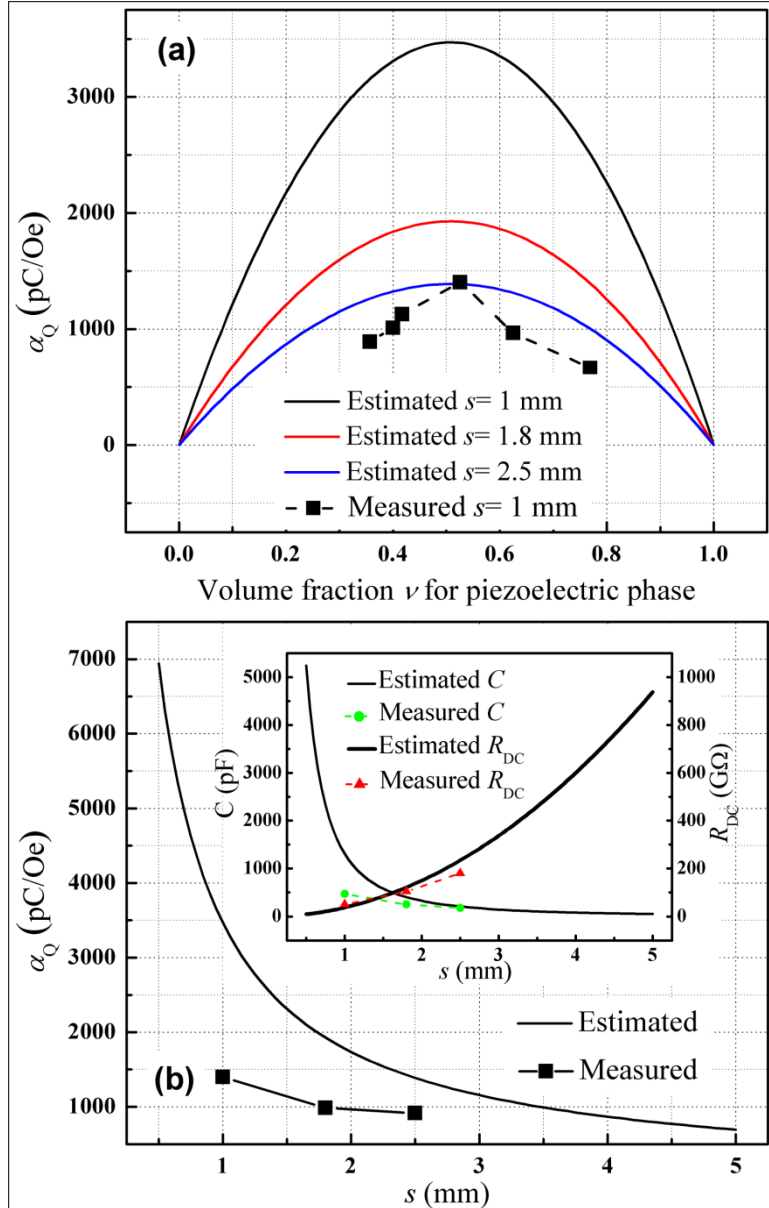


Figure 3. (a) Estimated and measured α_Q for multi-push-pull configuration Metglas/PZT-fiber composite as a function of volume fraction v for PZT-fibers phase. (b) Estimated and measured maximum α_Q at optimal v dependence on the s of Kapton® over the range of $0.5\text{mm} < s < 5 \text{ mm}$.

The inset shows the theoretical and experimental C and R_{DC} was a function of s of Kapton®, where V is the volume of the piezofibers in the ME composites (i.e., $V=L \times A$, A is the cross-area of the piezofibers). We can see that the α_Q of the multi-push-pull mode ME composites was proportional to the volume of piezofibers, and inversely proportional to the space of the ID-electrodes.

Figure 3 (a) shows α_Q for Metglas/PZT-fiber composites with various space $s=1\text{mm}$, 1.8mm and 2.5mm , which was directly plotted form Equation (5). The core composites were consisted of 5

PZT-fibers, each with dimensions of $40 \times 2 \times 0.2$ mm³. It can be seen that the variation in estimated α_Q for various space composites with piezoelectric phase thickness fraction v has the same trends as that in α_E . Also, the maximum values for $s=1$ mm, 1.8mm and 2.5mm are 3470pC/Oe, 1928pC/Oe and 1388pC/Oe, which was obvious decreased with increasing s . The corresponding experimental results for $s=1$ mm were also plotted Figure 3 (a). It was obvious that the measured α_Q obey the trends of the estimated ones, and the maximum measured value was 1402 pC/Oe at $v_m=0.53$, as predicted in Figure 3 (a). The plot of estimated and measured α_Q as a function of space was shown in Figure 3 (a). Both estimated and measured α_Q decreased with the s increase, and the measured values for $s=1$ mm, 1.8mm and 2.5mm are 1402pC/Oe, 985pC/Oe and 915pC/Oe, which was $2.48\times$, $1.96\times$ and $1.52\times$ smaller than the corresponding estimated values, respectively. The different proportional relations between the estimated and measured α_Q for various space can be contributed to difference between the theoretical and experimental capacitance. Hence, the capacitance and DC resistance was studied as a function of space, as shown in the inset of Figure 3 (b). The capacitance decreased with s increase, while the DC resistance increased with s increase. The measured capacitance values for $s=1$ mm, 1.8mm and 2.5mm are 472pF, 248pF and 181pF, which was $2.77\times$, $1.63\times$ and $1.15\times$ smaller than the corresponding estimated values. It is obvious that the proportional relations between estimated and measured capacitance can be determined from the ones in α_E and α_Q (i.e. $\alpha_Q = C \times s \times \alpha_E$). The large difference for estimated and measured α_Q or capacitance at low space might be due to an oversimplification of the theoretical model in terms of uniform polarization direction and non-dead zone in the PZT-fiber. From the inset, we can see the measured DC resistances for $s=1$ mm, 1.8mm and 2.5mm are 50GΩ, 108 GΩ and 180 GΩ, which are very close the estimated ones.

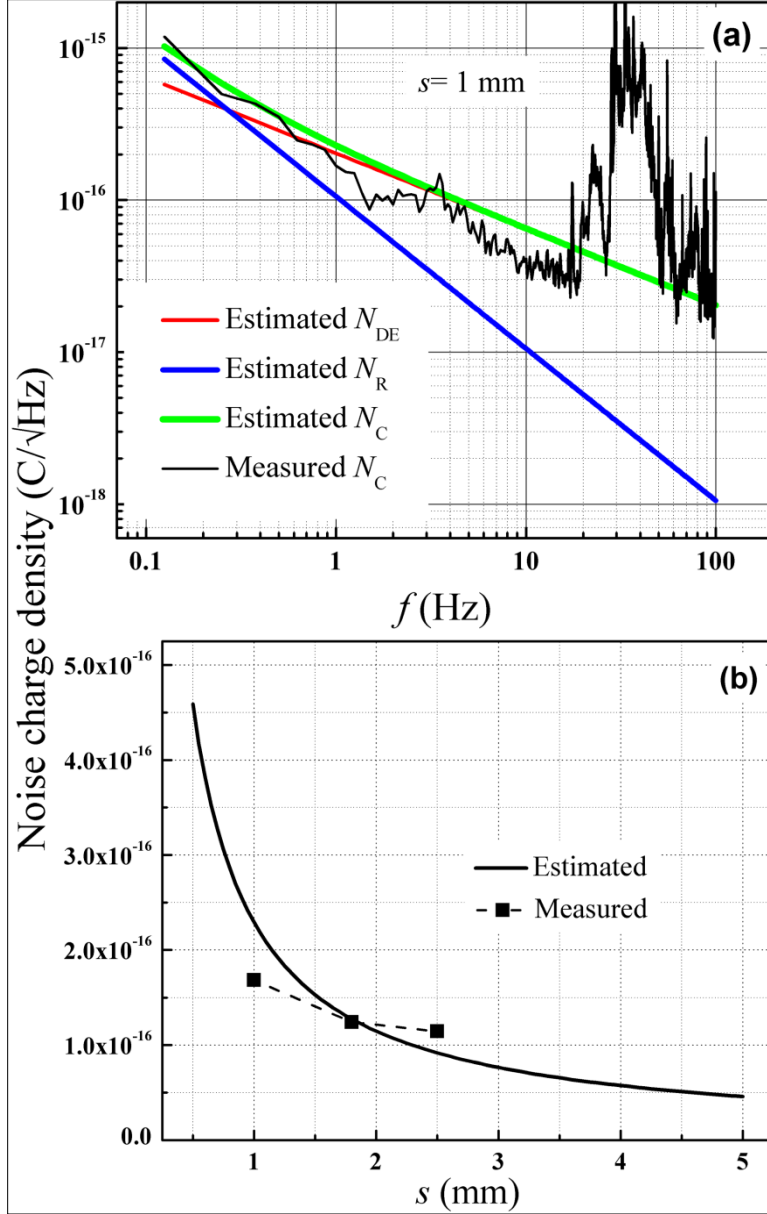


Figure 4. (a) Estimated and measured charge noise density of the Metglas/PZT-fiber sensor units, including constituent dielectric loss and DC resistance loss, over the frequency range of $0.125 \text{ Hz} < f < 100 \text{ Hz}$ for $s=1\text{mm}$. **(b)** Theoretical charge noise density as a function of s and the experimental data for the Metglas/PZT-fiber sensor.

The modeling results show that the DC resistance noise is dominant below 0.25 Hz. At interesting frequency $f=1 \text{ Hz}$, the total charge noise density was dominated by the dielectric loss noise.

The techniques described for the equivalent magnetic noise in ME composites focuses on the noise sources internal to the sensor, namely dielectric loss noise (N_{DE}) and DC leakage resistance noise (N_R). The total noise charge density contributed by the two significant noise sources can be estimated as:

$$N_t(C/\sqrt{Hz}) = \sqrt{N_{DE}^2 + N_R^2} = \sqrt{\frac{4kTC_P \tan \delta}{2\pi f} + \frac{1}{(2\pi f)^2} \frac{4kT}{R_{DC}}}, \quad (6)$$

The C_p of the sensor can be determined by the capacitance in one unit and the number of units (i.e., $C_p = \frac{^p\varepsilon_{33}V}{s^2}$), and the total dielectric loss was the same as $\tan\delta$ in one unit. The R_{DC} of the sensor is the sum values of n -units in parallel-connection (i.e., $R_{DC} = \frac{\rho s^2}{V}$, where ρ is the DC resistivity). Inputting the corresponding parameters to Equation (14), the total noise charge density (N_C) can be expressed as:

$$N_C(C/\sqrt{Hz}) = \frac{1}{s} \sqrt{\frac{4kT \tan \delta \rho s^2 V}{2\pi f} + \frac{1}{(2\pi f)^2} \frac{4kTV}{\rho}} \quad (7)$$

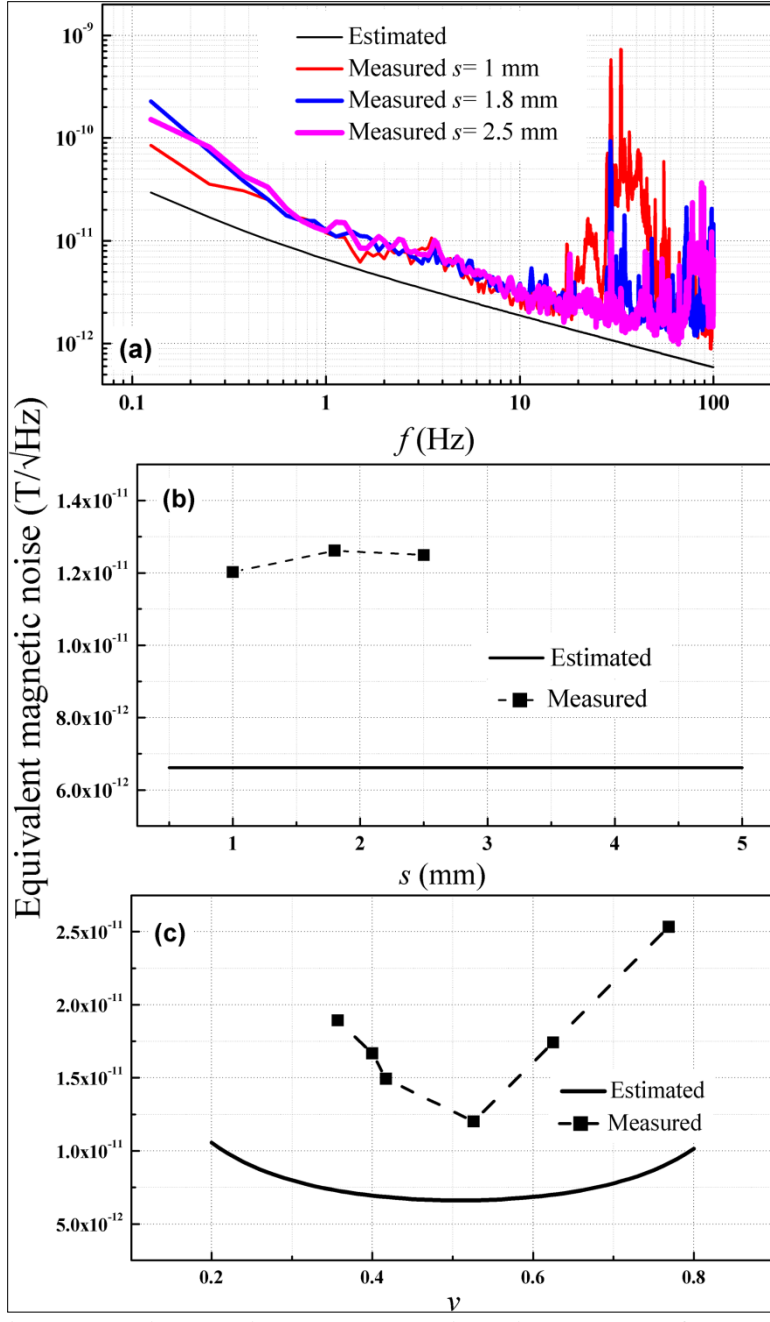


Figure 5. Theoretical modeling equivalent magnetic noise over the frequency range of 0.125 Hz < f < 100 Hz.

Experimental equivalent magnetic noise for $s = 1\text{mm}$, 1.8mm and 2.5mm over the frequency range of $0.125 \text{ Hz} < f < 100 \text{ Hz}$. (b) The estimated and measured 1 Hz equivalent magnetic noise as a function of s of Kapton®, which was directly plotted from (a). It shows estimated 1 Hz equivalent magnetic noise has no response to the s of Kapton®. (c) Theoretical 1 Hz equivalent magnetic noise vs PZT-fiber thickness ratio v and the experimental data for $s = 1\text{mm}$.

Figure 4 (a) shows the measured and modeled charge noise density of a Metglas/PZT-fiber sensor unit with $s=1\text{mm}$ in the frequency range of $0.125 < f < 100 \text{ Hz}$. The charge noise density due to $\tan\delta$ and the DC resistance were modeled based on Equation (6), using parameters listed in Table 2. Both the $\tan\delta$ and DC resistance noises contribute to the total noise floor at interesting frequency $f=1 \text{ Hz}$, but the magnitude of the $\tan\delta$ noise was $2.03\times$ larger than that of the DC resistance noise. From Equation (6), we can see the contributions of total theoretical noise charge density of Metglas/PZT-fiber sensor was only determined by the parameters of Metglas and PZT-fiber, but the magnitude of total theoretical noise charge density was inversely-proportional space of Kapton®, which was shown in Figure 4 (b). We observed similar trends in behavior of the experimental noise charge density. The noise charge density for $s=1\text{mm}$, 1.8mm and 2.5mm are $1.68\times10^{-16}\text{C}/\sqrt{\text{Hz}}$, $1.24\times10^{-16}\text{C}/\sqrt{\text{Hz}}$ and $1.14\times10^{-16}\text{C}/\sqrt{\text{Hz}}$, respectively. It also can be seen that the experimental noise charge density for $s=1\text{mm}$ was higher than the theoretical value, but the experimental noise charge density for $s=2.5\text{mm}$ was lower than the theoretical value. Because of the oversimplification of the theoretical model in terms of uniform polarization direction and non-dead zone in the PZT-fiber, resulting in a large variation in estimated and measured capacitance for $s=1\text{mm}$, in turn, the large difference between the estimated and measured capacitance lead to the modeling noise charge density is much higher than the experimental result. Whereas, the variation in estimated and measured capacitance for $s=2.5\text{mm}$ is much smaller, resulting in modeling noise charge density is even lower than the experimental result.

Then, the equivalent magnetic noise can be obtained from the α_Q of sensor and the total noise charge density:

$$\text{Equivalent magnetic noise } (T/\sqrt{\text{Hz}}) = \frac{N_c(C/\sqrt{\text{Hz}})}{\alpha_Q(C/T)} = \sqrt{\frac{4kT \tan\delta {}^p\epsilon_{33}}{2\pi fV} + \frac{1}{(2\pi f)^2} \frac{4kT}{{}^p\epsilon_{33}\alpha_E}} \quad (8)$$

It was importantly noted that the equivalent magnetic noise of the multi-push-pull mode sensor was independent on the space of the ID-electrodes, and inversely proportional to square root of the volume of piezofibers in the composites.

Figure 5 (a) presents the measured and simulated equivalent magnetic noise (in $T/\sqrt{\text{Hz}}$) of the ME Metglas/PZT-fiber laminate sensors, which was obtained through a conversion of the charge noise density and the ME charge coefficient. Except at frequencies where external vibration sources are present, the estimated and measured equivalent magnetic noises show the same trends. It can be predicted that the equivalent magnetic noise at a frequency has no response to the space of Kapton® from Equation (8), and the plot for $f=1\text{Hz}$ was shown in Figure 5 (b). The estimated 1 Hz equivalent magnetic noise for Metglas/PZT-fiber sensor was $6.6\text{pT}/\sqrt{\text{Hz}}$, and the measured 1 Hz equivalent magnetic noises for $s=1\text{mm}$, 1.8mm and 2.5mm are $12.0\text{pT}/\sqrt{\text{Hz}}$, $12.6\text{pT}/\sqrt{\text{Hz}}$ and $12.5\text{ pT}/\sqrt{\text{Hz}}$, which were directly plotted from Figure 5 (a). The difference of simulated and measured equivalent magnetic noise were resulted from the difference in ME charge coefficient and noise charge density, which have been discussed in Figure 3 (b) and Figure 4 (b), respectively. Finally, the equivalent magnetic noise dependence on the PZT-fiber thickness fraction was discussed, as shown in Figure 5 (c). It was obvious that the PZT-fiber thickness fraction has no influence to the noise charge density, but affects the ME charge

coefficient. Hence, the relationship between equivalent magnetic noise and PZT-fiber thickness fraction is inversely to the one between α_Q and PZT-fiber thickness fraction. As illustrated in Figure 3 (a), the simulated and measured α_Q reach highest value of 3470pC/Oe at $v_m=0.51$, and 1400pC/Oe at $v_m=0.53$, where the sensor exhibits the lowest estimated and measured equivalent magnetic noise, respectively.

A.3.1.2. Geometry-dependent ME coefficient

The analysis assumes small deformations, linear materials coefficients, and perfect interfacial bonding. For the solutions of Equations (1) and (2), the following boundary conditions were used:

$$\begin{aligned} {}^m S_2 &= {}^p S_2, \\ {}^m S_3 &= {}^p S_1, \\ {}^m T_3 &= {}^p T_3 = 0, \\ {}^m T_3(1-v)(1-\omega) + {}^p T_1 v \omega &= 0, \\ {}^m T_2(1-v)(1-\tau) + {}^p T_2 v \tau &= 0, \\ {}^p D_3 &= 0 \end{aligned} \quad (9)$$

where $v = \frac{t_p}{(t_p + 2t_m)}$, $\omega = \frac{w_p}{(w_p + w_m)}$, and $\tau = \frac{l_p}{(l_p + l_m)}$; w_m , t_m and l_m denote the width, thickness and length of magnetostrictive; and w_p , t_p and l_p denote the width and thickness of piezoelectric layer.

From Equations (1), (2) and (9), we can obtain

$$\begin{aligned} [{}^m s_{12} + \frac{{}^p s_{12} v \xi}{(1-v)(1-\xi)}] {}^m T_2 + [{}^m s_{11} + \frac{{}^p s_{11} v \omega}{(1-v)(1-\omega)}] {}^m T_3 - {}^p d_{31} {}^p E_3 &= -{}^m q_{33} {}^m H_3 \\ [{}^m s_{11} + \frac{{}^p s_{11} v \xi}{(1-v)(1-\xi)}] {}^m T_2 + [{}^m s_{12} + \frac{{}^p s_{12} v \omega}{(1-v)(1-\omega)}] {}^m T_3 - {}^p d_{31} {}^p E_3 &= -{}^m q_{31} {}^m H_3 \\ \frac{{}^p d_{31} v \xi}{(1-v)(1-\xi)} {}^m T_2 + \frac{{}^p d_{31} v \omega}{(1-v)(1-\omega)} {}^m T_3 - {}^p \epsilon_{33} {}^p E_3 &= 0. \end{aligned} \quad (10)$$

Next, we define the effective compliance coefficients as:

$$\begin{aligned} A &= [{}^m s_{12} + \frac{{}^p s_{12} v \xi}{(1-v)(1-\xi)}]; \quad B = [{}^m s_{11} + \frac{{}^p s_{11} v \omega}{(1-v)(1-\omega)}]; \quad C = [{}^m s_{11} + \frac{{}^p s_{11} v \xi}{(1-v)(1-\xi)}]; \\ D &= [{}^m s_{12} + \frac{{}^p s_{12} v \omega}{(1-v)(1-\omega)}]; \end{aligned} \quad (11)$$

and the effective piezoelectric coefficient as:

$$X = \frac{{}^p d_{31} v \xi}{(1-v)(1-\xi)}; Y = \frac{{}^p d_{31} v \omega}{(1-v)(1-\omega)}. \quad (12)$$

From Equation (10) and the above definitions, the ME coefficient in terms of the electric field ($E_3 = v {}^p E_3$) response to an applied magnetic field (H_3) can be expressed as:

$$\alpha_{ME} = -({}^m q_{33} v) \times \frac{(YC - XD)}{-BX {}^p d_{31} + AY {}^p d_{31} + BC {}^p \epsilon_{33} - YC {}^p d_{31} - AD {}^p \epsilon_{33} + XD {}^p d_{31}} \quad (13)$$

$$-({}^m q_{31} v) \times \frac{BX - AY}{-BX {}^p d_{31} + AY {}^p d_{31} + BC {}^p \epsilon_{33} - YC {}^p d_{31} - AD {}^p \epsilon_{33} + XD {}^p d_{31}}.$$

Harshe and Carman *et al.* obtained an expression for the L-T mode ME coefficient of the form

$$\alpha_{E,L-T} = \frac{-{}^p d_{31} (1-v)v ({}^m q_{31} + {}^m q_{33})}{{}^p \epsilon_{33} [({}^m s_{11} + {}^m s_{12})(1-v) + ({}^p s_{11} + {}^p s_{12})v] - 2({}^p d_{31})^2 v}. \quad (14)$$

The above equation corresponds to a special case of our geometry-dependent ME theory, in which one assumes $w_p=w_m$ and $l_p=l_m$ (i.e. $\xi=0.5$ and $\omega=0.5$). Thus, for the special case, the effective coefficients have the relationships of $A=D$, $B=C$, and $X=Y$.

In this section, the theoretical model is validated, via comparisons to other modeling results and to experimental data. Based on the model, analysis can be done on the effects of the parameter of the composite components, and on variation in geometry of the components. We will then compare our predictions to other theoretical models, and observe the general trends of the ME coefficient using the same materials with property parameters given in Table 3. We analyzed the theoretical models for magnetostrictive Metglas and piezoelectric PMN-PT laminates.

Table 3. Material parameters Metglas, and PMN-PT used for theoretical modeling.

Materials	${}^m s_{11}$ or ${}^p s_{11}$ ($10^{-12} \text{ m}^2/\text{N}$)	${}^m s_{12}$ or ${}^p s_{12}$ ($10^{-12} \text{ m}^2/\text{N}$)	${}^m q_{12}$ ($10^{-9} \text{ m}/\text{A}$)	${}^m q_{11}$ ($10^{-9} \text{ m}/\text{A}$)	${}^p d_{31}$ ($10^{-12} \text{ C}/\text{N}$)	ϵ_{33}/ϵ_0
Metglas	10	-5.2	-21.3	50.3	-	
PMN-PT	57.3	-34.1	-	-	-790	6650

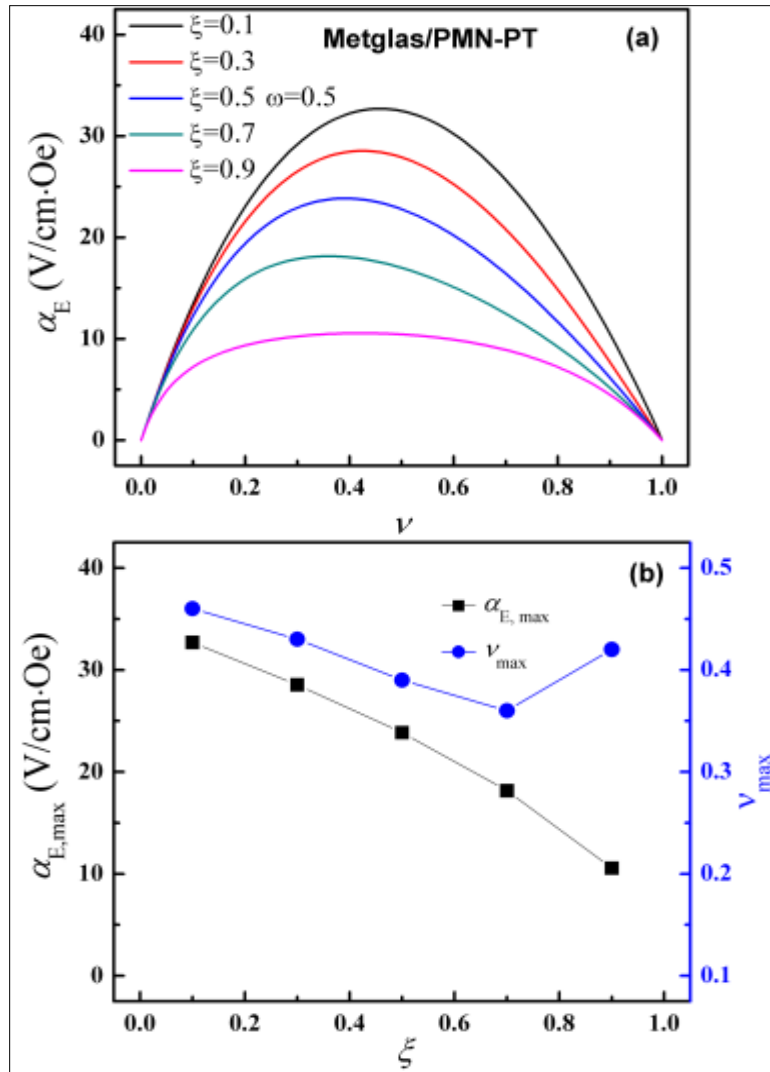


Figure 6. (a) Predicted dependence of α_E on thickness fraction v under various length fractions ξ and width fractions $\omega = 0.5$ (i.e. $w_p=w_m$) for the piezoelectric phase in the Metglas/PMN-PT multilayer composite. (b) Variation with ξ of maximum $\alpha_{E,\max}$ and the corresponding v_{\max} under $\omega = 0.5$.

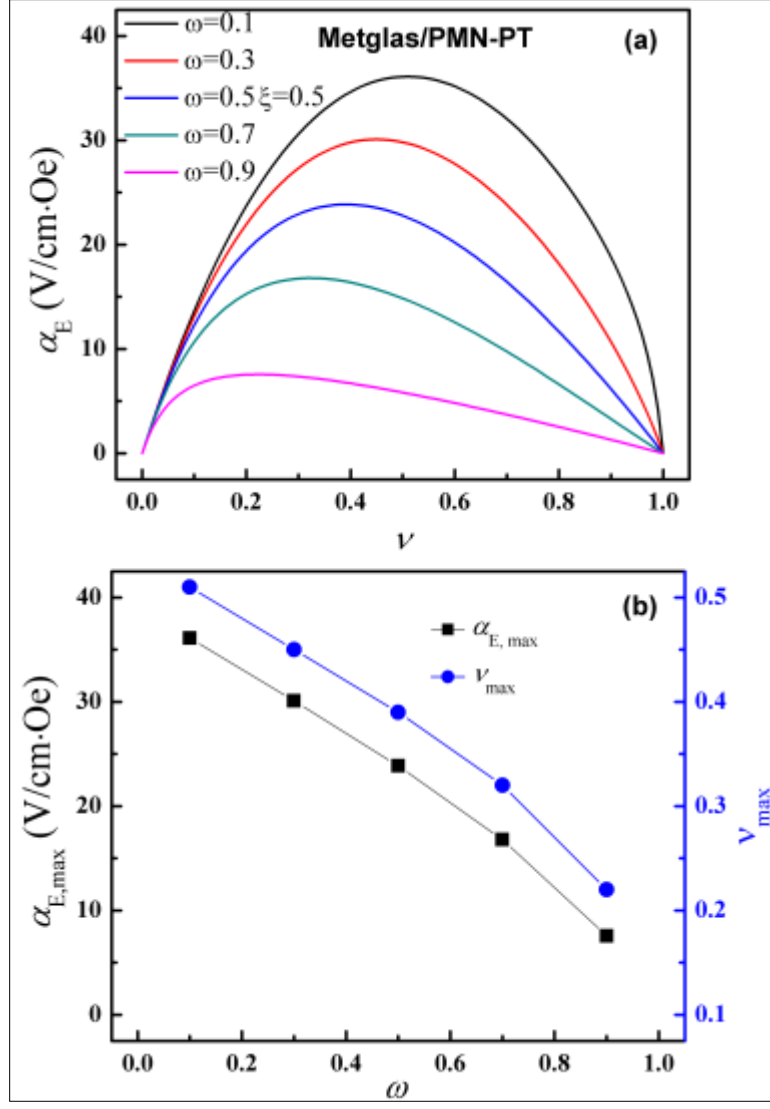


Figure 7. (a) Predicted dependence of α_E on thickness fraction v under various width fractions ω and length fractions $\xi=0.5$ (i.e. $l_p=l_m$) for the piezoelectric phase in the Metglas/PMN-PT multilayer composite. (b) Variation with ω of maximum $\alpha_{E,\max}$ and the corresponding v_{\max} under $\xi=0.5$.

Representative results for $\xi=0.5$ are presented in Figure 6 (a). The maximum theoretical value of α_E was as high as 23.9 V/cm·Oe for $\xi=0.5$ and $\omega=0.5$ under the constant of $v_{\max}=0.39$. The significant enhancement in α_E for Metglas/PMN-PT was due to the higher piezomagnetic coefficient for Metglas and the higher piezoelectric coefficient for PMN-PT. The variation in $\alpha_{E,\max}$ and the corresponding v_{\max} with ω is shown in Figure 6 (b). Both $\alpha_{E,\max}$ and corresponding v_{\max} , dramatically decreased with increase of ω .

Figure 7 (a) shows α_E as function of PMN-PT thickness fraction v for various length fraction ξ under a width fraction of $\omega=0.5$. The variation in $\alpha_{E,\max}$ and v_{\max} with ξ is shown in Figure 7 (b), which was not as significant as that with ω . An interesting observation is that the plot for $\xi=0.9$

was much flatter than the other composite geometries, with relatively higher values of α_E maintained for $0.2 < v < 0.8$.

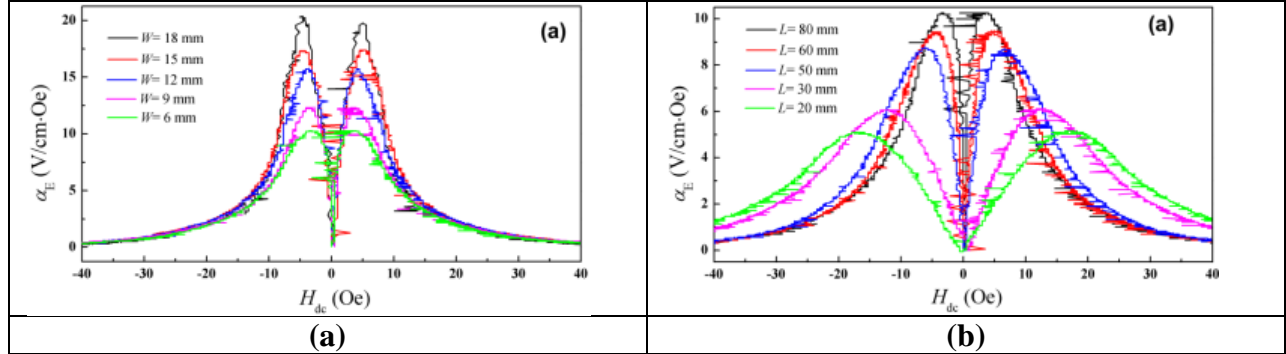


Figure 8. Experimental α_E as a function of H_{dc} for various widths and lengths of Metglas.

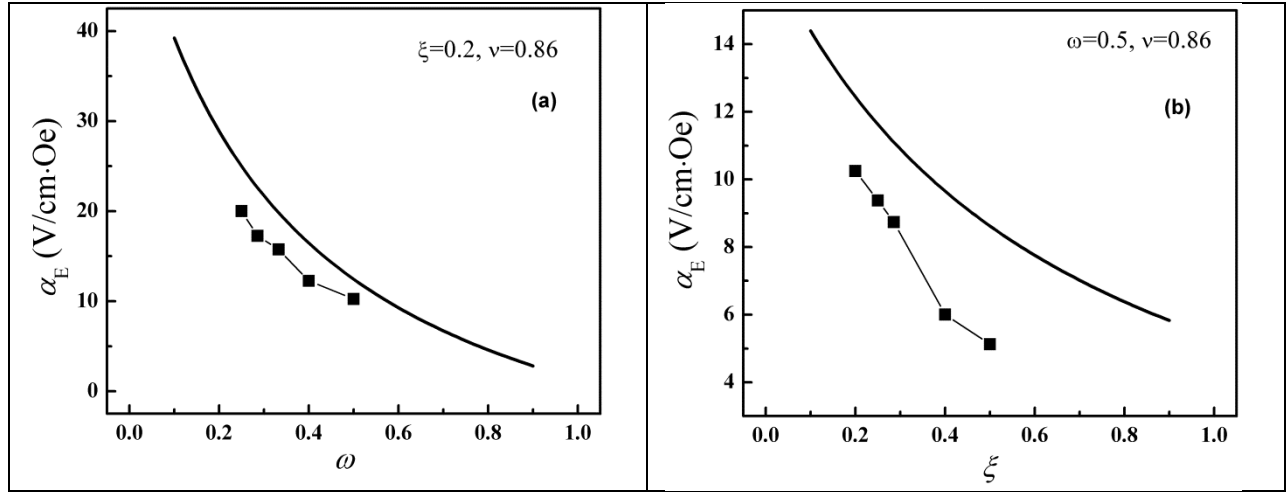


Figure 9. Comparison of theoretical (solid line) and experimental (line and symbol) α_E as function of: (a) width fraction ω under a length fraction $\xi=0.2$ and a thickness fraction $v=0.86$; (b) length fraction ξ under a width fraction $\omega=0.5$ and a thickness fraction $v=0.86$.

It is important to compare the theoretical predictions with experimental results. However, there have been few systematic studies of ME coefficient changes with component geometry. In case of experimental error due to sample fabrication, only one Metglas/PMN-PT composite was made, in which a thickness poled PMN-PT piezoelectric single crystal layer ($20 \times 6 \times 0.3 \text{ mm}^3$ with a $\parallel 10\parallel$ direction along thickness) was sandwiched between two-layer longitudinally magnetized Metglas foils ($80 \times 18 \times 0.025 \text{ mm}^3$). After sample fabrication, the width of the Metglas foil in this sample was successively trimmed to dimensions of 15 mm, 12 mm, 9 mm and 6 mm. The ME coefficient was characterized as function of H_{dc} for each width of the Metglas layers, as shown in Figure 8 (a). After testing the ME coefficient for the sample for a Metglas width of $w_m=6 \text{ mm}$, the length of Metglas was successively trimmed to from 80 mm to 60mm, 50 mm, 40 mm, 30 mm, and 20 mm, as shown in Figure 8 (b). At each length of the Metglas foils, the ME coefficient was measured. For these studies of changes in width, the thickness and length fractions of PMN-PT were $v=0.86$ and $\xi=0.2$ where the width fraction ω was designed to changes by trimming from 0.25 to 0.29, 0.33, 0.4 and 0.5. Figure 9 (a) shows the theoretical and

experimental values of α_E as function of ω for these various geometries: where the values of α_E correspond to the maximum ones in α_E vs H_{DC} . It can be seen that the trend of theoretical and experimental values of α_E exhibit excellent agreement, and that the prediction is about a factor of $1.5 \times$ larger than the experimental data. During these length change investigations, the values of $v=0.86$ and $\omega=0.5$ were held constant, and the length fraction was designed to successively change with trimming from 0.2 to 0.25, 0.29, 0.4 and 0.5. In this case, the changes in the theoretical and experimental values of α_E with ζ are shown in Figure 9 (b). Similar trends for predicted and measured values can be seen.

A.3.1.3. Bending mode sensors

We have modeled the ME coefficient in a bending mode magnetostrictive/piezoelectric laminate composites. A general expression for ME coefficient was obtained for N layer laminate composites under static and resonance frequencies. Compared with previously reported theoretical modeling, this model was closer to experimental results. In particular, new trends of ME coefficient were observed, which was significant important to sensor design for noise floor reduction by modulation in Phase II

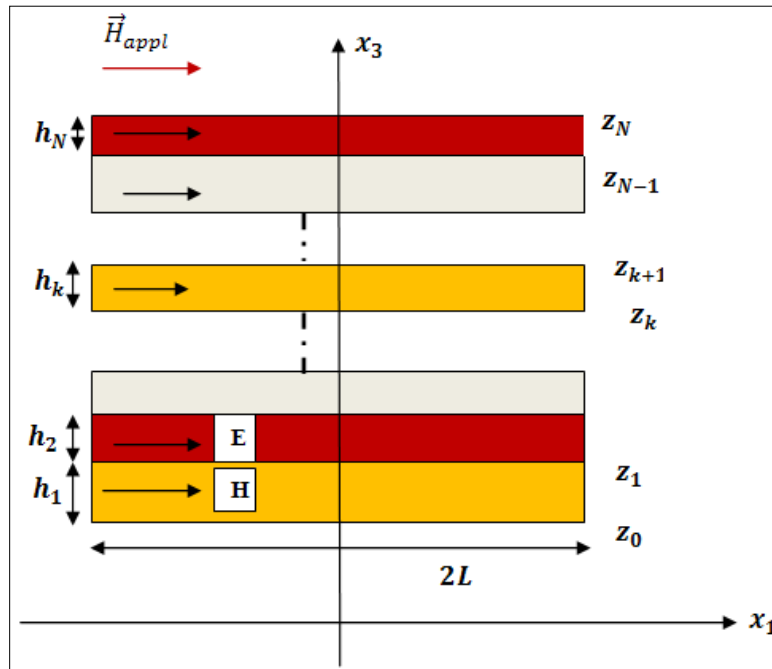


Figure 10. Magneto electric multilayer laminated composite.

The arrows indicate the direction of polarization in piezoelectric layer, applied magnetic field and induced magnetic field in ferromagnetic layer.

Consider an arbitrary laminated structure of length $2L$ and N layers. In this case, there is no middle plane of the bar that can serve as a plane of symmetry. For simplicity we will assume that the multilayer structure is two dimensional (i.e., a bar structure). In this case, the field functions depend only on the space coordinates x_1 and x_3 . The geometry and the magnetic loads are represented schematically in Figure 10. The x_1 axis in Cartesian coordinates is directed along the bar length, the x_2 axis is directed across the width, and the x_3 axis is orthogonal to them both. It

is assumed that the piezoelectric layers are poled in the x_1 direction. It should be mentioned that the proposed theory can be successfully applied to multilayer structures when the polarization direction of the piezoelectric layers is along the x_3 direction, or when some of them are along x_1 and along x_3 or x_2 .

We then assumed that the total thickness of the multilayers can be given by

$$\mathbf{h} = \sum_{k=1}^N \mathbf{h}_k = \sum_{k=1}^{N_p} \mathbf{h}_{kp} + \sum_{k=1}^{N_m} \mathbf{h}_{km} + \sum_{k=1}^{N_e} \mathbf{h}_{ke}, \quad (15)$$

where $N = N_p + N_m + N_e$ is the total number of layers; N_p is the number of ferroelectric layers; N_m is the number of ferromagnetic layers; N_e is the number of pure elastic ones; h_k ($k = 1, N$) is the thickness of the k^{th} layer; h_{kp} ($k = 1, N_p$) the thickness of the ferroelectric k^{th} layer; h_{km} ($k = 1, N_m$) the thickness of the ferromagnetic k^{th} layer; and h_{ke} ($k = 1, N_e$) the thickness of the elastic k^{th} layer. Later, we will use the following notations as well: $H_p = \sum_{k=1}^{N_p} h_{kp}$ which is the total thickness of the piezoelectric layers, $H_m = \sum_{k=1}^{N_m} h_{km}$ which is the total thickness of the piezomagnetic layers, $H_e = \sum_{k=1}^{N_e} h_{ke}$ which is the total thickness of the elastic layers, and $H = h = H_p + H_m + H_e$ which is the total thickness of the composite.

Basic assumptions and restrictions

We then make the following assumptions and restrictions:

- I) The layers are perfectly bonded together (i.e., no cracks or other type of imperfections).
- II) The Material of each layer is linearly elastic.
- III) Each layer is of uniform thickness.
- IV) The strains and displacements are small.
- IV) The length of the composite is much greater than the total thickness, i. e., $L \gg h$.
- V) The transverse shear stresses on the top and bottom surfaces of the laminate are zero.
- VI) Bernoulli's (Kirchhoff's) hypothesis are valid for any layer, i.e. the displacements in x_1 and x_3 directions can be given as

$$\begin{cases} \mathbf{u}_1(x_1, x_3) = \mathbf{u}(x_1) - x_3 \frac{\partial \mathbf{w}}{\partial x_1} \\ \mathbf{u}_3(x_1, x_3) = \mathbf{w}(x_1) \end{cases} \quad (16)$$

We also assume that the specimen was poled along the longitudinal (L) direction (i.e., x_1 -axis). The dc and ac magnetic fields were then applied along the L direction and across the planes of the contacts (\vec{H}_{appL}). The magnetostrictive and piezoelectric layers were assumed to be bonded together with an elastic bonding material-layer of a finite thickness.

Due to magnetostriction, an alternating magnetic field induces vibrations in the magnetostrictive layers, which propagates both across and along the specimen. Mechanical vibrations of the ferrite medium are transferred to the piezoelectric component, via mechanical bonding, wherein an electric field is induced by the piezoelectric effect. Our further considerations will be a case of coupled bending and longitudinal vibrations of this multilayer structure.

With the above assumptions of I) to VII), the equations of motions and Maxwell's electro-magneto static equations, the elastic, magnetic and electro elastic layers can be written as follows:

$$\mathbf{T}_{ij,i}^{(k)} = \rho_k \frac{\partial^2 \mathbf{u}_j^{(k)}}{\partial t^2} \quad (k = 1, 2, \dots N) \quad (17)$$

$$B_{i,i}^{(k)} = 0, \quad e_{ijm} H_{j,m}^{(k)} = 0 \quad (k = 1, 2, \dots N) \quad (18)$$

$$\mathbf{D}_{i,i}^{(k)} = \mathbf{0}, \quad e_{ijm} \mathbf{E}_{j,m}^{(k)} = \mathbf{0}, \quad (k = 1, 2, \dots N); \quad (19)$$

where $F_{i,i} = \frac{\partial F}{\partial x_i}$; e_{ijm} is the permutation symbol with $e_{ijm} = 1$ or -1 depending on whether the indices are in cyclic or anticyclic order, respectively and $e_{ijm} = 0$, otherwise, the superscript in parentheses denotes the number of the layer. The constitutive equations for the magnetostrictive, piezoelectric and pure elastic layers can then be expressed in the following forms:

Piezoelectric media

$$\begin{cases} S_{ip}^{(k)} = s_{pij}^{(k)} T_{jp}^{(k)} + d_{mi}^{(k)} E_m^{(k)} \\ D_{mp}^{(k)} = d_{mi}^{(k)} T_{ip}^{(k)} + \varepsilon_{mn}^{(k)} E_n^{(k)} \end{cases} \quad (k = 1, 2, \dots N_p; i, j = 1, \dots 6; m, n = 1, 2, 3); \quad (20)$$

Magnetostrictive media

$$\begin{cases} S_{im}^{(k)} = s_{mij}^{(k)} T_{jm}^{(k)} + q_{mi}^{(k)} H_m^{(k)} \\ B_{mm}^{(k)} = q_{mi}^{(k)} T_{im}^{(k)} + \mu_{mn}^{(k)} H_n^{(k)} \end{cases} \quad (k = 1, 2, \dots N_m; i, j = 1, \dots 6; m, n = 1, 2, 3); \quad (21)$$

Pure elastic media

$$S_{ij}^{(k)} = s_{Eij}^{(k)} T_{ji}^{(k)} \quad (k = 1, 2, \dots N_E; i, j = 1, \dots 6). \quad (22)$$

In Equations (20-22), we introduced the following notations: S_i and T_i are the strain and stress tensor components; E_m and D_m are the vector components of electric field and displacement; H_m and B_m are the vector components of magnetic field and induction; $s_{pij}^{(k)}$, $s_{mij}^{(k)}$ and $s_{Eij}^{(k)}$ are the compliance matrixes of the piezoelectric, piezomagnetic and pure elastic media, respectively; q_{mi} and d_{mi} are the piezomagnetic and piezoelectric coefficients; ε_{km} and μ_{km} are the dielectric permittivity and magnetic permeability matrixes, respectively. The sub indexes P , M and E correspond to the piezoelectric and piezomagnetic phases and substrate (i.e., pure elastic media) respectively; where the superscripts in the parentheses denote the number of the layer. If material of the layer is not specified then for compliances we will use notation $s_{ij}^{(k)}$. We assume that the symmetry of the piezoelectric phase is ∞m , and that of the piezomagnetic one is cubic.

As in elastic bar theory, the stresses T_2 and T_3 in the constitutive relations can be neglected compared to the stress T_1 , and it is assumed that the magneto-electro-elastic state does not depend on the x_2 coordinate. Within the scope of Bernoulli's (Kirchhoff's) hypothesis of beam bending theory only the strain S_1 is induced in a beam, given as

$$S_1 = \frac{\partial u_1(x_1, x_3)}{\partial x_1} = \frac{\partial u(x_1)}{\partial x_1} - x_3 \frac{\partial^2 w}{\partial x_1^2} = \varepsilon - x_3 \kappa; \quad (23)$$

where $\varepsilon = \frac{\partial u(x_1)}{\partial x_1}$ is a strain along the neutral axis and $\kappa = \frac{\partial^2 w}{\partial x_1^2}$ is a bending of the neutral axis.

Equation (A9) denotes the linear behavior of the strain S_1 over the entire cross section of the bending beam, whereas x_3 defines the distance from the neutral axis.

Boundary conditions

We next provide the most frequently used boundary conditions for the electrical quantities. If there are no electrodes on the surfaces of the bar and the layer on their surfaces is in contact with a non-conducting medium (i.e., insulating glue or a vacuum or air), the component of the electric induction vector D_3 normal to these surfaces equals zero:

$$D_3 = 0 \quad (24)$$

For the electrical field, magnetic field and magnetic induction components, the following boundary conditions should be satisfied

$$\mathbf{E}_1^{(k)} \Big|_{x_3=z_k} = \mathbf{E}_1^{(k+1)} \Big|_{x_3=z_k}; \mathbf{H}_1^{(k)} \Big|_{x_3=z_k} = \mathbf{H}_1^{(k+1)} \Big|_{x_3=z_k}; \mathbf{B}_3^{(k)} \Big|_{x_3=z_k} = \mathbf{B}_3^{(k+1)} \Big|_{x_3=z_k}; \quad (25)$$

where ($k = 0, 1, \dots, N + 1$) and the components with “0” or “N+1” superscript in parentheses indicate electromagnetic components with surrounding area to the laminate. Later, it will be assumed that the surrounding area is a vacuum. If the electrodes are in closed circuit condition with a known complex conductivity $Y = Y_0 + iY_1$, then

$$\mathbf{I} = \iint \frac{d\mathbf{D}_1}{dt} d\Gamma = 2VY; \quad (26)$$

where Γ is the surface over of one of the electrodes, V is an applied voltage and I is the magnitude of the current. If the electrodes are in open-circuit conditions, then the following integral condition for the current is satisfied

$$\mathbf{I} = \iint \frac{d\mathbf{D}_1}{dt} d\Gamma = \mathbf{0}. \quad (27)$$

The mechanical load on the surface is given that on the bar faces, namely

$$\mathbf{T}_6^{(N)} \Big|_{x_3=z_N} = \mathbf{q}_1^+; \mathbf{T}_6^{(N)} \Big|_{x_3=z_0} = \mathbf{q}_1^-; \mathbf{T}_3^{(N)} \Big|_{x_3=z_N} = \mathbf{q}_3^+; \mathbf{T}_3^{(N)} \Big|_{x_3=z_0} = \mathbf{q}_3^-; \quad (28)$$

where q_i^\pm are the forces applied on the surfaces $x_3 = z_N$ and $x_3 = z_0$. The boundary conditions on the composite edges should also be included as well. We will provide these conditions later in a paragraph related to vibration of multilayer composite.

In order to construct a theory of ME bars, some additional assumptions regarding the electrical and magnetic quantities must be made. As in the theory of piezoelectric shells and plates, the content of the hypotheses assumed depends on the electrical conditions on the surfaces of the ME layers. For the piezoelectric layers, we will make the following assumptions, which were previously justified by an asymptotic method for single-layer electro elastic plates and shells:

The electric field component $E_1^{(k)}(x_1, x_3)$ is not a function of the thickness coordinate x_3 , i.e.

$$E_1^{(k)}(x_1, x_3) = E_0^{(k)}(x_1) = E_0(x_1). \quad (29)$$

The magnetic field component $H_1^{(k)}(x_1, x_3)$ is not function of the thickness coordinate x_3 , i.e.

$$H_1^{(k)}(x_1, x_3) = H_0^{(k)}(x_1) = H_0(x_1). \quad (30)$$

The third component of magnetic induction is zero, i.e.

$$B_3^{(k)}(x_1, x_3) \equiv 0. \quad (31)$$

Note that due to assumption (29-31) the boundary conditions given in Eq (25) is automatically fulfilled. These three assumptions can be derived by the asymptotic integration of Maxwell's equations (18-19) in composite layers and surrounding areas. These assumptions are the first terms in an asymptotic representation.

Due to representation Equation (23), the induced stresses in the k^{th} layers of the various phases can be expressed as:

Piezoelectric layer

$$T_{1P}^{(k)} = \frac{1}{s_{P11}^{(k)}} (\varepsilon - x_3 \kappa - d_{11}^{(k)} E_1^{(k)}) \quad (k = 1, 2, \dots, N_P) \quad (A11)$$

Piezomagnetic layer

$$T_{1M}^{(k)} = \frac{1}{s_{M11}^{(k)}} (\varepsilon - x_3 \kappa - q_{11}^{(k)} H_1^{(k)}) \quad (k = 1, 2, \dots, N_M) \quad (A12)$$

Elastic layer

$$T_{1E}^{(k)} = \frac{1}{s_{E11}^{(k)}} (\varepsilon - x_3 \kappa) \quad (k = 1, 2, \dots, N_E). \quad (A13)$$

By integrating the stresses over the thickness, we can obtain the resultant tangential force T_1 in the following form

$$T_1 = \sum_{k=1}^N \int_{z_{k-1}}^{z_k} T_1^{(k)}(x_1, x_3) d x_3 = \sum_{k=1}^{N_P} \int_{z_{k-1}^P}^{z_k^P} T_{1P}^{(k)}(x_1, x_3) d x_3 + \sum_{k=1}^{N_M} \int_{z_{k-1}^M}^{z_k^M} T_{1M}^{(k)}(x_1, x_3) d x_3 + \sum_{k=1}^{N_E} \int_{z_{k-1}^E}^{z_k^E} T_{1E}^{(k)}(x_1, x_3) d x_3. \quad (35)$$

Using Equations (32-34), the expression in (35) for T_1 results in:

$$\mathbf{T}_1 = \mathbf{A}\boldsymbol{\varepsilon} - \mathbf{B}\boldsymbol{\kappa} - \mathbf{A}_{01}\mathbf{E}_0 - \mathbf{A}_{02}\mathbf{H}_0; \quad (36)$$

Where

$$\begin{aligned} \mathbf{A} &= \sum_{k=1}^{N_P} \frac{\mathbf{h}_{kP}}{s_{P11}^{(k)}} + \sum_{k=1}^{N_M} \frac{\mathbf{h}_{kM}}{s_{M11}^{(k)}} + \sum_{k=1}^{N_E} \frac{\mathbf{h}_{kE}}{s_{E11}^{(k)}}, \\ \mathbf{B} &= \sum_{k=1}^{N_P} \frac{1}{2s_{P11}^{(k)}} [(z_k^P)^2 - (z_{k-1}^P)^2] + \sum_{k=1}^{N_M} \frac{1}{2s_{M11}^{(k)}} [(z_k^M)^2 - (z_{k-1}^M)^2] + \sum_{k=1}^{N_E} \frac{1}{2s_{E11}^{(k)}} [(z_k^E)^2 - (z_{k-1}^E)^2], \\ \mathbf{A}_{01} &= \sum_{k=1}^{N_P} \frac{d_{11}^{(k)} \mathbf{h}_{kP}}{s_{P11}^{(k)}}, \quad \mathbf{A}_{02} = \sum_{k=1}^{N_P} \frac{q_{11}^{(k)} \mathbf{h}_{kM}}{s_{M11}^{(k)}} \end{aligned} \quad (37)$$

The resulting bending moment M_1 is calculated according to

$$M_1 = \sum_{k=1}^N \int_{z_{k-1}}^{z_k} x_3 T_1^{(k)}(x_1, x_3) d x_3 = \sum_{k=1}^{N_P} \int_{z_{k-1}^P}^{z_k^P} x_3 T_{1P}^{(k)}(x_1, x_3) d x_3 + \sum_{k=1}^{N_M} \int_{z_{k-1}^M}^{z_k^M} x_3 T_{1M}^{(k)}(x_1, x_3) d x_3 + \sum_{k=1}^{N_E} \int_{z_{k-1}^E}^{z_k^E} x_3 T_{1E}^{(k)}(x_1, x_3) d x_3. \quad (38)$$

Using (20)-(22), the expression in (26) for M_1 results in

$$\mathbf{M}_1 = \mathbf{B}\boldsymbol{\varepsilon} - \mathbf{D}\boldsymbol{\kappa} - \mathbf{C}_1\mathbf{E}_0 - \mathbf{C}_2\mathbf{H}_0; \quad (39)$$

Where

$$D = \sum_{k=1}^{N_P} \frac{1}{3s_{P11}^{(k)}} [(z_k^P)^3 - (z_{k-1}^P)^3] + \sum_{k=1}^{N_M} \frac{1}{3s_{M11}^{(k)}} [(z_k^M)^3 - (z_{k-1}^M)^3] + \sum_{k=1}^{N_E} \frac{1}{3s_{E11}^{(k)}} [(z_k^E)^3 - (z_{k-1}^E)^3] \quad (40)$$

$$\mathbf{C}_1 = \sum_{k=1}^{N_P} \frac{d_{11}^{(k)}}{2s_{P11}^{(k)}} [(z_k^P)^2 - (z_{k-1}^P)^2], \quad \mathbf{C}_2 = \sum_{k=1}^{N_M} \frac{q_{11}^{(k)}}{2s_{M11}^{(k)}} [(z_k^M)^2 - (z_{k-1}^M)^2]. \quad (41)$$

In the context of the above simplification, the open-circuit condition can be written in the following form

$$\sum_{k=1}^{N_P} \int_{z_{k-1}^P}^{z_k^P} \mathbf{D}_1^{(k)}(x_1, x_3) d x_3 = \mathbf{0}. \quad (42)$$

Using Equations (32-34) and the second equation in (21), the expression (42) results in:

$$C_3 E_0 + C_4 \varepsilon - C_5 \kappa = 0; \quad (43)$$

Where

$$\begin{aligned} C_3 &= \sum_{k=1}^{N_P} \varepsilon_{11}^{(k)} (1 - K_{1k}^2) h_{kP}, \quad C_4 = \sum_{k=1}^{N_P} \varepsilon_{11}^{(k)} r_{1k} h_{kP}, \\ C_5 &= \sum_{k=1}^{N_P} \frac{\varepsilon_{11}^{(k)} r_{1k}}{2} [(z_k^P)^2 - (z_{k-1}^P)^2], \quad K_{1k}^2 = \frac{(d_{11}^{(k)})^2}{\varepsilon_{11}^{(k)} s_{P11}^{(k)}}, \quad r_{1k} = \frac{d_{11}^{(k)}}{\varepsilon_{11}^{(k)} s_{P11}^{(k)}}. \end{aligned} \quad (44)$$

We then combine Equations (24), (27) and (31) together for further use

$$\begin{cases} A\varepsilon - B\kappa - A_{01}E_0 - A_{02}H_0 = T_1 \\ B\varepsilon - D\kappa - C_1E_0 - C_2H_0 = M_1 \\ C_3E_0 + C_4\varepsilon - C_5\kappa = 0. \end{cases} \quad (45)$$

Note that ε , κ , E_0 and H_0 are function of x_1 and time t . These unknown functions should be determined using the motion equation of (3), Maxwell's Equations of (18-19) and the boundary conditions on composite edges of $x_1 = \pm L$. From Equation (45), we can see that if the coefficient $B \neq 0$, then bending term κ can produce a tension T_1 and the strain ε can produce a bending moment M_1 , in other words, the bending and longitudinal modes are coupled. These two modes can be decoupled only when $B = 0$.

Next, note that the coefficient B is always zero for symmetrically laminated composites. For bar structures, it is well-known that the electro-elasticity relations can be simplified by choosing a position along the neutral axis so that the coefficient B in (45) vanishes:

$$B = \sum_{k=1}^{N_P} \frac{1}{2s_{P11}^{(k)}} [(z_k^P)^2 - (z_{k-1}^P)^2] + \sum_{k=1}^{N_M} \frac{1}{2s_{M11}^{(k)}} [(z_k^M)^2 - (z_{k-1}^M)^2] + \sum_{k=1}^{N_E} \frac{1}{2s_{E11}^{(k)}} [(z_k^E)^2 - (z_{k-1}^E)^2] = 0. \quad (46)$$

From this expression we can find z_0 as

$$z_0 = - \frac{\sum_{k=1}^{N_P} (h_{kP}^2 / s_{P11}^{(k)}) + \sum_{k=1}^{N_M} (h_{kM}^2 / s_{M11}^{(k)}) + \sum_{k=1}^{N_E} (h_{kE}^2 / s_{E11}^{(k)}) + 2 \sum_{k=2}^N (h_k / s_{11}^{(k)}) \sum_{k=1}^{N-1} h_k}{2 \sum_{k=1}^{N_P} (h_{kP} / s_{P11}^{(k)}) + 2 \sum_{k=1}^{N_M} (h_{kM} / s_{M11}^{(k)}) + 2 \sum_{k=1}^{N_E} (h_{kE} / s_{E11}^{(k)})}. \quad (47)$$

For bilayers, the position of the neutral axes is determined as

$$z_0 = - \frac{h_1^2 / s_{11}^{(1)} + h_2^2 / s_{11}^{(2)} + 2h_1 h_2 / s_{11}^{(2)}}{2(h_1 / s_{11}^{(1)} + h_{12} / s_{11}^{(2)})}. \quad (48)$$

Once the tension strain ε and bending κ are determined, the axial stress T_1 and bending moment M_1 can be found from Equation (45). If we neglect the edge effects of the composite (i.e., composite is long) and assume the state is quasi-static (i.e., no time dependence), then solutions of the motion equation (3) and Maxwell's Equations (18-19) can be obtained as $= \text{const}$, $\kappa = \text{const}$, $E_0 = \text{const}$ and $H_0 = \text{const}$.

Using the boundary conditions that the edges of composite are free of stresses and applied moments, then it can be determined that $T_1 = 0, M_1 = 0$.

The first two equations of (45) allow us to determine ε and κ in terms of E_0 and H_0 . Then using the 3rd equation of (33), we can express E_0 in terms of H_0 as

$$E_0 = -\frac{(C_2A-BA_{02})(BC_4-C_5A)+A_{02}C_4(B^2-AD)}{(B^2-AD)(C_3A+A_{01}C_4)+(C_1A-BA_{01})(BC_4-C_5A)} H_0. \quad (49)$$

Equation (49) expresses the relationship between the electric and magnetic fields at a fixed point in the piezoelectric media.

Definition of ME coefficient

We can define the ME voltage coefficient in a piezoelectric layer as

$$\alpha = \frac{\delta E}{\delta H}; \quad (50)$$

where δE is the electric field in the piezoelectric layer and δH is an applied magnetic field. The effective ME coefficient can then be defined as

$$\alpha_{eff} = \alpha_{ME} = \frac{1}{V} \int \alpha dV_P; \quad (51)$$

where V is the total volume of the composite multilayer; and V_P is the total volume of only the piezoelectric phase.

Using Equation (49), we can obtain

$$\alpha = -\frac{(C_2A-BA_{02})(BC_4-C_5A)+A_{02}C_4(B^2-AD)}{(B^2-AD)(C_3A+A_{01}C_4)+(C_1A-BA_{01})(BC_4-C_5A)}. \quad (52)$$

By applying (51) to (50), the final form for the effective ME coefficient becomes

$$\alpha_{ME} = -\frac{(C_2A-BA_{02})(BC_4-C_5A)+A_{02}C_4(B^2-AD)}{(B^2-AD)(C_3A+A_{01}C_4)+(C_1A-BA_{01})(BC_4-C_5A)} \frac{V_P}{V}. \quad (53)$$

Note that Equation (53) was derived for general multilayer composite structures, where bending-tension modes are present.

Particular CASES

We now consider several particular cases of Equation (53), which can be simplified. These are as follows:

- (1) Only tension is present. In this case, there is no bending mode; i.e., $\kappa = 0$ or $D \rightarrow \infty$.

$$\alpha_{ME} = \alpha_{ME}^T = -\frac{C_4A_{02}}{C_3A+A_{01}C_4} \frac{V_P}{V} \quad (54)$$

(2) Only bending is present. In this case, there is no tension strain: i.e., $\varepsilon = 0$ or $A \rightarrow \infty$.

$$\alpha_{ME} = \alpha_{ME}^B = -\frac{C_2 C_5}{C_3 D + C_1 C_5} \frac{V_P}{V} \quad (55)$$

(3) Symmetrically laminated composites. In this case, the bending and longitudinal modes are decoupled: i.e., $B = 0$.

$$(4) \quad \alpha_{ME} = \alpha_{ME}^S = -\frac{\frac{C_4 A_{02}}{A} + \frac{C_2 C_5}{D}}{\frac{C_3}{A} + \frac{A_{01} C_4}{A} + \frac{C_1 C_5}{D}} \frac{V_P}{V}. \quad (56)$$

Piezomagnetic-piezoelectric bi-layer: static ME coefficient

Following the above, we will consider the important case: that of piezomagnetic-piezoelectric bi-layers. In this case, the numbers of layers are

$$N_P = 1, N_M = 1, N_E = 0; \quad (57)$$

and the coordinates of the layers are given as (see Figure 10)

$$z_0 = -h_p, z_1 = 0, z_2 = h_m, z_0^P = -h_p, z_1^P = 0, z_0^m = 0, z_1^m = h_m. \quad (58)$$

We can then derive the following expressions for the coefficients in Eq (53), using Eqs. (37), (40) and (44):

$$\begin{aligned} A_{01} &= \frac{d_{11}}{s_{P11}} h_p, A_{02} = \frac{q_{11}}{s_{M11}} h_m, B = \frac{h_p^2}{2s_{P11}} (-1 + \gamma_1), A = \frac{h_p}{s_{P11}} (1 + \gamma_0), \\ D &= \frac{h_p^3}{3s_{P11}} (1 + \gamma_2), C_1 = -\frac{d_{11} h_p^2}{2s_{P11}}, C_2 = \frac{q_{11} h_m^2}{2s_{M11}}, C_3 = \varepsilon_{11} (1 - K_1^2) h_p, \\ C_4 &= \varepsilon_{11} r_1 h_p, C_5 = -0.5 \varepsilon_{11} r_1 h_p^2; \end{aligned} \quad (59)$$

where

$$\gamma_0 = \frac{s_{P11}}{s_{M11}} \frac{h_m}{h_p}, \gamma_1 = \frac{s_{P11}}{s_{M11}} \left(\frac{h_m}{h_p} \right)^2, \gamma_2 = \frac{s_{P11}}{s_{M11}} \left(\frac{h_m}{h_p} \right)^3, r_1 = \frac{d_{11}}{s_{P11} \varepsilon_{11}}, K_1^2 = \frac{d_{11}^2}{s_{P11} \varepsilon_{11}}. \quad (60)$$

Using these expressions for the coefficients in Eq (A36), and after algebraic rearrangements, we arrive to

$$\begin{aligned} \alpha_{ME} &= -\frac{q_{11} d_{11}}{s_{P11} \varepsilon_{11} h_p + h_m} \left\{ \frac{\gamma_0}{\gamma_0 + 1} + \frac{1}{\Delta_{01}} [\gamma_1 (\gamma_0 + 1) - \gamma_0 (\gamma_1 - 1)] \left[\frac{\gamma_1 - 1}{\gamma_0 + 1} + 1 \right] \right\} \times \\ &\quad \left\{ 1 - K_1^2 - K_1^2 \frac{1}{\Delta_{01}} [(\gamma_0 + 1) + (\gamma_1 - 1)] \left[\frac{\gamma_1 - 1}{\gamma_0 + 1} - 1 \right] + K_1^2 \frac{1}{\gamma_0 + 1} \right\}^{-1}; \end{aligned} \quad (61)$$

where $\Delta_{01} = (\gamma_1 - 1)^2 - \frac{4}{3} (\gamma_0 + 1)(\gamma_2 + 1)$.

Particular CASES for bi-layer composite structure

Similar particular cases for bi-layers can then be obtained analogous to those of multilayer composite laminates given in Equations (54-56). These are:

- (1) Only tension is present. In this case, there is no bending mode: i.e., $\kappa = 0$ or $D \rightarrow \infty$.

$$\alpha_{ME} = \alpha_{ME}^T = -\frac{q_{11}d_{11}}{s_{P11}\varepsilon_{11}} \frac{h_P}{h_P+h_m} \left\{ \frac{\gamma_0}{\gamma_0+1} \right\} \times \left\{ 1 - K_1^2 + K_1^2 \frac{1}{\gamma_0+1} \right\}^{-1}. \quad (62)$$

- (2) Only bending is present. In this case, there is no longitudinal strain: i.e., $\varepsilon = 0$ or $A \rightarrow \infty$.

$$\alpha_{ME} = \alpha_{ME}^B = \frac{q_{11}d_{11}}{s_{P11}\varepsilon_{11}} \frac{h_P}{h_P+h_m} \left\{ \frac{3}{4} \frac{\gamma_1}{\gamma_2+1} \right\} \times \left\{ 1 - K_1^2 + \frac{3}{4} K_1^2 \frac{1}{\gamma_2+1} \right\}^{-1}. \quad (63)$$

- (3) Symmetrically laminated composites. In this case, the bending and longitudinal modes are decoupled: i.e., $B = 0$.

$$\alpha_{ME} = \alpha_{ME}^S = -\frac{q_{11}d_{11}}{s_{P11}\varepsilon_{11}} \frac{h_P}{h_P+h_m} \left\{ \frac{\gamma_0}{\gamma_0+1} - \frac{3}{4} \frac{\gamma_1}{\gamma_2+1} \right\} \times \left\{ 1 - K_1^2 + K_1^2 \frac{1}{\gamma_0+1} + \frac{3}{4} K_1^2 \frac{1}{\gamma_2+1} \right\}^{-1} \quad (64)$$

The equations of motion in bar theory are obtained by integrating the three-dimensional equations of motion (17-19) over the bar thickness, i.e.

$$\frac{\partial T_1}{\partial x_1} + X_1 = \rho \frac{\partial^2 u}{\partial t^2} - \tilde{\rho} \frac{\partial^3 w}{\partial x_1 \partial t^2} \quad (65)$$

$$\frac{\partial Q}{\partial x_1} + X_3 = \rho \frac{\partial^2 w}{\partial t^2} \quad (66)$$

$$Q = \frac{\partial M_1}{\partial x_1} - \tilde{\rho} \frac{\partial^2 u}{\partial t^2} - \tilde{\rho} \frac{\partial^3 w}{\partial x_1 \partial t^2}; \quad (67)$$

where Q is a transverse shear stress in a cross sectional area of the composite; $X_1 = q_1^+ - q_1^-$; q_1^+ and q_1^- are the applied shear stresses to the top and bottom of the composite, respectively; $X_3 = q_3^+ - q_3^-$; q_3^+ and q_3^- are the applied normal stresses to the top and bottom of the composite, respectively; and

$$\rho = \sum_{k=1}^{N_P} h_{kP} \rho_{kP} + \sum_{k=1}^{N_M} h_{kM} \rho_{kM} + \sum_{k=1}^{N_E} h_{kE} \rho_{kE} \quad (68)$$

$$\tilde{\rho} = \sum_{k=1}^{N_P} \frac{\rho_{kP}}{2} [(z_k^P)^2 - (z_{k-1}^P)^2] + \sum_{k=1}^{N_M} \frac{\rho_{kM}}{2} [(z_k^M)^2 - (z_{k-1}^M)^2] + \sum_{k=1}^{N_E} \frac{\rho_{kE}}{2} [(z_k^E)^2 - (z_{k-1}^E)^2] \quad (69)$$

$$\tilde{\rho} = \sum_{k=1}^{N_P} \frac{\rho_{kP}}{3} [(z_k^P)^3 - (z_{k-1}^P)^3] + \sum_{k=1}^{N_M} \frac{\rho_{kM}}{3} [(z_k^M)^3 - (z_{k-1}^M)^3] + \sum_{k=1}^{N_E} \frac{\rho_{kE}}{3} [(z_k^E)^3 - (z_{k-1}^E)^3] \quad (70)$$

Note for static conditions that the time dependent terms are zero: in which case for $\frac{\partial}{\partial t} = 0$, the complete problem exactly divides into plane and bending problems. Dynamical Equations (65-67) do not enable the complete system of equations for the theory of asymmetrical laminated

electroelastic bars to be split into two decoupled systems for the tangential and transverse vibrations, as in the theory of bars of symmetrical structure. We next performed an asymptotic analysis of the equations of motion of the bar (65-67) to simplify them. We will present the complete solution of the system of equations for the theory of laminated ME elastic bars as the sum of the solution of homogeneous equations for free quasi-tangential vibrations, the solution of homogeneous equations for free quasi-transverse vibrations, and a particular solution of an inhomogeneous system of equations.

Using the constitutive relations (45) and the expressions $\varepsilon = \frac{\partial u(x_1, t)}{\partial x_1}$ and $\kappa = \frac{\partial^2 w(x_1, t)}{\partial x_1^2}$, the system of equations (65-67) can be expressed in terms of the displacements $u(x_1, t)$ and $w(x_1, t)$:

$$\begin{cases} A \frac{\partial^2 u}{\partial x_1^2} - B \frac{\partial^3 u}{\partial x_1^3} = \rho \frac{\partial^2 u}{\partial t^2} - \tilde{\rho} \frac{\partial^3 w}{\partial x_1 \partial t^2} - X_1 \\ B \frac{\partial^3 u}{\partial x_1^3} - D \frac{\partial^4 w}{\partial x_1^4} - \tilde{\rho} \frac{\partial^2 u}{\partial t^2} - \tilde{\rho} \frac{\partial^4 w}{\partial x_1^2 \partial t^2} = \rho \frac{\partial^2 w}{\partial t^2} - X_3. \end{cases} \quad (71)$$

For symmetrically laminated plates, the coefficient $B = 0$ and $\tilde{\rho} = 0$. In this case, the coupled system of dynamic Equation (71) splits into two simpler problems: a plane problem with

$$A \frac{\partial^2 u}{\partial x_1^2} = \rho \frac{\partial^2 u}{\partial t^2} - X_1; \quad (72)$$

and a bending one with

$$-D \frac{\partial^4 w}{\partial x_1^4} - \tilde{\rho} \frac{\partial^4 w}{\partial x_1^2 \partial t^2} = \rho \frac{\partial^2 w}{\partial t^2} - X_3. \quad (73)$$

From Equations (68-70), we can see that the coefficients ρ , $\tilde{\rho}$ and $\tilde{\rho}$ have different orders of total thicknesses for the composite: i.e., $\rho = h\rho_0$, $\tilde{\rho} = h^2\tilde{\rho}_0$, and $\tilde{\rho} = h^3\tilde{\rho}_0$, where ρ_0 , $\tilde{\rho}_0$, and $\tilde{\rho}_0$ are order of $O(1)$. We can obtain the same for the coefficients A , B and D , see Equations (37) and (40), i. e., $A = hA_0$, $B = h^2B_0$ and $D = h^3D_0$.

Decomposition of longitudinal and bending problems

These types of representations help us to be split the system of Equation (71) into two decoupled equations for tension and bending problems. The system of Equation (71), can then be expressed in the following convenient form:

$$\begin{cases} \frac{\partial^2 u}{\partial x^2} - \frac{1}{\omega_T^2} \frac{\partial^2 u}{\partial t^2} = \delta \left[\frac{B_0}{A_0} \frac{\partial^3 w}{\partial x^3} - \frac{\tilde{\rho}_0}{\rho_0} \frac{1}{\omega_T^2} \frac{\partial^3 w}{\partial x \partial t^2} \right] - \frac{L^2}{\omega_T^2 A_0} X_1 \\ \frac{1}{\omega_B^2} \frac{\partial^2 w}{\partial t^2} + \frac{\partial^4 w}{\partial x^4} = \delta \left[\frac{B_0}{\rho_0 L^2 \omega_B^2} \frac{\partial^3 u}{\partial x^3} - \frac{\tilde{\rho}_0}{\rho_0} \frac{1}{\omega_B^2} \frac{\partial^3 u}{\partial x \partial t^2} - \varepsilon \frac{\tilde{\rho}_0}{\rho_0} \frac{1}{\omega_B^2} \frac{\partial^4 w}{\partial x^2 \partial t^2} \right] - \frac{L^4}{\omega_B^2} X_3. \end{cases} \quad (74)$$

In Equation (74), we use the following notations: $x = \frac{x_1}{L}$; $\delta = \frac{h}{L}$ for nondimensional relative length and thicknesses, where generally $\delta \ll 1$; $\omega_T = \sqrt{\frac{A_0}{\rho_0 L^2}}$ is the angular frequency of the longitudinal volume waves and $\omega_B = \sqrt{\frac{D}{h\rho_0 L^4}}$ is that for bending volume waves.

It is easy to check that the following representation for u and w

$$\begin{cases} \mathbf{u}(x, t) = \sum_{i=0}^{\infty} \boldsymbol{\delta}^i \mathbf{u}_i(x, t) \\ \mathbf{w}(x, t) = \sum_{i=0}^{\infty} \boldsymbol{\delta}^i \mathbf{w}_i(x, t) \end{cases} \quad (75)$$

can decouple the system of equations (74) into the following set of equations:

$$\text{for zero iteration } \begin{cases} \frac{\partial^2 u_0}{\partial x^2} - \frac{1}{\omega_T^2} \frac{\partial^2 u_0}{\partial t^2} = -\frac{L^2}{\omega_T^2 A_0} X_1 \\ \frac{1}{\omega_B^2} \frac{\partial^2 w_0}{\partial t^2} + \frac{\partial^4 w_0}{\partial x^4} = -\frac{L^4}{\omega_B^2} X_3, \end{cases} \quad (76)$$

$$\text{for first iteration } \begin{cases} \frac{\partial^2 u_1}{\partial x^2} - \frac{1}{\omega_T^2} \frac{\partial^2 u_1}{\partial t^2} = \frac{B_0}{A_0} \frac{\partial^3 w_0}{\partial x^3} - \frac{\tilde{\rho}_0}{\rho_0} \frac{1}{\omega_T^2} \frac{\partial^3 w_0}{\partial x \partial t^2} \\ \frac{1}{\omega_B^2} \frac{\partial^2 w_1}{\partial t^2} + \frac{\partial^4 w_1}{\partial x^4} = \frac{B_0}{\rho_0 L^2 \omega_B^2} \frac{\partial^3 u_0}{\partial x^3} - \frac{\tilde{\rho}_0}{\rho_0} \frac{1}{\omega_B^2} \frac{\partial^3 u_0}{\partial x \partial t^2}. \end{cases} \quad (77)$$

The splitting of the complete dynamical problem into simpler plane and bending problems is radically different from the splitting in the case of a symmetrical bar structure. For a bar of symmetrical structure, the complete dynamical problem splits exactly into plane and bending problems. However, for a bar of asymmetrical structure, this splitting is approximate: the deflection is in the first equation of motion of (74) for the plane problem, and the tangential displacement u is in the second equation of motion (74) for the bending one. Splitting of the dynamic problem occurred true everywhere, except apart from the vicinities of the natural vibration frequencies.

Next based on equations (74), we will discuss some issues related to the bending-tension vibration of multilayer composites. The dynamic ME coefficient will be derived. As a particular case, bi-layer composites made of ferromagnetic-ferroelectric will be considered.

As an example, consider the harmonic vibrations of a multilayer bar. The top and bottom surfaces are free of stresses, i. e. $q_i^\pm = 0$, ($i=1,3$). Let us then find the solution in a zeroth order approximation, which holds everywhere except in the vicinities of the natural vibration frequencies. The equations of the plane problem have the form

$$\begin{cases} \frac{\partial^2 u_0}{\partial x^2} - \frac{\rho L^2}{A} \frac{\partial^2 u_0}{\partial t^2} = 0 \\ T_{10} = \frac{A}{L} \frac{\partial u_0(x, t)}{\partial x} - A_{01} E_0 - A_{02} H_0, \end{cases} \quad (78)$$

and the equations of the bending problem have the form

$$\begin{cases} \frac{\rho L^4}{D} \frac{\partial^2 w_0}{\partial t^2} + \frac{\partial^4 w_0}{\partial x^4} = 0 \\ M_{10} = -\frac{D}{L^2} \frac{\partial^2 w_0(x_1, t)}{\partial x^2} - C_1 E_0 - C_2 H_0 \\ Q_0 = \frac{1}{L} \frac{\partial M_{10}}{\partial x}. \end{cases} \quad (79)$$

For the vibration problem, we will assume all functions can use the following type of representations

$$u_0(x, t) = u_0(x)e^{i\omega t}, w_0(x, t) = w_0(x)e^{i\omega t}, E_0(x, t) = E_0 e^{i\omega t}, H_0(x, t) = H_0 e^{i\omega t}; \quad (80)$$

where $i = \sqrt{-1}$ and ω is the vibration frequency. When using this representations, it is easy to find that the general solution of (78-79)

$$u_0(x, t) = e^{i\omega t} [R_1 \sin(\lambda_T Lx) + R_2 \cos(\lambda_T Lx)] \quad (81)$$

$$w_0(x, t) = e^{i\omega t} [R_3 \sin(\lambda_B Lx) + R_4 \cos(\lambda_B Lx) + R_5 \sinh(\lambda_B Lx) + R_6 \cosh(\lambda_B Lx)]; \quad (82)$$

where $\lambda_T = \sqrt{\frac{\omega^2 \rho}{A}}$, $\lambda_B = \sqrt{\frac{\omega^2 \rho}{D}}$, and the coefficients R_n , ($n = 1, 2, 3, 4, 5, 6$) are unknown and should be determined from the boundary (edge) conditions.

We next have to examine the following boundary conditions applied to the edges of the laminated composite: both ends are simply-supported. At the edges, $x = \pm 1$ should satisfy

$$T_{10} = 0, w_0 = 0, M_{10} = 0. \quad (83)$$

Applying the boundary conditions (83) to the general solutions of (81-82), we can obtain the following representations for the displacements

$$u_0(x, t) = e^{i\omega t} \frac{A_{01} E_0 + A_{02} H_0}{A \lambda_T} \frac{\sin(\lambda_T Lx)}{\cos(\lambda_T L)} \quad (84)$$

$$w_0(x, t) = e^{i\omega t} \frac{C_1 E_0 + C_2 H_0}{2D \lambda_B^2} \left[\frac{\cos(\lambda_B Lx)}{\cos(\lambda_B L)} - \frac{\cosh(\lambda_B Lx)}{\cosh(\lambda_B L)} \right]. \quad (85)$$

For strain $\varepsilon = \frac{\partial u(x_1, t)}{\partial x_1}$ and bending $\kappa = \frac{\partial^2 w(x_1, t)}{\partial x_1^2}$, we can obtain the following

$$\varepsilon = \tilde{\varepsilon} e^{i\omega t} \frac{A_{01} E_0 + A_{02} H_0}{A}, \quad \kappa = \tilde{\kappa} e^{i\omega t} \frac{C_1 E_0 + C_2 H_0}{2D}; \text{ where } \tilde{\varepsilon} = \frac{\cos(\lambda_T Lx)}{\cos(\lambda_T L)} \quad (86)$$

is a magnitude of the strain, and where

$$\tilde{\kappa} = -\frac{\cos(\lambda_B Lx)}{\cos(\lambda_B L)} - \frac{\cosh(\lambda_B Lx)}{\cosh(\lambda_B L)} \quad (87)$$

is a magnitude of the bending.

We can then finally obtain the ME coefficients using the definitions of (50-51) and solutions (84-85). We deriving the following compact expression for the ME coefficient α_{ME} :

$$\alpha_{ME} \equiv \alpha_{ME}(\omega) = -\frac{H_P}{H} \frac{\Delta_{0I}}{\Delta_{0II}}; \quad (88)$$

where

$$\Delta_{0I} = \frac{A_{02}C_4}{A} \frac{\operatorname{tg}(\lambda_T L)}{\lambda_T L} + \frac{C_2 C_5}{2D} \left[\frac{\operatorname{tg}(\lambda_B L)}{\lambda_B L} + \frac{\operatorname{tgh}(\lambda_B L)}{\lambda_B L} \right] \quad (89)$$

$$\Delta_{0II} = C_3 + \frac{A_{01}C_4}{A} \frac{\operatorname{tg}(\lambda_T L)}{\lambda_T L} + \frac{C_1 C_5}{2D} \left[\frac{\operatorname{tg}(\lambda_B L)}{\lambda_B L} + \frac{\operatorname{tgh}(\lambda_B L)}{\lambda_B L} \right]. \quad (90)$$

From Equations (88-90) for the case of ferromagnetic-ferroelectric bi-layer composites, the ME coefficient α_{ME} can be derived as

$$\alpha_{ME} \equiv \alpha_{ME}(\omega) = -\frac{h_P}{h_P + h_m} \frac{\tilde{\Delta}_{0I}}{\tilde{\Delta}_{0II}}; \quad (91)$$

Where

$$\tilde{\Delta}_{0I} = \frac{q_{11}d_{11}}{s_{P11}\varepsilon_{11}} \frac{\gamma_0}{\gamma_0+1} \frac{\operatorname{tg}(\lambda_T L)}{\lambda_T L} - \frac{3}{8} \frac{\gamma_1}{\gamma_2+1} \left[\frac{\operatorname{tg}(\lambda_B L)}{\lambda_B L} + \frac{\operatorname{tgh}(\lambda_B L)}{\lambda_B L} \right] \quad (92)$$

$$\tilde{\Delta}_{0II} = 1 - K_1^2 + K_1^2 \frac{1}{\gamma_0+1} \frac{\operatorname{tg}(\lambda_T L)}{\lambda_T L} + K_1^2 \frac{3}{8} \frac{1}{\gamma_2+1} \left[\frac{\operatorname{tg}(\lambda_B L)}{\lambda_B L} + \frac{\operatorname{tgh}(\lambda_B L)}{\lambda_B L} \right]. \quad (93)$$

Please note that all notations in (91-93) are consistent to those one in (59-60).

Some Notes and Definitions

The frequency at which the ME coefficient $\alpha_{ME} \rightarrow \pm\infty$ is called the resonance frequency; whereas, the frequency were $\alpha_{ME} \rightarrow 0$ is called the anti-resonance one. The resonance frequency can be determined from the equation $\Delta_{0II} = 0$. The anti-resonance frequency can be determined from the equation $\Delta_{0I} = 0$. The number of resonance and anti-resonant frequencies are discrete and infinite: i.e. the transcendental equations (89-90) have an infinite and discrete number of zeros. If we assume $\omega \rightarrow 0$ in (88-90), or (91-93) for bi-layers, we can arrive to (54-56) or (61) for bi-layers. In other words, from the formulae for dynamic ME coefficients, we can derive the static ME coefficient as a particular case, assuming the vibration frequency approaches zero. If $D \rightarrow \infty$ in (88), we can obtain the dynamic ME coefficient for the pure longitudinal mode; and of $A \rightarrow \infty$ in (88), we arrive at the dynamic ME coefficient for the pure bending mode.

Furthermore, similar conclusions can be derived for bi-layer composites: i.e., if in (91) $\gamma_2 + 1 \rightarrow$

∞ , then one obtains a pure longitudinal mode; and if $\gamma_0 + 1 \rightarrow \infty$ in (91), one has a pure bending mode

To demonstrate the validity of the theory we will consider bi-layer laminate composites. In the calculations, we will use the following material parameters for Metglas-PZT (or NFO-PZT) composite bilayers given in Table 4. For numerical illustrations, the Metglas-PZT bilayer composite was chosen, as a model system, because it has higher piezoelectric and piezomagnetic coefficients.

We will also assume a laminate length $2L = 4 \cdot 10^{-2}m$ and that PZT thickness is $h_p = 2 \cdot 10^{-4}m$. First, we will determine the static magneto-electric coupling effects, and then the dynamic ones (i.e., effect of vibration frequency).

Table 4. Material parameters for lead zirconate titanate (PZT), nickel ferrite (NFO) and Metglas.

Materials	s_{11}	s_{12}	s_{13}	s_{33}	q_{11}	q_{13}	d_{13}	d_{11}	μ_{11}/μ_0	$\varepsilon_{11}/\varepsilon_0$	ρ
PZT	15.3	-5	-7.22	17.3			-175	400	1	1750	7600
NFO	6.5	-2.4			-680	125			3	10	7800
Metglas	10				50000				45000		7180

*compliance coefficient $s(\mathbf{10}^{-12}\mathbf{m}^2/\mathbf{N})$, piezomagnetic coupling $\mathbf{q}(\mathbf{10}^{-12}\mathbf{m}/\mathbf{A})$, piezoelectric coefficient $\mathbf{d}(\mathbf{10}^{-12}\mathbf{m}/\mathbf{V})$, density $\rho(\mathbf{10}^{-12}\mathbf{kg}/\mathbf{m}^3)$, permeability μ , and permittivity ε

Static magneto-electric coupling effects

The theoretical modeling of the low frequency tension-bending mode ME effect was based on a homogeneous strain-stress approach. However, configurationally asymmetry of a composite (for example, a bi-layer structure) must mean that the sample is bending under applied magnetic or electric fields. One of the principal objectives was to model the ME interactions in a magneto-electro-elastic multilayer composite taking into account flexural strains.

The ME voltage coefficient can be numerically calculated based on the analytical expressions derived in Equation (61), or its simplified counterpart Equation (62). In Figure 11 (a), the low-frequency ME voltage coefficient is shown as a function of the bilayer (i.e., Metglas and PZT) volume fractions. Comparisons of the ME voltage coefficient based on (61) yield models ignoring bending strain (62) and tension strain (63). In the figure, we can see that the maximum value of the ME coefficient is not the value predicted based only a longitudinal mode or on a bending mode: rather in fact, it was significantly lower value than that predicted at these points of maximum values. Figure 11 (b) shows the variation of the ME coefficient as a function of the Metglas-PZT thickness ratio. Comparisons were made based on formulas for the bending-tension mode (61), pure tension mode (62) and pure bending mode (63). Figure 11 (c) and (d) show a comparison of the asymmetric (61) and symmetric (64) models for the bending-tension mode. In this case, no significant difference between the predictions for the asymmetric ($B \neq 0$) and symmetric ($B = 0$) models were found. Comparison between theory and experiment are shown in Figure 11 (e).

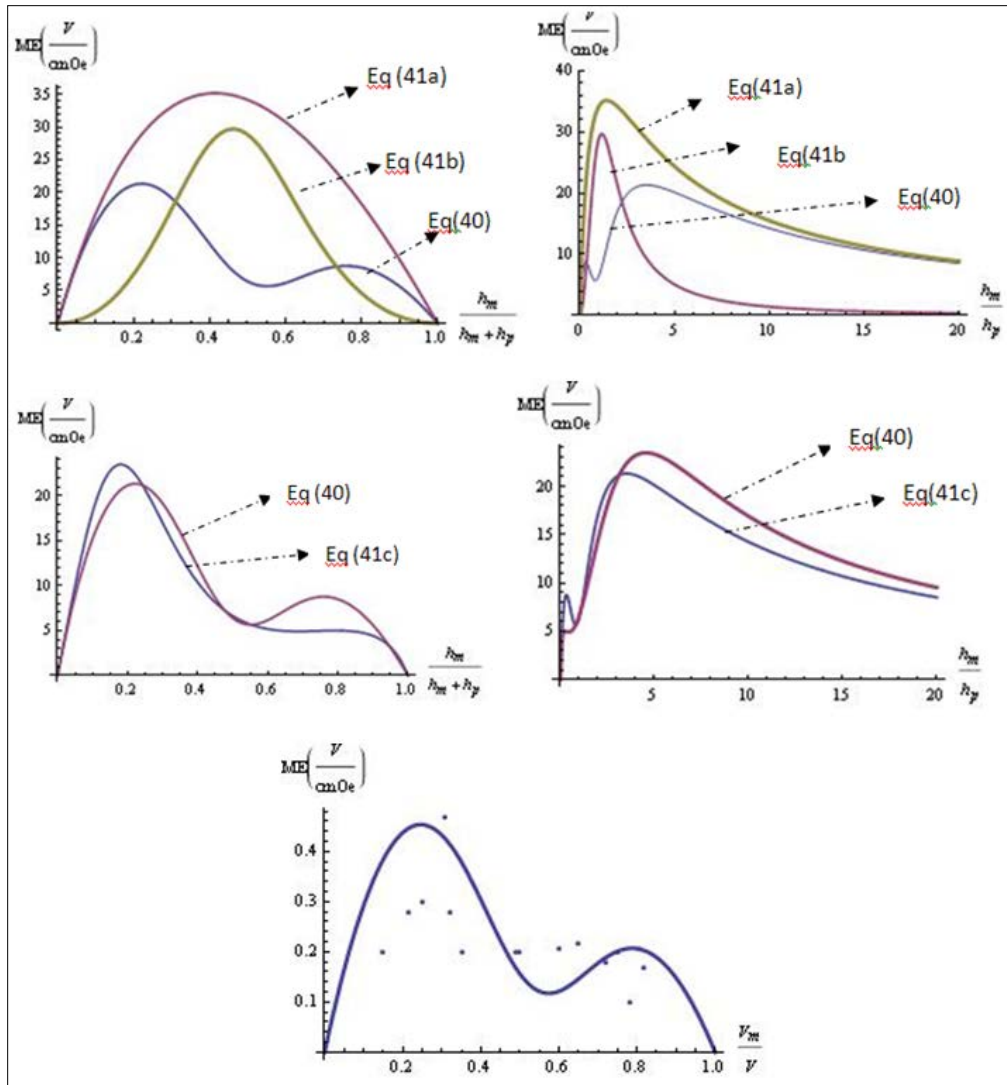


Figure 11. (a) Low-frequency ME voltage coefficient as a function of bilayer (Metglas and PZT) volume fraction. (b) Low-frequency ME voltage coefficient as a function of a bilayer thickness ratio. (c) Low-frequency ME voltage coefficient as a function of a bilayer volume fraction. (d) Low-frequency ME voltage coefficient as a function of a bilayer thickness ratio. (e) Low-frequency ME voltage coefficient as a function of bilayer (NFO-PZT) volume fraction.

(a) Comparison of ME voltage coefficient based on the exact model, model that ignores the bending strain and model that ignore tension strain. Results are for a PZT-Metglas bilayer. (b) Comparison of ME voltage coefficient based on the exact model that ignores the bending strain and model that ignore tension strain. Results are for a PZT-Metglas bilayer. (c) Comparison of ME voltage coefficient based on the exact model and symmetric model. Results are for a PZT-Metglas bilayer. (d) Comparison of ME voltage coefficient based on the exact model and symmetric model. Results are for a PZT-Metglas bilayer. (e) Comparison between the theory (solid line based on and data from Ref¹). Data presented for NFO-PZT bilayer.

We derived the dynamic ME coefficient and field functions (stress, strain, displacements), which allowed us to investigate the magneto-electro-elastic interactions in laminated composite. It is reasonable to expect that the magnitude of this interaction will be much larger in the region of the magneto-electro-elastic resonance. We will again consider the example of Metglas-PZT bilayers, analyzing the influence of the vibration frequency and geometry of the composite on the ME coefficient and the field functions.

In Figure 12 (a-c), the ME voltage coefficient is shown as a function of the vibration frequency $f = \omega/2\pi$ for different values of h_M/L . Comparisons of the ME voltage coefficient are based on calculations made using (78). The value of h_p/L was assumed to be 0.01. From this figure, one can clearly see the positions of the first resonance and anti-resonance frequencies: for example, when $\frac{h_M}{L} = 10^{-2}$, the first resonance and anti-resonance frequencies were around

$f_{1R} \approx 376.9\text{Hz}$ and $f_{1AR} \approx 318.1\text{Hz}$ respectively. Figure 12 (c) shows the dependence of the ME coefficient on frequency f (in large diapason of variation). We can see that overall the value of the ME coefficient increase until the first resonance frequency of the pure longitudinal mode f_{1L} : above which frequency, the overall behavior resembles that of the longitudinal mode (pure longitudinal mode is shown as a red dotted line).

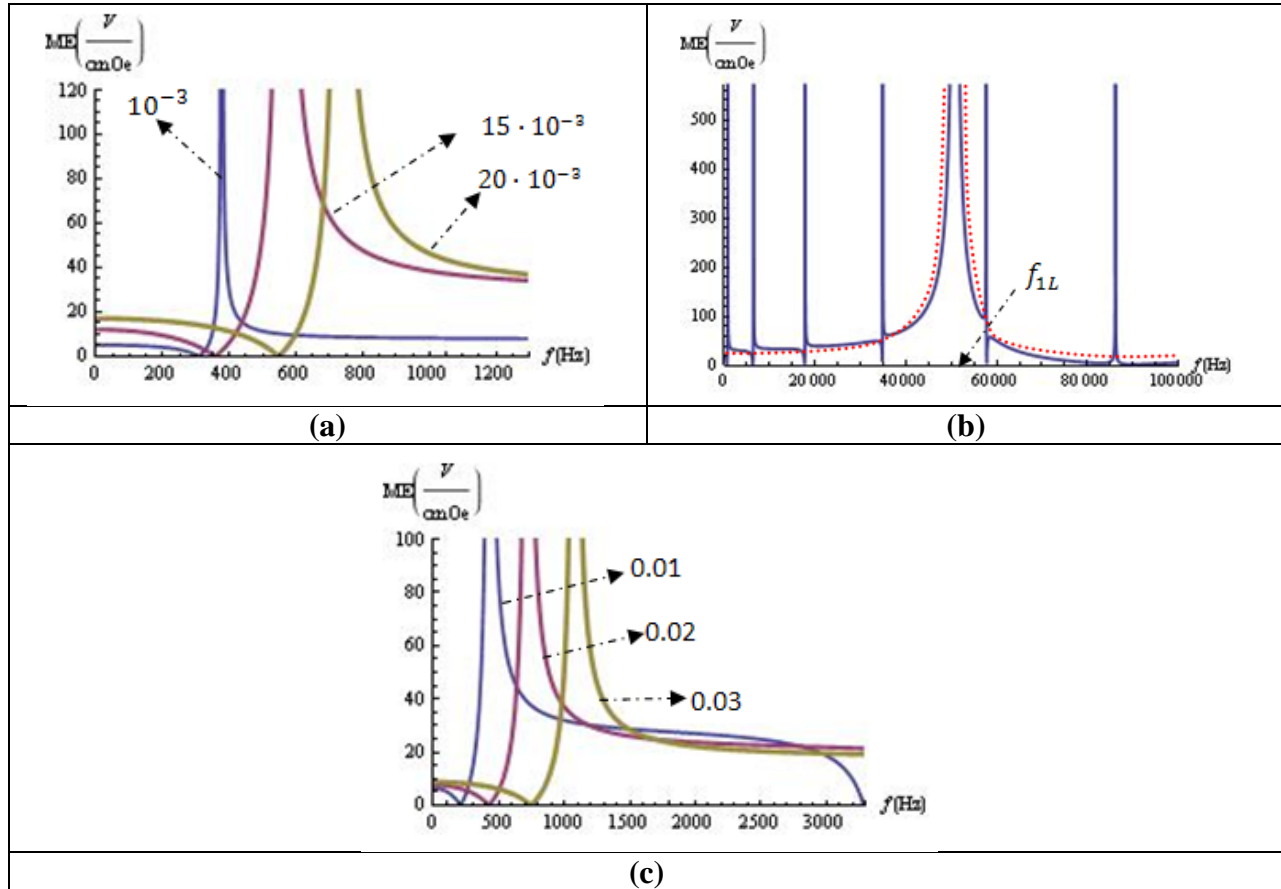


Figure 12. (a) ME voltage coefficient as a function of $f = \omega/2\pi$ for different values of h_M/L . (b) ME voltage coefficient as a function of $f = 2\pi/\omega$. (c) ME voltage coefficient as a function of $f = \omega/2\pi$ for different values of h_p/L .

(a) Comparison of ME voltage coefficient based on the Equation (91). Results are for a PZT-Metglas bilayer. The value of $h_P/L = 0.01$. (b) Results are for a PZT-Metglas bilayer. The value of $h_P/L = 0.01$, $h_M/L = 0.02$. (c) Comparison of ME voltage coefficient based on the Equation (91). Results are for a PZT-Metglas bilayer. The value of $h_M/L = 0.002$

In Figure 13 (a), the ME voltage coefficient is shown as a function of h_M/L for different values of $f = \omega/2\pi$. These values were calculated using Equation (91). In this figure we can see a strong dependence of the ME coefficient on f . An analogous type of behavior can also be seen for the ME voltage coefficient as a function of a h_P/L . Figure 13 (c) shows the ME voltage coefficient as a function of the bilayer (Metglas and PZT) volume fraction for different values of $f = 2\pi/\omega$. Again, we can see a strong dependence of the ME coefficient on f .

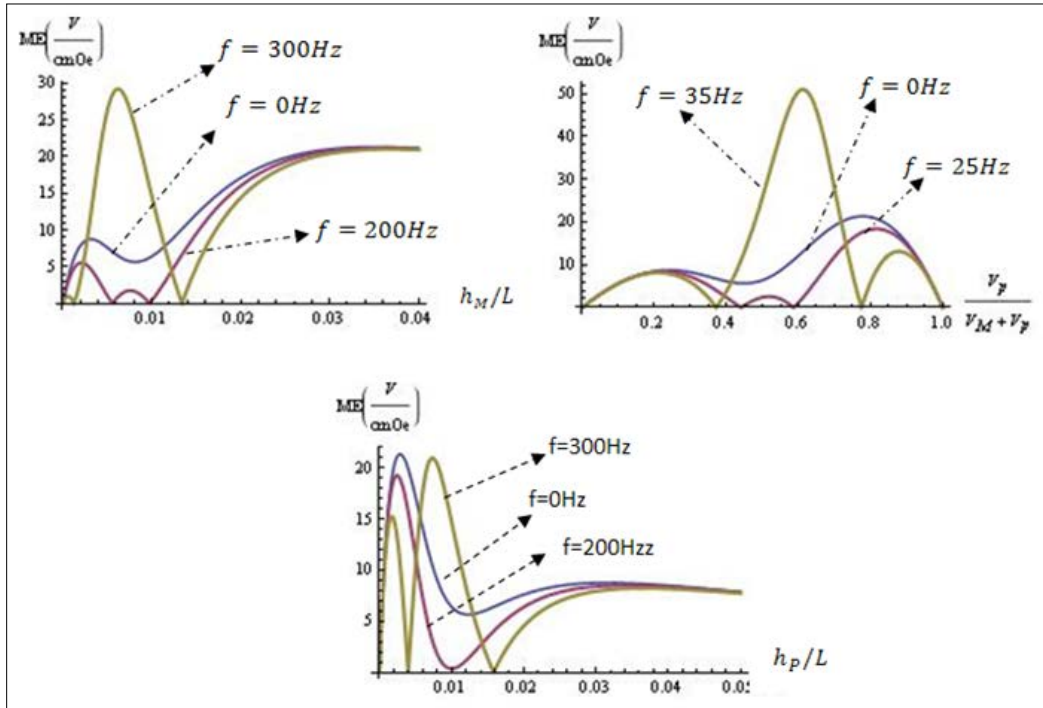


Figure 13. (a) ME voltage coefficient as a function of a h_M/L for different $f = 2\pi/\omega$ frequency values. (b) ME voltage coefficient as a function of bilayer (Metglas and PZT) volume fraction for different $f = 2\pi/\omega$ frequency values. (c) ME voltage coefficient as a function of a h_P/L for different $f = 2\pi/\omega$ frequency values.

(a) Comparison of ME voltage coefficient based on the Eq(A63). Results are for a PZT-Metglas bilayer. (b) Results are for a PZT-Metglas bilayer. (c) Comparison of ME voltage coefficient based on the Equation (78). Results are for a PZT-Metglas bilayer.

Figure 14 (a) shows the dependence of the dimensionless bending on f at different positions $x = x_1/L$. The values of $\frac{h_M}{L}$ were 0.001 and 0.01. It can be seen from the curves that the dimensionless bending increased as the vibration frequency approached the first anti-resonance frequency ($f_{1AR} \approx 318.1 \text{ Hz}$). Figure 14 (b) shows the dependence of the nondimensional bending on $x = x_1/L$, for different values of f on approaching to the first anti-resonance

frequency. Calculations using (74) showed that the bending increased rapidly as the vibration frequency approached the anti resonance. We can identify similar behavior for the strain, based on (86). As can be seen in Figure 14 (c), a rapid increase in the strain was found as frequency approached the resonant frequency of the longitudinal mode; $f_{1LR} \approx 58\text{kHz}$. Note in the vicinities of the resonance or anti-resonance frequencies of the bending-tension vibrations that the stresses and strains increased rapidly. Consequently, the applicability of the linear theory could be questionable. A more accurate theory should also include nonlinear terms.

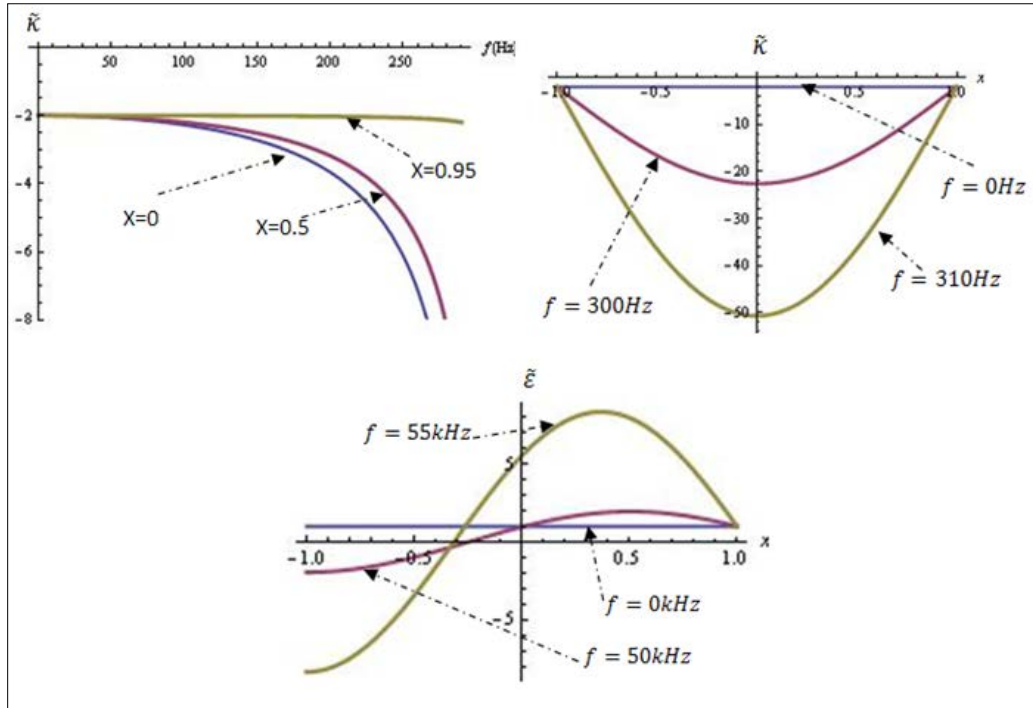


Figure 14. (a) Nondimensional bend as a function of $f = \omega/2\pi$ for different values of $x = x_1/L$. **(b)** Nondimensional bend as a function of x for different values of frequency f . **(c)** Nondimensional strain as a function of $x = x_1/L$ for different values of frequency f .

(a) Comparison based on the Equation (87). Results are for a PZT-Metglass bilayer. The values of $h_M/L = 0.001$, $h_P/L = 0.01$. (b) Comparison based on the Equation (87). Results are for a PZT-Metglass bilayer. The values of $h_M/L = 0.001$, $h_P/L = 0.01$. (c) Comparison based on the Equation (86). Results are for a PZT-Metglass bilayer. The values of $h_M/L = 0.001$, $h_P/L = 0.01$.

A.3.2. Noise contribution modeling

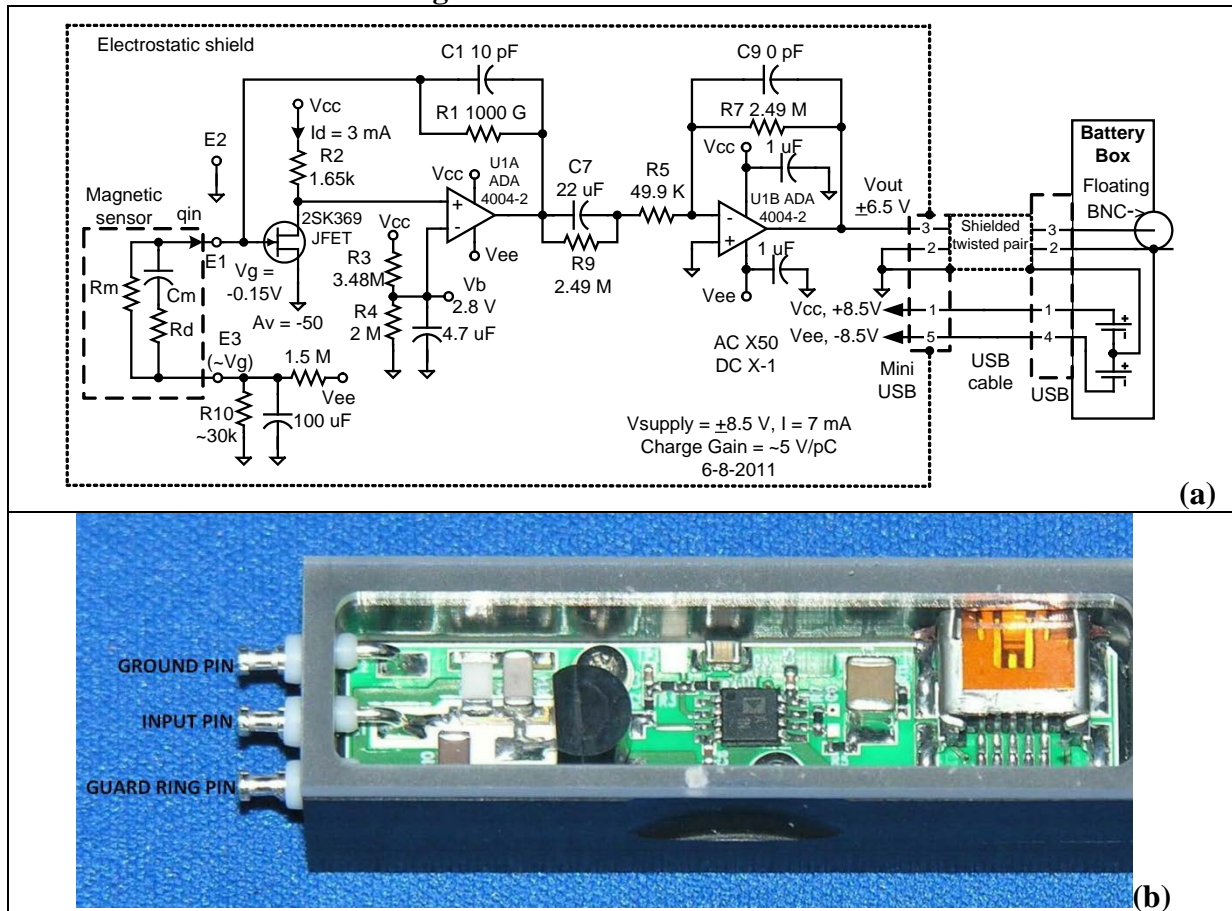


Figure 15. Schematic diagram and photograph of charge amplifier, showing the interface to the sensor and battery box.

The high level schematic diagram (Figure 15) shows how the JFET was incorporated into the two-stage Charge Amplifier; the sensor is connected on the left in the diagram and the battery box connection is shown on the right. Since the voltage gain of the JFET is inverting, its output must be connected to the positive side of the op-amp to provide negative feedback.

From the circuit, the noise contributions can be obtained in two parts: charge amplifier noise and sensor noise. For the charge amplifier noise, it was contributed by: voltage noise, current noise, op-amp voltage noise, op-amp current noise and Feedback resistance noise; for the sensor noise, it was dominated by dielectric loss noise and DC resistance noise. All the noise contribution items are summarized in Table 5.

Table 5. Model Equations for Charge noise density in C/ $\sqrt{\text{Hz}}$.

Contributing Term	Charge Noise Formula in (C/rtHz)
Voltage noise	$V_n(f) = (V_{n1}-V_{n1000}) / f + V_{n1000}$
Current noise	$I_n(f) = (I_{n1}-I_{n1000}) / f + I_{n1000}$
Op-amp voltage noise	$N_v(f) = 1/(2\pi f) V_n(f) (1+N_c C_s/C_f) / i2\pi f + 1/C_f R_f C_f$
Op-amp current noise	$N_i(f) = 1/(2\pi f) I_n$
Feedback resistance noise	$N_f(f) = 1/(2\pi f) (4 k_b T / R_f)^{1/2}$
Sensor leakage resistance noise	$N_s(f) = 1/(2\pi f) (4 k_b T N / R_s)^{1/2}$
Dielectric loss noise	$N_d(f) = (4 k_b T C_s \tan(\delta)/(2\pi f))^{1/2}$
Total Noise	$N_t(f) = (N_v^2 + N_i^2 + N_f^2 + N_s^2 + N_d^2)^{1/2}$

Then, we can predict the equivalent magnetic noise, and the dominated noise sources using above equations. For an example: a normal Metglas/PZT sensor with a spacing of 1mm ($C=420$ pF, $\tan\delta=0.02$, $R_{dc}=60$ G Ω , $\alpha_Q=1100$ pC/Oe), the equivalent magnetic noise and noise contributions can be predicted, as shown in Figure 16.

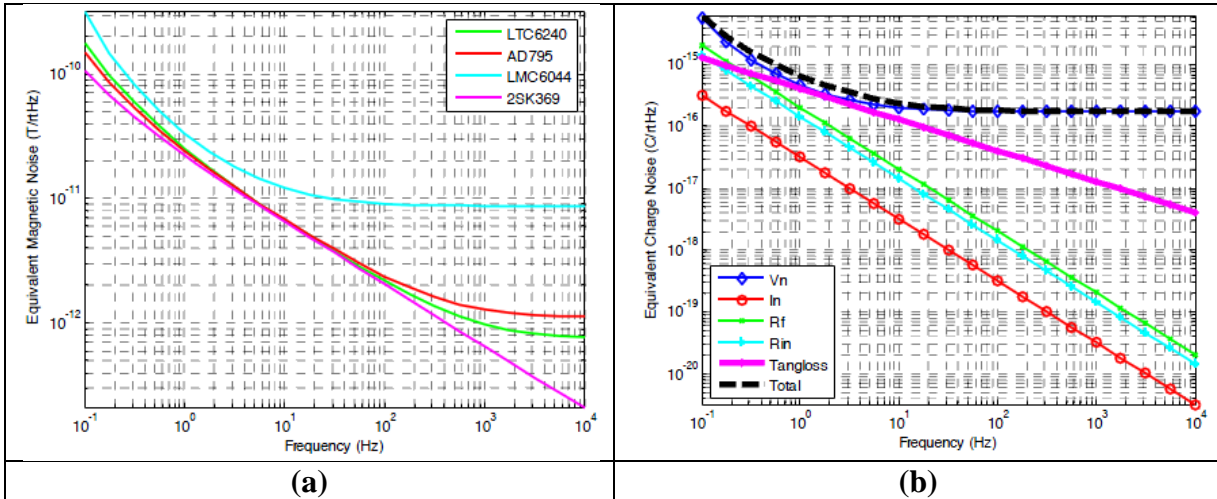


Figure 16. Predicted equivalent magnetic noise and the noise contributions for a normal Metglas/PZT sensor with a spacing of 1 mm.

From the predicted results, we can see that the internal noise was dominated by the dielectric loss noise, which was usually several times larger than the dc resistance noise. Hence, it is physically important and technologically interesting to reduce the dielectric loss of ME laminates.

A.3.3. ME coefficient enhancement

A.3.3.1. Constitute components

The PZN-PT and PMN-PT single crystals offer a much higher d_{33} than the PZT. Therefore, the ME response and the sensitivity are expected to be higher than the PZT based laminates. Our results shown in Figure 17 indeed confirm that for PZN-PT/PMN-PT the ME response is about 1.7 times higher than PZT that results in a 3-4 times lower noise floor. Note that the PZT/PZN-PT/PMN-PT and Metglas dimensions for this study were about $0.6 \times 2.5 \times 0.02$ cm 3 and $1 \times 8 \times 0.005$ cm 3 , respectively. The Metglas foils had higher magnetostriction coefficient λ of about 27 ppm.

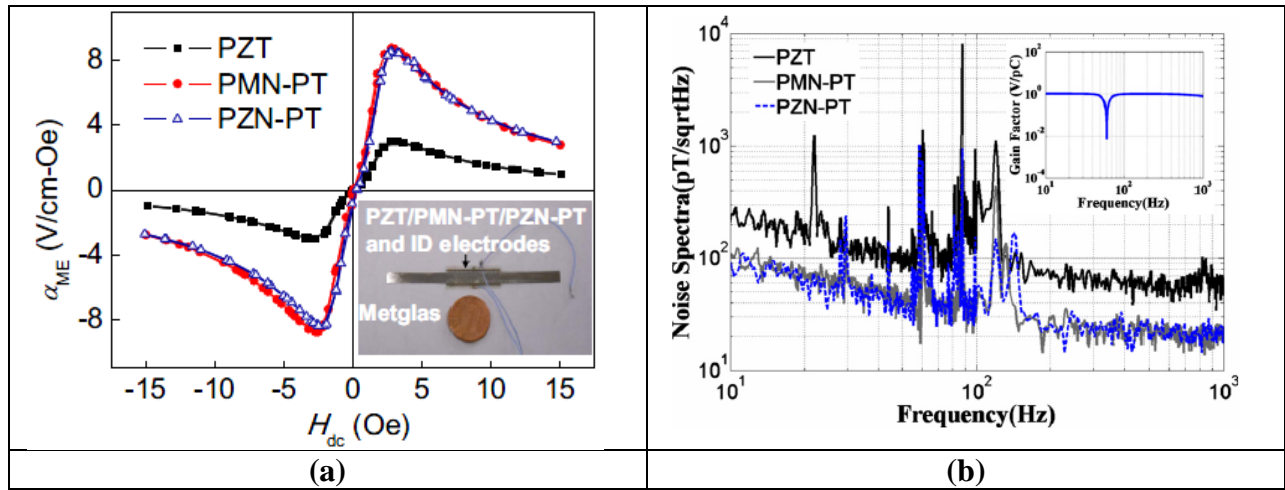


Figure 17. Comparison of (a) ME response and (b) noise floors for Metglas-PZT, Metglas-PZN-PT, and Metglas-PMN-PT laminates.

With the progress of noise reduction, we found CPSC PMN-PT was a good candidate for high ME coefficient and low equivalent magnetic noise. An extremely low equivalent magnetic noise sensor was made by CPSC PMN-PT and Metglas operated in M-P-P mode, as shown in Figure 18.

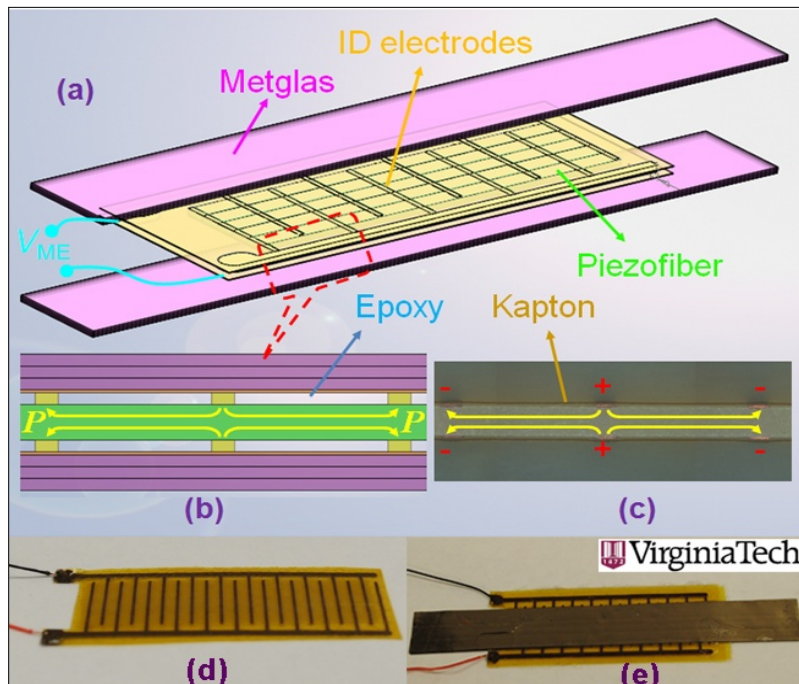


Figure 18(a) Schematic diagram of the Metglas/piezofiber configuration consisting of an ID electrodes/PMN-PT fibers core composite, and symmetric 3-layer Metglas actuators on the bottom and top of the core composite. (b) Illustration of the numerous alternating push-pull mode units. (c) Optical micrograph of a longitudinally poled push-pull element in the core composite. (d) and (e) Photographs of the ID electrode/piezofiber core composite and the complete Metglas/piezofiber ME sensor.

Under optimal DC magnetic bias ($H_{dc} \sim 8$ Oe), α_E reaches a maximum value of 52 V cm $^{-1}$ Oe $^{-1}$, as shown in Figure 19. The ME coefficient reported here is significantly higher than that previously reported for two-phase ME composites, regardless of constituent material types. The high ME coefficient is due to several factors: (i) optimum stress transfer in the current multi-push-pull mode, (ii) large $d_{33,m}$ and high permeability of magnetostrictive Metglas, (iii) high piezoelectric properties ($d_{33,p}$) of the PMN-PT piezofiber, (iv) optimum thickness ratio of Metglas to piezofiber, and (v) optimal ID electrodes distribution on Kapton. The ME charge coefficient (α_Q) is also presented in Figure 19. The maximum α_Q of 2680 pC Oe $^{-1}$ was obtained under a DC magnetic bias field of $H_{dc} \sim 8$ Oe.

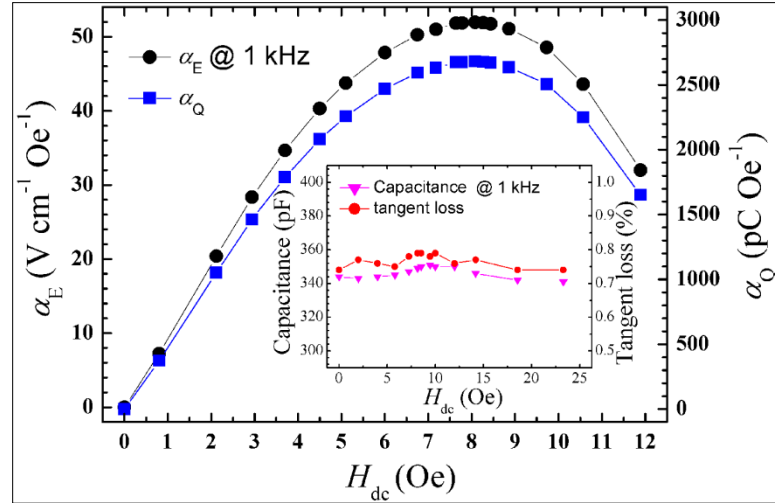


Figure 19. The magnetic field dependence of (a) the longitudinal magnetostrictive strain λ and (b) the ME voltage coefficient and ME charge coefficient of the Metglas/piezofiber sensor. (c) ME charge coefficient shows a flat response over the quasi-static frequency range.

The inset shows the capacitance and dielectric loss as a function of DC magnetic field. Measurements were made at 1 kHz.

Figure 20 shows the measured and modeled charge noise density, and the equivalent magnetic noise, of the ME sensor unit in the frequency range of $0.125 < f < 100$ Hz. Both the $\tan\delta$ and DC resistance noises contribute to the total noise floor at 1 Hz, but the magnitude of the $\tan\delta$ noise was $1.2\times$ larger than that of the DC resistance noise. Except at frequencies where external vibration sources are present, the modeled and measured charge density noises show good agreement. The equivalent magnetic noise spectrum shown in Figure 20 (b) was obtained through a conversion of the charge noise density spectrum using the ME charge coefficient. An extremely low equivalent magnetic noise of 5.1 pT Hz $^{-1/2}$ was found at 1 Hz, which is very close to the predicted value of 4.2 pT Hz $^{-1/2}$. In particular, the equivalent magnetic noise of the ME sensor unit was as low as about 1 pT Hz $^{-1/2}$ at a frequency of only several Hz. The extremely low equivalent magnetic noise that we observed obtained using PMN-PT fibers originated from a low charge noise density coupled with a giant ME charge coefficient. The extremely low equivalent magnetic noise makes this ME sensor particularly promising for use in ultralow magnetic field detection applications.

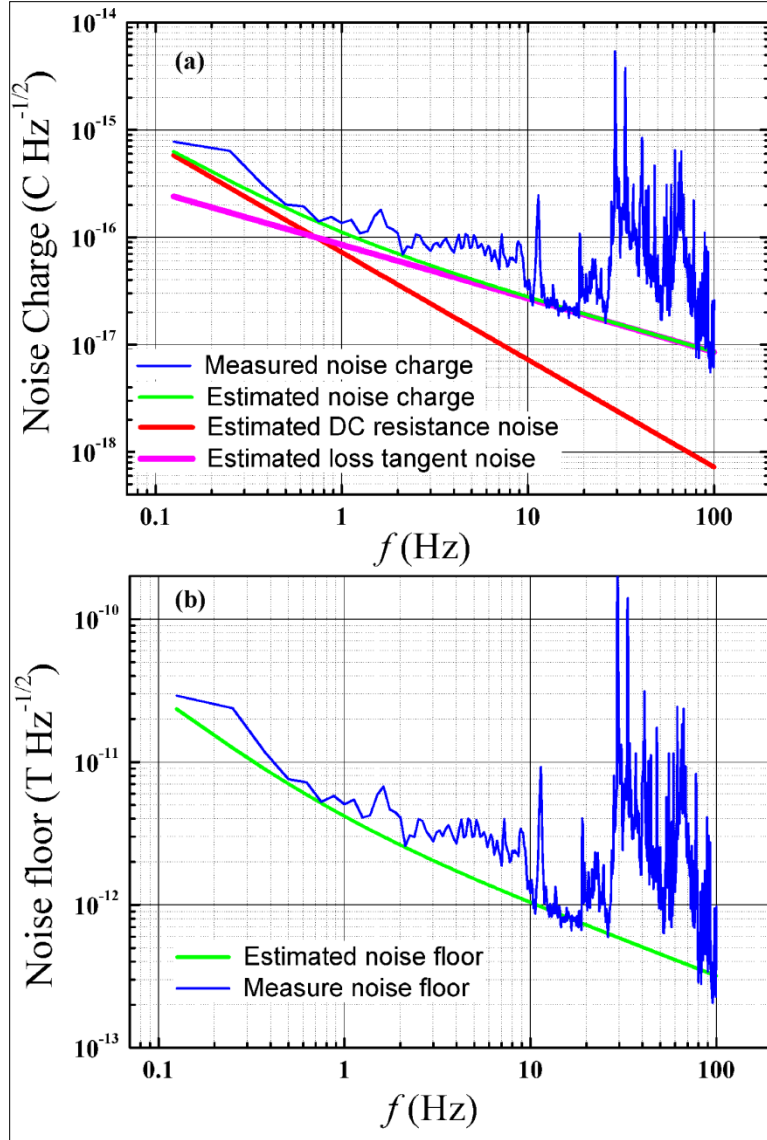


Figure 20. (a) Measured and estimated charge noise density of the proposed sensor unit, including constituent dielectric loss and DC resistance loss, over the frequency range of $0.125 \text{ Hz} < f < 100 \text{ Hz}$.

The modeling results show that the DC resistance noise is dominant below 0.6 Hz. At 1 Hz, the total charge noise density the dielectric loss noise and DC resistance noise contribute almost equally to total charge noise levels.

A.3.3.2. Operation modes

In the past, various modes of operation have been studied, including: longitudinal-longitudinal (LL)², longitudinal- transverse (LT)³, TL, TT, radial, push-pull and bending ones⁴. However, shear-mode PMN-PT single crystals have the highest piezoelectric coefficient values, as summarized in Table 6. Thus, in principle, ME laminate composites using PMN-PT as the piezoelectric layer operated in a shear mode should provide the largest ME coefficients.

Table 6. Constituent material parameters of PMN-PT for transverse-extensional, longitudinal-extensional, and shear modes.

Parameter	Piezoelectric constant (10^{-12} pC/N)			Elastic compliance (10^{-12} m 2 /N)			Dielectric constant	
	d_{31}	d_{33}	d_{15}	s_{11}^E	s_{12}^E	s_{55}^E	$\frac{\epsilon_{33}^T}{\epsilon_0}$	$\frac{\epsilon_{11}^T}{\epsilon_0}$
Transverse-extensional ^{a)}	-1883			112.0	-31.1		4033	
Longitudinal-extensional ^{b)}		2365		41.2	-17.3		6833	
Shear-extensional ^{c)}			6800	85.4		212.2		9540

a) Cited from Ref.⁵.

b) Cited from Ref.⁶.

c) Measured.

Figure 21 (a) shows a schematic diagram and the working principle of the proposed shear-mode ME laminate composite. The ME laminate consisted of two shear-mode PMN-PT layers, sandwiched between a longitudinally magnetized Terfenol-D plate and a mechanical clamping brass substrate. Single crystals of PMN-PT with dimensions of $10 \times 5 \times 0.5$ mm 3 were grown in-house using a modified Bridgman technique, with their $<111>$ and $<110>$ crystallographic axes oriented in the length and thickness directions [see Figure 21 (b)]. The properties of the PMN-PT samples were then characterized following the IEEE standard, as summarized in Table 6. The Terfenol-D plate was commercially supplied. They were of dimensions $40 \times 10 \times 1$ mm 3 , with their long axes were directed along the [112] direction. These Terfenol-D layers were then symmetrically stacked and bonded to PMN-PT ones using an epoxy resin. A brass substrate was bonded to the other side of the PMN-PT layers to form shear-mode three-phase ME laminate composites. In principle, the PMN-PT layers were operated in combined shear extensional and one-side longitudinal extensional modes, as illustrated in Figure 21 (c) and (d). The Terfenol-D generated an elongation/shrinkage motion in response to an applied magnetic field H , while, a longitudinal-stress was applied to one-side of the PMN-PT plates and while the other side was clamped. Thus, the PMN-PT was excited into a one-side longitudinal extensional motion (due to the end parts of Terfenol-D) and a shear extensional motion (due to the center part of Terfenol-D).

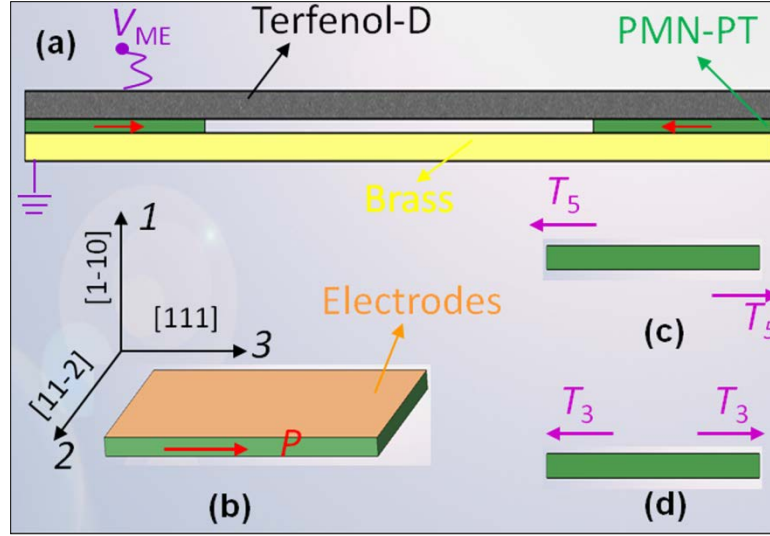


Figure 21. (a) Schematic diagram of the proposed shear mode three-phase magnetostriuctive/piezoelectric/brass heterostructure. (b) The coordinate system shows the crystalline directions of the PMN-PT single crystal. (c) and (d) illustrate the motion of the PMN-PT single crystal under shear extensional and longitudinal extensional stresses, respectively.

The arrows P and T_i ($i=3$ and 5) denote the polarization and stress directions. The Terfenol-D layer in the heterostructure has two functions: the end parts (bonded to PMN-PT) generate a longitudinal extensional stress T_3 , and the center part (unbounded to PMN-PT) produce a shear extensional stress T_5 .

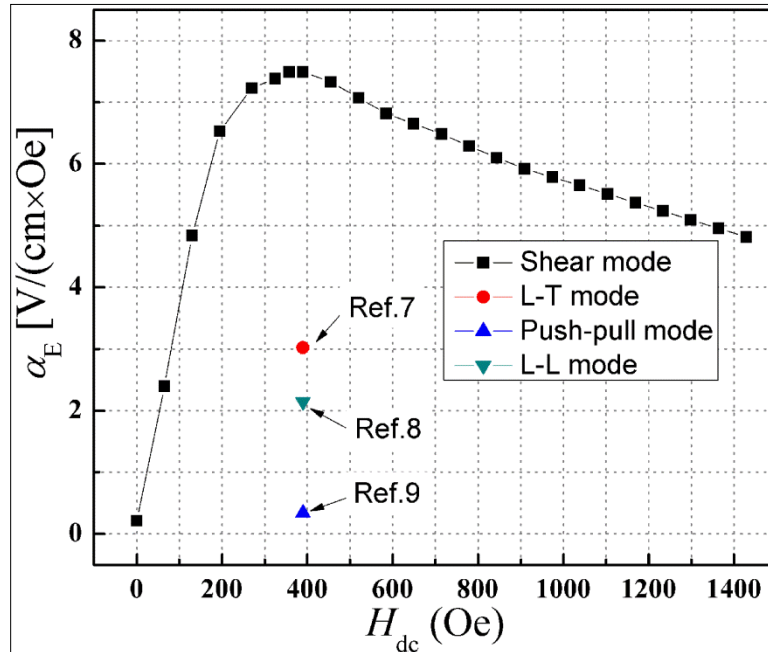


Figure 22. ME coefficient α_E as a function of dc magnetic bias H_{dc} for a shear-mode Terfenol-D/PMN-PT laminate composite.

The points denote the values of α_E for the L-L mode, L-T mode and push-pull mode Terfenol-D/PMN-PT laminate composites (see Refs.^{2,3,7}).

The functional form of the variation of α_E with H_{dc} was similar to that previously reported for magnetostrictive and piezoelectric composites^{2,3,7}, as shown in Figure 22. These data reveal that the value of α_E increased approximately linearly with increasing H_{dc} for low dc magnetic biases ($H_{dc} < 100$ Oe). A maximum value of 7.5 V/(cm×Oe) was observed at an optimal $H_{dc} \sim 400$ Oe, where values of α_E for other mode composites were also maximized^{2,3,7}. It can be seen in Figure 22 that the shear-mode α_E exhibits a $\times 2.5$, $\times 22.1$ and $\times 3.5$ enhancement relative to L-T⁷, L-L² (see Refs.^{3,9}) and push-pull⁹ modes, respectively.

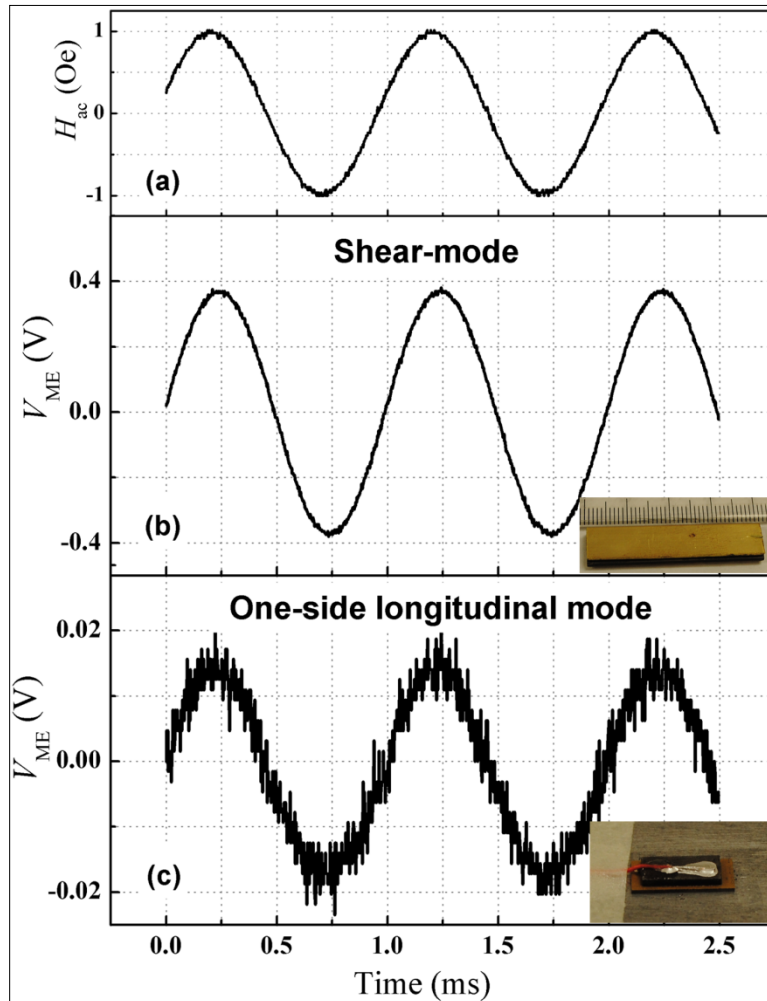


Figure 23 Time-domain waveforms of (a) applied ac magnetic field H_{ac} and ME output voltage V_{ME} for (b) the shear mode Terfenol-D/PMN-PT laminates and (c) a one-sided longitudinal-extensile laminate.

The inset shows the photos of the shear-mode and one-side longitudinal-mode laminate composites.

As mentioned above, the PMN-PT layers in our laminate heterostructure were operated with combined shear and one-sided longitudinal extensional motions. In order to separate the mechanism of the ME effect of the shear-mode laminate [see inset of Figure 23 (b)], an additional laminate composite that operated exclusively in a one-sided longitudinal mode was employed for comparative experiment. This pure one-sided longitudinal mode structure was made by a shear-mode PMN-PT sandwiched between a longitudinally magnetized Terfenol-D layer and an aluminum alloy clamping baseplate, as shown in the inset of Figure 23 (c). The induced output ME voltage V_{ME} in the time-domain for these shear [see Figure 23 (b)] and one-sided longitudinal [see Figure 23 (c)] mode laminates were measured in response to $H_{ac,peak}=1$ Oe at $f=1$ kHz [see Figure 23 (a)]. The results reveal that V_{ME} for the shear-mode laminate was much higher than that for the one-sided longitudinal mode one (i.e., by a factor of $19.7\times$). Clearly, the ME effect of the shear-mode laminate is dominated by the shear extensional motion, rather than the one-sided longitudinal extensional one.

The shear-mode Terfenol-D/PMN-PT heterostructure exhibited a higher ME coefficient than the traditional L-L, L-T and push-pull modes with the same constitute components. However, Terfenol-D has much lower piezomagnetic coefficient than Metglas foils. Thus, the ME coefficient of L-T mode Metglas/single crystal heterostructure was physically important and technologically interesting to investigated.

Besides the shear-mode sensor, we have also investigated a bending mode Metglas/Mn-doped PMN-PT heterostructure, as shown in Figure 24.

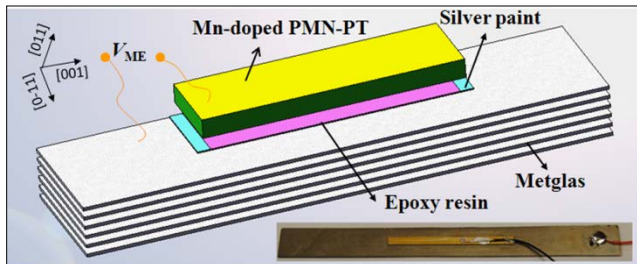


Figure 24. Schematic diagram and photograph of the proposed Metglas/Mn-doped PMN-PT bimorph heterostructure.

The ME charge coefficient α_Q was measured by a charge meter (Kistler type 5015), coupled with a lock-in amplifier (Stanford Research, SR-850), as a function of dc magnetic bias field H_{dc} in response to a constant ac magnetic drive of $H_{ac}=0.1$ Oe at frequency $f=1$ kHz for various Metglas layers N (where N was varied by successively peeling off layers). Both the excitation magnetic field and dc bias were applied along the length of the heterostructure. The measured results were then converted to α_E , as shown in Figure 25 (a). From this figure, it can be seen that the values of α_E for laminate with different N , was nearly zero at $H_{dc}=0$; dramatically increased as H_{dc} was increased; reached a maximum at a particular H_{dc} ; and subsequently decreased as H_{dc} was further increased. Figure 25 (b) shows a summary of the data given in Figure 25 (a), and reveals that the variation of the maximum value of α_E with N for the bimorph heterostructure. The value of α_E did not dramatically decrease after reaching a maximum with increasing N , as previously reported in sandwiched laminate. A high value of $\alpha_E=61.5$ V/cm·Oe can be seen at $N=5$, which was $1.2\times$ enhancement relative to $N=6$. It should be noted that prior reports for laminated

composites have focused on $N=6$. An abnormal thickness fraction-dependent α_E for bending mode ME laminates has been previously discussed elsewhere⁸.

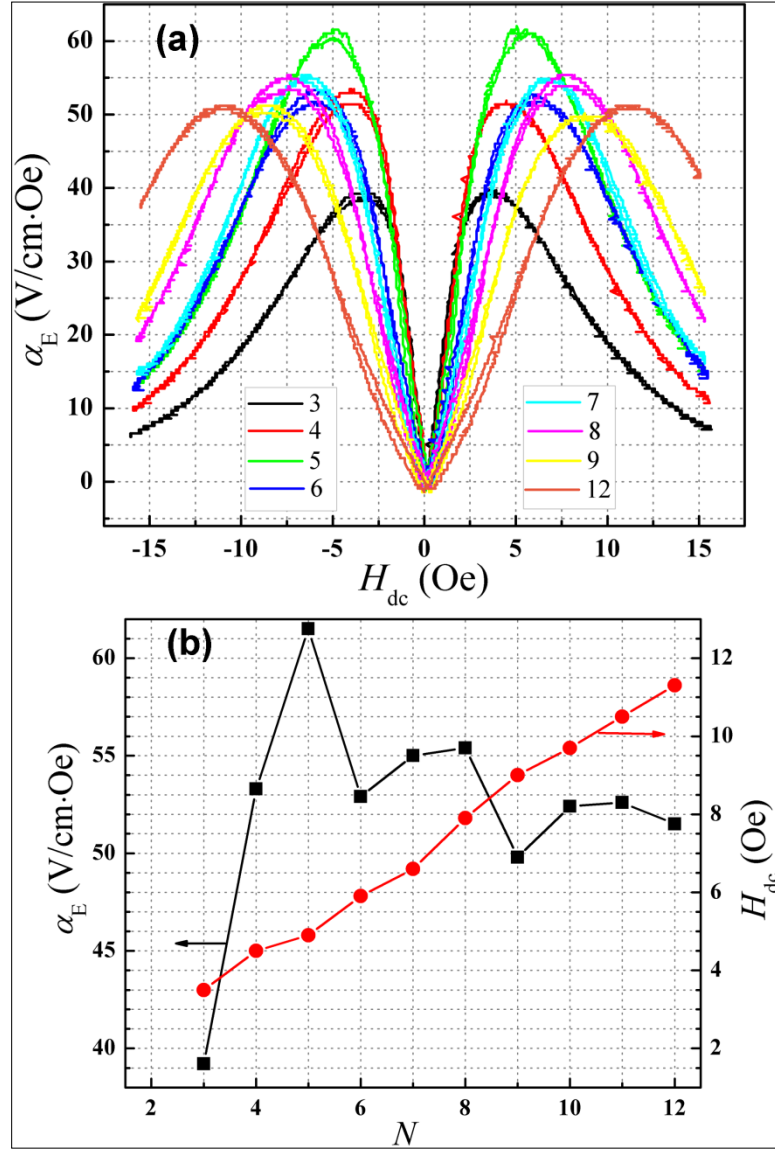


Figure 25. ME coefficient α_E as a function of dc magnetic bias field H_{dc} for various layers of Metglas.

The numbers indicate the number of Metglas layers (N). (b) Maximum α_E and the required optimal H_{dc} dependence of the number of Metglas of Metglas layers N .

The noise charge density and the equivalent magnetic noise of the current L-T mode Metglas/Mn-doped PMN-PT and the previously reported M-P-P Metglas/PMN-PT sensors are compared, as shown in Figure 26. First, the noise charge density due to $\tan\delta$ and R_{dc} of the two sensors presented in Figure 26 (a) were estimated using appropriate sensor parameters. For the M-P-P mode sensor, both $\tan\delta$ and R_{dc} noises contributed to the total noise charge density at 1 Hz, but the magnitude of the $\tan\delta$ noise was 1.2× larger than that of the R_{dc} noise. However, for the

L-T mode sensor, the total noise charge density at 1 Hz was dominated by R_{dc} noise, and the magnitude of R_{dc} noise was $45.5\times$ larger than that of the $\tan\delta$ noise: this is because $\tan\delta$ of the L-T mode sensor was extremely low ($\tan\delta=0.0014$) and R_{dc} was relatively low. It can be seen that the predicted 1 Hz noise charge density of the L-T mode sensor was $2\times$ higher than that of M-P-P mode one. This is because of the much higher R_{dc} noise of the L-T mode sensor, even though the $\tan\delta$ noises of the two modes were close. In this figure, the measured noise charge density of the L-T mode Metglas/Mn-doped PMN-PT sensor is also given. Except at frequencies where external vibration sources were present, the estimated and measured noise charge density exhibited good agreement, especially for 1 Hz and 10 Hz.

The estimated and measured equivalent magnetic noise spectra were given in Figure 26. The results show that the estimated 1 Hz equivalent magnetic noise of the L-T mode was still $1.3\times$ times higher than the M-P-P mode one (i.e., $5.5 \text{ pT}/\sqrt{\text{Hz}}$ to $4.2 \text{ pT}/\sqrt{\text{Hz}}$), whereas the 10 Hz value was $1.3\times$ times lower (i.e., $0.8 \text{ pT}/\sqrt{\text{Hz}}$ relative to $1.0 \text{ pT}/\sqrt{\text{Hz}}$). These results show that our L-T mode Metglas/Mn-doped PMN-PT sensor has a 1 Hz equivalent magnetic noise close to that previously reported for M-P-P mode Metglas/PMN-PT sensors, with a noise floor that drops off more rapidly with increasing frequencies. Experimentally, an ultralow equivalent magnetic noise of $6.2 \text{ pT}\sqrt{\text{Hz}}$ was found at 1Hz, which was close to the predicted value of $5.5 \text{ pT}\sqrt{\text{Hz}}$. Please note that the equivalent magnetic noise of the proposed ME sensor unit was lower than $1 \text{ pT}\sqrt{\text{Hz}}$ at $f=10 \text{ Hz}$. Furthermore, the current L-T mode Metglas/Mn-doped PMN-PT laminate has much lower equivalent magnetic noise at interesting $f=1\text{Hz}$ than the similar L-T mode Metglas/pure PMN-PT laminate (i.e., $6.2 \text{ pT}/\sqrt{\text{Hz}}$ to $10.8 \text{ pT}/\sqrt{\text{Hz}}$). These low equivalent magnetic noises observed for the L-T mode originate from a low $\tan\delta$ noise, coupled with a giant ME charge coefficient.

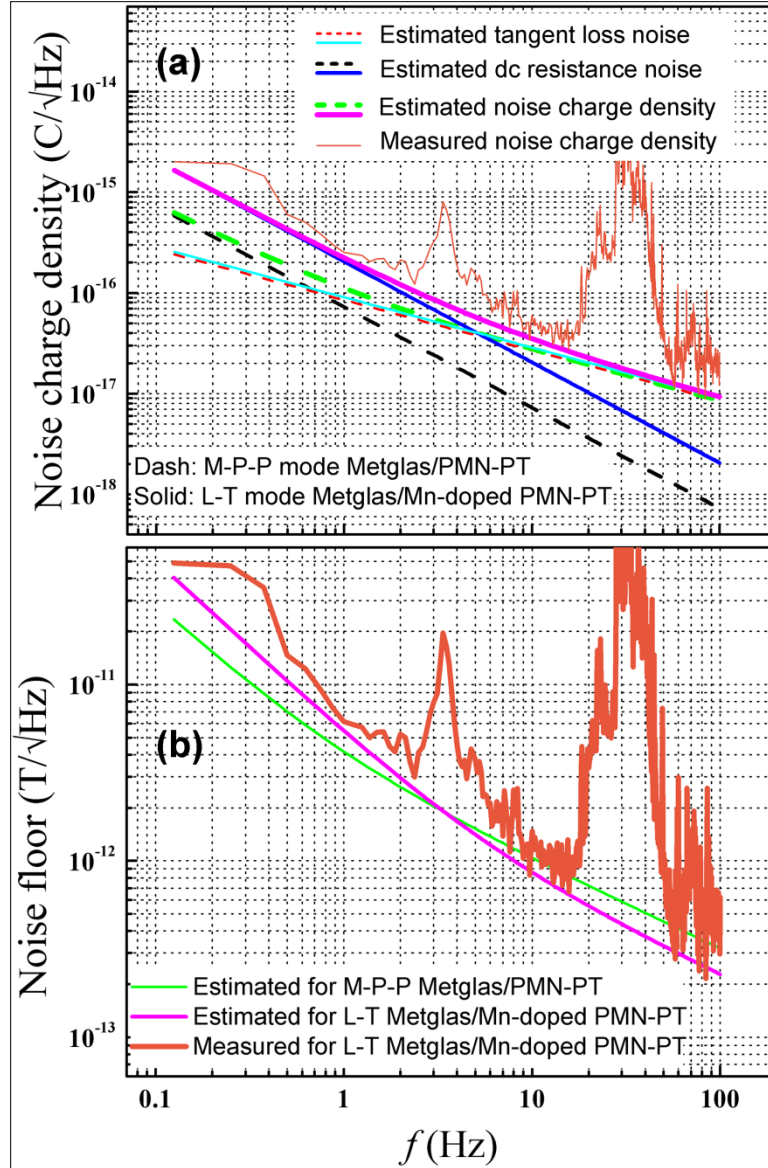


Figure 26. (a) Measured and estimated noise charge density and (b) equivalent magnetic noise for the multi-push-pull mode Metglas/PMN-PT sensor unit (Ref.⁹) and the proposed one over the frequency range of $0.125 \text{ Hz} < f < 100 \text{ Hz}$.

The noise contributions, including constituent dielectric loss and dc resistance loss, are compared.

A.3.3.3. Dumbbell shaped sensor

The proposed ME laminate composite was composed of six-layers of dumbbell-shaped magnetostrictive Metglas and a piezoelectric core composite consisting of two PZT fibers interrogated by a pair of Kapton® interdigitated (ID) electrodes, as shown in Figure 27 (a) and (b). The Kapton® films were attached to both the top and bottom surfaces of the two commercially available PZT fibers each with dimensions of $40 \times 2 \times 0.2 \text{ mm}^3$ using an epoxy resin to obtain a multi-push-pull geometry. The width of ID electrodes were $d=20\mu\text{m}$, and the distance

of adjacent electrodes was $s=0.5\text{mm}$ [see Figure 27 (c)]. Commercially supplied Metglas foils (Vacuumscheltze, Germany, annealed at 300°C) with thicknesses of $25\ \mu\text{m}$ and widths of 18 mm , were then cut into a dumbbell-shape: with end-flanges widths of $W_1=18\text{mm}$, and end-flanges lengths of $L_1=10\text{mm}$. The center cavity was the same length and width as the two PZT core fibers ($L_2=40\text{mm}$, $W_2=4\text{mm}$), as shown in Figure 27 (b). The total length ($L=80\text{mm}$) of the dumbbell-shaped Metglas was selected as a trade-off between the requirements for maximum magnetic flux concentration and the necessity to reduce the device size for practical application. In order to compare the ME properties of dumbbell-shaped designs with the traditional rectangular-shaped laminates, we altered the end-flange width from $W_1=18\text{mm}$, 12mm to 4mm . The ME coefficients and magnetic field sensitivities were then compared for the dumbbell and rectangular-shaped ME laminates using the same Kapton®/PZT-fiber core composites.

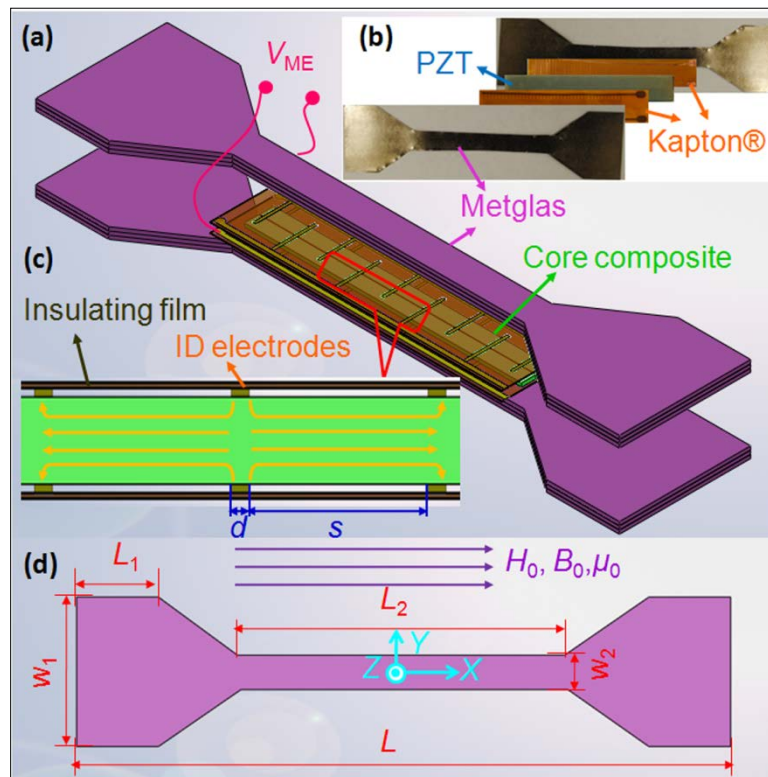


Figure 27. (a) Schematic diagram of dumbbell-shaped Metglas/piezofiber ME laminate with magnetic field amplification effect, (b) exploded view photo of constituent components: six-layers of magnetostrictive Metglas and a piezoelectric core composite consisting of two PZT fibers interrogated by a pair of Kapton® interdigitated (ID) electrodes. (c) Cross-sectional schematic diagram of the ID electrodes in a multi-push-pull configuration (d) and geometry of Metglas layers in barbell configuration showing width and length of end-flange.

The magnetic field was applied along the length direction of the laminate, i.e. axially.

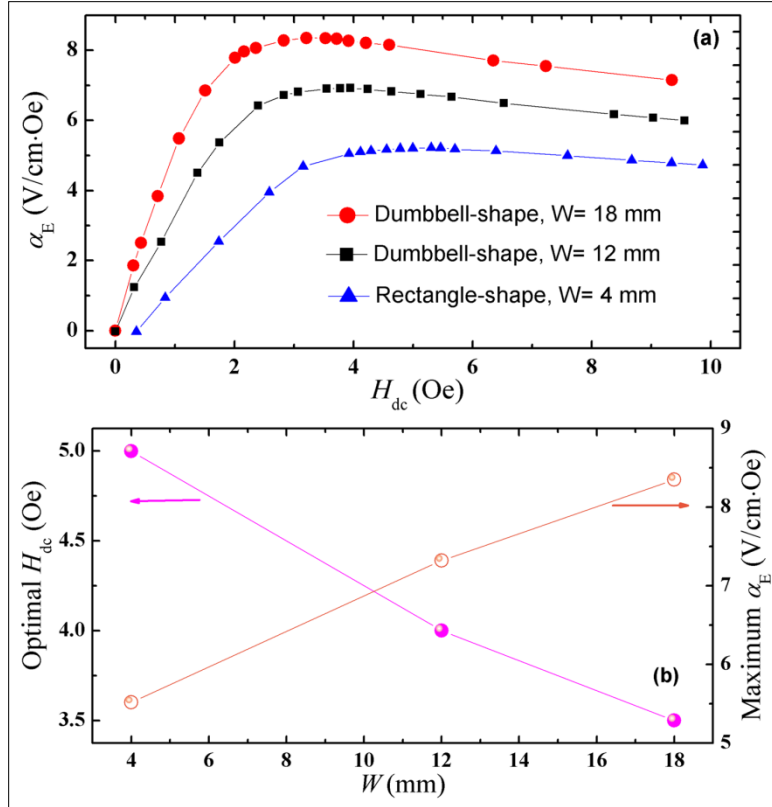


Figure 28. (a) 1 kHz ME coefficient of the dumbbell-shaped Metglas/piezofiber ME laminate as a function of DC magnetic field for various flange widths. (b) Dependence of optimal DC magnetic field and the maximum ME coefficient under optimal DC magnetic field on width of Metglas flange.

Figure 28 (a) shows α_E for the dumbbell ($W=18\text{mm}$ and 12mm) and rectangular-shaped ($W=4\text{mm}$) Metglas/PZT-fiber laminates as a function of DC magnetic bias (H_{dc}) in response to a Helmholtz coil driven AC magnetic field of $H_{ac}=0.1$ Oe at a frequency $f=1$ kHz. The value of α_E was determined derivatively from the ME charge coefficient α_Q and the capacitance (C) of the laminate composite. The values of α_Q were measured using a Stanford Research SR850 lock-in amplifier, together with a charge meter. The capacitance ($C=340$ pF) and dielectric loss ($\tan\delta=0.009$) at 1 kHz were measured using an impedance analyzer (Agilent 4294 A). For both the dumbbell ($W=18\text{ mm}$ and 12 mm) and rectangular-shaped ($W=4\text{mm}$) laminates, α_E was nearly zero under $H_{dc}=0$, increased to a maximum as H_{dc} was increased, and subsequently decreased as H_{dc} was further increased. A significant decrease in the optimal H_{dc} and an effective improvement in the maximum α_E for the dumbbell-shaped laminates are shown in Figure 28 (b). The traditional rectangular-shaped laminates had a relatively larger value of optimal bias ($H_{dc}=5$ Oe) and a lower maximum α_E (~ 5.5 V/cm·Oe). Whereas, for the dumbbell-shaped ($W=18\text{mm}$) design, the optimal H_{dc} was decreased to 3.5 Oe and the maximum value of α_E was increased to 8.5 V/cm·Oe. These changes in properties can be attributed to a concentration of magnetic flux by the dumbbell-shape of the Metglas, thus resulting in magnetic field amplification in the magnetostrictive strain actuator, and in turn leading to a higher effective α_E under lower H_{dc} . We then estimated the magnetic flux density distribution of the dumbbell ($W=18\text{mm}$ and 12 mm) and rectangular-shaped ($W=4\text{ mm}$) Metglas under a uniform external field of 1 Oe in free space

by finite element simulation using Ansoft's Maxwell 3D. A value of the relative magnetic permeability of $\mu_r = 20,000$ was used in the simulation. Figure 29 (a) shows the calculated in-plane magnetic flux density for the three geometric configurations considered. A trace of the magnitude of the magnetic flux density along the axial center-line of each geometry, presented in Figure 29 (b), shows increased flux density for all three geometries relative to free space due to the magnetic flux concentration effect of the high-permeability Metglas. In particular, the magnetic flux density in the center region of the dumbbell-shaped Metglas was significantly higher than that of rectangular-shaped ones. This is important as this center region geometrically corresponds to the piezoelectric core. Furthermore, the magnetic flux density within this magnetostrictive strain actuator region of the dumbbell-shaped Metglas displayed improved axial uniformity, as compared to the rectangular-shaped geometry. The relative magnetic field gain (axial flux density normalized to that of the rectangular geometry) is presented in Figure 29 (c). The magnetic field gain of the dumbbell-shape for $W=18\text{mm}$ and 12mm reached factors of $1.5\times$ and $1.2\times$, respectively. The magnetic flux concentration (termed here a self-amplified magnetic field) of the dumbbell-shaped design acted to simultaneously enhance the effective piezomagnetic coefficient $d_{33,m}$ of the ME laminates and to decrease the optimal required H_{dc} . Additionally, the wider dumbbell geometry exhibited an effective improvement of $1.5\times$ in α_E , and a reduction of $1.4\times$ in the required H_{dc} . These results reveal an important method by which to optimize the effective ME properties of the laminates, while not adversely affecting the sensor-concentrator volume.

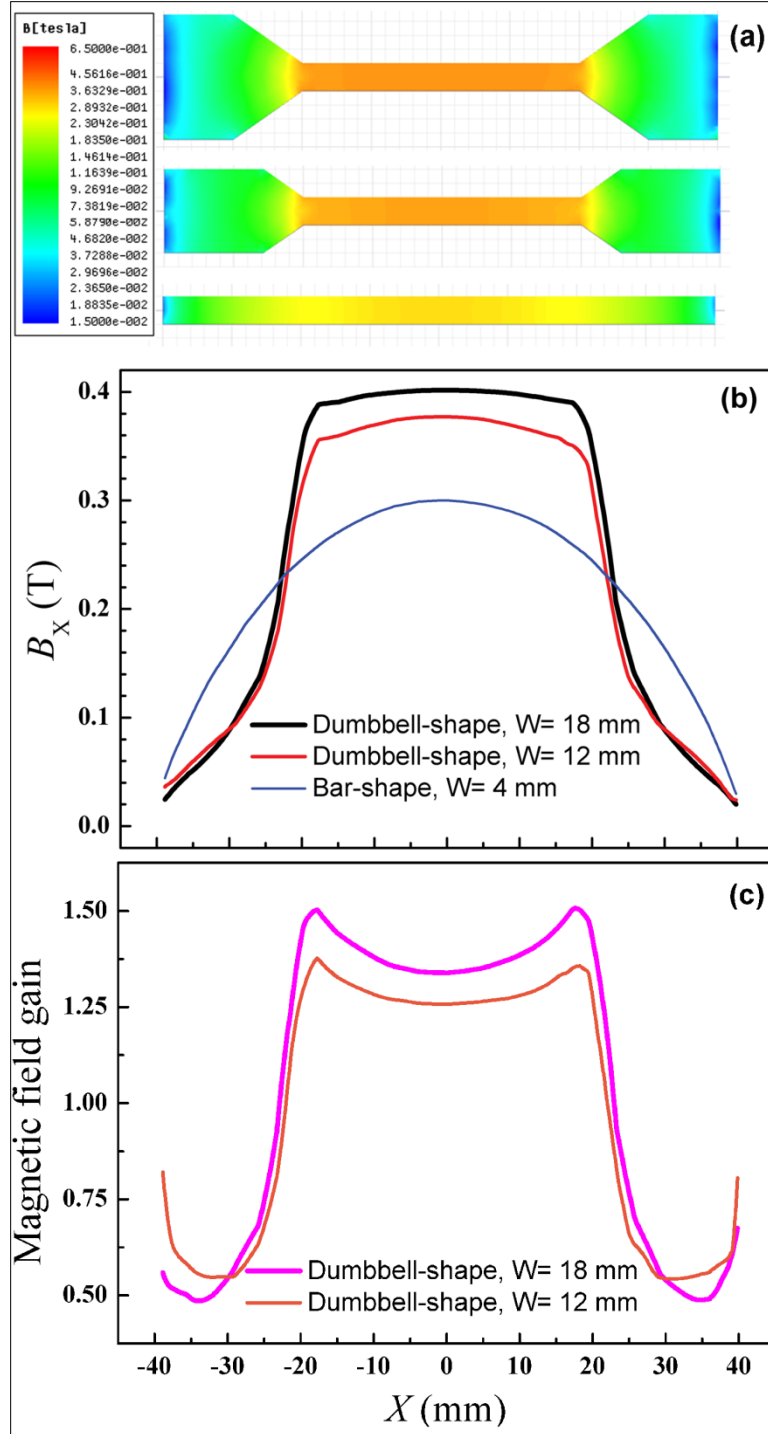


Figure 29. (a) Magnetic flux density distribution under a uniform external field of 1 Oe in free space obtained by numerical simulations using Maxwell 3D. (b) Line trace of magnetic flux density within Metglas sheets with dumbbell-/rectangle-shapes ($W=18$ mm, 12mm and 4mm) along axially centerline. The origin is the center of Metglas sheet (see Figure 27 (d)). (c) The relative magnetic field gain (as compared to rectangular-shape, $W=4$ mm) for the dumbbell-shaped designs ($W=18$ mm and 12mm), calculated by normalizing axial flux density trace to that of rectangular Metglas.

A.3.3.4. Self-stressed sensor

It is known that application of suitable stress to magnetostrictive materials results in a maximum value of the effective linear piezomagnetic coefficient. Under moderate stress, the piezoelectric coefficient of piezoelectric materials can also be increased. Thus, when suitably stress biased, the ME effect of magnetostrictive/piezoelectric laminate composites should also be enhanced. To apply a static stress to ME composites, a stiff frame and pre-stress screws can be used, which makes the unit size large and inconvenient to assemble. Alternatively, the application of an optimum dc electric voltage bias to the piezoelectric layer is similar in context to applying a static stress to the composites. Since the layers of ME laminates are epoxied together, inducing self-stress could be a good way by which to apply static stress to both phases. We have proposed two methods to induce self-stress to Metglas/PZT/Metglas laminates, as shown in Figure 30. Application of either a dc magnetic field to Metglas or a dc electric voltage to PZT was found to enhance the ME effects. These self-stressed ME laminate sensors were found to exhibit lower equivalent magnetic noise floors at low frequencies.

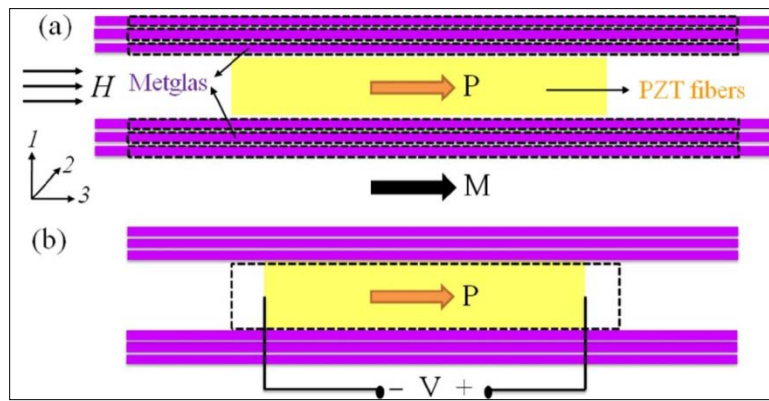


Figure 30. Schematic of the self-stress in the longitudinal section of a ME laminate configured in M-P-P mode.

(a) H_{dc} applied to the Metglas and (b) E_{dc} applied to the interdigitated electrode/PZT core composite. The dashed line illustrates the original shape without H_{dc} or E_{dc} .

Figure 31 (a) shows the value of α_E as a function of H_{dc} for the Metglas/PZT/Metglas laminates with different H_{bias} applied during curing of the epoxy. It can be seen that α_E increased as H_{dc} was increased; and subsequently decreased as H_{dc} was further increased. The maximum value of α_E increased with increasing magnetic fields until $H_{bias} = 20$ Oe, and then decreased with further increase in H_{bias} . As shown in Figure 31 (b), without self-stress in the laminate, the maximum value of α_E was 25.3 V/cm·Oe. However, for $H_{bias} = 20$ Oe, the maximum value of α_E was 31.4 V/cm·Oe, which was a factor of $1.24\times$ larger than that for $H_{bias} = 0$. This value of α_E in the self-stressed state is higher than any ever reported for ME laminates having a core PZT layer. Figure 31 (c) shows the maximum value of α_E of the laminates as a function of E_{bias} . The highest value was 29.2 V/cm·Oe for $E_{bias} = 2.4$ kV/cm, which was $1.15\times$ higher than the laminate without self-stress.

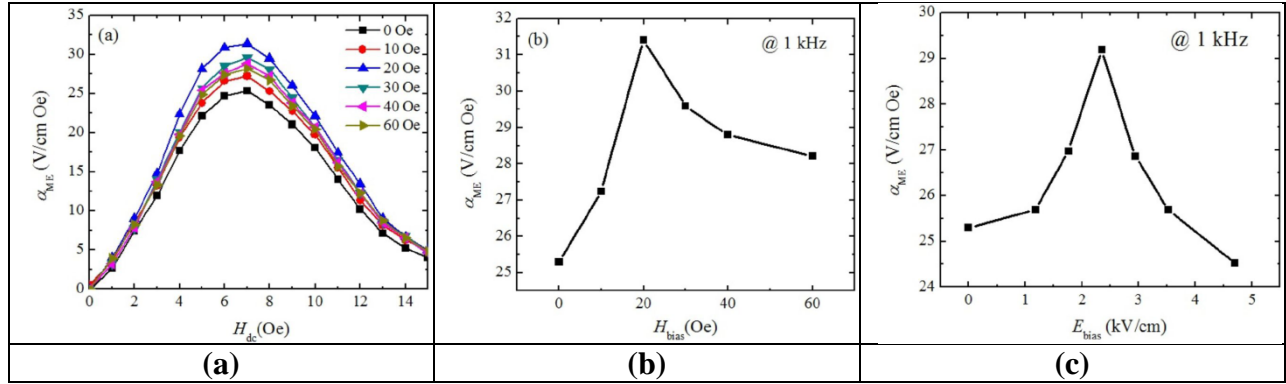


Figure 31. (a) The values of the α_E as a function of H_{dc} for Metglas/PZT/Metglas laminates epoxied together under various H_{bias} . (b) Maximum values of α_E as a function of H_{bias} . (c) Maximum values of α_{ME} as a function of E_{bias} . The data were measured at an ac magnetic field of $H_{ac} = 0.1$ Oe and at a frequency of $f=1$ kHz.

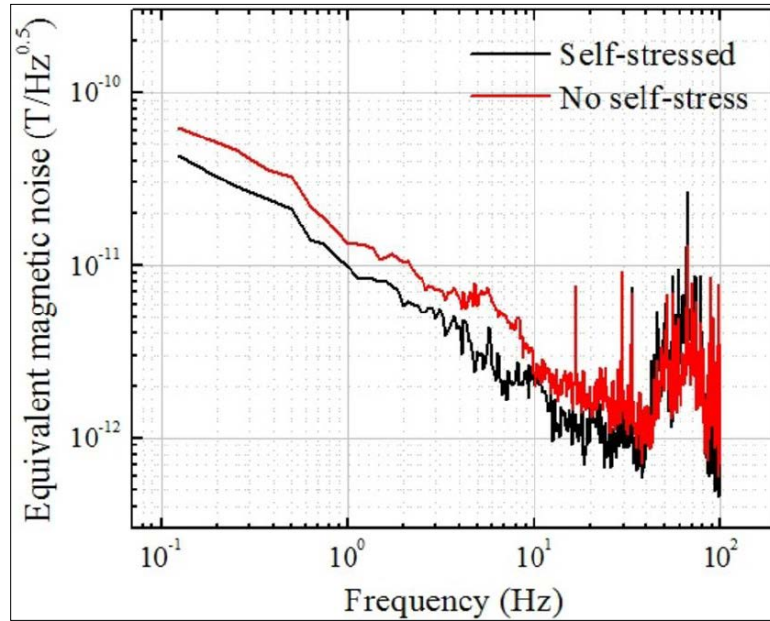


Figure 32. Equivalent magnetic noise floors of self-stress Metglas/PZT/Metglas laminates epoxied together under $H_{bias} = 20$ Oe, and laminate without self-stress.

Figure 32 shows the equivalent magnetic noise floor of the self-stressed Metglas/PZT/Metglas laminate epoxied together under $H_{bias} = 20$ Oe, which is compared to the laminate prepared without self-stress. The results show a decrease in the equivalent magnetic noise floor for the self-stressed laminate over the frequency range of $0.1 < f < 30$ Hz. At $f = 1$ Hz, the noise floor was reduced from $13.3 \text{ pT}/\sqrt{\text{Hz}}$ to $9.8 \text{ pT}/\sqrt{\text{Hz}}$, which was by a factor of about $1.35\times$.

A.3.3.5. Geometry-induced ME enhancement

From previous modeling, we found the ME coefficient in laminate composite was significant dependent on the geometry. In other word, the ME coefficient can be enhanced if we choose the optimum geometry of the two components. Thus, we fabricated several sensors, and experimentally approved the previous modeling, as shown in Figure 33 (a). They either had the

same width of Metglas ($w_m=10\text{mm}$) with different widths of the piezofiber layer (i.e., $N=3$ and 5), or the same width of piezofiber layer (i.e., $N=5$) with different width of Metglas ($w_m=10$ and 18mm). PZT bundles of dimensions $40\text{mm}\times 6\text{mm}$ and $40\text{mm}\times 10\text{mm}$ served as the cores of the laminates, which consisted of $N=3$ and $N=5$ PZT fiber each with dimensions of $40\text{mm}\times 2\text{mm}\times 0.18\text{mm}$. The PZT fibers were oriented along the length direction of the laminates, as shown in Figure 33 (b) and (c).

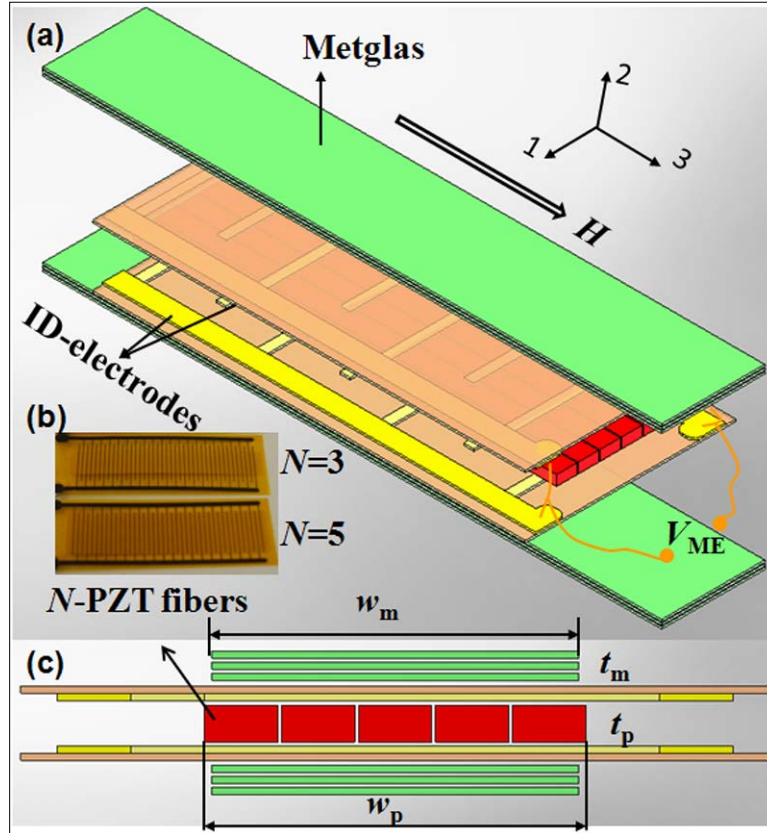


Figure 33. (a) Three-dimensional and (c) cross-sectional schematic illustration of the multi-push-pull mode Metglas/piezofiber heterostructure. (b) Photograph for the PZT-fiber core composites with $N=3$ and 5.

The width of the Metglas layer is w_m , and the width of PZT bundle is w_p (i.e., $w_p=2N$, width of each fiber is 2 mm and N is the number of fibers).

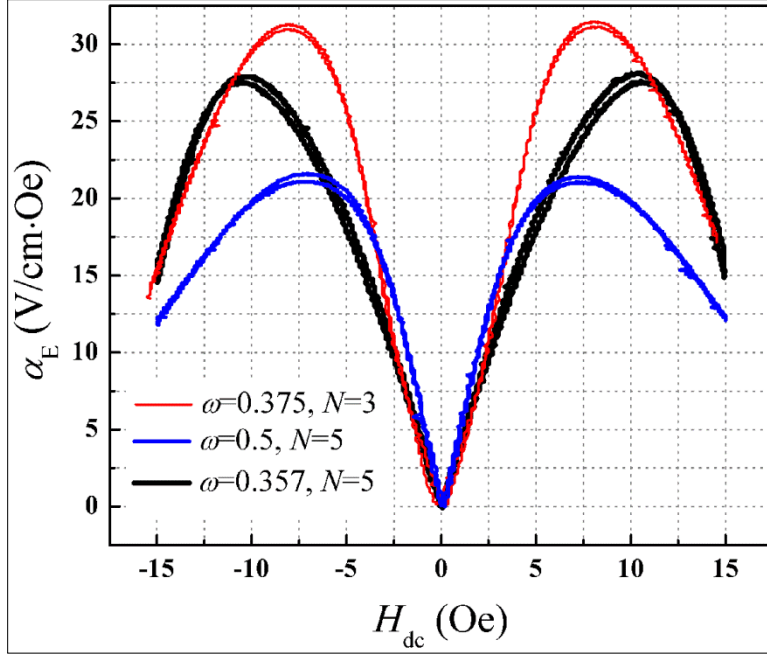


Figure 34. Measured ME coefficient α_E as a function of dc magnetic bias H_{dc} for various piezofiber width fraction ω .

Figure 34 shows the ME coefficient α_E as a function of H_{dc} for different width fraction of PZT-fiber with $\omega=0.375$ and $N=3$, $\omega=0.5$ and $N=5$, and $\omega=0.357$ and $N=5$. From this figure, it can be seen that the values of α_E increased from nearly zero at $H_{dc}=0$ Oe to a maximum at a particular H_{dc} , and then subsequently decreased as H_{dc} was further increased. One can also see that the maximum value of α_E for $\omega=0.375$ and 0.357 were larger than that for $\omega=0.5$, resulting corresponding 1.3 and 1.5 times enhancements in α_E . It should be noted that prior reports have focused on $\omega=0.5$. This indicates that there remains notable potential to further enhance the values of α_E by improving the interfacial bonding conditions. Additionally, we can see the values of α_E for $\omega=0.357$ was even lower than that for $\omega=0.375$. This might be due to higher demagnetization effects in Metglas when wider layers are used.

A.3.3.6. Electric-field tuning effect

In previous studies, the ME coefficient have been widely investigated as a function of magnetic fields, working modes, composite microstructures, interfacial bonding condition, and so on. While a number of studies of E control of the magnetic properties of nanosized thin films have been reported due to their relevance in voltage-driven memory applications with low power consumption, investigations of E tuning of ME properties in laminated composites has been deficient. In this quarter, we present an investigation an E tuning effect on the ME coefficient and equivalent magnetic noise for a multi-push-pull configuration Metglas/piezofiber heterostructure composite.

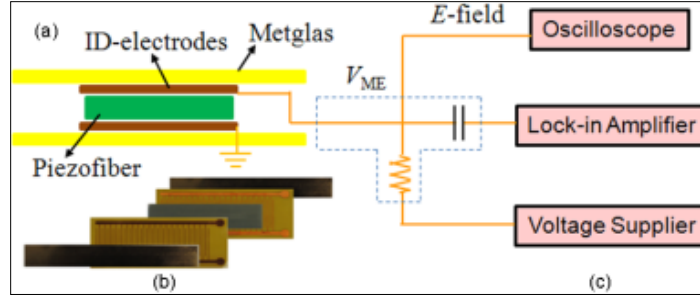


Figure 35. (a) Schematic diagram of the multi-push-pull configuration Metglas/PZT-fiber ME composite; (b) enlarged view of the constituent components: six-layers of magnetostrictive Metglas and a piezoelectric core composite consisting of five PZT fibers interrogated by a pair of Kapton® interdigitated (ID) electrodes; and (c) the electric field tuning effect measurement set-up.

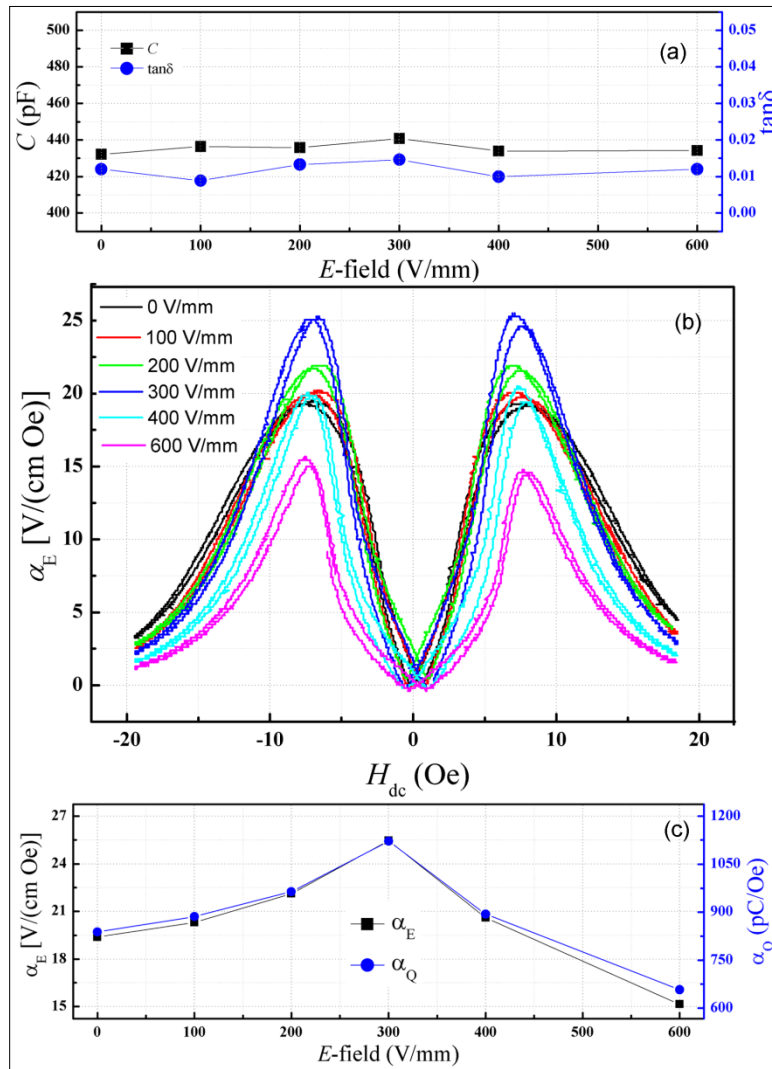


Figure 36. The capacitance and dielectric loss of a Metglas/PZT-fiber sensor as a function of applied E ; (b) dependence of α_E on H_{dc} under various applied E ; and (c) the maximum values of α_E and α_Q as a function of applied E .

Figure 35 (a) shows a schematic diagram and working principle of the multi-push-pull configuration for a Metglas/PZT-fiber heterostructure. The composite components were bonded together using epoxy resin, as shown in Figure 35 (b). The experimental arrangement for the measurement of the E tuned ME effect is illustrated in Figure 35 (c). A dc voltage was provided by a voltage supplier (Model 210-20R), which was applied to the ME composite through a dc port of a bias tee ($R=1M\Omega$, $C=1nF$). This E drive applied on the ME composite was monitored by an oscilloscope. The ME signals induced across the ID electrodes of the PZT-fiber layer were measured as a function of dc magnetic bias H_{dc} in response to a constant ac magnetic drive of $H_{ac}=0.1$ Oe at 1 kHz.

First, we characterized the dielectric properties of the Metglas/PZT-fiber laminate under various E using a LCR meter (HP 4284 A) coupled to a dc voltage supplier (Model 210-20R) via a blocking circuit. Representative data of the capacitance C and dielectric loss $\tan\delta$ at 1 kHz are shown in Figure 36 (a). We found that C and $\tan\delta$ were relatively invariant to the applied E over 0-600 V/mm, as the magnitude of the E induced dimension changes in the piezofiber were insufficient to appreciably alter the dielectric properties. Meanwhile, the dc resistance R_{dc} of the laminate was directly determined to be $60 G\Omega$ using a pA Meter/dc voltage source (HP 4140 B) based on Ohm law. These results indicate that the noise charge density of the sensor was independent on the applied E , which will be systematically shown in the next paragraph.

The ME coefficient α_E as a function of H_{dc} for the Metglas/PZT-fiber heterostructure under various applied E over 0-600V/mm is shown in Figure 36 (b). The value of α_E , here, is a derivative measurement determined from the ME charge coefficient α_Q and C of the sensor (i.e.

$\alpha_E = \frac{\alpha_Q}{s \times C}$): please note that the value of C was relatively insensitive to both the H_{dc} , and applied E [see Figure 36 (a)]. For all applied E , the values of α_E tended towards zero for $H_{dc} \approx 0$ Oe, increased to a maximum and then decreased with increasing of H_{dc} : which is attributable to a vanishing piezomagnetic coefficient ($d_{33,m}$) at $H_{dc} \approx 0$ Oe, and a peak $d_{33,m}$ value near an optimal $H_{dc} \approx 8$ Oe. The results also indicate that the maximum values of α_E and α_Q at the optimal H_{dc} are tunable by E , as shown in Figure 36 (b). The changes in α_E and α_Q were qualitatively similar, due to negligible changes of C with E .

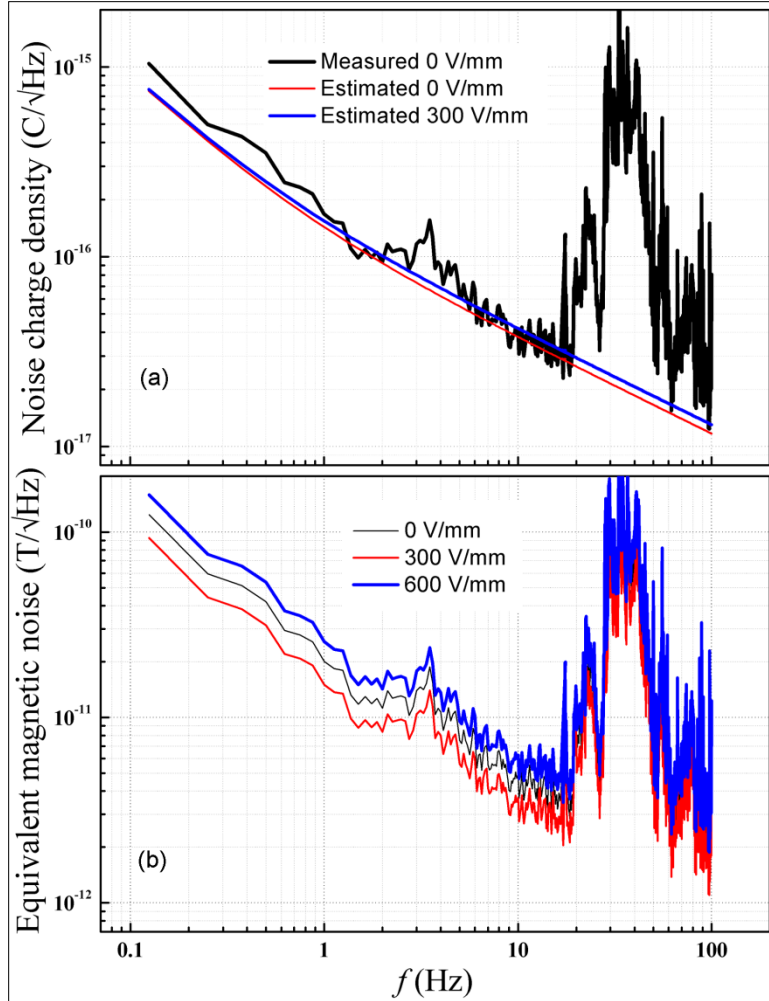


Figure 37. (a) Estimated noise charge densities of the proposed sensor unit under applied E of 0 V/mm and 300 V/mm and the measured values for $E=0$ V/mm, over the frequency range of $0.125 \text{ Hz} < f < 100 \text{ Hz}$. **(b)** Measured equivalent magnetic noise of the sensor unit under applied E of 0 V/mm, 300 V/mm and 600 V/mm.

These results are derivative measurements determined from the noise charge density without applying E and α_Q under various applied E fields.

After measuring the dielectric and ME properties, the Metglas/PZT-fiber laminate was connected to a low noise charge amplifier (CA) with a transfer function of 5.18 V/pC to form a sensor unit. The influence of E on the noise charge density and the equivalent magnetic noise was then studied. Figure 37 (a) shows the measured and predicted noise charge density under $E=0$ and 300 V/mm, for a ME sensor unit (laminate and CA) in the frequency range of $0.125 < f < 100$ Hz. The dominate noise charge density contributions due to $\tan\delta$ and R_{dc} sources were modeled using appropriate ME sensor parameters under various E as presented in Figure 37 (a). It can be seen that except at frequencies where external vibration sources are present, the modeled and measured noise charge densities for 0 V/mm showed good agreement. In particular, the values predicted for $E=0$ and 300 V/mm were nearly coincided over the entire measured frequency

range: this is because the noise contributions of C , $\tan\delta$, and R_{dc} were independent of E , as given by Figure 36 (a).

Figure 37 (b) shows the measured equivalent magnetic noise of the ME sensor unit over the frequency range of $0.125 < f < 100$ Hz for applied $E=0$, 300 and 600 V/mm. These results were obtained by converting the noise power density spectrum (PSD), directly measured in the absence of E , the gain of the charge amplifier, and α_Q for the corresponding value of E (i.e. $\sqrt{PSD} / (\text{gian} \times \alpha_Q)$). The equivalent magnetic noise at 1 Hz for $E=0$, 300 and 600 V/mm were 20.1, 15.0 and 25.6 pT/ $\sqrt{\text{Hz}}$, respectively. These results show that the equivalent magnetic noise can be reduced by a factor of $1.3\times$ under an $E=300$ V/mm, which is a direct result from the enhanced value of α_Q . Correspondingly, the 1 Hz equivalent magnetic noise was increased for $E=600$ V/mm due to the decreased α_Q .

A.3.4. Dielectric loss noise reduction

A.3.4.1. Interfacial bonding optimization

We have concentrated in optimizing the epoxy resin needed to bond the PZT fibers with the patterned copper electrode-Kapton tape. Earlier during our heterostructure preparation processing steps, we used to lay down a thick layer of epoxy on both sides of the PZT fibers and then used a laminator to bond the patterned copper electrode-Kapton tape on both sides of the PZT. This process used to offer epoxy thickness around 15-20 μm . After this, we used to cure the epoxy at about 50-60°C for about 3-4 hours and then used to bond the Metglas on both sides following the similar process described above. During our investigation, we understood that this process might give rise to an inhomogeneous epoxy distribution and thickness that might result in an inhomogeneous stress transfer from the Metglas layer to the PZT layer. This, in turn, can result in a higher noise floor than that one might obtain for a perfectly homogeneous epoxy. Further, the old process of laying down epoxy with hand and using the laminator, might depend on the amount of epoxy one is putting (dependent on person) that probably can give rise to individual dependent non-reproducible heterostructures with different sensitivities.

We improved the process steps in dealing with epoxy by (1) vacuum bag processing and (2) spin coating. We first concentrated on the vacuum bag processing. Just after putting the PZT and the patterned copper electrode-Kapton tape together with epoxy, we kept it in a vacuum bag for about 12 hours at room temperature to cure the epoxy. In the mean time, we made our 3 Metglas stack layers (each layer of about 25 μm thick) by putting epoxy followed by pressing and curing at about 50-60°C. Then, we pasted two of these three Metglas stack layers on both sides of the Kapton side of the patterned copper electrode-Kapton tape-PZT structure and kept it in the vacuum bag for about 10-12 hours. For the spin coating approach, we spin coat the epoxy at different rates (for example, 3000 or 3500 rpm) to make it homogeneous on PZT and then follow the above mentioned vacuum bag process to obtain the heterostructures.

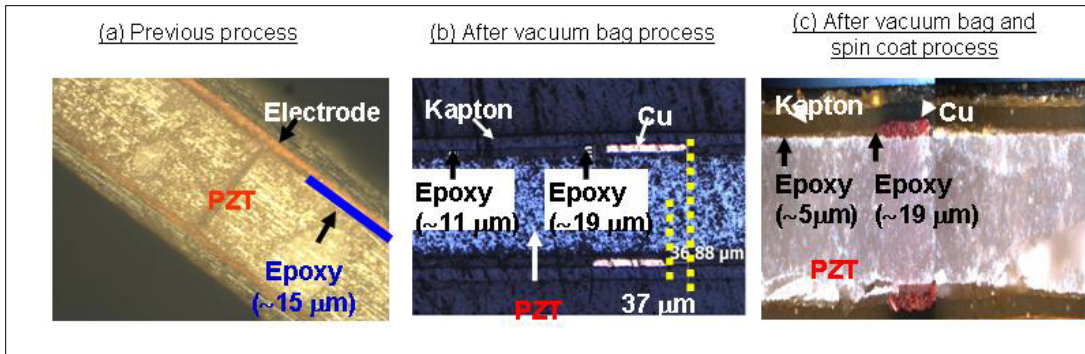


Figure 38. Images of the PZT-patterned electrode-Kapton tape structures after (a) previous process, (b) and (c) vacuum bag process, and (d) vacuum bag and spin coating process. The epoxy thicknesses are as indicated.

Table 7. Comparison of dielectric loss, ME responses with and without aluminum box, and with plastic box for a Metglas-PZT sensor.

Laminate	Dielectric loss (%)	ME voltage (V/Oe)	ME charge (pC/Oe)
Before	1.9	1.31	765
After vacuum bag	1.9	1.56	890
After vacuum bag and spin coating	1.1	1.80	1920

Figure 38 shows the images of the heterostructures after different processing. Part (a) shows a view of the PZT- copper electrode-Kapton tape structure. One can see that the in between epoxy was about 15 μm thick and it was pretty inhomogeneous. Part (b) shows the images of the structure after vacuum bag process. In (b), one can see that the epoxy thicknesses are different at different places. It indicates that the epoxy is much more homogeneous than the previous process and the epoxy close to the patterned copper electrode is about 19 μm thick, while it is about 11 μm thick away from the electrode. This picture clearly points out to the fact that the top Kapton surface might have a surface roughness of about 8-10 μm . Further, one can also see that the top copper electrode is about 37 μm off from the bottom electrode which can result in a lower ME response and can contribute to the increase in the noise floor response. Part (c) shows the image of the structure after both vacuum bag and spin coat process. The epoxy thickness is about 11 μm and looks quite homogeneous. The corresponding dielectric loss and ME properties of sensors using previous method and after interfacial bonding optimization, were presented in Table 7. It can be seen that the sensors using Spin-coat to form the interfacial bonding exhibited significantly lower dielectric loss and higher ME coefficients.

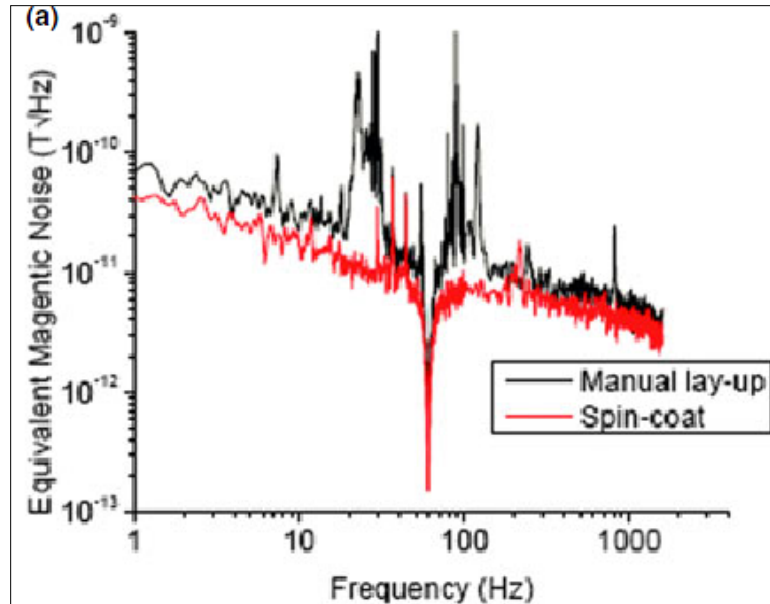


Figure 39. Equivalent magnetic noise spectrum of manual lay-up and spin-coat/vacuum bag technique.

Figure 39 shows the equivalent magnetic noise floor of sensor unit made by spin-coat/vacuum, compared to those made by the manual lay-up process. The noise floor at 1 Hz was ~ 40 pT/ $\sqrt{\text{Hz}}$, which was almost a factor of $2\times$ lower than the ~ 70 pT/ $\sqrt{\text{Hz}}$ for a ME unit containing a laminate made by the manual lay-up process. This reduction in equivalent magnetic noise was due to the enhancement in ME coefficient and the reduction in dielectric loss.

A.3.4.2. Poling optimization

For piezoelectric single crystals, the material properties are quite sensitive to the poling conditions. In order to gain a more comprehensive understanding on the effect of poling conditions on ME properties in Metglas/PMN-PT laminates, we explored the effects of poling procedure both on PMN-PT stand alone fibers and on PMN-PT/Metglas composite ME structures based on an automatic poling system, as shown in Figure 40. Optimal poling conditions result in an effective improvement in the ME coefficient, a significant reduction in equivalent magnetic noise, and a notable enhancement in magnetic field sensitivity.

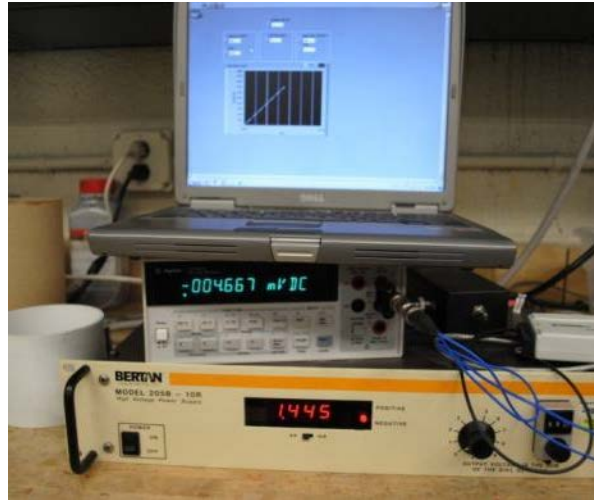


Figure 40. Computer display showing Labview interface ramping voltage to poling setup

Four commercially supplied PMN-PT samples each with length of 10mm were poled at a electric field of $E_1=1000$ V/mm, but at various temperatures and with different E -field ramp rates, as detailed in Table 8. For poling procedures (a) and (b), the PMN-PT samples were poled at room temperature under amaximum E_1 for 15 min, with voltage ramp rates of +100 V/min and -20 V/min. For procedures (c) and (d), the samples were poled at 120 °C under the maximum E_1 for 15 min, then maintained at half of E_1 with $E_2= 500$ V/mm during the cool down cycle. Ramp rates for procedures (c) and (d) were +100 V/min and -20 V/min for ramp-up and ramp-down, respectively. For each sample, ϵ_r , $\tan\delta$, and k_{33} was measured or determined by an impedance analyzer (*Agilent 4294 A*), and d_{33} was measured by a *Berlincount*-type meter. The parameters of the PMN-PT samples and the corresponding poling procedures are listed in Table 8. The dielectric constant of the PMN-PT fiber was insensitive to voltage ramp rate and exhibited negligible enhancement when poled at higher temperatures. Values of d_{33} and k_{33} for PMN-PT were significantly enhanced when poled at an elevated temperature of $T= 120^{\circ}\text{C}$, due to smaller domain sizes and more neutral domain wall configurations. However, the values of $\tan\delta$ decreased both with reduced voltage ramp rate and with increasing poling temperature. This might be because during the poling process, the domain walls in PMN-PT crystals are forced to align parallel to the poling field direction: mechanical stresses will develop, which may result in microcracks within the crystals. Thus, we poled the crystal at higher temperatures and/or using slower voltage rampings: as under these conditions poling is easier thus resulting in fewer microcracks, and consequently lower $\tan\delta$ values.

Table 8. Poling procedures for PMN-PT fibers, and the their properties poled under various procedures.

Poling procedures	T (°C)	E ₁ (V/mm)	E ₂ (V/mm)	Ramp up/down (V/min)	ε _r ^{a)}	tanδ ^{a)} (%)	d ₃₃ ^{b)} (pC/N)	k ₃₃ ^{c)} (%)
a	25	1000	0	100	3850	2.1	920	0.74
b	25	1000	0	20	3890	1.7	980	0.76
c	120	1000	500	100	3980	1.6	1140	0.83
d	120	1000	500	20	3950	1.1	1280	0.85

^{a)} 16-times average method (Experimental error<1%).

^{b)} 5-points average method (Experimental error~2%).

^{c)} Resonance-antiresonance method (Experimental error<1%).

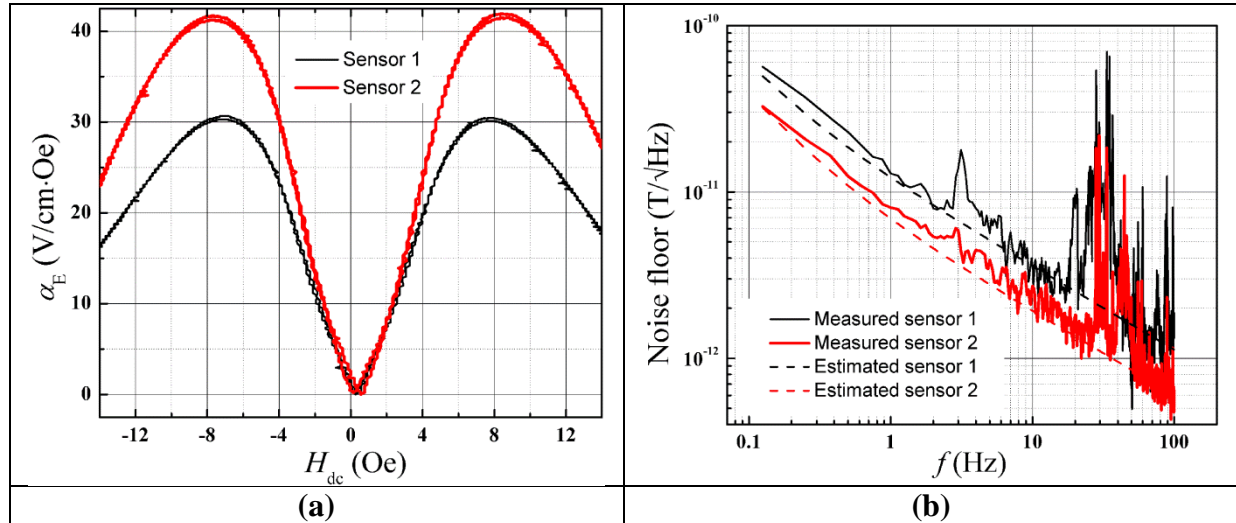


Figure 41. (a) ME voltage coefficient as a function of magnetic bias field for the Metglas/PMN-PT fiber heterostructures poled by different procedures: denoted as sensor #1 and sensor #2, respectively. **(b)** Theoretical and experimental equivalent magnetic noise spectra for the two sensor units.

The capacitance ($C=670$ pF, 685 pF) and dielectric loss factors ($\tan\delta=0.022$, 0.012) of the two laminates were then measured using an impedance analyzer. The DC resistance was determined to $R_{DC}=61\text{G}\Omega$ and $59\text{G}\Omega$ for the two laminates, based on Ohm's law using the current-to-voltage data from a pA Meter/DC voltage source (HP 4140B) α_E of the two Metglas/PMN-PT laminates, derivative values determined from α_Q , the capacitance C_p of the sensor and the length of an interdigitated unit were characterized as a function of H_{dc} at room temperature under zero stress bias using an in-house automated measurement system. For both sensors, α_E increased with increasing H_{dc} up to about $H_{dc}=8$ Oe, where a maximum value was reached. Above 8 Oe, α_E subsequently decreased with increase of H_{dc} as shown in Figure 41 (a). The maximum values of α_E for the two sensors poled using procedures (a) and (d) were 31 V/cm·Oe and 42 V/cm·Oe, respectively. These results demonstrate that optimal poling conditions result in an increase of α_E by a factor of $1.4\times$. Corresponding maximum values of α_Q were 1760 pC/Oe and 2450 pC/Oe respectively. This enhancement is a direct consequence of the increase in the piezoelectric properties originating from the optimal poling conditions.

The equivalent magnetic noise floor of the two ME laminate sensor units (sensor packages and low-noise SAIC JFET charge amplifier) was first predicted by considering the constituent noise sources of dielectric loss (N_{DE}) and DC leakage resistance (N_R), and then measured inside a high-mu-metal magnetic shielding chamber in the frequency range of $0.125 < f < 100$ Hz as shown in Figure 41 (b). The experimental equivalent magnetic noises of the two sensor units were deduced from the noise power spectrum in V^2/Hz directly obtained from a Dynamic Signal Analyzer (Stanford Research, SR-785), the experimental values of α_Q [in C/T], and the charge amplifier transfer function (5.18 V/pC).

In Figure 41 (b), it can be seen that except at frequencies where external vibration sources are present, the trend of the modeled and measured equivalent magnetic noise for each of the two sensor units show good agreement. The experimental values are slightly higher than the theoretical values, which might be due to an oversimplification of the theoretical model in terms of electrical charge amplifier and external thermal noise sources. In particular, the experimental equivalent magnetic noises at $f=1$ Hz for the two sensors units poled following procedures (a) and (d) were $12.9 \text{ pT}/\sqrt{\text{Hz}}$ and $8.0 \text{ pT}/\sqrt{\text{Hz}}$, respectively. A significant reduction of $1.6\times$ in the equivalent magnetic noise was achieved solely through optimization of the poling conditions.

A.3.4.3. Single crystal sensors

Single crystal ferroelectrics, such as lead magnesium niobate-lead titanate (PMN-PT) near the morphotropic phase boundary between ferroelectric rhombohedral and ferroelectric tetragonal phases, exhibit ultrahigh piezoelectric coefficients of $\sim 2000 \text{ pC/N}$ and low tangent losses of $\sim 0.5\%$: as listed in Table 9. In particular, it has been found that Mn substitutions in PMN-PT is effective achieving in higher coercive fields, and lower dielectric permittivities and tangent losses due to the selectively pinning of 180° domain wall motions¹⁰. For example, in $<001>$ -oriented 1mole% Mn-doped PMN-29PT, giant piezoelectric coefficient $d_{33}=2000 \text{ pC/N}$ and extremely low $\tan\delta=0.07\%$, have been reported, as summarized in Table 9. The superior properties of Mn-doped PMN-PT single crystal provide opportunities for realization higher magnetic field sensitivity through a combination of giant ME effects and ultralow equivalent magnetic noise.

Table 9. Property parameters for multi-push-pull mode Metglas/PMN-PT and L-T mode Metglas/Mn-doped PMN-PT sensors and the related pure single crystals.

ϵ_{33}	$\tan\delta$	d_{33} or d_{31} [pC/N]	C [pC]	$\tan\delta$	R_{dc} [GΩ]	α_E [V/cmOe]	α_Q [pC/Oe]
<001>-PMN-PT ^a			M-P-P mode Metglas/PMN-PT ^c				
7000	0.005	2000	344	0.008	80	52	2680
<110>-Mn-doped PMN-PT ^b			L-T mode Metglas/Mn-doped PMN-PT				
1300	0.001	1800	3120	0.0014	10	61.5	3914

^a Cited from Ceracomp Co., Ltd.

^b Measured based on IEEE standards.

^c Cited from Ref.⁹

The dielectric and ME properties of various single crystal sensors were listed in Table 10. From these results, we can see that the Mn-doped PMN-PT sensors exhibited relative low dielectric loss, whereas, the repeatability of these sensors were poor due to the segregation of Mn substitution during single crystal growth. One also can see that the CPSC PMN-PT based sensors have superior ME properties and relative low dielectric loss.

Table 10. Properties of PZN-PT, PMN-PT and Mn-doped PMN-PT sensors.

Spacing	C (pF)	$\tan\delta$	R_{dc} (GΩ)	αV (V/Oe)	αQ (pC/Oe)
PZN-PT with length of 30mm					
S= 1 mm	1#	558	1.43%	~80	3.66
	2#	567	1.33%	~80	4.23
	3#	567	1.45%	~80	3.79
PMN-PT with length of 40mm					
S= 1mm	1#	666	1.1%	~60	2.78
	2#	690	1.28%	~60	2.81
	3#	670	1.21%	~65	2.8
S= 2mm	1#	208	1.3%	~110	3.5
	2#	211	1.2%	~105	3.7
	3#	213	1.3%	~110	3.9
Mn-doped PMN-PT with length of 40mm					
S= 1.5mm	1#	356	1%	~120	3.3
	2#	368	0.9%	~120	3.8
	3#	281	1%	~120	3.3
	4#	458	0.8	~120	3.8
S= 2mm	1#	289	0.8%	190	4.8
	2#	285	0.9%	185	4.8
	3#	288	1.1%	190	5.5
S= 2.5mm	1#	175	0.7%	195	5.8
CPSC PMN-PT with length of 40mm					
S= 2mm	1#	244	1.37%	~130	5.1
	2#	255	1.45%	~130	4.8
	3#	259	1.55%	~130	4.85
	4#	256	1.4%	~130	5.4
S= 1.8mm	1#	344	0.75	90	5.7
	2#	350	0.7	~90	5.9

A.3.5. Sensor stacking for noise floor reduction

In our previous study, we found sensors in series or in parallel connection can reduce the equivalent magnetic noise and enhance the magnetic field sensitivity¹¹.

A.3.5.1. Effect of mutual inductance

First, the effect of distance between a pair of Metglas/PZT-Metglas ME laminated sensors was studied. An optimum distance was found that is important for the application of ME sensor array to have higher values of α_E , and this enhanced performance at an optimum distance is due to flux

concentration effects, i.e., the sensors in the pair have mutual inductance effects, as shown in Figure 42 (a).

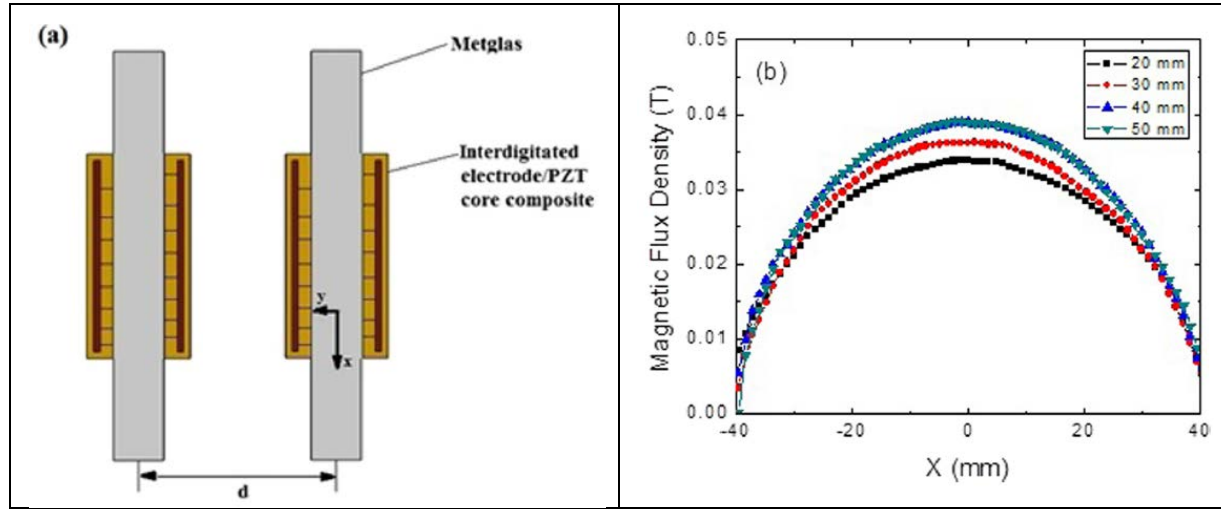


Figure 42. (a) Schematic representation of a pair of Metglas/PZT L-L mode ME laminates separated by a distance d . (b) Magnetic flux density of the Metglas foils along the x -axis at $y=0$, $z=0$ when another identical foil was placed at various distances from it.

The external magnetic field was 0.1 Oe.

Finite element simulation using MAXWELL was performed for Metglas foils of the same directions as our laminates, as shown in Figure 42 (b). As can be seen, when the distance between the two Metglas foils was 20 mm, the magnetic flux density at the center region (-20 mm to 20 mm), where the Kapton/PZT core composite was bonded, was the lowest. The flux density became higher in this region as the spacing between the two foils was increased. When the distance was 40 mm and 50 mm, the flux density was nearly equal, which means that mutual inductance between foils is small. Such an effect depended on the size of the sensors. For sensors with various dimensions, the distance at which the effect of mutual inductance can be neglected should be different.

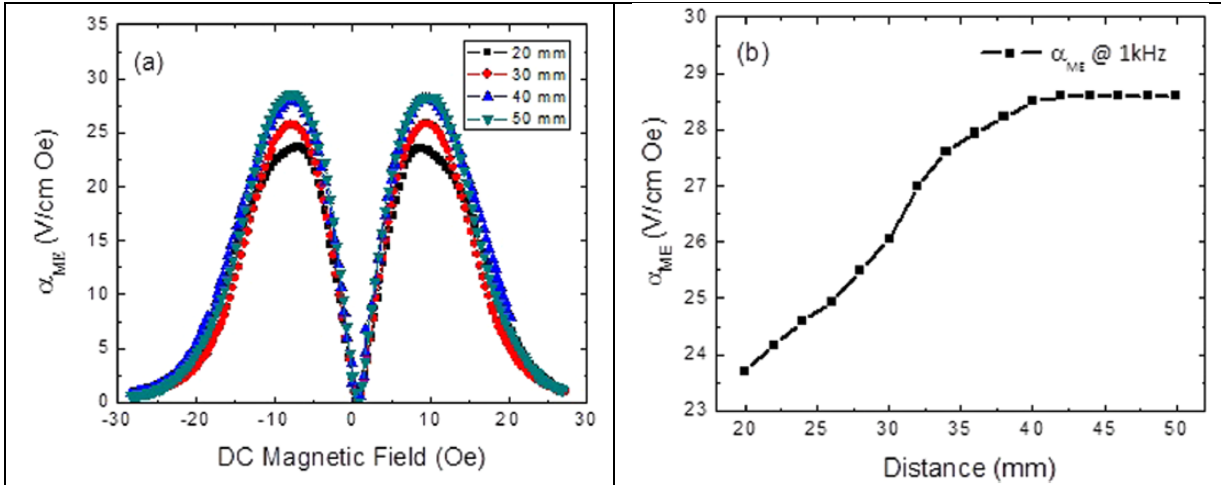


Figure 43. (a) the value of α_E as a function of H_{dc} for one Metglas/PZT laminate when another one was placed at different distance from it. (b) The maximum value of α_E as a function of distance between two Metglas/PZT laminates.

The data were measured at 1 kHz and $H_{ac}=0.1$ Oe.

As shown in Figure 43 (a), the value of α_E was largest when the laminates were separated from each other by at least 40 mm. the maximum value of α_E was then 28.5V/cm·Oe under a DC bias of 8.9 Oe. When the distance between these two laminates was <40 mm, the value of α_E was reduced, for example, at 20 mm, the maximum value of α_E was 23.6 V/cm·Oe under a $H_{dc}=8.9$ Oe, a 17% reduction with respect to that at 40 mm. Figure 43 (b) shows the maximum value of α_E as a function of distance between these two laminates. One can see that the maximum value of α_E increased as the distances between the two laminates was increased. When the distance was>40 mm, the maximum value of α_E was the same as for each sensor with an infinite separation.

A.3.5.2. Sensor array

Based on the above results, we have developed a sensor array (4×4 sensors) to further to reduce the noise floor.

Totally, we made four ME sensor units to construct the ME sensor array. The four units were placed in a square holder inside the shielding chamber. As shown in Figure 44, the distance between the centers of two units was 8 cm.

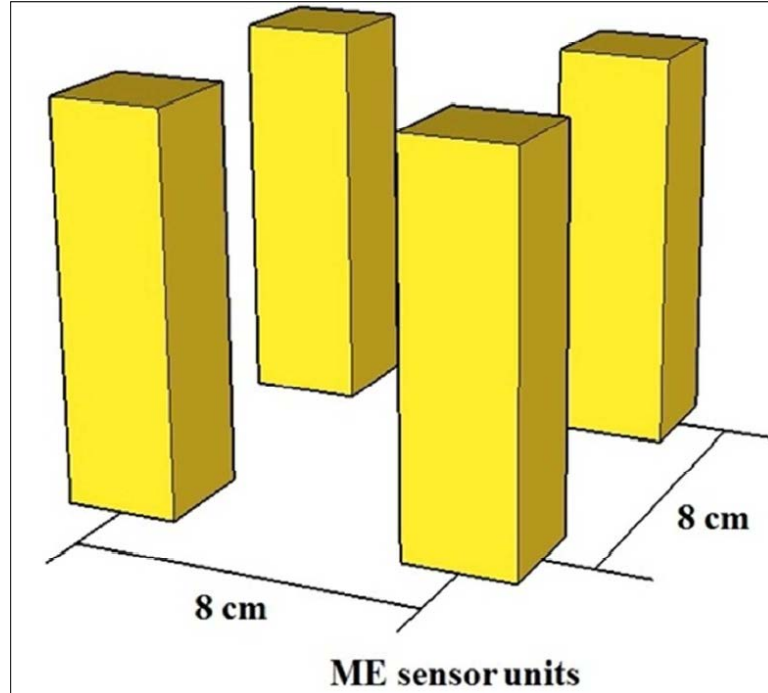


Figure 44. Schematic representation of the ME sensor arrays of four units.

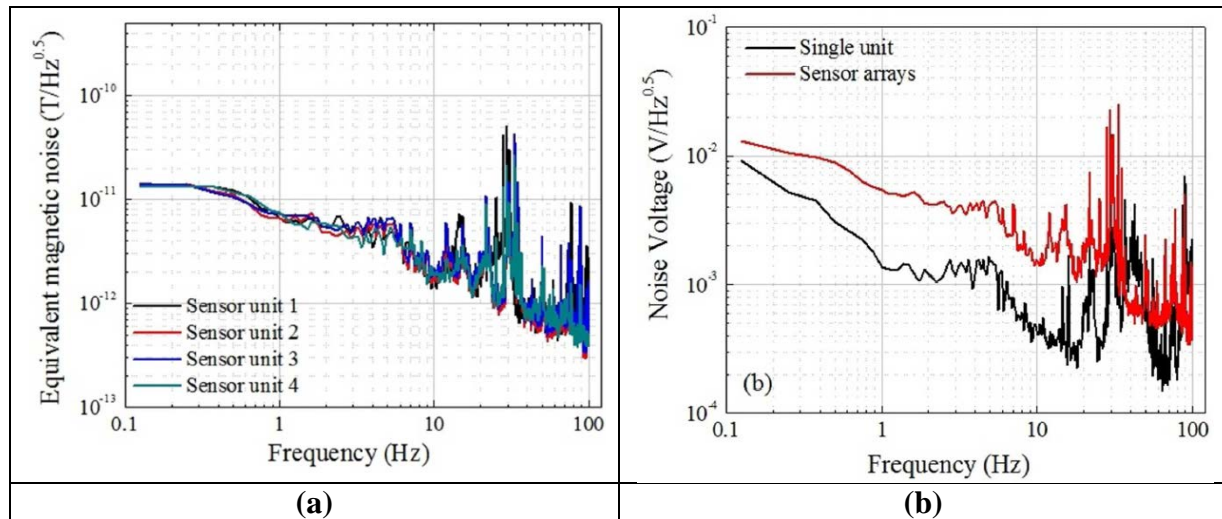


Figure 45. (a) Equivalent magnetic noise spectra for four ME sensor units over the frequency range of $0.125\text{Hz} < f < 100\text{Hz}$. (b) Background voltage noise of single unit and calculated noise of the sensor array.

Figure 45 (a) shows the equivalent magnetic noise spectra for these four ME sensor units. Over the frequency range of $0.125\text{Hz} < f < 100\text{Hz}$, the noise floors can be seen to be nearly equivalent for the various units. Extremely low noise floor of $7 \text{ pT}/\sqrt{\text{Hz}}$ were found at 1Hz. Figure 45 (b) shows the voltage noise spectra of a single ME sensor unit and a sensor array over the frequency range $0.125\text{Hz} < f < 100\text{Hz}$. Because the sensor array was formed by sensor unit in parallel connection, thus the noise voltage spectra of a sensor array was higher than that of a sensor unit.

Then, the equivalent magnetic noise of the sensor array can be calculated to be $\sim 3.5 \text{ pT}/\sqrt{\text{Hz}}$ from the noise voltage spectra and the ME charge coefficient.

A.3.6. ME sensor gradiometer

A.3.6.1. Gradiometer for AC magnetic dipole localization

First, the theory of ac magnetic dipole localization was studied. The magnetic field \mathbf{B} created by a dipole with a moment \mathbf{M} at distance R from the dipole is given as

$$\mathbf{B}(\mathbf{x}, \mathbf{y}, \mathbf{z}) = \frac{\mu_0}{4\pi} \frac{3\mathbf{R}(\mathbf{M} \cdot \mathbf{R}) - \mathbf{M}\mathbf{R}^2}{\mathbf{R}^5}; \quad (94)$$

Where $\mu_0 = 4\pi \cdot 10^{-7} \text{ H/m}$ is the permeability of free space, and R is the scaled distance. The tensor matrix form for equation (96) is

$$\begin{vmatrix} \mathbf{B}_x \\ \mathbf{B}_y \\ \mathbf{B}_z \end{vmatrix} = \frac{\mu_0}{4\pi R^3} \begin{vmatrix} 3x'^2 - 1 & 3x'y' & 3x'z' \\ 3y'z' & 3y'^2 - 1 & 3y'z' \\ 3z'x' & 3z'y' & 3z'^2 - 1 \end{vmatrix} \begin{vmatrix} \mathbf{M}_x \\ \mathbf{M}_y \\ \mathbf{M}_z \end{vmatrix}; \quad (95)$$

where

$$x' = \frac{x}{R}, \quad y' = \frac{y}{R}, \quad z' = \frac{z}{R}, \quad R = \sqrt{x^2 + y^2 + z^2}. \quad (96)$$

After normalizing, the components of the scalar magnetic moments of \mathbf{M} are

$$\mathbf{M}_x = \sin\beta \cos\gamma \mathbf{M}, \quad \mathbf{M}_y = \sin\beta \sin\gamma \mathbf{M}, \quad \mathbf{M}_z = \cos\beta \mathbf{M}. \quad (97)$$

Where β is the angle between the dipole moment and the z-axis, and γ is that between the dipole moment and the x-axis. Equation (99) can then be rewritten as:

$$\begin{vmatrix} \mathbf{B}_x \\ \mathbf{B}_y \\ \mathbf{B}_z \end{vmatrix} = \frac{\mu_0 M}{4\pi R^3} \begin{vmatrix} 3x'^2 - 1 & 3xy & 3xz \\ 3yz & 3y'^2 - 1 & 3yz \\ 3zx & 3zy & 3z'^2 - 1 \end{vmatrix} \begin{vmatrix} \sin\beta \cos\gamma \\ \sin\beta \sin\gamma \\ \cos\beta \end{vmatrix} \quad (98)$$

If a solenoid has surface area, S , current, I , and N identical turns, its moment strength M takes the form $M = INS$.

A Grid Search (GS) algorithm provides a robust mathematical approach for determining the maximum likelihood of an objective function. Here, we adopted an iterative GS refinement method to perform a systematic search for a dipole over a defined grid of points. As a first step, a 3-dimentional initial region $\psi = [x_1, x_2] \times [y_1, y_2] \times [z_1, z_2] \in D^3$ was established containing the source and the triple-axis receivers (i, j , and k). The equivalent distance grid can then be defined as¹³

$$\begin{aligned} \psi = & \left\{ (x, y, z)^T \mid x = x_1 + \frac{k_x}{n+1}(x_2 - x_1), k_x = 1, \dots, n, y = y_1 + \frac{k_y}{n+1}(y_2 - y_1), k_y = 1, \right. \\ & \left. n, z = z_1 + k_z(n+1)z_2 - z_1, k_z = 1, \dots, n. \right. \end{aligned} \quad (99)$$

Please note that an evaluation was applied during each mutation and only a single newborn point was re-used in the next iteration. To this end, the problem evolved into searching sub-optimal points statistically among limited possible solutions and restricting their resolutions, rather than solving equation (99). Thus the applied GS became an efficient means by scanning regions of feature space to quickly approach an area with the high possibility of leaving an object to be detected. Accordingly we then spent most of the computational time where there was the largest probability of find a dipole.

Figure 46 (a) illustrates the configuration of the dipole (illustrated by α , β and γ) and three tri-axis ME sensor devices (denoted as i, j, and k) used in this study. Each triple-axis sensor consisted of three single-axes ME sensor units, where the sensors were mutually perpendicular to each other to enable measuring the three magnetic field components B_x , B_y , and B_z . The corresponding CAs were enclosed in the bottom solid plastic housing of each sensor, including battery support. Triple-axis magnetometers i and j were separated by 40 cm in the x-direction, and the one k was separated from the i-j centerline by 30 cm in the y-direction. A datalogger was utilized to collect output signals from the CAs at 100 samples/sec, with a full-scale of 1 V and a dynamic range of 60 dB. MATLAB scripts were used to perform signal processing. The sensor detection units were placed parallel to each other, and the y-components of the sensors were all aligned with the geomagnetic field.

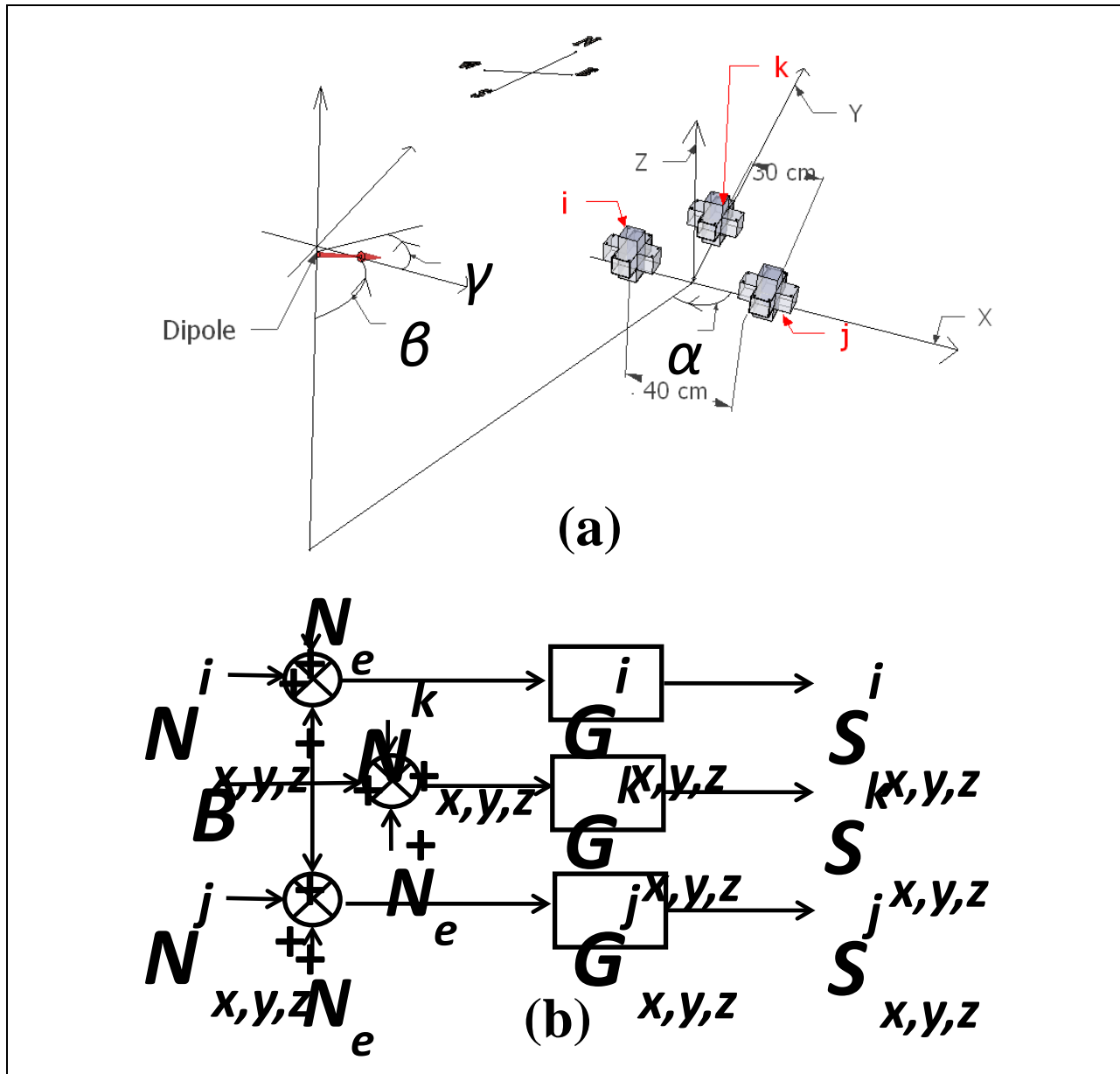


Figure 46. (a) Schematic illustration of test layout, where the tensor ME sensors are constructed in three linear orthogonal directions. (b) Block diagram of signal collection model.

The baseline between sensor *i* and *j* is 40cm and that between sensor *k* to the central point of sensor *i* and *j* is 30cm.

To model the magnetic dipole, a solenoid coil was driven by a signal generator producing an AC sine wave signal B . Please note that the three triple-axis magnetometers (*i*, *j*, *k*) were exposed to the same external noise N_e ; and that each one should have incoherent intrinsic noises of $N_{x,y,z}^i$, $N_{x,y,z}^j$, and $N_{x,y,z}^k$ respectively. The dipole signal and noise sources from the nine sensors of the three triple-axis magnetometer were integrated separately via a CA. A block diagram of the signal collection is shown in Figure 46 (b). The gain of each sensor was $G_{x,y,z}^i$, $G_{x,y,z}^j$, and $G_{x,y,z}^k$.

The charge signals that were detected were converted into the voltage ones ($S_{x,y,z}^i$, $S_{x,y,z}^j$, and $S_{x,y,z}^k$), which were then recorded by a datalogger.

In order to locate magnetic dipoles by the GS algorithm, a test was performed where a solenoid “dipole” driven at 7 Hz was placed at (0.5m, -1.0m, 0.74m) with $(\alpha, \beta, \gamma) = (26.58^\circ, 90^\circ, 90^\circ)$ relative to the origin of the coordinate system. Representative PSD plots of the received sensor signal (RSS) for the three triple-axis gradiometers (i, j, and k) are presented in Figure 47 (a), 47 (b) and 47 (c) respectively. The amplitude of the 7 Hz peaks in each the PSD is the dipole that we are trying to localize.

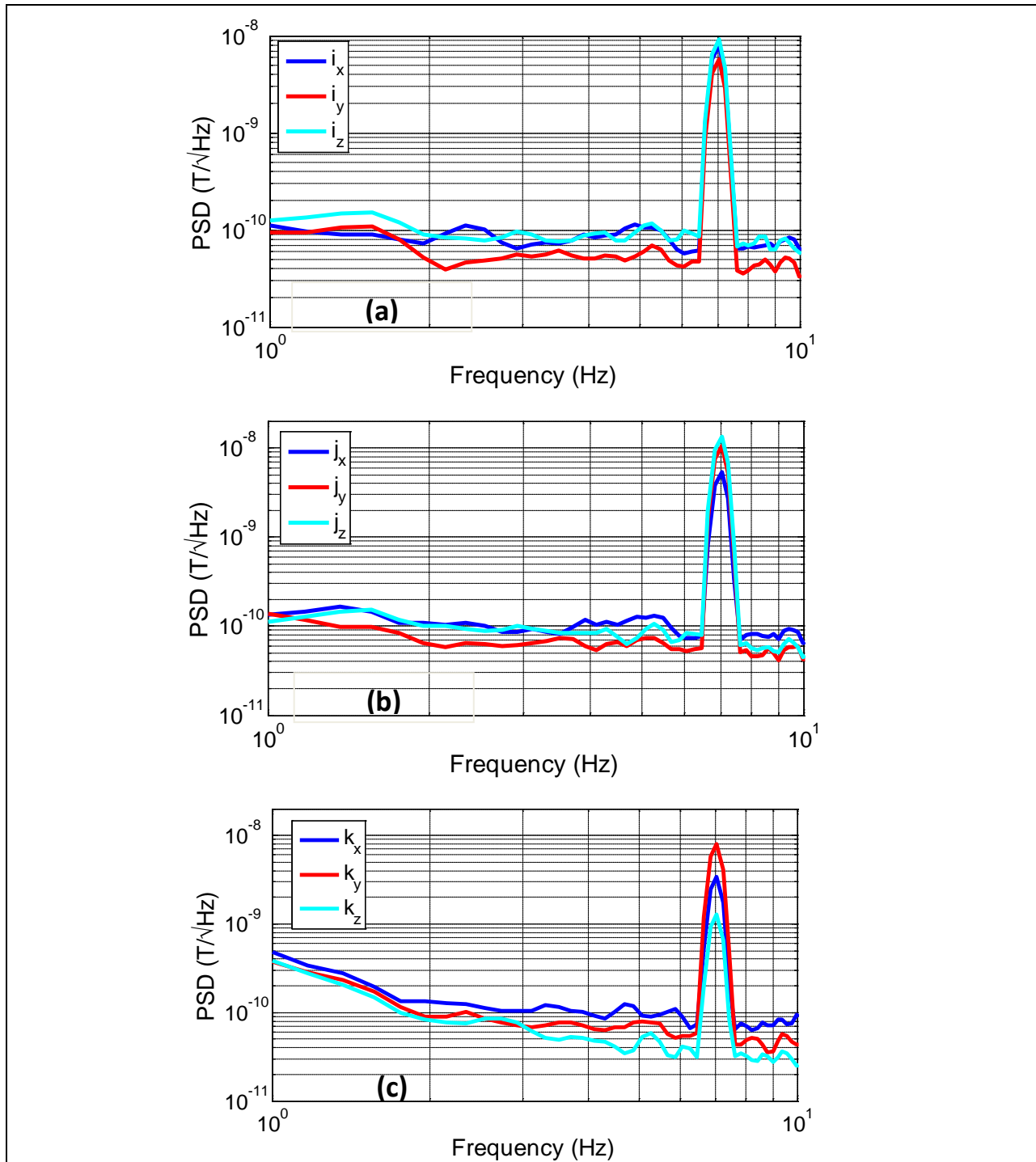


Figure 47. Power spectral density of applied AC magnetic dipole at $f=7$ Hz on (a) sensor i, (b) sensor j and (c) sensor k in x-axis (blue curve), y-axis (red curve) and z-axis (cyan curve)

Execution of the GS algorithm estimation for dipole localization yielded (0.46m, -1.24m, 0.77m). This corresponded to 6.0%, 10% and 13.5% errors in the x, y and z locations respectively, and error in range of 9.02% relative to the actual position as illustrated in Figure 48

(a). Different orientations of the dipoles were considered and tests were performed with changes in (α, β, γ) , as illustrated in Figure 48 (a), (b) and (c). The results show as the dipole angles change that the accuracy of localization decreased modestly. Figure 48 (a), (d) and (e) demonstrate that the accuracy decreases as target distance along the y-direction increases. All the data and localization error were summarized in Table 11.

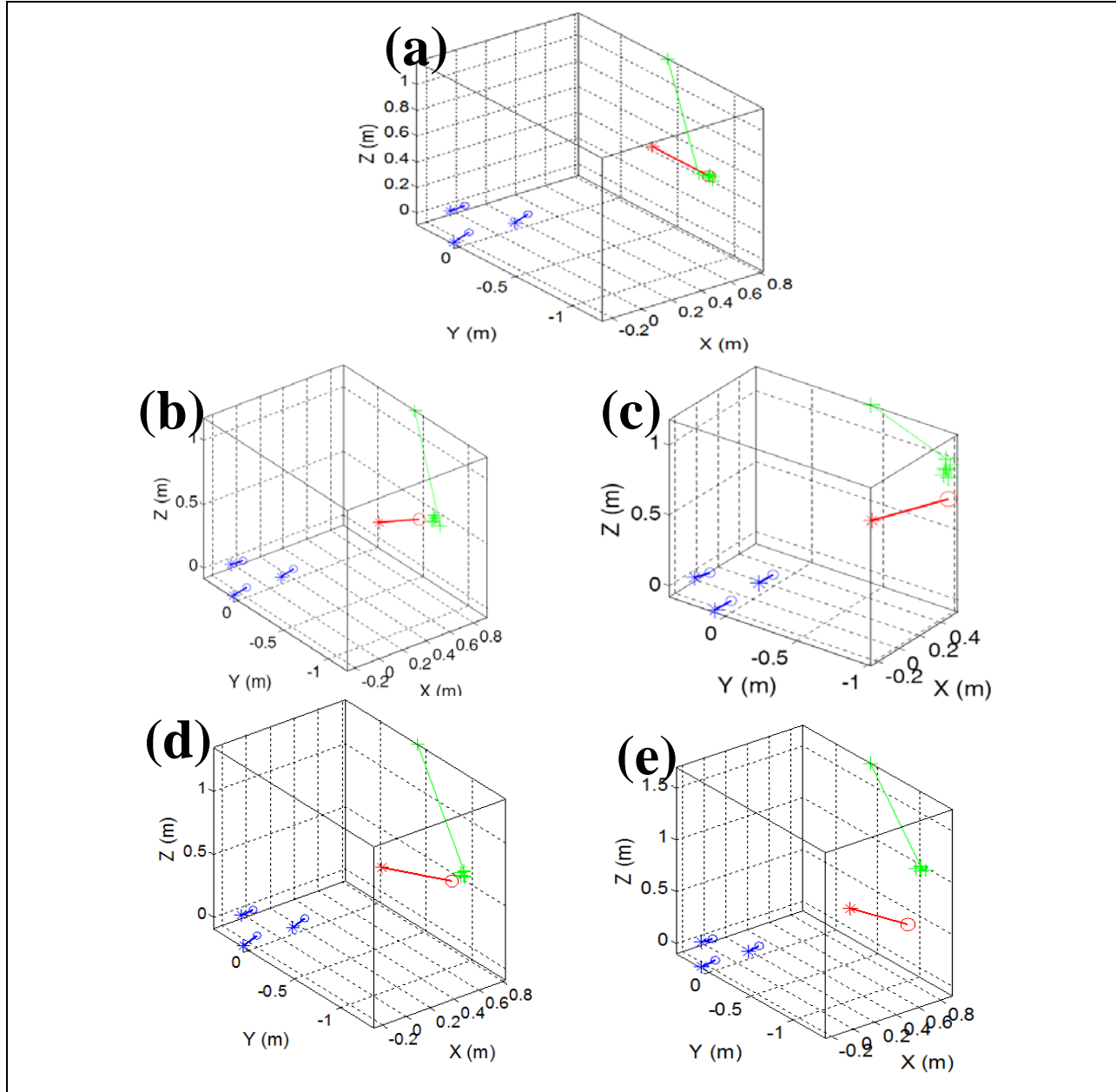


Figure 48. Estimation for dipole position (green cross) based on SRR (blue line and star head) by three tensor ME sensors (blue open circles) responding to solenoid dipole (red open circle) with moment direction (red line and star head) with different dipole moment directions as in (a), (b) and (d), and with different distance in y as in (a), (d) and (e).

Table 11. Target dipole localization as a function of (α , β , γ) and y

Test	(α , β , γ) in unit of degree	True position (x, y, z) in unit of m	Search position (x, y, z) in unit of m	Localization error in 3-axis	Errors in range
a	(26.58, 90, 90)	(0.5, -1, 0.74)	(0.47, -1.10, 0.84)	(6%, 10%, 13.5%)	9.02%
b	(26.58, 26.58, 90)	(0.5, -1, 0.74)	(0.49, -1.15, 0.80)	(2%, 15%, 8.1%)	10.69%
c	(26.58, 26.58, 68)	(0.5, -1, 0.74)	(0.49, -0.98, 0.93)	(2%, 2%, 25.7%)	7.19%
d	(26.58, 90, 90)	(0.5, -1.2, 0.74)	(0.47, -1.33, 0.87)	(6%, 11.4%, 18.7%)	10.79%
e	(26.58, 90, 90)	(0.5, -1.4, 0.74)	(0.68, -1.26, 1.15)	(36%, 10%, 55.4%)	10.59%

Our findings have demonstrated that we can use triple-axis ME sensors to locate magnetic dipoles with good precision. The localization was made computationally efficient by use of a GS algorithm. Such efficient localization of magnetic dipole is important to application of passive ME magnetic sensors.

A.3.6.2. Gradiometer for external noise rejection

Measurements were conducted in an open environment (magnetically unshielded) in our laboratory. Figure 49 (a) shows the experimental configuration for the gradiometer measurements. A matched pair of ME gradiometer sensors G 1 and G 2 were oriented parallel to the geomagnetic north with a center-to-center separation distance of D=0.2 m. A magnetic dipole, represented by a solenoid coil driven by a signal generator, produced an AC sine wave signal at 7 Hz. Let \mathbf{R} be the 2D x-y plane position where the coil was placed. The coil was rotated along the perimeter of a circle with a radius $R = |\mathbf{R}| = 1$ m centered on the sensor pair. The radial position of the coil (θ_1) and its orientation relative to the x axis (θ_2) were controlled such that the magnetic dipole pointed towards the center of the gradiometer array. The field was studied as the coil was rotated from 0 to 180°. The output signals from the sensors in the time-domain were collected via a CR5000 datalogger and sampled at a rate of 100 Hz and a 1 V dynamic range. The magnetic field strengths at each testing point were recorded in 100 seconds, and a fast Fourier transform (FFT) was then performed via Matlab to calculate the power spectral density (PSD) for the two output signals as a function of frequency.

Figure 49 (b) gives the background noise PSD plots of our gradiometer over a frequency range of $1 < f < 10$ Hz. The data show that the y-component of the sensors (G_{1y} and G_{2y}) had nearly identical equivalent background noises of 300 pT/ $\sqrt{\text{Hz}}$ over this bandwidth, increasing some and decreasing slightly at lower and higher frequencies respectively. Direct subtraction of two magnetic sensors output signals can reject the coherent environmental noise source and yield the gradiometer noise floor. In Figure 49 (b), the differential noise floor for the y-axis sensors ($G_{1y} - G_{2y}$) was determined to be 20 pT/ $\sqrt{\text{Hz}}$ for $1 < f < 10$ Hz. One can also see in this figure that the individual sensor noise floor for the x-component sensors (G_{1x} and G_{2x}) was about 110 pT/ $\sqrt{\text{Hz}}$, and their differential output ($G_{1x} - G_{2x}$) was about 40 pT/ $\sqrt{\text{Hz}}$ over the same bandwidth. It is

important to note that the equivalent gradiometer noise floor of the y-axis and x-axis sensors were about 15x and 2.75x respectively lower than that of the corresponding individual sensors. This enables enhanced detection sensitivity by gradiometers, and will contribute to a higher SNR during signal detection.

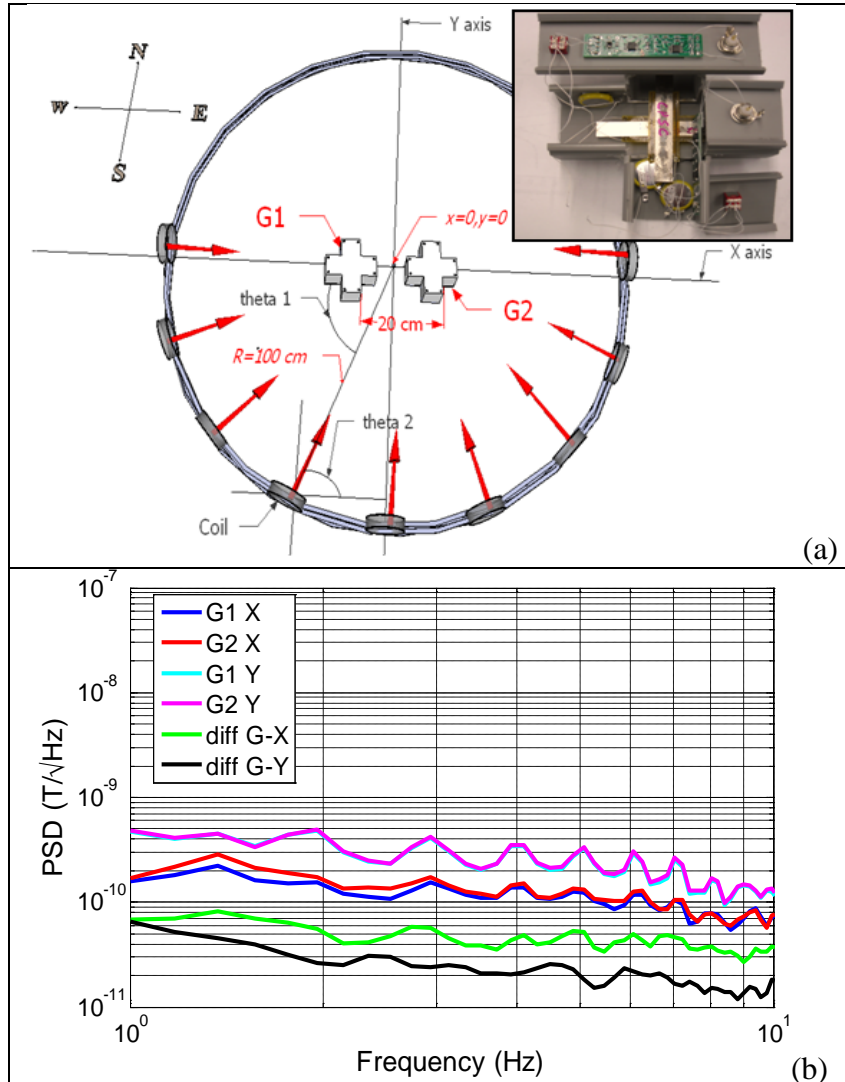


Figure 49. (a) Diagram of experimental layout as the coil position is rotated from 0 to 180 degree for our two biaxial ME magnetometers. (b) Power spectral density curves of the background noise for sensors G_{1x} and G_{2x} (blue and red curves respectively), sensors G_1 and G_2 (cyan and pink curves respectively), and gradiometric noise floor signals diff (G_x) and diff (G_y) (green and black curves respectively).

The inset is a photo of a prototype biaxial ME magnetometer.

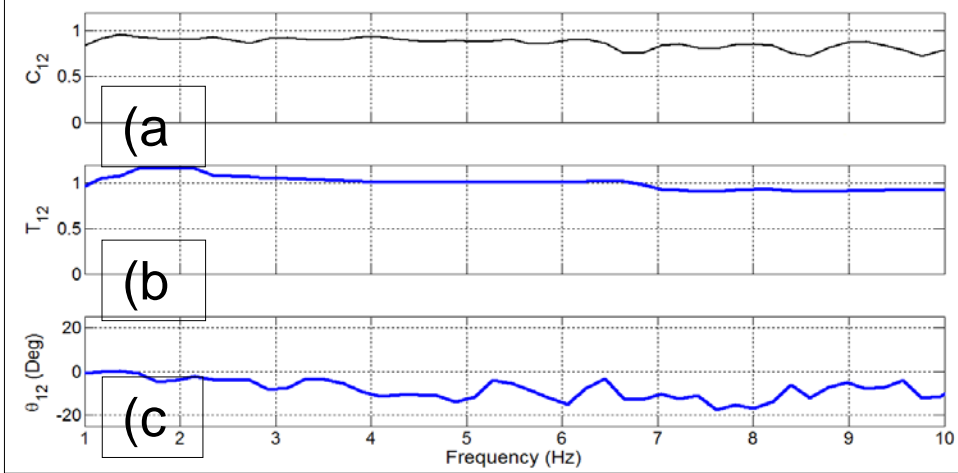


Figure 50. (a) Coherence value, (b) relative amplitude difference and (c) phase shift for G1_x and G2_x.

Figure 50 (a) shows the coherence $C_{x_1x_2}(f)$ between G1_x and G2_x which was slightly lower than unity: the transfer functions $T_{12}(f)$ of S_1 and S_2 , which are the Fourier transforms of G1_x and G2_x, were evaluated by their relative ratios as defined as:

$$T_{12}(f) = \frac{S_2(f)}{S_1(f)}. \quad (100)$$

The smoothing transfer function amplitude $|T_{12}(f)|$ is shown in Figure 50 (b), can be given as:

$$Amplitude \equiv |T_{12}(f)| = \frac{|S_2(f)|}{|S_1(f)|}. \quad (101)$$

The amplitude ratio, $|T_{12}(f)|$, was also close to unity with ± 0.1 variance. Figure 50 (c) shows phase discrepancy $\theta_{12}(f)$ between S_1 and S_2 , which can be estimated as:

$$Phase \equiv \theta_{12}(f) = ArcTan\left(\frac{\text{Im}(T_{12}(f))}{\text{Re}(T_{12}(f))}\right). \quad (102)$$

For matched sensors, when $|T_{12}| = 1 + \varepsilon$ with $\varepsilon \ll 1$ and $\arg(T_{12}) = \theta \ll 1$, the coherent noise rejection efficiency is :

$$Rejection\ efficiency = \frac{1}{\sqrt{\varepsilon^2 + \theta^2}}. \quad (103)$$

In Figure 50 (c), we can see that the phase shift was about -20° or -0.39 rad, which contributes to a rejection efficiency of $2.78x$ together with the amplitude factor effects. Thus, the equivalent

gradiometric noise floor was about $2.75 \times$ lower than that of the individual sensors for $G1_x$ and $G2_x$.

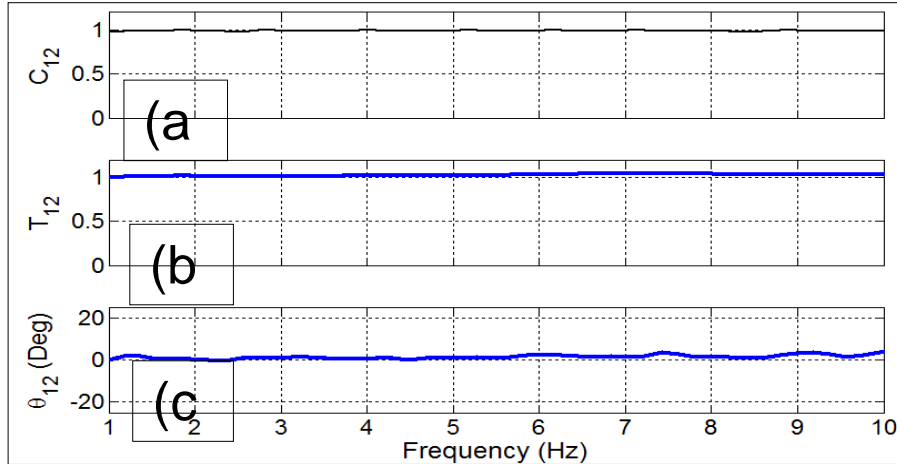


Figure 51. (a) Coherence value, (b) relative amplitude difference and (c) phase shift for $G1_y$ and $G2_y$.

The coherence $C_{y_1y_2}(f)$ between the y-axis sensors $G1_y$ and $G2_y$ was analyzed similarly, as shown in Figure 51 (a). The value of $C_{y_1y_2}(f)$ remained constant at $C_{y_1y_2}(f)=1$, indicating better coherence than that of $C_{x_1x_2}(f)$. Figure 51 (b) shows the absolute amplitude ratio which was also nearly unity, which shows that $G1_y$ and $G2_y$ have nearly identical magnetic field strengths. The value of $\theta_{12}(f)$ shown in Figure 51 (c) reveals a phase shift of 4° (0.07 rad). By employing Equation (106), we can determine that the rejection efficiency for $G1_y$ and $G2_y$ was $14.3x$, which is confirmed by Figure 49 which had a gradiometer noise floor of 20 pT/ $\sqrt{\text{Hz}}$ from an individual sensor noise level of 300 pT/ $\sqrt{\text{Hz}}$.

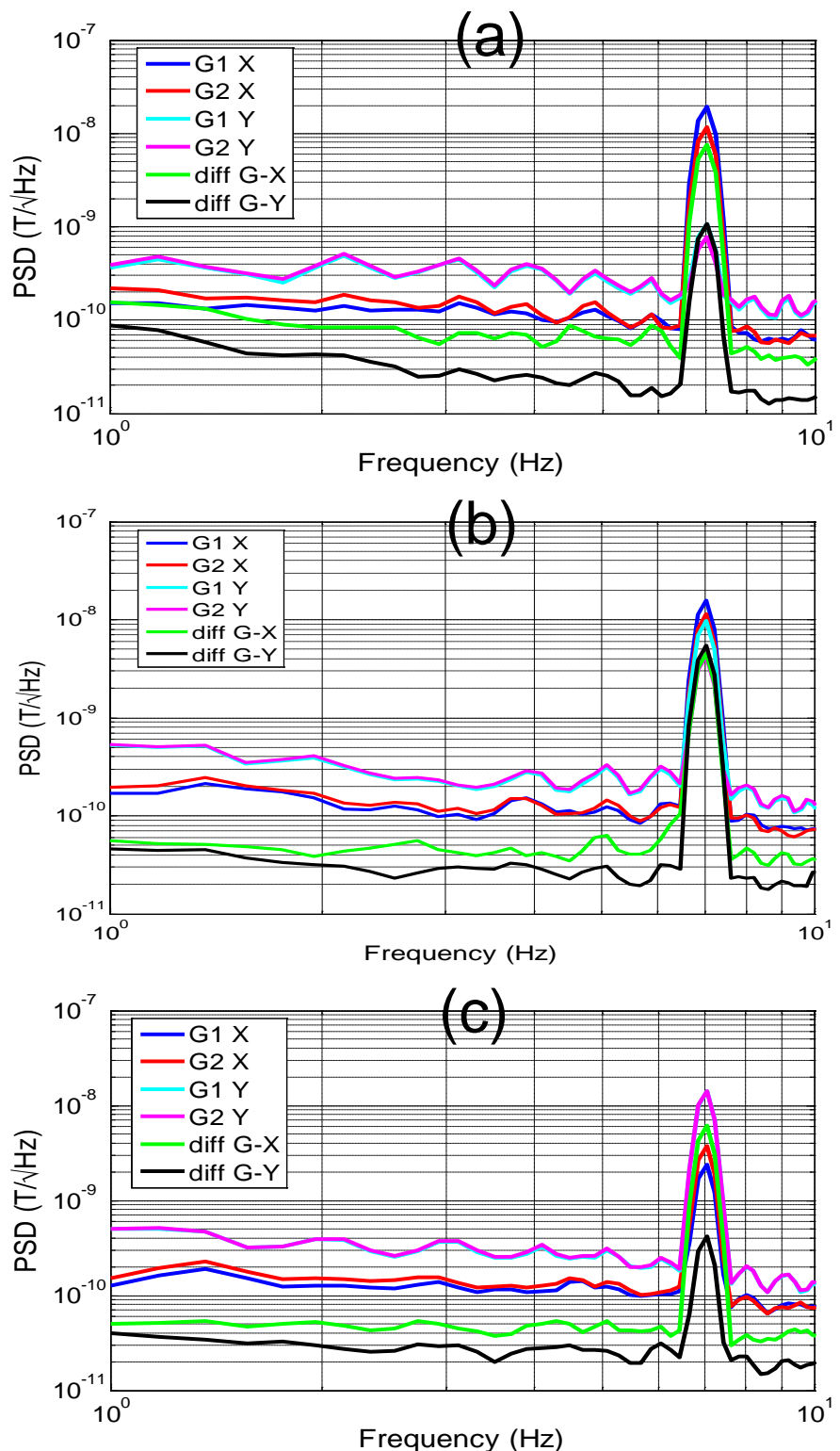


Figure 52. Power spectral density curves at (a) $\theta_1=0^\circ$, (b) $\theta_1=30^\circ$, (c) $\theta_1=90^\circ$ for sensor $G1_x$ and $G2_x$ (blue and red curves respectively), sensors $G1_y$ and $G2_y$ (cyan and pink curves respectively), and gradiometric noise floor signals $\text{diff } (G_x)$ and $\text{diff } (G_y)$ (green and black curves respectively).

At a frequency of $f=7$ Hz, when the angle between the target source and the central point of the gradiometers was $\theta_1=0^\circ$, the induced magnetic fields on G_{1x} and G_{2x} were maximum as shown in Figure 52 (a). In this figure, it can be seen that the gradiometer noise floors remained at a level lower than that of the individual sensors. If a small magnetic anomaly was nearby (assuming a magnetic amplitude of 100 pT in the quasi-static frequency domain), it would readily be sensed by the ME gradiometer but not the individual ME sensors. The magnetic strengths of G_{1y} and G_{2y} sensors were smaller than that along the x-axis as they are perpendicular to the dipole. Under ideal conditions when the sensor can be treated as a physical point, the G_{1y} and G_{2y} sensors should not have a magnetic response to the dipole at $\theta_1=0^\circ$. When the dipole was moved to $\theta_1=30^\circ$, it can be seen that the induced magnetic fields on the G_{1y} and G_{2y} sensors increased whereas that of G_{1x} and G_{2x} slightly decreased, as shown in Figure 52 (b). For $\theta_1=90^\circ$, G_{1y} and G_{2y} had nearly the same induced magnetic field strength ($f=7$ Hz) due to a strong coherence to the same source (see Figure 52 (c)). The induced magnetic field amplitudes on G_{1x} and G_{2x} should be the same, due to the same relative distances to the dipole. However, G_{1x} and G_{2x} exhibited a discernable variance in the output signals, resulting from an inherent difference due to variations in sensors phases (see Figure 50). The magnetic fields at other points ($\theta_1=45^\circ$, 60° , 120° , 135° , 150° and 180°) were also recorded and signal processing conducted to compute the PSD amplitude. Table 12 gives the calibrated observed values for the sensors as a function of θ_1 .

Table 12. Calibrated observed data for sensors of magnetic field as a function of θ_1

θ_1 (deg)	G_{1x} (n T)	G_{2x} (n T)	G_{1y} (n T)	G_{2y} (n T)
0	19.25	11.62	1.08	0.78
30	15.95	11.46	9.8	4.3
45	11.11	9.98	11.98	6.31
60	6.42	8.82	15	9.78
90	- 2.38	3.78	14.12	14.18
120	-8.23	-5.55	9.9	15.66
135	-9.9	-10.31	7.74	14.72
150	-11.26	-15.97	5.02	11.63
180	-11.57	-20.28	0.67	1.66
Noise	0.104	0.104	0.266	0.260

B. Christophe Dolabdjian, Universite de Caen

The objective of this task was to analyze and to improve, to give a noise model of the Magneto(elasto)Electric(M.E.) sensors. We demonstrate how we evaluate the equivalent magnetic sensor noise for the full range frequency response of the sensor. This model is based on the physical Mason's equations and includes the main intrinsic sensor noise sources.

Associated to the electronic voltage or charge amplifier, we can predict the total equivalent magnetic noise of the sensors over its wide frequency bandwidth. Once, this model was well compared to experiments. These goals have all been met, as described in the pages that follow.

B.3.1. Sensor noise modeling

1-D Model of piezoelectric layer.

In this part, we have analyzed with the help of the Mason's model the theoretical ME laminated sensor noise in the one Dimension and Longitudinal-Transverse mode “1D/L-T” mode ($l \gg w \& l \gg t_{lam}$) in order to evaluate the physical noise limit of the magneto electric laminated composites sensors versus given hypothesis^{16,17}. We have considered a simple 1D model for the 31 (transverse) mode. The piezoelectric materiel layer has a length, l , width, w , and thickness, t_p . The electric field E and the electric displacement D are in direction 3. The stress and strain are in direction 1. The sketch view of the layer is presented in Figure 53.

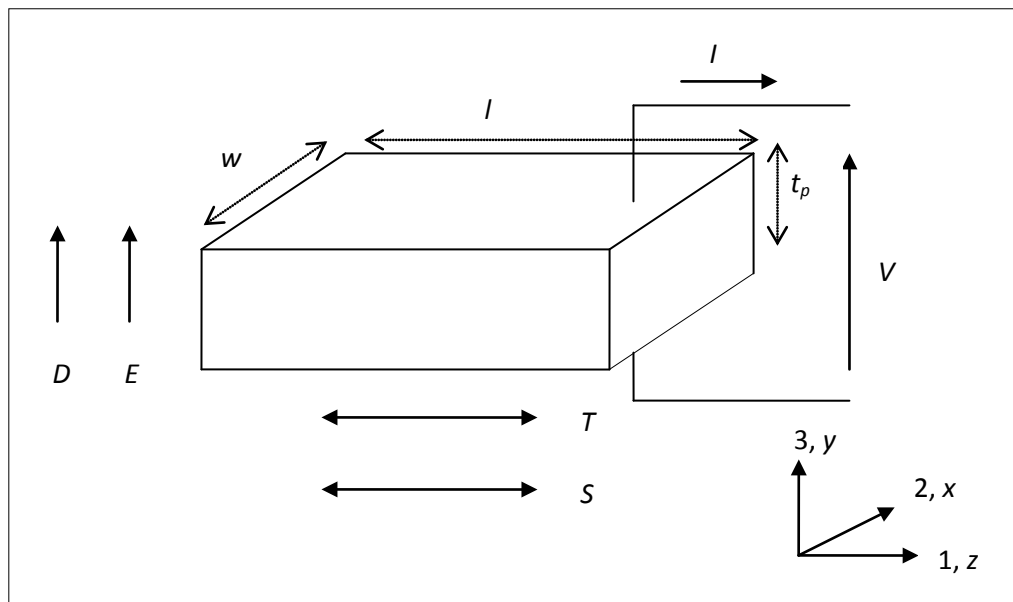


Figure 53.Piezoelectric layer with associated parameters.

Figure 54 presents a piezoelectric layer with parameters to study. Strain S and stress T are in direction 1, electric displacement D and electric field E are transversal, that is to say, in direction 3. So, we write the parameters under the form S_1 ; T_1 and D_3 E_3 . V is the electric voltage appearing between the two surfaces of the piezoelectric layer. I is the electric current. Before detailing the model of piezoelectric layer, we have to remind some classical parameters or equations.

The first is the one dimensional (1-D) propagation speed of elastic wave solution. It defines the speed, v , of elastic wave in a 1-D solid and can be written as

$$v = ae^{-ikz} + be^{ikz} \quad (104)$$

Where a and b are two parameters, e is the exponential symbol, i is $\sqrt{-1}$, k is the elastic wave number, z is the position on the piezoelectric layer. From above formula, we obtain by derivation

$$\frac{\partial v}{\partial z} = \frac{\partial(ae^{-ikz} + be^{ikz})}{\partial z} = -ikae^{-ikz} + ikbe^{ikz} = -ik(ae^{-ikz} - be^{ikz}) \quad (105)$$

The second is the characteristic impedance Z of the piezoelectric layer.

$$Z = \frac{c}{v} = \frac{ck}{\omega} \quad (106)$$

where v , c , k , and ω are the propagation speed of elastic wave, the piezoelectric constant, the wave number and the angular speed of elastic wave, respectively, in the piezoelectric layer.

The third is a general mathematical equality which will be utilized in following section. It can be written as

$$\operatorname{tg} \frac{\theta}{2} = \frac{1}{\sin \theta} - \frac{1}{\operatorname{tg} \frac{\theta}{2}} \quad (107)$$

where θ is expressed in radians.

We detail below the elastic and electric equations.

The Elastic equations.

The constitutive elastic equations present the relations between the forces at the two extremities of piezoelectric layer $F_{1,p}F_{2,p}$ and the vibration speed v_1 and v_2 appearing at these extremities. If we consider that the electric current I can be easily obtained from the derivation of the electric displacement D , we start our calculation from¹⁸

$$T_1 = c_{11}^D S_1 - h_{31,p} D_3 \quad (108)$$

where T_1 is the stress in direction 1, S_1 is the strain in direction 1, D_3 is the electric displacement in direction 3, c_{11}^D is the rigidity coefficient under a certain electric displacement D , $h_{31,p}$ is the piezoelectric coefficient. We have to search the relation between the forces and vibration speed at the extremities of piezoelectric layer. We know that the strain S is the derivation of

displacement $S = \frac{\partial u}{\partial z}$ where u is the position of one point on the piezoelectric layer and z the

axial direction. The vibration speed, v , is the time derivation of the position, which can be written as $v = \frac{\partial u}{\partial t}$. In order to find out the vibration speed, we derive the previous stress formula

$$\frac{\partial T_1}{\partial t} = c_{11}^D \frac{\partial S_1}{\partial t} - h_{31,p} \frac{\partial D_3}{\partial t} \quad (109)$$

The current density is the derivation of electric displacement and given by

$$J(t) = \frac{\partial D_3}{\partial t} \quad (110)$$

So,

$$\frac{\partial T_1}{\partial t} = c_{11}^D \frac{\partial}{\partial t} \frac{\partial u}{\partial z} - h_{31,p} J(t) \quad (111)$$

If the $(l w)$ product is the surface section, of piezoelectric layer, we obtain

$$\frac{\partial T_1}{\partial t} = c_{11}^D \frac{\partial v}{\partial z} - h_{31,p} \frac{I(t)}{lw} \quad (112)$$

We substitute the vibration speed by the given solution

$$\frac{\partial T_1}{\partial t} = c_{11}^D \left[-ik(ae^{-ikz} - be^{ikz}) \right] - \frac{h_{31,p} I(t)}{lw} \quad (113)$$

By the Fourier transform, it yields to

$$i\omega T_1 = -ikc_{11}^D (ae^{-ikz} - be^{ikz}) - \frac{h_{31,p} I}{lw} \quad (114)$$

From above formulas, we can find the expression of F_1 and F_2 at the two extremities of the piezoelectric layer

$$\begin{cases} F_{1_{-1,p}} = -A_p T_{1_{-1}} = \zeta_p (ae^{-ikz_1} - be^{ikz_1}) - \frac{ih_{31,p} I}{\omega} \frac{t_p}{l} \\ F_{2_{-1,p}} = -A_p T_{2_{-1}} = \zeta_p (ae^{-ikz_2} - be^{ikz_2}) - \frac{ih_{31,p} I}{\omega} \frac{t_p}{l} \end{cases} \quad (115)$$

where F_{1_1} and F_{2_1} are the force at left and right extremities, in direction 1, respectively, T_{1_1} and T_{2_1} are the stresses at the corresponding extremities in direction 1, $\zeta_p = \frac{c_{11}^D k}{\omega} A_p$ is the characteristic impedance of piezoelectric layer, ω the angular speed, $A_p (= w t_p)$ is the cross-sectional surface of piezoelectric layer. With the help of the previous equations, we can evaluate the two parameters a and b . The vibration speeds at the two extremities can be written as

$$\begin{cases} v_1 = v(z_1) = ae^{-ikz_1} + be^{ikz_1} \\ v_2 = -v(z_2) = -(ae^{-ikz_2} + be^{ikz_2}) \end{cases} \quad (116)$$

From the above equations, we obtain

$$\begin{cases} a = -\frac{v_1 e^{ikz_2} + v_2 e^{ikz_1}}{2i \sin kl} \\ b = \frac{v_1 e^{-ikz_2} + v_2 e^{-ikz_1}}{2i \sin kl} \end{cases} \quad (117)$$

By inserting a and b in the above equations above and making some simplifications, we arrive to

$$\begin{cases} F_{1,p} = \zeta_p \left(-i \frac{1}{\sin kl} (v_1 + v_2) + itg \frac{kl}{2} v_1 \right) - \frac{ih_{31,p} I}{\omega} \frac{t_p}{l} \\ F_{2,p} = \zeta_p \left(-i \frac{1}{\sin kl} (v_1 + v_2) + itg \frac{kl}{2} v_2 \right) - \frac{ih_{31,p} I}{\omega} \frac{t_p}{l} \end{cases} \quad (118)$$

Electric equations.

The constitutive electric equations present the relations between electric voltages, electric currents and vibration speeds at the two extremities of piezoelectric layers. The electric field is given by the equation

$$E_3 = \beta_{33}^S D_3 - h_{31,p} S_1 \quad (119)$$

where $h_{31,p}$ and β_{33}^S are the piezoelectric coefficient of piezoelectric layer and the inversion of the dielectric coefficient under a strain, S , respectively. The electric voltages V is deduced by the integration of electric field E_3 as

$$V(t) = - \int_{-\frac{t_p}{2}}^{\frac{t_p}{2}} E_3(t) dz_3 \quad (120)$$

So,

$$V(t) = - \int_{-\frac{t_p}{2}}^{\frac{t_p}{2}} (\beta_{33}^S D_3(t) - h_{31,p} S_1(t)) dz_3 = h_{31,p} \frac{u_{1_1}(t) - u_{1_2}(t)}{l} \int_{-\frac{t_p}{2}}^{\frac{t_p}{2}} dz_3 - \int_{-\frac{t_p}{2}}^{\frac{t_p}{2}} \beta_{33}^S D_3(t) dz_3 \quad (121)$$

where u_{1_1} and u_{1_2} are the displacements at the extremities of piezoelectric layer. After derivation in time, we obtain

$$\frac{V(t)}{dt} = -\int_{-\frac{t_p}{2}}^{\frac{t_p}{2}} \beta_{33}^s J_3(t) dz_3 + h_{31,p} \left(\frac{v_{1_1}(t) - v_{1_2}(t)}{l} \right) \int_{-\frac{t_p}{2}}^{\frac{t_p}{2}} dz_3 = -\beta_{33}^s \frac{I_3(t)}{lw} t_p + h_{31,p} \frac{t_p}{l} (v_1(t) + v_2(t)) \quad (122)$$

where $v_{1_1} (= v_1(t))$ and $v_{1_2} (= -v_2(t))$ are the displacements at both extremities of piezoelectric layer. With the help of the Fourier transform,

$$\begin{aligned} i\omega V(\omega) &= -\beta_{33}^s \frac{I_3(\omega)}{lw} t_p + h_{31,p} \frac{t_p}{l} (v_1(\omega) + v_2(\omega)) \\ V(\omega) &= h_{31,p} \frac{t_p}{i\omega l} (v_1(\omega) + v_2(\omega)) - \frac{\beta_{33}^s t_p I(\omega)}{i\omega lw} \end{aligned} \quad (123)$$

We define

$$C_i = \frac{lw}{\beta_{33}^s t_p} \quad (124)$$

as the capacity of piezoelectric layer. It leads to the voltage value

$$V(\omega) = \frac{h_{31,p} t_p}{i\omega l} (v_1(\omega) + v_2(\omega)) - \frac{I(\omega)}{i\omega C_i} \quad (125)$$

With the help of these equations, we can design the equivalent electric model of piezoelectric layer as given in Figure 54.

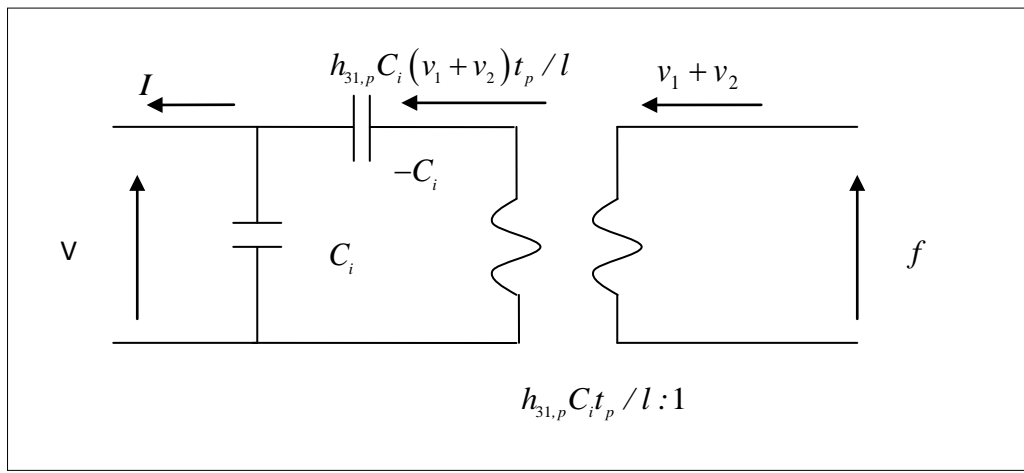


Figure 54. Presents the equivalent electric scheme of piezoelectric layer.

f is the dynamic force. The vibration speeds v_1 and v_2 are considered as mechanical currents. The coupling between the two parts of circuit is an equivalent transformer with the transfer coefficient $h_{31,p} C_i t_p / l : 1$.

To summarize, the 1-D model yields the constitutive piezoelectric equations

$$\begin{cases} F_{1,p} = \zeta_p \left(-i \frac{1}{\sin kl} (v_1 + v_2) + itg \frac{kl}{2} v_1 \right) - \frac{i h_{31,p} I}{\omega} \frac{t_p}{l} \\ F_{2,p} = \zeta_p \left(-i \frac{1}{\sin kl} (v_1 + v_2) + itg \frac{kl}{2} v_2 \right) - \frac{i h_{31,p} I}{\omega} \frac{t_p}{l} \\ V = h_{31,p} \frac{t_p}{i \omega l} (v_1 + v_2) - \frac{I}{i \omega C_i} \end{cases} \quad (126)$$

1-D Model of magnetostrictive layer

- **Magnetic equations**

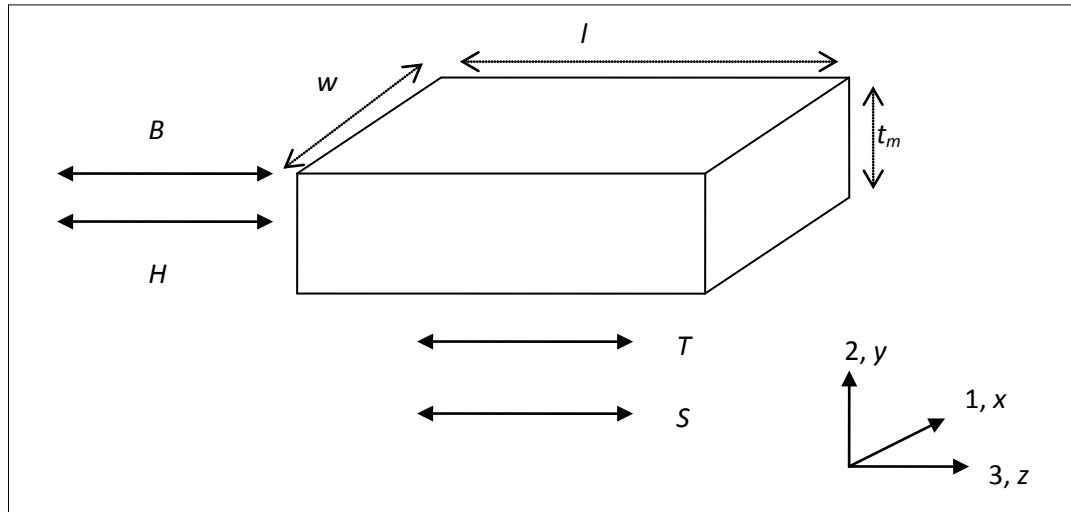


Figure 55. Sketch view of the magnetostrictive layer with associated parameters.

Figure 55 presents a magnetostrictive layer with its lateral dimensions ($l \times w \times t_m$). The magnetic field H and magnetic flux B , stress T and strain S are in the direction 3. We will detail the relations between the vibration speed, forces and magnetic field. So, the first formula¹⁹ is given by

$$S_3 = s_{33,m}^H T_3 + d_{33,m} H_3 \quad (127)$$

The derivation of this formula yields

$$\frac{\partial S_3}{\partial t} = s_{33,m}^H \frac{\partial T_3}{\partial t} + d_{33,m} \frac{\partial H_3}{\partial t} \quad (128)$$

where $s_{33,m}^H$ and $d_{33,m}$ are the flexibility under a magnetic field H and the piezoelectric constant, respectively. We substitute S_3 by $S_3 = \frac{\partial u}{\partial z}$

$$\frac{\partial}{\partial t} \frac{\partial u}{\partial z} = s_{33,m}^H \frac{\partial T_3}{\partial t} + d_{33,m} \frac{\partial H_3}{\partial t}, \quad (129)$$

And v as the vibration speed

$$\frac{\partial v}{\partial z} = s_{33,m}^H \frac{\partial T_3}{\partial t} + d_{33,m} \frac{\partial H_3}{\partial t} \quad (130)$$

As previously detailed, the vibrational speed v solution is given by $v = ae^{-ikz} + be^{ikz}$. The reduction yields to

$$\frac{\partial}{\partial z} (ae^{-ikz} + be^{ikz}) = s_{33,m}^H i\omega T_3 + d_{33,m} i\omega H_3 \quad (131)$$

and to

$$-ik(ae^{-ikz} + be^{ikz}) = s_{33,m}^H i\omega T_3 + d_{33,m} i\omega H_3 \quad (132)$$

with the Fourier Transform. We also evaluate a and b with the previous formulas. We obtain

$$\begin{cases} a = \frac{v_1 e^{ikz_2} + v_2 e^{ikz_1}}{2i \sin kl} \\ b = \frac{v_1 e^{-ikz_2} + v_2 e^{-ikz_1}}{2i \sin kl} \end{cases} \quad (133)$$

So,

$$\frac{-k}{\omega s_{33,m}^H} \left(\frac{v_2}{i \sin kl} + \frac{v_1}{itgkl} \right) = T_{3_1} + \frac{d_{33,m}}{s_{33,m}^H} H_3 \quad (134)$$

with T_{3_1} the stress at the left extremity in direction 3. The force at the left extremity can be written as

$$\begin{aligned} F_{1,m} &= -A_m T_{3_1} = \frac{k A_m}{\omega s_{33,m}^H} \left(\frac{v_2}{i \sin kl} + \frac{v_1}{itgkl} \right) + \frac{d_{33,m}}{s_{33,m}^H} A_m H_3 \\ F_{1,m} &= \zeta_m \left(\frac{v_2}{i \sin kl} + \frac{v_1}{itgkl} \right) + \frac{d_{33,m}}{s_{33,m}^H} A_m H_3 \end{aligned} \quad (135)$$

where $A_m (= wt_m)$ is the cross sectional surface of magnetostrictive layer. Similarly, the force at the right extremity is

$$\begin{aligned} F_{2,m} &= -A_m T_{3-2} = \frac{kA_m}{\omega s_{33,m}^H} \left(\frac{v_1}{i \sin kl} + \frac{v_2}{itgkl} \right) + \frac{d_{33,m}}{s_{33,m}^H} A_m H_3 \\ F_{2,m} &= \zeta_m \left(\frac{v_1}{i \sin kl} + \frac{v_2}{itgkl} \right) + \frac{d_{33,m}}{s_{33,m}^H} A_m H_3 \end{aligned} \quad (136)$$

where $\zeta_m \left(= \frac{kA_m}{\omega s_{33,m}^H} \right)$ is the characteristic impedance of the magnetostrictive layer.

To summarize, the 1-D model yields the constitutive magnetostrictive equations

$$\begin{cases} F_{1,m} = \zeta_m \left(\frac{v_2}{i \sin kl} + \frac{v_1}{itgkl} \right) + \frac{d_{33,m}}{s_{33,m}^H} A_m H_3 \\ F_{2,m} = \zeta_m \left(\frac{v_1}{i \sin kl} + \frac{v_2}{itgkl} \right) + \frac{d_{33,m}}{s_{33,m}^H} A_m H_3 \end{cases} \quad (137)$$

1-D Model of a 3 layers laminated sensor.

The 1-D model of a ME laminated sensor (one piezoelectric layer and two magnetostrictive layers under sandwich form) is presented in Figure 56.

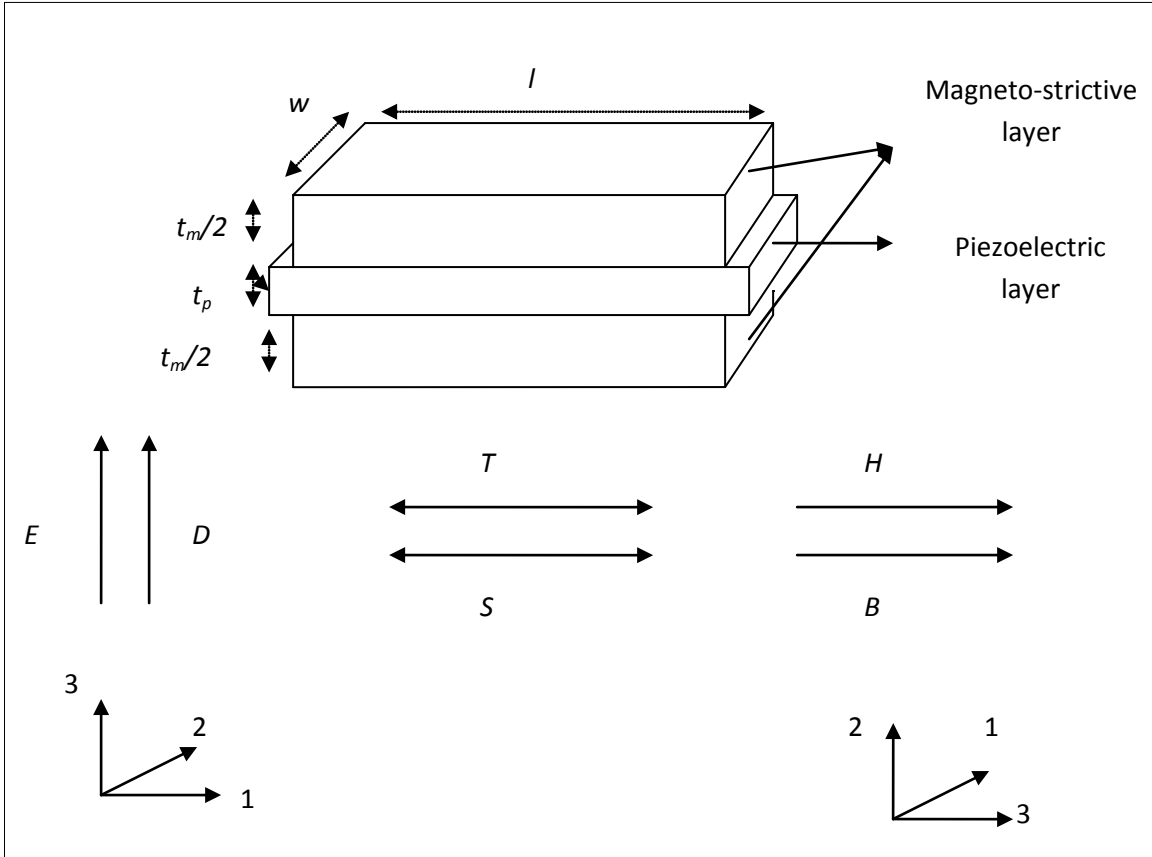


Figure 56. Sketch view of the ME laminated sensor with associated parameters.

Figure 56 presents the 1-D model with 2 layers of magnetostrictive and 1 layer of piezoelectric material. The parameters E , D and H , B are in direction 3 of their self-axes. The dimension of piezoelectric and magnetostrictive is $l \times w \times t_p$ and $l \times w \times t_m$, respectively. With equations of previous parts, we can write the forces at both sensor extremities as

$$\begin{cases} F_1 = F_{1,m} + F_{1,p} \\ F_2 = F_{2,m} + F_{2,p} \end{cases} \quad (138)$$

We rewrite these two equations as

$$\begin{cases} F_1 = (\zeta_p + \zeta_m) \left(\frac{-v_1 \operatorname{tg} \frac{kl}{2}}{i} + \frac{(v_1 + v_2)}{i \sin kl} \right) + \frac{i h_{31,p} I}{\omega} \frac{t_p}{l} + \frac{d_{33,m} A_m}{s_{33,m}^H} H_3 \\ F_2 = (\zeta_p + \zeta_m) \left(\frac{-v_2 \operatorname{tg} \frac{kl}{2}}{i} + \frac{(v_1 + v_2)}{i \sin kl} \right) + \frac{i h_{31,p} I}{\omega} \frac{t_p}{l} + \frac{d_{33,m} A_m}{s_{33,m}^H} H_3 \end{cases} \quad (139)$$

We bring to mind that

F_1 and F_2 are the forces on two extremities of ME laminated sensor

ω is the angular vibration speed

ζ_p and ζ_m are the characteristic impedances of piezoelectric layer and magnetostrictive

layer, respectively, with $\zeta_m = \frac{k_m A_m}{\omega s_{33,m}}$ and $\zeta_m = \frac{c_{31,p} k_p A_p}{\omega} = \frac{k_p A_p}{s_{11,p}^D \omega}$

v_1 et v_2 are the vibration speeds at two extremities of sensor

k is the wave number in sensor

l is the length of the layers

i is the imaginary number $\sqrt{-1}$

$h_{31,p}$ is the piezoelectric constant

I is electric current

$d_{33,m}$ is the magnetostrictive constant

A_m is the side surface of magnetostrictive layer

$s_{33,m}$ is the flexibility coefficient of magnetostrictive material

H_3 is the magnetic field to sense in direction 3

If we consider the electric equation as well, we obtain

$$\left\{ \begin{array}{l} F_1 = (\zeta_p + \zeta_m) \left(\frac{-v_1 \operatorname{tg} \frac{kl}{2}}{i} + \frac{(v_1 + v_2)}{i \sin kl} \right) + \varphi_p \left(\frac{h_{31,p} t_p}{i \omega l} (v_1 + v_2) - V \right) + \varphi_m H_3 \\ F_2 = (\zeta_p + \zeta_m) \left(\frac{-v_2 \operatorname{tg} \frac{kl}{2}}{i} + \frac{(v_1 + v_2)}{i \sin kl} \right) + \varphi_p \left(\frac{h_{31,p} t_p}{i \omega l} (v_1 + v_2) - V \right) + \varphi_m H_3 \\ V = \frac{h_{31,p} t_p}{i \omega l} (v_1 + v_2) - \frac{I}{i \omega C_i} \end{array} \right. \quad (140)$$

$$\left\{ \begin{array}{l} F_1 = (Z_1 v_1 + Z_2 (v_1 + v_2)) + \varphi_p V' + \varphi_m H_3 \\ F_2 = (Z_1 v_1 + Z_2 (v_1 + v_2)) + \varphi_p V' + \varphi_m H_3 \\ V' = \left(\frac{\varphi_p (v_1 + v_2)}{i \omega C_i} - V \right) \\ V = V' + V - \frac{I}{i \omega C_i} \Rightarrow V' = \frac{I}{i \omega C_i} = \frac{-I_{C_i}}{i \omega C_i} - I_z Z = \frac{-I_{C_i} + I_z}{i \omega C_i} \Rightarrow Z = \frac{1}{i \omega (-C_i)} \end{array} \right. \quad (141)$$

So, an electrical equivalent circuit from above equations can be deduced. It is presented in Figure 57.

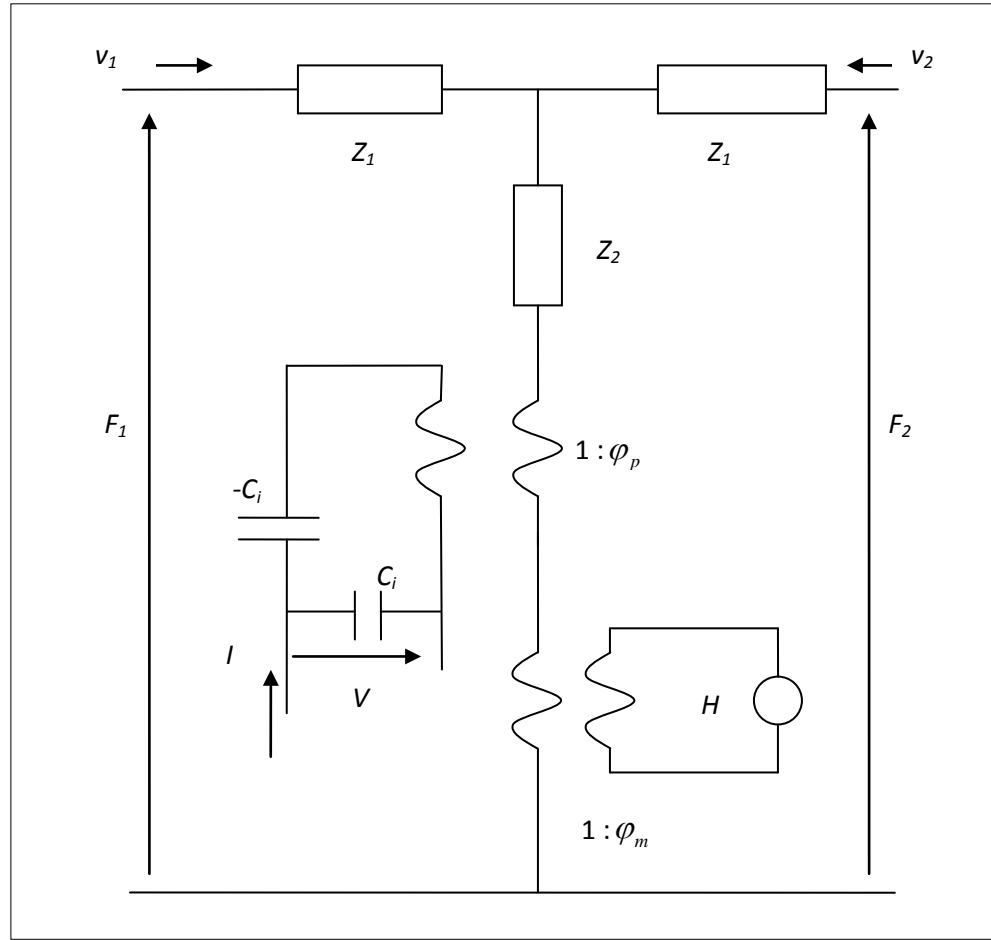


Figure 57. Sketch view of the electrical 1-D L-T mode equivalent circuit of a magnetoelectric laminated sensor.

Figure 57 presents the complete 1D L-T mode equivalent circuit of ME laminated sensor. Notice that the magnetic field H and voltage V or current I are linked versus the vibration speed. We define four parameters

$$\varphi_p = h_{31,p} C_i \frac{t_p}{l} \text{ the coupling coefficient of the piezoelectric layer,}$$

$$\varphi_m = \frac{d_{33,m} A_m}{s_{33,m}^H} \text{ the coupling coefficient of the magnetostrictive layer,}$$

$$Z_1 = (\zeta_p + \zeta_m) i t g \frac{kl}{2} \text{ and } Z_2 = (\zeta_p + \zeta_m) \frac{1}{i \sin kl} \text{ the equivalent mechanical impedances,}$$

$$C_i = \frac{lw}{\beta_{33}^s t_p} = \frac{\epsilon_{33}^s lw}{t_p} \text{ the capacitor value of piezoelectric layer.}$$

In free boundary conditions and **at low frequency**, the forces F_1 and F_2 at the two extremities are nulls ($F_1 = F_2 = 0$). The equivalent circuit could be simplified as given in Figure 58. The mechanical resistance can be written for the quasi static state $\omega \ll 2\pi f_r$ ($f_r = \sqrt{v}/2l$, is the mechanical resonance frequency of the system), as

$$\begin{aligned} Z_{mech} &= Z_1 // Z_1 + Z_2 = \frac{-i}{2} (\xi_p + \zeta_m) \left(\tan \frac{kl}{2} - \frac{2}{\sin kl} \right) = \frac{-i}{2} (\zeta_p + \xi_m) \cot \frac{kl}{2} \\ Z_{mech} &\approx -\frac{1}{2} i \left(\frac{k_m A_m}{\omega_m s_{33,m}^H} + \frac{k_p A_p}{\omega_p s_{11,p}^D} \right) \frac{2}{kl} \approx -i \left(\frac{A_m}{s_{33,m}^H} + \frac{A_p}{s_{11,p}^D} \right) \frac{1}{vkl} \end{aligned} \quad (142)$$

With $k l < 1$.

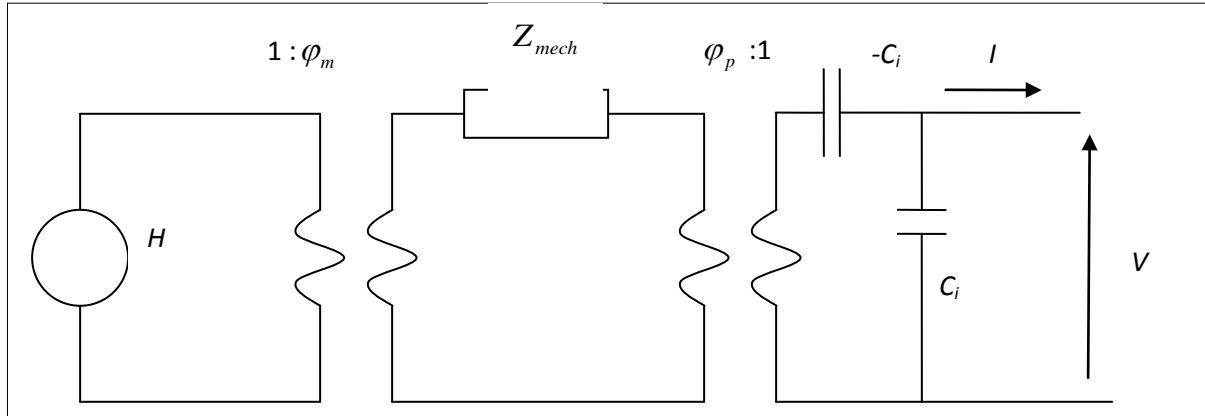


Figure 58. Simplified equivalent circuit under free boundary conditions and at low frequency. Z_{mech} ($= Z_1 // Z_1 + Z_2$) is the mechanical impedance

We define n as the thickness ratio of the piezoelectric and magnetostrictive layers, then

$$Z_{mech} = Z_1 // Z_1 + Z_2 = -i \left(\frac{n}{s_{33,m}^H} + \frac{1-n}{s_{11,p}^D} \right) \frac{A}{vkl} = -i \left(\frac{n}{s_{33,m}^H} + \frac{1-n}{s_{11,p}^D} \right) \frac{A}{\omega l} \quad (143)$$

with $A = w(t_p + t_m)$ the cross section surface of sensor.

In free boundary conditions and **around the resonance frequency**, the forces F_1 and F_2 at the two extremities are always nulls ($F_1 = F_2 = 0$). The equivalent circuit can be simplified as given in figure 8. The mechanical resistance can be written as

$$Z_{mech} = Z_1 // Z_1 + Z_2 = -\frac{j}{2} \rho v A_{Lam} \cot \frac{kl}{2} \quad (144)$$

The equivalent mechanical impedance can be simplified by using the following formula, that is $\frac{\tan x}{x} = -\sum_n \frac{2}{x^2 - (n^2 \pi^2 / 4)}$ (n is odd). So, it yields to

$$Z_{mech} = -\frac{1}{2} i \rho v A \left(\frac{\frac{\pi^2}{4} - \frac{k^2 l^2}{4}}{kl} \right) = i \omega \frac{\rho v A k l}{8 \omega} + \frac{1}{i \omega \frac{8 k l}{\rho v A \pi^2 \omega}} \quad (145)$$

Under the resonance conditions, the wave length λ is equal to $2l$, where l is the length of sensor, so the wave number in sensor $k = \frac{2\pi}{\lambda} = \frac{2\pi}{2l} = \frac{\pi}{l}$. So, the mechanical impedance can be reduced as

$$Z_{mech} = i \omega \frac{Z_0 \pi}{8 \omega} + \frac{1}{i \omega \frac{8}{Z_0 \pi \omega}} = i \omega L_{mech} + \frac{1}{i \omega C_{mech}} \quad (146)$$

With

$$L_{mech} = \frac{Z_0 \pi}{8 \omega}, \quad C_{mech} = \frac{8}{Z_0 \pi \omega} \text{ and } Z_0 = \rho v A = \left(\frac{n}{s_{33,m}^H} + \frac{1-n}{s_{11,p}^D} \right) \frac{A}{\omega} = \left(\frac{n}{s_{33,m}^H} + \frac{1-n}{s_{11,p}^D} \right) \frac{\pi A}{\omega_s l} \quad (147)$$

The equivalent mechanical resistance of ME laminated sensor is given by²⁰

$$R_{mech} = \frac{\omega_s L_{mech}}{Q_{mech}} = \frac{\pi Z_0}{8 \omega_s} \quad (148)$$

where Q_{mech} is the mechanical quality coefficient and ω_s is the resonance frequency. By including the resistance (magnetic or mechanical loss), R_{mech} , as dissipation, we obtain a new expression of the impedance (*cf.* Figure 59) as

$$Z_{mech} = R_{mech} + i \omega L_{mech} + \frac{1}{i \omega C_{mech}} \quad (149)$$

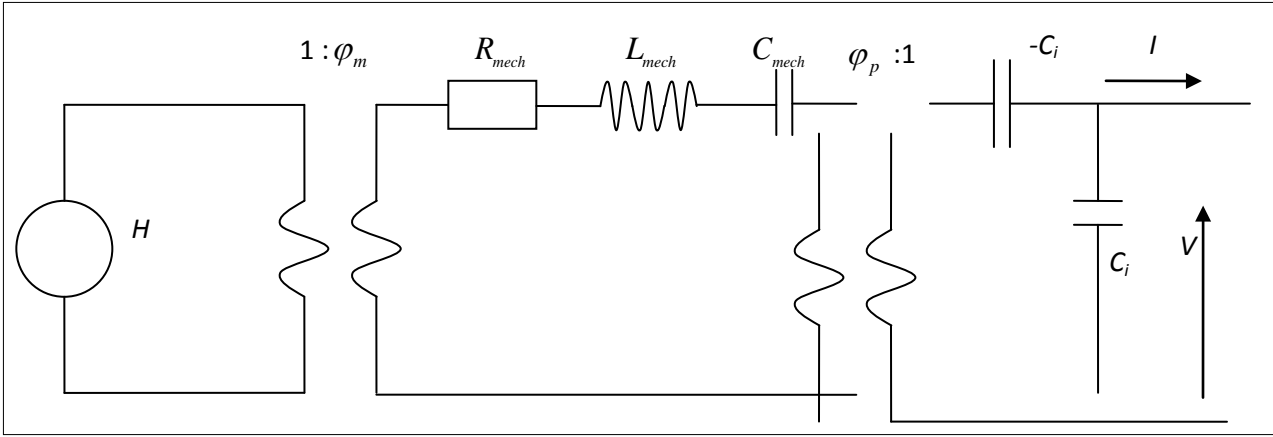


Figure 59. Sketch view of the equivalent circuit under free boundary conditions and at the resonance frequency. Z_{mech} ($= R_{mech} + j \omega L_{mech} + 1/j \omega C_{mech}$) is the mechanical impedance at the resonance frequency.

ME charge coefficient and ME voltage coefficient for the 1-D L-T mode of laminated sensor at low frequency.

From the simplified equivalent circuit given in Figure 59, we are able to give the ME voltage coefficient

$$\alpha_{ME}^V|_{I=0} = \frac{dV}{dH} = \left| \frac{\frac{\varphi_m}{i\omega C_i Z_{mech}}}{\frac{\varphi_p}{\varphi_p}} \right| = \left| \frac{\varphi_m \varphi_p}{i\omega C_i Z_{mech}} \right|, \quad (150)$$

the ME current coefficient

$$\alpha_{ME}^I|_{V=0} = \frac{dI}{dH} = \left| \frac{\frac{\varphi_m}{i\omega C_i - \frac{Z_{mech}}{\varphi_p}}}{\frac{\varphi_p}{\varphi_p}} \right| = \left| \frac{i\omega C_i \varphi_m \varphi_p}{\varphi_p^2 - i\omega C_i Z_{mech}} \right|, \quad (151)$$

and the ME charge coefficient

$$\alpha_{ME}^Q|_{V=0} = \left| \frac{1}{i\omega} \frac{dI}{dH} \right| = \frac{dQ}{dH} = \left| \frac{C_i \varphi_m \varphi_p}{\varphi_p^2 - i\omega C_i Z_{mech}} \right| \quad (152)$$

After inserting $C_i \left(= \frac{\epsilon_{33}^s l w}{t_p} = \epsilon_{33}^s \frac{l w}{(1-n) t_{lam}} \right)$ in the above formula, the ME charge coefficients are given by

$$\alpha_{ME}^V = \frac{dV}{dH} = \left| \frac{\varphi_m \varphi_p}{i\omega C_i Z_{mech}} \right| = \left| \frac{\frac{d_{33,m} t_m w}{s_{33,m}^H} h_{31,p} \left(\varepsilon_{33}^S \frac{l w}{t_p} \right) t_p}{i\omega \left(\varepsilon_{33}^S \frac{l w}{t_p} \right) (-i) \left(\frac{n}{s_{33,m}^H} + \frac{1-n}{s_{11,p}^D} \right) \frac{w t_{lam}}{k l v}} \right| = \left| \frac{\frac{d_{33,m} n}{s_{33,m}^H} h_{31,p} t_p}{\left(\frac{n}{s_{33,m}^H} + \frac{1-n}{s_{11,p}^D} \right)} \right| = \left| \frac{n(1-n) d_{33,m} h_{31,p} s_{11,p}^D t_{lam}}{s_{11,p}^D n + s_{33,m}^H (1-n)} \right| \left[\text{V/A} \cdot \text{m}^{-1} \right], \quad (153)$$

$$\alpha_{ME}^I = \frac{dI}{dH} = \left| \frac{\omega C_i \varphi_m \varphi_p}{\varphi_p^2 - i\omega C_i Z_{mech}} \right| = \left| \omega \frac{n d_{33,m} h_{31,p} s_{11,p}^D \varepsilon_{33}^S w l}{n s_{11,p}^D + (1-n) s_{33,m}^H (1 - s_{11,p}^D h_{31,p}^2 \varepsilon_{33}^S)} \right| \left[\text{A/A} \cdot \text{m}^{-1} \right], \quad (154)$$

$$\alpha_{ME}^O = \frac{dQ}{dH} = \frac{\alpha_{ME}^I}{\omega} = \left| \frac{n d_{33,m} h_{31,p} s_{11,p}^D \varepsilon_{33}^S w l}{n s_{11,p}^D + (1-n) s_{33,m}^H (1 - s_{11,p}^D h_{31,p}^2 \varepsilon_{33}^S)} \right| \left[\text{C/A} \cdot \text{m}^{-1} \right], \quad (155)$$

respectively.

ME charge coefficient and ME voltage coefficient for the 1-D L-T mode of laminated sensor at the resonance frequency.

From the simplified equivalent circuit given in Figure 59, we are able to give the ME voltage coefficient

$$\alpha_{ME}^{V,f_s} = \left| \frac{dV}{dH} \right| = \left| \frac{\varphi_m \varphi_p}{i\omega C_0 \left(R_{mech} + i\omega L_{mech} + \frac{1}{i\omega C_{mech}} \right)} \right| \quad (156)$$

Because $\omega^2 = \omega_s^2 = \frac{1}{L_{mech} C_{mech}}$, $i\omega L_{mech} + \frac{1}{i\omega C_{mech}}$ equals 0 at resonance frequency. We reduce the previous term as

$$\alpha_{ME}^{V,f_s} = \left| \frac{dV}{dH} \right| = \left| \frac{\varphi_m \varphi_p}{i\omega_s C_0 R_{mech}} \right| = \left| \frac{8 Q_m \varphi_m \varphi_p}{\pi \omega_s C_0 Z_0} \right| \quad (157)$$

We substitute $\varphi_p, \varphi_m, C_0$ and Z_0 with their expressions, $Z_0 = \rho v A = \left(\frac{n}{s_{33,m}^H} + \frac{1-n}{s_{11,p}^D} \right) \frac{A}{v}$ and

notice that $\frac{\omega}{v} = k = \frac{2\pi}{\lambda} = \frac{2\pi}{2l} = \frac{\pi}{l}$.

We obtain

$$\alpha_{ME}^{V,f_s} = \left| \frac{dV}{dH} \right| = \left| \frac{8Q_m \frac{wt_m d_{33,m}}{s_{33,m}} \frac{wd_{31,p}}{s_{11,p}^D}}{\pi^2 \epsilon_{33}^S \frac{lw}{t_p} \left(\frac{n}{s_{33,m}^H} + \frac{1-n}{s_{11,p}^D} \right) A} \right| \quad (158)$$

By reducing, the above formula becomes

$$\alpha_{ME}^{V,f_s} = \left| \frac{dV}{dH} \right| = \left| \frac{8Q_m n(1-n) d_{33,m} d_{31,p} t_{lam}}{\pi^2 \epsilon_{33}^S (ns_{11,p}^D + (1-n)s_{33,m}^H)} \right| \quad (159)$$

After inserting $\varphi_p = h_{31,p} C_0 \frac{t_p}{l}$; $\varphi_m = \frac{d_{33,m} wt_{h,m}}{s_{33,m}}$; $C_0 = \frac{lw}{\beta_{33}^S t_h} = \frac{\epsilon_{33}^S lw}{t_p}$, the ME charge coefficients are given by

$$\alpha_{ME}^{V,f_s} = \left| \frac{dV}{dH} \right| = \left| \frac{8Q_m n(1-n) d_{33,m} h_{31,p} s_{11,p}^D t_{lam}}{\pi^2 ns_{11,p}^D + (1-n)s_{33,m}^H} \right| \approx \left| \frac{8Q_m}{\pi^2} \alpha_{ME}^V \right|_{k_{31}^2 \ll 1} [V/A \cdot m^{-1}], \quad (160)$$

(we assume that $s_{11,p}^D h_{31,p}^2 \epsilon_{33}^S \ll 1$)

$$\alpha_{ME}^{Q,f_s} = \frac{1}{\omega_s} \frac{dI}{dH} = \frac{dQ}{dH} = \left| \frac{8Q_m}{\pi^2} \frac{nd_{33,m} h_{31,p} s_{11,p}^D \epsilon_{33}^S lw}{ns_{11,p}^D + (1-n)s_{33,m}^H} \right| \approx \left| \frac{8Q_m}{\pi^2} \alpha_{ME}^Q \right|_{k_{31}^2 \ll 1} [C/A \cdot m^{-1}], \quad (161)$$

$$\alpha_{ME}^{I,f_s} = \frac{dI}{dH} = \left| \frac{8Q_m \omega_s}{\pi^2} \frac{nd_{33,m} h_{31,p} s_{11,p}^D \epsilon_{33}^S lw}{ns_{11,p}^D + (1-n)s_{33,m}^H} \right| \approx \left| \frac{8Q_m}{\pi^2} \alpha_{ME}^I \right|_{k_{31}^2 \ll 1} [A/A \cdot m^{-1}], \quad (162)$$

respectively. Notice that $s_{11,p}^D = (1 - k_{31}^2) s_{11,p}^E$ in L-T mode.

Expected equivalent magnetic noise level 1-D L-T mode of a 3 layers laminated sensor by using a charge amplifier at low frequency.

By using previous development, we are able to predict the theoretical ultimate noise of the sensor. The electronic design is given in Figure 60.

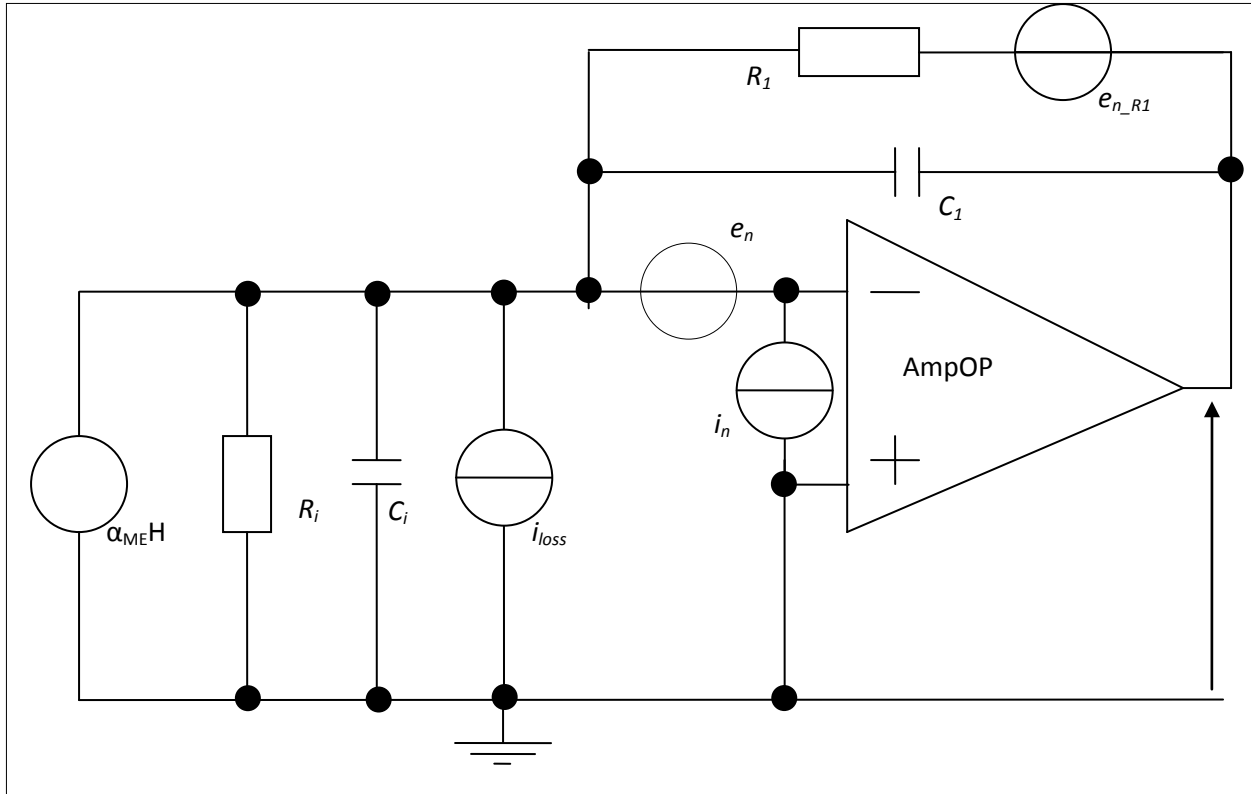


Figure 60. Sketch view of the current charge preamplifier electronics.

The equivalent magnetic noise of the sensor have been evaluated as

$$b_{n_Teq}^2(f) = \frac{1}{\alpha_{ME}^2(f)} \left[\frac{1}{(2\pi f)^2} \left(i_n^2(f) + \frac{4k_b T}{R_1} + \frac{4k_b T}{R_i} + \frac{e_n^2(f)}{R_1^2} + \frac{e_n^2(f)}{R_i^2} \right) + q_{n_vibr}^2(f) + (C_1 + C_i)^2 e_n^2(f) \right] + b_n^2(f) + \frac{4k_b T C_i}{2\pi f \alpha_{ME}^2(f)} \text{Tan}(\delta(f)) \quad (163)$$

with $R_i \gg R_1$ and a transfer function in (V/T) of

$$T_r(f) \approx \frac{\alpha_{ME}^2(f)}{C_1}, \quad (164)$$

if $(R_1 C_1 \omega)^2 \gg 1$ or $R_1 \gg (C_1 \omega)^{-1}$. The charge coefficient is given by

$$\alpha_{ME}^Q = \frac{dQ}{dB} = \frac{1}{\mu_0} \left(\frac{n t_p d_{33,m} h_{31,p} s_{11,p}^D C_i}{s_{11,p}^D n + s_{33,m}^H (1-n) (1 - s_{11,p}^D h_{31,p}^2 \varepsilon_{33}^S)} \right) [\text{C/T}] \quad (165)$$

Taking account, strictly, of the sensor parameter and the Op-Amp noise sources, we obtain an equivalent magnetic noise of the sensor

$$b_{n_Teq}^2(f) = \left(\mu_0 \frac{s_{11,p}^D n + s_{33,m}^H (1-n) (1 - s_{11,p}^D h_{31,p}^2 \varepsilon_{33}^S)}{nd_{33,m} h_{31,p} s_{11,p}^D \varepsilon_{33}^S l w} \right)^2 \left[\frac{1}{(2\pi f)^2} \left(i_n^2(f) + \frac{4k_b T}{R_i} + \frac{e_n^2(f)}{R_i^2} \right) \right] + \\ + \left(\mu_0 \frac{s_{11,p}^D n + s_{33,m}^H (1-n) (1 - s_{11,p}^D h_{31,p}^2 \varepsilon_{33}^S)}{nd_{33,m} h_{31,p} s_{11,p}^D} \right)^2 \frac{4k_b T}{2\pi f_i \varepsilon_{33}^S l w t_p} \tan(\delta(f)) \\ + \left(\mu_0 \frac{s_{11,p}^D n + s_{33,m}^H (1-n) (1 - s_{11,p}^D h_{31,p}^2 \varepsilon_{33}^S)}{n t_p d_{33,m} h_{31,p} s_{11,p}^D} \right)^2 e_n^2(f) \quad (166)$$

Taking account of the main noise contribution, we obtain a theoretical noise level of

$$b_{n_Teq}(f) = \left(\mu_0 \frac{s_{11,p}^D n + s_{33,m}^H (1-n) (1 - s_{11,p}^D h_{31,p}^2 \varepsilon_{33}^S)}{nd_{33,m} h_{31,p} s_{11,p}^D} \right) \sqrt{\frac{i_n^2(f)}{(2\pi f \varepsilon_{33}^S l w)^2} + \frac{e_n^2(f)}{(2\pi f \varepsilon_{33}^S l w R_i)^2} + \frac{4k_b T}{2\pi f_i \varepsilon_{33}^S l w t_p} \tan(\delta(f))} \quad (167)$$

to an ultimate value of

$$b_{n_Teq}(f) = \left(\mu_0 \frac{s_{11,p}^D n + s_{33,m}^H (1-n) (1 - s_{11,p}^D h_{31,p}^2 \varepsilon_{33}^S)}{nd_{33,m} h_{31,p} s_{11,p}^D} \right) \sqrt{\frac{4k_b T}{2\pi f_i \varepsilon_{33}^S l w t_p} \tan(\delta(f))} \quad (168)$$

By using classical piezoelectric and magnetostrictive parameters, as given in table 1, we are able to evaluate the sensor noise performance versus n . To simplify the analysis, we will plot

$$b_{n_Teq}(f) \sqrt{l w t_{lam}} = b_{n_Teq}(f) \sqrt{V_{vol}} = \mu_0 \left(\frac{s_{11,p}^D n + s_{33,m}^H (1-n) (1 - s_{11,p}^D h_{31,p}^2 \varepsilon_{33}^S)}{nd_{33,m} h_{31,p} s_{11,p}^D} \right) \sqrt{\frac{4k_b T}{2\pi f \varepsilon_{33}^S (1-n)} \tan(\delta(f))} \\ b_{n_Teq}(f) = \mu_0 \left(\frac{s_{11,p}^D n + s_{33,m}^H (1-n) (1 - s_{11,p}^D h_{31,p}^2 \varepsilon_{33}^S)}{nd_{33,m} h_{31,p} s_{11,p}^D} \right) \sqrt{\frac{4k_b T}{2\pi f \varepsilon_{33}^S l w t_p} \tan(\delta(f))} [\text{T}/\sqrt{\text{Hz}}] \quad (169)$$

where V_{vol} ($= l w t_{lam}$) is the volume of the sensor. The curve is given in figure 10. This analysis shows that there is an optimal value of n (≈ 0.8). Furthermore, we have evaluated if the limit of the sensor noise is close the fundamental physical minimal energy level, $\hbar \approx 10^{-34}$ J/Hz. Indeed, for a magnetic sensor or magnetometer, the energy resolution can be given by $\varepsilon = \frac{b_n^2 V}{2\mu_0}$ [J/Hz]. It

yields for the current sensor, with theoretical and piezoelectric or magnetostrictive parameters listed in Table 13, to

$$\varepsilon = \frac{b_n^2 V}{2\mu_0} = \frac{b_{n_Teq}^2(f) V_{vol}}{2\mu_0} = \left(\frac{s_{11,p}^D n + s_{33,m}^H (1-n)(1-s_{11,p}^D h_{31,p}^2 \varepsilon_{33}^S)}{nd_{33,m} h_{31,p} s_{11,p}^D} \right)^2 \left(\frac{k_b T \mu_0}{\pi f \varepsilon_{33}^S (1-n)} \text{Tan}(\delta(f)) \right) \approx 7 \cdot 10^{-22} [\text{J/Hz}] \quad (170)$$

(equivalent to $45 \text{ pT}/\sqrt{\text{Hz}}$ @ $f = 1 \text{ Hz}$) with $n = 0.8$. This value has to be compared to standard SQUID sensor theory where

$$\varepsilon = \frac{4k_b T L}{R} \approx 9.310^{-33} [\text{J/Hz}] \quad (171)$$

with $T = 4.2 \text{ K}$, $L = 100 \text{ pH}$ and $R = 10 \Omega$. For example, Table 13 gives the different magnetic energy resolutions for sensors.

Table 13. Comparison of different magnetic sensor energy resolution

Device	Energy Resolution $\varepsilon (\text{J/Hz})$
SQUID w/pickup	$1 \cdot 10^{-30}$
SERF	$3 \cdot 10^{-29}$
Hybrid GMR/SC	$4 \cdot 10^{-29}$
GMI	$6 \cdot 10^{-28}$
AMR	$7 \cdot 10^{-26}$
CSAM	$2 \cdot 10^{-25}$
He4	$4 \cdot 10^{-24}$
Fluxgate	$3 \cdot 10^{-23}$
GMR w/feedback	$4 \cdot 10^{-23}$
Hall	$5 \cdot 10^{-23}$
TMR	10^{-25}
TMR w/FC	10^{-19}
Magneto(Elasto)Electric	$\approx 10^{-22}$

Expected equivalent magnetic noise level 1-D L-T mode of a 3 layers laminated sensor by using a voltage amplifier at low frequency.

Similarly as for our previous development, we have analyzed the equivalent noise model of a voltage preamplifier electronic as given in Figure 61.

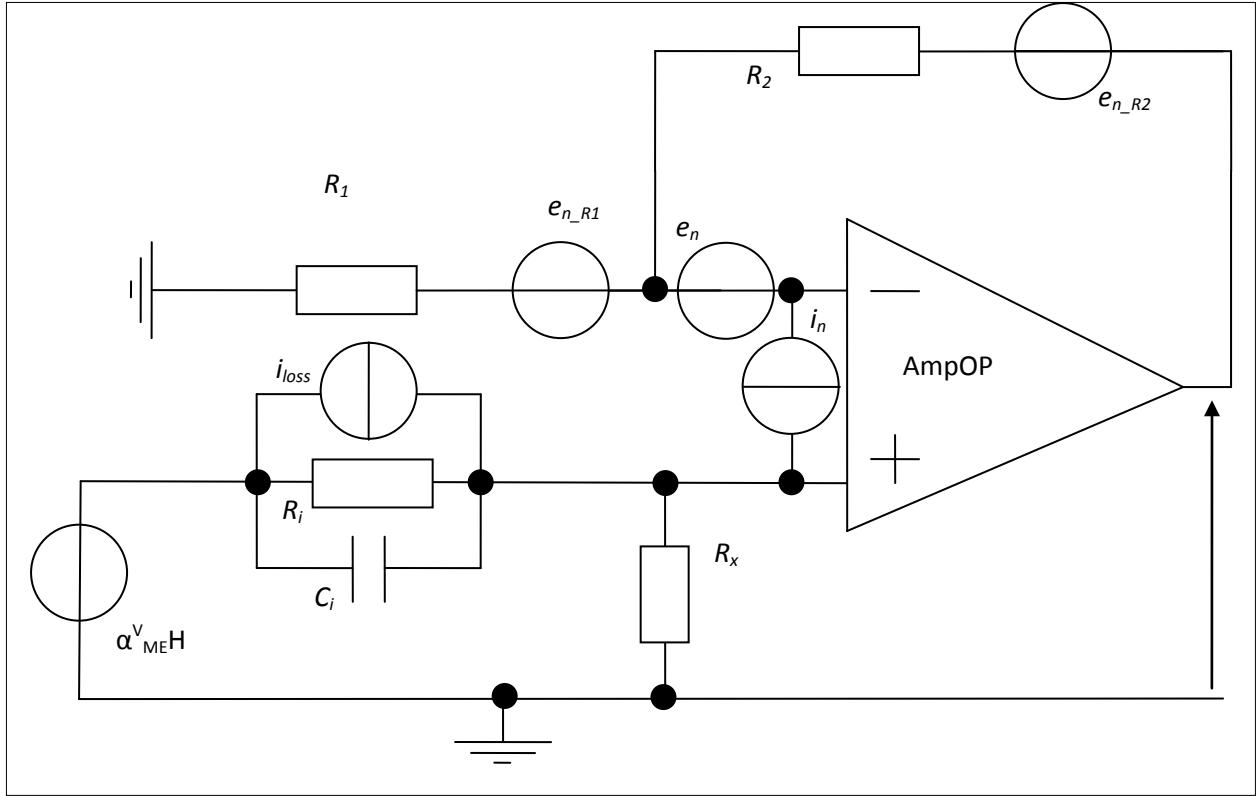


Figure 61. Sketch view of the voltage preamplifier electronics.

The equivalent voltage noise of the system is given by

$$e_{n_tot}^2 \approx \left(1 + \frac{R_2}{R_1}\right)^2 \left[e_n^2 + \left(R_1 // R_2\right)^2 i_n^2 + \left(\frac{R_i R_x}{R_i + R_x}\right)^2 \frac{1}{1 + \left(\frac{R_i R_x}{R_i + R_x} C_i \omega\right)^2} \left(i_n^2 + i_{n_R_x}^2 + i_{n_R_i}^2 + i_{loss}^2\right) \right] \quad (172)$$

Hereafter, the term $\left(R_1 // R_2\right)^2 i_n^2$ will be considered negligible. The output transfer function in (V/T) is

$$T_r^V = \frac{\alpha_{ME}^V}{\mu_0} \left(1 + \frac{R_2}{R_1}\right) \left(\frac{R_x}{R_x + R_i}\right) \frac{(1 + jR_i C_i \omega)}{\left(1 + j \frac{R_i R_x}{R_x + R_i} C_i \omega\right)} \quad (173)$$

The latter can be simplified under the following conditions:

If

$$R_i \gg R_x, \quad T_r^V = \frac{\alpha_{ME}^V}{\mu_0} \left(1 + \frac{R_2}{R_1}\right) \left(\frac{R_x}{R_i}\right) \frac{(1 + jR_i C_i \omega)}{(1 + jR_x C_i \omega)} \quad (174)$$

If

$$R_i \ll R_x, T_r^V = \frac{\alpha_{ME}^V}{\mu_0} \left(1 + \frac{R_2}{R_1} \right) \quad (175)$$

If

$$R_i \rightarrow \infty, T_r^V = \frac{\alpha_{ME}^V}{\mu_0} \left(1 + \frac{R_2}{R_1} \right) \frac{jR_x C_i \omega}{(1 + jR_x C_i \omega)} \quad (176)$$

We obtain an equivalent magnetic noise of the sensor with associated voltage preamplifier electronics given by

$$b_n^2 \approx \left(\mu_0 \frac{s_{11,p}^D n + s_{33,m}^H (1-n)}{d_{33,m} h_{31,p} s_{11,p}^D t_p n} \right)^2 \frac{1}{(1 + (R_i C_i \omega)^2)} \left\{ \left(\frac{\left(1 + \left(\frac{R_i R_x}{R_i + R_x} C_i \omega \right)^2 \right)^2}{\left(\frac{R_x}{R_i + R_x} \right)^2} e_n^2 + R_i^2 (i_n^2 + i_{n-R_i}^2 + i_{n+R_i}^2 + 4k_b T C_i 2\pi f \tan(\delta(f))) \right) \right\} + b_n^2(f) \quad (177)$$

After reduction and taking account of the sensor parameters, we obtain the equivalent magnetic noise of the sensor

$$b_n^2 \approx \left(\mu_0 \frac{s_{11,p}^D n + s_{33,m}^H (1-n)}{d_{33,m} h_{31,p} s_{11,p}^D t_p n} \right)^2 \left\{ \frac{R_i^2 i_n^2 + \frac{R_i^2}{R_x^2} e_n^2 + \frac{R_i}{R_x} e_n^2 + 4k_b T R_i + R_i^2 4k_b T C_i 2\pi f \tan(\delta(f))}{(1 + (R_i C_i \omega)^2)} + e_n^2 \right\} \quad (178)$$

With similar hypothesis used for a charge amplifier, if $(R_i C_i \omega)^2 \gg 1$ or $R_i \gg (C_i \omega)^{-1}$, we obtain

$$b_n^2 \approx \mu_0 \left(\frac{s_{11,p}^D n + s_{33,m}^H (1-n)}{d_{33,m} h_{31,p} s_{11,p}^D t_p n 2\pi f C_i} \right)^2 \left(i_n^2 + \frac{e_n^2}{R_x^2} + \frac{e_n^2}{R_x R_i} + i_{n-R_i}^2 + 4k_b T 2\pi f C_i \tan(\delta(f)) \right) + \left(\frac{s_{11,p}^D n + s_{33,m}^H (1-n)}{d_{33,m} h_{31,p} s_{11,p}^D t_p n} \right)^2 e_n^2 \quad (179)$$

$$b_n^2 \approx \left(\mu_0 \frac{s_{11,p}^D n + s_{33,m}^H (1-n)}{d_{33,m} h_{31,p} s_{11,p}^D n \epsilon_{33}^S l w} \right)^2 \left(\frac{1}{(2\pi f)^2} \left(\frac{4k_b T}{R_i} + i_n^2 + \frac{e_n^2}{R_x^2} + \frac{e_n^2}{R_x R_i} \right) \right) + \left(\mu_0 \frac{s_{11,p}^D n + s_{33,m}^H (1-n)}{d_{33,m} h_{31,p} s_{11,p}^D n} \right)^2 \frac{4k_b T}{2\pi f \epsilon_{33}^S l w t_p} \tan(\delta(f)) + \left(\mu_0 \frac{s_{11,p}^D n + s_{33,m}^H (1-n)}{d_{33,m} h_{31,p} s_{11,p}^D t_p n} \right)^2 e_n^2 + b_n^2(f) \quad (180)$$

So, the theoretical noise level is given by

$$b_{n_V}^2(f) = \left(\mu_0 \frac{s_{11,p}^D n + s_{33,m}^H (1-n)}{nd_{33,m} h_{31,p} s_{11,p}^D} \right) \sqrt{\frac{i_n^2(f)}{(2\pi f \epsilon_{33}^S lw)^2} + \frac{e_n^2(f)}{R_x^2 (2\pi f \epsilon_{33}^S lw)^2} + \frac{e_n^2(f)}{R_i R_x (2\pi f \epsilon_{33}^S lw)^2} + \frac{4k_b T}{2\pi f_i \epsilon_{33}^S lwt_p} \tan(\delta(f))} \quad [\text{T}/\sqrt{\text{Hz}}], \quad (181)$$

to an ultimate equivalent value as by using a charge amplifier of

$$b_n(f) = \left(\mu_0 \frac{s_{11,p}^D n + s_{33,m}^H (1-n)}{nd_{33,m} h_{31,p} s_{11,p}^D} \right) \sqrt{\frac{4k_b T}{2\pi f_i \epsilon_{33}^S lwt_p} \tan(\delta(f))} \quad [\text{T}/\sqrt{\text{Hz}}] \quad (182)$$

Or

$$b_n(f) = \left(\mu_0 \frac{ns_{11,p}^E (1 - k_{31,p}^2) + (1-n)s_{33,m}^H}{nd_{33,m} g_{31,p}} \right) \sqrt{\frac{4k_b T}{2\pi f_i \epsilon_{33}^S lwt_p} \tan(\delta(f))} \quad [\text{T}/\sqrt{\text{Hz}}] \quad (183)$$

So, no real difference could be observed between both amplifiers (charge and current) in theory if the optimal conditions on the resistors have been considered and $(1 - k_{31,p}^2) \approx 1$. Equations mainly differ on the frequency time constant for the output transfer in (V/T) and associated e_n noise versus R_i or R_x . If *all things being equal*, it lets to conclude that if $R_i > R_x$, it will be better to use a charge amplifier and, if $R_x > R_i$, it will be better to use a voltage amplifier. So, we expect similar noise level measurements, if the sensor noise is predominant and that the preamplifiers are well done!

Expected equivalent magnetic noise level 1-D L-T mode of a 3 layers laminated sensor by using a charge amplifier at the resonance frequency.

Also, we have evaluated the equivalent noise model around the frequency by using a charge amplifier. Around the resonance, the voltage noise is given by

$$e_{n_T}^2(f_s) = \left| \frac{1}{C_1 \omega_s} \right|^2 \left[i_{n_R1}^2(f_s) + i_n^2(f_s) + i_{loss}^2(f_s) \right] + \left| 1 + \frac{C_i}{C_1} \right|^2 e_n^2(f_s) \quad (184)$$

It yields to the equivalent magnetic noise given by

$$b_{n_tot}^2 \approx \frac{\left| \frac{1}{\omega_s} \right|^2 \left[i_{n_R1}^2(f_s) + i_n^2(f_s) + i_{loss}^2(f_s) \right] + |C_1 + C_i|^2 e_n^2(f_s)}{\left| \frac{8Q_m}{\mu_0 \pi^2} \frac{nd_{33,m} h_{31,p} s_{11,p}^D \epsilon_{33}^S lw}{ns_{11,p}^D + (1-n)s_{33,m}^H} \right|^2} \quad (185)$$

and an ultimate noise of

$$b_{n,f_s} \approx \mu_0 \frac{\pi^2}{8Q_m} \left| \frac{ns_{11,p}^D + (1-n)s_{33,m}^H}{nd_{33,m}h_{31,p}s_{11,p}^D} \right| \sqrt{\frac{4k_b T}{2\pi f_s \varepsilon_{33}^S l w t_p} \tan(\delta(f))} \quad (186)$$

So, we obtain with a $Q_m \approx 50$, $f_s = 30$ kHz and data given in table 1 of

$$b_{n_tot} \approx \frac{55,836}{Q_m \sqrt{f_s}} \approx 6.5 \text{ [fT}/\sqrt{\text{Hz}}] \quad (187)$$

By neglecting the acceleration noise of the piezoelectric element, see after.

Expected equivalent magnetic noise level 1-D L-T mode of a 3 layers laminated sensor by using a voltage amplifier at the resonance frequency. Also, we have evaluated the equivalent noise model around the frequency by using a voltage amplifier. Around the resonance, the voltage noise is given by

$$e_n^2 = \left(1 + \frac{R_2}{R_1} \right)^2 \left(e_n^2(f_s) + (R_1 // R_2)^2 i_n^2(f_s) \right) + (Z_i // R_x)^2 \left(1 + \frac{R_2}{R_1} \right)^2 \left(i_n^2(f_s) + i_{n_{-R_i}}^2(f_s) + i_{n_{-R_x}}^2(f_s) + i_{loss}^2(f_s) \right) + \left(\frac{R_2}{R_1} \right)^2 e_{n_{-R_1}}^2(f_s) + e_{n_{-R_2}}^2(f_s) \quad (188)$$

It yields to the equivalent magnetic noise given by

$$\begin{aligned} b_{n,V,f_s}^2 &\approx \frac{e_n^2(f_s) + \left| \frac{R_i R_x}{R_x (1 + j R_i C_i \omega_s)} + R_i \right|^2 (i_n^2(f_s) + i_{n_{-R_i}}^2(f_s) + i_{n_{-R_x}}^2(f_s) + i_{loss}^2(f_s))}{\left| \frac{1}{\mu_0} \frac{8Q_m}{\pi^2} \frac{n(1-n)d_{33,m}h_{31,p}s_{11,p}^D t_{lam}}{ns_{11,p}^D + (1-n)s_{33,m}^H} \right|^2} \\ &\approx \left| \frac{4k_b T}{2\pi f_s} \frac{\varepsilon_{33}^S l w}{t_p} \tan(\delta(f)) \right|^2 \\ &\approx \left| \frac{1}{\mu_0} \frac{8Q_m}{\pi^2} \frac{nd_{33,m}h_{31,p}s_{11,p}^D \varepsilon_{33}^S l w}{ns_{11,p}^D + (1-n)s_{33,m}^H} \right|^2 \end{aligned} \quad (189)$$

and a similar ultimate noise of

$$b_{n,f_s} \approx \mu_0 \frac{\pi^2}{8Q_m} \left| \frac{ns_{11,p}^D + (1-n)s_{33,m}^H}{nd_{33,m}h_{31,p}s_{11,p}^D} \right| \sqrt{\frac{4k_b T}{2\pi f_s \varepsilon_{33}^S l w t_p} \tan(\delta(f))} \quad (190)$$

Expected equivalent magnetic noise level, 1-D, for all modes (LL, TL, LT, TT and LL push-pull) of a 3 layers laminated sensor by using a voltage amplifier at low frequency.

Similarly, as in our previous report, we have detailed the sensitivity and noise for L-L, T-L, L-T, T-T and L-L_{Push-Pull} sensor mode. Results are given in the tables below for the basic sensor sketch-view given in Figure 62.

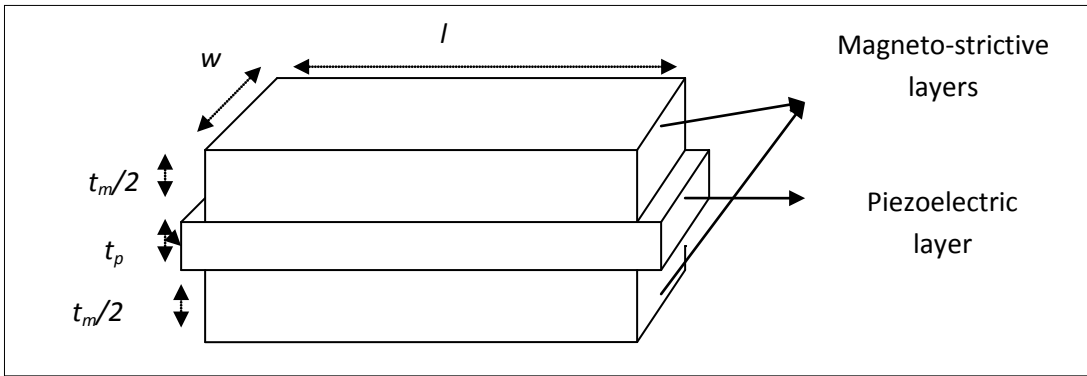


Figure 62. Sketch-view of the sensor.

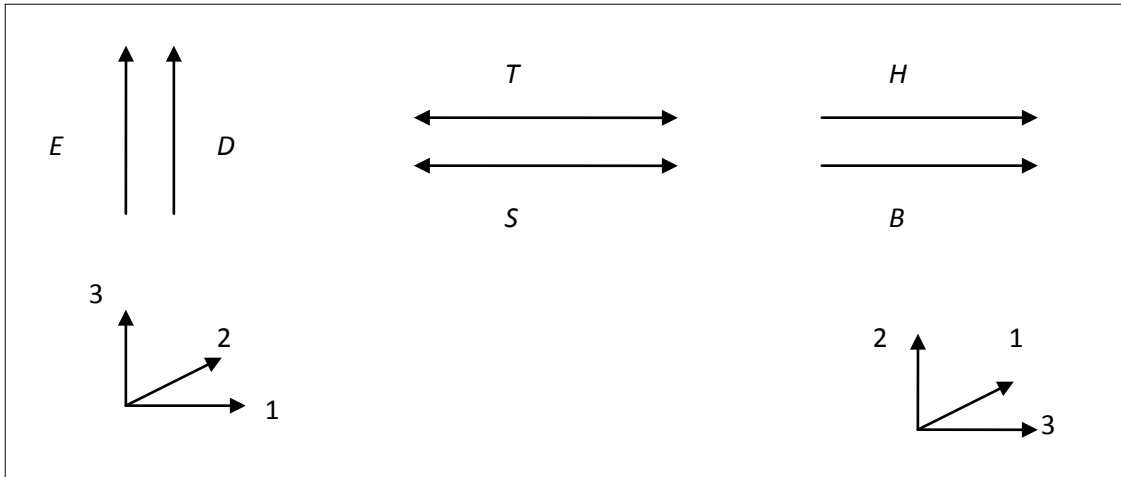


Figure 63. Associated axes for LT mode.

The constitutive equations used for this model are given below. It helps to solve the system.

$$\begin{cases} S_p = s_p^E T + d_p E \\ D = d_p T + \varepsilon^T E \end{cases} \quad \begin{cases} S_m = s_m^H T + d_m H \\ B = d_m T + \mu^T H \end{cases} \quad (191)$$

Or

$$\begin{cases} E = \beta^T D - g_p T \\ S_p = s_p^D T + g_p D \end{cases} \quad \begin{cases} S_m = s_m^H T + d_m H \\ B = d_m T + \mu^T H \end{cases} \quad (192)$$

Table 14. Calculations Synthesis Associated to the Four Main Modes and, also for the LL Push-Pull Mode.

Mode	Model A	Model B	Sensitivity V/(A.m) or C/(A.m)
L-L	$C_0 = \frac{wt_p}{l} \mathcal{E}_{33}^S$ $\varphi_p = \frac{wt_p}{l} \frac{d_{33,p}}{s_{33,p}^E}$ $\varphi_m = \frac{wt_m d_{33,m}}{s_{33,m}^H}$ $Z_{mech} = -j \left(\frac{n}{s_{33,m}^H} + \frac{1-n}{s_{33,p}^E} \right) \frac{A}{kvl}$	$C_0 = \frac{wt_p}{l} \mathcal{E}_{33}^S$ $\varphi_p = \frac{g_{33,p}}{s_{33,p}^D} C_0$ $\varphi_m = \frac{wt_m d_{33,m}}{s_{33,m}^H}$ $Z_{mech} = -j \left(\frac{n}{s_{33,m}^H} + \frac{1-n}{s_{33,p}^D} \right) \frac{A}{kvl}$	$\frac{dV}{dH} = \frac{ng_{33,p} d_{33,m} l}{ns_{33,p}^D + (1-n)s_{33,m}^H}$ $\frac{dQ}{dH} = \frac{nd_{33,p} d_{33,m} wt_p}{ns_{33,p}^E + (1-n)s_{33,m}^H}$
T-L	$C_0 = \frac{wl}{t_p} \mathcal{E}_{33}^S$ $\varphi_p = \frac{wt_p}{l} \frac{d_{33,p}}{s_{33,p}^E}$ $\varphi_m = \frac{wt_m d_{31,m}}{s_{11,m}^H}$ $Z_{mech} = -j \left(\frac{n}{s_{11,m}^H} + \frac{1-n}{s_{33,p}^E} \right) \frac{A}{kvl}$	$C_0 = \frac{wt_p}{l} \mathcal{E}_{33}^S$ $\varphi_p = \frac{g_{33,p}}{s_{33,p}^D} C_0$ $\varphi_m = \frac{wt_m d_{31,m}}{s_{11,m}^H}$ $Z_{mech} = -j \left(\frac{n}{s_{11,m}^H} + \frac{1-n}{s_{33,p}^D} \right) \frac{A}{kvl}$	$\frac{dV}{dH} = \frac{ng_{33,p} d_{31,m} l}{ns_{33,p}^D + (1-n)s_{11,m}^H}$ $\frac{dQ}{dH} = \frac{nd_{33,p} d_{31,m} wt_p}{ns_{33,p}^E + (1-n)s_{11,m}^H}$
L-T	$C_0 = \frac{wl}{t_p} \mathcal{E}_{33}^S$ $\varphi_p = w \frac{d_{31,p}}{s_{11,p}^E}$ $\varphi_m = \frac{wt_m d_{33,m}}{s_{33,m}^H}$ $Z_{mech} = -j \left(\frac{n}{s_{33,m}^H} + \frac{1-n}{s_{11,p}^E} \right) \frac{A}{kvl}$	$C_0 = \frac{wl}{t_p} \mathcal{E}_{33}^S$ $\varphi_p = \frac{g_{31,p}}{s_{11,p}^D} C_0$ $\varphi_m = \frac{wt_m d_{33,m}}{s_{33,m}^H}$ $Z_{mech} = -j \left(\frac{n}{s_{33,m}^H} + \frac{1-n}{s_{11,p}^D} \right) \frac{A}{kvl}$	$\frac{dV}{dH} = \frac{ng_{31,p} d_{33,m} t_p}{ns_{11,p}^D + (1-n)s_{33,m}^H}$ $\frac{dQ}{dH} = \frac{ng_{31,p} d_{33,m} lw}{ns_{11,p}^E + (1-n)s_{33,m}^H}$
T-T	$C_0 = \frac{wl}{t_p} \mathcal{E}_{33}^S$ $\varphi_p = w \frac{d_{31,p}}{s_{11,p}^E}$ $\varphi_m = \frac{wt_m d_{31,m}}{s_{11,m}^H}$ $Z_{mech} = -j \left(\frac{n}{s_{11,m}^H} + \frac{1-n}{s_{11,p}^E} \right) \frac{A}{kvl}$	$C_0 = \frac{wl}{t_p} \mathcal{E}_{33}^S$ $\varphi_p = \frac{g_{31,p}}{s_{11,p}^D} C_0$ $\varphi_m = \frac{wt_m d_{31,m}}{s_{11,m}^H}$ $Z_{mech} = -j \left(\frac{n}{s_{11,m}^H} + \frac{1-n}{s_{11,p}^D} \right) \frac{A}{kvl}$	$\frac{dV}{dH} = \frac{ng_{31,p} d_{31,m} t_p}{ns_{11,p}^D + (1-n)s_{11,m}^H}$ $\frac{dQ}{dH} = \frac{nd_{31,p} d_{31,m} lw}{ns_{11,p}^E + (1-n)s_{11,m}^H}$

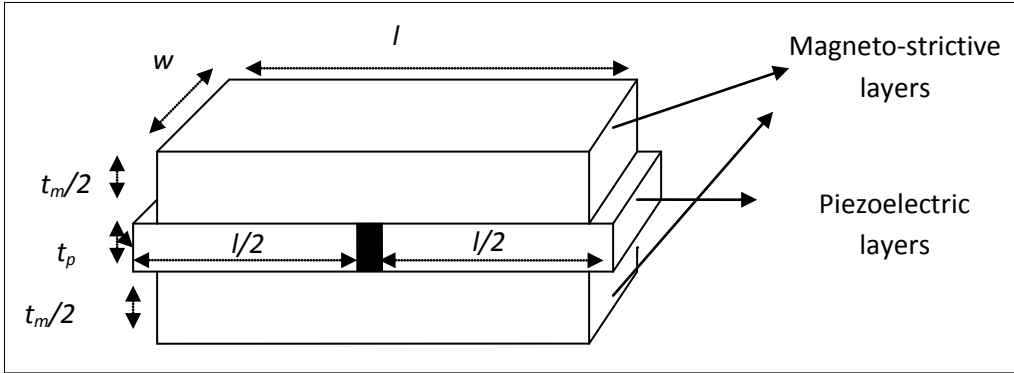


Figure 64. Sketch-view of a push-pull sensor.

Table 15. Calculations Synthesis Associated to the Four Main Modes and, also for the LL Push-Pull Mode.

Mode	Model A	Model B	Sensitivity
L-L Push-pull (2 sections)	$C_0 = \frac{t_p w}{l_1} \varepsilon_{33}^S$ $\varphi_p = \frac{w t_p}{l_1} \frac{d_{33,p}}{s_{33,p}^E}$ $\varphi_m = \frac{w t_m}{s_{33,m}^H} d_{33,m}$ $Z_{mech} = -j \left(\frac{n}{s_{33,m}^H} + \frac{1-n}{s_{33,p}^E} \right) \frac{A}{k v l_1}$	$C_0 = \frac{t_p w}{l_1} \varepsilon_{33}^S$ $\varphi_p = \frac{g_{33,p}}{s_{33,p}^D} C_0$ $\varphi_m = \frac{w t_m}{s_{33,m}^H} d_{33,m}$ $Z_{mech} = -j \left(\frac{n}{s_{33,m}^H} + \frac{1-n}{s_{33,p}^D} \right) \frac{A}{k v l_1}$	$\frac{dV_1}{dH} = \frac{n g_{33,p} d_{33,m} l_1}{n s_{33,p}^D + (1-n) s_{33,m}^H}$ $\frac{dQ_1}{dH} = \frac{n d_{33,p} d_{33,m} t_p w}{n s_{33,p}^E + (1-n) s_{33,m}^H}$ where $l_1 = l/2$

Notice that $\left| \frac{dV}{dH} \right| = \left| \frac{dV_1}{dH} \right|$ and $\left| \frac{dQ}{dH} \right| = 2 \left| \frac{dQ_1}{dH} \right| \dots$

These results enable us to modelized the ME sensor as electric circuits as shown in Figure 65.

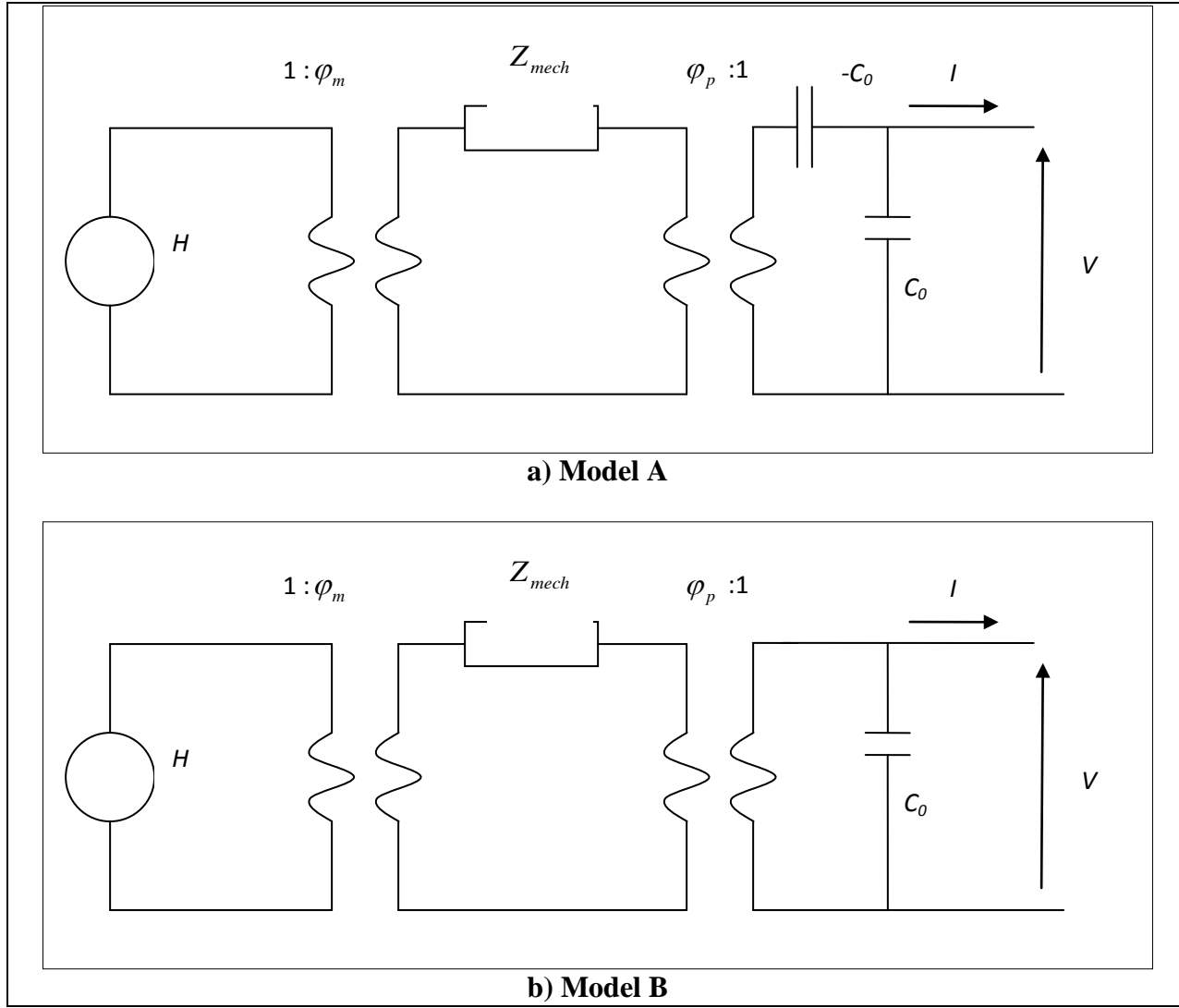


Figure 65. Electric equivalent circuits (Models A & B) of a ME sensor by using 1-D Mason Model.

Similarly as in the previous report, the equivalent magnetic noise of the sensor is given by taking into account, strictly, the sensor parameter and the OpAmp noise sources. We obtain an optimal equivalent magnetic noise of the sensor

$$b_{n_Teq}^2(f) \Big|_{V=0} \approx \frac{\mu_0^2}{\alpha_{ME}^o(f)^2} \left[\frac{1}{(2\pi f)^2} \left(i_n^2(f) + \frac{4k_b T}{R_i} + \frac{e_n^2(f)}{R_i^2} \right) + C_i e_n^2(f) \right] + \frac{4\mu_0^2 k_b T C_0}{2\pi f \alpha_{ME}^o(f)^2} \tan(\delta(f)) + b_n^2(f) \quad [\text{T}^2/\text{Hz}] \quad (193)$$

when using a charge amplifier and

$$b_{n_Teq}^2(f) \Big|_{I=0} \approx \frac{\mu_0^2}{\alpha_{ME}^v(f)^2} \left(e_n^2 + \frac{R_i^2}{(1+(R_i C_i \omega)^2)} (i_n^2 + i_{n-R_i}^2 + 4k_b T C_0 2\pi f \tan(\delta(f))) \right) + b_n^2(f) \quad [\text{T}^2/\text{Hz}] \quad (194)$$

for using a voltage amplifier. It yields respectively to an ultimate noise

$$b_{n_Teq}(f) \approx \frac{\mu_0}{\alpha_{ME}^v(f)} \sqrt{\frac{4k_b T C_0}{2\pi f} \tan(\delta(f))} [\text{T}/\sqrt{\text{Hz}}] \quad (195)$$

And

$$b_{n_Teq} \approx \frac{\mu_0}{\alpha_{ME}^v(f)} \sqrt{4k_b T 2\pi f C_0 \tan(\delta(f))} [\text{T}/\sqrt{\text{Hz}}] \quad (196)$$

Notice that $C_0 = (1 - k_{ij}^2) C_i \approx 0.5$ to 1 C_i .

The table hereafter summarizes the ultimate theoretical magnetic sensor noise associated to this description at low and resonance frequencies, ideally. The theoretical resonance frequency is given by

$$f_r = \frac{v}{2l} = \frac{\sqrt{\frac{n}{s^H} + \frac{1-n}{s^{E(D)}}}}{2l\sqrt{\rho}} = \frac{\sqrt{\frac{n}{s^H} + \frac{1-n}{s^{E(D)}}}}{2l\sqrt{n\rho_m + (1-n)\rho_p}} = \frac{1}{2l} \sqrt{\frac{s^{E(D)}n + (1-n)s^H}{s^H s^{E(D)}(n\rho_m + (1-n)\rho_p)}} \quad (197)$$

Table 16. Calculations Synthesis Associated to the Four Main Modes and, also for the LL Push-Pull Mode.

Mode	$\alpha_{ME}^v(f)$	C_0	$b_{n_Teq,V}(f) [\text{T}/\sqrt{\text{Hz}}]$
L-L	$\frac{ng_{33,p}d_{33,m}l}{ns_{33,p}^D + (1-n)s_{33,m}^H}$	$\frac{wt_p}{l}\mathcal{E}_{33}^S$	$\mu_0 \frac{ns_{33,p}^D + (1-n)s_{33,m}^H}{nh_{33,p}s_{33,p}^D d_{33,m}} \sqrt{\frac{4k_b T}{2\pi f t_p w l} \tan(\delta(f))}$
T-L	$\frac{ng_{33,p}d_{31,m}l}{ns_{33,p}^D + (1-n)s_{11,m}^H}$	$\frac{wt_p}{l}\mathcal{E}_{33}^S$	$\mu_0 \frac{ns_{33,p}^D + (1-n)s_{11,m}^H}{nh_{33,p}s_{33,p}^D d_{31,m}} \sqrt{\frac{4k_b T}{2\pi f t_p w l} \tan(\delta(f))}$
L-T	$\frac{ng_{31,p}d_{33,m}t_p}{ns_{11,p}^D + (1-n)s_{33,m}^H}$	$\frac{wl}{t_p}\mathcal{E}_{33}^S$	$\mu_0 \frac{ns_{11,p}^D + (1-n)s_{33,m}^H}{nh_{31,p}s_{11,p}^D d_{33,m}} \sqrt{\frac{4k_b T}{2\pi f t_p w l} \tan(\delta(f))}$
T-T	$\frac{ng_{31,p}d_{31,m}t_p}{ns_{11,p}^D + (1-n)s_{11,m}^H}$	$\frac{wl}{t_p}\mathcal{E}_{33}^S$	$\mu_0 \frac{ns_{11,p}^D + (1-n)s_{11,m}^H}{nh_{31,p}s_{11,p}^D d_{31,m}} \sqrt{\frac{4k_b T}{2\pi f t_p w l} \tan(\delta(f))}$
L-L Push-pull (mSeg. or Cap. in //)*	$\frac{1}{m} \left(\frac{ng_{33,p}d_{33,m}l}{ns_{33,p}^D + (1-n)s_{33,m}^H} \right)$	$m \frac{wt_p}{l}\mathcal{E}_{33}^S$	$\mu_0 \frac{ns_{33,p}^D + (1-n)s_{33,m}^H}{nh_{33,p}s_{33,p}^D d_{33,m}} \sqrt{\frac{4k_b T}{2\pi f t_p w l} \tan(\delta(f))}$

* Theoretical behavior

Table 17. Calculations Synthesis Associated to the Four Main Modes and, also for the LL Push-Pull Mode.

Mode	$\alpha_{ME}^Q(f)$	C_0	$b_{n_Teq,Q}(f)[T/\sqrt{Hz}]$
L-L	$\frac{nd_{33,p}d_{33,m}wt_p}{ns_{33,p}^E + (1-n)s_{33,m}^H}$	$\frac{wt_p}{l}\epsilon_{33}^S$	$\mu_0 \frac{ns_{33,p}^D + (1-n)s_{33,m}^H(1-k_{33,p}^2)}{ng_{33,p}d_{33,m}} \sqrt{\frac{4k_b T}{2\pi f l w t_p \epsilon_{33}^S}} \tan(\delta(f))$
T-L	$\frac{nd_{33,p}d_{31,m}wt_p}{ns_{33,p}^E + (1-n)s_{11,m}^H}$	$\frac{wt_p}{l}\epsilon_{33}^S$	$\mu_0 \frac{ns_{33,p}^D + (1-n)s_{11,m}^H(1-k_{33,p}^2)}{ng_{33,p}d_{31,m}} \sqrt{\frac{4k_b T}{2\pi f l w t_p \epsilon_{33}^S}} \tan(\delta(f))$
L-T	$\frac{nd_{31,p}d_{33,m}lw}{ns_{11,p}^E + (1-n)s_{33,m}^H}$	$\frac{wl}{t_p}\epsilon_{33}^S$	$\mu_0 \frac{ns_{11,p}^D + (1-n)s_{33,m}^H(1-k_{31,p}^2)}{ng_{31,p}d_{33,m}} \sqrt{\frac{4k_b T}{2\pi f l w t_p \epsilon_{33}^S}} \tan(\delta(f))$
T-T	$\frac{nd_{31,p}d_{31,m}lw}{ns_{11,p}^E + (1-n)s_{11,m}^H}$	$\frac{wl}{t_p}\epsilon_{33}^S$	$\mu_0 \frac{ns_{11,p}^D + (1-n)s_{11,m}^H(1-k_{31,p}^2)}{ng_{31,p}d_{31,m}} \sqrt{\frac{4k_b T}{2\pi f l w t_p \epsilon_{33}^S}} \tan(\delta(f))$
L-L Push-pull (mSeg. or Cap. in //)*	$m \left(\frac{nd_{33,p}d_{33,m}t_p w}{ns_{33,p}^E + (1-n)s_{33,m}^H} \right)$	$m \frac{wt_p}{l}\epsilon_{33}^S$	$\mu_0 \frac{ns_{33,p}^D + (1-n)s_{33,m}^H(1-k_{33,p}^2)}{ng_{33,p}d_{33,m}} \sqrt{\frac{4k_b T}{2\pi f l w t_p \epsilon_{33}^S}} \tan(\delta(f))$

* Theoretical behavior

Table 18. Calculations Synthesis Associated to the Four Main Modes and, also for the LL Push-Pull Mode.

Mode	$\alpha_{ME,Res}^V(f)$	C_0	$b_{n_Teq,V}(f)[T/\sqrt{Hz}]$
L-L	$\frac{8Q_m}{\pi^2} \frac{ng_{33,p}d_{33,m}l}{ns_{33,p}^D + (1-n)s_{33,m}^H}$	$\frac{wt_p}{l}\epsilon_{33}^S$	$\frac{8\mu_0 Q_m}{\pi^2} \frac{ns_{33,p}^D + (1-n)s_{33,m}^H}{nh_{33,p}s_{33,p}^D d_{33,m}} \sqrt{\frac{4k_b T}{2\pi f_{res} t_p wl \epsilon_{33}^S}} \tan(\delta(f))$
T-L	$\frac{8Q_m}{\pi^2} \frac{ng_{33,p}d_{31,m}l}{ns_{33,p}^D + (1-n)s_{11,m}^H}$	$\frac{wt_p}{l}\epsilon_{33}^S$	$\frac{8\mu_0 Q_m}{\pi^2} \frac{ns_{33,p}^D + (1-n)s_{11,m}^H}{nh_{33,p}s_{33,p}^D d_{31,m}} \sqrt{\frac{4k_b T}{2\pi f_{res} t_p wl \epsilon_{33}^S}} \tan(\delta(f))$
L-T	$\frac{8Q_m}{\pi^2} \frac{ng_{31,p}d_{33,m}t_p}{ns_{11,p}^D + (1-n)s_{33,m}^H}$	$\frac{wl}{t_p}\epsilon_{33}^S$	$\frac{8\mu_0 Q_m}{\pi^2} \frac{ns_{11,p}^D + (1-n)s_{33,m}^H}{nh_{31,p}s_{11,p}^D d_{33,m}} \sqrt{\frac{4k_b T}{2\pi f_{res} t_p wl \epsilon_{33}^S}} \tan(\delta(f))$
T-T	$\frac{8Q_m}{\pi^2} \frac{ng_{31,p}d_{31,m}t_p}{ns_{11,p}^D + (1-n)s_{11,m}^H}$	$\frac{wl}{t_p}\epsilon_{33}^S$	$\frac{8\mu_0 Q_m}{\pi^2} \frac{ns_{11,p}^D + (1-n)s_{11,m}^H}{nh_{31,p}s_{11,p}^D d_{31,m}} \sqrt{\frac{4k_b T}{2\pi f_{res} t_p wl \epsilon_{33}^S}} \tan(\delta(f))$
L-L Push-pull (mSeg. or Cap. in //)*	$\frac{8Q_m}{\pi^2 m} \left(\frac{ng_{33,p}d_{33,m}l}{ns_{33,p}^D + (1-n)s_{33,m}^H} \right)$	$m \frac{wt_p}{l}\epsilon_{33}^S$	$\frac{8\mu_0 Q_m}{\pi^2} \frac{ns_{33,p}^D + (1-n)s_{33,m}^H}{nh_{33,p}s_{33,p}^D d_{33,m}} \sqrt{\frac{4k_b T}{2\pi f_{res} t_p wl \epsilon_{33}^S}} \tan(\delta(f))$

* Theoretical behavior

Table 19. Calculations Synthesis Associated to the Four Main Modes and, also for the LL Push-Pull Mode.

Mode	$\alpha_{ME}^Q(f)$	C_0	$b_{n_Teq,Q}(f)[T/\sqrt{Hz}]$
L-L	$\frac{8Q_m}{\pi^2} \frac{nd_{33,p}d_{33,m}wt_p}{ns_{33,p}^E + (1-n)s_{33,m}^H}$	$\frac{wt_p}{l}\epsilon_{33}^S$	$\frac{8\mu_0 Q_m}{\pi^2} \frac{ns_{33,p}^D + (1-n)s_{33,m}^H(1-k_{33,p}^2)}{ng_{33,p}d_{33,m}} \sqrt{\frac{4k_b T}{2\pi f_{res} l w t_p \epsilon_{33}^S} \tan(\delta(f))}$
T-L	$\frac{8Q_m}{\pi^2} \frac{nd_{33,p}d_{31,m}wt_p}{ns_{33,p}^E + (1-n)s_{11,m}^H}$	$\frac{wt_p}{l}\epsilon_{33}^S$	$\frac{8\mu_0 Q_m}{\pi^2} \frac{ns_{33,p}^D + (1-n)s_{11,m}^H(1-k_{33,p}^2)}{ng_{33,p}d_{31,m}} \sqrt{\frac{4k_b T}{2\pi f_{res} l w t_p \epsilon_{33}^S} \tan(\delta(f))}$
L-T	$\frac{8Q_m}{\pi^2} \frac{nd_{31,p}d_{33,m}lw}{ns_{11,p}^E + (1-n)s_{33,m}^H}$	$\frac{wl}{t_p}\epsilon_{33}^S$	$\frac{8\mu_0 Q_m}{\pi^2} \frac{ns_{11,p}^D + (1-n)s_{33,m}^H(1-k_{31,p}^2)}{ng_{31,p}d_{33,m}} \sqrt{\frac{4k_b T}{2\pi f_{res} l w t_p \epsilon_{33}^S} \tan(\delta(f))}$
T-T	$\frac{8Q_m}{\pi^2} \frac{nd_{31,p}d_{31,m}lw}{ns_{11,p}^E + (1-n)s_{11,m}^H}$	$\frac{wl}{t_p}\epsilon_{33}^S$	$\frac{8\mu_0 Q_m}{\pi^2} \frac{ns_{11,p}^D + (1-n)s_{11,m}^H(1-k_{31,p}^2)}{ng_{31,p}d_{31,m}} \sqrt{\frac{4k_b T}{2\pi f_{res} l w t_p \epsilon_{33}^S} \tan(\delta(f))}$
L-L Push-pull (mSeg. or Cap. in //)*	$\frac{8mQ_m}{\pi^2} \frac{nd_{33,p}d_{33,m}t_p w}{ns_{33,p}^E + (1-n)s_{33,m}^H}$	$m \frac{wt_p}{l}\epsilon_{33}^S$	$\frac{8\mu_0 Q_m}{\pi^2} \frac{ns_{33,p}^D + (1-n)s_{33,m}^H(1-k_{33,p}^2)}{ng_{33,p}d_{33,m}} \sqrt{\frac{4k_b T}{2\pi f_{res} l w t_p \epsilon_{33}^S} \tan(\delta(f))}$

* Theoretical behavior

So, these tables give us the ultimate magnetic sensor noise level given by the theoretical Mason 1-D equations for each model.

Theoretically, we can notice that (L-L Push-pull as example):

$$\frac{b_{n_Teq,V}(f)}{b_{n_Teq,Q}(f)} = \frac{\mu_0 \frac{ns_{33,p}^D + (1-n)s_{33,m}^H}{nh_{33,p}s_{33,p}^D d_{33,m}} \sqrt{\frac{4k_b T}{2\pi f t_p w l \epsilon_{33}^S} \tan(\delta(f))}}{\mu_0 \frac{ns_{33,p}^D + (1-n)s_{33,m}^H(1-k_{33,p}^2)}{ng_{33,p}d_{33,m}} \sqrt{\frac{4k_b T}{2\pi f l w t_p \epsilon_{33}^S} \tan(\delta(f))}} \quad (198)$$

$$\frac{b_{n_Teq,V}(f)}{b_{n_Teq,Q}(f)} \approx 1 + \frac{k_{33,p}^2}{ns_{33,p}^D + (1-n)s_{33,m}^H} \quad (199)$$

It yields to:

$$b_{n_Teq,Q}(f) \leq b_{n_Teq,V}(f) \quad (200)$$

Noise level at the sensor resonance.

In order to evaluate the true noise level at the sensor resonance, we have investigated the mechanical sensor noise source given by

$$a_n = \sqrt{\frac{4k_B T \omega_{res}}{mass Q_{mech}}} [g/\sqrt{Hz}] \quad (201)$$

Where k_B , T , ω_{res} , mass, Q_{mech} are the Boltzmann constant, the temperature, the resonant frequency, the mass of laminates and the mechanical quality factor of the laminates. It yields to evaluate the mechanical noise source as

$$f_n = \text{mass} \times a_n = \sqrt{\frac{4k_B T \omega_{res} \text{mass}}{Q_{mech}}} [\text{N}/\sqrt{\text{Hz}}] \quad (202)$$

So, the laminate model can be studied with the mechanical noise source as given in Figure 66.

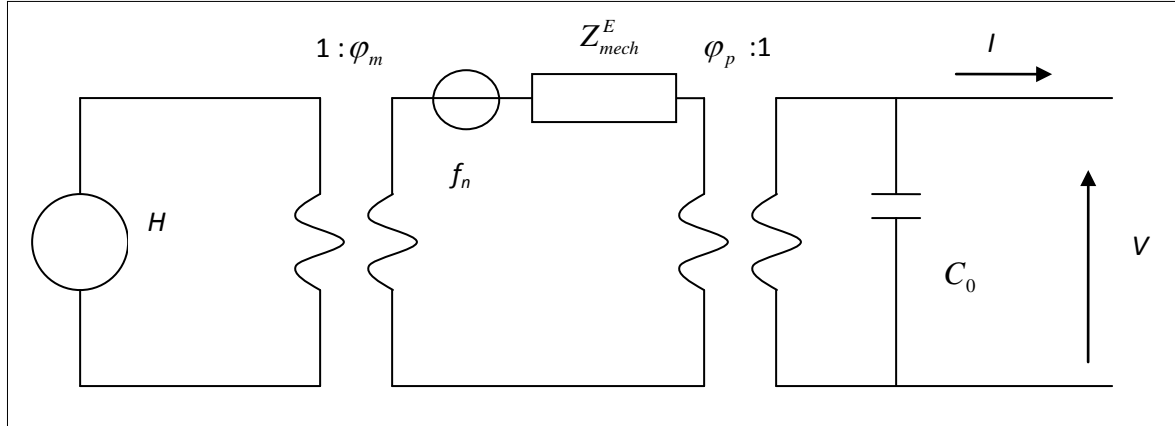


Figure 66. Lamine model with associated mechanical noise source.

The transfer function for the mechanical noise is deduced from the simplified model given in Figure 66, where the input of the system is the force f . V and I , the electrical voltage and current are the outputs of the system

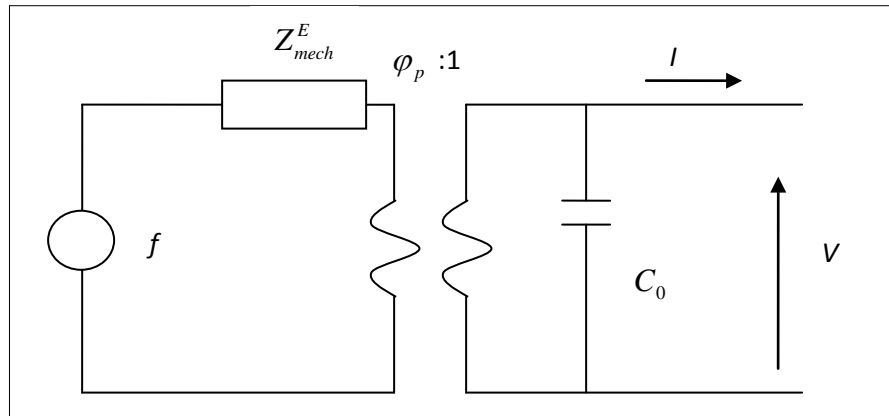


Figure 67. Simplified lamine model.

In L-L mode, we have, previously, defined

- the Mechanical resistance: $Z^E_{mech} = -j \left(\frac{n}{s_{33,m}^H} + \frac{1-n}{s_{33,p}^E} \right) \frac{A}{kvl} \quad (203)$

where A ($= t_{lam} \times w$) side surface of laminates; $s_{33,m}^H$ and $s_{33,p}^E$ flexibilities coefficient for magnetostrictive and piezoelectric materials; k elastic wave number; v elastic wave speed; l length of laminates.

$$- \text{the Elastic-electric coupling coefficient: } \varphi_p = \frac{A_p}{l} \frac{d_{33,p}}{s_{33,p}^E} \quad (204)$$

where A_p ($= t_p \times w$) side surface of piezoelectric layer, $d_{33,p}$ piezoelectric constant.

$$- \text{the Laminates capacitance: } C_0 = \frac{A_p}{l} \varepsilon_{33,p} \quad (205)$$

where $\varepsilon_{33,p}$ dielectric constant of the piezoelectric material.

So, the relation between V , I and f is given by

$$f = \frac{I + j\omega C_0 V}{\varphi_p} Z_{mech}^E, \quad (206)$$

and yields under open circuit condition ($I=0$)

$$V = \frac{\varphi_p}{j\omega C_0 Z_{mech}^E} f, \quad (207)$$

and under short circuit condition ($V=0$)

$$I = \frac{\varphi_p}{Z_{mech}^E} f \text{ or } Q = \frac{\varphi_p}{j\omega Z_{mech}^E} f \quad (208)$$

After inserting φ_p and Z_{mech}^E in the above formula, we are able to evaluate the output charge noise generated, in [C/\sqrt{Hz}] unit, by the mechanical noise force, as

$$q_n = \frac{\frac{A_p}{l} \frac{d_{33,p}}{s_{33,p}^E}}{j\omega \times -j \left(\frac{n}{s_{33,m}^H} + \frac{1-n}{s_{33,p}^E} \right) \frac{A}{kvl}} f_n = \frac{d_{33,p}}{1 - \left(2 - \frac{s_{33,p}^E}{s_{33,m}^H} \right) n + \left(1 - \frac{s_{33,p}^E}{s_{33,m}^H} \right) n^2} f_n. \quad (209)$$

Or

$$q_n = \left(\frac{d_{33,p}}{1 - \left(2 - \frac{s_{33,p}^E}{s_{33,m}^H} \right) n + \left(1 - \frac{s_{33,p}^E}{s_{33,m}^H} \right) n^2} \right) \sqrt{\frac{4k_B T \omega_{res} mass}{Q_{mech}}} \text{ [C/}\sqrt{\text{Hz}}\text{]} \quad (210)$$

By using the charge amplifier FCL-2, the output voltage noise e_n in [V/ $\sqrt{\text{Hz}}$] unit is written as

$$e_n = \frac{Q_n \times Gain}{C_1} = \frac{Gain}{C_1} \frac{d_{33,p}}{1 - \left(2 - \frac{s_{33,p}^E}{s_{33,m}^H} \right) n + \left(1 - \frac{s_{33,p}^E}{s_{33,m}^H} \right) n^2} \sqrt{\frac{4k_B T \omega_{res} mass}{Q_{mech}}} \quad (211)$$

where $Gain$ is the second stage gain of the charge circuit FCL-2 and C_1 (=10 pF) is the classical output capacitor of the sensor. Similarly, the output voltage noise, e_{n_res} , appearing around the resonance is

$$e_{n_res} = \frac{8Q_{mech}}{\pi^2} e_n. \quad (212)$$

So, the equivalent magnetic noise could deduced from previous equation, as

$$b_n = \frac{1}{\alpha_{ME}^Q} \left(\frac{d_{33,p}}{1 - \left(2 - \frac{s_{33,p}^E}{s_{33,m}^H} \right) n + \left(1 - \frac{s_{33,p}^E}{s_{33,m}^H} \right) n^2} \right) \sqrt{\frac{4k_B T \omega_{res} mass}{Q_{mech}}} \quad (213)$$

Ultimately, we can evaluate the lowest equivalent magnetic noise of ME sensor as

$$b_n = \frac{\mu_0}{m n d_{33,m}} \left(\frac{n s_{33,p}^E + (1-n) s_{33,m}^H}{1 - \left(2 - \frac{s_{33,p}^E}{s_{33,m}^H} \right) n + \left(1 - \frac{s_{33,p}^E}{s_{33,m}^H} \right) n^2} \right) \sqrt{\frac{4k_B T \pi \sqrt{\frac{(n s_{33,p}^E + (1-n) s_{33,m}^H)((1-n)\rho_p + n\rho_m)}{s_{33,p}^E s_{33,m}^H}}}{Q_{mech} w t_p (1-n)}} \quad (214)$$

where m is the number of segments in LL Push-Pull mode sensor.

Similarly, the equivalent magnetic noise appearing at around resonance is roughly, if the equivalent magnetic sensor noise is the dominant source at the output.

$$b_{n_res} = b_n \quad (215)$$

Presently, we predict that the lowest magnetic noise of the ME could be given by

$$\begin{aligned} b_{n,Q}^2(f) = & \left(\mu_0 \frac{ns_{33,p}^E + (1-n)s_{33,m}^H}{nwt_p d_{33,m} d_{33,p}} \right)^2 \left[\frac{1}{(2\pi f)^2} \left(i_n^2(f) + \frac{4k_B T}{R} + \frac{e_n^2(f)}{R^2} \right) \right] \\ & + \left(\mu_0 \frac{ns_{33,p}^E + (1-n)s_{33,m}^H}{n d_{33,m} d_{33,p}} \right)^2 \frac{4k_B T}{2\pi f \epsilon_{33}^S lwt_p} \tan(\delta(f)) \\ & + \left(\frac{\mu_0}{m n d_{33,m}} \frac{ns_{33,p}^E + (1-n)s_{33,m}^H}{1 - \left(2 - \frac{s_{33,p}^E}{s_{33,m}^H} \right) n + \left(1 - \frac{s_{33,p}^E}{s_{33,m}^H} \right) n^2} \right)^2 \frac{4k_B T \pi \sqrt{\frac{(ns_{33,p}^E + (1-n)s_{33,m}^H)((1-n)\rho_p + n\rho_m)}{s_{33,p}^E s_{33,m}^H}}}{Q_{mech} w t_p (1-n)} \\ & + \left(\mu_0 \frac{ns_{33,p}^E + (1-n)s_{33,m}^H}{n lwd_{33,m} d_{33,p}} \right)^2 e_n^2(f) \end{aligned} \quad (216)$$

and ideally to

$$b_{n,Q}^2(f) = \left(\mu_0 \frac{ns_{33,p}^E + (1-n)s_{33,m}^H}{n d_{33,m} d_{33,p}} \right)^2 \frac{4k_B T}{2\pi f \epsilon_{33}^S lwt_p} \tan(\delta(f)) + \frac{1}{m^2} \left(\frac{\mu_0}{n d_{33,m}} \frac{ns_{33,p}^E + (1-n)s_{33,m}^H}{1 - \left(2 - \frac{s_{33,p}^E}{s_{33,m}^H} \right) n + \left(1 - \frac{s_{33,p}^E}{s_{33,m}^H} \right) n^2} \right)^2 \frac{4k_B T \pi \sqrt{\frac{(ns_{33,p}^E + (1-n)s_{33,m}^H)((1-n)\rho_p + n\rho_m)}{s_{33,p}^E s_{33,m}^H}}}{Q_{mech} w t_p (1-n)}, \quad (217)$$

in L-L mode, as exemplify hereafter. To conclude, the equivalent magnetic noise sensor behavior versus f for the latter equation and is given in Figures 68 (a) and (b), respectively.

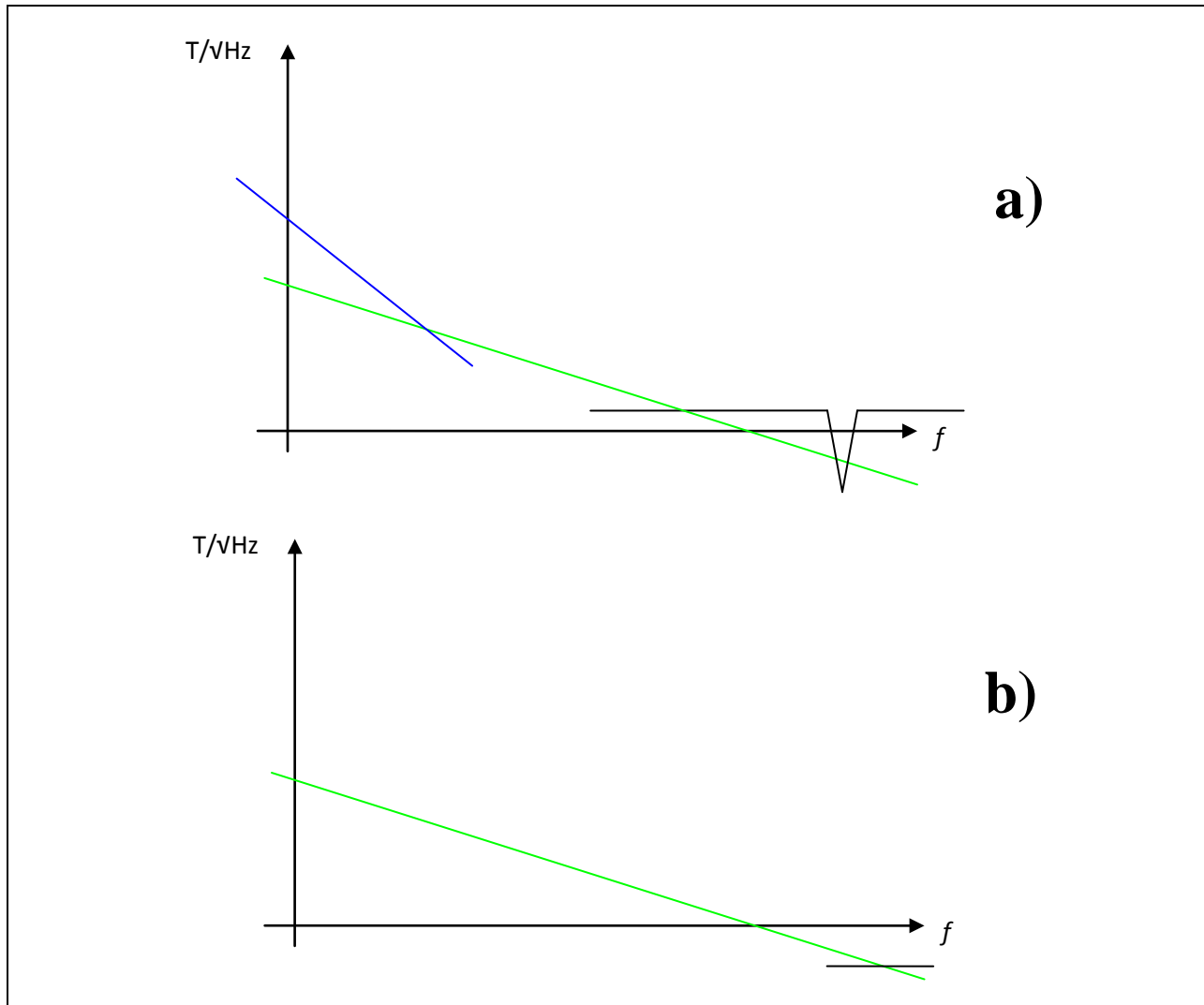


Figure 68. Expected equivalent magnetic noise behavior versus the frequency and given by the model, a) including the full model, b) including the ideal model.

B.3.2. Measurement

Hereafter, we present the set-up of the sensor characterization and the equivalent magnetic noise measurements obtained with the two best tested sensors.

The set-up of noise procedure measurements is summarized in Figure 69. We can notice the use of a vacuum vessel for the sensor. Without the use of a vacuum vessel, sensor performances were reduced by an acoustic sensed vibrational noise appearing at low frequency (*cf.* Figure 70).

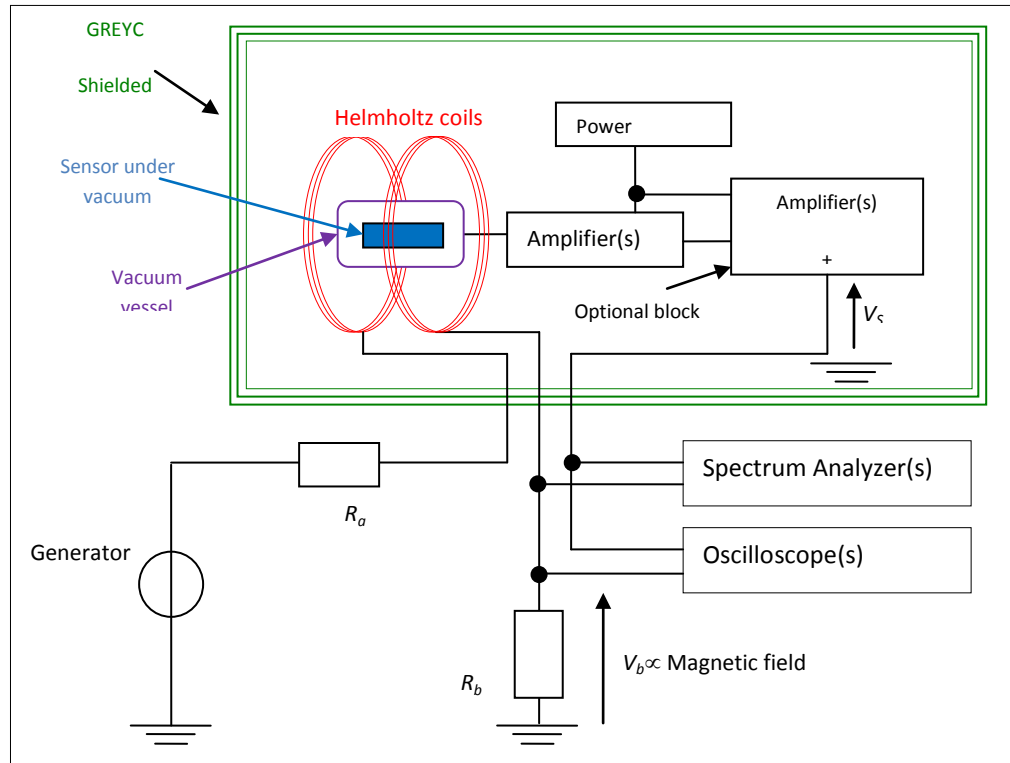


Figure 69. Setup of sensor characterization



Figure 70. View of a) theD.U.T.& b) GREYC Shielding room

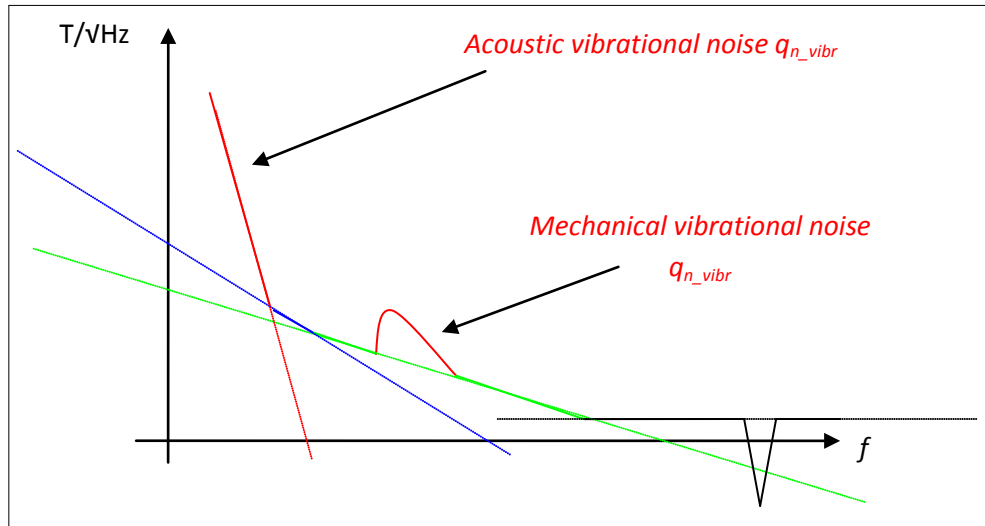
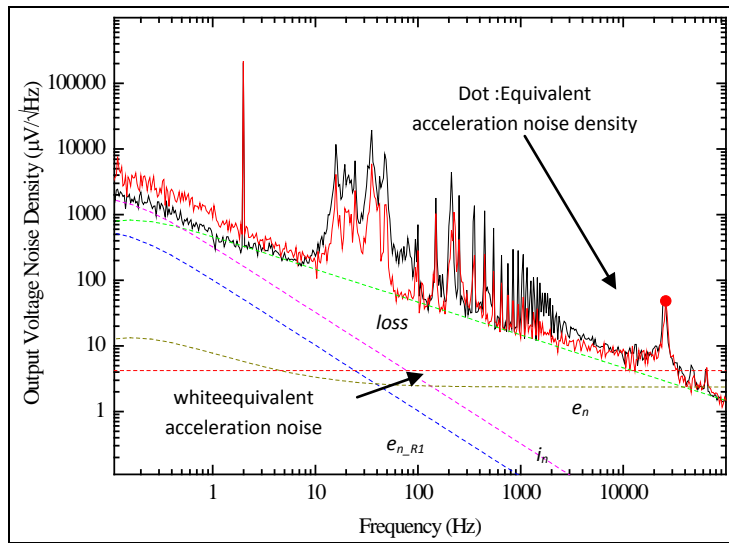


Figure 71. Expected equivalent magnetic noise behavior given by the model.

Comparison to experimental results.

The following figures well compare the theoretical model and experimental evaluations.



* It didn't include the resonance effect

Figure 72. Output voltage noise for laminates F21 (black) and F22 (red) with the use of the charge FCL-2 amplifier.

The dashed curves are the simulated curves. Notice that the ME resonance frequency appears at around 26 kHz with an increase of the noise level.

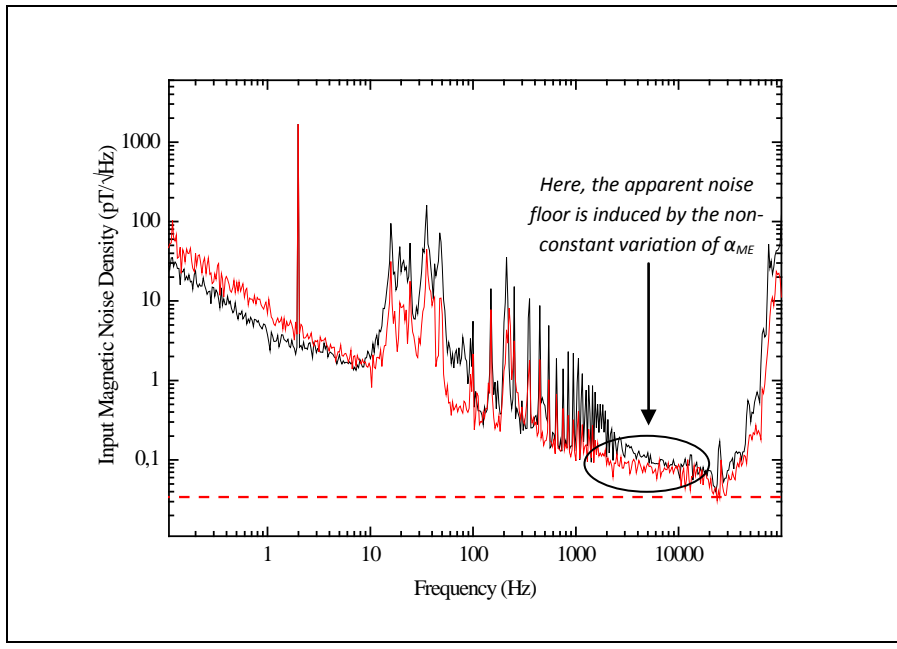


Figure 73. Equivalent input magnetic noise level for the laminates F21 (black) and F22 (red).

The dashed red line corresponds to the equivalent magnetic noise induced by the mechanical noise source at the resonance frequency.

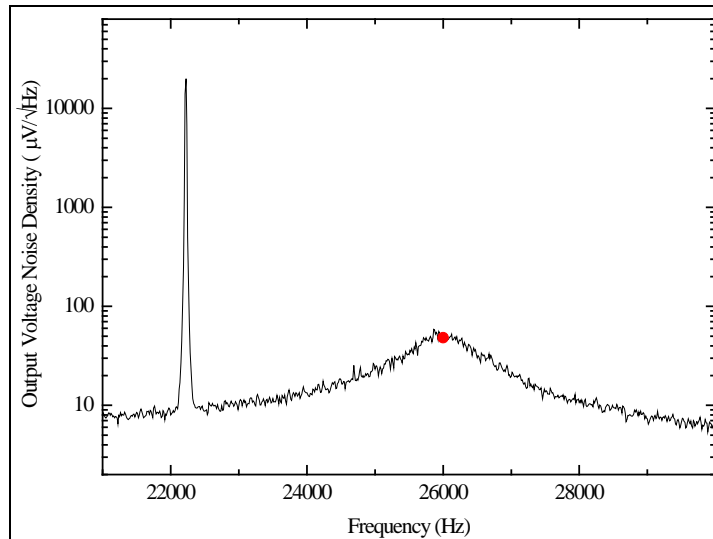


Figure 74. Zoom around the resonance of the output voltage noise level for the F22 laminate.

The red point corresponds to the equivalent magnetic noise induced by the mechanical noise source at the resonance frequency (cf. theoretical model).

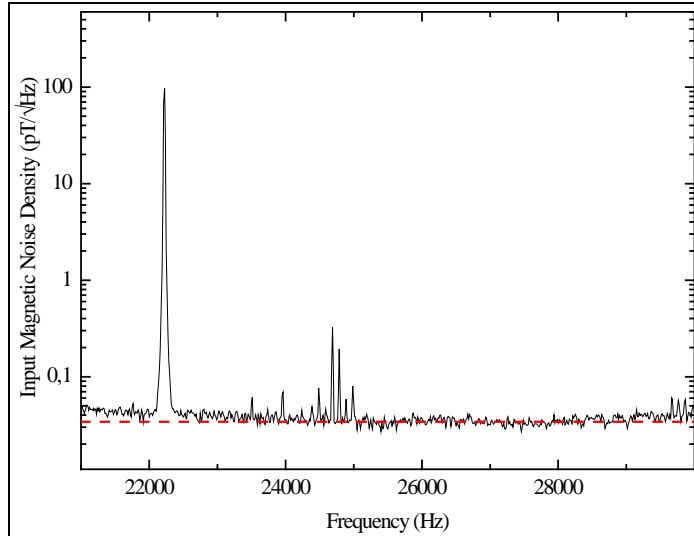


Figure 75. Zoom around the resonance of the equivalent input magnetic noise level for the F22 laminate.

The dashed red line corresponds to the equivalent magnetic noise induced by the mechanical noise source (cf. theoretical model).

Notice the simulation noise curves fit very well with the experiments noise curves for both the output voltage noise and the equivalent magnetic noise.

B.3.3. Magnetometer development

We have developed magnetometers and implemented an efficient feed-back system as given in Figure 76.

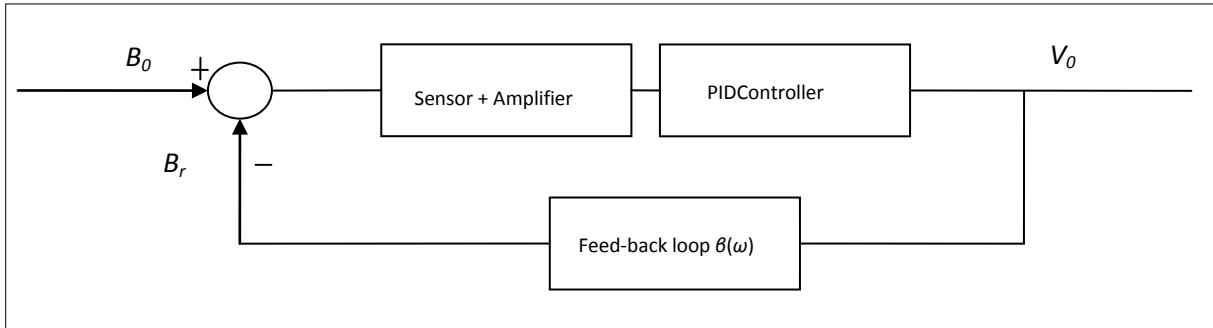


Figure 76. View of the feedback loop design.

We define the transfer function in open loop as

$$T_{r_open}(j\omega) = \frac{\alpha_{ME}^{\varphi}(j\omega)}{C_1} \frac{jR_1 C_1 \omega}{1 + jR_1 C_1 \omega} C_{PID}(j\omega) \quad (218)$$

It leads to a closed loop transfer function given by

$$T_{r_cl}(j\omega) = \frac{T_{r_open}(j\omega)}{1 + T_{r_open}(j\omega)\beta(j\omega)} \quad (219)$$

where $\beta(j\omega) \left(\approx \frac{\mu_0 N}{2(R + R_{coil})\sqrt{a^2 + r^2}} \approx \frac{\mu_0 N}{2aR} \right)$ is the feed-back coil transfer in (T/V) with a (half coil radius) $\gg r$ (coil length) & $R \gg R_{coil}$. The closed loop transfer function could be simplified as

$$T_{r_cl}(j\omega) = \frac{\frac{\alpha_{ME}^o(j\omega)}{C_1} jR_1 C_1 \omega C_{PID}(j\omega)}{1 + jR_1 C_1 \omega + \frac{\alpha_{ME}^o(j\omega)}{C_1} jR_1 C_1 \omega C_{PID}(j\omega) \frac{\mu_0 N}{2(R + R_{coil})\sqrt{a^2 + r^2}}} \approx \frac{2aR}{\mu_0 N} [\text{V/T}] \quad (220)$$

The measured open and the closed-loop transfer functions and phase behavior are given in Figures 77 and 78, as example.

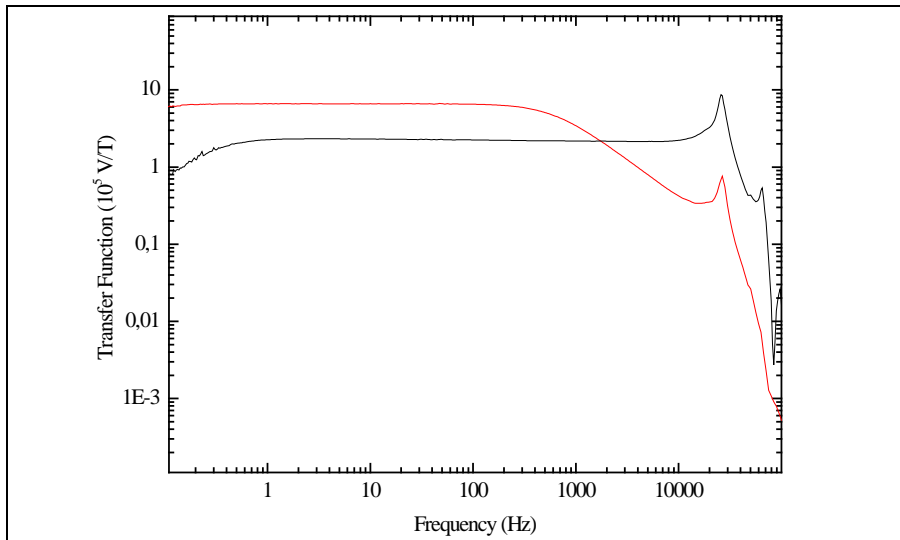


Figure 77. Magnetic field transfer function of sensor F20 and GREYC classical electronics (Black) without feedback system, (Red) with feedback system.

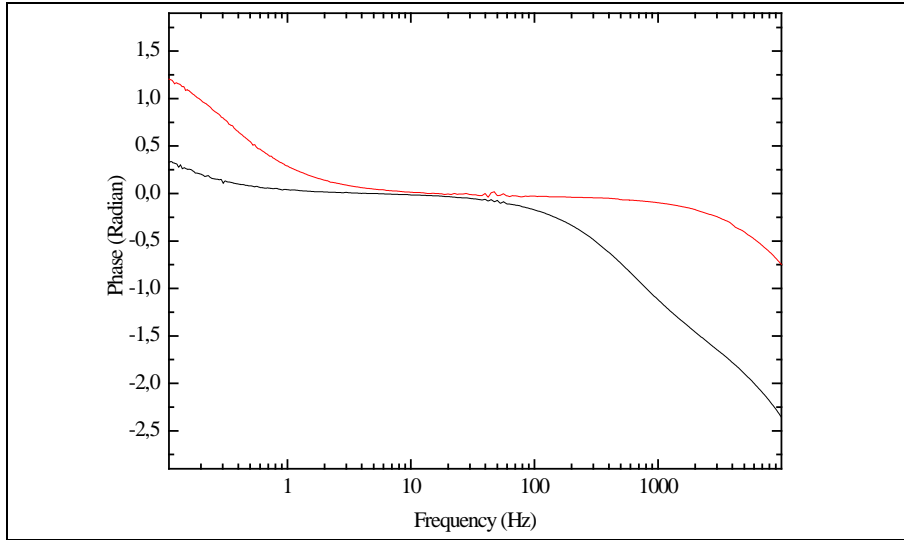


Figure 78. Phase of sensor F20 and GREYC classical electronics (Black) without feedback system, (Red) with feedback system.

Angular response.

We have tested the angular response of the magnetometer versus a magnetic dipole moment as presented in Figure 79.

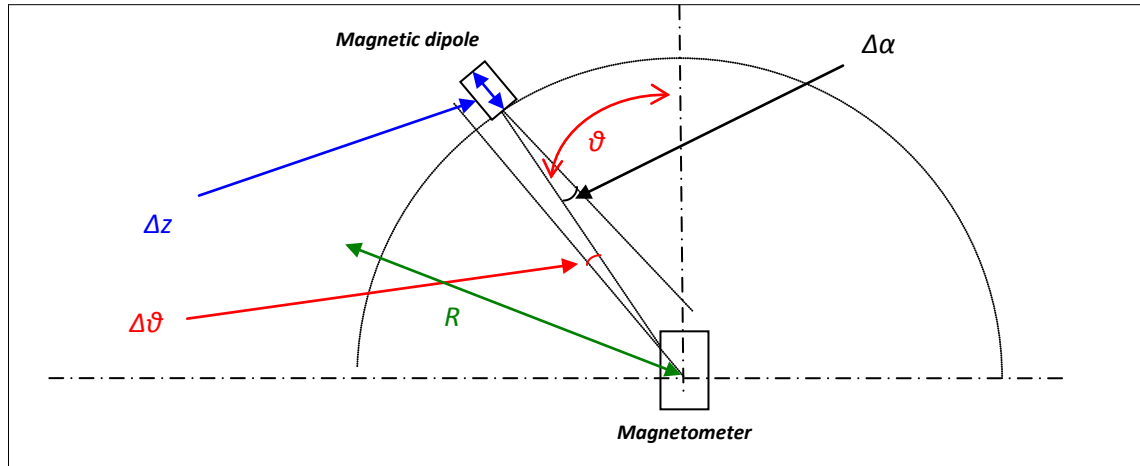


Figure 79. Experimental set-up with the magnetometer and dipole moment used as a magnetic source.

All given angles help to give the accuracy of the measurement..

The response of the magnetometer versus a magnetic dipole moment is given in Figure 80. We observe a good agreement with the theory. In the next subsection, we shall analyze the effect of the angle uncertainties on the response. We are able to evaluate the magnetic field sensed by the magnetometer as

$$B = \frac{\mu_0 m}{2\pi z^3} \cos(\theta) \cos(\alpha) \quad (221)$$

where m is the amplitude of the dipole (A.m^2). So, the total error on the sensed magnetic field, B , is given by

$$\begin{aligned} \varepsilon_B &= \frac{\partial B}{\partial \alpha} \cdot [\Delta \alpha] + \frac{\partial B}{\partial \theta} \cdot [\Delta \theta] + \frac{\partial B}{\partial z} \cdot [\Delta z] \\ \varepsilon_B &= -\sin(\alpha) \cos(\theta) \frac{\mu_0 m}{2\pi z^3} \cdot [\Delta \alpha] \\ &\quad -\cos(\alpha) \sin(\theta) \frac{\mu_0 m}{2\pi z^3} \cdot [\Delta \theta] \\ &\quad -\cos(\alpha) \cos(\theta) \frac{3\mu_0 m}{2\pi z^4} \cdot [\Delta z] \end{aligned} \quad (222)$$

where $\Delta\alpha$, $\Delta\theta$, Δz are the uncertainties associated to the angles (of the magnetometer, magnetic dipole moment) and on the radius, respectively. We define the interval errors as $\Delta\alpha \in [-5^\circ, 5^\circ]$, $\Delta\theta \in [-5^\circ, 5^\circ]$ and $\Delta z \in [-2 \text{ cm}, 2 \text{ cm}]$. The associated error limits are plotted in Figure 80 (red dots).

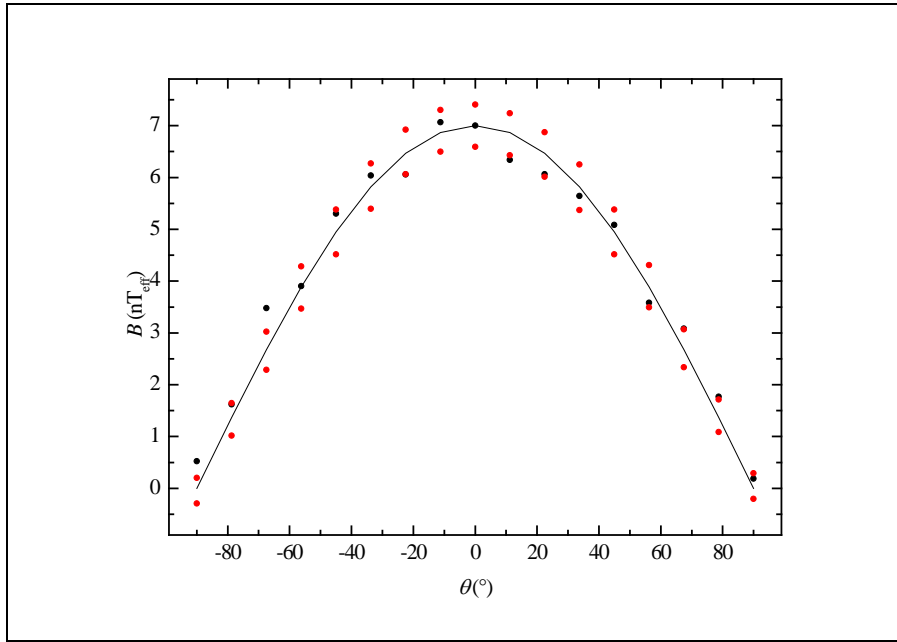


Figure 80. Black dots, red dots and line give the experimental measurement, measurement uncertainties, for the given interval errors $\Delta\alpha \in [-5^\circ, 5^\circ]$, $\Delta\theta \in [-5^\circ, 5^\circ]$, $\Delta z \in [-2 \text{ cm}, 2 \text{ cm}]$, and the theoretical response of the magnetometer, respectively.

The radius R is 1 m and the applied field frequency is 2 Hz.

B.3.4. Gradiometer development

We have analyzed and compared the gradiometer performances to a fluxgate (*cf.* Figure 81). The equivalent input magnetic noise is given in Figure 82 for each sensor outputs (V_1 to V_4 .)

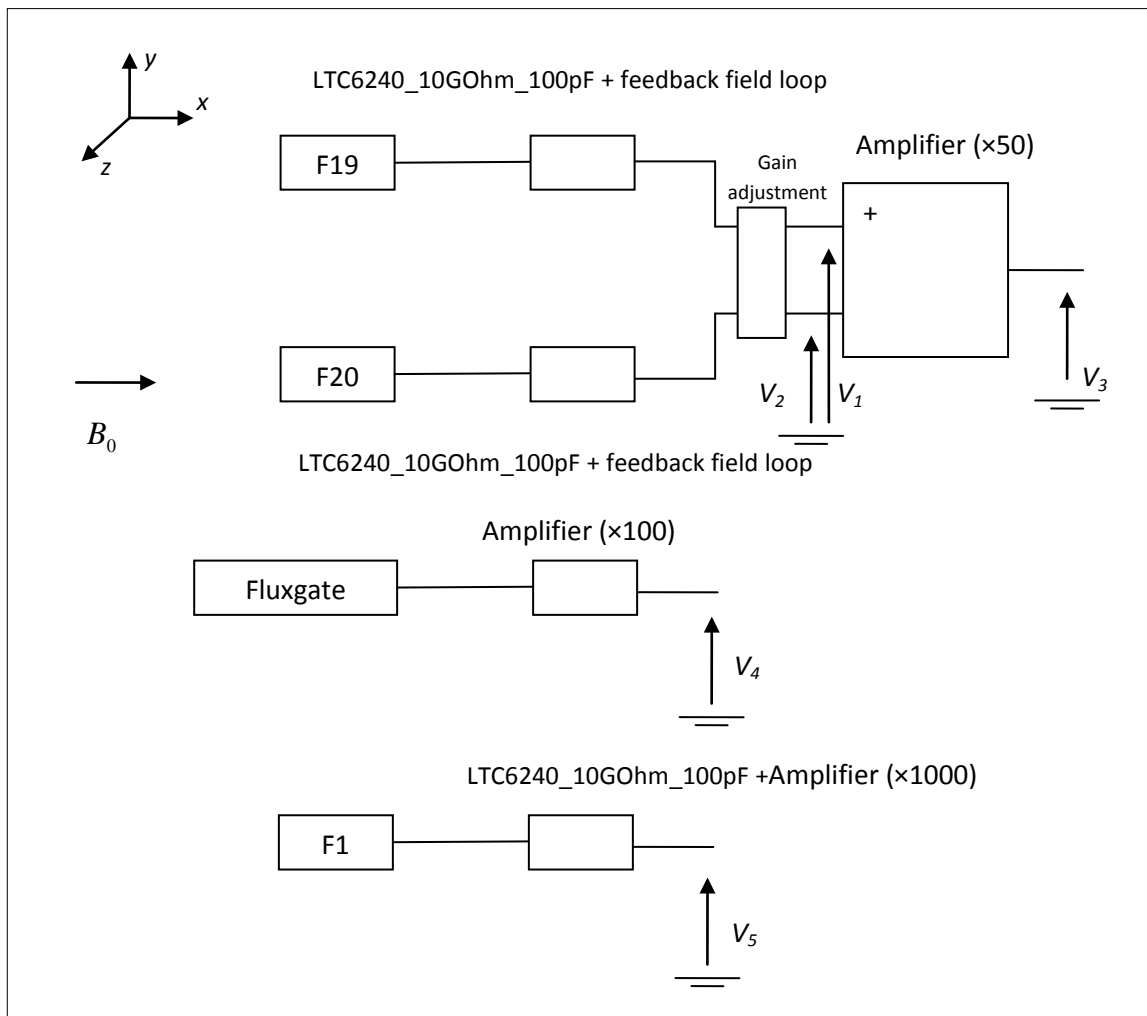


Figure 81. Experimental set-up.

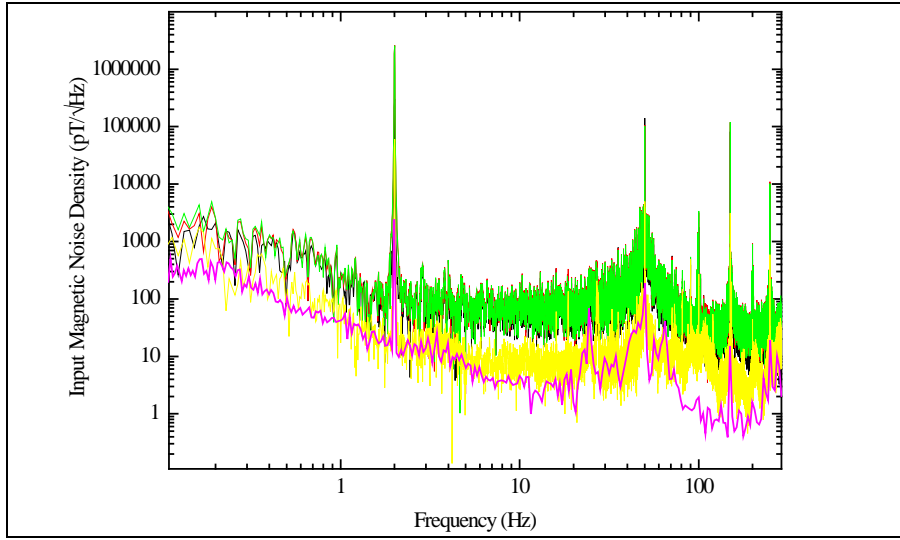


Figure 82. Equivalent input magnetic noise of V_1 , V_2 , V_3 , V_4 (red, green, yellow and black curves respectively).

The pink curve is the intrinsic magnetic noise of F19 or F20 sensor (with LTC6240).

Based on the set-up, we have measured the spatial transfer function of the magnetometer. The benchmark, CMMR and transfer function are given in Figure 83, Figure 84 and Figure 85. The used base line is 20 cm and the magnetic moment is $4.2 \text{ mA}_{\text{peak}} \cdot \text{m}^2$ at 2 Hz for $z < 10 \text{ cm}$ and is $21 \text{ mA}_{\text{peak}} \cdot \text{m}^2$ at 2 Hz for $z > 10 \text{ cm}$.

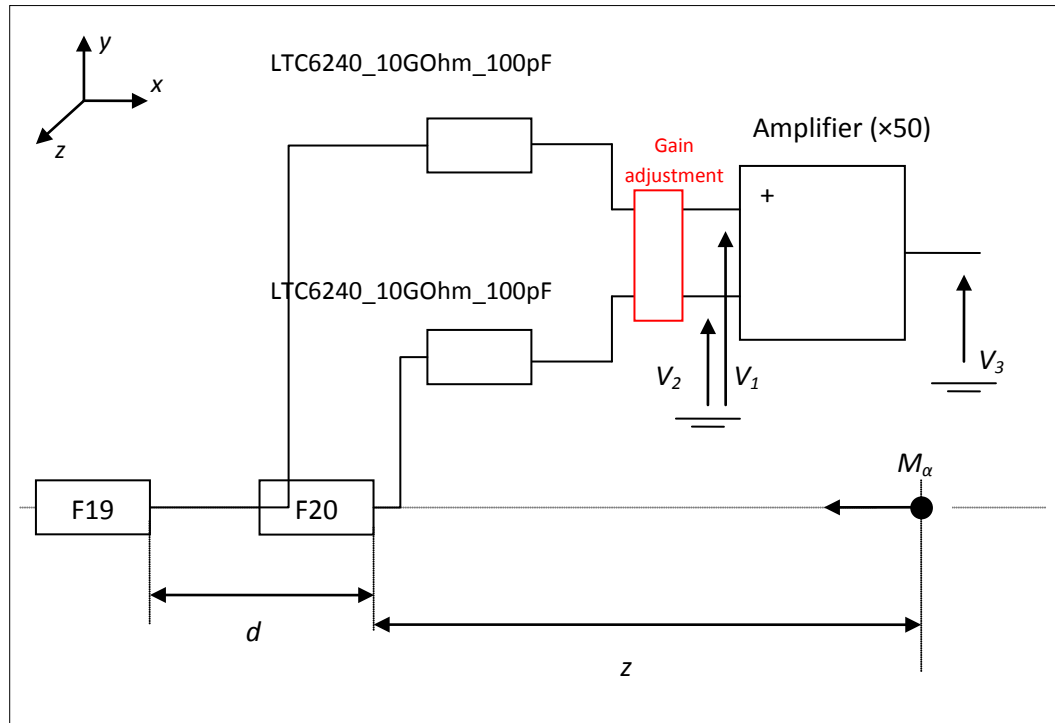


Figure 83. Set-up (d is the gradiometer base line and z the distance between the sensors to the magnetic moment).

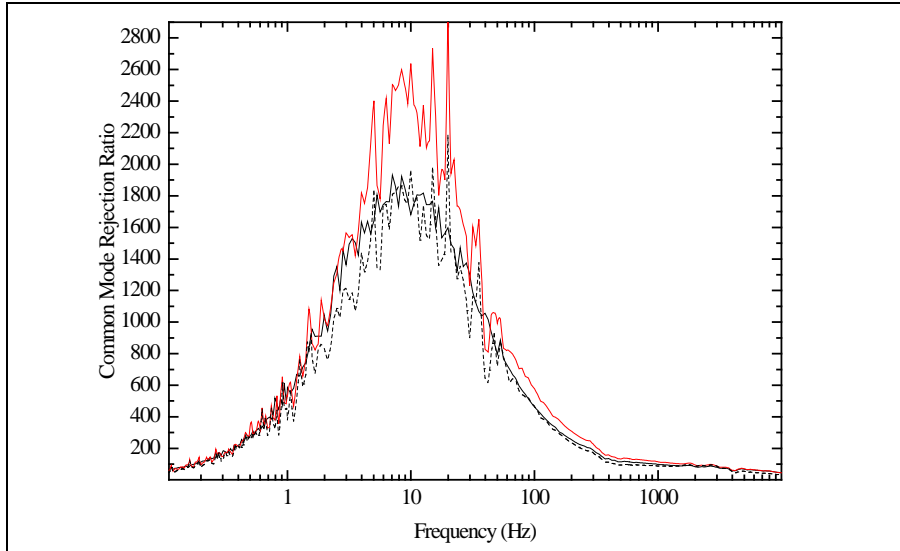


Figure 84.Theoretical (black curve) and experimental (red curve) CMRR evaluation corresponding to the measurement a) and b) given in figures 15 and 16, respectively.

Dashed black line corresponds to the simplified CMRR model.

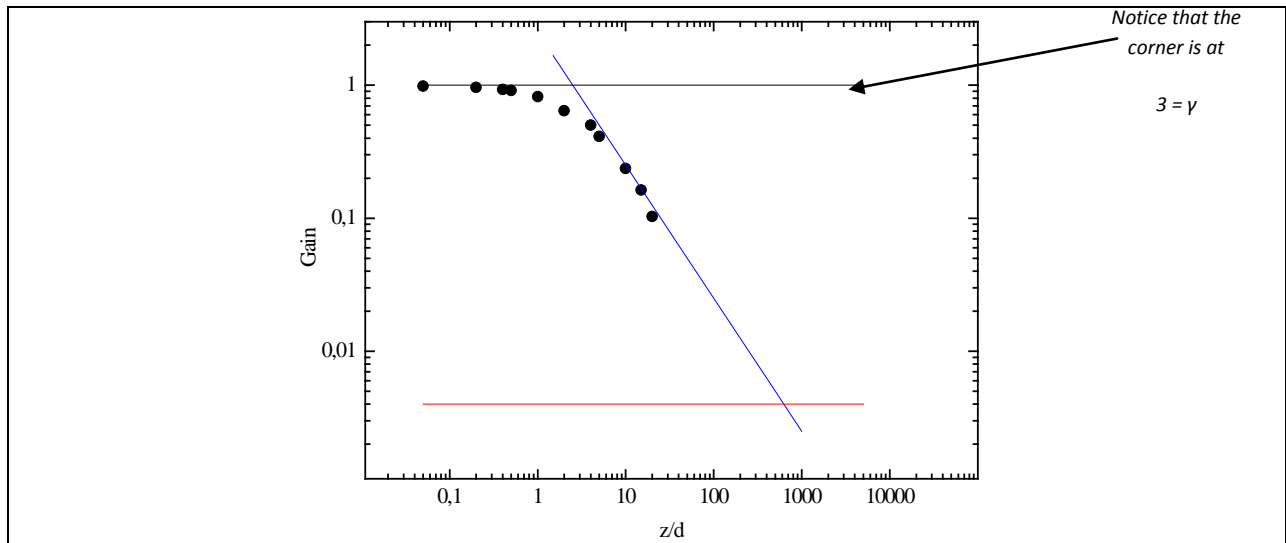


Figure 85. Spatial transfer function of the gradiometer V_3/V_2 in Log-Log scale. z and d are the distance of the source to the gradiometer and gradiometer base-line, respectively.

In Log-Log scale figure, the blue line indicates the well gradiometer behavior slope as $\text{d}Bx/\text{d}x$ and the red line give the theoretical limit of this slope with a CMRR of 250 (cf. §.III). Therefore, we are able to measure the effective gradient of a far field, in the given set-up, for $z > 2 \text{ m}$ ($z/d = 10$), experimentally, to $z < 200 \text{ m}$ ($z/d = 1000$), theoretically.

Theoretical description.

In this subsection, the transfer function of the gradiometer is evaluated with the help of the sensed magnetic field

$$B = \frac{\mu_0}{2\pi} \frac{m}{z^3} \quad (223)$$

where m and \mathbf{z} are the magnetic dipole moment and the distance from the first magnetometer to the magnetic source, respectively. So, the sensed field is given by

$$B_1 = \frac{\mu_0}{2\pi} \frac{m}{z_1^3} \quad (224)$$

And

$$B_2 = \frac{\mu_0}{2\pi} \frac{m}{z_2^3} \quad (225)$$

for the first and second magnetometer, with $z_2 = z_1 + d$. The two magnetometer transfer functions T_{r_1} and T_{r_2} enable us to evaluate the gradiometer transfer function, $\vec{\Delta} = \vec{T}_{r_1} - \vec{T}_{r_2}$.

We have analyzed two cases.

Case 1 - There is no tilt between the both magnetometers.

$$V_1 = \vec{B}_1 \cdot \vec{T}_{r_1} = \frac{\mu_0}{2\pi} \frac{\vec{m}}{z_1^3} \cdot \vec{T}_{r_1} = \frac{\mu_0}{2\pi} \frac{\vec{m}}{z_1^3} \cdot \left(\vec{T}_{r_2} + \vec{\Delta} \right) \text{ and } V_2 = \vec{B}_2 \cdot \vec{T}_{r_2} = \frac{\mu_0}{2\pi} \frac{\vec{m}}{z_2^3} \cdot \vec{T}_{r_2}, \quad (226)$$

The gradiometer output is given by

$$V_3 = \frac{\mu_0}{2\pi} \frac{\vec{m}}{z_1^3} \cdot \left(\frac{1}{z_1^3} \left(\vec{T}_{r_2} + \vec{\Delta} \right) - \frac{1}{(z_1 + d)^3} \vec{T}_{r_2} \right) = \frac{\mu_0}{2\pi} \frac{\vec{m}}{z_1^3} \cdot \left[\left(\frac{1}{z_1^3} - \frac{1}{(z_1 + d)^3} \right) \vec{T}_{r_2} + \frac{\vec{\Delta}}{z_1^3} \right] \quad (227)$$

It yields to the spatial transfer function

$$\left| \frac{\vec{V}_3}{\vec{V}_1} \right| = \left| \frac{\frac{\mu m}{2\pi} \left[\left(\frac{1}{z_1^3} - \frac{1}{(z_1 + d)^3} \right) \vec{T}_{r_2} + \frac{\vec{\Delta}}{z_1^3} \right]}{\frac{\mu m}{2\pi} \frac{1}{z_1^3} \vec{T}_{r_1}} \right| \quad (228)$$

Notice that, if $z_1 \gg d$, the transfer function is

$$\left| \frac{\vec{V}_3}{\vec{V}_1} \right| = \left| \frac{\left(1 - \frac{z_1^3}{(z_1 + d)^3} \right) + \frac{\vec{\Delta}}{\vec{T}_{r_2}}}{1 + \frac{\vec{\Delta}}{\vec{T}_{r_2}}} \right| = \left| \frac{\frac{\vec{\Delta}}{\vec{T}_{r_2}}}{1 + \frac{\vec{\Delta}}{\vec{T}_{r_2}}} \right| \approx \left| \frac{\vec{\Delta}}{\vec{T}_{r_2}} \right| \approx \left| \frac{\vec{\Delta}}{\vec{T}_{r_1}} \right| = \frac{1}{CMRR} \quad (229)$$

and, if $z_1 \ll d$,

$$\left| \frac{\vec{V}_3}{\vec{V}_1} \right| \approx \left| \frac{1 + \frac{\vec{\Delta}}{\vec{T}_{r_2}}}{1 + \frac{\vec{\Delta}}{\vec{T}_{r_2}}} \right| = 1, \quad (230)$$

respectively.

Case 2 - There is a small tilt, θ , between the two magnetometers

Similarly,

$$V_1 = \vec{B}_1 \cdot \vec{T}_{r_1} = \frac{\mu}{2\pi} \frac{\vec{m}}{z_1^3} \cdot \vec{T}_{r_1} = \frac{\mu}{2\pi} \frac{\vec{m}}{z_1^3} \cdot \left(\vec{T}_{r_2} + \vec{\Delta} \right) \text{ and } V_2 = \vec{B}_2 \cdot \vec{T}_{r_2} = \frac{\mu}{2\pi} \frac{\vec{m}}{z_2^3} \cdot \vec{T}_{r_2} \cos(\theta), \quad (231)$$

The gradiometer output is given by

$$V_3 = \frac{\mu m}{2\pi} \left(\frac{1}{z_1^3} \left(\vec{T}_{r_2} + \vec{\Delta} \right) - \frac{1}{(z_1 + d)^3} \cos(\theta) \vec{T}_{r_2} \right) = \frac{\mu m}{2\pi} \left[\left(\frac{1}{z_1^3} - \frac{1}{(z_1 + d)^3} \cos(\theta) \right) \vec{T}_{r_2} + \frac{\vec{\Delta}}{z_1^3} \right] \quad (232)$$

It yields to the spatial transfer function

$$\left| \frac{\vec{V}_3}{\vec{V}_1} \right| = \left| \frac{\frac{\mu m}{2\pi} \left[\left(\frac{1}{z^3} - \frac{1}{(z + d)^3} \cos(\theta) \right) \vec{T}_{r_2} + \frac{\vec{\Delta}}{z^3} \right]}{\frac{\mu m}{2\pi} \frac{1}{z_1^3} \vec{T}_{r_1}} \right| = \boxed{\left| \frac{\left(1 - \frac{z_1^3}{(z_1 + d)^3} \cos(\theta) \right) + \frac{\vec{\Delta}}{\vec{T}_{r_2}}}{1 + \frac{\vec{\Delta}}{\vec{T}_{r_2}}} \right|} \quad (233)$$

Notice that, if $z_l \gg d$ and $\theta > 0^\circ$, the transfer function is

$$\left| \frac{\vec{V}_3}{\vec{V}_1} \right| = \left| \frac{\left(1 - \frac{z_l^3}{(z_l + d)^3} \cos(\theta) \right) + \frac{\vec{\Delta}}{\vec{T}_{r_2}}}{1 + \frac{\vec{\Delta}}{\vec{T}_{r_2}}} \right| \approx \left| \frac{\vec{\Delta}}{\vec{T}_{r_1} \cos(\theta)} \right| = \frac{1}{CMRR} \frac{1}{\cos(\theta)} \quad (234)$$

and, if $z_l \ll d$ and $\theta > 0^\circ$,

$$\left| \frac{\vec{V}_3}{\vec{V}_1} \right| = \left| \frac{\left(1 - \frac{z_l^3}{(z_l + d)^3} \cos(\theta) \right) + \frac{\vec{\Delta}}{\vec{T}_{r_2}}}{1 + \frac{\vec{\Delta}}{\vec{T}_{r_2}}} \right| \approx \left| \frac{1 + \frac{\vec{\Delta}}{\vec{T}_{r_2}}}{1 + \frac{\vec{\Delta}}{\vec{T}_{r_2}}} \right| = 1, \quad (235)$$

respectively.

Effect of the tilt on the spatial transfer function.

We present in Figure 86 the spatial transfer functions of the gradiometer versus a tilt of one of the two magnetometers. Results fit well with the theory and help to give the ultimate sensor performances.

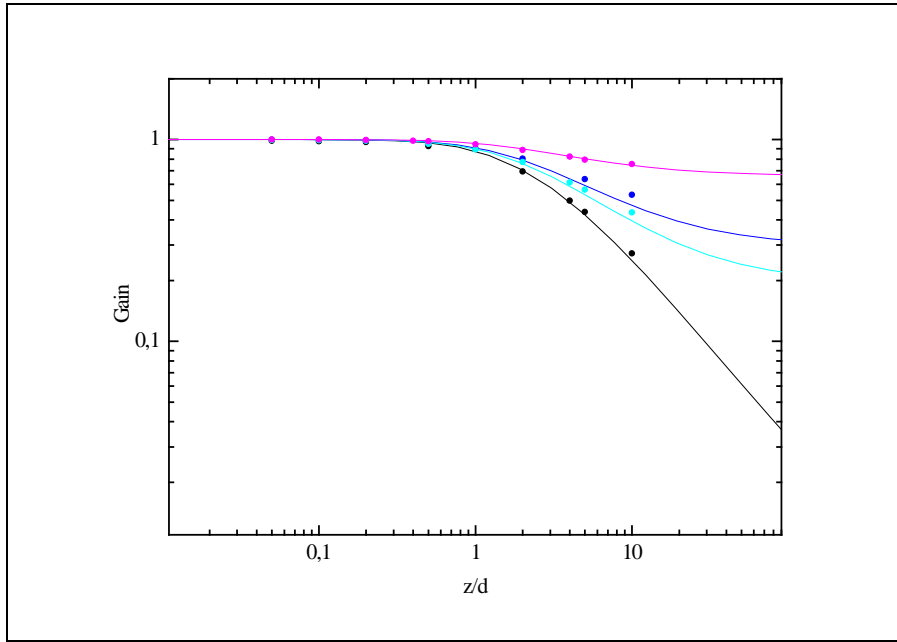


Figure 86. Effect of the tilt between the two magnetometers on the spatial transfer function of the gradiometer.

The dots and curves give the experimental and theoretical, V_3/V_I ratio values versus z/d for different tilts. The angles vary from 0° , 36° , 45° et 70° (black, blue-green, blue, purple).

B.3.5. Magnetic source localization

Based on the previous set-up, we have analyzed the source localization versus gradiometer performances. A sketch view is given in Figure 87.

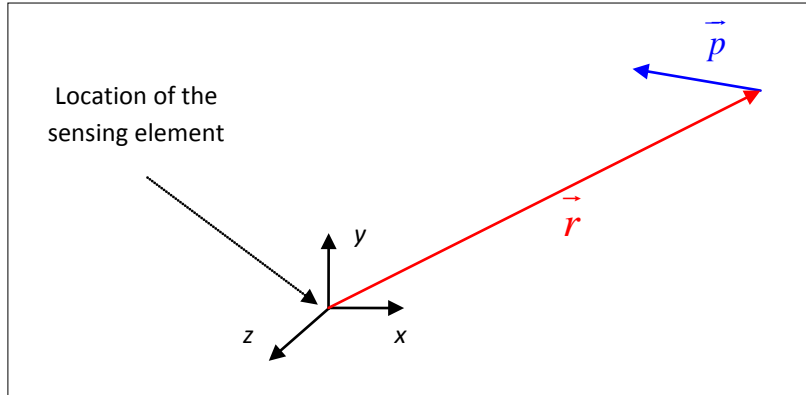


Figure 87. Sketch view of a source localization. \vec{r} and \vec{p} are the 3D spatial position and orientation of the magnetic moment, respectively.

In this subsection, magnetic dipole, \vec{p} , localization and orientation are evaluated as the function of the gradiometer performances. The sensed magnetic field, \vec{B} , induced by the magnetic moment is given by

$$\vec{B} = \frac{\mu_0}{4\pi} \text{Curl} \left(\frac{(\vec{p} \times \vec{r}) - \vec{s}}{|\vec{r} - \vec{s}|^3} \right) = \frac{\mu_0}{4\pi} \frac{3(\vec{p} \cdot \vec{n})\vec{n} - \vec{p}}{r^3} \quad (236)$$

where \vec{r} is the 3D spatial position of the magnetic moment and \vec{s} is the position where sensing element is placed. Let us consider the field, \vec{B}' , at the point $\vec{n}dr$. We can easily write

$$\vec{B}' = \frac{\mu_0}{4\pi} \frac{3(\vec{p} \cdot \vec{n})\vec{n} - \vec{p}}{(r + dr)^3}. \quad (237)$$

It yields to

$$\overline{\Delta B} = \vec{B} - \vec{B}' = \frac{\mu_0}{4\pi} \left(3(\vec{p} \cdot \vec{n})\vec{n} - \vec{p} \right) \left(\frac{\partial}{\partial r} \frac{1}{r^3} dr \right) = -\frac{3}{r} \vec{B} dr. \quad (238)$$

Also, the difference of the vectors can be written using the gradient of the magnetic fields as

$$\overrightarrow{\Delta B} = \overrightarrow{B} - \overrightarrow{B}' = \begin{pmatrix} \frac{\partial B_x}{\partial x} & \frac{\partial B_y}{\partial x} & \frac{\partial B_z}{\partial x} \\ \frac{\partial B_x}{\partial y} & \frac{\partial B_y}{\partial y} & \frac{\partial B_z}{\partial y} \\ \frac{\partial B_x}{\partial z} & \frac{\partial B_y}{\partial z} & \frac{\partial B_z}{\partial z} \end{pmatrix} \vec{n} dr = G \vec{n} dr = -\frac{3}{r} \vec{B} dr . \quad (239)$$

So, the position \vec{r} could be evaluated by

$$\vec{n} r = \vec{r} = -3G^{-1} \vec{B} = -3G^{-1} \begin{Bmatrix} B_x \\ B_y \\ B_z \end{Bmatrix}. \quad (240)$$

With $x, y, z > 0$, we are able to evaluate the uncertainty of the sensor position in 2D considering the gradiometer performances, as an example. The calculation yields to the evaluation of the position $\vec{\tilde{r}}$ as

$$\vec{\tilde{r}} = \begin{Bmatrix} \tilde{x}_i \\ \tilde{y}_i \\ \tilde{z}_i \end{Bmatrix} \approx 3 \left\{ \begin{array}{l} \frac{-\left(B_{yx}^2 - B_{xx}B_{yy}\right)\left(B_{yx}B_y - B_{yy}B_x\right) - \left(B_{yx}^2 - B_{xx}B_{yy}\right)\left(B_{yx} - B_{yy}\right)b_n + \left(B_{yx} - B_{yy}\right)\left(-B_yB_{xx} + (B_x + B_y)B_{yx} - B_xB_{yy}\right)b_{n_grad}}{\left(B_{yx}^2 - B_{xx}B_{yy}\right)^2} \\ \frac{-\left(B_{xx}B_{yy} - B_{yx}^2\right)\left(B_{xx}B_y - B_{yx}B_x\right) - \left(B_{xx}B_{yy} - B_{yx}^2\right)\left(B_{xx} - B_{yx}\right)b_n + \left(B_{xx} - B_{yx}\right)\left(B_yB_{xx} - (B_x + B_y)B_{yx} + B_xB_{yy}\right)b_{n_grad}}{\left(B_{yx}^2 - B_{xx}B_{yy}\right)^2} \\ 0 \end{array} \right\} \quad (241)$$

where $B_{ij} = \frac{\partial B_i}{\partial j}$ are the components of the gradient matrix, B_i are the sensed field and b_n (T/\sqrt{Hz}) and b_{n_grad} ($(T/m)/\sqrt{Hz}$) are the magnetic noise and the gradient magnetic noise associated to the set-up measurement. This analysis is exemplified in Figure 88 for the localization of a magnetic moment at 2 Hz with ME sensing elements. The green circle gives the uncertainty of the source location versus the magnetic sensor noise and the magnetic noise gradient. The blue, green, and red arrows indicate the reference magnetic moment, the solution obtained by using the equation above and the averaged solution. The amplitude of the magnetic moment is obtained by solving the equation.

$$\tilde{\tilde{\mu}} = \begin{Bmatrix} \mu_x \\ \mu_y \end{Bmatrix} \approx \frac{4\pi}{\mu_0} \begin{pmatrix} \left(2\tilde{x}_i^2 - \tilde{y}_i^2\right) & \left(3\tilde{x}_i \tilde{y}_i\right) \\ \left(\tilde{x}_i^2 + \tilde{y}_i^2\right)^{\frac{5}{2}} & \left(\tilde{x}_i^2 + \tilde{y}_i^2\right)^{\frac{5}{2}} \\ \left(3\tilde{x}_i \tilde{y}_i\right) & \left(2\tilde{y}_i^2 - \tilde{x}_i^2\right) \\ \left(\tilde{x}_i^2 + \tilde{y}_i^2\right)^{\frac{5}{2}} & \left(\tilde{x}_i^2 + \tilde{y}_i^2\right)^{\frac{5}{2}} \end{pmatrix}^{-1} \begin{Bmatrix} B_x + b_n \\ B_y + b_n \end{Bmatrix}. \quad (242)$$

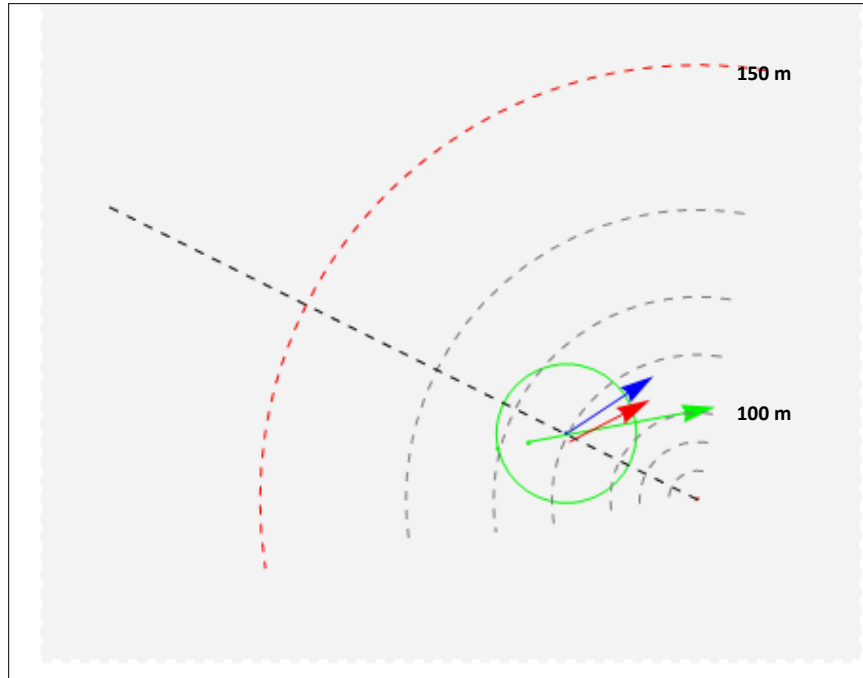


Figure 88. Example of a source localization in 2D versus sensor performances.

The green circle gives the uncertainty of the source location versus the magnetic sensor noise and the magnetic noise gradient. The blue, green, and red arrows indicate the reference magnetic moment, the solution obtained by matrix inverse method and the averaged solution.

C. Keith McLaughlin, SAIC

C.3.1. Applications and System Concepts.

Under this task SAIC worked with Virginia Tech staff to design and analyze data collections that demonstrate the HUMS Phase 1 ME sensor. Demonstrations included the localization of AC dipoles with an array of 3-component ME sensors. Presentations were made at reviews and a paper was presented at the November 2011 Material Research Society meeting in Boston.

C.3.2. Array Design.

Under this task SAIC worked with Virginia Tech staff to explore design considerations for ME sensor arrays. The first deliverable under this task was delivered in 2010, “Phase 1 Array Design Objectives”.

A key array design consideration is the interaction of closely spaced ME sensors. Flux shared by two or more sensors constitutes a mutual inductance that may either increase or decrease sensor sensitivity (ME coefficient). SAIC and Virginia Tech staff conducted simulations and measurements to derive a set of useful design strategies for arrangement of ME sensors.

Simulations and a theoretical treatment are reported in the SAIC monthly reports.

The second deliverable under this task, “Phase 2 Array Design Objectives,” is satisfied by the following discussion derived from a presentation to the Materials Research Society in 2011, “ME Sensor Self-Noise, Power, and Volume Trade-Space”.

C.3.2.1. Overview

Passive magneto-electric (ME) sensors (constructed from piezoelectric-magnetostrictive heterostructures) occupy a unique and advantageous region of the self-noise versus power versus size/volume magnetic sensor trade-space. We compare ME sensors in this trade-space with a survey of available technologies. The passive piezoelectric-magnetostrictive heterostructure transduces magnetic energy into electrical energy and therefore only the readout electronics consumes energy. At low frequencies (< 10 Hz) the passive ME sensor self-noise is generally limited by a combination of the $1/f$ noise of the charge amplifier, the $1/f$ noise of leakage resistance, and the $1/\sqrt{f}$ noise of the intrinsic loss of the piezoelectric material. At high frequencies (> 100 Hz), the passive ME sensor self-noise is limited by the equivalent input white-noise of the charge amplifier. The low-noise versus power envelope of the trade-space is therefore determined by the readout electronics noise trade with power. If the battery volume for a fixed lifetime is included in the sensor volume budget, then the electronics noise versus power trade establishes the self-noise versus volume trade-space. A sensor designer can optimize the size, weight, power and cost of the sensor in this trade-space. We discuss low-power, long-life sensing applications for which passive ME sensors are well positioned as well as packaging and integration considerations that may be unique to ME sensors.

C.3.2.2. ME Technology Trade-Space

Magneto-electric sensors transduce magnetic energy to mechanical strain energy to electrical energy through a magnetostrictive material mechanically coupled to a piezoelectric material. A charge or voltage amplifier outputs an analog voltage that is recorded using standard recording devices. Only the readout electronics consumes energy. Figure 89 shows the trade space of ME sensors in the context of commercial magnetic sensors. Table 20 lists a range of performance characteristics for three classes of laminate ME sensors that occupy a unique noise-volume-

power trade space. Sensor self-noise depends upon three factors; 1) the volume of the magnetostrictive and piezoelectric materials, 2) the quality of the transduction materials, and 3) the design and power draw of the readout electronics. Therefore incremental decreases in sensor self-noise are therefore attained with incremental increases in volume, power, and/or cost. We divide the sensors and readout electronics into three categories. In the first category, inexpensive materials are assembled into small laminates with ultra-low-power charge amplifiers (0.1-1 mW). When we include the power and volume required by the readout electronics, this class of ME laminate sensors may be made as small as 1 cm wide by 1 cm long by <0.1 cm thick and are competitive with commercial magnetoresistive sensors in size and power. As the sensors are lengthened from 1 to 10 cm long and the charge amplifier power increased, the self-noise is reduced to levels comparable with commercial fluxgate sensors at a fraction of the power consumption. With added volume further decreases in self-noise may be achieved; 4-8 laminates may be wired in parallel (stacked configurations) and flux concentrators may be added. However, these sensors are ultimately limited by quality factor of the inexpensive piezoelectric materials and stacking efficiency is limited by the proximity of the stacked laminates (> 1 cm separation required to reduce their mutual negative inductance). Finally, by substituting higher quality single crystal piezoelectrics, stacking the outputs of multiple charge amplifiers, and adding flux concentrators, noise levels below 1 pT/rtHz at 1 Hz may theoretically be attained. The power requirements and volumes of these devices would still make them competitive with increased cost of materials. This represents the primary challenge to materials science to manufacture high-Q piezoelectric crystals with a suitable form factor at low cost.

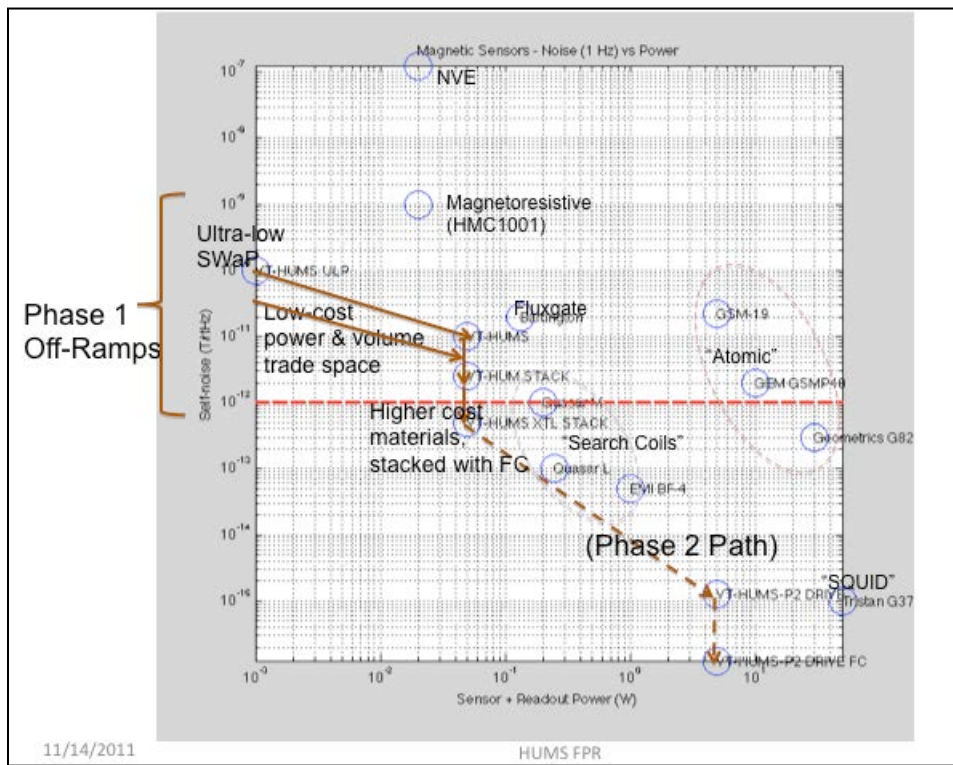


Figure 89. Phase 1 ME sensors in the context of available Commercial Off The Shelf (COTS) magnetic sensors.

ME sensors lie along a trade-space line of noise vs power where sensors and charge amplifiers may be stacked in parallel and charge amplifiers may be low-power and noisy or high-power and quiet.

Table 20. Three Passive ME Sensor Classes.

Sensor	Volume / Size	Power	Noise @1 Hz	Unit Cost	Comment
Ultra-low power, size, & cost with noise comparable to mag-resistive	1 – 2 (CC)/ 1-10 (cm)	0.1-1 mW	30-1000 pT/rtHz	Materials: \$10-20	Noise floor trades through electronics power (.1-1 mW) & sensor size (1-10 cm). No stacking.
Low power, size & cost with noise comparable to fluxgate	2-200 (CC)/ 10-20 (cm)	1-200 mW	6-30 pT/rtHz	Materials: \$10-50	Noise floors limited by Q of piezo, stacking efficiency and trades between electronics power and noise.
Small size, with noise better than fluxgate	200-1000 (CC)/ 10-50 (cm)	200 mW	0.5-1 pT/rtHz	Materials: \$250-\$1000	Noise floor limited by high-Q piezo material, stacked ultra-low-noise electronics, flux concentrator

•ME sensors favor "gum-stick" form-factors (e.g. 10 x 1 x 0.1 cm)
 •Stacked sensors should be offset by ~1cm to minimize mutual inductance
 •Arrays or gradiometers may be constructed from all classes of sensors.

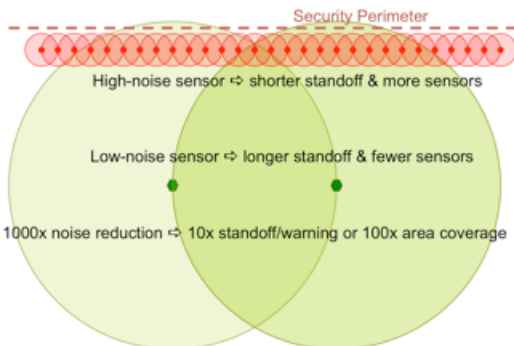
C.3.2.3. Potential Applications

As we highlighted above, the primary advantage of passive ME laminate sensors is their small size, low power, and low material cost for comparatively low self-noise. They represent a disruptive technology because battery volume dominates the size, volume, cost and logistics of a mass-produced autonomous long-life persistent magnetic sensor. ME sensor technology significantly reduces required battery volume to support a persistent sensor for a 1-2 year lifetime. We highlight an application area that may exploit the potential for small, low-cost persistent sensors.

C.3.2.4. Persistent Perimeter Monitoring

Error! Reference source not found. illustrates the concept of perimeter monitoring. Sensors are spaced approximately twice the distance of detecting an intruder at an X probability. Therefore the probability of detection will be greater than $2X-X^2$ that one or more sensors detect the intruder. One or more lines of detectors may be utilized for added security in depth; increase probability of detection and lower false alarms on the perimeter. Regardless of the spacing required for a given level of security, the cost is linear in the length of perimeter and unit cost per sensor. For a long-life sensor, the size and weight is ultimately determined by the battery and hence the power of the sensing unit. We consider a 1 km perimeter with magnetoresistive, fluxgate, and ME sensors monitored by an ultra-low power microcontroller and mesh radio (~ 3 mW) and a fixed battery energy density (1300 Amp-hr/Liter). Detection range scales inversely with sensor noise. While the fluxgate sensors have a longer detection range the ME sensors have the final advantage in lower unit cost and power consumption (smaller battery).

Persistent and ubiquitous wide-area & perimeter ISR



- Sensitive, low SWaP and low cost sensors enable new approaches to monitor large areas for the military & DHS.
- Short detection range of low-SWaP sensors or cost of low-noise sensors has made persistent and ubiquitous monitoring uneconomical.

1000 m perimeter with 3 lines of 3-axis sensors for 2 yr lifetime:

Sensor Type	Detection Range (m)	# Sensors	Unit Cost *	Total Cost (\$)	Unit Sensor Volume ** (CC)
Magnetoresistive (3 nT, 12 mW)	1	3000	\$100	\$300,000	500
Flux gate (3 pT, 100 mW)	10	300	\$2000	\$600,000	2000
Magnetoelectric (30 pT, 1 mW)	5	600	\$100	\$60,000	250

* Unit cost is dominated by sensor for flux gate and by processor, battery, radio, and package for MR and ME sensors

** Unit Volume dominated by power requirements for processor and radio for ME sensor

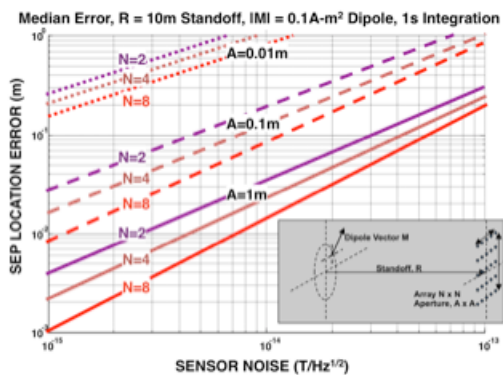
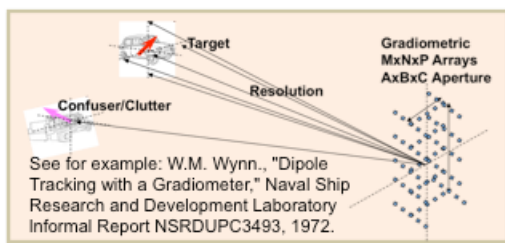
Figure 90. Low-noise magnetometers may be placed further apart and further back from the perimeter.

Likewise, a low-noise magnetometer will provide earlier alert. Low size, weight, and power (SWaP), and cost of an ME sensor is particularly attractive.

C.3.2.5. Target Localization and Tracking

Once a target has crossed a perimeter, one or more sensors must track the target. Alternatively, a small array may track a target by sensing the gradient of the radiated field. This concept is illustrated in Figure . Algorithms for tracking have been described by Wynn and others. The angular resolution of a small array is a function of the target signal-to-noise ratio (SNR), the number of sensors in the array, and the ratio of the aperture of the array to the target distance. ME sensors are particularly suitable for construction of arrays, given their low SWaP and material cost.

Standoff Target Detection, Localization and Tracking



11/14/2011

HUMS FPR



7

Figure 91. The concept for detection of CW magnetic sources with a gradiometer (upper left), performance projections as a function of sensor noise, stand-off, aperture, and number of sensors (lower-left), and a Phase 1 2x2 gradiometer.

C.3.2.6. Packaging and Integration

There are several packaging and integration concerns unique to ME sensors. First, the charge amplifier and sensor must be carefully shielded from electric fields that induce charge noise. Therefore, the charge amplifier must be located close to the ME laminate and the package shielded with a thin conducting foil to act as a “Faraday Cage”. Second, because the ME sensor is strain sensitive; it may transduce environmental vibration and/or sound pressure conducted through the packaging. Third, sensor and charge amplifier leakage resistance, and piezoelectric quality factor are sensitive to moisture and the sensors must be appropriately packaged. A mechanically stiff, hermetic package is therefore desirable with a thin conductive foil.

C.3.3. Signal and Image Processing

Under this task SAIC worked with Virginia Tech staff to explore signal processing and target localization algorithms. A HUMS MATLAB toolkit was developed for signal simulation and target localization using a grid search algorithm.

The deliverable under this task, “Imaging Options and Performance Predictions”, is satisfied with the memo “Signal processing software for arrays and gradiometers” which follows:

The purpose of this memo is to begin the process of defining signal processing subsystem concepts and algorithms for the VaTech consortium HUMS array and gradiometer. Signal processing (SP) is a subsystem in the VaTech HUMS array. Figure 92 illustrates that the SP subsystem interfaces with the data acquisition subsystem. Subsystems for a HUMS array include the ME sensors, charge amplifiers, power for the charge amplifiers, cabling, test gear, a multi-channel digitizer, a data archiver and signal processing. If required, the array may require one or more accelerometers for noise cancelation. After data archiving signal processing will estimate vector components of the “ambient” magnetic field, gradients of the vector field and sensor noise levels.

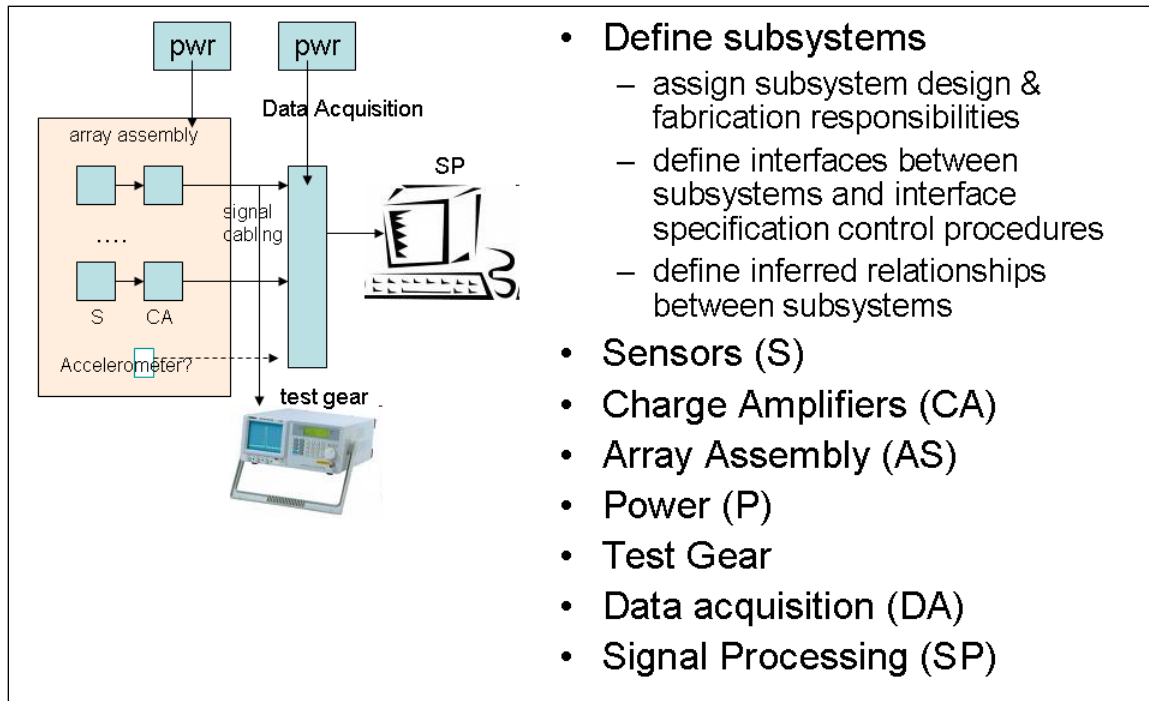


Figure 92. Subsystems for a HUMS array include the sensors, charge amplifiers, power for the charge amplifiers, cabling, test gear, a multi-channel digitizer, a data archivist and signal processing.

C.3.3.1. SigProc Subsystem

The objective of signal processing is to estimate the coherent signal (vector components of the magnetic field) and incoherent “noise” for an array of magnetometers. The signal processing may have to compensate for inevitable calibration and phase errors and mitigate sensor and clutter noise. SAIC and VaTech will develop a specific suite of algorithms for VaTech to manipulate and perform statistical analysis of HUMS array data. There is no requirement for real-time processing. It is envisioned that processing would be conducted in an offline, interactive, post-data collection environment by multiple members of the team. The signal processing subsystem does not replace test equipment that would be operated prior to and during data collection runs. A short “strawman” listing of SigProc subsystem functional requirements follows:

- Interface:
 - at a minimum a MATLAB “toolkit” of functions & scripts available from the command line
 - a GUI is TBD
- Read archive data.
 - convert input TBD formats to output TBD formats as required
- Perform Quality Control.
 - generate displays of spectra, waveforms, etc...
- Estimate coherent and incoherent noise of individual and multiple sensors.
 - review and select data windows for analysis
 - compute standard statistical estimates of noise
 - compute standard statistical estimates of coherence (correlation)
 - compute incoherent and coherent components
 - estimate transfer functions between components
- Estimate optimal filters to minimize “beam” noise.
 - review and select data windows for analysis
 - ABF or MVDR algorithms
- Estimate optimal filters for field gradients.
 - review and select data windows for analysis
 - derivatives of ABF and MVDR
- Portability, documentation, ...
 - MATLAB code is sufficient (platform independent)
 - Standard configuration management
 - Standard MATLAB toolkit or library “help” documentation
 - Tutorial

C.3.3.2. Algorithms

We look at three useful algorithms in this memo. Each is coded in MATLAB.

- fdpef() – frequency-domain prediction error filter – an algorithm for stripping vibration clutter or other signals from ME sensors based on the LMS algorithm.
- tfestimate() – transfer function estimate (SigProc Toolbox) – an algorithm for estimating the transfer functions of ME sensors (or between sensors) in a cluttered environment.
- abf() – time domain adaptive beam former – Shen’s algorithm for adaptively forming a beam from an array of ME sensors.
- mscohere() – magnitude squared coherence (SigProc Toolbox) – used to estimate noise of sensors using the estimated coherent and incoherent fractions of signal energy in two time series.

C.3.3.3. Data Set

We will illustrate signal processing with data collected in September 2009. Table 21 and Figure 93 show the experimental test setup. Ten ME sensors (VT1-10) were epoxied to cinder blocks

with two 3-component Bartington (BT1-2) reference sensors, two 3-component reference accelerometers (A1-1), and a pair of reference microphones (M1-2). For the purposes of this illustration we will use the Bartington “Z” and accelerometer “X” components as defined in Figure 93. The “-Z” axis was oriented 20-30 degrees east of the local magnetic north (this should have been measured). The “X” axis was oriented vertical. The data was collected at 44 kHz on a 24 channel Alesis 24-bit digitizer. The data was then low-pass filtered and decimated. We will use this data to illustrate procedures for 1) removing vibration noise from sensors, 2) estimating transfer functions and 3) forming an adaptive array and estimating the gradient across the array.

Table 21. Sensor channels and calibration

Channel	Sensor	Calibration	Units
3	VT3 (650 pC/Oe)	7.69 e-7	T/count
6	VT6 (512 pC/Oe)	9.76 e-7	T/count
8	VT8 (507 pC/Oe)	9.86 e-7	T/count
13,16	Bartington mag03 (100,000 V/T)	5.0 e-5	T/count
17,20	Accel Vertical (100 mV/g))	5.0 e+1	g/count

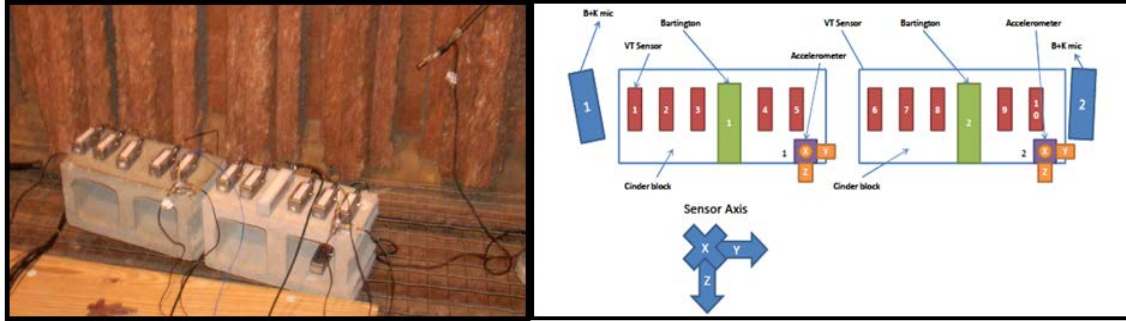


Figure 93. Sensors were mounted on cinder blocks. Note locations and orientations of VT #6 (VT6) and Bartington 1 (B1) and Bartington 2 (B2).

C.3.3.4. Vibration Noise Cancelation

We will first illustrate the use of the reference accelerometer to cancel noise. Rotational vibration (rocking) is a significant source of noise for a vector magnetometer in the Earth’s field. For small angle of rotation of a sensor of length, L, with a rotational rate spectrum N_0 (in units of radians/sec/rtHz) we expect a “noise” component of $B_R = B_0 (L/2) N_0$, where B_0 is the component of the Earth’s field in the direction of the sensor. We only have one accelerometer on the cinder block and can not make a complete description of the rotational motion of the block, but we can make an upper estimate of the rocking spectrum from the vertical accelerometer spectrum, $N_0 = N_A / (L_1/2) / (2 \pi f)$, where N_A is the vertical acceleration spectrum (in units of m/s/s/rtHz), and L_1 is the short axis of the block. At the test location, 42.3913N, 71.1572W, the horizontal magnitude of the field is about 19,800 nT (see <http://www.ngdc.noaa.gov/geomagmodels/struts/calcIGRFWMM>). Figure 94 is an upper estimate of the rocking noise on the magnetic sensors assuming $L = 0.06$ m, and $L_1 = 0.2$ cm, and $B_0 = 1.8e-5$ T. The acceleration time histories for A1 and A2 are shown in the upper panel. The bottom panel shows the spectral estimate, $B_R = N_A B_0 (L/2) / (L_1/2) / (2\pi f)$. There are several peaks in the rocking spectrum and it has a general $1/f^2$ character. In particular, there are prominent peaks at 12-14 Hz and 92-95 Hz. The rocking motion contamination at 1 Hz may be

as high as 2 nT/rtHz. The acceleration spectrum is nearly flat above 150 Hz indicating that the accelerometers may not have been sufficiently sensitive to fully resolve the acceleration spectrum above 150 Hz. The fall-off above 200 Hz is due to the anti-alias filter applied prior to decimation.

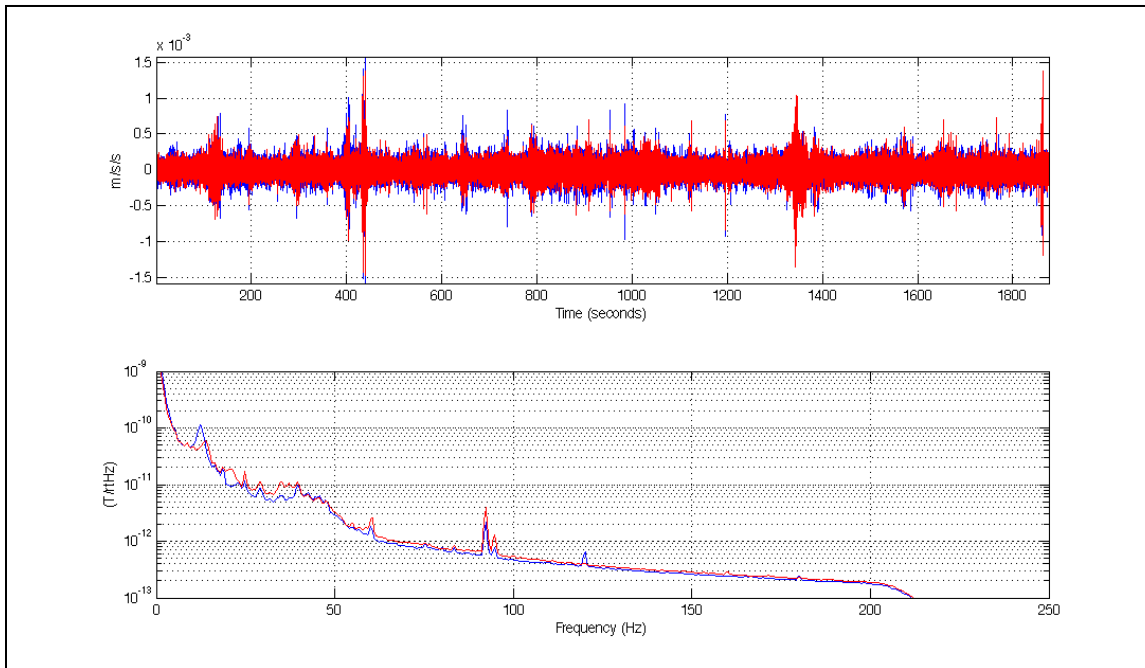


Figure 94. (Top) Time history of the vertical accelerometers, A1 (blue), A2 (red). **(Bottom)** An upper estimate of the equivalent magnetic noise due to the rocking motion of the cinder block from A1 (blue) and A2 (red) assuming all accelerations are caused by rocking around the worst possible axis.

Note that the acceleration time history amplitude is not stationary. In general the acceleration spectra are similar but there are important differences in the motion of the two blocks below 50 Hz.

A frequency-domain version of the Widrow-Hoff LMS algorithm (Figure 95) was used to adaptively remove rocking motion recorded on the magnetometers as indicated by the accelerometers. The algorithm minimizes the residual time series produced by using the acceleration time series to predict the magnetic time series, $|Z(t)| = |X(t) - A(t) \otimes Y(t)|$ where $X(t)$ is the magnetic time series, $Y(t)$ is the acceleration time series and $A(t)$ is an adaptive filter. The symbol \otimes indicates a convolution. Because the environment evolves, $A(t)$ slowly evolves with time.

The LMS algorithm is a practical approach to canceling (removing) interference using reference sensors (see for example Nayef et al., Freire and S. C. Douglas, Voytovych et al., Bick et al., and Penna et al.). The algorithm will strip from the time series $X(t)$ signals that are common to $X(t)$ and $Y(t)$ such as the rocking motion of the cinder block. However, if any “true” magnetic signals are picked up by the accelerometer, then they too will also be removed from the magnetometer signal (e.g. the 60Hz hum from the power grid may contaminate the accelerometer). Figure 96 -

Figure 98 show examples of the time series and the spectra resulting from this cancellation process for VT3, VT6, and VT8. These examples demonstrate that the rocking response was not the same for the three units. VT3 is noisier than VT6 and VT8, but is also more susceptible to vibration.

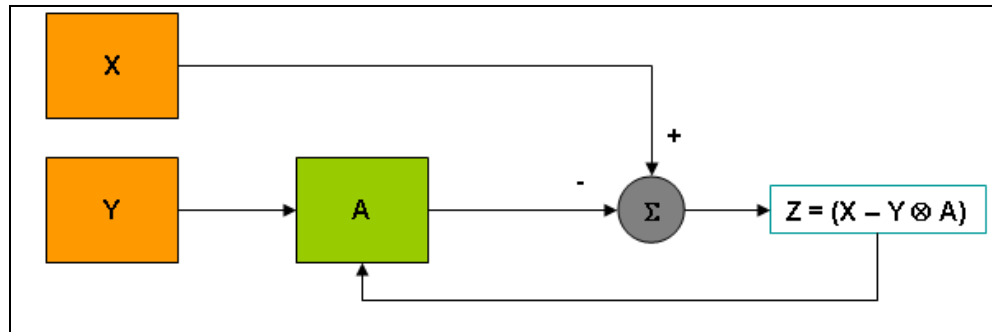


Figure 95. The adaptive Widrow-Hoff LMS algorithm estimates a filter, A, to transform Y to X.

The result, $Z = (X - A^* Y)$, is the portion of X that is not predicted by the time series Y. The feedback loop acts to update A proportional to the error signal, Z.

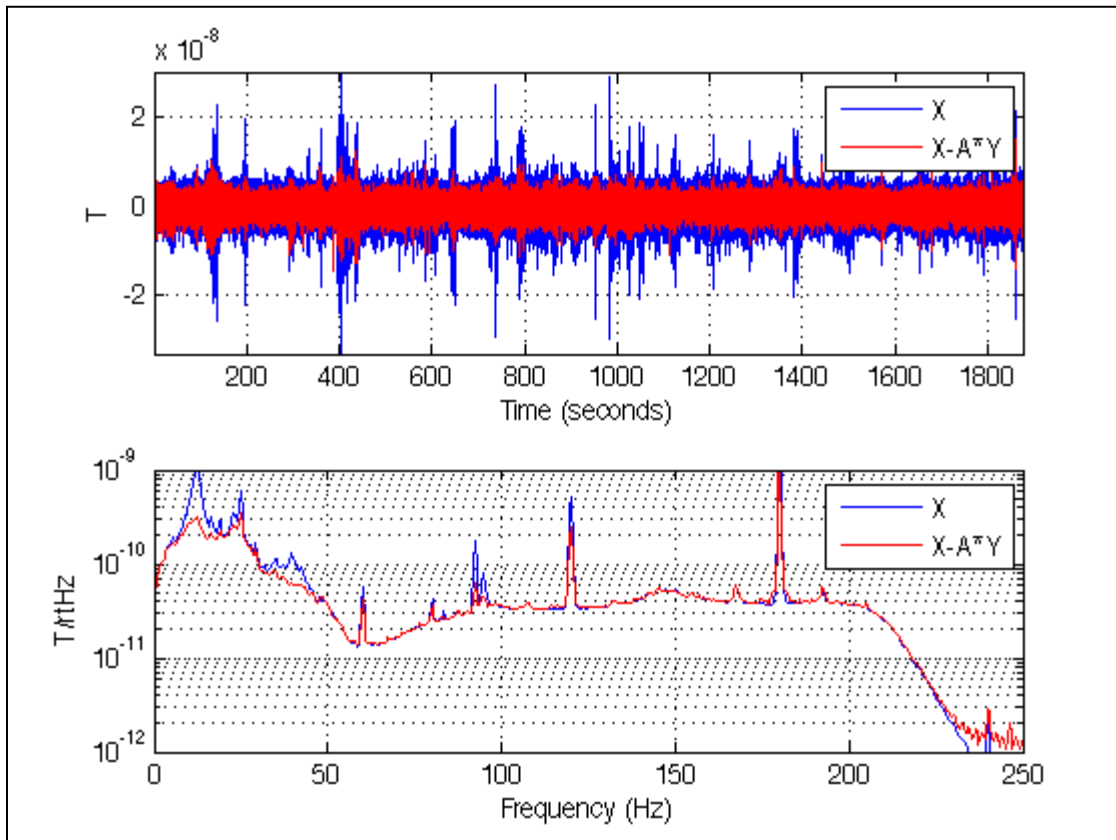


Figure 96. LMS stripping algorithm applied to VT3 using accelerometer A1.

The top panel shows the before (blue) and after (red) time series. The bottom panel shows the before and after mean spectra. Note that the peaks below 50 Hz and as well as the peaks near 95 Hz are reduced.

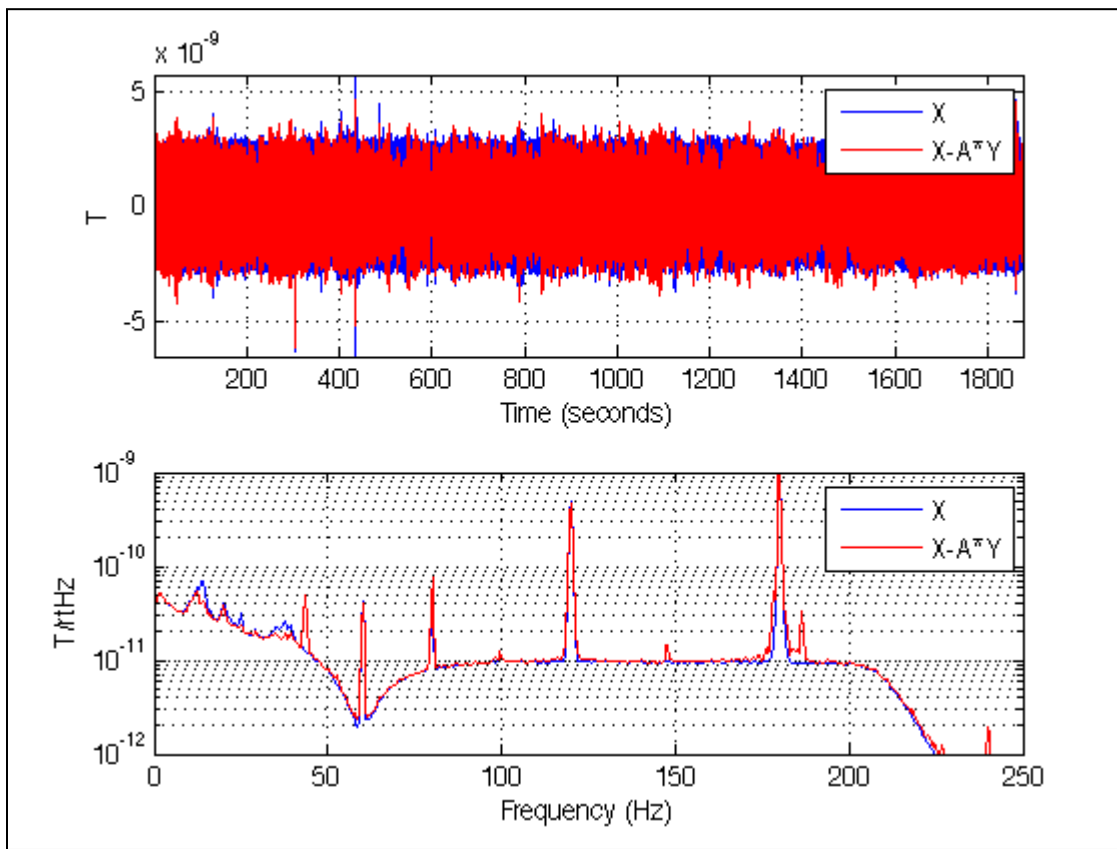


Figure 97. LMS stripping algorithm applied to VT6 using accelerometer A2.

Top panel shows before and after time series. Bottom panel shows the mean spectra. Note that the peaks below 50 Hz are reduced.

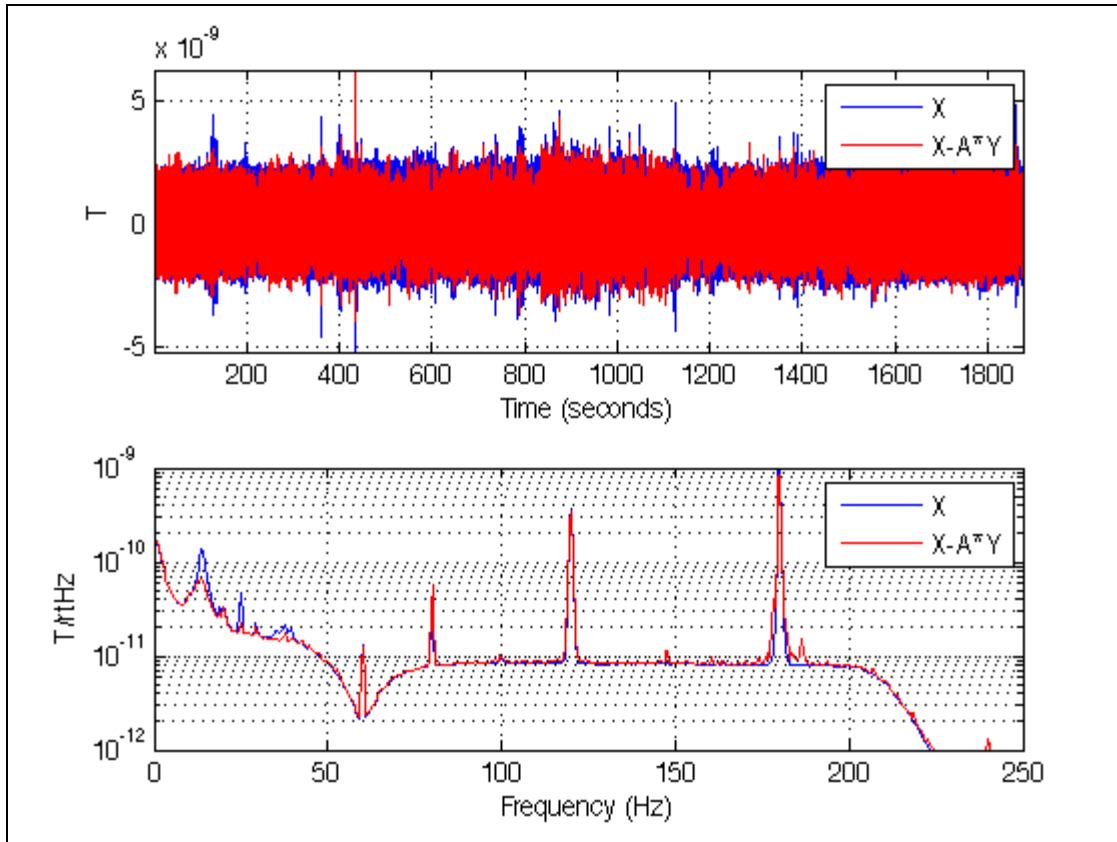


Figure 98. LMS stripping algorithm applied to VT8 using accelerometer A2.

Top panel shows before and after time series. Bottom panel shows the mean spectra. Note that the peaks below 50 Hz are reduced.

A second use of the stripping algorithm is to remove a time varying narrow band tone from a time series. This is useful because the largest clutter signal in each of the sensors is the 3rd harmonic of the power line (180 Hz). The procedure is to insert a pure sine wave into the LMS algorithm and allow the algorithm to solve for the slow time variation of the phase and amplitude required to minimize the residual. Figure 99 shows the time domain plot with VT3 before and after stripping the 180 Hz signal from the time series. The adaptive LMS algorithm is useful because the phase and amplitude of the 180 Hz tone changes with time (non-stationary). It is superior to a narrowband filter because it is exceedingly narrow and introduces a minimal phase shift away from the pure tone.

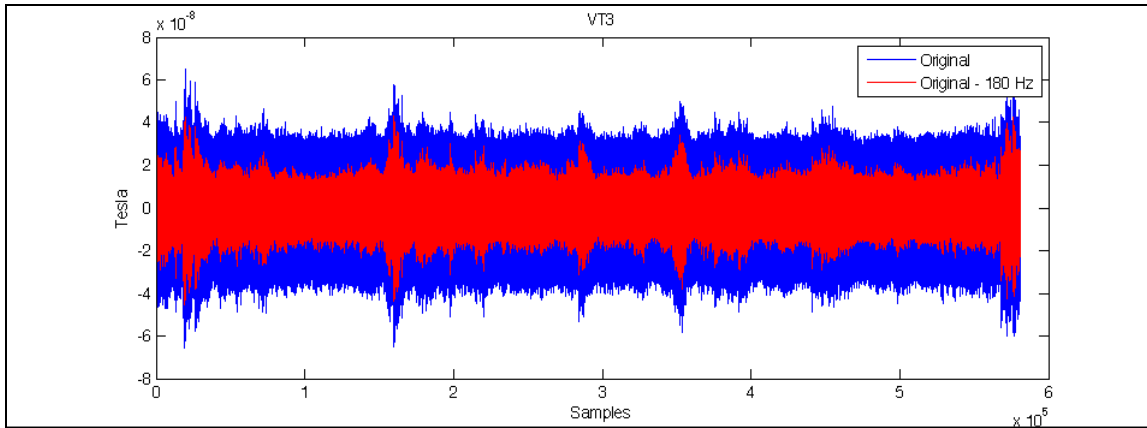


Figure 99. VT3 time series before and after adaptive removal of the 180 Hz tone.

C.3.3.5. Transfer Response Estimation

We next estimate the transfer responses of VT3, VT6, and VT8 with respect to the Bartington fluxgate reference sensors. We assume the Bartington reference sensor has a zero phase response. We want to check for gross differences in responses between sensors and make corrections to a flat phase response if possible for future processing. If sensors have different phase responses they can not be stacked. We use a standard MATLAB signal processing toolbox function that estimates the transfer function, $T_{XY}(f) = \langle P_{XY}(f)/P_{YY}(f) \rangle$ using Welch averaging indicated by the $\langle \rangle$ operator. $T_{XY}(f)$ is the complex transfer function as a function of frequency and P_{XY} , P_{XX} , P_{YY} are the XY, XX, and YY cross-spectra respectively. $T_{XY}(f)$ is a good estimate of the transfer function when the coherence, $C_{XY}(f) = \langle P_{XY}(f)/(P_{XX}(f) P_{YY}(f))^{1/2} \rangle$ is significantly greater than zero. The assumption is that the sensor noise components in P_{XY} and P_{YY} average to zero. In our example, the Bartington is the Y time series and VT3, VT6, and VT8 are the X time series.

The transfer function estimates based on 30 minutes of data in a low clutter environment (run4) are shown in Figure 100. The complex transfer function estimated by the MATLAB routine “tfestimate” have been smoothed with a median filter. The responses are noisy but still interpretable. The responses show a deep 60 Hz notch with a phase shift of one. Note that VT8 is inverted relative to VT6. The amplitude and phase responses of VT6 and VT8 are quite similar except for the polarity inversion. VT3 sensitivity is actually somewhat higher (~2x) than the nominal estimate. VT6 and VT8 sensitivities are higher than nominal below 50 Hz and low than nominal above 70 Hz. The VT3 phase response is considerably more erratic due to higher sensor noise levels but the instrument may have a different low frequency response.

Figure 101 shows a repeat of the exercise with a longer time window with a higher clutter level. We multiplied VT8 before processing to correct for the inversion. Because of the longer time period and the higher clutter level, the responses are much less noisy. The median filter has smoothed over most of the frequencies with poor coherence but there are still artifacts near 5, 120, and 180 Hz. Even accounting for the notch filter 180 degree phase shift, the sensors do not have flat phase responses (i.e. they are dispersive). VT6 and VT8 have nearly the same phase responses. The VT3 phase response is clearly different at low frequencies.

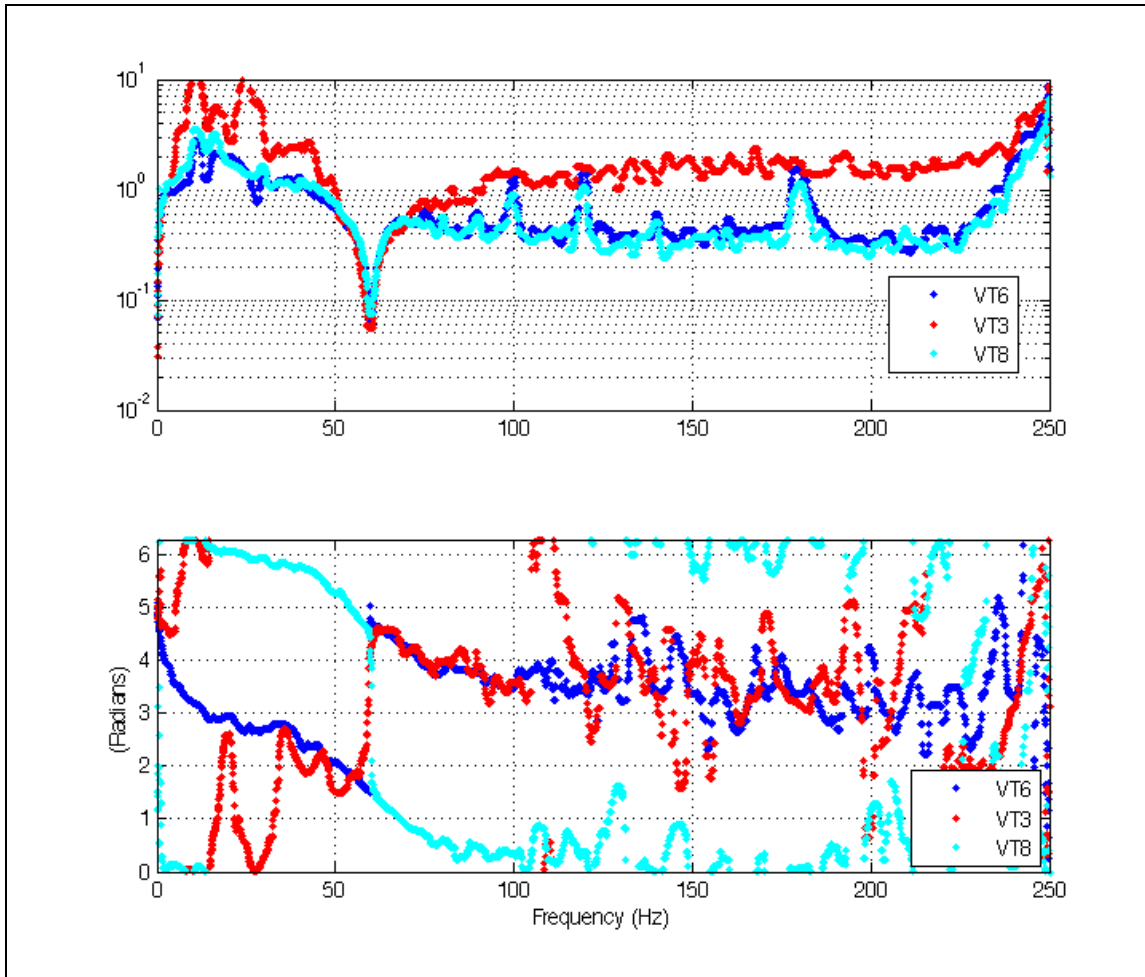


Figure 100. Relative response with respect to Bartington mag03 for VT3, VT6, and VT8.

Top panel displays the relative amplitude spectrum and bottom panel displays the relative phase response.

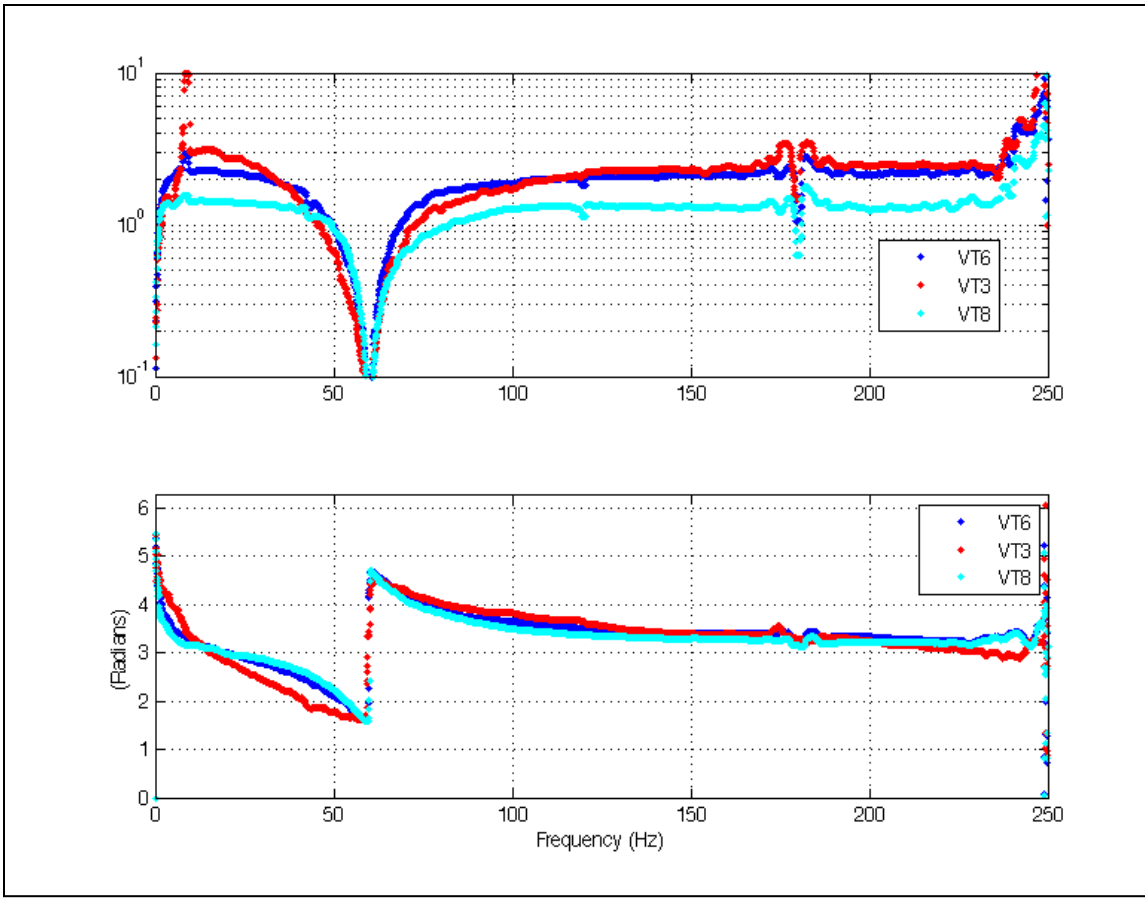


Figure 101. A repeat of the response response determination with respect to a Bartington mag03 fluxgate for VT03, VT6, and VT8 for a longer time period and a higher clutter level.

Note the phase difference below 50 Hz between the VT3 (red) and the VT6 (blue) and VT8 (cyan).

C.3.3.6. A Strawman Adaptive Beamformer and Gradiometer

Figure 102 illustrates our strawman concept for a simple 3-element adaptive beamformer and gradiometer. The N-element gradiometer may be generalized. Three sensors are combined to make the best estimate of the mean field which we will refer to as the “beam”. The Adaptive Beamformer (ABF) algorithm is based on the algorithm of Shen (1979) and has been successfully applied to seismic (McLaughlin et al 2005), infrasound, and magnetic data. The ABF algorithm is a multidimensional application of the Widrow-Hoff LMS algorithm. Filters for each individual channel are derived that provide a “least mean square” error between the channel and the beam under the constraint that the individual filters sum to unity (delta function). The algorithm has several very useful properties. First of all, in the limit of stationary noise, the algorithm converges to weights (filters) inversely proportional to the sensor noise of each channel. In this manner, noisy sensors are down weighted and quiet sensors are up weighted. A second property of the algorithm is that in the limit of stationary noise, filters converge to compensate for amplitude miss-matches between sensors and the beam. A third property is that filters converge to cancel stationary coherent noise that is not on the beam (common to all sensors). In this way, a tone present on only one sensor or out of phase across multiple sensors is

canceled. A fourth property of the adaptive algorithm is that it slowly adjusts for changes in the noise environment (non-stationary). There are time-domain and frequency domain versions of the algorithm. A frequency version is closely related to the Minimum Variance Distortionless Response (MVDR) algorithm. Both algorithms are being investigated as candidates for optimal beam and gradient estimation. As with both the ABF and MVDR the number of interfering signals that can be canceled is proportional to the number of array elements.

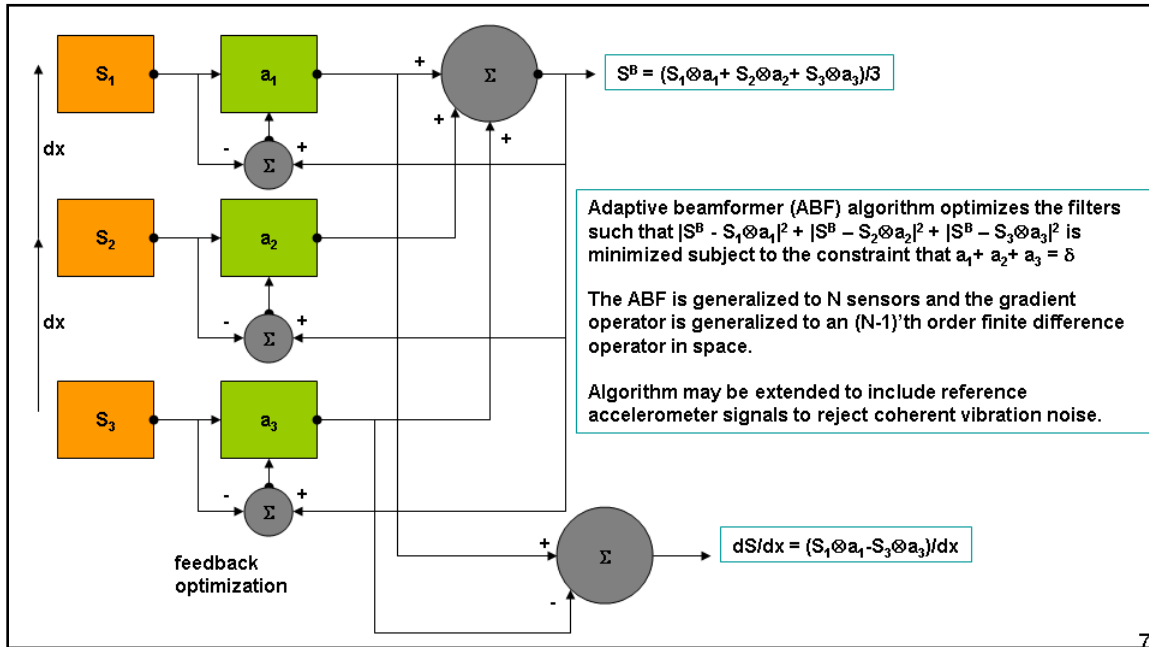


Figure 102. A simple 3-element adaptive beamformer and gradiometer array extendable to $N > 2$ channels.

To illustrate the ABF algorithm, I have chosen to form an array composed of VT3, VT6, and VT8. The processing had several steps:

1. I normalized all sensors to the median level at 180 Hz (the strongest signal).
2. I striped the 180 Hz tone using the LMS algorithm.
3. I striped vibration motion using the LMS algorithms and the reference accelerometer.
4. I corrected for the smooth phase responses shown above to match the Bartington reference sensor.
5. I ran the time-domain version of the ABF on the three channels, VT3, VT6, and VT8.

The results are shown in Figure 103. Figure 103 compares the CBF with the ABF. The ABF and CBF are similar across the 1-200 Hz bandwidth except for many narrowband tones that are not common to all sensors (VT3, VT6 and VT8). Figure 104 compares the median CBF and ABF spectra to the individual median VT3, VT6, and VT8 spectra. VT3 is the noisiest and contains many narrowband tones not present in VT6 and VT8 spectra. We presume these are vibration modes of the VT3. Formally, the CBF = (VT3+VT6+VT8)/3 and consequently it contains portions of the VT3 vibration modes that are not coherent with VT6 and VT8. The ABF spectra are less than or close to the minimum of all the three sensors across the band. If the three sensors were matched and their sensor noise was uncorrelated, then we would expect to see the CBF and

ABF 1/sqrt(3) lower (4.8 dB) lower. Instead we see the ABF is generally just about equal to the quietest sensor (VT6 or VT8) at each frequency.

We can define the gain of the ABF and CBF as $\text{ABF_Gain} = -20 * \text{Log10}(\text{ABF}/\text{P}^*)$ and $\text{CBF_Gain} = -20 * \text{Log10}(\text{CBF}/\text{P}^*)$, where $\text{P}^* = ((|\text{VT3}|^2 + |\text{VT6}|^2 + |\text{VT8}|^2)/3)^{1/2}$ is the mean power spectra of VT3, VT6, and VT8. The gain is shown as a function of time and frequency (lower left) and a median value versus time (lower right) of Figure . The largest median gain is in the 1-20 Hz bandwidth where the sensors were most affected by vibration. If the ABF is the best estimate of the mean field, then we can begin to estimate a gradient with the differences between the individual sensors and the ABF. The spectra of differences between each individual sensor and the ABF as estimates of the gradient spectra are plotted in Figure 106. The gradiometer spectra are compared with a noise level estimate for VT6 and VT8 based on their mutual coherence (magenta). The gradiometer spectra are above the noise level for frequencies above 40 Hz. The analysis indicates that the gradient estimates are probably not reliable below 40 Hz.

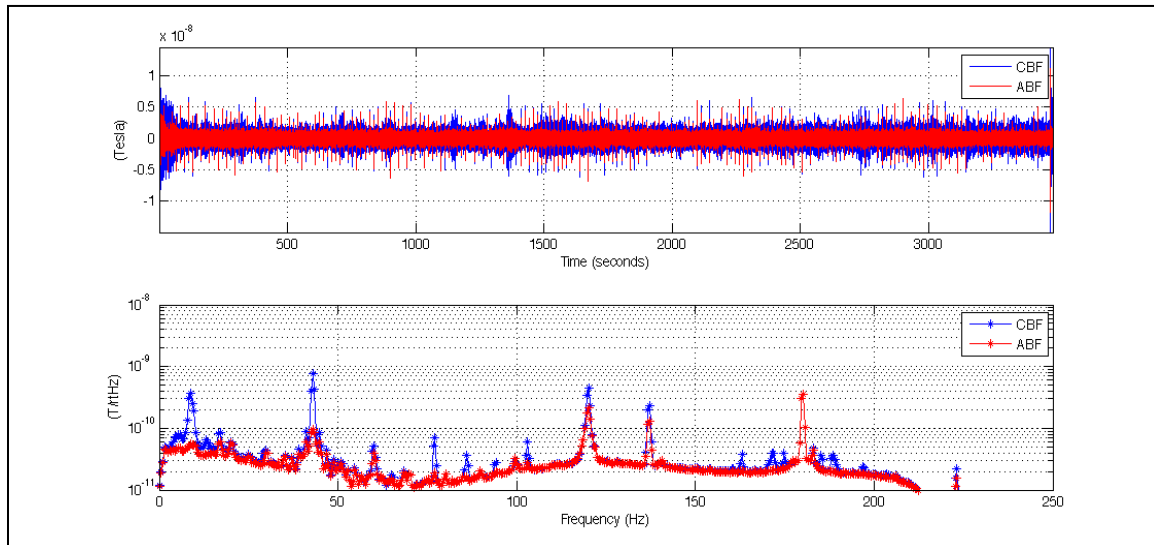


Figure 103. The top panel shows the time domain signal for the conventional beamformer (CBF blue) and the adaptive beamformer (ABF red). The bottom panel shows the median spectra of each.

The ABF and CBF are similar across the 1-200 Hz bandwidth except for many narrowband tones that are not common to all three sensors (VT3, VT6 and VT8).

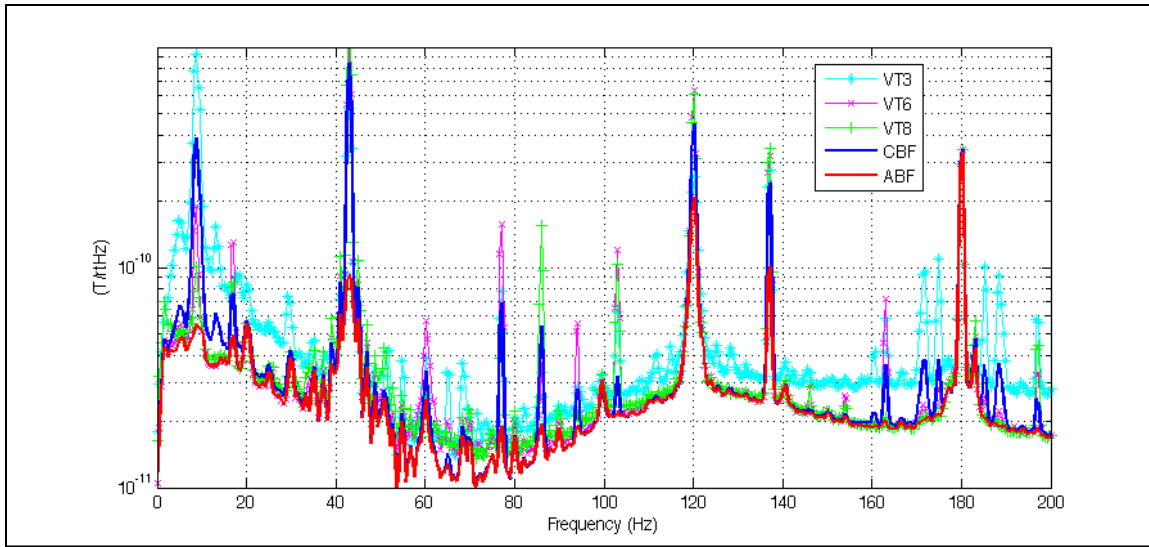


Figure 104. The median CBF and ABF spectra are compared to the median VT3, VT6, and VT8 spectra.

VT3 is noisier and contains many narrowband tones not present in VT6 and VT8 spectra. The $\text{CBF} = (\text{VT3} + \text{VT6} + \text{VT8})/3$ consequently contains portions of the VT3 spectra that are not coherent with VT6 and VT8. The ABF spectra is less than or close to the $\min(\text{VT3}, \text{VT6}, \text{VT8})$ across the band.

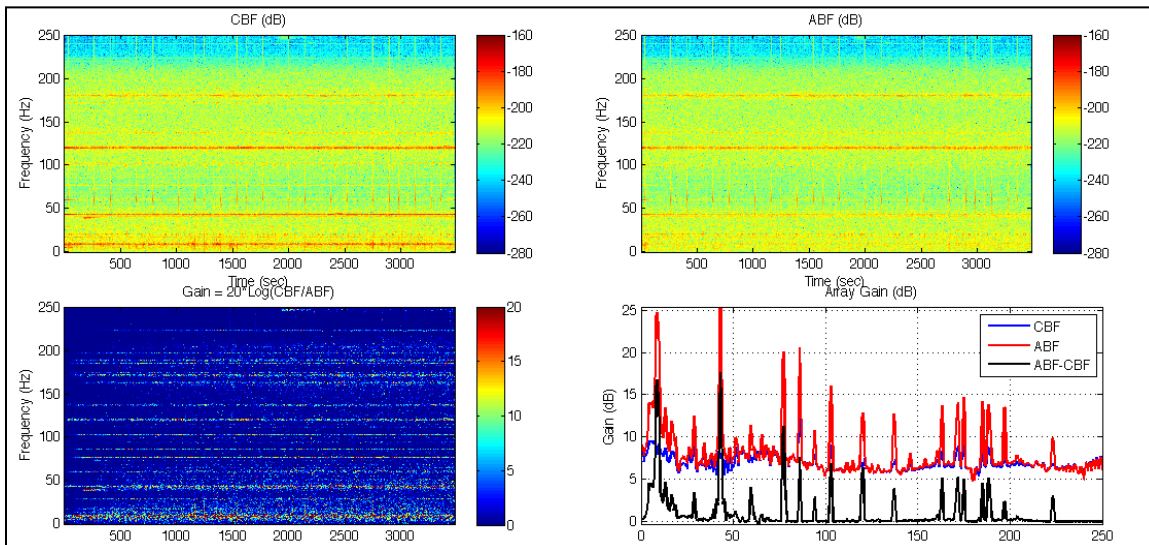


Figure 105. Spectrogram of the CBF (upper left) is compared with the spectrogram of the ABF (upper right). The gain is shown as a function of time and frequency (lower left) and a median value versus time (lower right).

The gain of the ABF with respect to the CBF can be defined as $\text{ABF-CBF Gain} = -20 * \text{Log10}(\text{ABF}/\text{CBF})$. The largest excess ABF gain is in the 1-20 Hz bandwidth where sensors were most affected by vibration.

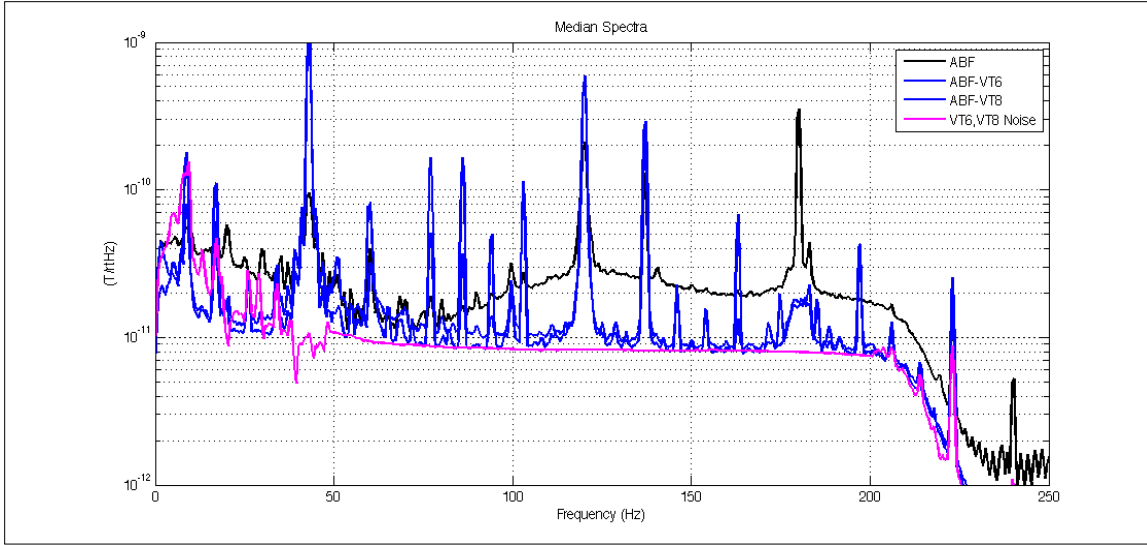


Figure 106. The differences between the VT6 and VT8 sensors (the quietest of the sensors) and the ABF are good estimates of the gradient spectra.

The gradiometer spectra (blue) are compared with a noise level estimate for VT6 and VT8 from their coherence (magenta). The gradient spectra are nearly always less than the ABF spectra (black). The gradiometer spectra (blue) are above the noise level (magenta) for frequencies above 40 Hz. The signal at 43 Hz is a controlled source close to the array and the local gradient spectra may exceed the mean spectra for this nearby source. The analysis shows that the gradient spectra below 40 Hz may not be reliable.

C3.4. Low-Noise Electronics

Under this task SAIC designed, developed and delivered a series of ultra-low-noise (ULN) charge amplifiers specifically designed for passive readout of magneto-electric (ME) sensors near 1 Hz. At the beginning of the project, the noise from the charge amplifier was comparable to or exceeded the sensor noise (0.3-0.4 fC/ $\sqrt{\text{Hz}}$). Our final delivery was 32 miniaturized UNL charge amplifiers, custom packaged to facilitate integration with arrays of ME sensors, with average charge noise at 1 Hz between 0.05 and 0.08 fC/ $\sqrt{\text{Hz}}$.

C.3.4.1. Opamp-Based Low-Noise Charge Amplifier

We began the task by modeling the noise of the existing Virginia Tech operational amplifier (opamp) based charge amplifier, and surveying alternative commercially available opamps. Our analysis showed that the opamp current noise dominates below about 10 Hz while voltage noise dominates above 10 Hz, so we selected the Analog Devices AD795 opamp whose 0.6 fA/ $\sqrt{\text{Hz}}$ noise current is the lowest in its class.

We constructed a noise model for a two-stage charge amplifier in order to analyze and optimize the noise performance, as shown in Figure . It shows that the noise is dominated by the opamp current noise below 10 Hz and voltage noise above. Setting the value of the feedback resistor in the charge amplifier circuit to 200 G Ω reduced its noise contribution to below that of the opamp, providing optimal performance from the AD795. A comparison of noise spectra of the new charge amplifier to that of the LMC6044-based charge amplifier from Virginia Tech (Figure)

shows the reduction in noise at 1 Hz and above. The improvement is primarily due to the use of the lower-noise, higher-voltage opamp used in the first stage and the larger value of the feedback resistor

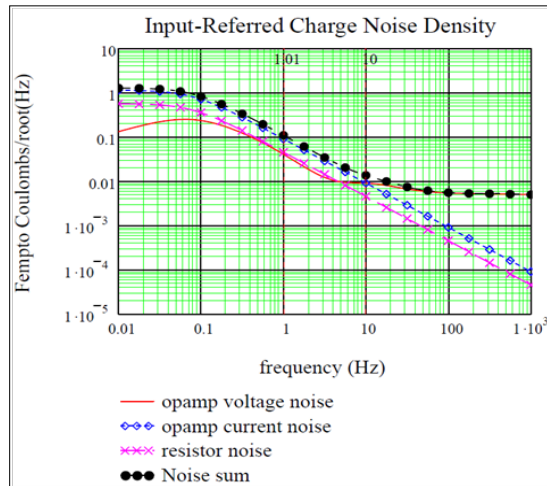


Figure 107. Predicted Charge Noise Density

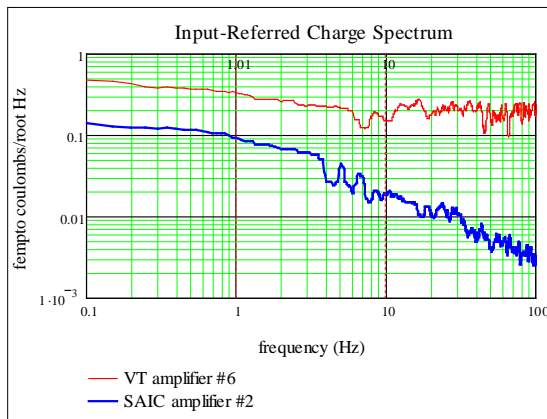


Figure 108. Charge noise spectra for the new charge amplifier compared to the current amplifier provided by Virginia Tech.

Figure 109 shows a schematic of the charge amplifier circuit. The charge amplifier was packaged in an aluminum box to shield it from electromagnetic noise. Two prototypes were delivered to Virginia Tech in January, 2010, and two more in May, 2010. The design, predicted and measured noise characterization, and instructions for use were described in Huntley (January, 2010).

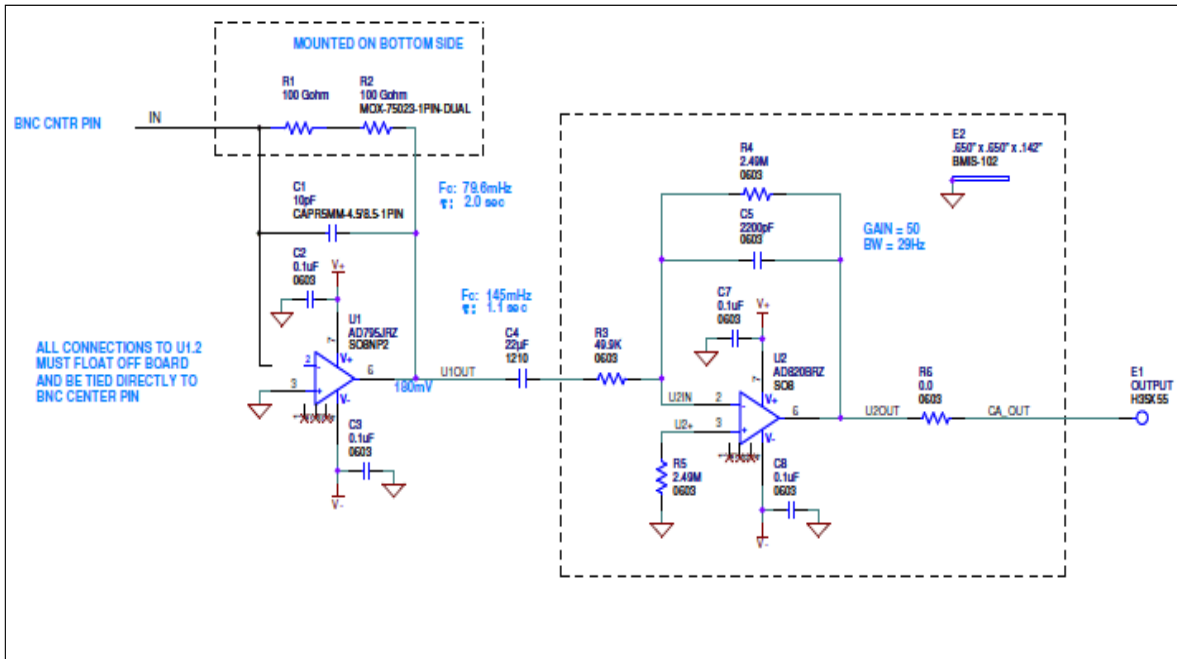


Figure 109. Schematic of prototype low-noise charge amplifier.

C.3.4.2. FET-Based Low-Noise Charge Amplifier

In an effort to further reduce the electronic noise from this circuit, we considered both uncooled and cooled discrete JFETs as front-ends to the charge amplifier. We evaluated FETs from InterFET, Linear Systems, MOXTEK, and Toshiba. Most of the FETs (shown in blue in Figure) have current noise similar to or higher than the opamp we used (AD795), but some have considerably lower voltage noise. Several FETS from MOXTEX (MX-NN) had promising noise specifications but were considered too expensive for this project (over \$300 per FET). The current noise (Shot noise) of the FET input can theoretically be reduced $3\text{dB}/10^\circ\text{C}$ by cooling. We made an uncalibrated measurement of the change in current noise in a discrete FET and found the reduction in the leakage current to be consistent with this model, and considered several options for cooling the FET, including constructing a custom thermoelectric cooler (TEC). However, our investigations showed that this would only be worthwhile if the charge amplifier current noise is the dominant contributor to the total sensor noise, which our noise models show is not the case.

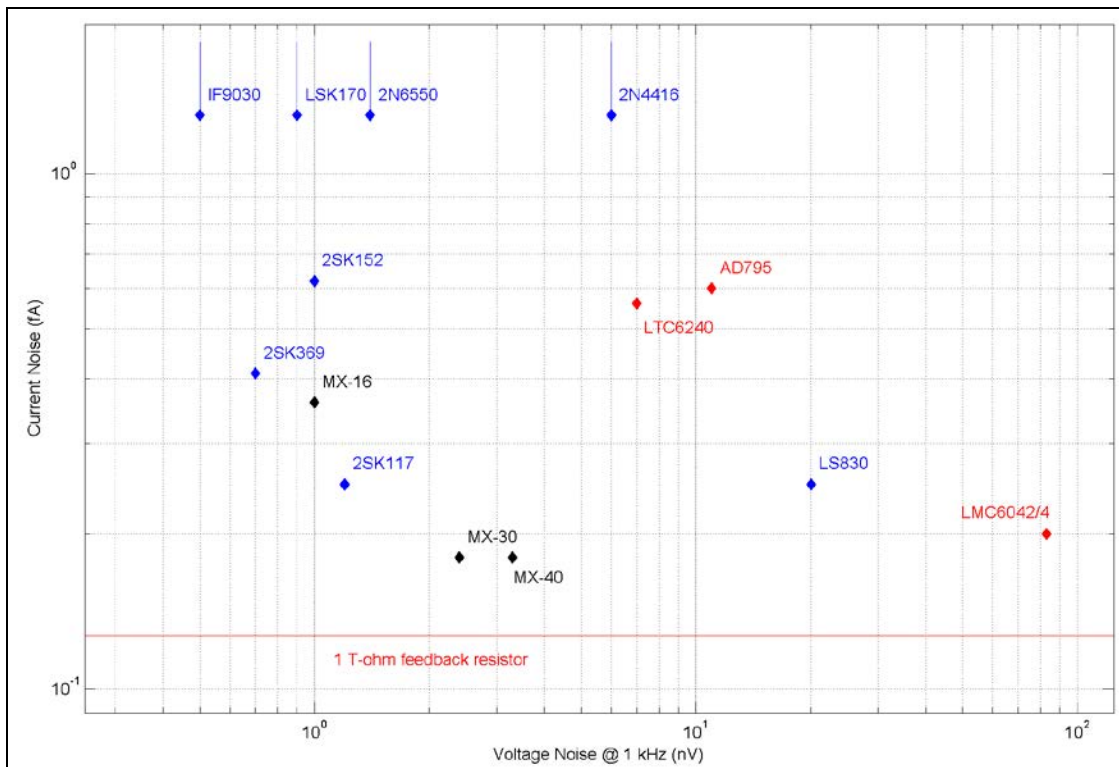


Figure 110. Current and voltage noise for a selection of FETs that might be used in the first stage of the charge amplifier.

Several opamps, including the AD795, are shown in red for reference. The red line is the equivalent current noise from a 1 TΩ feedback resistor.

A more promising approach to reducing the effective system noise is to exploit the lower voltage noise of the JFET to allow amplification of the signal by multiple sensors in parallel. Stacking N “matched sensors” adds coherent signals and incoherent noise such that SNR should increase proportional to \sqrt{N} , provided the sensor phase responses are matched and the noise are incoherent. However, the voltage noise of the charge amplifier is proportional to $V_n * (1 + N C_m/C_f)$, where V_n is the voltage noise of the input stage of the amplifier, C_m is the capacitance of the sensor, and C_f is the feedback capacitance. The charge signal from N sensors in parallel increases as $N*C_m$, but the noise will increase by the same factor unless the small voltage noise can suppress it.

The design of the FET-based charge amplifier is shown in Figure . The design was optimized for ME laminate sensors with high leakage resistance (>30 G-Ohm). The JFET used in the first stage was selected to provide optimal performance for stacked sensors to provide superior noise characteristics at 1 Hz. The design also supports drive options in the range of 1 to 30 kHz with or without stacked sensors.

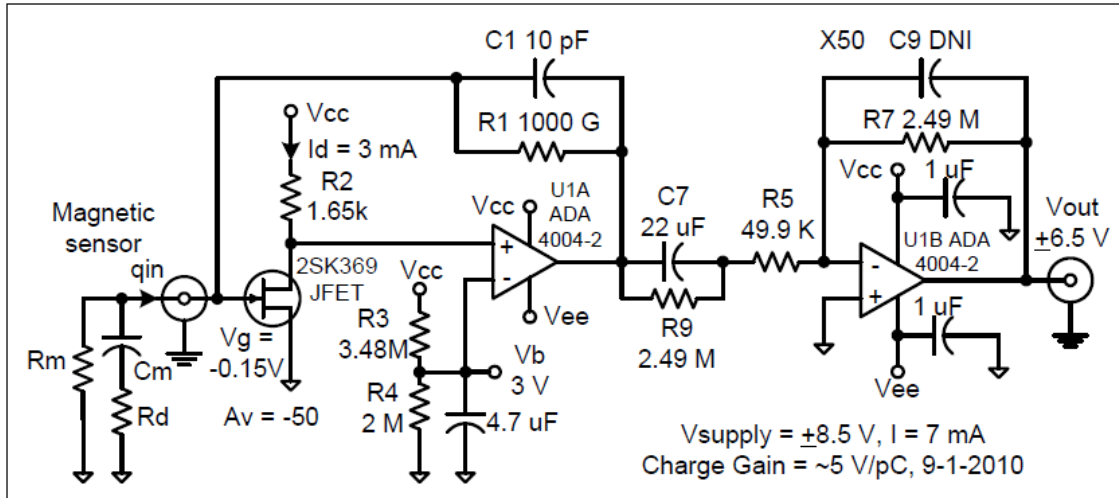
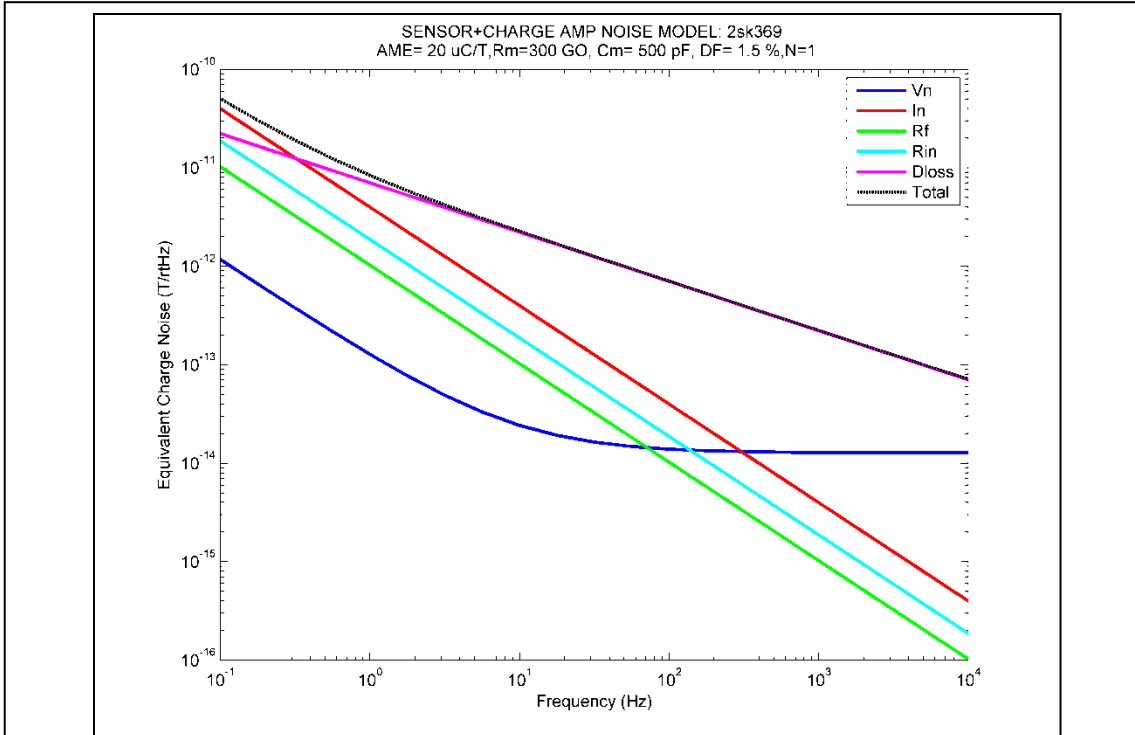


Figure 111. Schematic of the JFET-based charge amplifier.

The combined noise model for the charge amplifier and sensor, summarized in Figure , was central to optimizing the charge amplifier and identifying key noise contributions of the sensor. The leakage resistance and the dielectric loss of the sensors were found to be key contributors to the system noise. If the leakage resistance decreases as the sensor response is increased, this term could become dominant as sensors are stacked. The dielectric loss is due to a material property but is proportional to the square root of the capacitance. In general, if the sensor capacitance and leakage resistance are determined by the piezoelectric material constants and the inter-digitated design, we expect them to be inversely related.



Noise Term	Formulas
Charge-amp voltage (V_n)	$1/2\pi f V_n(f) (1+N C_m/C_f) (i 2\pi f + 1/(R_f C_f)) C_f / \alpha_E$
Charge-amp current (I_n)	$1/2\pi f I_n(f) / \alpha_E$
Feedback resistance (R_f)	$1/ (2\pi f)(4 k_b T / R_f)^{1/2} / \alpha_E$
Sensor leakage resistance (R_{in})	$1/ (2\pi f)(4 k_b T N / R_m)^{1/2} / \alpha_E$
Sensor dielectric loss (D_{loss})	$(4 k_b T N C_m \tan(\delta) / 2\pi f)^{1/2} / \alpha_E$

Figure 112. Combined noise model for a JFET-based charge amplifier and laminate ME sensor.

C_m and R_m are the sensor capacitance and leakage resistance, C_f and R_f are the feedback capacitance and resistance, k_b is the Boltzmann constant, T is the temperature, $\tan\delta$ the dielectric loss factor, N is the number of sensors in a stack, α_E is the sensor charge coefficient, and ω is the frequency in radians. The feedback resistor (R_f) and capacitor (C_f) correspond to R1 and C1 in the circuit diagram in Figure .

After considering a variety of low-noise JFETs which traded off current noise and voltage noise, as noted above, we concluded that minimizing the voltage noise was most beneficial since it can suppress an increase in the sensor capacitance (C_m in Figure). Reducing the voltage noise allows us to increase the charge gain of the sensor by stacking sensors without commensurately increasing the noise contribution. We consequently selected the Toshiba 2SK369 as the JFET front end to our charge amplifier.

Minimizing the feedback resistance contribution to the noise required the selection of a very high value (1 T-Ohm) resistor. Use of this feedback resistance requires that the leakage resistance of sensor remains high (> 30 G-Ohm) in order to prevent saturation of the charge amplifier. The JFET-based charge amplifier board and its EMI protective enclosure are shown in Figure . The 1 T-Ohm feedback resistor is “floated” on the back side of the board to minimize charge leakage. The 2SK369 JFET is the prominent black device directly connected to the input (bottom).

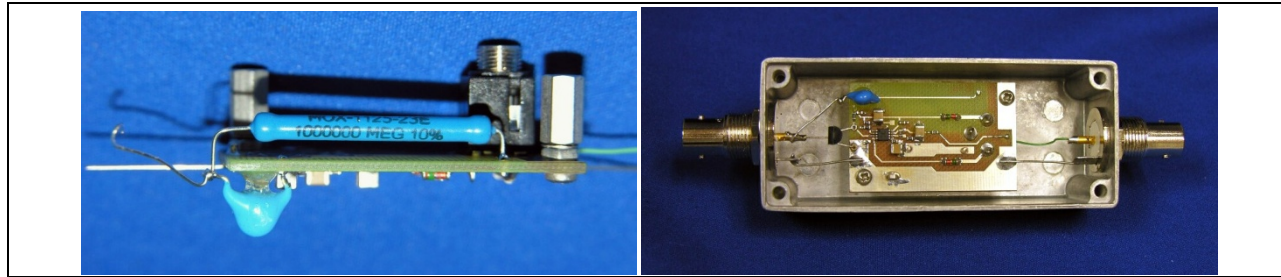


Figure 113. Photo of JFET-based charge amplifier board: a side view (top), and inside the enclosure (bottom).

Gain and noise levels were measured for four charge amplifiers at 1 Hz. Their charge noise spectra were found to be very consistent (Figure), and the measured values of the gain and noise at 1 Hz closely match the design values of 5 V/pC and 0.06 fC/ $\sqrt{\text{Hz}}$.

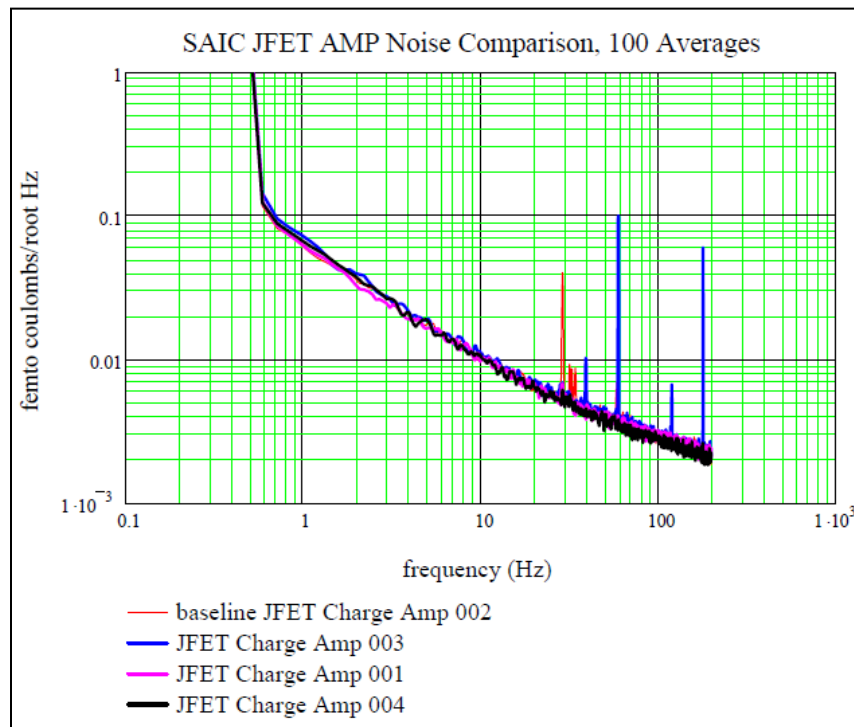


Figure 114. Measured charge noise of four JFET-based charge amplifiers.

For PZT-based ME sensors, dielectric loss dominates the sensor charge noise. In Figure and Figure 116 we examine the potential benefits of stacking several sensors. Figure shows the noise models for a single sensor with a noise level of $10 \text{ pT}/\sqrt{\text{Hz}}$ at 1 Hz ($\alpha_E = 18 \text{ C/T}$, $C_m = 500$

pF, $R_m = 300$ G-Ohm, and $\tan(\delta) = 1.5\%$) on the left and a stack of 16 such sensors on the right. The perfect stack of $N=16$ would have an effective noise level of $\sim 2\text{pT}/\sqrt{\text{Hz}}$. Modeling a speculative improved ME sensor with a 3x enhancement in α_E and a 10x reduction in dielectric loss, we plot the noise models for $N=1$ and a stack of $N=16$ in Figure . This set of plots show the reductions in the 1 Hz noise level that might be achieved with additional reduction in the dielectric loss increase in the charge coefficient.

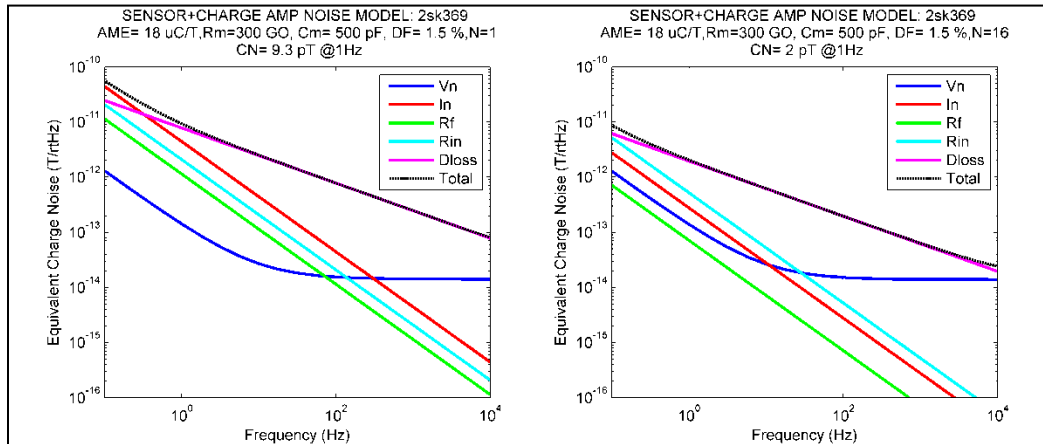


Figure 115. Noise model for sensor plus charge amplifier showing improvements achievable by stacking.

The plot on the left is for single sensor while the plot on the right is for a stack of 16 sensors in parallel.

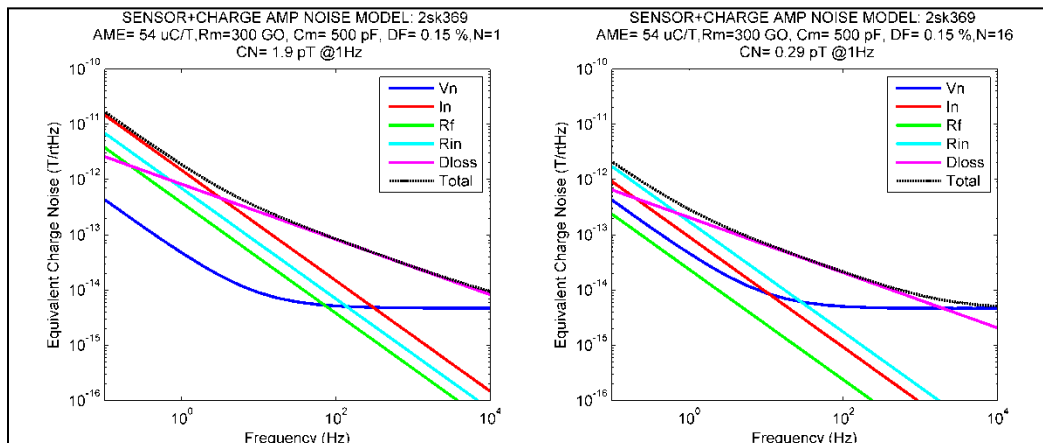


Figure 116. Noise model for a notional next generation of sensor plus charge amplifier showing improvements from enhanced charge coefficient and reduced dielectric loss.

The plot on the left is for single sensor while the plot on the right is for a stack of 16 sensors in parallel.

Two JFET-based charge amplifiers were delivered to Virginia Tech in September, 2010. The design, predicted and measured noise characterization, and instructions for use of the JFET-based charge amplifier were described in Huntley (September, 2010).

C.3.4.3. Miniaturized FET-Based Low-Noise Charge Amplifier

Beginning in early 2011, SAIC designed and fabricated a miniaturized version of the JFET-based charge amplifier to facilitate integration with the ME sensor into an array configuration.

Reducing the size of the circuit required replacing the air-isolated feedback resistor with a surface-mounted resistor on a very-high resistance circuit-board. We also modified the circuit to provide USB connector oriented to the side to improve cable connections. The populated circuit board is shown on the left in Figure . The large black square on the left is the JFET, while the large orange square on the right is the mini-USB connector. The charge amplifier board is protected by a custom plastic enclosure to avoid damage and inadvertent contamination of the PCB surface, which can introduce significant noise, as shown on the right in Figure . The large orange square on the left is copper foil that provides a good electrical contact with the mini-USB connector. Unlike the previous versions of the charge amplifier, this enclosure does not provide EMI shielding, which must be provided by the enclosure that holds the charge amplifier and sensor.

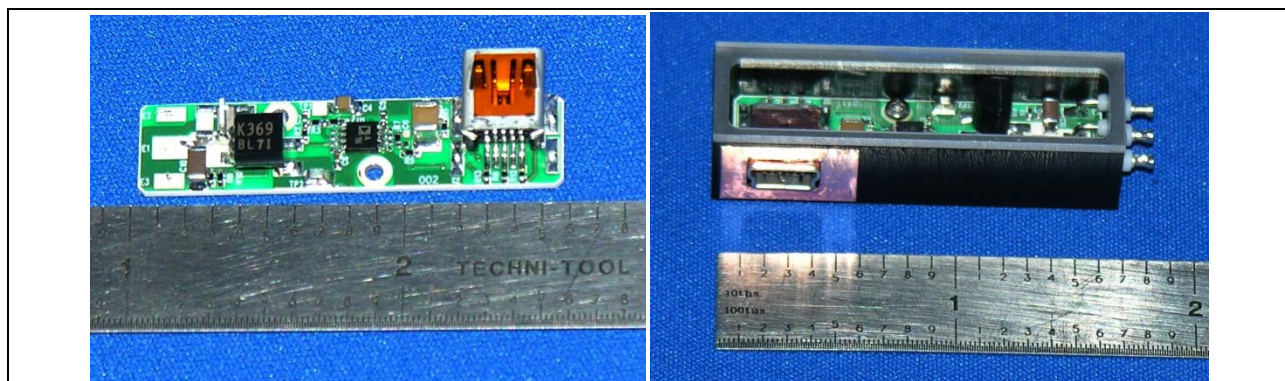


Figure 117. Miniaturized JFET-based charge amplifier, bare and packaged in protective box with clear lid.

Forty-five (45) miniaturized JFET-based charge amplifiers were fabricated and tested. The results were largely consistent, showing slightly higher noise at 1 Hz than the previously delivered larger JFET-based charge amplifiers. Nine of the charge amplifiers were rejected for either high noise at 1 Hz, high DC offset, or high sensitivity to vibration, giving a yield of around 80%. The measured values of the charge gain, gate voltage (V_g), DC output voltage and the noise with an open input (red) or with a 440 pF test capacitor on the input (blue), shown in Figure , were found to be reasonably uniform; the average values are shown in Table 22. Eight of the units (higher serial number in Figure) built using a 2SK369GR were found to have a noise approximately 30% lower than units built using of the original 2SK369BL (Table 23).

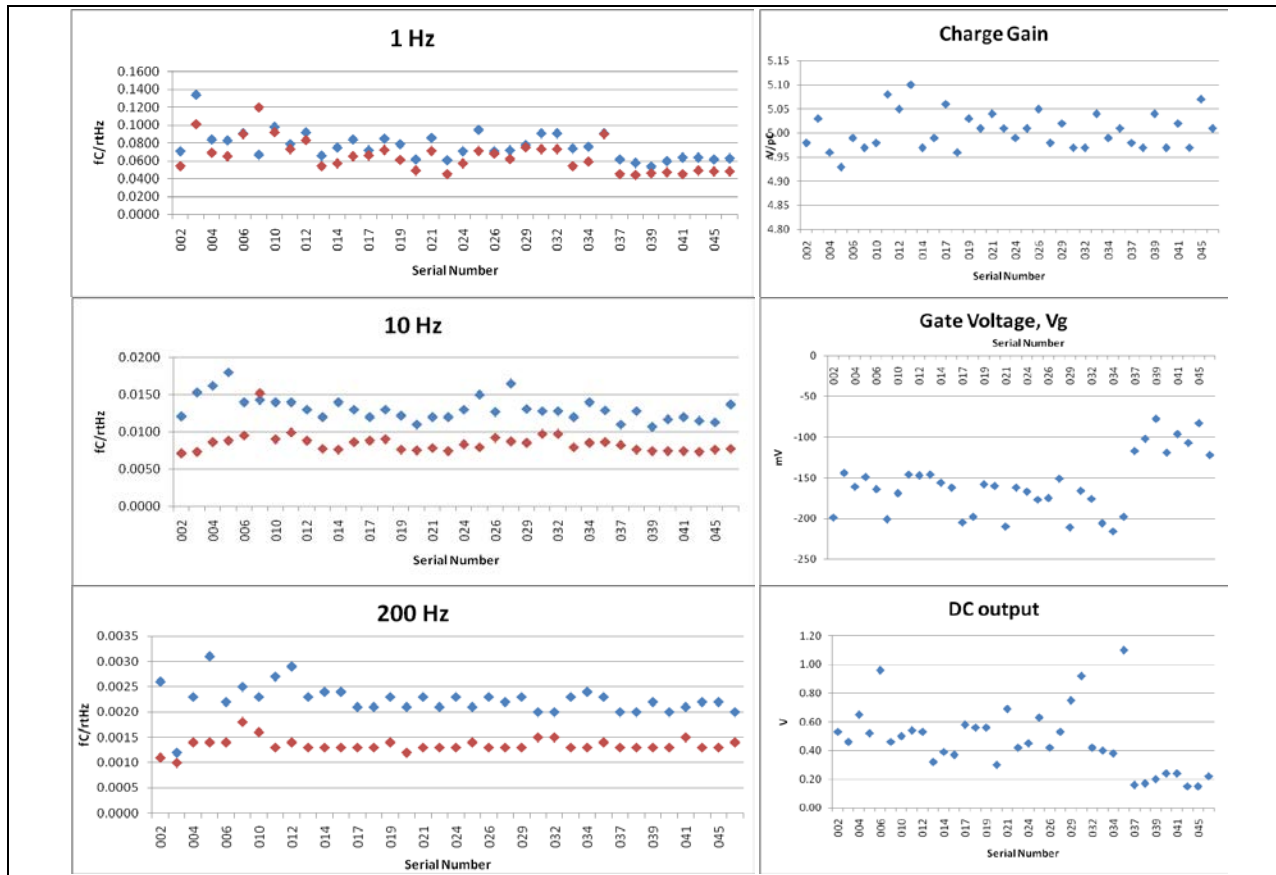


Figure 118. Distributions of noise and other characteristics of the miniaturized charge amplifiers, after removing rejected units.

Table 22. Average characteristics of the miniaturized charge amplifiers, excluding rejected units.

Serial Number	Charge gain (V/pC)	Gate voltage, Vg (mV)	DC output (V)	noise w/ 440 pF test capacitor (fC/rtHz)			open input (fC/rtHz)		
				1 Hz	10 Hz	200 Hz	1 Hz	10 Hz	200 Hz
average	5.01	-158.43	0.47	0.077	0.0131	0.0022	0.065	0.0084	0.0013
std dev	0.04	37.18	0.23	0.015	0.0016	0.0003	0.018	0.0014	0.0001

Table 23. Comparison of average characteristics of miniaturized charge amplifiers using a 2SK369GR JFET (top) and 2SK369BL JFET (bottom).

		noise w/ 440 pF test capacitor (fC/rtHz)			noise w/ open input (fC/rtHz)		
		1 Hz	10 Hz	200 Hz	1 Hz	10 Hz	200 Hz
average	2SK369GR	0.061	0.0118	0.0021	0.047	0.0076	0.0013
average	2SK369BL	0.081	0.013	0.002	0.070	0.009	0.001

Thirty-two units were delivered to Virginia Tech, two units were provided to ARL, and two units were retained at SAIC. The design, predicted and measured noise characterization, and instructions for use were described in Huntley (June, 2011).

D. Jiefang Li, Passive Sensors

D.3.1. Materials Issues and Characterization

D.3.1.1. Metglas and Metglas/Epoxy Characterization:

Metglas/Epoxy Interface:

We studied the Metglas and epoxy relationship on the surface of the Kapton outside of the core of the sensor. We placed a complete understanding of the mechanics of this phase of the sensor.

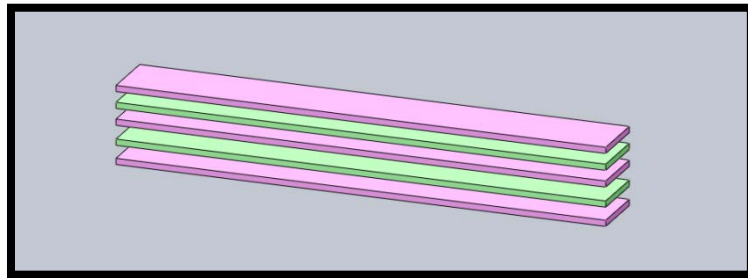


Figure 119. Illustration of three layers of Metglas with two bonding layers of epoxy.

A mathematical model was constructed that confirmed our assumptions that the strain transfer of the magnetostrictive material was a function of the mechanical properties and thickness of the epoxy, as shown in Figure 119. If we are to assume the interaction force is F , and the cross section of Metglas and epoxy is S_M and S_E then the stress of Metglas and epoxy can be shown as:

$$\sigma_M = F / S_M \quad (243)$$

$$\sigma_E = F / S_E \quad (244)$$

The volume ratio of Metglas to epoxy is given by:

$$\frac{V_M}{V_E} = \frac{S_M}{S_E} \quad (245)$$

The Young's modulus of Metglas and epoxy are E_M and E_E , respectively. Combining these equations will give an expression for the magnetostriction of the three layers of Metglas and epoxy composite:

$$\lambda_C = \sigma_M / E_M = F / S_M E_M = F / k V_M E_M \quad (246)$$

If the magnetostriction of Metglas is λ_M , then the magnetostriction of the composite, λ_C , is:

$$\lambda_C = \lambda_M - \frac{\sigma_E}{E_E} = \lambda_M - \frac{F}{S_E E_E} = \lambda_M - \frac{F}{k V_E E_E} \quad (247)$$

From (D1.11) and (D1.12), we can get one expression for the composite magnetostriction:

$$\lambda_c = \lambda_m \frac{V_E E_E}{V_E E_E + V_M E_M} \quad (248)$$

It is obvious from this equation that for a given magnetostrictive phase, the Young's modulus and volume of epoxy dictate the overall strain of the composite. However, experimental data is still lacking to confirm this expression is true for our composite. This is made more complicated by variables in the attachment of the Metglas to the PZT/Kapton core. This quarter work was done to explore the Kapton-Metglas and Metglas-Metglas interfaces. Table 24 shows the excess variability in sensor properties. Sensors in Table 24. This table shows an increase in properties with change in Metglas attachment improvements for PZT cores with similar electrical properties. reveal very similar loss and capacitance values yet charge and ME voltage differ greatly.

Table 24. This table shows an increase in properties with change in Metglas attachment improvements for PZT cores with similar electrical properties.

		Capacitance	Dielectric loss	ME voltage	ME charge
PZT sensor	Previous	384	1.7%	1913	940
	Present	385	2.01%	2073	1065
PMN-PT sensor	Previous	677	2.01%	2620	1720
	Present	711	2.05%	2870	2168
CPSC sensor	Previous	820	2.3%	1850	1520
	Present	867	2.1%	3590	3045

Current layup techniques are utilizing the vacuum pump and heat press to increase epoxy flow and provide thin uniform layers within the Metglas laminate stack. Observations have been made that suggest the level of vacuum pressure may dictate the thickness of the epoxy layer. ME properties have been enhanced in sensors made with lower vacuum pressures or pressures closer to ambient pressure. These results suggest a more formal investigation into epoxy thickness as a function of vacuum pressure is needed. The results of initial experiments on this task are shown in Table 25 below. The vacuum pressure applied for Metglas adhesion to the PZT cores is varied. The PZT core electrical properties are in close agreement prior to Metglas attachment. With this in mind, the results should reflect only the quality of Metglas adhesion. Although a small trend in upward ME voltage as vacuum pressure is decreased is seen, the difference in the minimum and maximum values are still within the range of measurement repeatability noise seen in past experiments.

Table 25. Experimental results for pressure dependence cure on Metglas properties.

Pressure (in.Hg)	Capacitance (pF)	Dielectric loss	Resistance (GΩ)	ME voltage (mV/Oe)	ME charge (pC/Oe)
-16	398	1.61%	60	1.57	895
-12	403	2.23%	61	1.61	920
-8	418	1.58%	65	1.79	1000
-6	411	1.50%	70	1.82	970

Earlier attempts to strengthen the Metglas bond to the sensor core were not fruitful in increasing ME voltage. Attempts to thin the layers of epoxy within the Metglas stacks above and below the sensor core also should have optimized the strain transfer, however, ME voltages are still not increasing in a predictable fashion. Some of the unpredictable nature may be due to lack of precise control of variables such as cure pressure. Current vacuum bagging techniques may not be as repeatable or as controllable as previously thought. To test these assertions, experiments to determine the effect of cure pressure on strain transfer and therefore ME voltage will be done using a different pressing mechanism. To accomplish a more controllable and constantly repeatable cure pressure a simple press has been proposed.

The proposed press is based on the equation for force.

$$P = \frac{mg}{S} \quad (249)$$

Where m is the mass of the hammer and additional weights, S is the area of force for the ME composite/Metglas. For the press platen to sufficiently cover the complete 8 cm sample, the platen was designed to be 10 cm in diameter. Using this dimension the calculated minimum mass would need to be approximately 21 kg. By designing a platen with a mass equal to approximately 20 kg, additional weights can be added in small increments to precisely and repeatably control the force. An illustration showing the design and the added weights is shown in Figure 120.

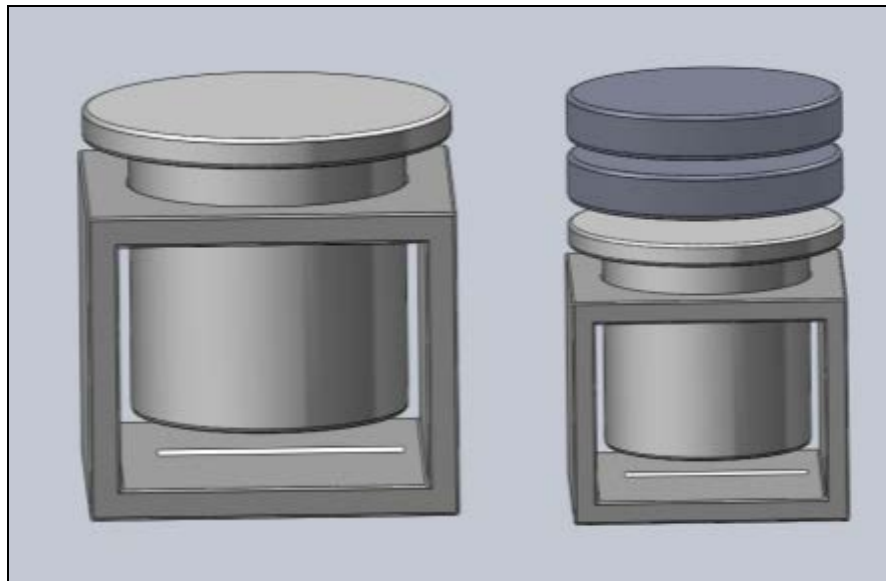


Figure 120. Metglas press for controlling curing pressure.

Other notable increases in ME voltage have been obtained from poorly adhered Metglas which is counterintuitive and may well mean ME voltage is a poor indicator of uniform construction. It is thought that if one side of the sensor has poorly adhered Metglas then the well adhered side dominates the output and performs almost entirely in a bending mode. One sensor in particular with one well adhered Metglas layer (on top of core) and one poorly adhered layer (below core) revealed a promising ME voltage of 1.91V/Oe (1815pC/Oe).

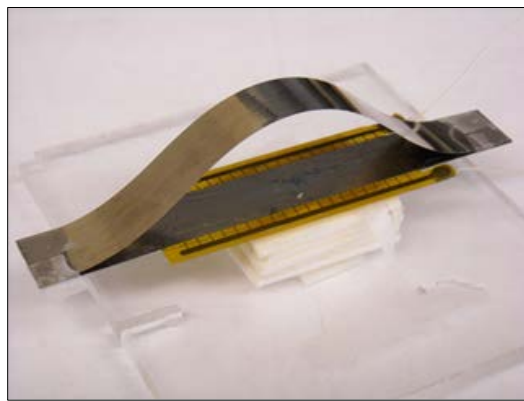


Figure 121. Sensor with one additional 9 cm piece of Metglas attached to top.

The top layer was then separated from the core altogether with only the ends of the Metglas still adhered and the ME voltage was still large at 1.3V/Oe (1230pC/Oe). However, releasing one end completely showed a small increase from the initial output to 1.96V/Oe (1685 pc/Oe). The maximum output 2.04 V/Oe was achieved by removing the top layer of Metglas completely. These observations have led to more inspection into bending mode operation and manipulation of the methods and forms of attaching Metglas. The newest experiments in Metglas attachment involve adding additional layers by attaching them only at the ends to see the effects on output. A set of tests were done without any extra Metglas added, one with an additional 8 cm piece

attached on the ends of one layer and one with an additional 9 cm piece attached on the ends of one layer (shown in Figure 121).

The results (shown in Table 26) reveal no appreciable difference in ME voltage output for the three different scenarios. However, the H_{dc} bias needed to achieve optimum bias is interesting to note. The addition of the 9 cm Metglas strip decreased the H_{dc} bias although the maximum ME voltage is not increased. Although, the attachment has not changed the mode of sensor operation it has served to somehow increase flux concentration. This may prove an advantage in future sensor biasing requirements.

Table 26. ME Voltage output and Hdc bias for three conditions of Metglas.

Test condition	DC bias	ME voltage (V/Oe)	Optimized bias	ME voltage (V/Oe)
Without Metglas	8.51Oe (0.32 V)	1.755	8.51 Oe	1.755
8 cm long	8.51Oe (0.32V)	1.663	10.05 Oe	1.742
9 cm long	8.51Oe (0.32 V)	1.716	7.66 Oe	1.724

Metglas:

In an effort to simplify construction and reduce variables associated with the magnetostrictive composite of Metglas and epoxy, a thicker Metglas was evaluated for replacement as the magnetostrictive phase. A thicker section of Metglas may be able to replace the three layer composite of the previous Metglas by maintaining the same quantity of flux capture while also increasing strain transfer by avoiding multiple epoxy–Metglas interfaces. Experiments were performed with the previous arrangement of Metglas-epoxy composites using Metglas that is approximately 21 microns thick with epoxy. The results of these experiments were compared to a similar sensor core with 40 micron thick Metglas attached.

Table 27. ME properties with changing Metglas thickness

		Capacitance (pF)	Dielectric loss	ME voltage (V/Oe)	ME charge (pC/Oe)
Thin Metglas/PMN-PT	3-layer	620-670	2.2-2.5%	~3	2320-2450
Thick Metglas/PMN-PT	1-layer	608	2.4%	0.42	352
	2-layer	~608	~2.4%	0.52	440
	3-layer	~608	~2.4%	0.73	618

D.3.1.2. Core Epoxy

Core Epoxy Selection:

To increase the understanding of the epoxy properties and their effect on the sensor properties, sensors were constructed using different types of epoxy. It is thought that increased flexibility of the cured epoxy may be responsible for the enhanced sensor properties observed with the Stycast

epoxy brand. Epoxies were chosen over a range of glass transition temperatures in an effort to observe a trend in performance with changing elasticity. The most flexible epoxy chosen was a urethane casting compound. The urethane compounds have a large range of glass transition temperature but all are well below the Stycast T_g of 25°C. The Epotek epoxy was chosen because of its high T_g which is above the West Systems epoxy blend currently used for the Metglas-epoxy composite on the exterior of the sensor. Epoxy with a T_g below room temperature should remain “rubbery” even after cure and those with glass transitions greater than room temperature should become more brittle after curing.

Test results showed no obvious trend in dielectric loss or capacitance with changing epoxy elasticity. The impedance angle is also listed in Table 28 as an indication of effective poling. The impedance angle for each of the four sensors revealed no obvious trend in impedance angle yet illustrates the randomness of effective poling. It may be that the deficiency in poling is a direct result of the epoxy which cured between the copper electrode surface and the PZT. More work needs to be done to insure that little to no epoxy exists between the copper electrodes and the PZT. The sample with the best poling condition was the West Systems glue which is more brittle than the Stycast that is currently used.

Table 28. Core electrical property deviations with different interior epoxy.

	Glass Transition	Hardness	Measured Cap. (10kHz)	Measured Loss (10kHz)	Impedance Angle (1600V poling)
Urethane	<0C	ShoreA80 (Shore D30)	517pF	4.0%	-54°
Stycast	<25C	Shore A62	459pF	1.7%	-14.2°
W.Systems	52.2C	ShoreD83	867pF†	6.1%†	-3.23°
Epotek	>95C	ShoreD67	423.3pF	3.8%	-23°

†= values recorded at 1kHz.

As noted earlier, the presence of epoxy may lead to poor poling and lower than expected impedance angles. The loss contribution from this interface was modeled in much the same way as the piezoelectric fibers in an earlier section. The ideal interface is illustrated in Figure 122 below. This scenario assumes there is no epoxy between the electrodes and the piezoelectric fibers.

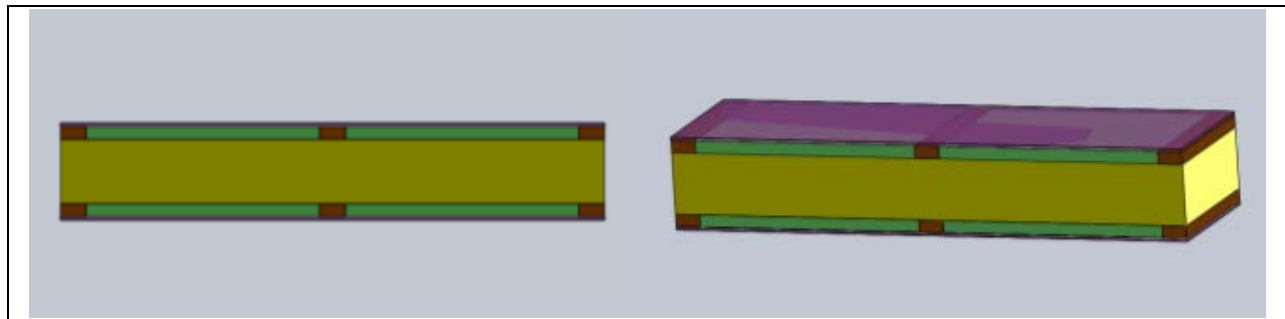


Figure 122. Schematic of calculated condition with ideal electrode connection.

The equivalent circuit for this diagram (Figure 123) can also be constructed and used for analysis.

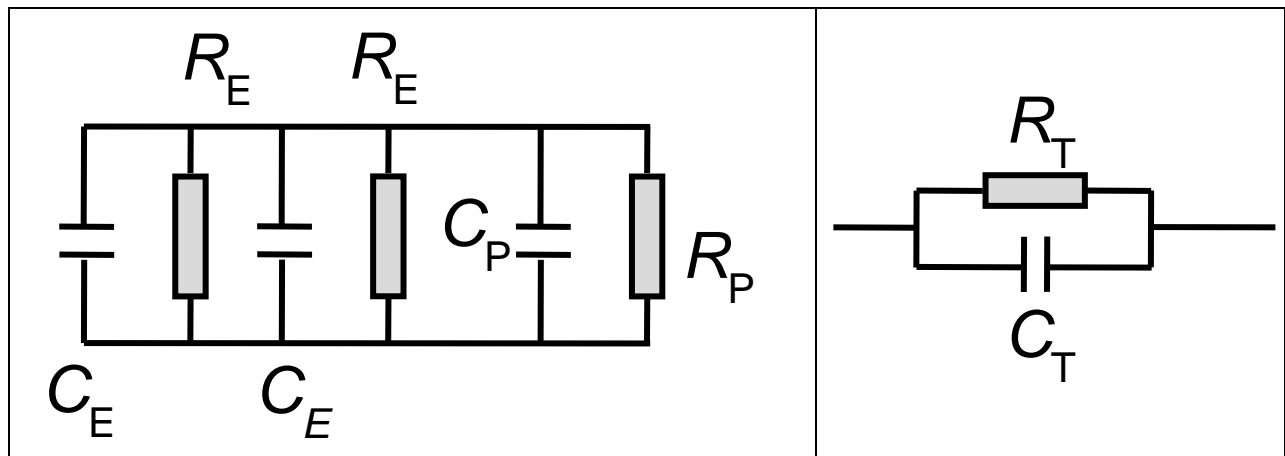


Figure 123. Equivalent circuit for ideal bonding electrode bonding condition.

From the simplified equivalent circuit, we can easily obtain the total resistance (R_T) and capacitance (C_T):

$$R_T = \frac{\frac{1}{2}R_E R_P}{\frac{1}{2}R_E + R} \quad (250)$$

$$C_T = 2C_E + C_P \quad (251)$$

The total dielectric loss can be written:

$$\begin{aligned}
 \tan \delta_T &= \frac{1}{\omega C_T R_T} \\
 &= \frac{1}{\omega \left(\frac{1}{2} R_E R_P \right) (2C_E + C_P)} \\
 &= \frac{\frac{1}{2} R_E + R_P}{\omega R_E C_E R_P + \frac{1}{2} \omega R_E C_P R_P} \\
 &= \frac{\frac{1}{2} R_E + R_P}{\frac{R_P}{\tan \delta_E} + \frac{\frac{1}{2} R_E}{\tan \delta_P}} \\
 &= \tan \delta_P \left[\frac{\left(\frac{1}{2} R_E + R_P \right) \tan \delta_E}{R_P \tan \delta_P + \frac{1}{2} R_E \tan \delta_E} \right]
 \end{aligned} \tag{252}$$

The dielectric constant and dielectric loss of the Stycast epoxy used in the core of the composite were measured in the lab and found to be 3.7, and 0.4%. The PZT dielectric constant and loss has been reported to be as low as ~ 1900 and 1.2% at low frequency, respectively. Using these values the relationships for the epoxy and piezoelectric phase can be determined. Using the relationships it can be seen that the loss in the ideal condition is based solely on the loss of the piezoelectric phase.

$$\tan \delta_T \approx \tan \delta_P \tag{253}$$

However, a more realistic representation of the interface is given in Figure 124.

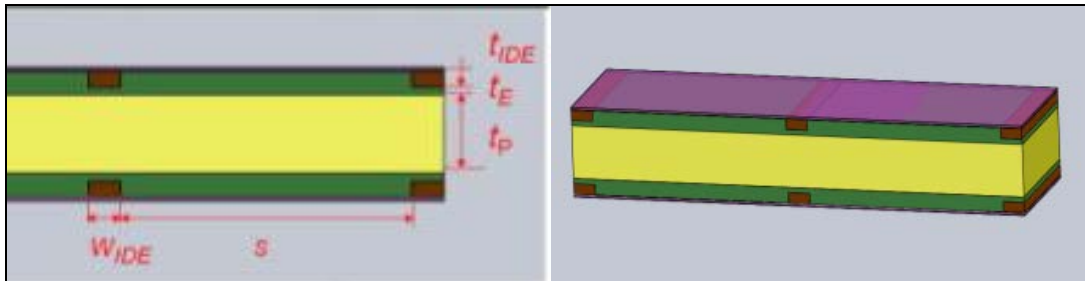


Figure 124. Illustration of actual electrode interface to piezoelectric fibers.

The equivalent circuit for the non-ideal interface is illustrated below in Figure 125. Calculations are made easier by simplifying the circuit from the initial circuit (top) to the simplified circuit (bottom).

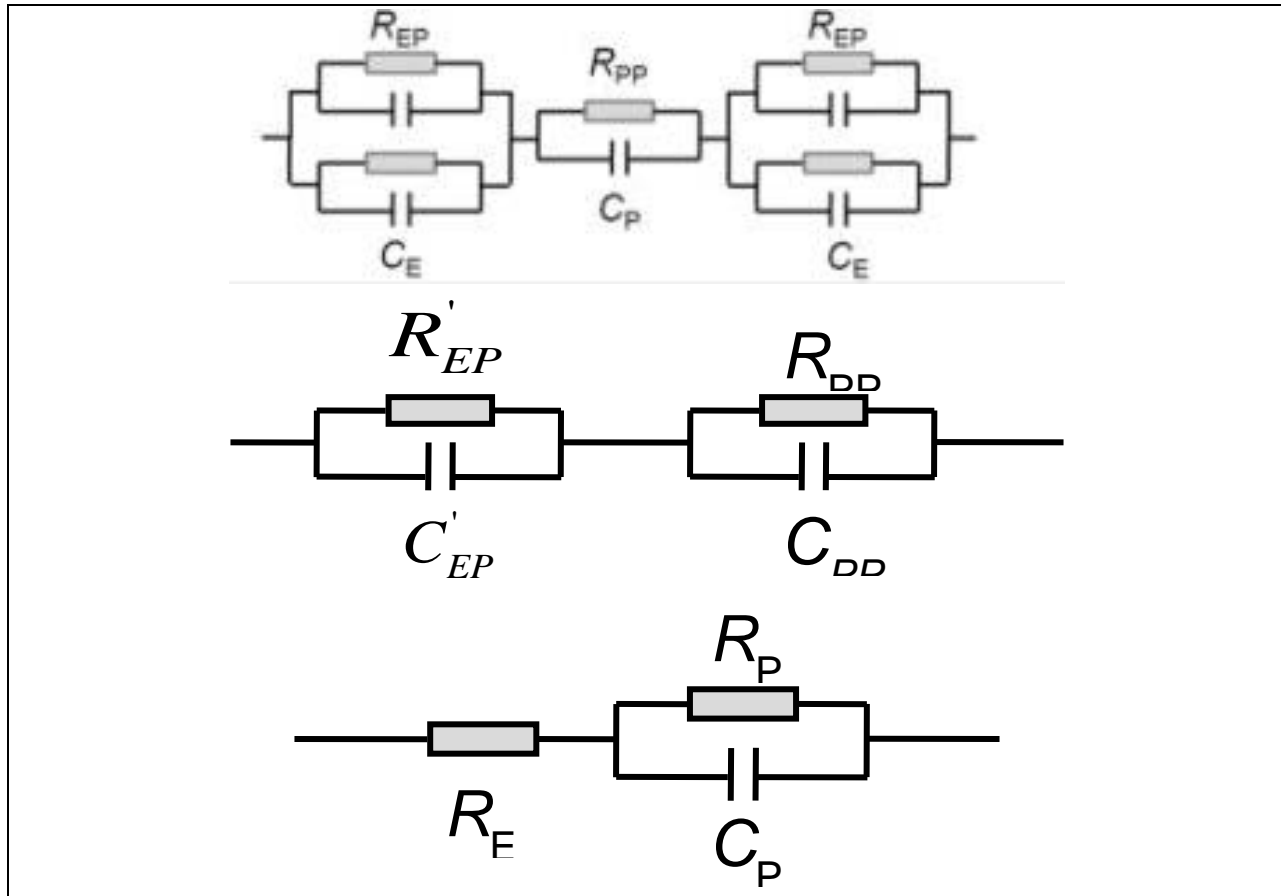


Figure 125. Equivalent circuit for the non-ideal bonding of electrodes to piezoelectric fibers simplified from top to bottom.

The simplified composite can be represented by R_P and C_P in parallel with an epoxy resistance, R_E , based on the thickness of the epoxy, t_E . The capacitance of the interfacial bonding (t_E) was ignored because it was negligible to the capacitance of PZT fibers. The $\tan \delta$ at low frequency can then be written as:

$$\begin{aligned}
 \tan \delta &= \omega R_E (C_P + \frac{1}{\omega^2 R_P C_P}) + \frac{1}{\omega R_P C_P} \\
 &= \frac{1}{\omega R_P C} (1 + \frac{R_E}{R_P}) \dots \text{(Low frequency)} \quad (254)
 \end{aligned}$$

From Equation 254, if the C_E is larger, the R_E must be smaller.

$$C_E = \frac{\epsilon_E S}{t_E} \quad (255)$$

And from this it is easy to conclude that if the layer of epoxy is small, the C_E increases and the R_E is lowered. This condition results in a smaller dielectric loss of the sensor. As the t_E is reduced the sensor approaches the ideal condition and therefore approaches the loss of the piezoelectric phase found earlier. The other observation from these calculations is that the electrode width has some effect on the loss as well. If the electrode width is increased, s will be increased, C_E is larger, and the R_E is smaller, then dielectric loss of sensor should also be decreased.

Experiments are being planned to find methods of constructing sensors with even less epoxy between the copper traces of the electrodes and the surface of the PZT. However, poling breakdown and moisture mitigation still need to be addressed as well. Decreasing the amount of epoxy alone may not effectively reduce the loss and may result in less moisture mitigation.

One option that has been entertained is creating a softer, more pliable interface for contacting the PZT surface. The copper traces were coated with a liquid tinning solution (Figure 126) in hopes of 1) creating an intermediate layer that could be more easily pressed against the surface of the PZT and 2) lead to an epoxy free joint by utilizing a hot press to bond the low melting point tin to the surface of the PZT.

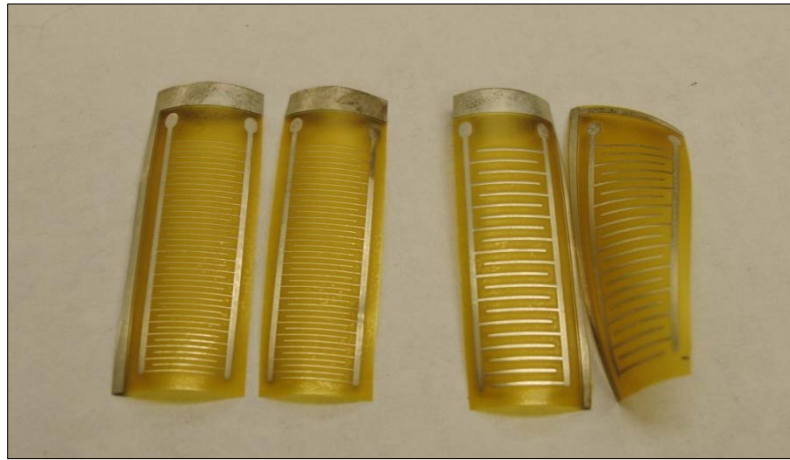


Figure 126. Copper electrodes after coating with liquid tinning solution.

D.3.1.3. Kapton and interdigit vs ME response of sensors

We have fabricated sensors using ID electrodes and Kapton™ tapes of different thickness. Previously sensors were fabricated using 17 μm thick copper ID electrodes on 25 μm thick Kapton™ tapes. Reducing the thickness of the copper and Kapton™ layers should bring the magnetostrictive ad piezoelectric layers into closer proximity, improving ME response through increased stress transfer. Sensors were therefore manufactured with electrodes consisting of 4 μm copper traces on 12.5 μm thick tapes. Moreover, widths and spacings of the ID electrodes were also varied in an attempt to maximize the ME response of the laminate structure. Figure

127 shows the noise floor measurement of several sensors with different interdigit/electrode configurations. The trend seems to suggest that narrower digits with larger interspacings seem to result in lower noise.

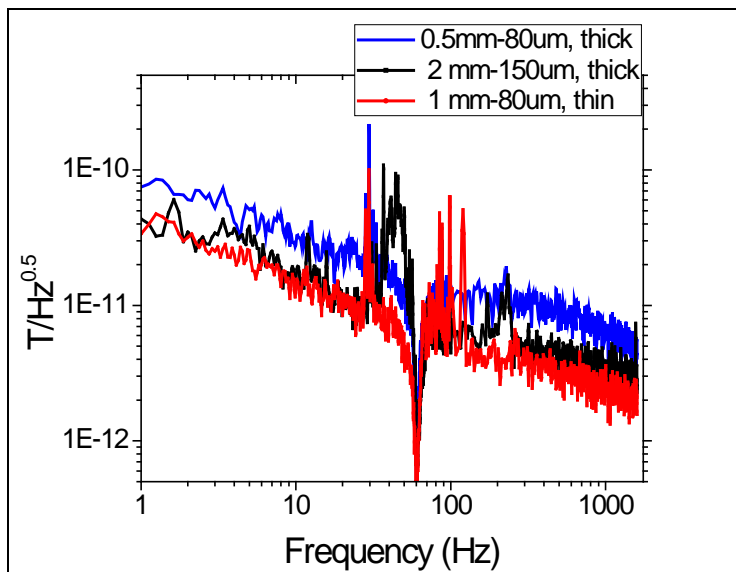


Figure 127. Noise floor comparison of sensors fabricated with various interdigit geometries and Kapton® thicknesses.

Table 29. Summary of ME response of sensors fabricated with different thickness electrode and differently spaced interdigits.

Electrode Dimensions (Cu width-ID spacing)	Kapton Thickness/ Cu Thickness	ME voltage (V)	Output charge (pC)
2mm-150μm	25(μm)/17(μm)	2.2020	753.1
1mm-150μm	25(μm)/17(μm)	1.565	1517
1mm-80μm	25(μm)/17(μm)	1.680	1660
0.75mm-80μm	25(μm)/17(μm)	1.360	2296.3
0.75mm-80μm	25(μm)/17(μm)	1.218	1960.2
0.5mm-80μm	25(μm)/17(μm)	0.833	2364.5
1mm-150μm	12.5(μm)/4(μm)	1.5038	1364.4
1mm-80μm	12.5(μm)/4(μm)	1.5170	1410.8
0.75mm-80μm	12.5(μm)/4(μm)	1.2125	1906.2

Table 29 summarizes the ME voltage response and output charge characteristics of sensors fabricated with different electrode geometries. Decreasing the spacing between digits tends to decrease output voltage and raise output charge, while changes in digit width and electrode thickness have little effect on ME voltage and output charge.

Electrode Geometry:

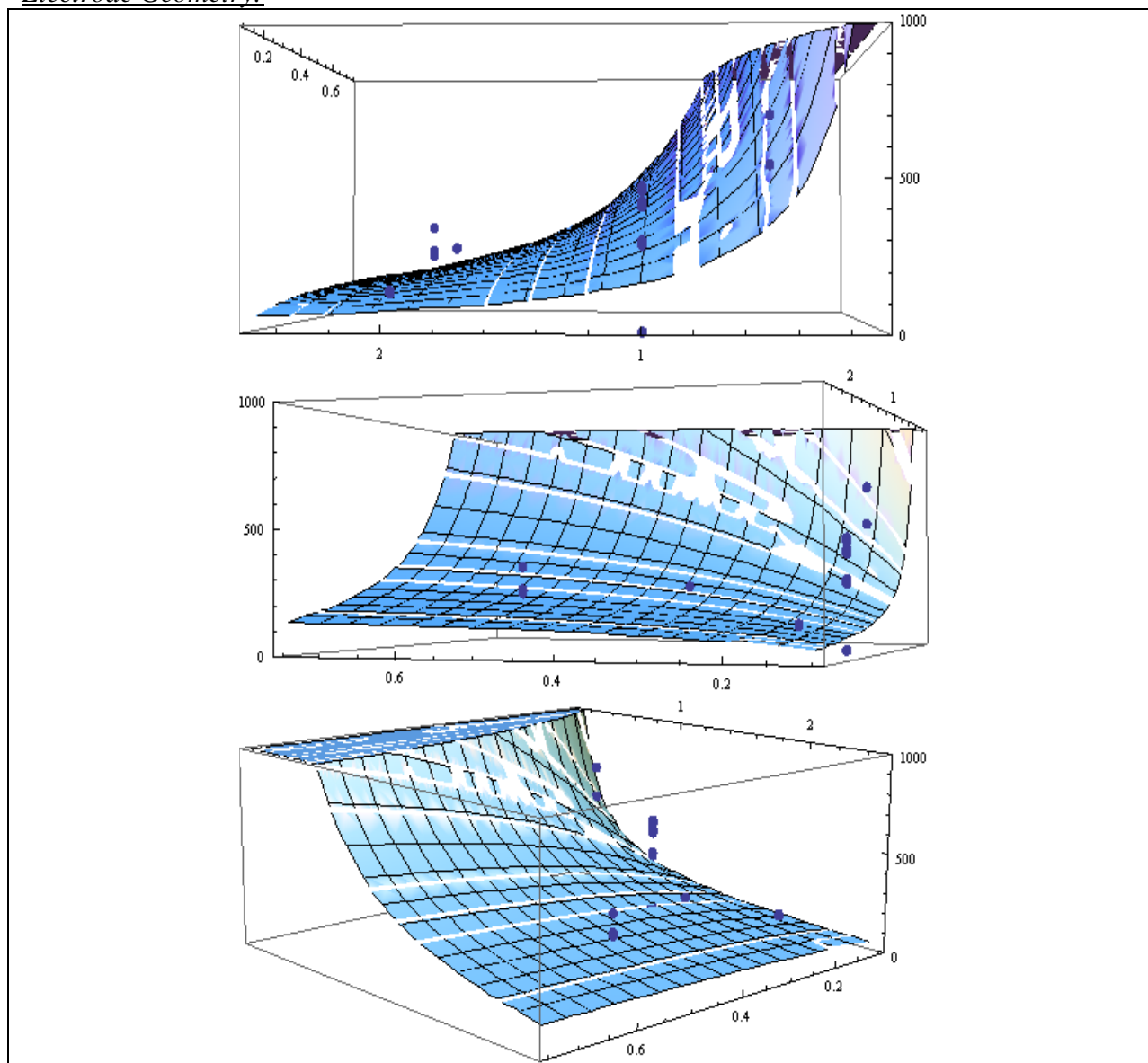


Figure 128. Comparison of current PZT sensors characteristics to previously modeled values based on previous obtained empirical data.

Electrode modeling albeit relatively accurate continues to improve as more sensors are manufactured. The current model shown in Figure 128 was constructed using empirical data from past experiments with different electrode spacing. A survey of current PZT based sensors made with advances in fabrication and poling was utilized for comparison with previous modeled values. The model is constructed by estimating sensor capacitance based on electrode geometry and a constant-width dead zone assumption. The following have constant-width dead zones equal to that of the electrode fingers, and an epoxy thickness of $0.5\mu\text{m}$. Inclusion of loss values should help to improve estimations but agreement is still very close. We hope to use the model to experiment with different electrode trace widths and spacing. Application specific

quantities like charge, voltage and capacitance can be obtained by varying the dimensions referenced by the model diagram.

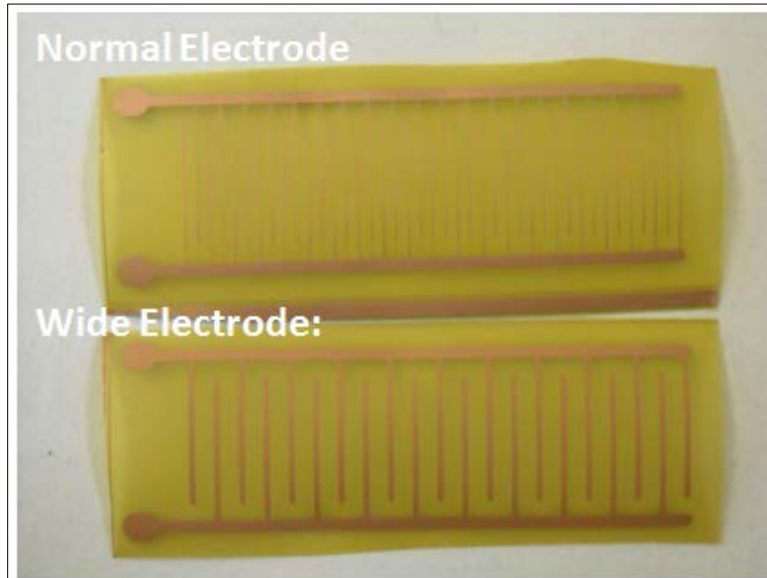


Figure 129. Comparison of most often used electrode spacing, labeled Normal Electrode, and new modeled geometry.

To test the validity of our empirical model and determine if electrode geometry indeed affects loss as the model predicted, an electrode spacing and trace width was chosen from the modeled parameters.

A sensor was made using a PZT core and the wider electrodes. The wide electrode has trace width of 300 microns which is twice as thick as the most commonly used electrode and the distance between digits is 2.5mm compared to the normal 1 mm spacing. From the model the new spacing should decrease the 1Hz equivalent magnetic noise from $\sim 23 \text{ pT}/\sqrt{\text{Hz}}$ to $14 \text{ pT}/\sqrt{\text{Hz}}$.

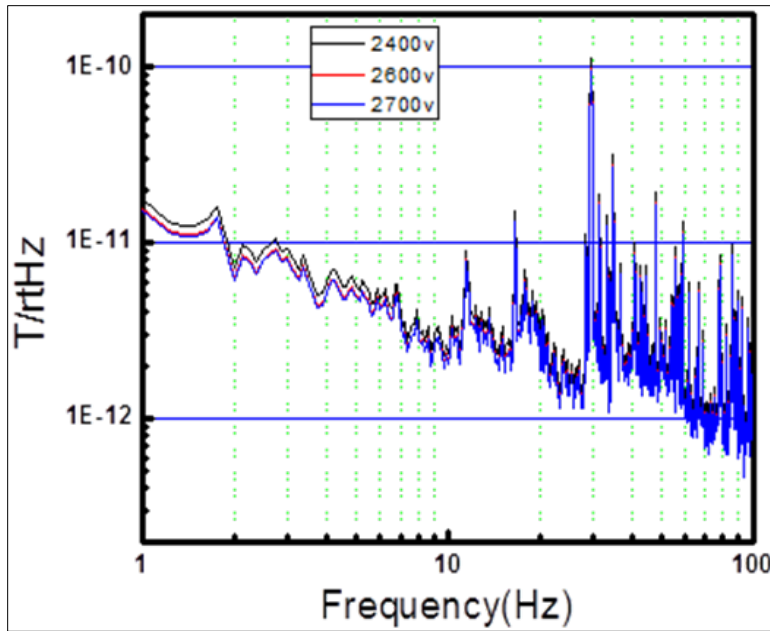


Figure 130. Equivalent noise floor with increasing charge due to larger poling voltage assuming electrical noise pattern stays the same.

The new spacing requires some optimization to obtain the ideal poling voltage which increases as interdigit spacing increases. Preliminary calculations using the E_c of the PZT, trace width and spacing suggested 2400V. However, attempts to add more voltage did result in larger charge output which ultimately leads to a lower noise floor. The noise floor was measured using the charge obtained at a poling voltage of 2400V. Upon repoling the charge was increased considerably. The predicted noise floor is shown in Figure 130, along aside the original trace. The noise floor plot shown was obtained with the 2400V poling and converted to show the effect of increased charge assuming all electrical noise stays constant. This is encouraging because it very closely approaches the modeled prediction of $14 \text{ pT}/\sqrt{\text{Hz}}$.

Since PMN-PT possesses a much lower dielectric loss than PZT, sensors were made using the new electrode spacing and PMN-PT as the piezoelectric phase. The results of the experiment are tabulated in Table 30. ME charge and capacitance showed very small reductions when compared to the 0.85mm spacing quantities. However, a considerable increase in ME voltage was obtained while also decreasing the dielectric loss by more than 30%. The model has proven to be a useful and necessary tool in predicting and specifying sensor properties.

Table 30. Mn doped PMNPT used with two differing electrode spacings showing loss reduction of larger spacing.

Spacing	C (pF)	$\tan\delta$ (%)	α_V (V/Oe)	α_Q (pC/Oe)
0.85mm	495	1.1	2.3	1500
1.5mm	307	0.68	2.98	1345

Electrode Selection:

We compared electrodes made with different Kapton substrates to select a vendor and technique for future production. Because Kapton thickness and composition varies so much from

distributor to distributor we felt we could further reduce variables in sensor qualities by choosing a single thickness and manufacturer for all future sensor electrodes.

A copper coated Kapton from Dupont was chosen in two different thicknesses (13 and 27 micron). Electrodes fabricated from these two types were compared to an electrode made using Kapton from a Shanghai manufacturer which was 29 microns thick. Also, one of each type had a layer of gold plated onto the copper surface in an effort to keep the copper surface from oxidizing. More than one interdigital spacing was made with each Kapton. The two spacings compared were the most often utilized 0.85mm and the new 1.5mm.

Sensors were made by different people utilizing all configurations and compared to determine which performed best. It was deciding from these tests to continue with the Shanghai manufacturer. The gold coated had very little overall effect on sensor performance and will not be added to future electrodes. Following the tests, the Kapton specifications were received from the Shanghai manufacturer and in house characterization of loss, moisture absorption and thickness will follow.

Electrode geometry (spacing, trace thickness and trace width) is as important to electrode performance as Kapton substrate. This quarter we continued to research the different electrode geometries. The intention of this research is to collect as much experimental data as possible to steer future fabrication direction. After determining electrode spacing and line width effect on the sensor electrical properties it may be possible to adjust future sensors to meet specified electrical quantities based solely on electrode dimension. This month two PMN-PT sensors were constructed with electrodes having a 2mm interdigit spacing and two were made with a 2.5mm interdigit spacing. The trace widths of each set were also changed so one was made with a 150 micron trace width and one with a 250 micron trace width. The measured properties are presented in Table 31.

Table 31. Properties of four PMN-PT sensor using different electrode trace width and interdigit spacings

Electrodes		C (pF)	α_V (V/Oe)	α_Q (pC/Oe)	$\tan\delta$ (%)
0.2 mm PMN-PT 2 mm d	250um trace	384 (298)	4.36	1900	1.33
	150um trace	306 (233)	4.54	1668	1.39
0.2 mm PMN-PT 2.5 mm d	250um trace	234 (188)	4.82	1599	1.21
	150um trace	186 (145)	4.50	1293	1.35

From the table it can be seen that a smaller trace width seems to reduce the measured capacitance. However, other sensor quantities are dependent on many more variables and a generalized trend or rule cannot be determined by direct measurement comparison. The ME voltage and output charge depend largely on integrity of the Metglas phase. Although it seems the widest spacing and the largest trace produces the largest ME voltage more testing needs to be done before this can be assumed to be a trend. The largest charge was found with the narrower spacing and the wide trace. These tests may lead us to tailor our geometry to the application but

more data is needed for trend determination.

Variable Electrode Thickness

We also optimized electrode characteristics such as Kapton and copper thickness while also utilizing a supplier that recognizes our interest in maintaining consistent supply with consistent specifications. In the past, we have selected optimum performing electrodes and found that subsequent batches did not perform as well as others. The goal was to choose an electrode based on empirical data and then give these specifications to the supplier of choice. Current electrodes are made from both domestic and international suppliers.

We chose to experiment with three different electrode scenarios. The electrodes used are listed in Table 32 below and all have an copper trace interdigit spacing of 2mm center to center.

Table 32. Electrodes available for experiments to determine optimum characteristics.

	Kapton thickness (um)	Cu trace thickness (um)	Overall thickness (um)
Electrode 1	12	9	21
Electrode 2	18	13	31
Electrode 3	20	18	38

A sample of the data from the experiments is shown in Figure 131. This batch of samples was made by the same individual. This type of experiment was performed to better disregard fabrication variables among various persons.

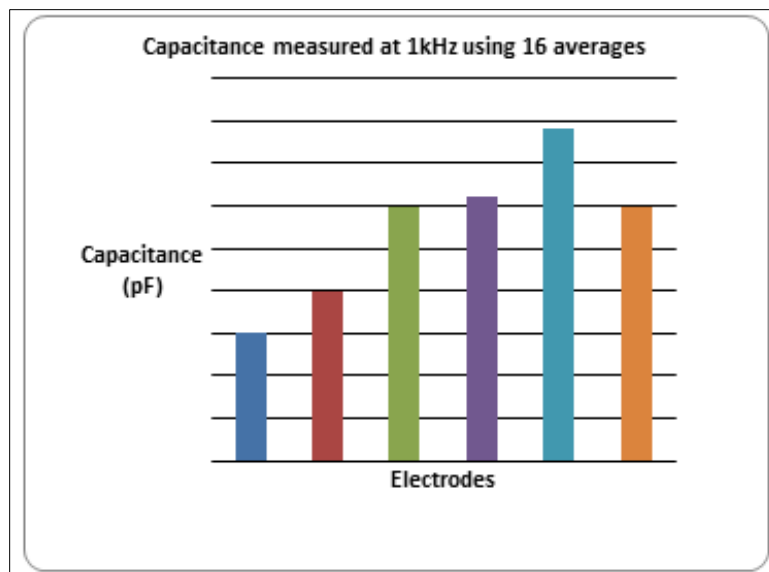


Figure 131. Measured capacitance data for a single batch of samples made with different electrodes.

Each electrode was used twice in this test and one can see from this data that the capacitance has a large degree of variability in samples of the same as well as different electrode thicknesses. For 18/13 electrodes, there is approximately 3% difference in the capacitance measurements and for 12/9 electrodes, a 5% change is visible. Only the 20/18 electrodes seem to remain consistent

at less than 1% deviation. It is not feasible to average the two similar electrodes and compare them to the other types because the deviation among same types is on the same scale as that for different types. As for capacitance change with changing electrode these results remain inconclusive. Figure 132 shows a comparison of measured dielectric loss of the same data set. From this it is apparent that all the electrodes seem to fall below 2% loss and the trend in loss is very close to the opposite trend in capacitance. However, the deviations in both sets are still inconclusive. A more thorough data set is still being accumulated.

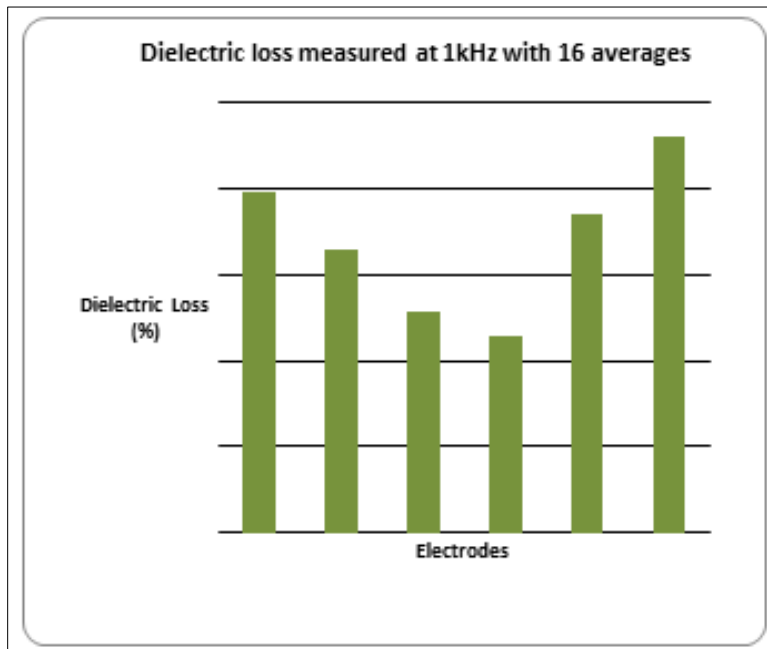


Figure 132. Measured dielectric loss data for a single batch of samples made with different electrodes.

The most interesting observation derived from this set of experiments is the effect of electrode thickness on ME voltage and charge measurements. One can see the total thickness of the electrodes used in this experiment differ greatly with electrode one ($21\text{ }\mu\text{m}$) measuring nearly double the thickness of electrode three ($38\text{ }\mu\text{m}$). Because two electrodes are used in every sensor this change is also doubled which should move the Metglas much further from the centerline of a sensor made with different electrodes. For example, a PZT ($200\mu\text{m}$) sensor made with two $21\mu\text{m}$ electrodes can be no thinner than $242\text{ }\mu\text{m}$. The same sensor made with electrode three could be no thinner than $276\text{ }\mu\text{m}$. This represents an overall change of $30\mu\text{m}$ which should have a large effect on the strain transfer mechanism that yields ME voltage when field is applied to our sensor. Figure 133 shows the ME voltage characteristics for the batch of samples previously discussed in figures one and two. The thickest of the three electrodes is in the center and exhibits the largest ME voltage. The thinnest electrode is at the far right and the output seems quite lower. The deviation in the results doesn't allow for any large conclusion but it does seem that the added distance doesn't hurt the performance of the sensor rather it may increase the sensor performance. This is counterintuitive when considering the increased distance from the PZT centerline and its effect on the mechanism of strain transfer.

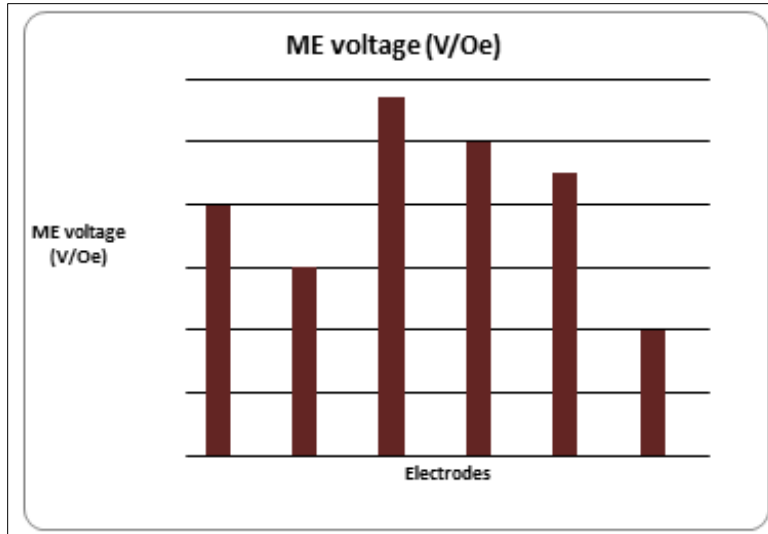


Figure 133. Measured ME voltage output for a single batch of samples made with different electrodes.

Electrode Layout

A new and improved electrode pattern was designed. The new Kapton sheet of electrodes will have a much larger footprint than earlier iterations. This large print will allow for a larger number of sensors to be made in one fabrication cycle. The new layout shown in Figure 134 shows how the symmetry can be used to make as little as twelve sensors at one time in eight separate cycles or as many as 48 at one time in a single cycle. The flexibility is necessary in this stage to allow for smaller batches in experimental stages.

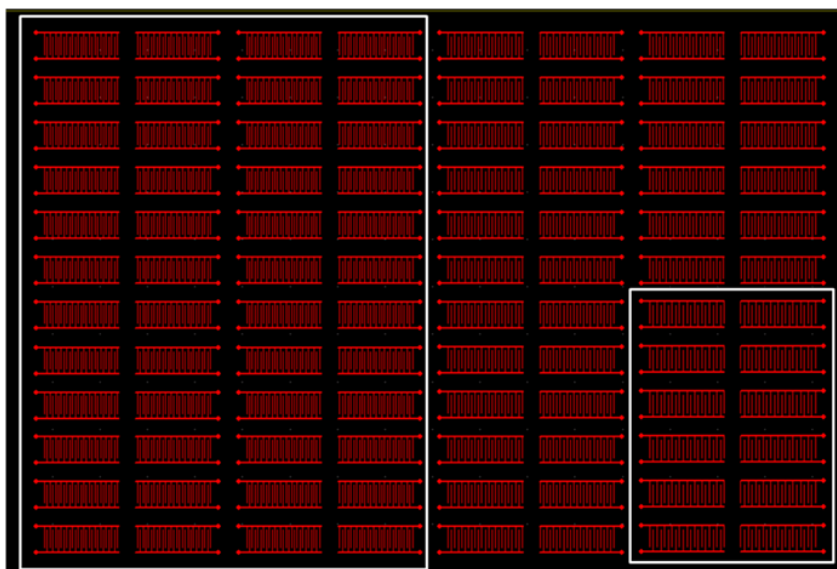


Figure 134. New improved large footprint electrode layout.

D.3.1.4. Piezoelectric Phase: Loss Analysis

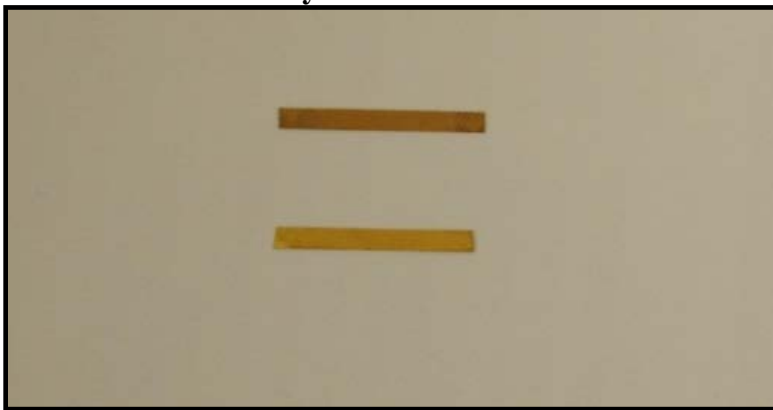


Figure 135. Gold sputtered PZT fibers used for dielectric loss tests.

Sensor component characterization was performed to understand the piezoelectric contributions to sensor loss. Loss measurements of the most recently fabricated sensors are between 1.5 and 2.5 percent. We would like to establish a model of the sensor that allows us to find the loss floor. To accomplish this, it was important to know the minimum loss possibly achieved by the core piezoelectric phase. Tests to characterize this component of the sensor involved testing the dielectric loss of the core material outside of the sensor construction.

Individual PMN-PT and PZT fibers were sputtered with gold for dielectric measurements outside of the sensor. Results show an unpoled loss for PMN-PT of greater than 4% (Figure 136). After poling, the dielectric loss decreases to well below 2% (Figure 137). Although this value is much higher than the 0.5% stated by the manufacturer, it very closely resembles the overall measured loss of our constructed sensor. This may lead to the assumption that epoxy loss values are less important in the overall loss of the sensor and the loss of the sensor is only a function of the minimum loss and poling quantity of the piezoelectric phase.

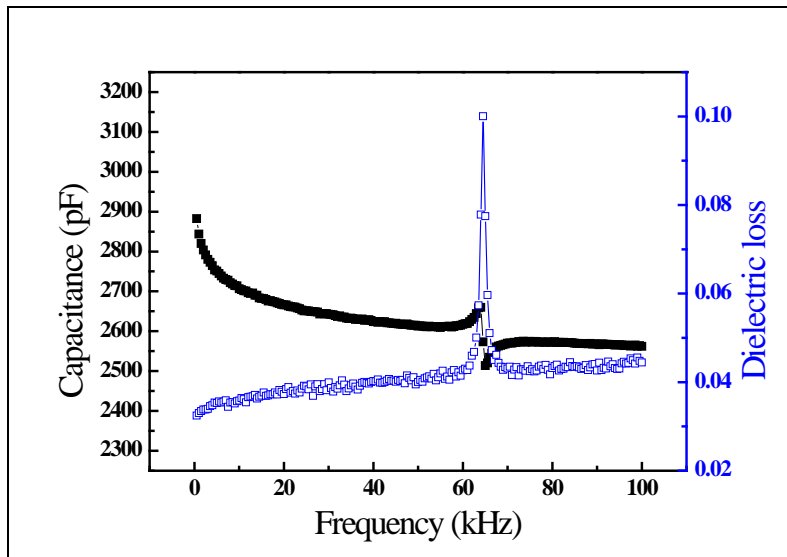


Figure 136. Unpoled capacitance and loss values for PMN-PT showing loss >4% at low frequency.

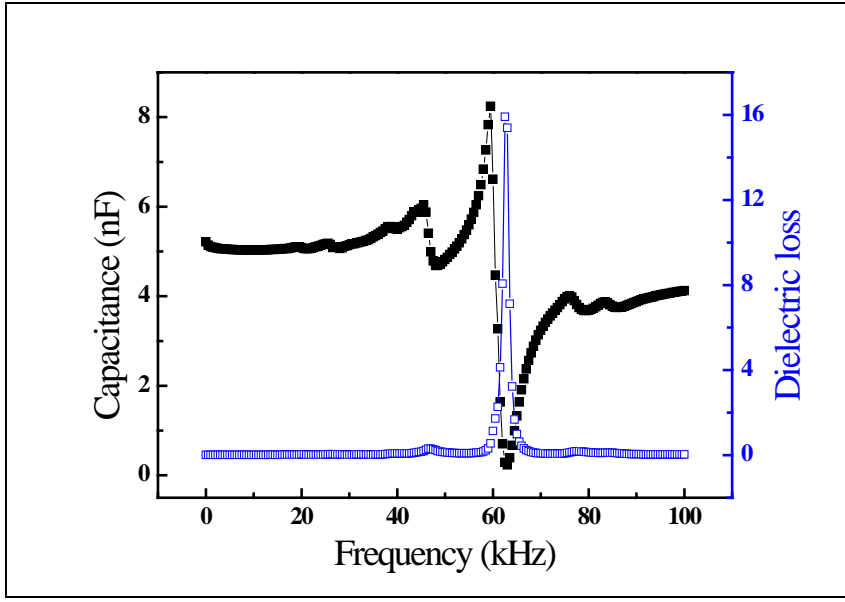


Figure 137. PMN-PT capacitance and loss data after poling showing loss of 1.42 to 1.68% from 1 to 10 kHz.

The dielectric loss of the completed sensors was higher than expected at 2% and above. Contributions from the epoxy and Kapton are expected but the reported losses are larger than calculated. Reported losses for the epoxy are well below 2% and experimentally measured losses are as low as 0.15%. Data sheets for the epoxy report values of loss but did not consistently report measurement frequency. The Kapton insulating layer has a reported loss of well below 0.3% depending on thickness. These values, if true, imply that the piezoelectric phase has a higher loss than previously thought. To insure the piezoelectric phase of our sensors have a loss similar to the reported values, tests were performed on a variety of different piezoelectric materials.

Piezoelectric fibers were again sputtered with a gold layer for conductivity and poled using poling voltages listed in Table 31. Previous tests only tested PMN-PT and PZT fibers. Each fiber was then measured using the LCR meter and a dielectric test measurement fixture to determine dielectric loss at 1kHz.

Results of these tests show loss values that are inconsistent with reported values. These results indicate that overall constructed sensor losses could be a result of higher than expected values of piezoelectric phase loss. The experimental values may reveal an inhomogeneity in the piezoelectric material that arises randomly in fully constructed sensors. Confirmation of low piezoelectric phase loss before sensors are constructed may lead to better understanding of overall sensor loss.

Table 33. Loss characteristics of several different varieties of piezoelectric core material available for manufacturing.

Materials	Dimension (mm ³)	Poling (V)	Tanδ (%)
PZT	10×2×0.2	500	1.7
PMN-PT	4×2×0.2	200	2
Mn-doped PMN-PT	10×2×0.2	300	0.8
PZN-PT	10×2×0.2	300	2

All dielectrics (except vacuum) have two types of losses. One is a conduction loss, representing the flow of actual charge through the dielectric. The other is a dielectric loss due to movement or rotation of the polarization, atoms or molecules in an alternating electric field.

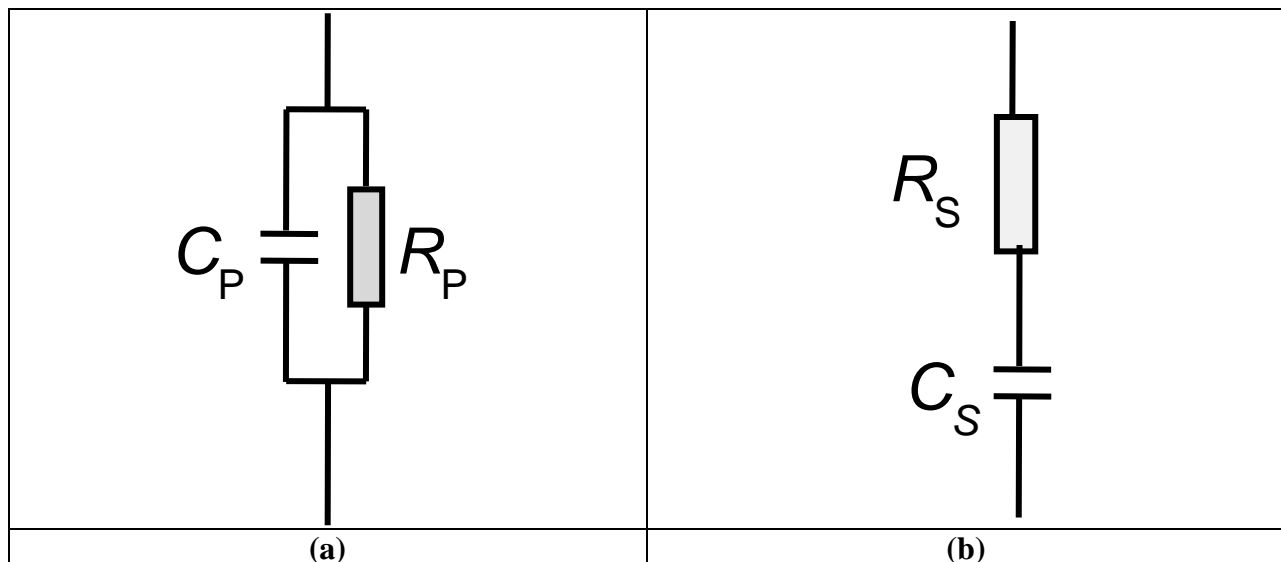


Figure 138. Equivalent circuit for dielectric materials for conduction loss (a) and rotation loss (b).

For our piezoelectric materials, the dielectric loss mainly results from the conduction loss. Using the equivalent circuit from Figure 138 an equivalent circuit model can be constructed for the dielectric loss in our piezoelectric materials. This equivalent circuit is shown in Figure 139.

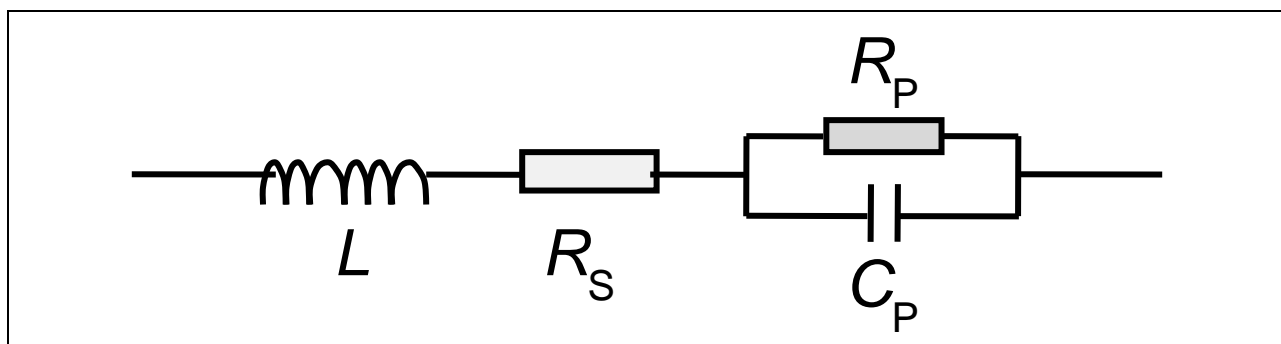


Figure 139. Equivalent circuit to model the dielectric loss in our piezoelectric material.

From the equivalent circuit, the impedance can easily be calculated to be:

$$Z = j\omega L + R_s + R_p // \frac{1}{j\omega C_p} \quad (256)$$

$$Z = j\omega L + R_s + \frac{R_p}{j\omega C_p R_p + 1} \quad (257)$$

We know the impedance has the form of:

$$Z = R + jX \quad (258)$$

Then, we got the impedance:

$$Z = R_s + \frac{R_p}{1 + \omega^2 R_p^2 C^2} + j \frac{\omega L - \omega R_p^2 C + \omega^2 R_p^2 L C^2}{1 + \omega^2 R_p^2 C^2} \quad (259)$$

We assume the equivalent capacitance is C_s , then

$$\frac{1}{j\omega C_s} = j \frac{\omega L - \omega R_p^2 C + \omega^2 R_p^2 L C^2}{1 + \omega^2 R_p^2 C^2} \quad (260)$$

The ideal total capacitance can then be easily calculated for the low frequency to be:

$$C_t = \frac{1}{\omega^2 R_p^2 C} \quad (261)$$

The total dielectric loss being written as:

$$\tan \delta = \frac{1}{\omega R_p C} \left(1 + \frac{R_s}{R_p} \right) \quad (262)$$

We measured the dielectric loss of the piezofiber at low frequencies, and the results were even larger than that given in the data sheet. From equation (20) at low frequency, we can conclude that it is because the setup had greater than expected contact resistance and this will be researched further.

Piezoelectric Phase Loss

It was discussed above that either excess epoxy at the interface between the interdigitated electrodes and piezoelectric phase or a property of the piezoelectric phase itself was a source of significant loss. We attempt, here, to carefully consider each variable associated with the attachment and proper and efficient poling of the piezoelectric phase.

Past experiments have observed higher dielectric loss is normally associated with low impedance angles. Ideal poling will result in an impedance angle of positive 90 degrees which would indicate a complete realignment of domains. An unpoled sample has an impedance angle of -80 degrees and represents a random alignment of domains. Poling regimes can change with piezoelectric phase and poling direction. It is also best if the poling procedures are tuned carefully to the piezoelectric phase and tailored for each known coercive field (E_c). Using tips from this reference we began improvements on our poling setup and poling programs.

First, improvements were made to increase the sample temperature to 100°C. This was accomplished with a heated oil bath and hotplate. The hotplate with a digital setpoint can be adjusted to achieve temperatures in any time allotted. Wada et al suggested temperature increases and decreases be kept to approximately 1°C/min.

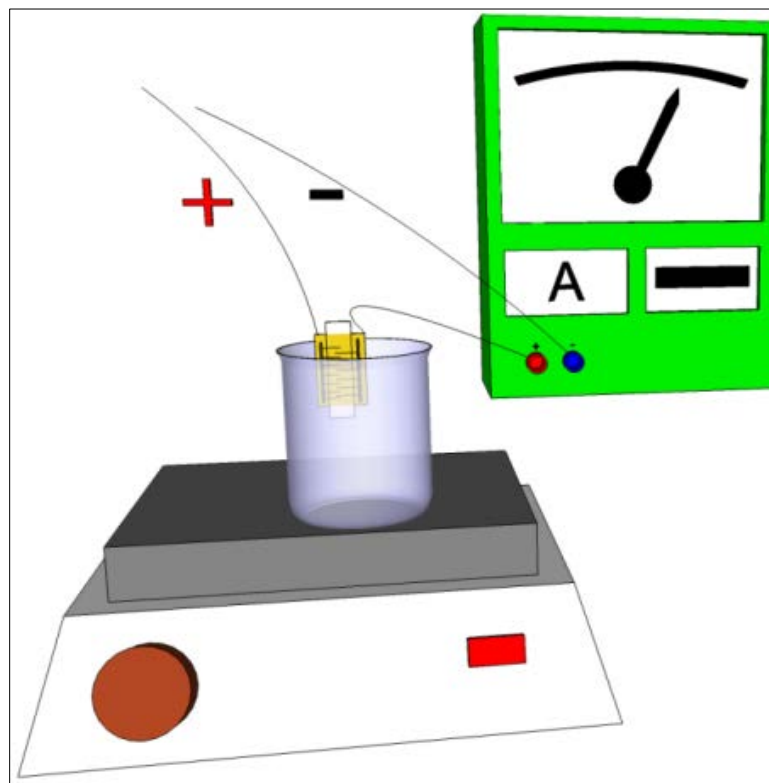


Figure 140. Schematic illustrating wiring used to measure and monitor sample poling currents.

Secondly, we reduced connection issues by making samples easier to attach and avoiding often difficult soldering connections.

Wada et al suggested sample current be kept to a minimum and never be allowed to increase beyond 1 μ A. To accomplish this we began monitoring the current with the serial output of the power supply. However, early attempts revealed this connection did not have the resolution needed to observe the current at the scale needed. The final iteration of the current monitoring setup simply placed a 6-digit ammeter in the circuit with the poling sample and monitored current directly (Figure 140).

The largest improvement was to digitally control the output power supply voltage via an A-D converter on a computer utilizing Labview software. The Labview interface allowed any desired poling voltage increase or decrease and a timed soak. Manual adjustment of the poling setup is still possible using a switch (black box to right of computer) that converts control but manual adjustment may spike current and require a large amount of operator time.

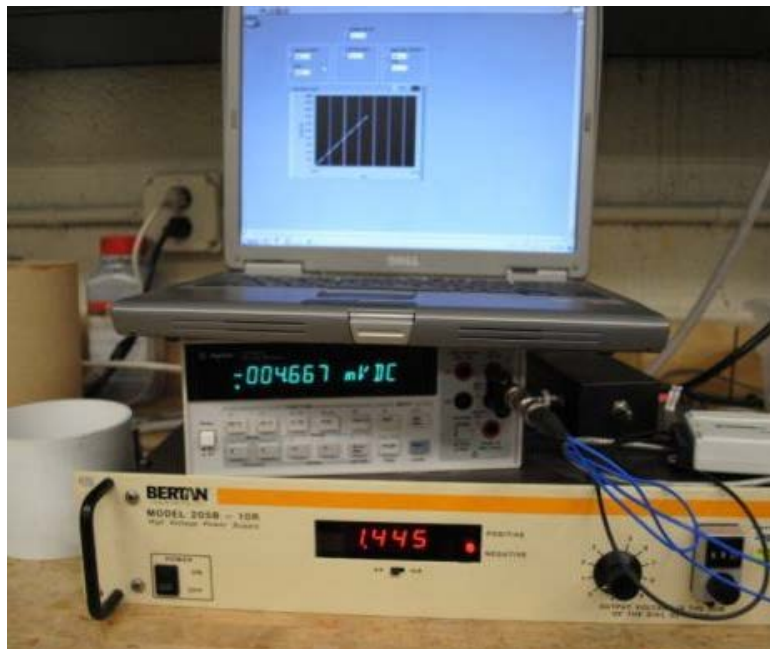


Figure 141. Computer display showing Labview interface ramping voltage to poling setup

Several samples have now been poled with the new improved poling setup. Wada et al suggested in their article that property sample coercivity be determined and that the poling regime adjusted to slow voltage increases in this area. With our PZT samples and the geometry of our most common interdigitized electrode this value is between 885 and 1000°C. Current will increase quickly when voltage nears the calculated coercivity of the piezoelectric. For our poling setup, it was decided that the ramp rate chosen would not exceed the fastest ramp rate possible in the vicinity of the piezoelectric coercivity. Therefore our initial ramp rates were slow.

The first sample poled on the new setup was made using PZT as the piezoelectric core. The voltage was increased at 160V/min, held for 15 minutes at 1650V and then decreased at 500V/min. Table 34 below compares one previous sample to the sample poled utilizing the new setup. The impedance angle was greatly increased with the new regime and the loss dropped accordingly. More PZT samples will be done and the programmed ramp rate, soak temperatures and dwell times will be optimized.

Table 34. Comparison of poling effects on current PZT cores versus previously poled PZT cores.

	C (pF)	Tanδ (%)	Phase angle (°)
Previous	~400	1.5–2	-30–46
Present	408	1.24	21

PMN-PT samples were also poled with the new poling configuration. PMN-PT samples were poled at a rate of 60V/min to 600V, held for 15 minutes then decreased at 200V/min. The result was a better poled sample. The impedance angle measurement reveals a large impedance angle approaching 40°. The loss was also measured to be 1.27% which is lower than previous values of between 2.5 and 3% and presents a considerable improvement.

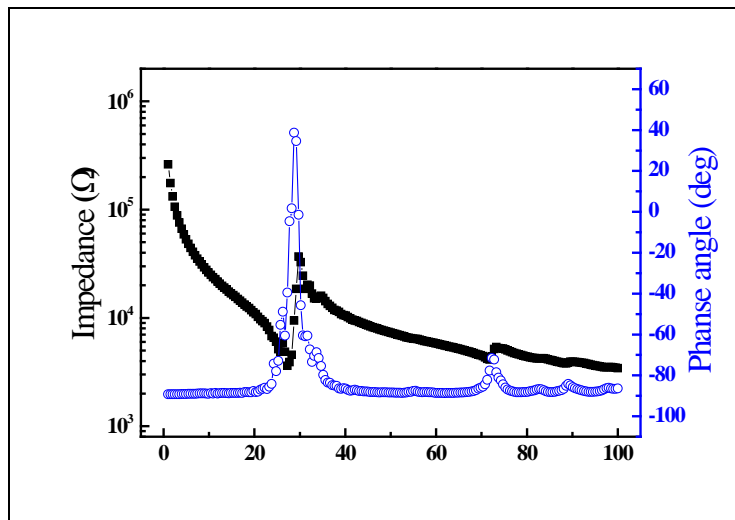


Figure 142. Impedance angle measurement for PMN-PT samples poled

In the weeks following the poling configuration upgrades more samples of more types were poled. The losses of these samples were compared to the datasheet values from the manufacturer. The comparisons are outlined in Table 35.

Table 35. Comparison of datasheet and experimentally observed loss values

Material	Tanδ (%) datasheet	Tanδ (%) Exp. Fiber	Tanδ (%) Sensor	Tanδ (%) Previous sensor
PZT	1.2	N/A	0.8%	1.0%-2%
PMN-PT (Korea)	0.5	1.8-2.0	1.2%-1.4%	~2.5%
Mn PMN-PT (Shanghai)	0.1	0.4	N/A*	0.8%
PZN-PZT (Virginia Tech)	0.2-0.4	0.6	0.6%	0.5%-2%
PMN-PT (CPSC)	0.5	1.0	0.75%	2.0%
PMN-PT (Shanghai)	0.2-0.5	0.2-0.5*	0.4% LT Mode	N/A

The benefits of the new poling station can easily be seen from the new results recorded in Table 35 above. The most common piezoelectric phase in our sensors is PZT and PMN-PT. It can be seen in the comparison above that we have made considerable improvement in reducing loss. The PZT losses have approached and sometimes exceeded the loss values reported in manufacturer data sheets (column 1). PMN-PT purchased from Korea and Shanghai both had low loss values as reported in manufacturer data sheets and although we are yet to approach data sheet values, we have exceeded our past sensor losses by almost 50% in the case of the Korean PMN-PT.

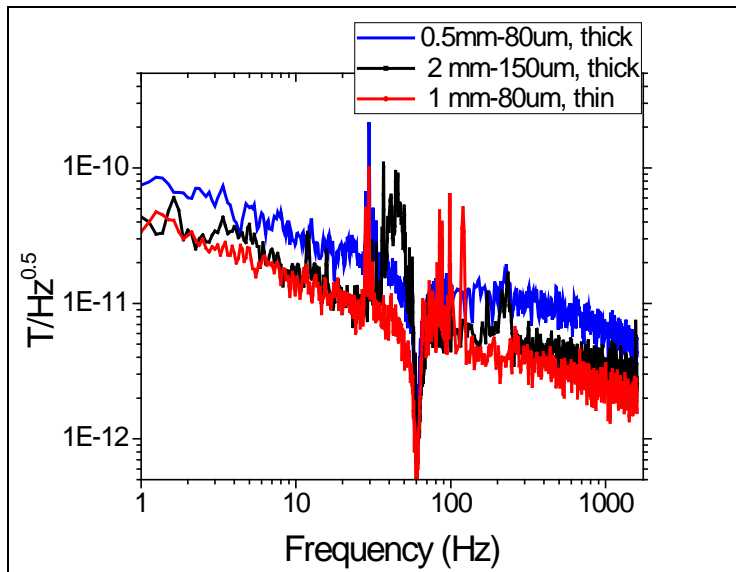


Figure 143. Noise floor comparison of sensors fabricated with various interdigit geometries and Kapton® thicknesses.

D.3.2. Fabrication

Efforts were made to control epoxy application with a method that is more conducive to mass production. Previous successful attempts to improve epoxy application included but were not limited to spin coating epoxy onto the PZT fibers. While this method was successful and repeatable, it would not easily allow for increased production. We are now beginning experiments with the process of epoxy screen printing.

The screen printing of epoxy utilizes a conventional screen utilized in other common printing processes with Stycast epoxy as the medium. The epoxy is mixed and applied using a rubber squeegee pressed through a prestressed mesh (Figure 144). The opening and thickness of the mesh are used to control the ratio of epoxy to void space on the substrate. The substrate in our process is a bundle of PZT fibers.

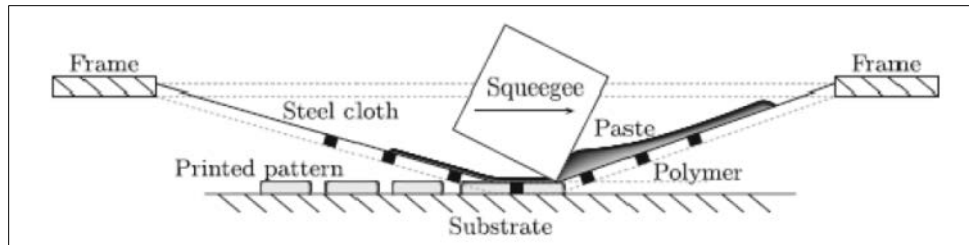


Figure 144. Diagram outlining screen printing process.

Preliminary tests were done with one 325 mesh. This mesh should create a pattern on the PZT covering 50% of the area with epoxy and leaving a void space of 50%. The resulting thickness of epoxy areas should be between 23 and 28 microns as shown in Figure 145. Immediately following application, the sample is exposed to vacuum pressure from the vacuum bagging step. This uniform pressure will reduce the printed thickness and distribute the epoxy evenly throughout the entire substrate surface.

MESH COUNT	WIRE DIAMETER	MESH OPENING	OVERALL THICKNESS	% OPEN AREA	WET PRINT	SCREEN TENSION (N/CM)
325	.0009/23	.002/51	.002/51	51	.001/25	16
325	.0011/28	.002/51	.0024/61	42	.001/25	22
C325	.0011/28	.002/51	.0020/51	42	.0007/18	19
360	.0006/15	.0022/56	.0014/36	60	.0009/25	17
400	.00075/19	.0018/46	.0015/38	49	.0007/18	16
400	.001/25	.0015/38	.0020/51	36	.0008/20	21
C400	.001/25	.0015/38	.0013/33	36	.0007/18	19

Figure 145. Screen printing mesh characteristics.

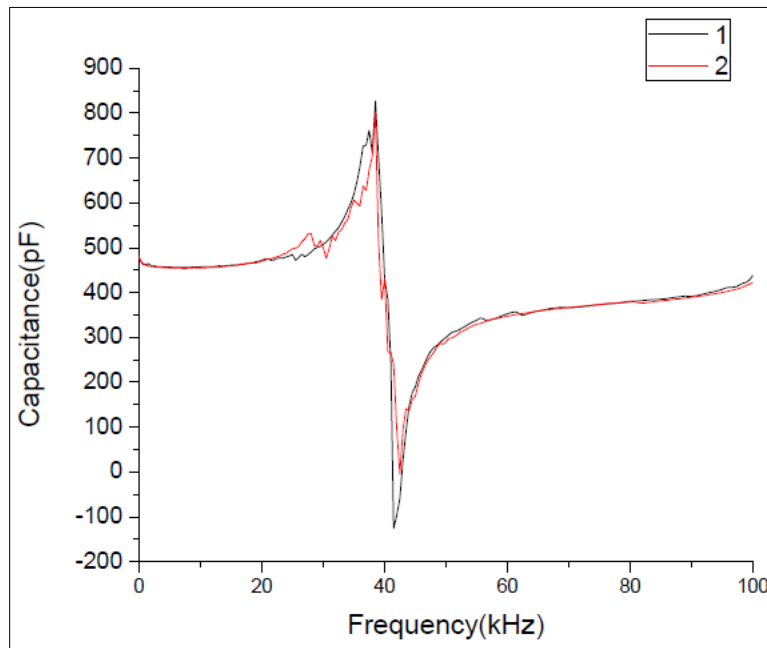


Figure 146. Capacitance curves of two samples manufactured using Styccast epoxy applied with a 325 screen printing mesh.

Two samples were fabricated using the newly proposed technique. The post-poling capacitance curves of the two samples are compared to each other in Figure 146 below to confirm that they are nearly identical and achieve a capacitance value normally seen from sample prepared with the previous spin coat application. This is encouraging and will lead to more attempts to both increase scale and compare/contrast electrical quantities as a function of mesh size. A mesh size of 400 is likely to achieve a thinner epoxy interface, as seen in column one of Figure 145, and may improve the capacitance values further. A 400 mesh screen was purchased so experiments could continue with screen application and increasing scale.

With the 400 mesh screen printing technique eight sensors were fabricated. The eight sensors are shown in Figure 147. Properties are currently being measured to determine repeatability. However, repeatability will increase as the process itself becomes more familiar. The immediate goal was to realize the time and labor needed for this scale of production and match it with the other steps in the process. Process shortcomings are not always related to the initial layup step. Post-layup steps also need to be optimized to insure efficient overall process flow. Advances in lead attachment, poling and Metglas layup needs to researched further to insure each step moves at the same rate as core layup. Metglas attachment has been successfully addressed and will be discussed more in depth in the next section. Advances in poling will mean poling eight sensors at one time. The current poling setup can be expanded to accommodate more sensors and research will be done this month to make that happen in an efficient manner.



Figure 147. Increase to eight sensors produced simultaneously through a screen printing process of epoxy application.

Repeatability

We made progress towards production of sensors. Eight sensors were made simultaneously using a press type fixture. This evolved into eight sensors fabricated simultaneously utilizing a screen printing application of epoxy. The eight screen printed sensors are shown in Figure 147. Screen

printing epoxy application has proved to be quite repeatable from sensor to sensor. A batch of four was made and measured at the same time to determine repeatability. The sensor characteristics for the four sample batch are shown in Table 36. The capacitance of these sensors shows the greatest deviation but it remains below 10%. The loss and ME voltage are nearly identical from sensor to sensor. However, the ME voltage depends largely on the Metglas application which has also improved in the last several months.

Repeatability will increase as the process itself becomes more familiar. The immediate goal is to realize the time and labor needed for this scale of production and match it with the other steps in the process. Process shortcomings are not always related to the initial layup step. Post-layup steps also need to be optimized to insure efficient overall process flow. Advances in lead attachment, poling and Metglas layup needs to be researched further to insure each step moves at the same rate as core layup. Metglas attachment has been successfully addressed. Advances in poling will mean poling eight sensors at one time.

Table 36. Single batch property distributions of PZT sensors using screen printing epoxy application.

PZT/Metglas	C (pF)	α_V (V/Oe)	α_Q (pC/Oe)	$\tan\delta$ (%)
1	428	2.09	1212	1.37
2	415	2.05	1199	1.32
3	412	2.03	1194	1.37
4	401	1.98	1180	1.38

Repeatability of PMN-PT sensors was also examined to determine variability in sensor fabrication independent of screen print methods. Utilizing PMN-PT sensors constructed for previous experiments we can compare and contrast the properties to determine advances in repeatability. Four PMN-PT sensors fabricated for previous experiments with 2.5mm ID spaced electrodes were compared. The measured properties of the sensors are shown in Table 37. One observation easily seen from the table is the deviation in properties from sensor 1 and the rest of the dataset. Sensors 2, 3 and 4 are very closely matched with no more than 2% difference in any of the electrical properties. The addition of sensor 1 changes the deviation to nearly 7% from the average in charge and approximately 3% from the average capacitance. Although there is an outlier in the dataset, the quantities are still within the 10% deviation for all properties. Yet, the data shows a smaller gap of only a few percent deviations is easily a possibility.

Table 37. Measured properties of PMN-PT sensors made with similar 2.5mm ID electrodes as a comparison of property repeatability.

Sensor (2.5mm ID spacing)	C (pF)	α_V (V/Oe)	α_Q (pC/Oe)	$\tan\delta$ (%)
1	241	4.82	1599	1.21
2	254	5.20	1746	1.16
3	247	5.21	1778	1.19
4	248	5.22	1756	1.28

D.3.3. Study of ME sensor nonlinearity

D.3.3.1. Signal distortion at maximum α_E :

We studied the signal distortion (second harmonic, third harmonic, ...) of our PZT/Metglas sensor when an optimized dc magnetic bias was used to get a maximum ME coefficient α_{ME} . These investigations were done at the request of SAIC and CNRS-Caen. They were considered necessary information in order to begin to consider modulation methods to enhance detection electronics.

Test setup: A lock-in amplifier (SR-850) was used to provide a sine wave (300Hz or 1kHz). In order to drive the coil properly, we used a $\times 100$ amplifier to boost this ac signal and increased the drive capability at the same time. The PZT sensor output was sent to the “signal in” terminal of the lock-in amplifier SR-850. The detailed information is shown in Figure 148.

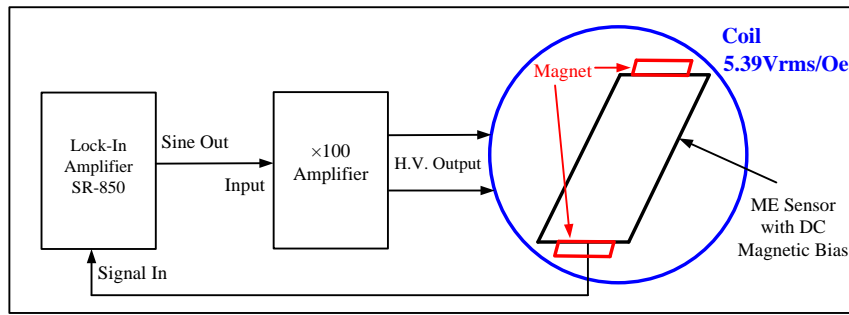


Figure 148. Test setup for determining signal distortion (second harmonic, third harmonic...)

The magnets were adjusted so that a maximum α_{ME} could be obtained. For example, as shown in Figure 149, the DC magnetic field should be around 7.5Oe. It is worth mentioning that we could also adjust the DC magnetic field to get the set point where the slope of the α_E is maximum (again, as shown in Figure 149, the DC magnetic field should be around 2.5Oe).

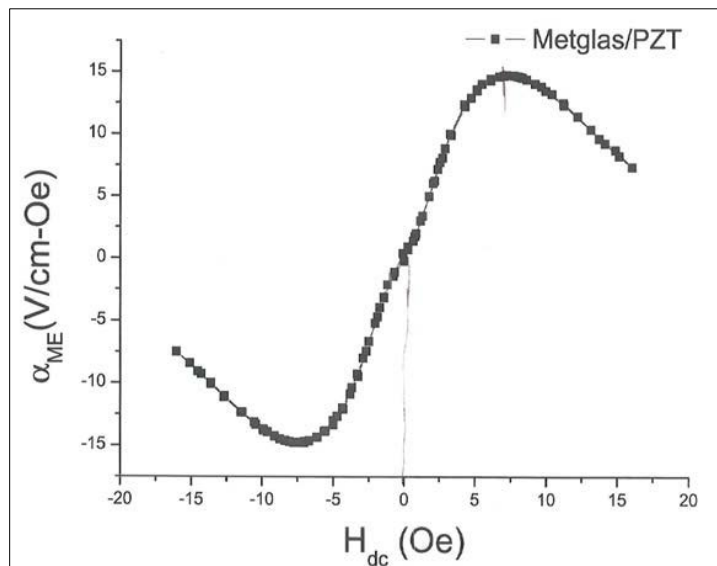


Figure 149. Experimental α_E versus bias field for a Metglas/PZT composites

D.3.3.2. Harmonics as function of f and ac drive amplitude

Measurements were made at dc magnetic biases close to the maximum in α_E - H_{dc} curve, the maximum in the slope of the α_E - H_{dc} curve, and the minimum in the α_E - H_{dc} curve.

Near maximum in α_E :

Figures 150(a) and (b) show the first and second harmonic as a function of frequency, respectively. These data were taken for a dc bias near the maximum value of α_E . The results show the presence of a significant 2nd order harmonic, in particular when the sensor is driven near its resonance conditions where the displacement is amplified. Clearly, the ME voltage response has second harmonic distortions. These harmonics are large enough to offer the potential for a cross-modulation detection method.

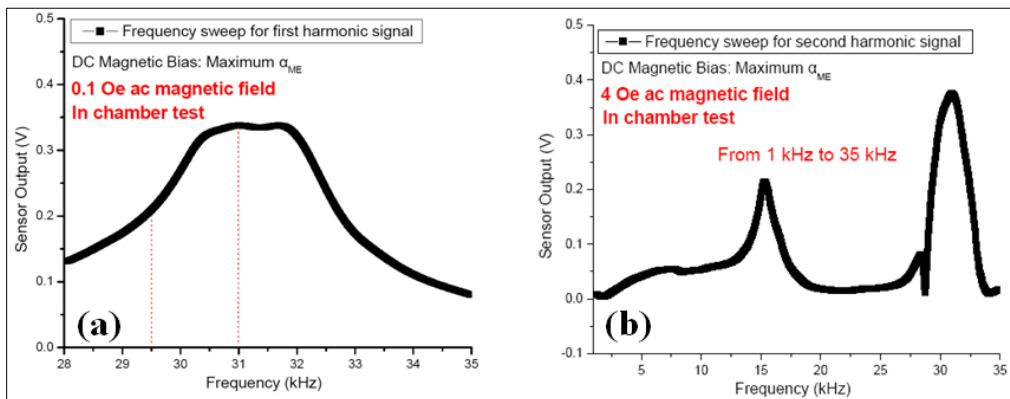


Figure 150. ME voltage as a function of frequency for (a) 1st harmonic, and (b) 2nd harmonic.

This data was taken near the maximum in the α_E - H_{dc} curve.

In Figures 151(a) and (b), we show the dependence of the first and second harmonic responses on the applied ac magnetic field H_{ac} . Data are shown at three different frequencies of 1kHz (far away from the EMR), 29.5kHz (near the EMR), and 31kHz (at the EMR). In Part (a), we can see that the first harmonic depends linearly on H_{ac} for all frequencies studied. In Part (b), we can see at low frequencies that the 2nd harmonic is very small, over the range of ac fields investigated. However, with increasing frequency as the EMR was approached, the 2nd harmonic increased in magnitude. Inspection of the figure will reveal a strongly nonlinear dependence of the output voltage on ac magnetic drive.

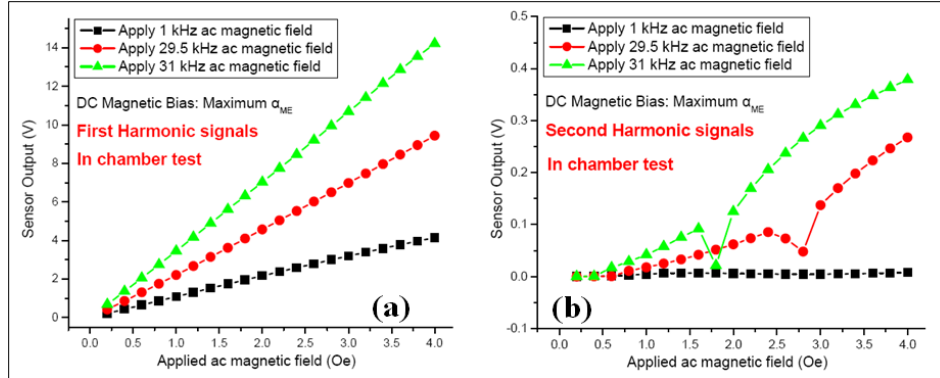


Figure 151. ME voltage as a function of ac drive amplitudre at various frequencies for (a) 1st harmonic, and (b) 2nd harmonic.

This data was taken taken near the maximum in the αE -Hdc curve.

Near maximum in slope of αE with H_{dc} :

Next, in Figure 152, we show corresponding results taken near the maximum in the slope of the αE -H_{dc} curve. These data again show that the first harmonic is linearly dependent on H_{ac}, and that there are significant 2nd order harmonics present in the ME voltage signal. However, in this case, we found that the 2nd harmonic was notably stronger at lower frequencies (f=1kHz), than near the EMR conditions; although, notable magnitudes were found at all frequencies studied.

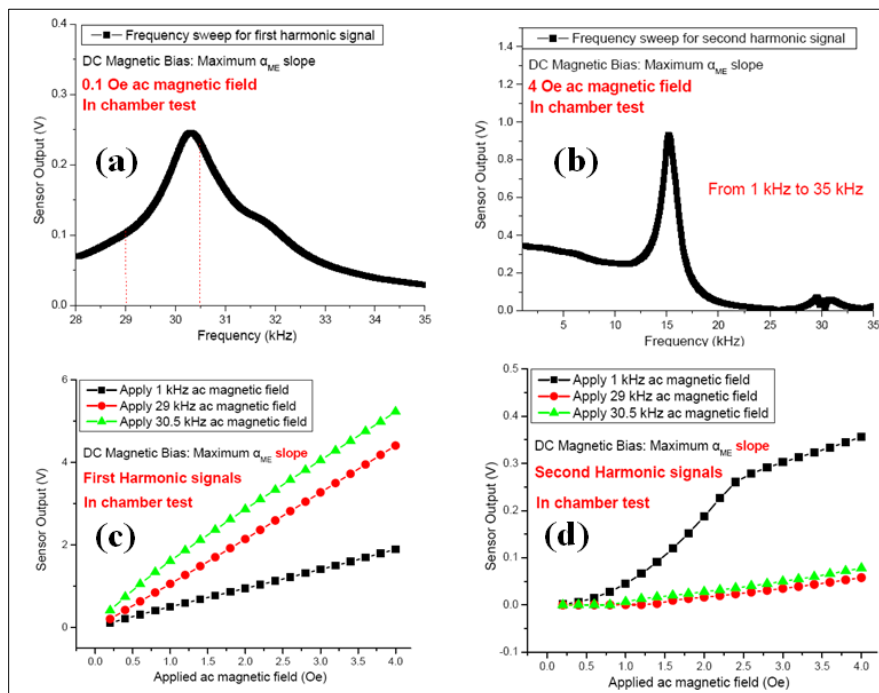


Figure 152. ME voltage as a function of frequency for (a) 1st harmonic, and (b) 2nd harmonic; and the ME voltage as a function of ac magnetic drive at various frequencies for (c) 1st harmonic, and (d) 2nd harmonic.

This data was taken taken near the maximum in the slope of the αE -Hdc curve.

Near minimum in α_E :

Finally, in Figure 153, we show corresponding results taken near the minimum in α_E . These data show a very weak first harmonic, where it was difficult to determine whether it depended linearly on H_{ac} or not. Please note that the 2nd order harmonic signal was much stronger than the first: i.e., the anharmonic contributions dominate the total response under small dc bias fields when α_{ME} is small. We found that the 2nd harmonic was notably strong only at lower frequencies (f=1kHz), and nearly zero at the EMR.

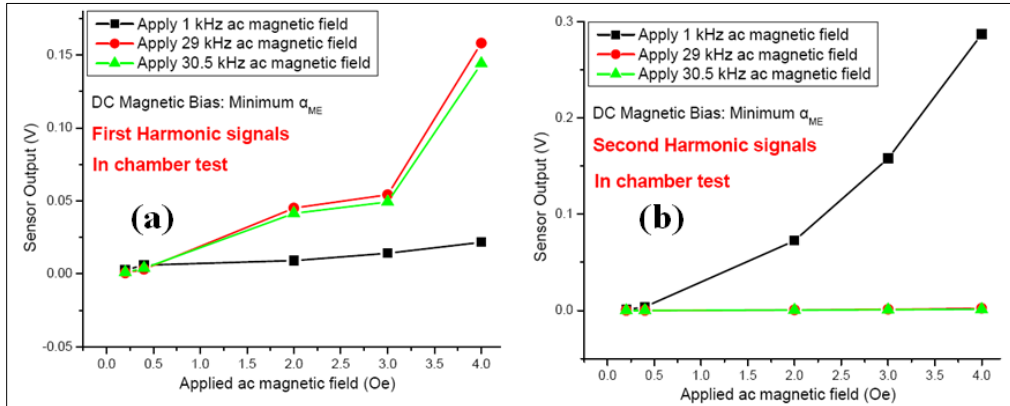


Figure 153. ME voltage as a function of ac drive amplitude at various frequencies for (a) 1st harmonic, and (b) 2nd harmonic.

This data was taken near the minimum in α_E -Hdc.

D.3.3.3. Comparison of nonlinearities of various sensors

α_E vs. H_{dc} curves under different ac magnetic fields

We compared the test results of the single crystal sensor with the test results of Metglas/PZT and Metglas/PMN-PT ME laminate sensors in Figures 154 (a) and (b), respectively. For Metglas/PZT, around $H_{dc}=0$, we found that the slope was notable lower, than it was near $H_{dc}=5$ Oe. Such a change in slope was not found for the Metglas/PMN-PT ME laminate.

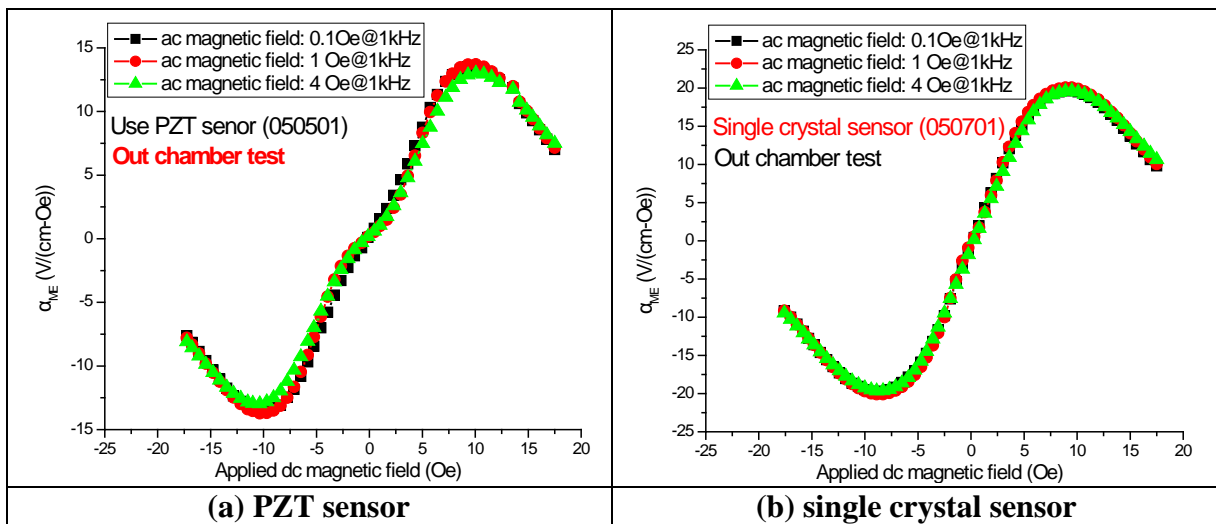


Figure 154. Calibrated α_E vs. H_{dc} curves of PZT sensor and single crystal sensor.

α_E vs. H_{ac} curves under different dc magnetic fields

Next, we show the dependence of α_{ME} on the value of the ac drive. Data were taken at different H_{dc} values of 1Oe, 2Oe, 3Oe, 4.8Oe (near maximum in slope of α_E with H_{dc}) and 9.5Oe (at maximum in α_E). Data are shown in Figure 155a for Metglas/PZT-fiber and in Figure 155b for Metglas/PMN-PT single crystal fiber laminates. These data reveal nonlinearity of α_E with H_{ac} for Metglas/PZT-fiber laminates, where the value of α_E was found to decrease some with increasing H_{ac} . The maximum nonlinearity was found near the field level, where the change in slope was found in the $\alpha_E - H_{dc}$ relation was observed in Figure 155. Much less nonlinearity was observed for Metglas/PMN-PT fiber laminates

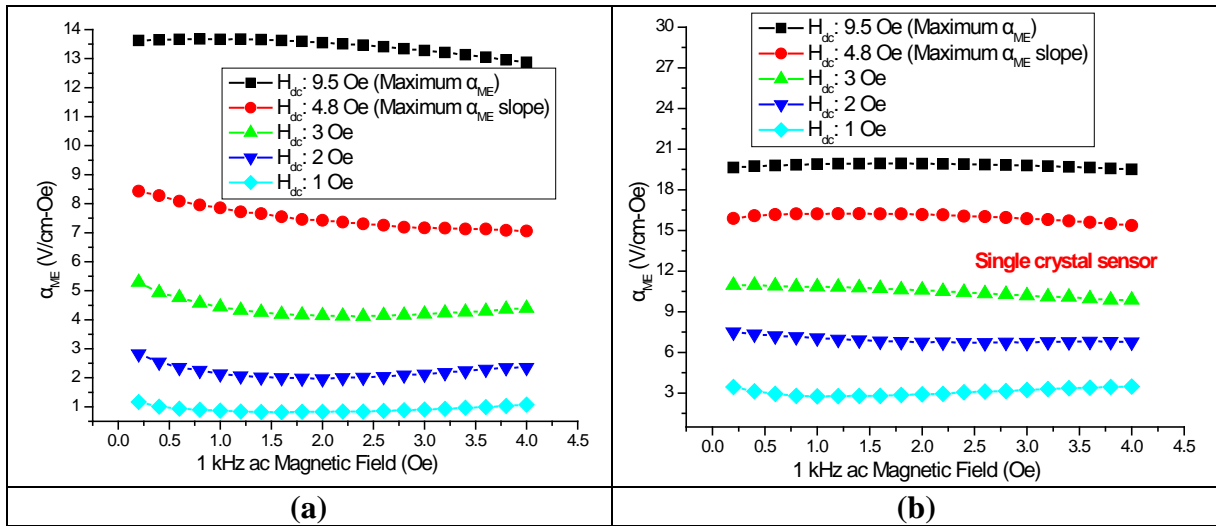


Figure 155. Calibrated α_E vs. H_{ac} curves (a) for Metglas/PZT sensor, and (b) Metglas / single crystal fiber sensor.

D.3.3.4. Cross-modulation effect at different f , H_{dc} and H_{ac}

We also worked on an external drive modulation method that should allow for remediation of noise at frequencies below the external drive frequency. The sensor was modulated via an external coil that is driven at frequency f_0 . Two assumptions that validate this technique are that the α_{ME} coefficient was nonlinear, and that the incident magnetic field was small compared to the drive magnitude. We performed initial experiments in quantifying the nonlinearity of our α_{ME} coefficient for various ac and dc magnetic fields. We also explored the nonlinearity and relative strength of higher order harmonics at different bias and incidence strengths (Figure 156a). We found that driving the sensor with an external coil does in fact act to modulate the signal, resulting in the offset sidebands in the power spectrum, (Figure 156b). The relative power of the signal contained in the sidebands depends on the ratio of drive to incident fields, and their relative frequencies.

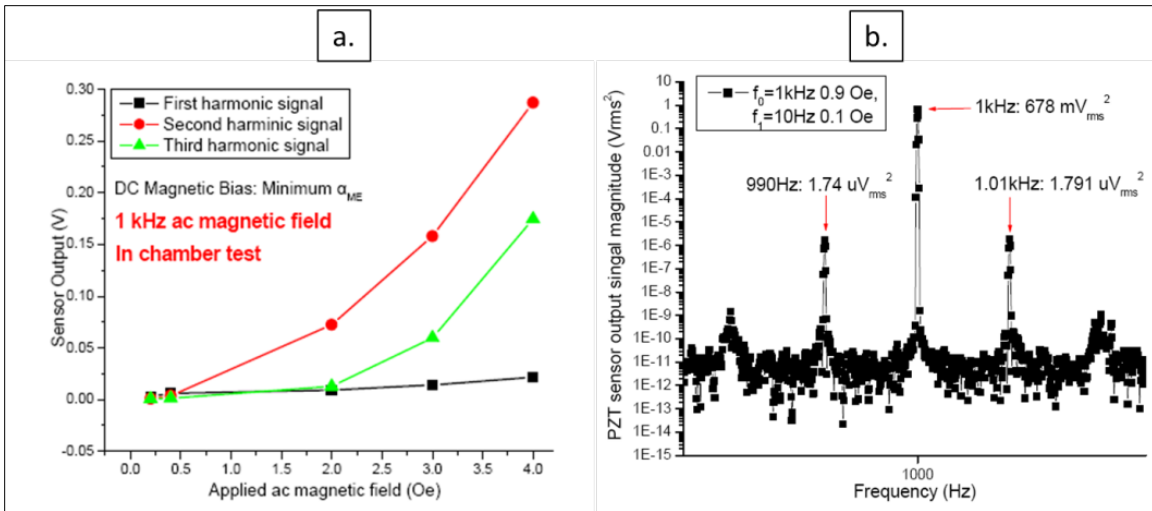


Figure 156. (a) Nonlinear ME response with respect to bias field and (b) verification of modulation of incident field resulting in sideband signals.

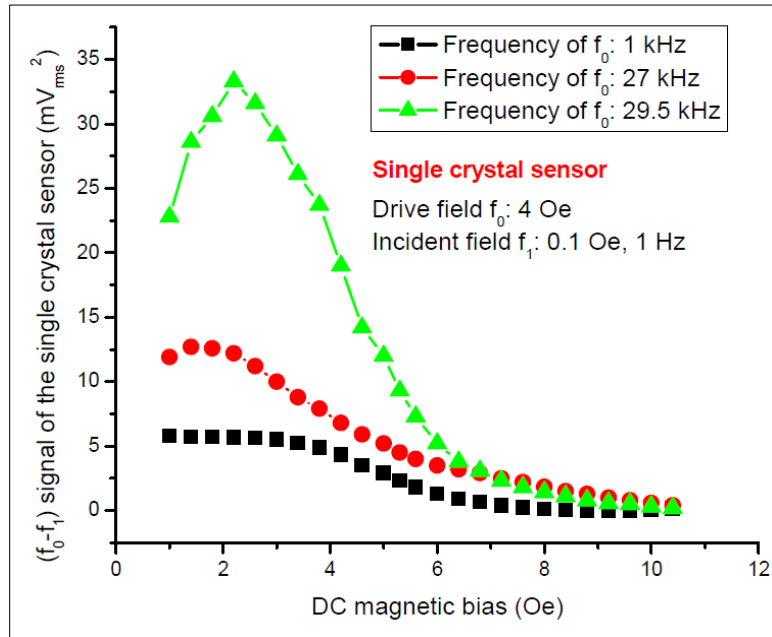


Figure 157. Magnitude of modulated side-band as a function of H_{dc} .

We focused specifically on biasing field and drive field conditions that resulted in maximum f_0-f_1 signal strength. Our test results show that the magnitude of the modulated side-band signal is a complex function of the applied DC bias field (Figure 157). The maximum sideband signal strength occurs at roughly 2.8 Oe for quasi-single crystal PMN-PT piezoelectric cores and is relatively insensitive to drive frequency. The data also highlight the fact that changes in bias field (e.g. from the Earth's magnetic field) will cause changes in the strength of the sideband signal. It might therefore be necessary to correct the bias of the sensor for the orientation within Earth's field.

Our experiments suggested that a maximum α_{ME} for the PMN-PT sensor should occur at ~ 2 Oe regardless of drive frequency. We therefore modulated our signal at resonance for various DC bias strengths and found a maximum α_E at $H_{dc} = 2.8$ Oe (Figure 158). We then found that the magnitude of α_{ME} was a function of drive strength as well, yielding a local maximum at $H_{ac} \approx 2.5$ Oe, and then scaling linearly with drive strength (Figure 159).

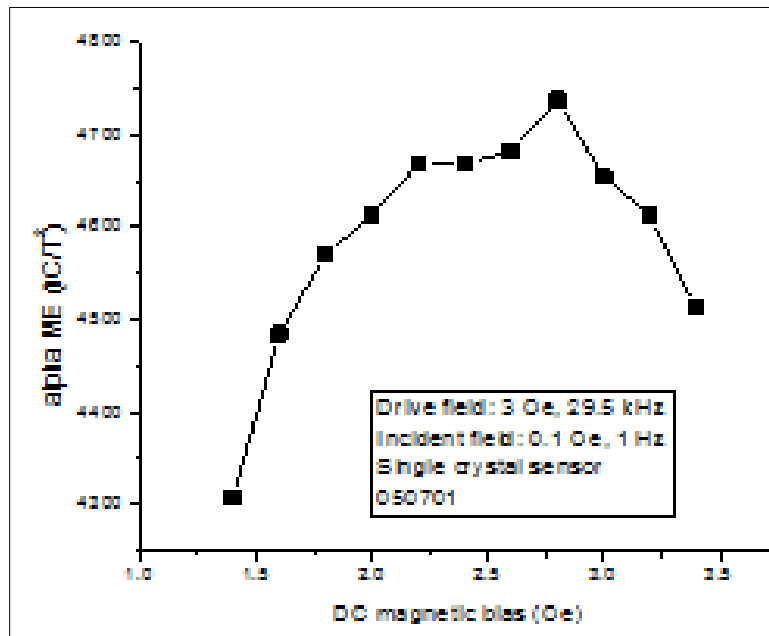


Figure 158. ME response to bias field strength at resonance for PMN-PT sensor.

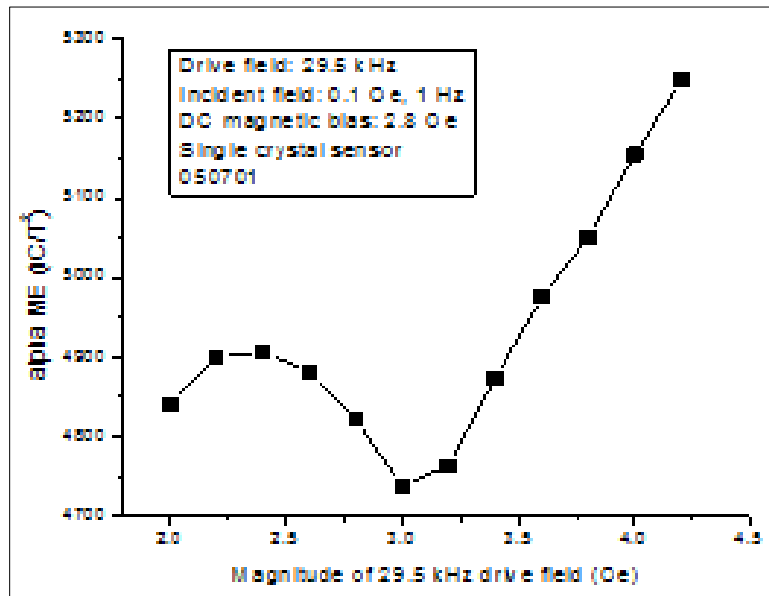


Figure 159. ME response to AC drive field strength at resonance for PMN-PT sensor.

D.3.4. Sensor arrays

D.3.4.1. Initial Design

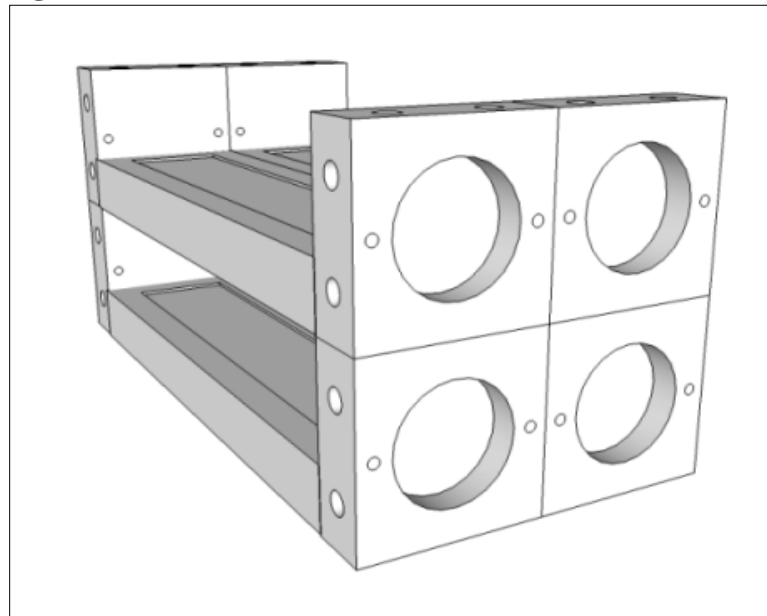


Figure 160. 2 by 2 array prototype.

An array design was detailed that would allow for the mounting, connection and experimentation of four ME sensors in a 2 by 2 array. The drawing in Figure 160 shows only one of the many possible configurations. The end closest reveals the space for the fixed bias magnets on the end of each piece. All pieces were removable and reconfigurable. Tests could be done in single fixtures alone or with additional fixtures attached. Figure 161 illustrates how each individual fixture was designed to be removed and rotated.

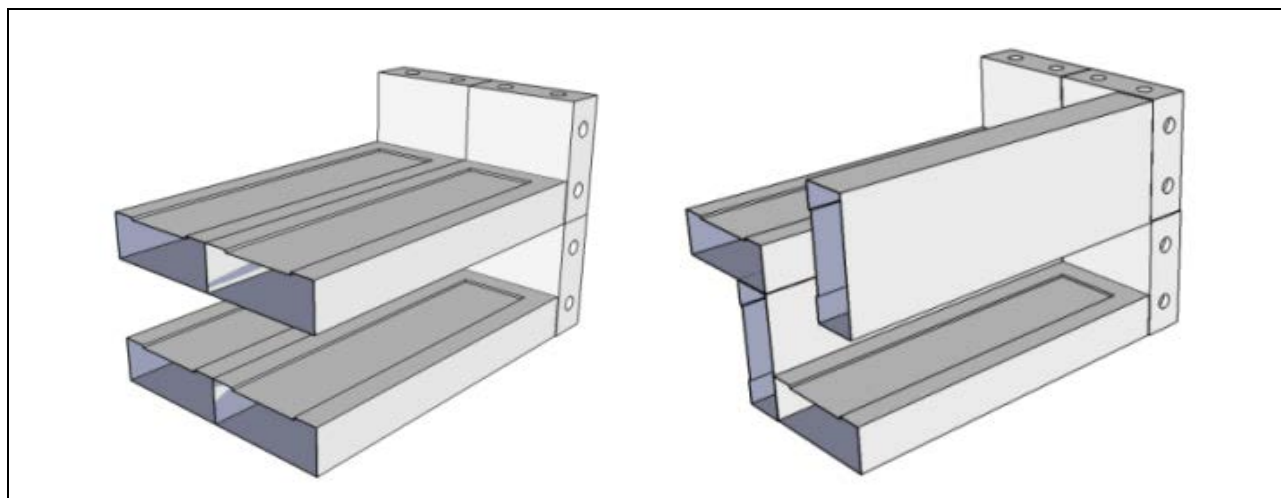


Figure 161. Example of possible orientation changes available using symmetric package.

Initial Fabricated Package



Figure 162. Photo of fabricated assembly with one attached sensor for illustration.

A prototype of our array design was fabricated by a local machine shop and shown in Figure 162 with one ME sensor mounted. The mounted sensor leads move to the outside through small through holes on each side of the permanent bias magnet. Proposed upgrades to this design include stand offs above the sensor for mounting a charge amplifier. Also, sensor connection after the charge amplifier needs to be addressed.

Integration of charge amplifiers was an important next step. Proposed drawings of charge amplifier attachment were created soon after single sensor experiments began and were created with flexibility in mind. These drawings utilized the open space in the current package to either house and connect one charge amplifier to the complete multi-sensor array or include a single charge amplifier for each independent module.

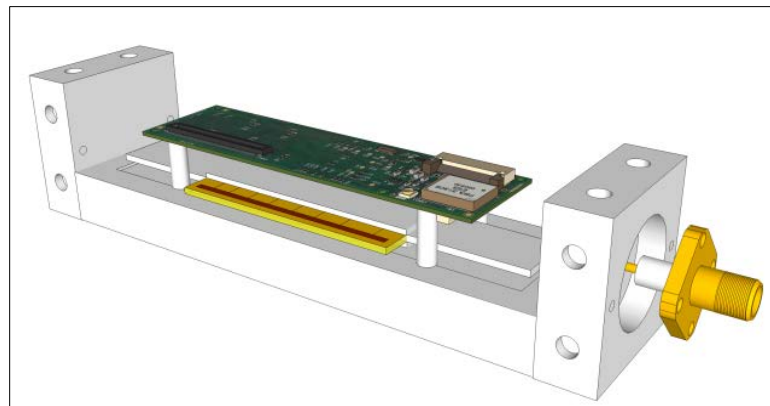


Figure 163. Drawing of single sensor with individual charge amplifier mounted above.

Proposed drawings show a new charge amplifier constructed by Virginia Tech, with a smaller footprint, mounted on top of the sensor using standoffs. The charge amplifier is no wider than a fabricated sensor and doesn't exceed the footprint allotted for the sensor. Attachment to the charge amplifier would be made inside the fixture and the signal will be output with a miniature SMA connector attached to one face of the module. The design shown in Figure 163 has not accounted for proper mounting of the SMA fitting nor does it show batteries or the charge amplifier switch. Experiments with newly fabricated charge amplifiers containing full size batteries and switches were performed to see if the method of charge amplifier mounting could easily be accomplished.

The thinner charge amplifier was soldered and batteries were attached underneath. The complete charge amplifier was then mounted above the sensor using homemade standoffs with the correct height to allow another module to be attached above and still not contact sensor below. A double pole-single throw switch is normally used for switching the charge amplifier. The switch, however, is much too large to use the sensor module as designed. The footprint of the switch needs to be decreased to allow it to fit inside the module and not impede other modules. The SMA fitting was attached to the end using small gauge hard copper wire.

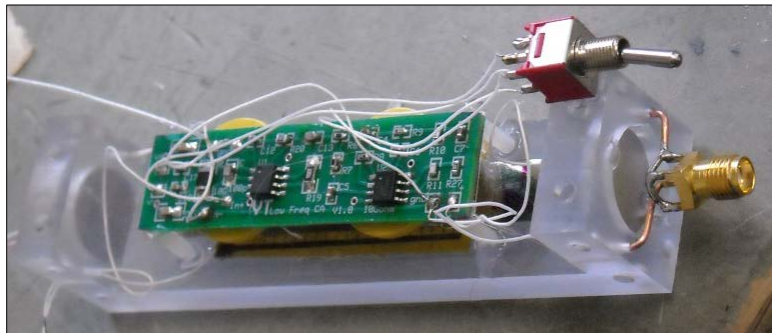


Figure 164. Single module with new thin charge amplifier and SMA fitting attached.

Initial Array Experiments:

We worked with stacking sensors into arrays in an attempt to decrease the noise floor by either increasing the output charge of the array, or by tuning the impedance of the array.

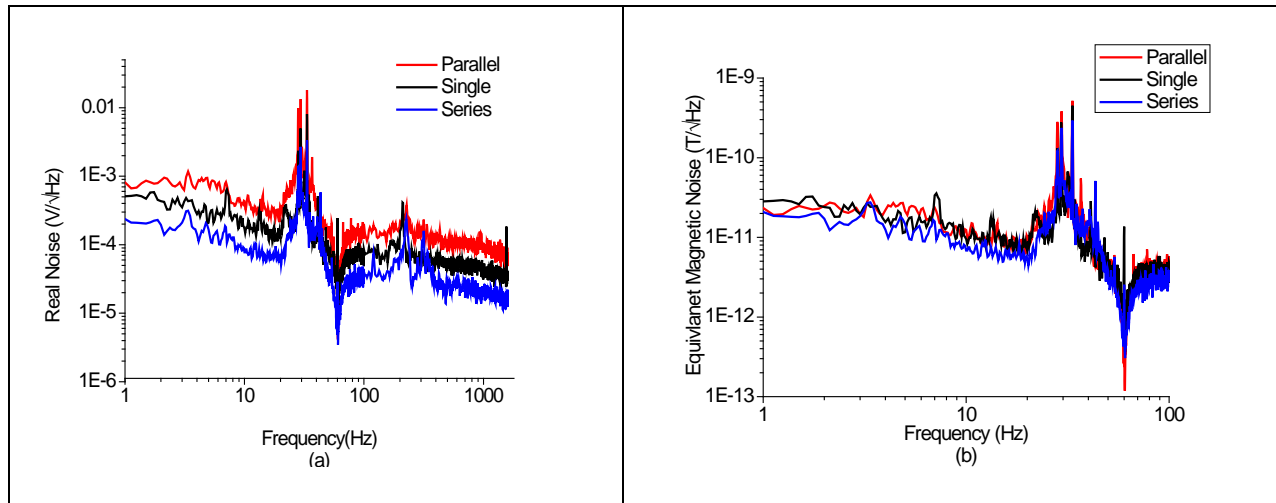


Figure 165. (a) Real voltage noise of parallel (red trace), single (black trace) and series (blue trace) sensor configurations. (b) equivalent magnetic noise of arrays showing that shift in voltage noise due to impedance change is offset by increased output charge

The decreased parallel resistance for the parallel configuration results in higher voltage noise.

Figure 165a shows the real voltage noise of a parallel array, a series array, and a single sensor. The parallel array shows a significantly higher noise floor, most likely due to the dramatic decrease in parallel resistance (and small increase in capacitance) versus either the series connection or the single sensor. While the parallel array has a roughly 3.5 times higher voltage noise (8.1×10^{-4} V/ $\sqrt{\text{Hz}}$ vs. 2.3×10^{-4} V/ $\sqrt{\text{Hz}}$ at 1 Hz), the increase in output charge of the parallel combination from 930 pC/Oe to 2780 pC/Oe results in no net change in equivalent noise floor for the different array configurations (Figure 165b).

While constructing the stacked arrays, we noticed that sensor-to-sensor flux interaction tends to affect the output charge of the individual sensors, and therefore affects the net performance of the array. We explored configurations with no spacing between constituent sensors (i.e. multilayer sensors) to 1 cm spacing between adjacent sensors. Sensors placed at 1 cm and connected with parallel electrical configuration showed much higher output charge than the multilayer sensor unit. We hope to use empirical electrical modeling and commercial FEM magnetic modeling to determine optimum array configuration and geometry in the next several months.

Also, we began exploration of multiple sensor configurations for use with the new array packaging scenario. The array package prototype allowed for four sensors to be used together. The drawings developed assumed a symmetrical 2 by 2 array would be best for the first round of testing. However, it is still not clear what electrical and physical configuration is optimum. We began preliminary testing for the optimum configuration by constructing four sensors that were closely matched in electrical properties. The four sensors and their electrical properties are listed in Table 38. The similarity in properties is easily seen from the table. The α -charge and α -voltage do not deviate more than 10%. The loss is nearly constant for all four sensors at close to 1.7%.

Table 38. Matching sensors manufactured for array testing.

Sensor	α_V (V/Oe)	α_Q (pC/Oe)	R_{dc} (GΩ)	$\tan\delta$ (%)	Phase shift (°)
1	2167.4	1266.5	24.7	1.8	162.48
2	2170.5	1176.6	37.7	1.6	162.49
3	2193.2	1308.0	32.9	1.9	162.48
4	2249.1	1360.5	66.2	1.7	162.42

Experiments to determine optimum sensor spacing were performed. These initial tests utilized only two of the four sensors and varied the spacing between the top and bottom of the sensors oriented in similar directions. The sensors were electrically assembled in a parallel condition. Table 39 reveals a slight increase in ME characteristics with increasing spacing between sensors. Obviously, more tests will need to be completed to determine if the trend continues in a linear fashion and narrow the applicable ranges. The largest spacing tested in these experiments resulted in an ME voltage very near to that of the single sensor ME voltage.

Table 39. Changes in ME charge and voltage as a function of spacing.

Sensor	α_V (V/Oe)	α_Q (pC/Oe)
2 in parallel (approx. 4.8mm spacing)	1996.2	2136.5
2 in parallel (approx. 6.3mm spacing)	2062.7	2195.3
2 in parallel (approx.. 7.9mm spacing)	2101.7	2236.0

Preliminary calculations about the effect of electrical orientation suggested that series connections should increase ME voltage characteristics in an additive fashion. Parallel electrical connections could serve to double the α -charge and capacitance but not affect the α_E . To verify these assumptions tests were performed with multiple sensors configured in series and parallel connections. Table 40 shows the results of both experiments. For the sensors connected in series, the ME voltage increases for two sensors in series but increases do not continue as expected for the connection of three and four sensors in series. The output charge changed but this variation can be expected due to the imperfect match of sensors.

Table 40. Change in ME properties with series additions.

Sensor	α_V (V/Oe)	α_Q (pC/Oe)
Series Combinations		
2 in series	3013.6	1136.2
3 in series	3018.5	927.4
4 in series	4165.1	1092.0
Parallel Combinations		
2 in parallel	1996.2	2136.5
3 in parallel	1860.0	2780.6
4 in parallel	2258.0	4201.6

For parallel connections of two, three and four sensors the ME voltage varied but stayed very near to the value measured for a single sensor as expected. The charge, however, was again not

increased in an additive fashion. The charge was expected to triple for three sensors and quadruple for four sensors. The charge increased but not linearly as predicted. Notable observations from these initial experiments indicate the deviation from a linear increase in voltage characteristics for series connections and charge characteristics for parallel connections. However, the loss values remain consistent regardless of connections.

Table 41. Comparison of parallel and series sensor combinations and their effect on loss characteristics.

Sensor	α_V (V/Oe)	α_Q (pC/Oe)	R_{dc} (GΩ)	$\tan\delta$ (%)
4 in parallel	2258.0	4201.6	12.5	1.8
4 in series	4165.1	1092.0	107.5	1.5

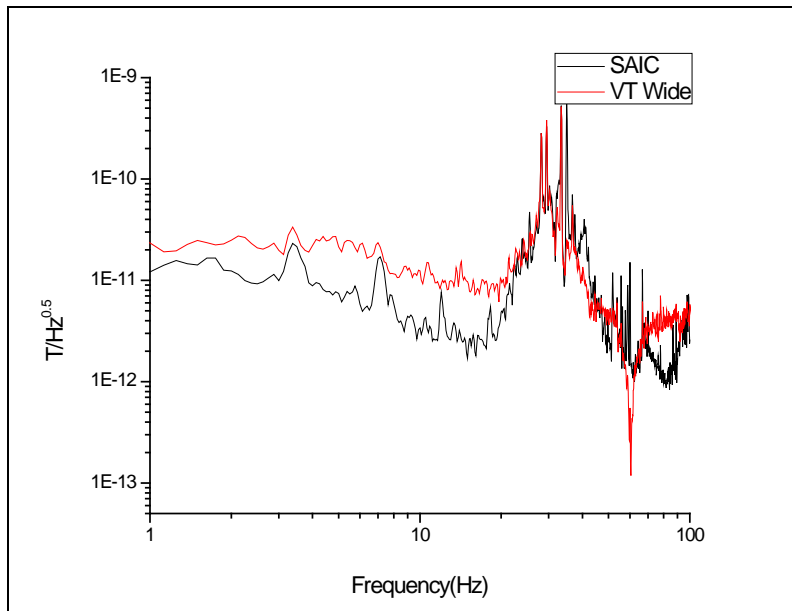


Figure 166. Noise floor measurements for three sensors in parallel.

Noise floor measurements were also done to determine which electrical scenario resulted in the best noise floor measurement. Noise floor tests were done for three sensors connected in parallel and series using both the SAIC and VT constructed charge amplifiers. The lowest noise floor measurement at 1 Hz was achieved with the SAIC charge amplifier. The results for the parallel connection show noise levels to be approximately $11\text{pT}/\text{Hz}^{1/2}$ and the series connections show a low noise level of approximately $19\text{pT}/\text{Hz}^{1/2}$. These tests show a decrease in noise level is achieved when sensors are connected in parallel. However, these deviations exist because of the choice of charge amplifier. The values for the VT constructed charge amplifier do not change much with the change in electrical connections and stay very close to $20\text{pT}/\text{Hz}^{1/2}$.

To determine if the fourfold increase in output charge experienced by connecting four sensors in parallel would then translate to a lower noise floor on increased sensitivity, the noise floor was measured with four sensors in parallel. The SAIC charge amplifier again revealed the better

noise floor measurement and the noise floor was measured to be $10 \text{ pT}/\text{Hz}^{1/2}$ at 1 Hz with a sensitivity measurement of 0.09nT using a SNR greater than 2.

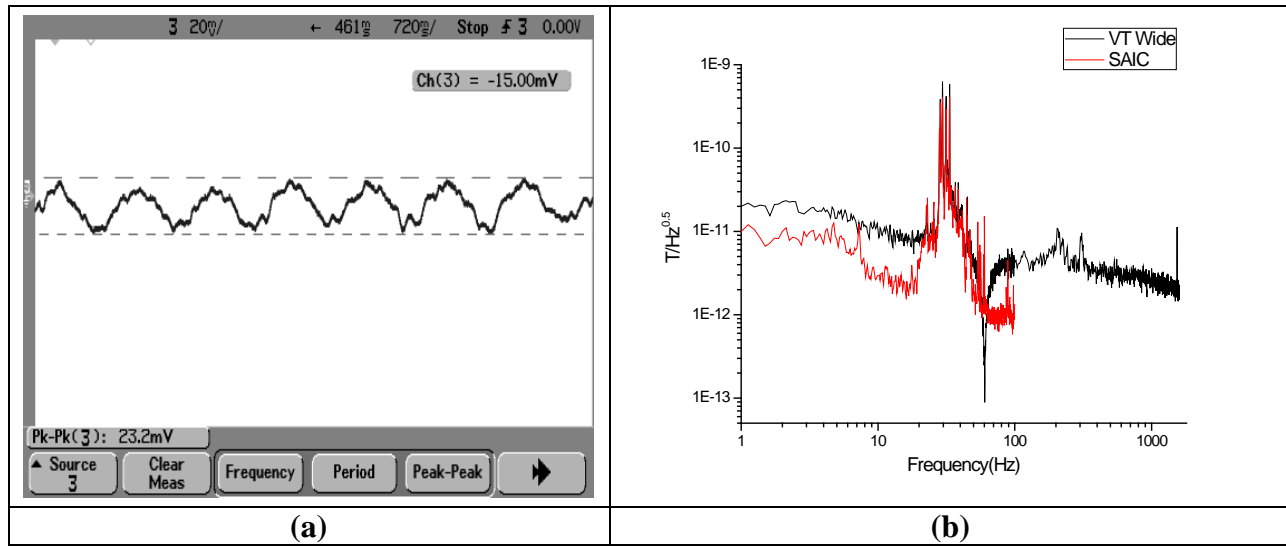


Figure 167. (a) Four parallel sensor sensitivity measurement showing SNR>2, Pk-Pk: 23.2mV@ 0.09nT @ 1Hz and (b) noise floor measurement of approximately 10pT using SAIC charge amplifier.

D.3.4.2. Revised Design



Figure 168. Virginia Tech constructed low frequency charge amplifiers for each module in the 2 by 2 array.

Two different experiments were performed to establish maximum and minimum boundary limits for sensor spacing. The first of these experiments utilized the PSU constructed array package. This package is designed to bias each sensor individually. The open construction allows for either multiple sensors in each unit or individual charge amplifiers with each unit. We attached individual charge amplifiers to each unit in our 2 by 2 sensor array. This configuration allowed us to reliably test individual package noise floors for direct comparison of multiple sensor noise

floors for the same package type. Also, the close proximity of the connections reduced noise from extraneous wiring.

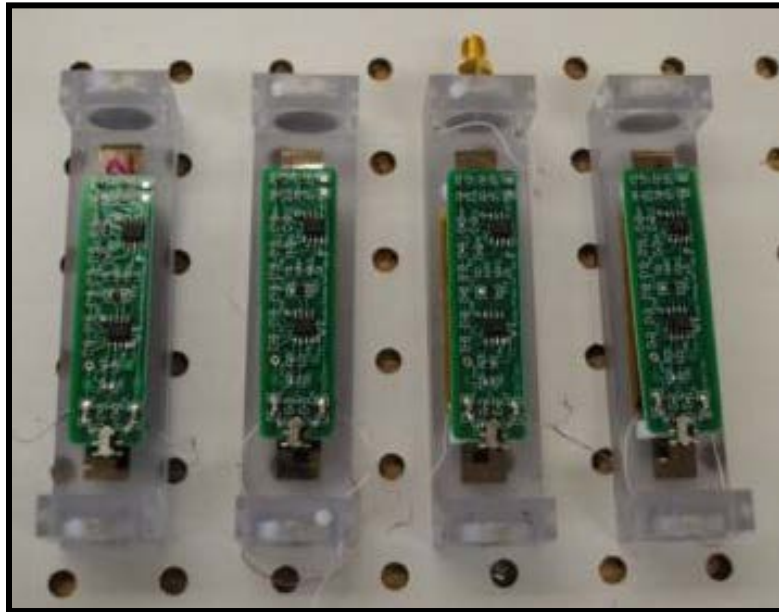


Figure 169. low frequency charge amplifiers mounted to individual sensor modules.

Figure 168 shows four low frequency charge amplifiers constructed by Virginia Tech for mounting with each sensor. Figure 169 shows the mounted charge amplifiers mounted to modules in the array package. Once mounted and tested, the flexibility of the package design will allow for many orientation experiments to be performed. Figures 170a and b illustrate only two of the intended orientations for experimentation.

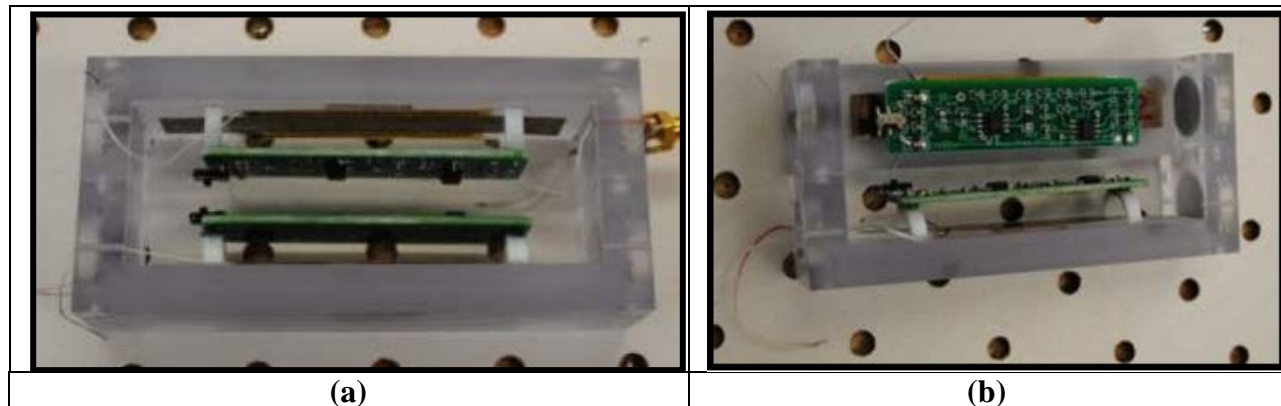


Figure 170. (a) Modules oriented with charge amplifiers close together (b) modules oriented out of plane in an effort to increase flux capture.

Each module was then equipped with an individual switch and set of batteries. The output of each was connected to individual SMA fittings. The modules did not lose any flexibility when fitted with the extra circuits and batteries. Assessing the output noise characteristics for the array and individual sensors now required four simultaneous channels. Data was collected with a

datalogger and used for signal processing. Experiments were conducted in and out of the noise and vibration isolation chamber. Configurations could be altered to determine the best performance. The large size of the package and the presence of four distinct high permeability strips imposed an extra degree of difficulty when measuring inside a Helmholtz coil. Careful calibration of fields before and during tests needed to be done to insure accurate results. More ideal experiment geometry might include an incident field from a fixed distance. This geometry will reduce field interaction from submersion of high permeability material within the field.

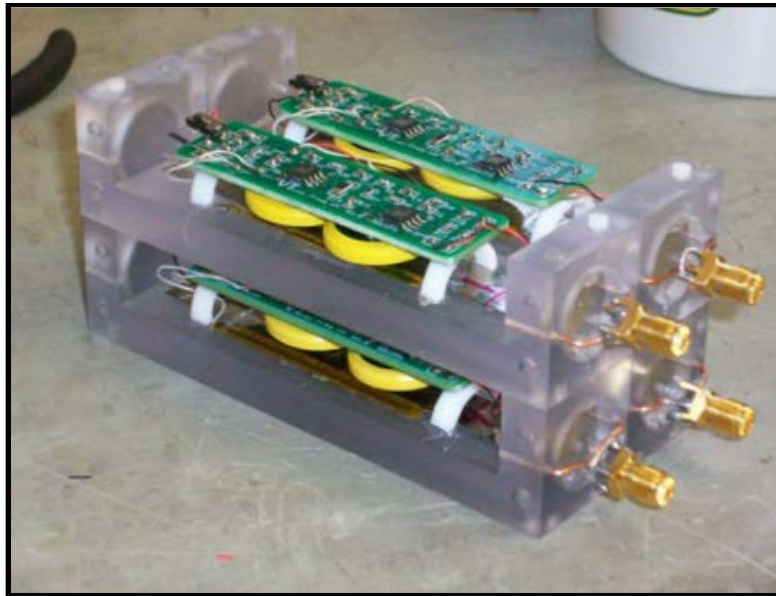


Figure 171. PSU array modules with individual charge amps and batteries ready for configuration experiments

Experiments:

Sensor interactions in array configurations were studied utilizing different combinations of sensors. It was thought that sensor combinations could achieve higher signal while simultaneously reducing coherent noise, thus resulting in overall increased signal to noise ratios. Experimental models suggested a possible improvement in noise floor. Contributions to the less than optimum observed performance of these combinations may arise from incompatibility between the additive sensor electrical quantities and our choice of charge amplifiers. The charge amplifiers being used were designed to accommodate single sensor applications and the electrical properties changed by serial and parallel configurations may fall outside the optimum parameters of the original design. The tests shown in this section were done by comparing the response of the JFET SAIC charge amplifier and the VT constructed wide band circuit. Changes were also made in the sensor orientation to confirm the sensors were exposed equally to both the AC and DC bias.

Tests with four sensors connected in parallel using first the VT constructed charge amplifier (Figure 172) and the SAIC JFET charge amplifier (Figure 173) were plotted to determine a trend in noise floor response.

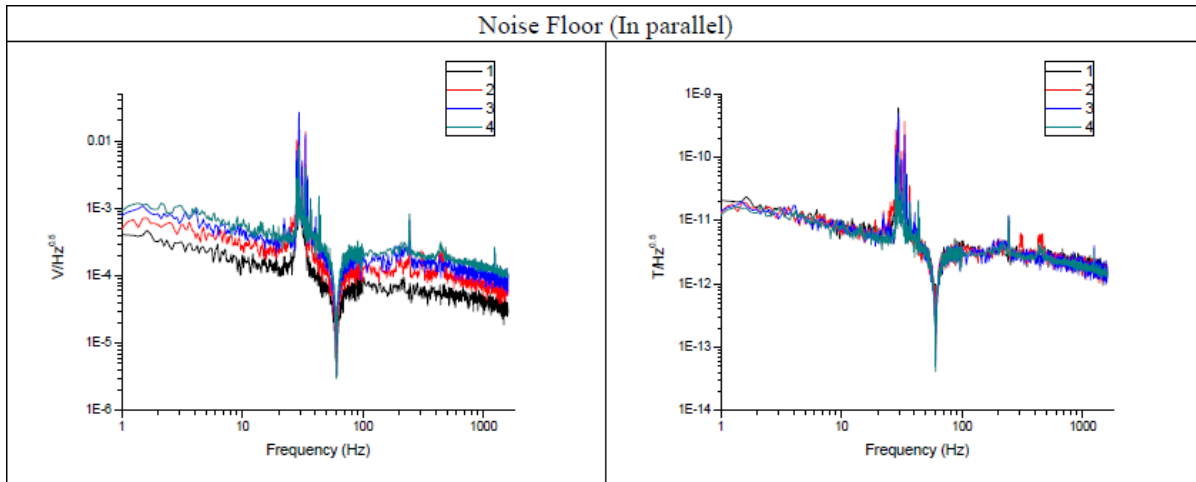


Figure 172. Noise floor tests of four sensors connected in parallel using VT constructed wide band charge amplifier.

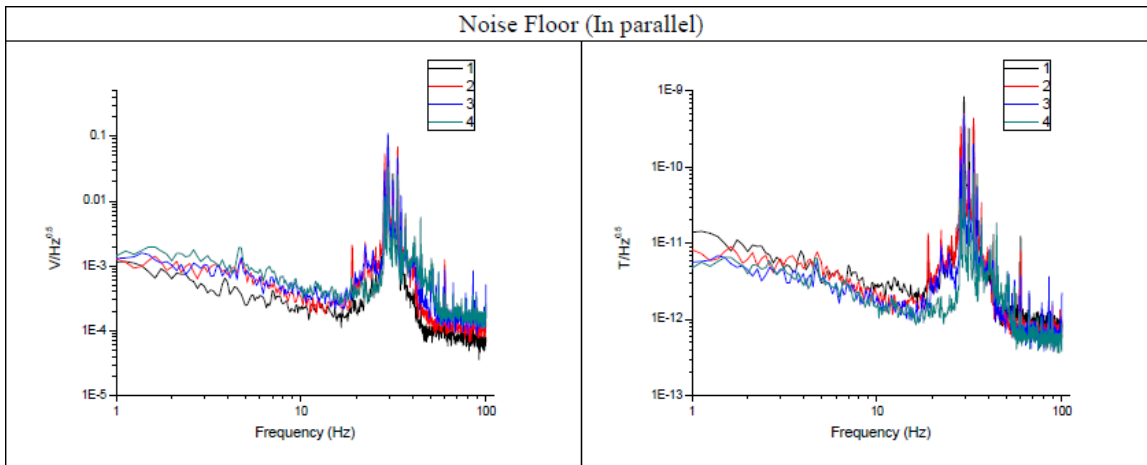


Figure 173. Noise floor tests of four sensors connected in parallel using charge amplifier constructed by SAIC.

Although decreasing noise floor trends exist with both charge amplifiers, the SAIC JFET circuit showed a more obvious lowering of the noise floor. With a single sensor the noise floor is nearly $15 \text{ pT}/\sqrt{\text{Hz}}$ and decreases as sensors are connected in parallel to reach as low as $4 \text{ pT}/\sqrt{\text{Hz}}$. The same sensors were also retested in a series connection with both amplifiers. Similar plots were made of the VT charge amplifier response (Figure 174) and the SAIC JFET response (Figure 175) below. Again, the noise floor tends to decrease in both cases. However, the largest improvement of the four possible configurations again exists with the SAIC JFET amplifier. A noise floor of $10 \text{ pT}/\sqrt{\text{Hz}}$ is observed when all four sensors are connected in series.

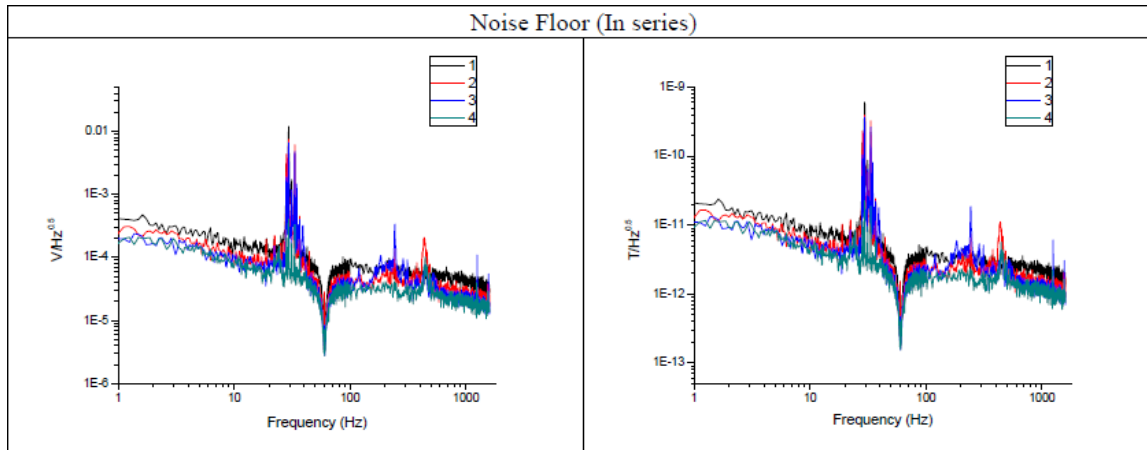


Figure 174. Noise floor tests of four sensors connected in series and measured using VT constructed made wide band charge amplifier.

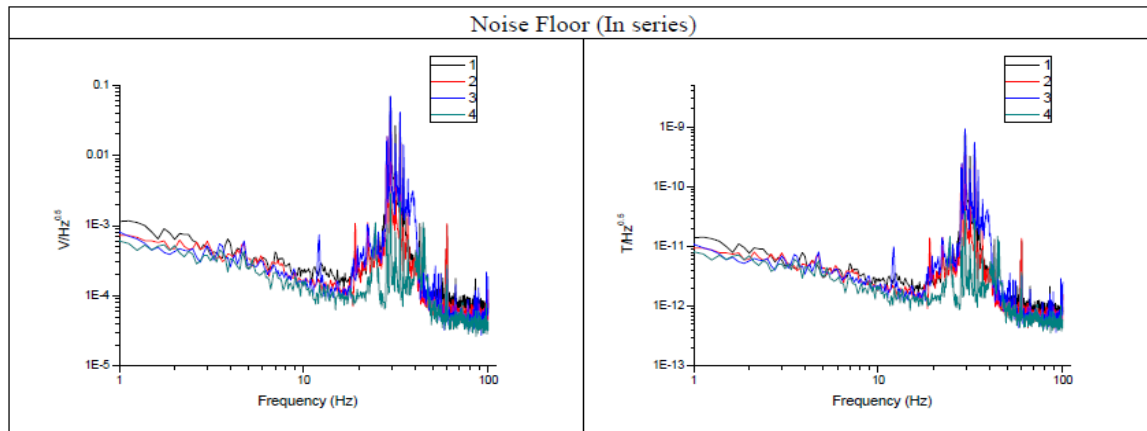


Figure 175. Noise floor tests of four sensors connected in series using JFET charge amplifier constructed by SAIC.

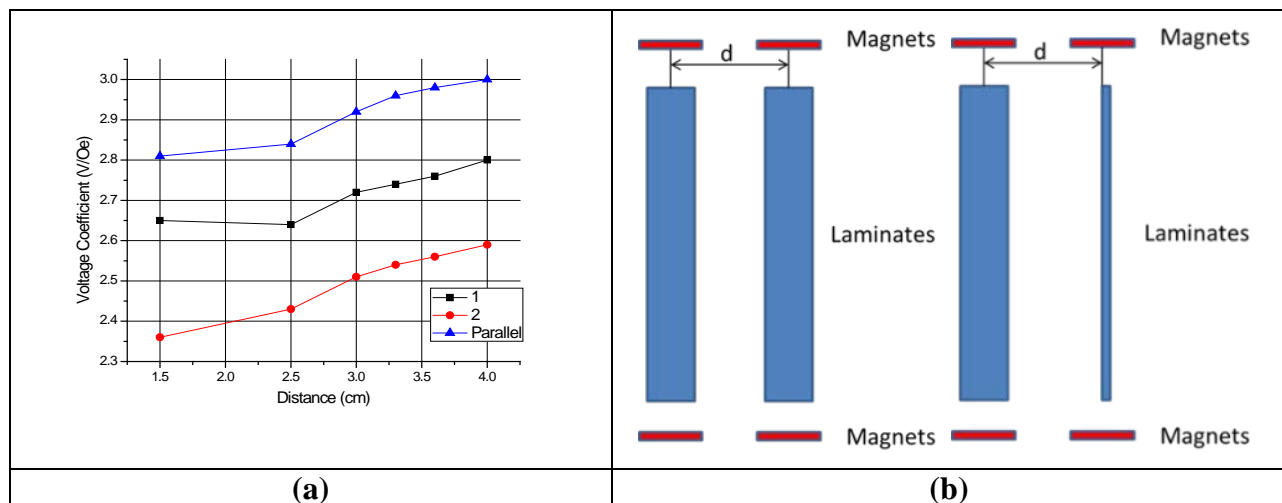


Figure 176. (a) sensors packaged with individual bias in the same plane. (b) Sensors packaged with individual bias magnets oriented in different planes.

Separation distance has been shown to effect the ME charge and voltage coefficients. Observations from those experiments suggested an interaction may occur between sensors leading to less than predicted results. Also, it may have been a result of uneven or less than optimum biasing conditions. Here, time was spent focusing on both of these variables. First, separation distance was varied for each of the promising configurations. Figure 176 shows the two configurations utilized.

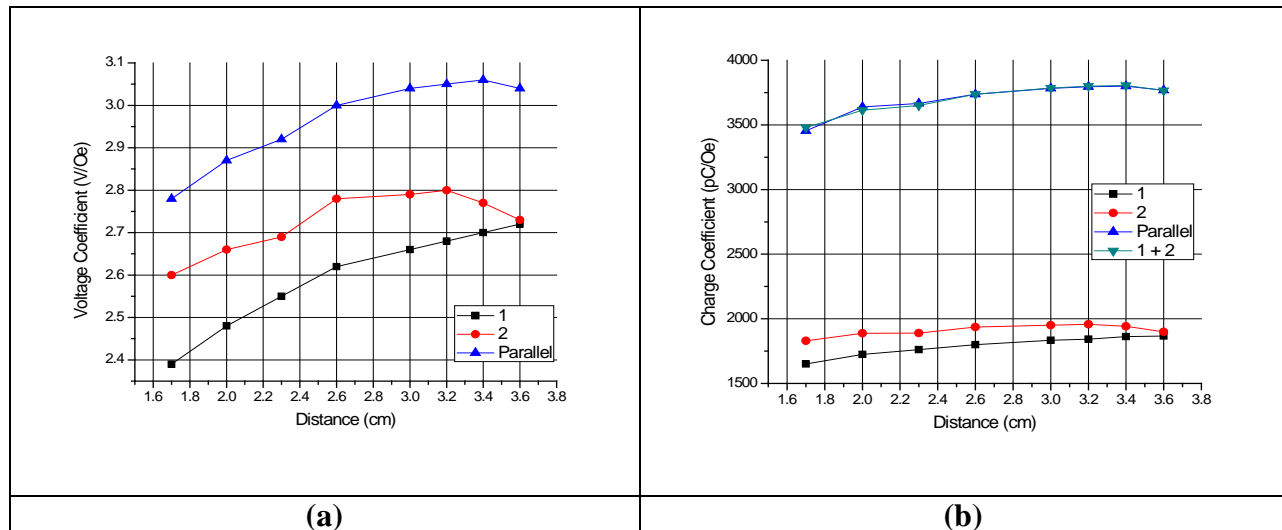


Figure 177. (a) parallel ME voltage output as a function of in-plane center-to-center separation distance. (b) ME charge output as a function of in plane separation distance.

The in-plane condition (Figure 177a) was tested inside a large Helmholtz coil driven with a 0.1 Oe_{rms} field at 1kHz. Care was taken to fabricate a coil large enough to insure the test was performed within the uniform field area of the coil. The sensors were electrically connected in a parallel configuration and the distance between sensors was adjusted symmetrically. The ME voltage and charge were measured throughout the span using a lock-in analyzer and plotted to observe the trends (Figure 177). The results so far suggest ME coefficients of both charge and voltage can behave differently in the individual sensor regardless of the symmetry of the experiment. The maximum ME charge and voltage of the parallel connection was achieved at a center-to-center in plane spacing of approximately 3.6 cm. The ME voltage experiences a parallel increase with spacing change of approximately 13% from 2.77V/Oe to 3.05V/Oe. The charge remained more constant and only experienced approximately 7% change with the spacing difference. The maximum ME charge seen here is 3750pC/Oe at an in plane center-to-center parallel spacing of 3.4cm.

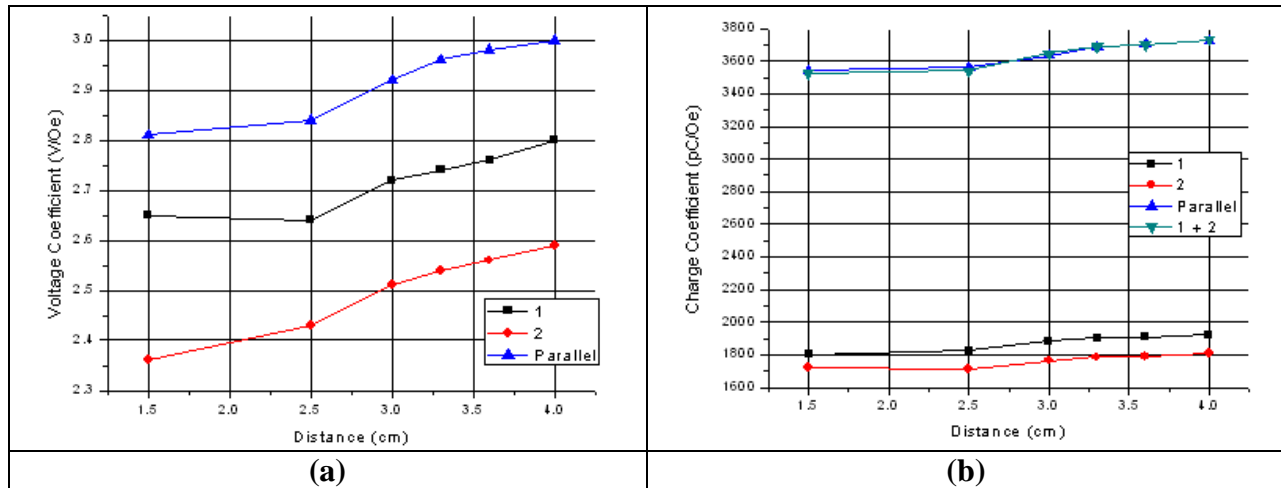


Figure 178. (a) parallel ME voltage output as a function of out-of-plane center-to-center separation distance. (b) ME charge output as a function of out of plane separation distance.

Array module:

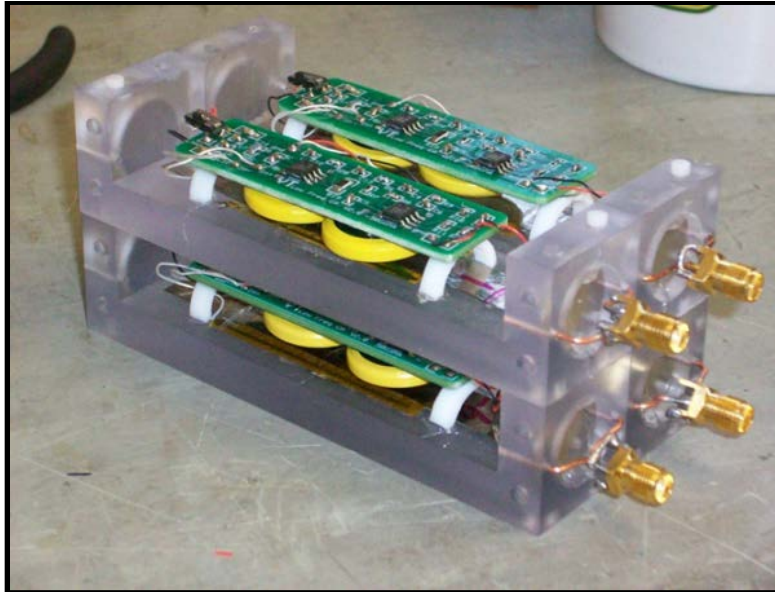


Figure 179. PSU array modules with individual charge amps and batteries ready for configuration experiments.

Each module was upgraded to include its own VT constructed low frequency charge amplifier with switch and batteries. The output of each is connected to individual SMA fittings. The modules did not lose any flexibility when fitted with the extra circuits and batteries. Assessing the output noise characteristics for the array and individual sensors now requires four simultaneous channels. Experimental data will be collected with a datalogger and used for signal processing. Experiments can now be conducted in and out of the noise and vibration isolation chamber. Configurations can be altered to determine the best performance. The large size of the package and the presence of four distinct high permeability strips impose an extra degree of difficulty when measuring inside a Helmholtz coil. Careful calibration of fields before and during tests will need to be done to insure results are accurate. More ideal experiment geometry

might include an incident field from a fixed distance. This geometry will reduce field interaction from submersion of high permeability material within the field.

The PSU array module was redesigned for the addition of the SAIC proposed charge amplifier which will replace the larger VT charge amplifier (see Fig.62). To properly mount the charge amplifier without utilizing stand-offs or mounting flanges, a center beam was used instead of single platform as before. With a symmetrical center beam, the sensor can be mounted off center to one side and the charge amplifier mounted on the remaining side. The spaces were symmetrical which gave a great deal of flexibility. We can either mount multiple sensors opposite a charge amp or multiple sensors on both sides without a charge amp. We could even mount multiple charge amps (one on top and bottom) if required. The new charge amplifier had a much smaller footprint for integration into the PSU module. SAIC reworked the circuit to minimize space in the package and decided to provide mini-USB connectors for output signal and battery input. The USB will leave the SAIC package at a right angle and will extend past the edge of the module. The metal on the USB can then be attached to any shielding surrounding the enclosure. Also, the USB can be oriented to either side or even upwards to accommodate any configuration changes we might make when placing modules together. The input to the charge amplifier from the sensor will be done via three pin terminals seen in Figure 179. Wires from the sensor to the pins can be routed through the center beam for soldering.

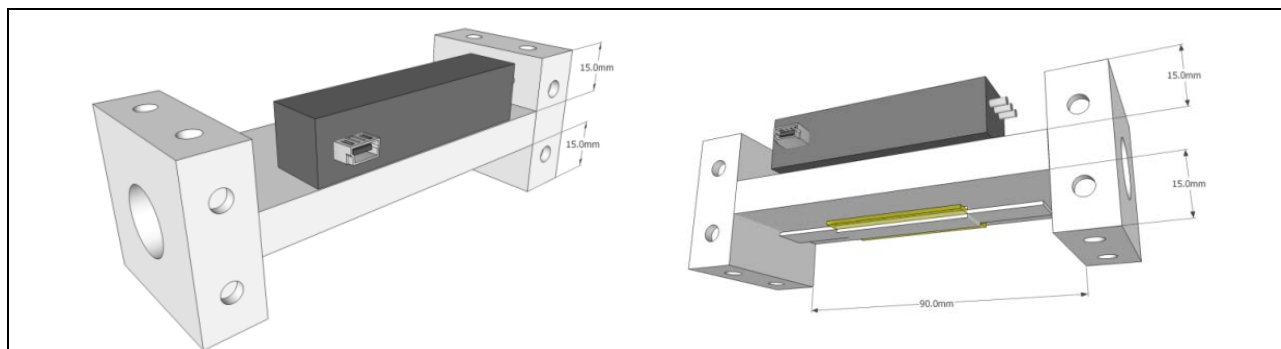


Figure 180. New PSU array module design with SAIC charge amplifier.

The design utilized the same magnets as the previous design and will be placed at the centerline of the module. The square shape and symmetrical arrangement will allow for all the same configurations as the original. The square dimension has been increased to be 40 mm instead of the previous 25.4mm. This was due to previous sensor proximity tests which suggest 40 mm results in the optimum ME properties of the individual sensors.

Array Sensor Configuration:

Experiments with multiple sensors connected or “stacked” were performed utilizing sensors of different compositions. The tests reported in this section were done utilizing PZT based sensors. They were fabricated using the most common electrode spacing of 0.85 mm between neighboring electrodes. The electrical properties of the individual sensors were closely matched and the representative properties are shown in the first row of Table 42 below. The properties of the sensors after connecting in series and then parallel (Figure 181) are shown in the second row of Table 42. The series/parallel configuration was chosen in an effort to double charge while keeping loss and capacitance similar to that of a single sensor. The resistance of this

configuration should also remain as low as that of a single sensor.

Table 42. Comparison of individual sensor properties to properties of stacked sensors in serial/parallel combination.

	C(pF)	α_V (V/Oe)	α_Q (pC/Oe)	$\tan\delta$ (%)
Individual PZT/Metglas	530	2.1	1350	1.2
Total PZT stack	552	4	2650	1.2

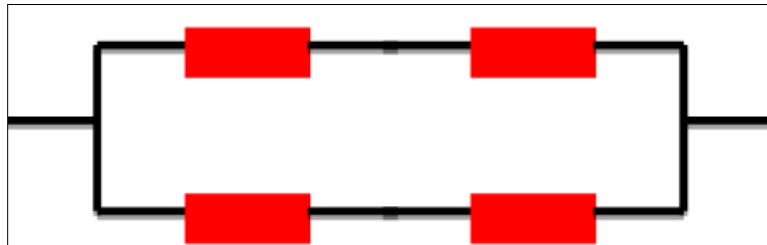


Figure 181. Electrical Configuration used in sensor stacking experiments.

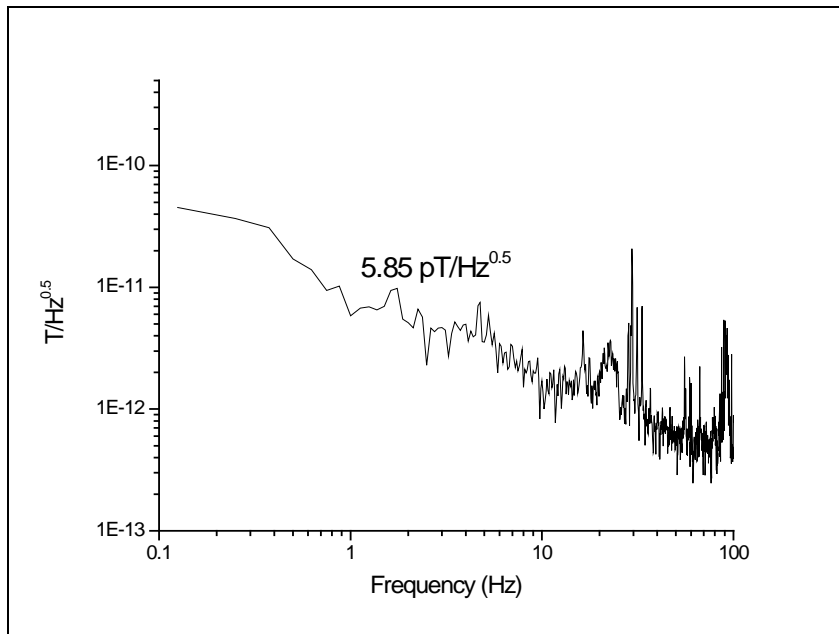


Figure 182. Noise floor for four stacked PZT sensors using serial/parallel configuration

The increase in charge should help to lower the noise floor of the sensor. All the other sensor quantities should resemble a single sensor when viewed by the charge amplifier minimizing any charge amplifier mismatch. The noise floor was measured using this configuration and was found to be as low as $5.85 \text{ pT}/\sqrt{\text{Hz}}$ (Figure 182). PZT based sensors normally have noise floor values as high as $20 \text{ pT}/\sqrt{\text{Hz}}$ when measured individually. This configuration realizes a 70% drop in the noise floor value.

The same experiment was then performed for sensors based on PMN-PT as the piezoelectric phase. PMN-PT sensors normally possess lower noise floors and higher charges than that of PZT based sensors. The same series/parallel configuration was utilized in this experiment. Four identical PMN-PT sensors were fabricated. The characteristics of the individual sensors are shown in Table 43 below. Again, stacking in this configuration should double the charge while keeping the other quantities equal to that of an individual sensor. In the case of PMN-PT, this means a total stacked charge of 3565 pF.

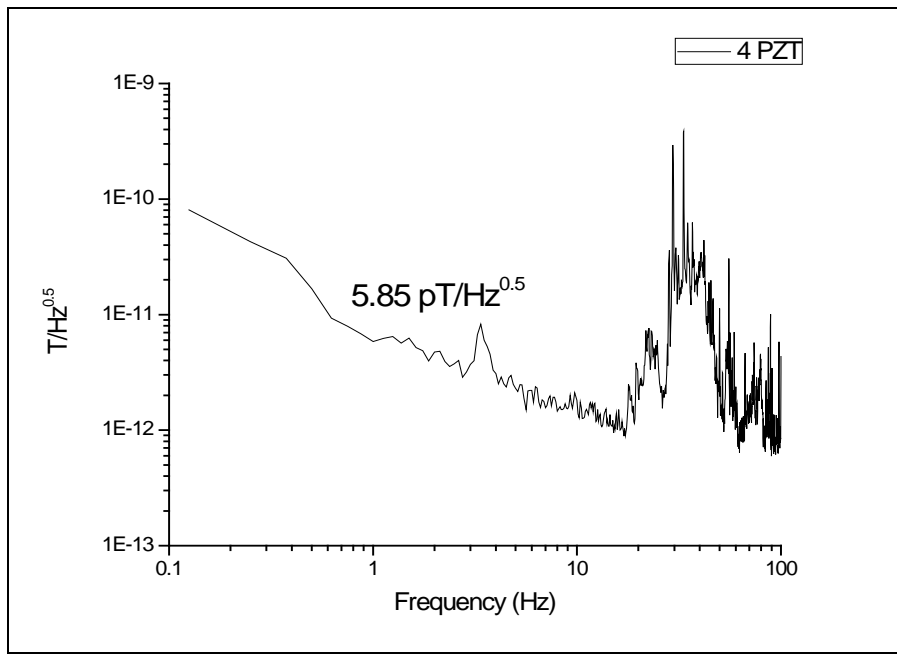


Figure 183. Noise floor for four stacked PMN-PT sensors using serial/parallel configuration.

Table 43. Comparison of individual PMN-PT sensors to four PMN-PT sensors stacked in serial/parallel configuration.

	C(pF)	α_v (V/Oe)	α_Q (pC/Oe)	$\tan\delta$ (%)
Individual PMN-PT/Metglas	550	2.85	1850	1.7
Total PMN-PT stack	552	6.16	3565	1.7

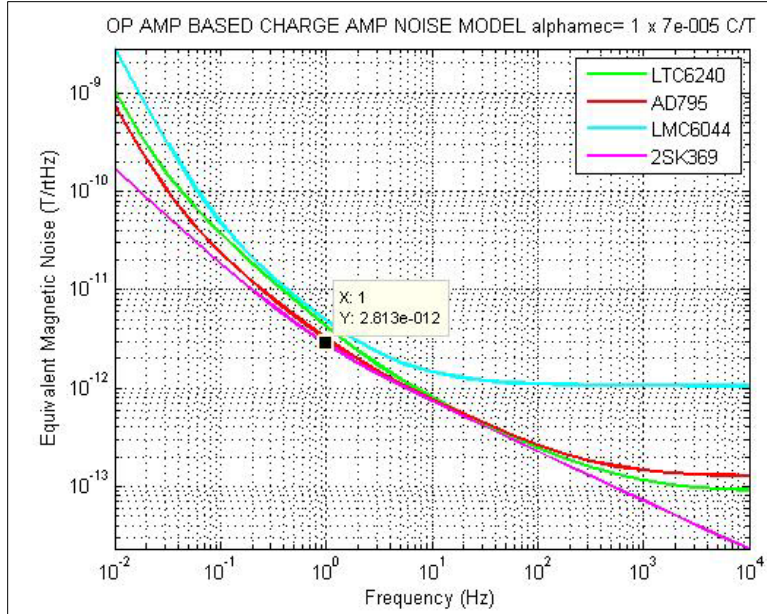


Figure 184. Noise floor of four stacked PMN-PT sensors in serial/parallel configuration.

The noise floor was measured for this configuration in the hopes it would be much lower than that of the PZT based sensors because of the increase in charge. Normal noise floor values for a single PMN-PT sensor are in the neighborhood of 9-10 pT/ $\sqrt{\text{Hz}}$. The noise floor measured using the stacked PMN-PT sensors was exactly the same as that of the PZT sensors (5.85 pT/ $\sqrt{\text{Hz}}$). Modeling of this configuration based on ideal sensor qualities and exact summing of charge predicted a much lower noise floor (3.5 pT/ $\sqrt{\text{Hz}}$) for the PMN-PT stacks. However, this configuration may not be the optimum configuration for the PMN-PT sensors.

To better understand how the choice of configuration affects the noise floor, a MATLAB model was utilized. The model uses sensor specific electrical quantities (measured) and plots their contributions to the equivalent magnetic noise. Because charge amplifier voltage noise and impedance play a role in the equivalent magnetic noise, plots for each possible charge amplifier are overlayed to illustrate the advantages and disadvantages of each type when attached to the sensor configuration.

Example predictions of this model can be seen in Figure 185. The predictions in Figure 185 are for four PMN-PT sensors in parallel configuration. These curves were obtained using α_q , α_v , sensor loss, sensor impedance and capacitance of four individual sensors. The measured individual characteristics were used to predict electrical quantities after attaching in series. These quantities were used for the model and curves plotted for each possible charge amplifier configuration.

Figure 185 suggests more than one charge amplifier is capable of minimizing the noise floor. For the parallel configuration we expect a noise floor value of 2.81 pT/ $\sqrt{\text{Hz}}$.

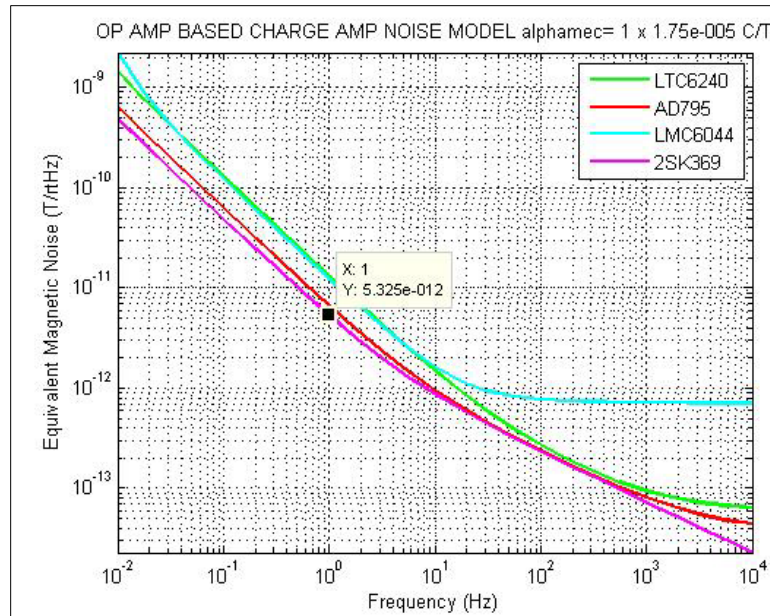


Figure 185. MATLAB model of predicted equivalent magnetic noise utilizing four PMN-PT sensors in parallel configuration.

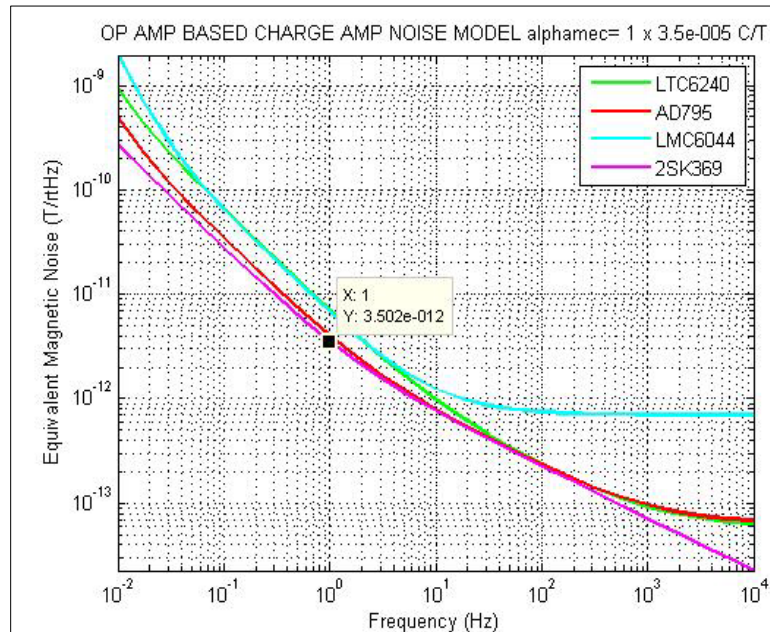


Figure 186. MATLAB model of equivalent magnetic noise using four PMN-PT sensors in parallel configuration.

The model was also used for both the series and parallel/series hybrid configuration of four PMN-PT sensors. The series connection is simply four sensors in series. The parallel/series hybrid configuration is two sets of series connected PMN-PT sensors connected in parallel. The modeled results for the series connection are shown in Figure 186. From the graph the lowest noise floor value will be achieved with the 2SK369 JFET charge amplifier. The equivalent

magnetic noise value for this charge amplifier and the measured electrical quantities for our sensors is $5.33 \text{ pT}/\sqrt{\text{Hz}}$.

The objective of using the parallel/series combination was to combine four sensors in a configuration that matched the impedance and capacitance values of a single sensor. It was thought that the charge amplifier may not properly match the increased impedance of four series sensors or the increased capacitance of four parallel sensors. The parallel/series connection will have impedance and capacitance characteristics of a single sensor. Figure 186 reveals the modeled noise floor values based on the series/parallel connection. The predicted equivalent 1 Hz magnetic noise floor for the 2SK369 JFET charge amplifier is $3.50 \text{ pT}/\sqrt{\text{Hz}}$. This is very close to that of the parallel connection.

From the simulation it is possible to reduce the noise floor below $3 \text{ pT}/\sqrt{\text{Hz}}$ using PMN-PT sensors in parallel configuration. Four PMN-PT were fabricated and electrical characteristics were used in this modeling. After modeling, the noise floor for the parallel configuration was measured.

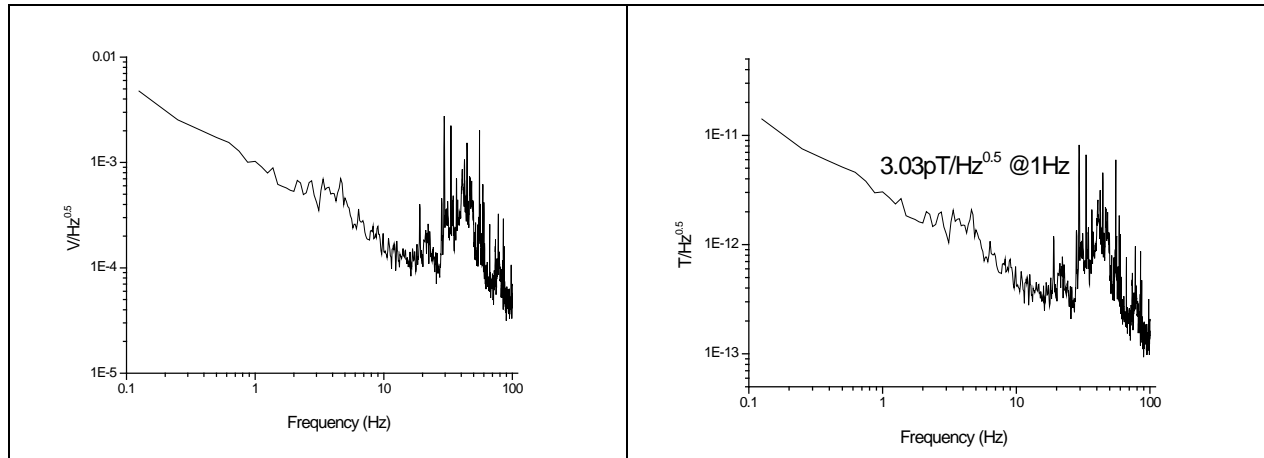


Figure 187. Measured noise floor of four PMN-PT using a parallel connection.

The results of the noise floor measurement are shown in Figure 187 above. Four PMN-PT sensors in a parallel configuration measure $3.03 \text{ pT}/\sqrt{\text{Hz}}$ compared to a modeled value of $2.81 \text{ pT}/\sqrt{\text{Hz}}$. The difference in modeled and measured values may be due to sensor mismatch.

D.3.4.3. Sensor Stacking

Testing was done for stacked sensors. Tests were initially performed by stacking 4 sensors together with one charge amplifier for the set. The charge amplifier used was a JFET charge amplifier made by SAIC. The tests were then redone using 8 sensors stacked with one charge amplifier so that loss and ME properties could be compared. Samples were arranged around a square PVC tube to decrease sensor interference. Earlier tests have proven this geometrical layout to be the best. The optimum geometry for 8 stacked sensors can be seen in Figure 188 below.

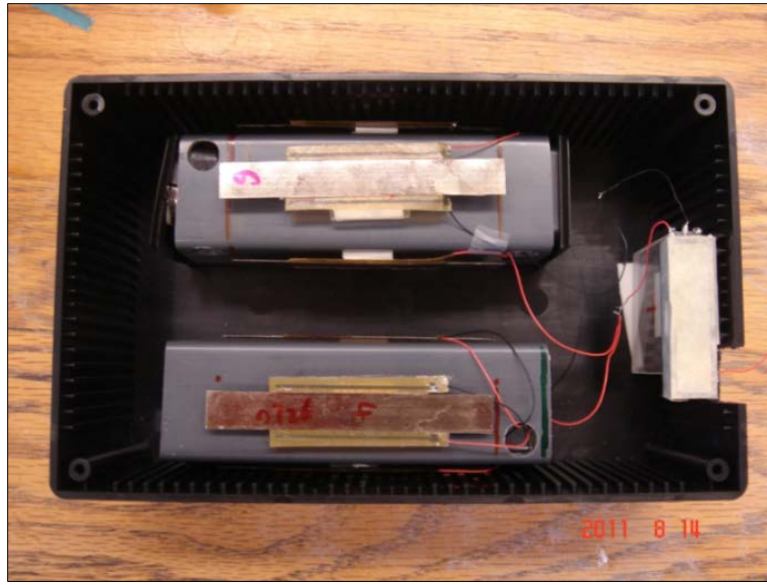


Figure 188. Testing protocol and pattern established for sensor stacking tests.

A list of sensors used for the experiments and the results of each is shown in Tables 44 and 45 below. It can be seen from Table 44 below that the capacitance of the eight sensor stack was exactly the sum of the two four sensor stacks. Also the loss for the eight sensor stack never increased beyond the value of the largest four sensor stack. And the charge value for all eight sensors stacked together was exactly the sum of the charges for the individual 4 sensor stacks. It is therefore very easily to calculate charge, loss and capacitance for future stacking experiments. The disadvantage is the amplitude of the ME voltage and leakage resistance make them difficult to measure. Also, noise floor measurements were not on the magnitude expected. The magnitude of each of these properties was larger than our normal values and is presenting us with new difficulties.

Table 44. Sensors fabricated for stacking experiments and recorded ME properties.

2mm-d	C(pF)	α_V (V/Oe)	α_Q (pC/Oe)	$\tan\delta$ (%)
1	175	2.62	832	1.30
2	178	2.35	726	1.23
3	180	2.70	880	1.20
4	194	3.00	1000	1.43
5	158	2.31	636	1.40
6	178	2.09	652	1.30
7	175	2.45	700	1.42
8	180	2.37	720	1.46

Table 45. Properties of stacked sensors utilizing only one JFET charge amplifier for set.

	C(pF)	α_V (V/Oe)	α_Q (pC/Oe)	$\tan\delta$ (%)	R_{dc} (G Ω)
1-4 stacked in parallel	702	4.05	3273 (95.2% of the sum of four)	1.34	28.6
5-8 stacked in parallel	650	3.80	2580 (95.3%)	1.40	
1-8 stacked in parallel	1350	Cannot measure	3273+2580=5853	1.40	15.0

E. Shashank Priya, Virginia Tech

E.3.1. Synthesis of Ferroelectric PZT Fibers using Sol-gel Technique

At the beginning, we successfully fabricated micron-diameter long PZT ceramic fibers via sol-gel route by controlling the hydrolysis degree and concentration of precursor sol. The schematic diagram of fiber drawing process and optical microscopy images of drawn fibers are shown in Figure 189 (a) and (b). By changing fiber pulling speed (10–50 cm/s) and diameter of glass rod (5–10 mm), gel fibers with various diameters ranging from 15 to 70 μm were obtained as shown in Figure 189 (b).

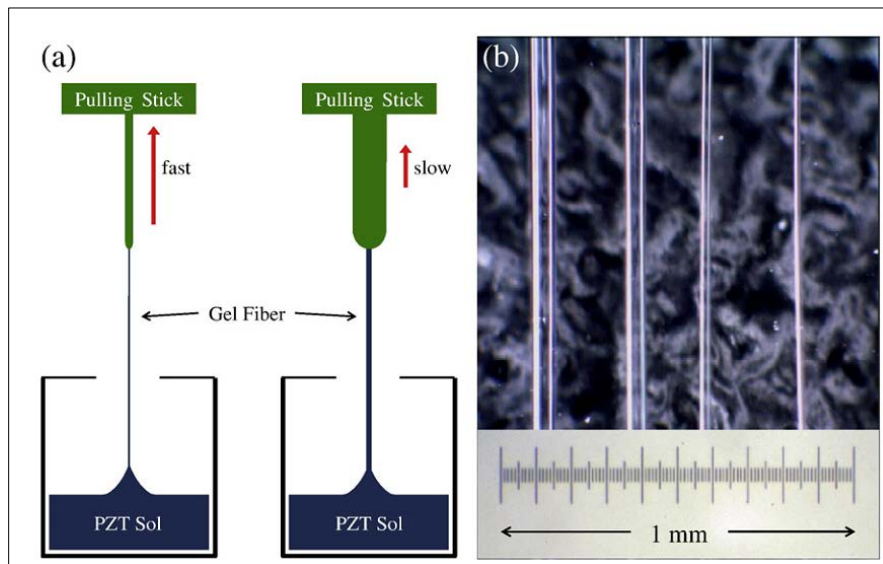


Figure 189. (a) Schematic diagram of drawing process of PZT gel fibers and (b) optical microscopy image of PZT gel fibers drawn from #5.0 solution.

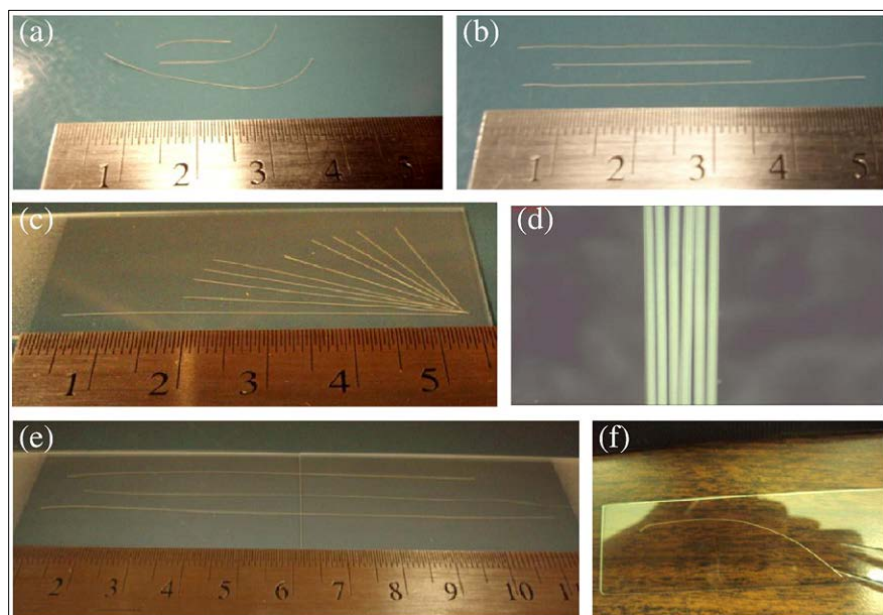


Figure 190. Picture of PZT ceramic fibers sintered at 950 °C for 10 h: (a) from #2.5 solution, (b) from #5.0 solution, and (c)–(f) from #5.0-2 .4 M solution

PZT gel fibers were converted in to ceramic fibers by conventional sintering process. Figure 190 shows the picture of PZT ceramic fibers sintered at 950 °C for 10 h in air. As seen in Figure 190 (a) and (b), fibers from the solution #2.5 were usually bent and broken after sintering while those from #5.0 solution maintained their straight shape. We think that gel fibers from #2.5 solution may contain larger amount of organic than those from #5.0 because of the difference in hydrolysis degree of metal-alkoxide. An optimum PZT sol was obtained near 2.4 M molarity (#5.0–2.4 M) and very long PZT gel fibers (several meters) could be drawn without any discontinuity. Figure 190 (c)–(f) shows the sintered PZT fibers from #5.0-2.4 M solution. Straight and long PZT ceramic fibers (Figure 190 (e)) were obtained with homogeneous thickness (Figure 190 (d)), high aspect ratio (N 3000) and good mechanical flexibility (Figure 190 (f)).

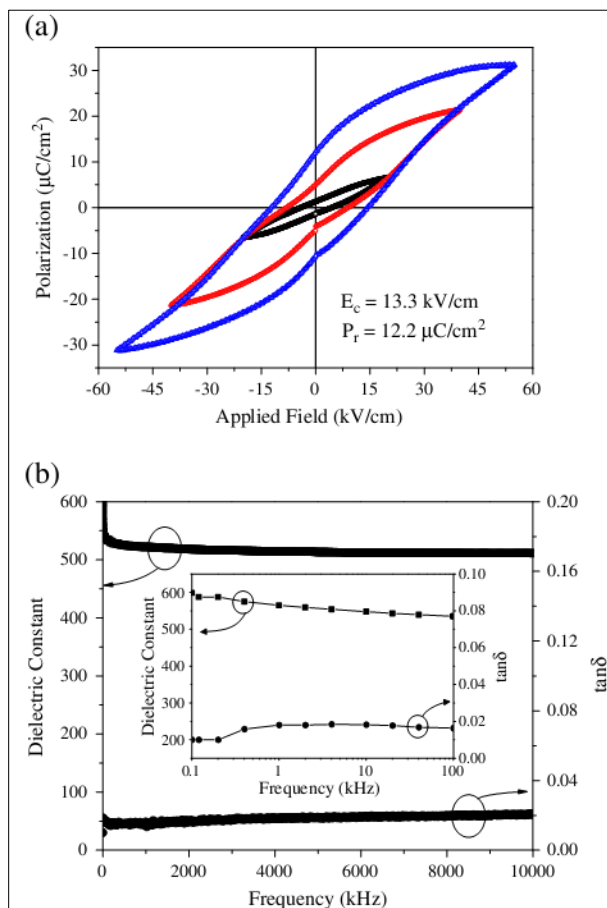


Figure 191. (a) Polarization vs. electric field curve measured at 0.1 Hz and (b) dielectric constant and loss factor at various frequencies for 1–3 composite.

Inset of (b) shows dielectric constant and loss factor at low frequencies ranging from 100 Hz to 100 kHz.

The electrical properties of sol–gel P ZT fibers were measured by fabricating 1–3 composite disks consisting of 400 PZT fibers in epoxy matrix (West System: 105 resin and 206 hardener , USA). This composite was polished to a thickness of 700 μm and electrodes were deposited on

top and bottom. The actual area of exposed fiber cross- section was found to be $\sim 0.7 \text{ mm}^2$. Figure 191 shows the polarization vs. electric field ($P-E$) and dielectric properties of the composite. The 1–3 composite clearly showed $P-E$ hysteresis loops with coercive field and remanent polarization of 13.3 kV/cm and $12.2 \mu\text{C}/\text{cm}^2$ respectively. Dielectric constant of this composite was measured to be 565 with loss factor of 0.018 at 1 kHz.

E.3.2. [001] Textured PMN-PT Ceramics

Up to now, we have optimized the piezoelectric performance and texture degree, and quantified the effect of BT template concentration on the texture degree and resulting changes in properties of PMN-PT. For the first time, we show that even 1 vol% template can provide >90% texture degree.

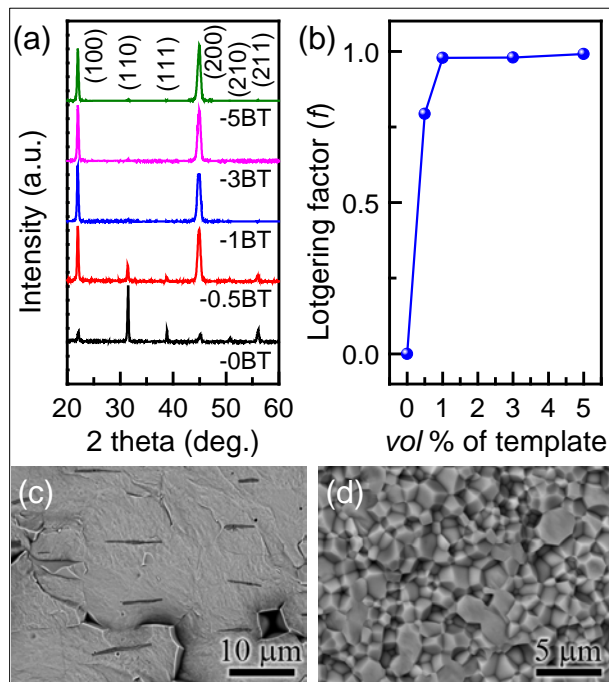


Figure 192. (a) XRD patterns of PMN-PT-xBT ceramics; **(b)** Texture degree of PMN-PT ceramics as a function of BT concentration; cross-sectional SEM image of **(c)** PMN-PT-1BT and **(d)** PMN-PT-0BT ceramic.

Figure 192(a) shows the XRD patterns of PMN-PT- x BT sintered specimens. All patterns display pervoskite structure without pyrochlore phase. With the introduction of template, the intensities of $(00l)$ peaks increases rapidly while other peaks have almost negligible intensity, indicating the induction of texture. Figure 192 (b) shows the texture degree computed by Lotgering factor method as a function of BT concentration. PMN-PT-0BT represents the random polycrystalline ceramics. With increase of BT template content, the texture degree increases dramatically and then saturates for PMN-PT-1BT. Figure 192 (c) displays the cross-sectional SEM images of PMN-PT-1BT specimen. It clearly shows brick wall-like structure. BT templates (black lines) were well aligned in the matrix and there were no residual random-oriented matrix grains (similar to PMN-PT-0BT as shown in Figure 192 (d)). This microstructure is consistent with the high texture degree as indicated by XRD. These results clearly show that PMN-PT-1BT with 1

vol% template was almost fully textured ($f = 0.98$). This is a significant achievement with important implications towards application of piezoelectric ceramics. We found that optimum dimension for BT template microcrystals to achieve high texture degree was in the vicinity of length: 5~10 μm , and thickness: 0.5~1 μm . At these dimensions the required growth distance for inducing texture in the matrix is dramatically reduced on the order of ~3 – 7 μm .

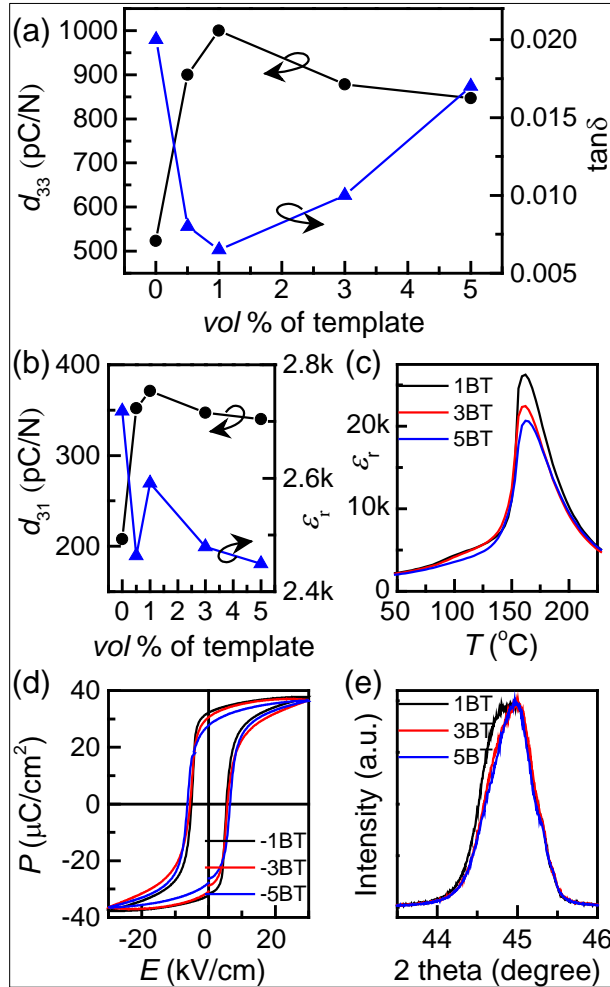


Figure 193. (a,b) Dielectric and piezoelectric properties of PMN-PT- x BT ceramics; (c) Dielectric permittivity as a function of temperature for PMN-PT- x BT ceramics; (d) Polarization (P) vs. electric field (E) hysteresis loops of PMN-PT- x BT ceramics; and (e) XRD patterns of PMN-PT- x BT ceramics.

Figure 193 (a) shows the piezoelectric coefficient (d_{33}) and dielectric loss ($\tan\delta$) of PMN-PT- x BT specimen. With increase of BT content, the d_{33} increases dramatically and achieves the maximum value of 1000 pC/N at $x = 1$, corresponding to the texture development as shown in Figure 192 (b). In this range ($0 \leq x \leq 1$), the enhancement of piezoelectric response is attributed to the texture engineering which develops domain configurations similar to that in the single crystal. Further increasing the BT content, the d_{33} gradually decreases. Similar trend can also be observed in the change of d_{31} as shown in Figure 193 (b). The change of $\tan\delta$ is opposite to the variation of d_{33} . The lowest value of $\tan\delta$ (~0.6%) was achieved for PMN-PT-1BT ceramic,

which is about $1/3^{\text{rd}}$ of the magnitude obtained for most of the soft piezoelectric ceramics ($>2.0\%$). High piezoelectric response with low loss makes PMN-PT-1BT system an ideal substitute for currently deployed soft piezoelectrics.

In the case of ϵ_r , Figure 193 (b) shows that the relative permittivity for the poled PMN-PT-xBT at room temperature decreases with increasing x in the range of $x > 1$. Same tendency of maximum relative permittivity for unpoled PMN-PT-xBT can be found in the Figure 193 (c). No obvious T_c shift in PMN-PT-xBT specimen indicates BT is very stable in PMN-PT ceramics. Therefore, the decrease of ϵ_r may be associated with the elastoelectric composite effect due to the introduction of low permittivity BT template ($\epsilon_t=130$ in $<001>$ direction). Figure 193 (d) shows the polarization (P) vs. electric field (E) for the PMN-PT-xBT specimen in the range of $x > 1$. It can be seen that P_r decreases and coercive field (E_c) increases with increasing BT template content (x), which indicates that the domain motion and switching became more difficult. This phenomenon may be attributed to clamping effect of BT template. The stress comes from the lattice mismatch between BT template and PMN-PT matrix, and also from their large difference in electromechanical properties. The stress build-up also results in phase shift from rhombohedral side to tetragonal side. Although fine BT template crystals were used which reduces the magnitude of stress, the width of (002) peaks decreases indicating phase shift from MPB (coexistence of rhombohedral and tetragonal phase) to tetragonal side as shown in Figure 193 (e). Therefore, elastoelectric composite effect and clamping effect can be suggested to degrade the piezoelectric property when texture degree saturates.

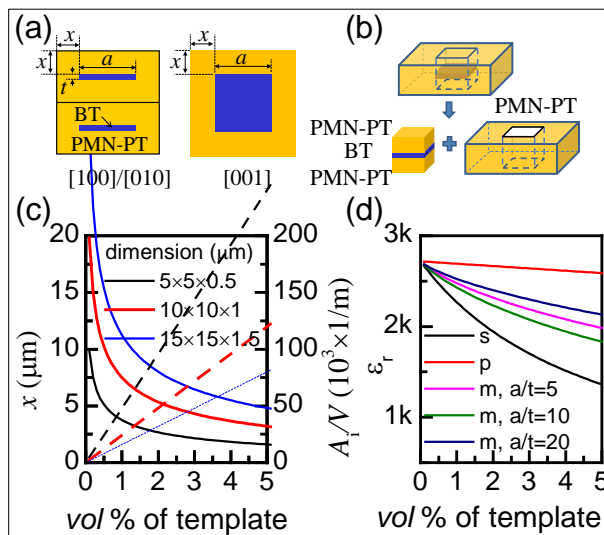


Figure 194. (a) Schematic illustration of grains of textured ceramic (left: [100] or [010] view, and right: [001] view). (b) Required growth distance (x) of matrix crystal (solid line) and specific interface area (A_i/V) (dashed line) as a function of the volume fraction and dimensions of template. (c) Schematic illustration of single templated grain. (d) Calculated relative permittivity of fully textured PMN-PT ceramic as a function of the volume fraction and dimensions of BT template.

Textured PMN-PT ceramics can be considered as a composite consisting of matrix PMN-PT and BT templates as shown in Figure 194 (a). In ideal condition, the required growth distance (x) of

PMN–PT crystal on BT template for 100% texture degree can be calculated by the following equation:

$$\frac{a^2 t}{V_T} = (2x + a)^2 (2x + t) \quad (263)$$

where a is the dimension of template plane, t is the thickness of template and V_T is the volume fraction of template. Figure 194 (b) shows the variation of x as a function of the volume fraction and dimensions of template. Higher is the template content shorter is the growth distance, thus easier it is to achieve full texture. As shown in Figure 194 (c), this composite can be considered as both parallel and series connections between PMN-PT matrix and BT template. When the composite is composed of only parallel connection, the effective permittivity of composite ($\epsilon_{parallel}$) was calculated by using Equation (264). On the other hand, when the composite is composed of only serial connection, the effective permittivity of composite (ϵ_{serial}) can be calculated by using Equation (265) given as:

$$\epsilon_{parallel} = \epsilon_t V_T + \epsilon_m (1 - V_T) \quad (264)$$

$$\epsilon_{serial} = \left[\frac{\epsilon_t \epsilon_m}{\epsilon_m V_T + \epsilon_t (1 - V_T)} \right] \quad (265)$$

where $\epsilon_m \epsilon_m$ is the relative permittivity of PMN-PT matrix and ϵ_t is the relative permittivity of BT template crystal. Since our textured sample is composed of both parallel and serial connection between PMN-PT matrix and BT templates (Fig. 6(c)), the relative permittivity of this composite structure (ϵ_{mixed}) was calculated by following expression:

$$\epsilon_{mixed} = \left[\frac{\epsilon_m \frac{4x^2 + 4ax}{2x + t} + \frac{a^2 \epsilon_t \epsilon_m}{2x \epsilon_m + t \epsilon_t}}{\frac{(2x + a)^2}{2x + t}} \right] \quad (266)$$

Figure 194 (d) shows the theoretical relative permittivity for 100% textured ceramics as a function of the volume fraction and dimensions of template. Here, the relative permittivity is calculated from Equations (264)-(266) by using $\epsilon_m = 2718$ for PMN-PT matrix grains and $\epsilon_t \epsilon_t = 130$ for $<001>$ BT template.

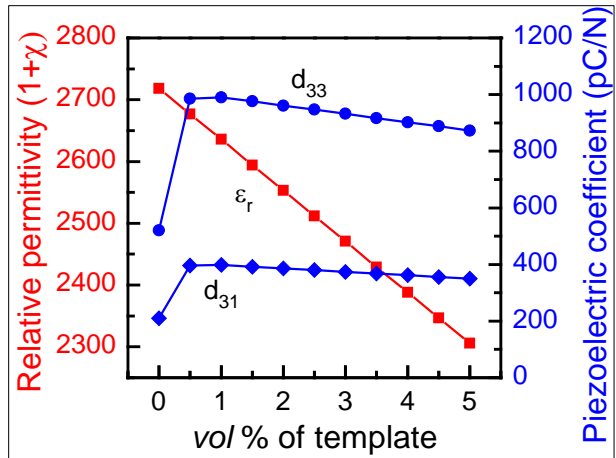


Figure 195. Theoretical prediction of dielectric and piezoelectric properties of textured PMN-PT ceramics as a function of BT template volume fraction.

As shown in Figure 195 (b), the specific interface area (A_i/V) related to clamping effect increases linearly with the BT template content. To further clarify the clamping effects of BT template content, texture degree, and material property mismatches between PMN-PT and BT on the dielectric and piezoelectric properties of the textured PMN-PT ceramics, we modeled the electrical behavior of the system by accounting the microstructural boundary conditions. The theoretically predicted dielectric and piezoelectric properties of textured PMN-PT ceramics are plotted as a function of BT template volume fraction in Figure 195, exhibiting good agreement with the experimental measurements shown in Figure 193 (a, b), especially for the piezoelectric strain coefficients d_{33} and d_{31} . These results confirm that [001] texturing of PMN-PT significantly improves the ceramic properties, while BT template content decreases the composite properties through mechanical clamping effect and interfacial mismatch. In conclusion, we quantify the effect of BT template heterogeneity on the texture degree and piezoelectric properties of PMN-PT ceramics. Inhomogeneity effect (elastoelectric composite effect, clamping strain) was clarified by theoretical models. Almost full [001] texture ($f=0.98$) was achieved at very low template volume fraction (1%). This is an important advancement in texture engineering of PMN-PT ceramics that promises to provide high-performance piezoelectric materials at significantly lower cost.

E.3.3. [001] Textured Pb(Mg_{1/3}Nb_{2/3})O₃-PbZrO₃-PbTiO₃ Ceramics

We synthesized of textured PMN-PZT ceramics with highly improved piezoelectric properties ($d_{33} > 1000$ pC/N, $g_{33} > 50 \times 10^{-3}$ Vm/N and $\tan \delta < 1.2\%$). Generally, high d_{33} piezoelectric materials possess low g_{33} value and vice versa as shown in Figure 196 (a) because d_{33} is usually proportional to square root of dielectric constant of piezoelectric materials. However, our textured PMN-PZT exhibited both high d_{33} and high g_{33} values due to template-controlled dielectric characteristics. The high d_{33} and g_{33} values are of importance for high magnetoelectric (ME) charge coefficient and voltage coefficient of ME sensors respectively. Therefore, combining with low loss value, the textured PMN-PZT is expected to yield a high performance of sensor.

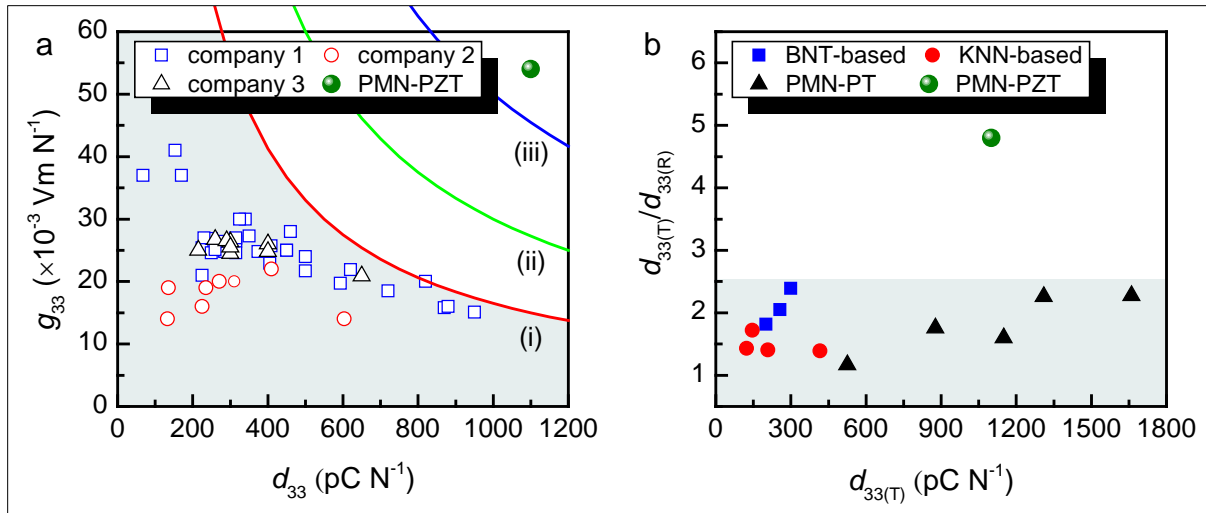


Figure 196. (a) Comparison of g_{33} and d_{33} values of various piezoelectric ceramics. (b) Comparison of $d_{33(T)}/d_{33(R)}$ ratio vs. $d_{33(T)}$ of various textured piezoelectric ceramics.

Different colored lines (i), (ii) and (iii) indicate the plots of $g_{33} \cdot d_{33} = c$ function; (i) $c = 16500 \times 10^{-15} \text{ m}^2 \text{ N}^{-1}$, (ii) $c = 30000 \times 10^{-15} \text{ m}^2 \text{ N}^{-1}$ and (iii) $c = 50000 \times 10^{-15} \text{ m}^2 \text{ N}^{-1}$. The $d_{33(T)}$ and $d_{33(R)}$ represent d_{33} of textured ceramic and that of randomly oriented counterpart respectively. BNT and KNN represent $(\text{Bi}_{1-x}\text{Na}_x)\text{TiO}_3$ and $(\text{K}_{1-x}\text{Na}_x)\text{NbO}_3$ compositions respectively.

Table 46. Piezoelectric and dielectric properties of PMN-PZT piezoelectrics: randomly oriented ceramic (R-ceramic), <001> textured ceramic (T-ceramic) and <001> single crystal (S-crystal).

Properties	R-ceramic	T-ceramic	S-crystal (⁸)
Piezoelectric charge constant, d_{33} (pC/N)	230	1100	1530
Electromechanical coupling constant, k	$0.4 (k_p)$	$0.84 (k_p)$	$0.93 (k_{33})$
Relative dielectric permittivity, ϵ_{33}/ϵ_0	915	2310	4850
Piezoelectric voltage constant, g_{33} ($\times 10^{-3} \text{ Vm/N}$)	28.4	53.8	35.6
$d_{33} \cdot g_{33}$ ($\times 10^{-15} \text{ m}^2/\text{N}$)	6532	59180	54468
Remanent polarization, P_r ($\mu\text{C/cm}^2$)	30	36	29
Coercive field, E_c (kV/cm)	8.2	7.4	4.5
Curie temperature, T_c ($^\circ\text{C}$)	233	204	211

Table 46 summarizes the piezoelectric and dielectric properties of randomly oriented ceramic (R-ceramic), <001> textured ceramic (T-ceramic) and <001> single crystal (S-crystal) of PMN-PZT composition. T-ceramic exhibited giant d_{33} of 1100 pC N^{-1} which is 4.8 times higher than that of

R-ceramic (230 pC N^{-1}). This increasing ratio of d_{33} value between R- and T-ceramic (4.8) was much higher than that of the other textured piezoelectric ceramics (usually less than 2.5) as shown in Figure 196 (b).

We have modified tube furnace for fabrication of large size textured samples. The tape casting and lamination processes have also been optimized for stable and uniform fabrication of large scale fibers by controlling casting speed, blade width and lamination pressure parameters. The scale of textured piezoelectric ceramics has been dramatically increased. Long PMN-PZT textured fibers with dimensions of 70 mm x 5 mm x 0.5 mm (Figure 197) were fabricated and sent to Dr. Srinivasan's team for their sensor fabrication.

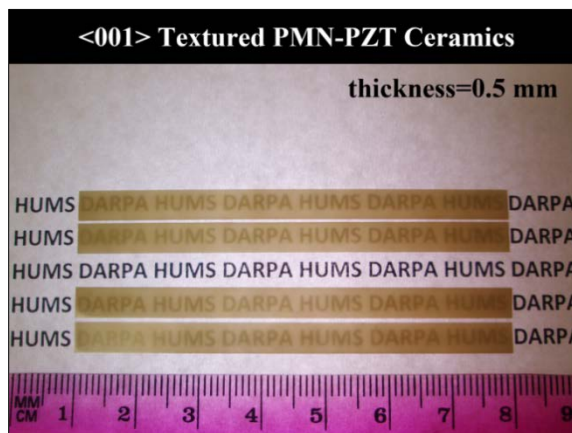


Figure 197. Photo image of textured PMN-PZT fibers.

E.3.4. Mn doped [001] Textured $\text{Pb}(\text{Mg}_{1/3}\text{Nb}_{2/3})\text{O}_3$ - PbZrO_3 - PbTiO_3 Ceramics

Besides the fiber fabrication of high d and g with low loss textured piezoelectrics, we have tried to develop high performance textured piezoelectrics for resonance mode ME sensor applications. To enhance the ME response at electromechanical resonance, the core piezoelectrics in ME composite should have high mechanical quality factor (Q_m) along with high piezoelectric coefficients (d and g) and low dielectric loss. Since most of existing piezoelectric compositions show that hard piezoelectrics with high Q_m usually have low d value, achieving high Q_m , high d and low loss together from single piezoelectric is quite challenging. To address this task, we have considered textured hard piezoelectrics and investigated Mn-modified textured PMN-PZT ceramics because Mn has been widely used for hardening PZT ceramics.

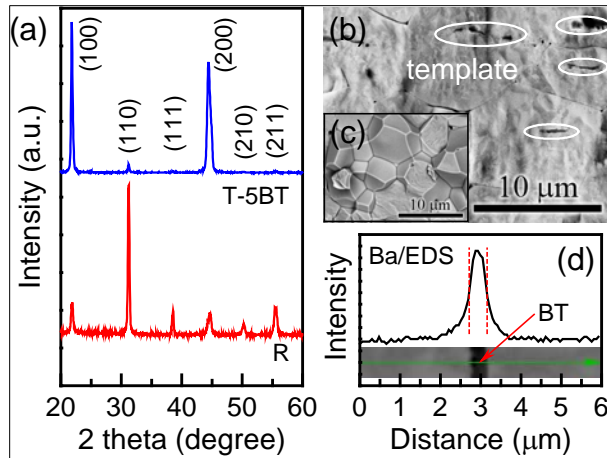


Figure 198. (a) XRD patterns of randomly oriented and textured MnO₂ doped PMN-PZT ceramics with 5 vol% BT template (abbreviated as R and T-5BT, respectively); SEM images of (b) T-5BT and (c) R ceramic; (d) line scanning element analysis of EDS across BT and PMN-PZT matrix.

Figure 198 (a) shows the XRD patterns of randomly oriented and textured MnO₂-doped PMN-PZT ceramics with 5 vol% BT (R and T-5BT ceramics, respectively). All the samples showed perovskite structure. Compared to the R ceramic, the *00l* reflection peaks of T-5BT ceramic were enhanced exhibiting high Lotgering factor of 96% that indicates a strong pseudo-cubic <001> orientation of textured grains in the T-5BT ceramic. The SEM image of the T-5BT ceramic showed a brick wall-like microstructure with well aligned BT templates (black lines) in the matrix as shown in Figure 198 (b) while the R ceramics showed homogeneous equiaxed grains (Fig. 10(c)). Table 47 shows the dielectric and piezoelectric properties of randomly oriented pure PMN-PZT (R-pure ceramic), R ceramic and T-5BT ceramic poled and measured at room temperature. The piezoelectric properties of T-5BT ceramic were enhanced compared to those of R-pure and R ceramics. Note that the Q_m and tan δ of the T-5BT ceramic were improved together with the d and k coefficients clearly demonstrating presence of “hard” and “soft” combinatory characteristics. Both d_{33} and Q_m of the T-5BT ceramic were 4 times higher and tan δ was 6.5 times lower than those of R-pure ceramic. This result confirms that the combination of texturing and Mn-doping is effective for developing high power piezoelectrics.

Table 47. Dielectric and piezoelectric properties of randomly oriented pure PMN-PZT, randomly oriented and textured MnO₂ doped PMN-PZT ceramics (abbreviated as R-pure, R and T-5BT, respectively).

Properties	$\varepsilon_{33}^T/\varepsilon_0$	$\tan \delta$ (%)	d_{33} (pC/N)	d_{31} (pC/N)	k_{31}	g_{33} (10^{-3} Vm/N)	g_{31} (10^{-3} Vm/N)	Q_m	T_m (°C)
R-pure	915	1.9	230	-78	0.27	28	-9.6	102	234
R	765	0.32	180	-69	0.27	27	-10	747	225
T-5BT	1723	0.29	680	-230	0.52	45	-15	428	198

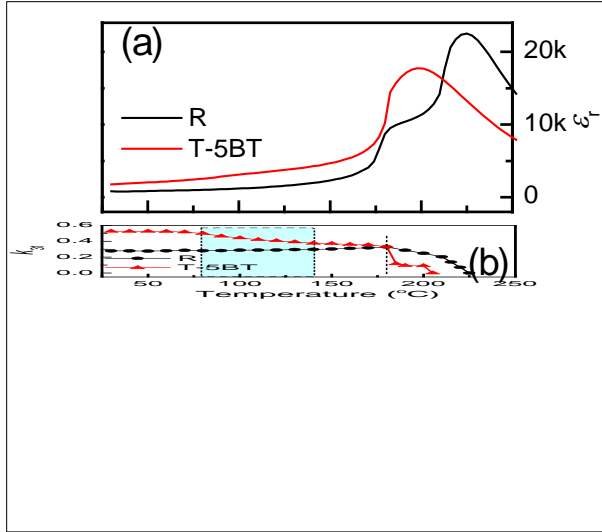


Figure 199. (a) Dielectric constant ($\epsilon_{33}^T/\epsilon_0$) and (b) electromechanical coupling coefficient (k_{31}) of R and T-5BT ceramic as a function of temperature.

Figure 199 (a) shows the dielectric permittivity as a function of temperature for random and textured Mn doped PMN-PZT ceramics. There are two obvious peaks for random ceramics located at ~ 180 °C and 225 °C. The first dielectric anomaly is the rhombohedral to tetragonal phase transformation temperature (T_{R-T}), while the second one is related to the Curie temperature (T_C). For textured ceramics, there is only one obvious peak located at 198 °C attributed to T_C . The decrease of T_C is due to the existence of low T_C BT template indicating shift in the composition towards rhombohedral side. Although, the T_C of T-5BT textured ceramics was still high on the order of 198 °C, we found that T-5BT ceramic has problem related to temperature stability of piezoelectric properties. As it can be seen in Figure 199 (b) that the k_{31} of T-5BT ceramic started to degrade from 75 °C while the R ceramic showed a stable tendency up to 180 °C (T_{R-T} of R ceramic). In order to understand this problem, we first analyzed the spontaneous polarization of T-5BT ceramic to precisely confirm the contribution of R-T transition. The pyroelectric current (I_P) of the ferroelectrics under variation of temperature is given as $I_P = (dP_s/dT) \cdot (dT/dt)$, where P_s is spontaneous polarization, T is temperature and t is time. Usually, the I_P of ferroelectrics shows a sharp increase at phase transition temperatures (e.g. at T_{R-T} and T_C of R ceramic as shown in Figure 200 (a)). The T-5BT ceramic also exhibited a sharp I_P peak at 180 °C, however, there was another broad peak in the range $75 \sim 140$ °C. There was no obvious T_{R-T} peak of T-5BT ceramic in Figure 200 (a), therefore, this peak was not associated with the rhombohedral-tetragonal phase transition. Figure 200 (b) shows the I_P vs. temperature curve of the T-5BT ceramic poled at 140 °C. It can be clearly seen in this figure that broad peak found in Figure 200 (a) in the region $75 \sim 140$ °C has vanished. Since the T_C of BT is 120 °C, the BT template in T-5BT ceramic could be depoled at higher temperature. However, starting temperature of degradation was much lower than 120 °C as seen in Figure 198 (b) and more obvious in the d_{33} plot shown in Figure 200 (c). This result indicates that the depoling of BT templates is not the sole reason for electromechanical degradation and broad peak in the Figure 200 (a), and gave us insight to consider the role of template and template-matrix interface.

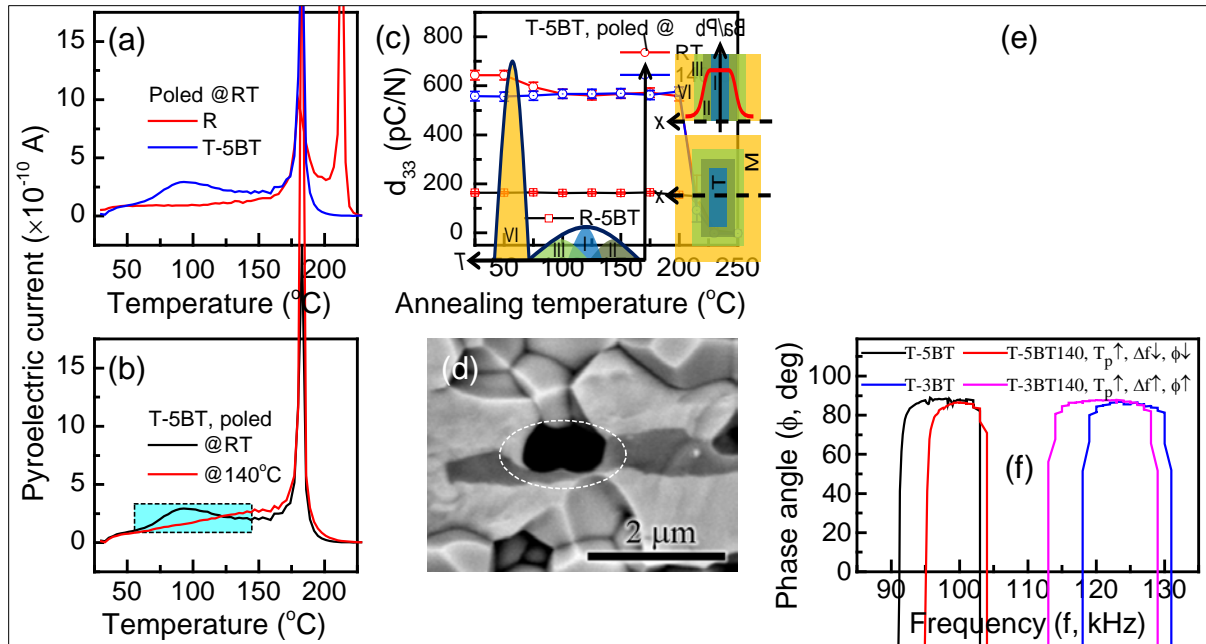


Figure 200. Pyroelectric current vs. temperature curves

(a) R and T-5BT ceramics poled at room temperature and (b) T-5BT ceramics poled at room temperature and 140 °C; (c) d_{33} of R and T-5BT ceramics poled at room temperature and 140 °C as a function of annealing temperature; (d) SEM of partially dissolved BT template; (e) schematic diagram of the concentration gradient that exists in the vicinity of the template – matrix interface; (f) the effect of the poling temperature and template content on degree of poling condition.

We investigated the microstructure of T-5BT ceramic in detail and found that some of the porous BT templates were partially dissolved during the texturing process (Figure 200 (d)). Figure 200 (e) schematically illustrates the concentration gradient that exists in the vicinity of the template – matrix interface using the microstructure and EDS analysis. There are four distinct regions in this diagram. Region I corresponds to the pure BT template, region II corresponds to the diffused area with high Ba/Pb concentration, region III corresponds to the region with slightly lower concentration ratio of Ba/Pb, and region IV represents pure matrix composition or no Ba. The diffusion of Ba into the matrix was confirmed from EDS line scanning data (Figure 198 (d)) showing that “interface region” with the width of ~1 μm was formed in the vicinity of BT template. The interface region could have composition corresponding to mixture of perovskites $(\text{Pb}, \text{Ba})[(\text{Mg}_{1/3}\text{Nb}_{2/3}), \text{Zr}, \text{Ti}]\text{O}_3$ and the T_c of the interface region can be lowered depending upon the concentration of Ba. All the component systems corresponding to PMN, BMN, BZ have been shown to have much lower T_c than BT. Thus, the variation of Ba/Pb concentration across this interface region results in the wide depoling temperature range which explains the broad pyroelectric current peak in Figure 199 (a) as schematically depicted in Figure 200 (e). Therefore, the degradation between 75 to 140 °C can be associated with the depoling of template which has lower paraelectric-ferroelectric transition temperature and the formation of interface region. In this scenario, the piezoelectric properties of the system can be controlled by: (i) lowering the template content, and (iii) poling the ceramic at temperatures higher than T_c of

template and interface region. Based on this hypothesis, the content of BT template was decreased to reduce the interface volume in the ceramic and poling temperature was increased to 140°C. Figure 200 (f) shows the effect of the poling temperature and template content. A much higher degree of poling was found in the T-3BT ceramic poled at 140 °C confirming our hypothesis.

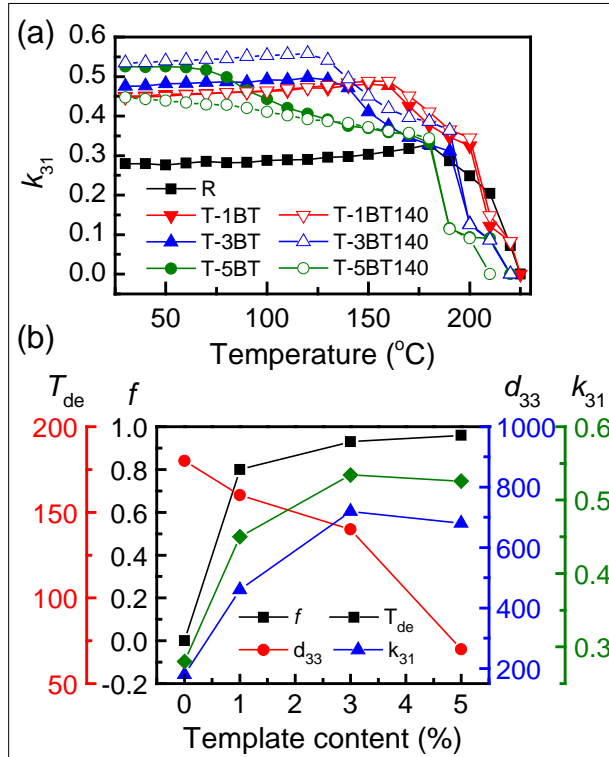


Figure 201. (a) k_{31} vs. temperature characteristics of randomly oriented and textured MnO_2 doped PMN-PZT ceramics with 1, 3 and 5 vol% BT template poled at 140 °C (abbreviated as R, T-1BT140, T-3BT140 and T-5BT140, respectively); **(b)** Lotgering factor (f), degradation temperature (T_{de}), d_{33} and k_{31} of textured MnO_2 doped PMN-PZT ceramics as a function of BT template content.

Figure 201 (a) shows the k_{31} vs. temperature curves of MnO_2 doped PMN-PZT ceramics textured with 1, 3 and 5 vol% BT and subsequently poled at 140 °C (T-1BT140, T-3BT140 and T-5BT140 ceramics, respectively). The T-5BT140 ceramic showed a gradual declining tendency in k_{31} even though the degradation slope was decreased as compared to that of T-5BT ceramic, illustrating the significance of Ba diffusion and formation of the interface region. However, the 3BT140 ceramic exhibited quite stable and high k_{31} (> 0.53) in a wide temperature range from room temperature to 130 °C. This result confirms that as the volume of interface region which has low T_C and relatively poor piezoelectricity was decreased by decreasing the BT content, an improved k_{31} with high degradation temperature (T_{de}) was obtained. Furthermore, there was no obvious change in k_{31} around 120 °C indicating that the formation of interface region is dominant factor in the degradation rather than the depoling of pure BT template. In the case of T-1BT140 ceramic, the T_{de} was increased up to 160 °C due to further reduced volume of interface region,

however, the k_{31} value was decreased because of low texture degree (Lotgering factor of 80 %) as shown in Figure 201 (b).

In summary, we investigated the piezoelectric properties of textured MnO₂ doped PMN-PZT ceramics. The combination of texturing and hardening effect was confirmed to be suitable for developing high power piezoelectric materials possessing excellent “hard and soft” combinatory characteristics. The effect of template content on temperature stability of piezoelectric properties was investigated. The results show that the content and chemical stability of BT template significantly affects the piezoelectric properties and temperature stability of PZT-based textured ceramics. Mn-doped PMN-PZT textured ceramics containing 3 vol% BT exhibited excellent piezoelectric properties $d_{33} = 720 \text{ pC/N}$, $k_{31} = 0.53$, $Q_m = 403$, $\tan \delta = 0.3\%$ along with good temperature stability ($T_{de} = 130 \text{ }^\circ\text{C}$). These combinatory characteristics are very important in designing magnetoelectric (ME) laminate composites operating in the vicinity of electromechanical resonance.

E.3.5. Fiber Fabrication Using Dicing

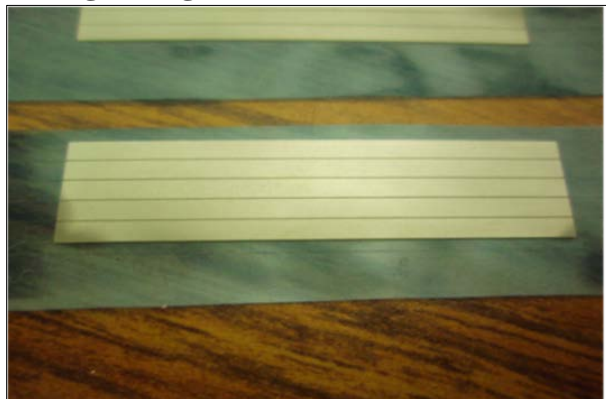


Figure 202. Optical image of texture fiber set.

We found the principal disadvantages of piezoelectric fiber using sol-gel method are the difficulty of processing and handling piezoceramic fibers during manufacture. An alternative method of construction using individual square cross-section fibers, which diced from lower cost piezoceramic wafers, was used. As shown in Figure 202, a set of textured PMN-PT fibers (40mm*2mm*0.2mm) can fabricated using dicing method.

E.3.6. Co-fired Textured Magnetoelectric Composite

In contrast to bonding, co-firing of layered ME composite provides compatibility with current industrial production process commonly used for fabrication of multilayer capacitors (MLCs). Recently, ME sensor based upon Ni-BaTiO₃ MLCs was reported which laid the foundation for future commercialization of this technology. The magnitude of α_E was found to be $7.1 \text{ mV cm}^{-1} \text{ Oe}^{-1}$ which is extremely low but the overall cost is also extremely low (~\$0.01). In order to increase the ME effect while keeping the cost down, materials with large magnetostrictive and piezoelectric coefficient are needed in the co-fired configuration. We fabricated a co-fired magnetostrictive/piezoelectric/magnetostrictive (M/P/M) laminate structure with Ag inner electrode. For the first time, we demonstrate integration of textured microstructure with the co-fired structure. Texturing by template grain growth (TGG) process was found to overcome the

fundamental limitations imposed by piezoelectric material. Compositions corresponding to $\text{Pb}(\text{Mg}_{1/3}\text{Nb}_{2/3})\text{O}_3$ -32.5PbTiO₃ [PMN-PT] and $(\text{Ni}_{0.6}\text{Cu}_{0.2}\text{Zn}_{0.2})\text{Fe}_2\text{O}_3$ [NCZF] were used as piezoelectric and magnetostrictive materials respectively. The fabrication process was based on standard LTCC process which guarantees the cost to be on the order of ~\$0.01.

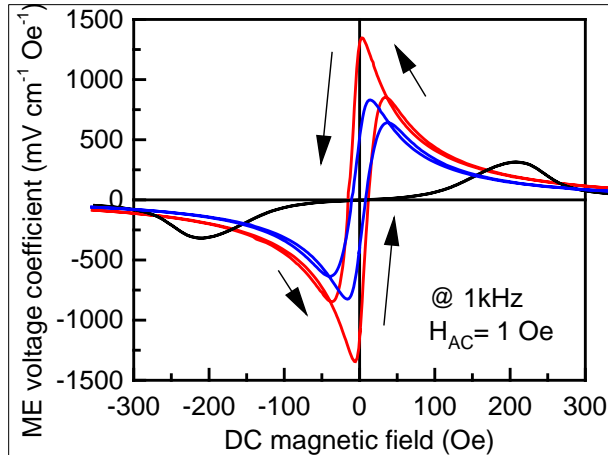


Figure 203. ME voltage coefficients (α_E) of co-fired NCZF/T-PMN-PT/NCZF (C-N/T/N), NCZF/R-PMN-PT/NCZF (C-N/R/N), and epoxy bonded Metglas/R-PMN-PT/Metglas (B-M/R/M) laminate

Figure 203 shows the change in ME voltage coefficient (α_E) as a function of DC magnetic field at off-resonance frequency of 1 kHz. Although the magnetostriction of Metglas ($\lambda=40$ ppm) is twice that of NCZF ($\lambda \approx 20$ ppm), maximum α_E of epoxy bonded Metglas/random-PMN-PT/Metglas (abbreviated as B-M/R/M) laminate is less-than-half of that of co-fired NCZF/random-PMN-PT/NCZF (abbreviated as C-N/R/N). Further improvement was achieved for co-fired textured sample (C-N/T/N). A giant ME volatage coefficient (>1200 mV cm⁻¹ Oe⁻¹) at zero-bias was achieved in C-N/T/N composite. Compared to ME coefficient of 30 mV cm⁻¹ Oe⁻¹ obtained for NKNLS-NZF/Ni/NKNLS-NZF trilayer laminate (40X) and ~400 mV cm⁻¹ Oe⁻¹ obtained for functionally graded Ni-NZFO-PZT composites (3X) at zero-bias, our co-fired composite exhibited extremely high response.

In conclusion, NCZF/PMN-PT/NCZF layered composite with Ag inner electrodes were successfully co-fired at low temperature (930 °C). The co-fired NCZF/textured PMN-PT/NCZF layered composites exhibited 5X increase in α_E compared to Metglas/PMN-PT/Metglas.

E.3.7. Effect of Loss Factors on the Dynamic ME Response

We report the correlation between intensive and extensive losses in piezoelectric materials with the frequency dependent response of layered magnetoelectric (ME) composites. Three different piezoelectric compositions were synthesized to achieve varying loss characteristics allowing a systematic interpretation of changes in ME coupling in terms of loss components. The measured dielectric and piezoelectric properties are shown in Table 48.

Table 48. Material parameters of piezoelectric compositions used in this study.

at 1kHz	d_{31} (pC/N)	ϵ_{33} ($\times 10^{-9}$ F/m)	k_{31}	Q_m	g_{31} ($\times 10^{-3}$ Vm/N)	S_{11}^E ($\times 10^{-12}$ m 2 /N)
PMS	-63.85	5.12	0.283	2291	-12.47	9.9
MPZN	-121.35	13.88	0.282	664	-8.74	13
PZN	-204.39	19.36	0.372	85	-10.56	16

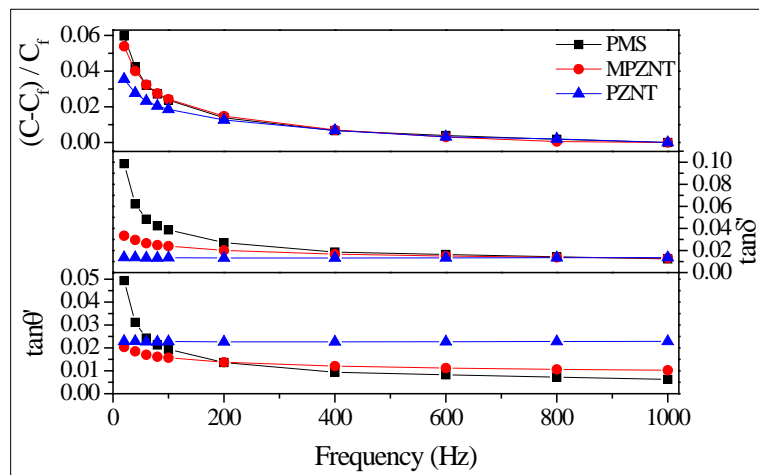


Figure 204. The rate of capacitance change, dielectric loss and piezoelectric loss of PMS, MPZN and PZN piezoelectric compositions measured in the frequency range of 20 Hz ~ 1 kHz.

We observed frequency dependence of capacitance change rate, dielectric ($\tan\delta'$) and piezoelectric ($\tan\theta'$) loss factors of these samples as shown in Figure 204. Three compositions showed different rate of increase with decreasing frequency. Hard PMS composition exhibited the most significant increase while soft PZN showed stable behavior of losses in overall range. This trend was well matched to the ME behavior of laminates in the same frequency range as shown in Figure 205. ME voltage coefficient of Metglas/PMS was rapidly dropped in low frequency region while Metglas/PZN showed stable response in ME voltage output.

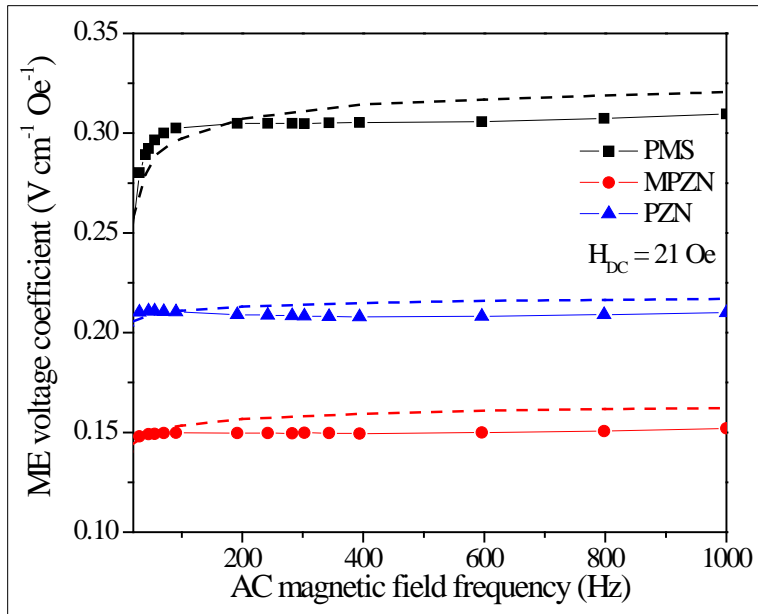


Figure 205. Magnetoelectric voltage coefficient of PMS / Metglas, MPZN / Metglas and PZN / Metglas laminates measured in H_{AC} frequency range of 20 Hz ~ 1 kHz under H_{DC} of 21 Oe.

Dashed lines indicate calculated magnetoelectric voltage coefficient. It can be clearly seen that the decreasing rate of coefficient of PMS / Metglas is the most rapid in low frequency range.

Since deterioration of ME voltage output is directly related to increase in magnetic noise, stable ME voltage in low frequency region is very important for high sensitivity. Therefore, a good strategy to obtain high sensitivity would be the design of piezoelectric composition which has low loss and high voltage constant in low frequency range.

E.3.8. Direct and Converse ME effect

Due to giant enhancement in the magnitude of ME coefficient at the electromechanical resonance, a combination of 2–2 laminate structure operating at resonance presents a tremendous opportunity for configuring the magnetoelectric devices. However, we noticed a serious discrepancy about the reported peak position of DME and CME. In this work, we analyze the direct and converse effect in laminate composites of magnetostrictive and piezoelectric materials. Our results deterministically show that direct magnetoelectric (ME) effect is maximized at antiresonance frequency while the converse ME effect is maximized at resonance frequency of the laminate composite as shown in Figure 206.

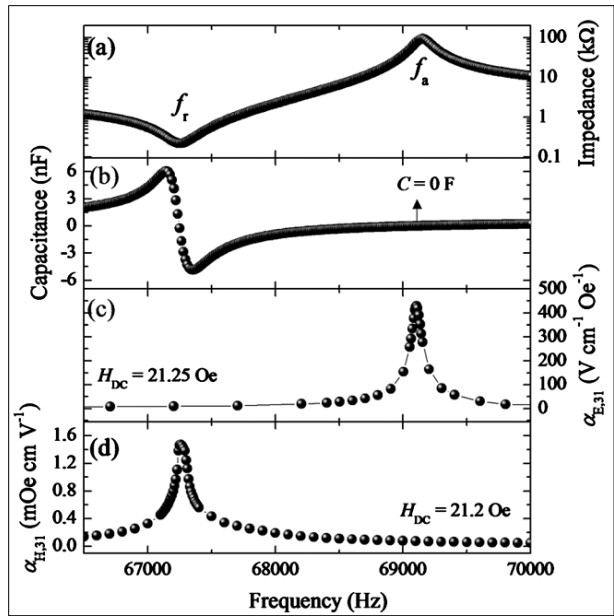


Figure 206. (a) Impedance versus frequency of the P-layer, (b) capacitance versus frequency of the P-layer, (c) $\alpha_{E,31}$ versus $H_{1,\text{ac}}$ frequency, and (d) $\alpha_{H,31}$ versus $E_{3,\text{ac}}$ frequency characteristic of the MP laminate.

By using piezoelectric constitutive equations and combining it with resonance boundary conditions. The dominant factor controlling the position of peak ME coefficient was found to be frequency dependent capacitance of piezoelectric layer. This study will provide guidance toward the development of magnetic field sensors based on direct effect and communication components based on converse effect.

F. Gopalan Srinivasan, Oakland University

F.3.1. Sample synthesis

Samples of Ni-Metglas-PZT and Metglas-Ni-PZT were studied. Annealed, 99.98 % pure nickel foil (obtained from Goodfellow Cambridge Limited, England) was used. We used iron-based Metglas (No.2605SA-1 provided by Metglas Inc., Conway, SC) ribbons. The ribbons are 25 μm in thickness and contained 20-50 nm crystallites. Vendor supplied PZT (No.851, American Piezo Ceramics, Mackeyville, PA) was used in the composites. Samples were made with 5-8 cm \times 1 cm \times 0.04 cm PZT, and 160 μm thick Ni and 25 μm thick Metglas of similar lateral dimensions. The PZT with silver electrodes was initially poled in an electric field of 30 kV/cm by heating it to 150 C in an oil bath. It was then bonded to Ni and Metglas with a 2 to 3 μm thick layer of epoxy (West System 105-resin and 206-hardner).

F.3.2. Low-frequency ME effects

Representative data on variation of the ME voltage coefficient (MEVC) α_E with H_0 are shown in Figure 207 for PZT-Ni-Metglas and PZT-Metglas-Ni samples. The data are for Metglas thickness of 75 μm . Consider first the data for PZT-Ni-Metglas in Figure 207 (a). The MEVC is ~ 1.6 V/cm Oe for $H_0 = 0$. With increasing H_0 the magnitude of MEVC decreases to zero for a bias field of 5-7 Oe. Beyond this zero-crossing, further increase in the bias field results in a sharp increase in MEVC to a maximum value of 3.5 V/cm Oe. The large zero-bias MEVC can only be due to a torque which arises from interaction between the in-plane ac field H_1 and a transverse grading induced magnetization. Compositional grading of ferrites are shown to result in such an internal field. The torque produces a bending moment in the magnetic layer direction and gives rise to ME output at zero magnetic bias field.

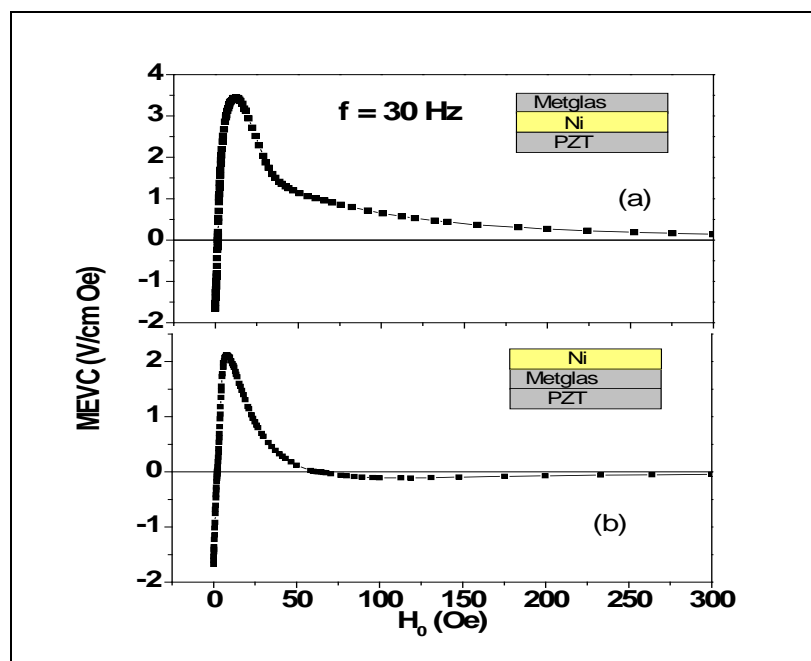


Figure 207. Magnetoelectric voltage coefficient (MEVC) as a function of the bias field H_0 for samples of PZT and ferromagnetic layers with Ni and Metglas.

The Metglas thickness is 75 μm . The bias field H_0 and ac field H_I are parallel to the sample plane.

We investigated the zero-field ME effects in detail. The PZT-Ni-Metglas sample was located in a magnetically shielded chamber to achieve $H_0 = 0$ and subjected to an in-plane ac field of 100Oe. The ME voltage was measured with a spectrum analyzer. Results of these measurements are shown in Figure 208. One observes a near-constant ME response independent of the frequency f of the ac field. The MEVC corresponds to 0.5 V/cm Oe, and is smaller than the value in Figure 207.

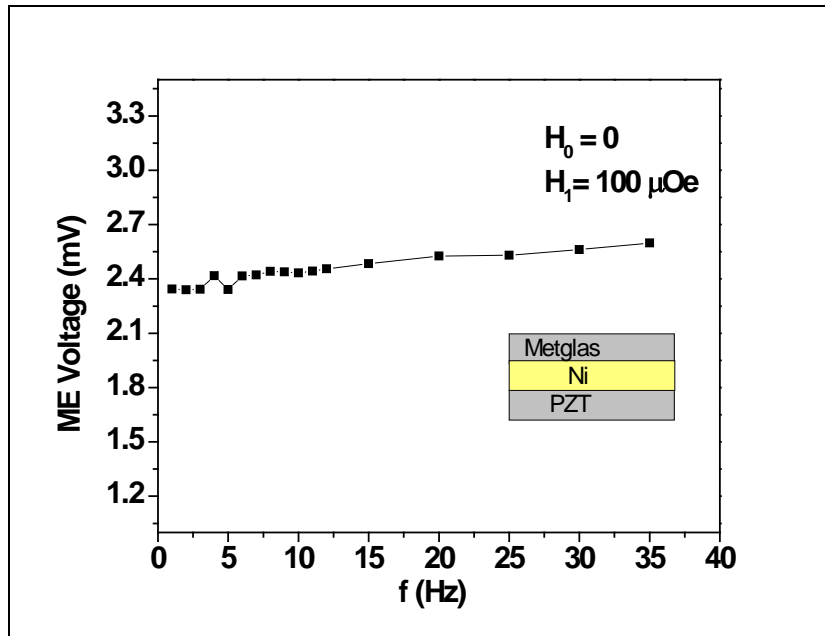


Figure 208. The zero-bias ME voltage as a function of frequency f of the ac field H_I measured for a sample of PZT-Ni and 75 μm thick Metglas.

Next we focus on the zero-bias ME coupling in magnetization graded samples. We prepared samples with Metglas thickness varying from 25 to 125 μm (or the number of layers $L = 1-5$) and measured the ME response as in Figure 207. Figure 209 shows $\alpha_{E,0}$ as a function of L for the magnetization graded samples. With increasing Metglas thickness, one observes a rapid rise in $\alpha_{E,0}$ to a peak value for $L = 3$ and is followed by a sharp fall for higher L . The zero-bias ME voltage is vanishingly small for $L = 5$.

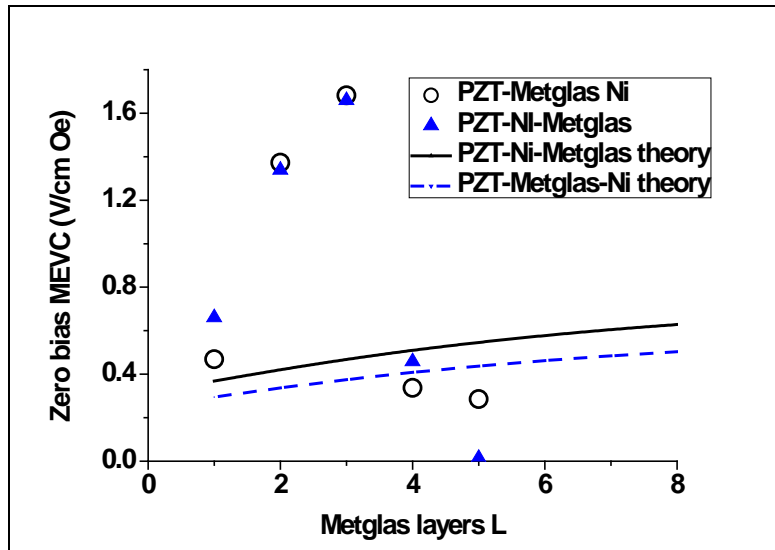


Figure 209. Zero-bias MEVC obtained from data as in Figure 209 as a function of number of Metglas layers L for magnetization graded samples.

The lines represent theoretical values.

F.3.3. ME response at bending resonance

An ME phenomenon of interest is the coupling at bending resonance. Measurements of zero-bias MEVC as a function of frequency of the ac magnetic field were carried out in the magnetically shielded chamber and typical results are shown in Figure 210. The data for a sample of PZT-Ni-25 μm thick Metglas shows a peak value at the resonance frequency of 170 Hz. Similar measurements on samples with a series of Metglas thickness and the peak $\alpha_{E,0}$ is shown in Figure 211. The data reveals a much stronger ME coupling at resonance in PZT-Ni-Metglas than for PZT-Metglas-Ni.

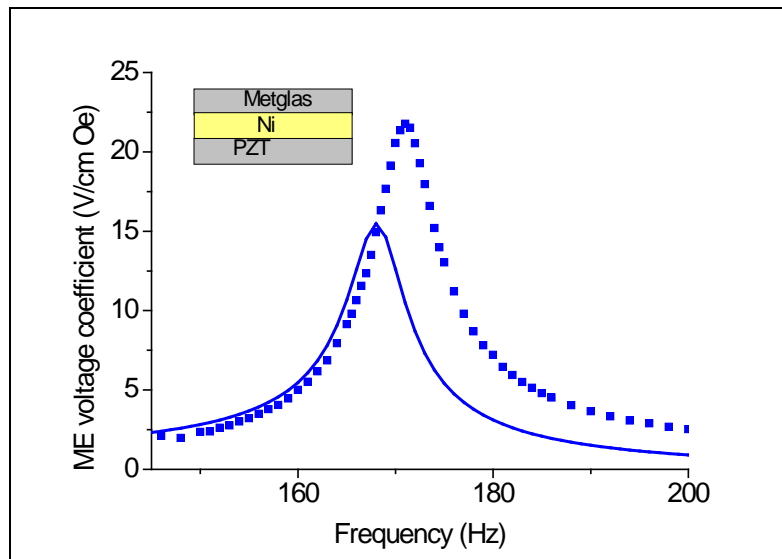


Figure 210. Magnetolectric voltage coefficient for $H_0 = 0$ as a function of frequency f of the ac magnetic field H_1 for a sample of PZT-Ni-25 μm thick Metglas.

The peak in MEVC corresponds to bending resonance in the sample clamped at one end. The symbols are data and the solid line is theoretical estimates.

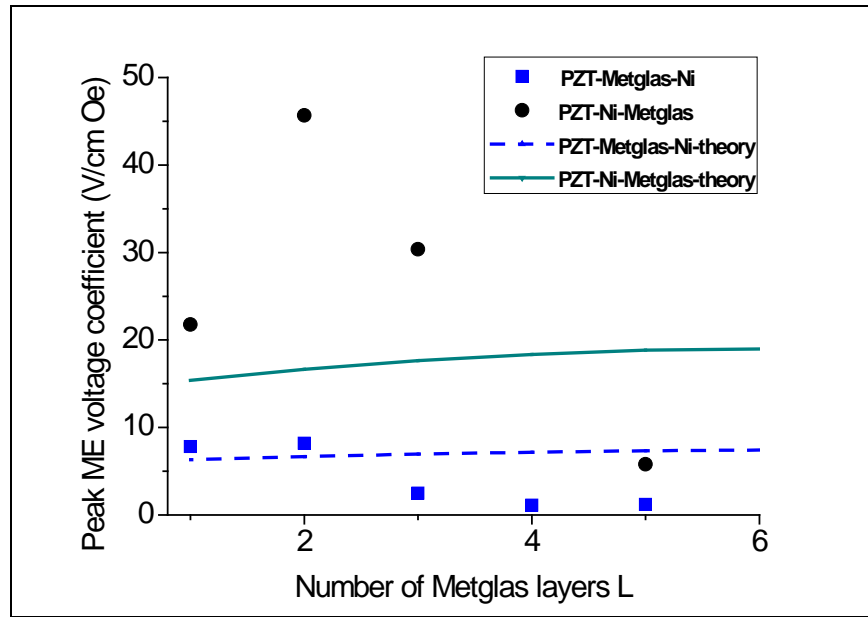


Figure 211. The resonance value of zero-bias MEVC versus number of Metglas layers in the magnetization graded samples. The solid and dashed lines are theoretical values.

F.3.4. Magnetic noise measurements

Noise measurements were done in a mu-metal shielded chamber. The sensor was subjected to an ac field produced by a Helmholtz coil. The output was amplified and fed to a spectrum analyzer. The voltage noise was converted to magnetic noise with the transfer function estimated from MEVC data as in Figure 207. Data on magnetic noise N vs f and at bending resonance frequency are shown in Figure 212. N is on the order of $2.4 \text{ nT}/\sqrt{\text{Hz}}$ @ 1 Hz and $70 \text{ pT}/\sqrt{\text{Hz}}$ at bending resonance.

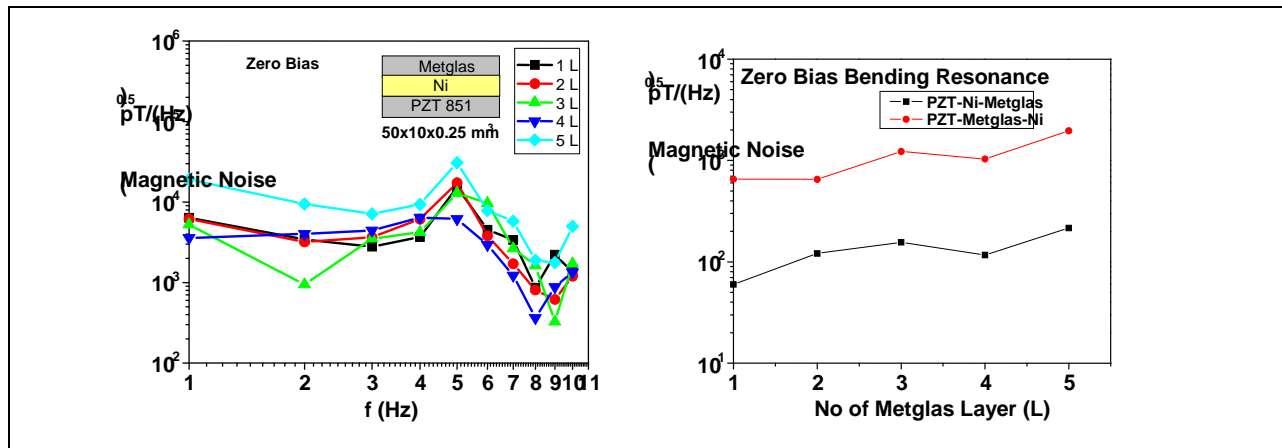


Figure 212. Magnetic noises at low-frequency and at bending resonance at zero-bias for PZT-Ni Metglas sensors.

F.3.5. Noise reduction strategies

F.3.5.1. q- and d- graded Sensors

When both the piezomagnetic and piezoelectric coefficients are graded, a general increase in MEVC (Figure 213a) is measured. The most significant finding, however, is the decrease in the magnetic noise (Figure 213b) by a factor of 5 to 8 compared to *q*-only graded samples (Figure 212) due to reduction in pyroelectric noise.

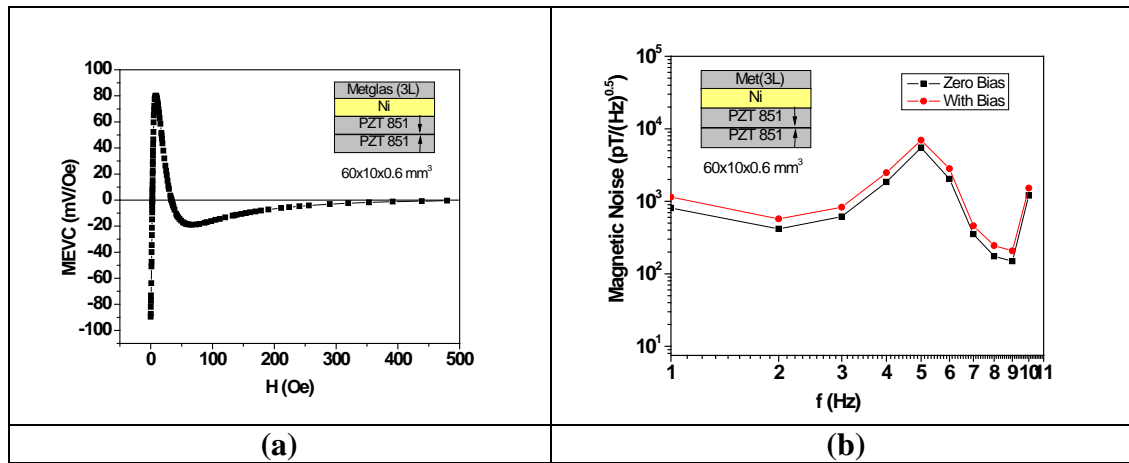


Figure 213. (a) MEVC vs H and (b) Noise vs f for *q*- and *d*- graded sensors.

F.3.5.2. Sensors with annealed Metglas

Metglas when annealed for 1 hr at 400 C under high vacuum is found to have higher piezomagnetic coefficient than unannealed samples. Sensors of oppositely poled PZT-nickel and 3 layers of annealed Metglas (of thickness 25 μ m) were prepared. Figure 214a shows ME sensitivity vs *H* and Figure 214b shows the noise spectrum for the sensor. The sensitivity increases by 50% and the noise $N \sim 250$ pT/ $\sqrt{\text{Hz}}$.

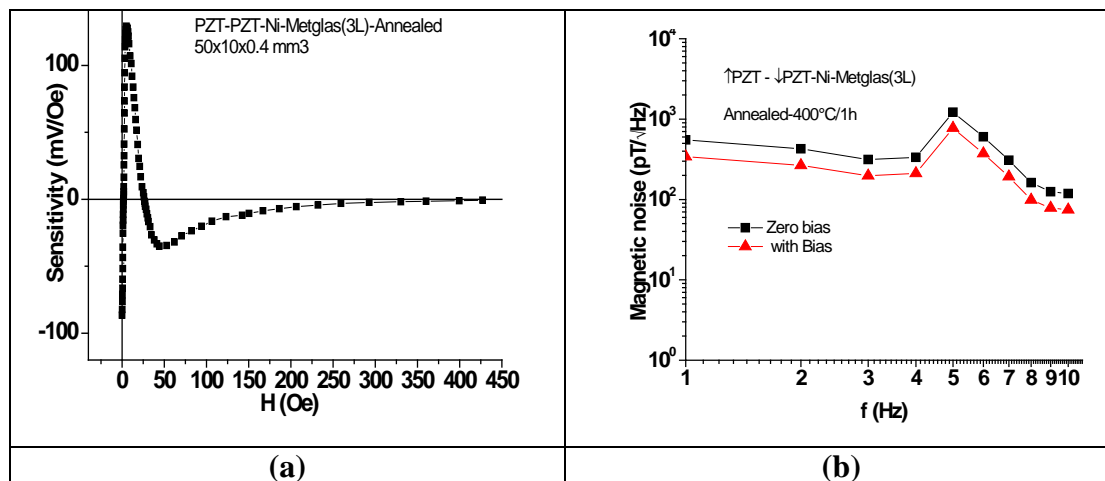


Figure 214. (a) MEVC vs H and (b) N vs f with bias and zero bias condition. for *q*- and *d*- graded sensors with annealed Metglas

G. Vince Harris, Northeastern University

G.3.1. Modulation sensing method vs. DC biasing method

A modulation sensing method has been utilized to reduce the low frequency noise floor of magnetic fields sensed by magnetoelectric composites. Traditionally, ME composite sensors are biased with an optimal H_{dc} to achieve optimal sensitivity. The H_{dc} requires use of either an electromagnet or permanent magnets which add volume, weight, and cost to the magnetic field sensing apparatus. Provided in the following section is an overview of the latest evolution of the modulation sensing technique and results demonstrating its ability to reduce low frequency noise floor.

The experimental setup for the modulation sensing technique has been improved to exhibit higher SNR, higher sensitivity, and lower 0-Hz noise floor than the conventional DC biasing method for both Northeastern University's Metglas/PZT/Metglas heterostructural laminate composite, and Virginia Tech's highly-sensitive Metglas/poled-PZT/Metglas heterostructural laminate magnetic field sensors. The improvements include the use of a preamplifier prior to lock-in detection to raise the internal noise floor of both sensors above the noise floor associated with the detection electronics, specifically the lock-in amplifier. A new hall probe was purchased to improve the accuracy of low AC H-field amplitude measurements. Finally, a new dual Helmholtz coil shown in Figure 215 was fabricated to produce nearly uniform fields of 9 cm long, which is greater than the length of the largest ME sensor.

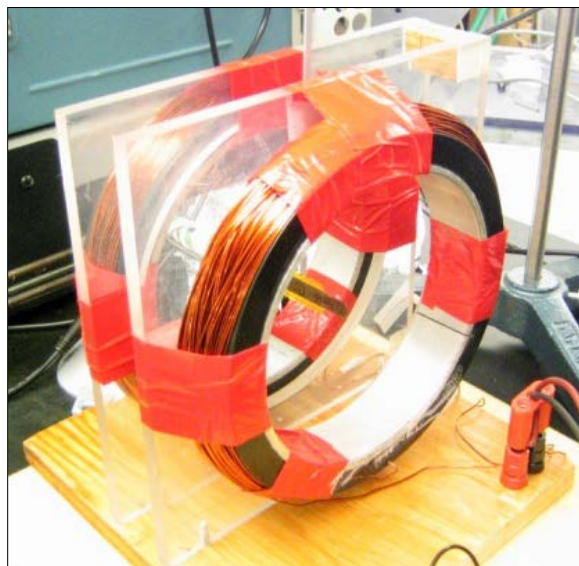


Figure 215. New dual Helmholtz coil exhibiting ~9 cm uniform magnetic field capability.

The test signal frequency was set to 25 Hz to illustrate the low frequency 1/f noise spectra. In addition, due to the frequency dependence of sensor sensitivity, a 25 Hz test H-field more closely results in ME sensitivity levels that a 1 Hz signal would generate. The amplitude of the test signal was also reduced from 1 Oe to 0.10 Oe. For the DC biasing method, a DC H-field was applied and its amplitude swept from 0-50 Oe. Voltage spectral density measurements of the output of each sensor were captured at intervals of 0, 1, 2.5, 5, 7.5, 10, 15, 20, 30, and 50 Oe. The DC biasing experimental setup is shown below in Figure 216.

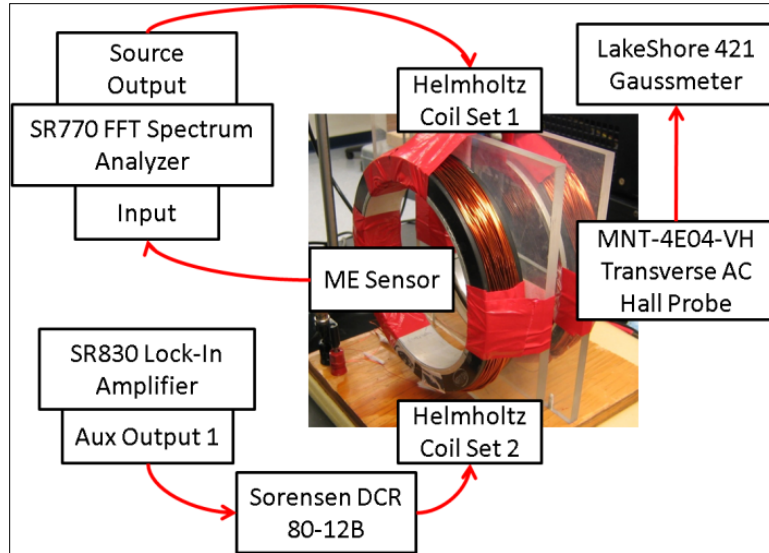


Figure 216. Block diagram of the DC biasing method.

For the modulation sensing method, a 0.25 Oe modulation field was superimposed with the test field and the modulation field was swept from 10 KHz to 70 KHz. VSD measurements of both sensors were captured at modulation frequency intervals of 10, 20, 30, 40, 50, 60, and 70 KHz. The modulation sensing technique experimental setup is shown in Figure 217.

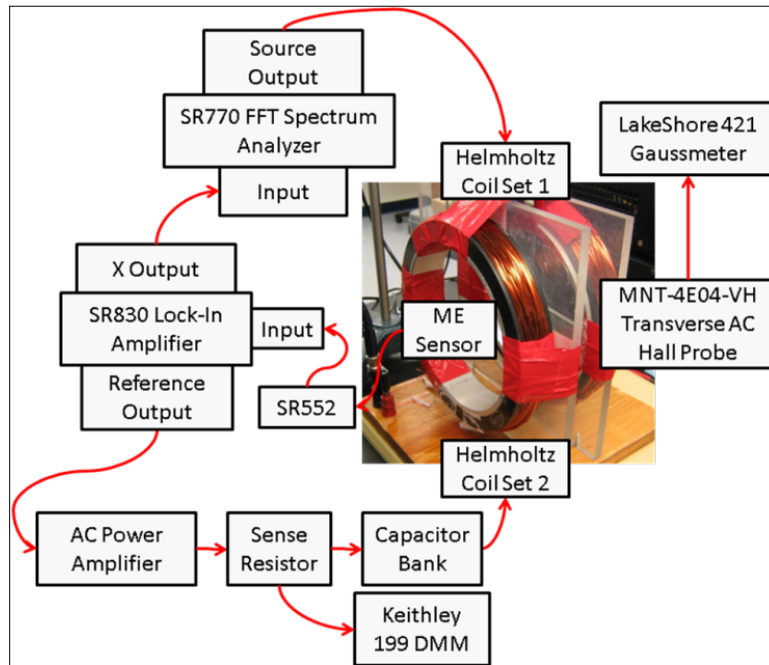


Figure 217. Block diagram of the modulation sensing technique.

New complete sets of data were captured using the dual Helmholtz coil in both the DC biasing method and the modulation sensing technique configurations. The following HUMS quarterly update shows the results of those measurements and provides a comparison between DC biasing and modulation sensing schemes, indicating that the modulation technique has the ability to

improve the SNR, sensitivity, and 0-Hz noise floor of ME sensor measurements in addition to providing superior mitigation of environmental, harmonic, and spurious noise.

Presented in Figure 218 is a comparison of the DC biasing method to the modulation sensing technique. Northeastern's sensor (Sensor 1) is shown in the dashed blue trace and VT's sensor (Sensor 2) is shown in the solid red trace. These plots represent the relative SNR, sensitivity, and noise floor between the detected 25 Hz test signal point and the lowest frequency bin measurement made using SR770 FFT spectrum analyzer corresponding to the 0-Hz bin.

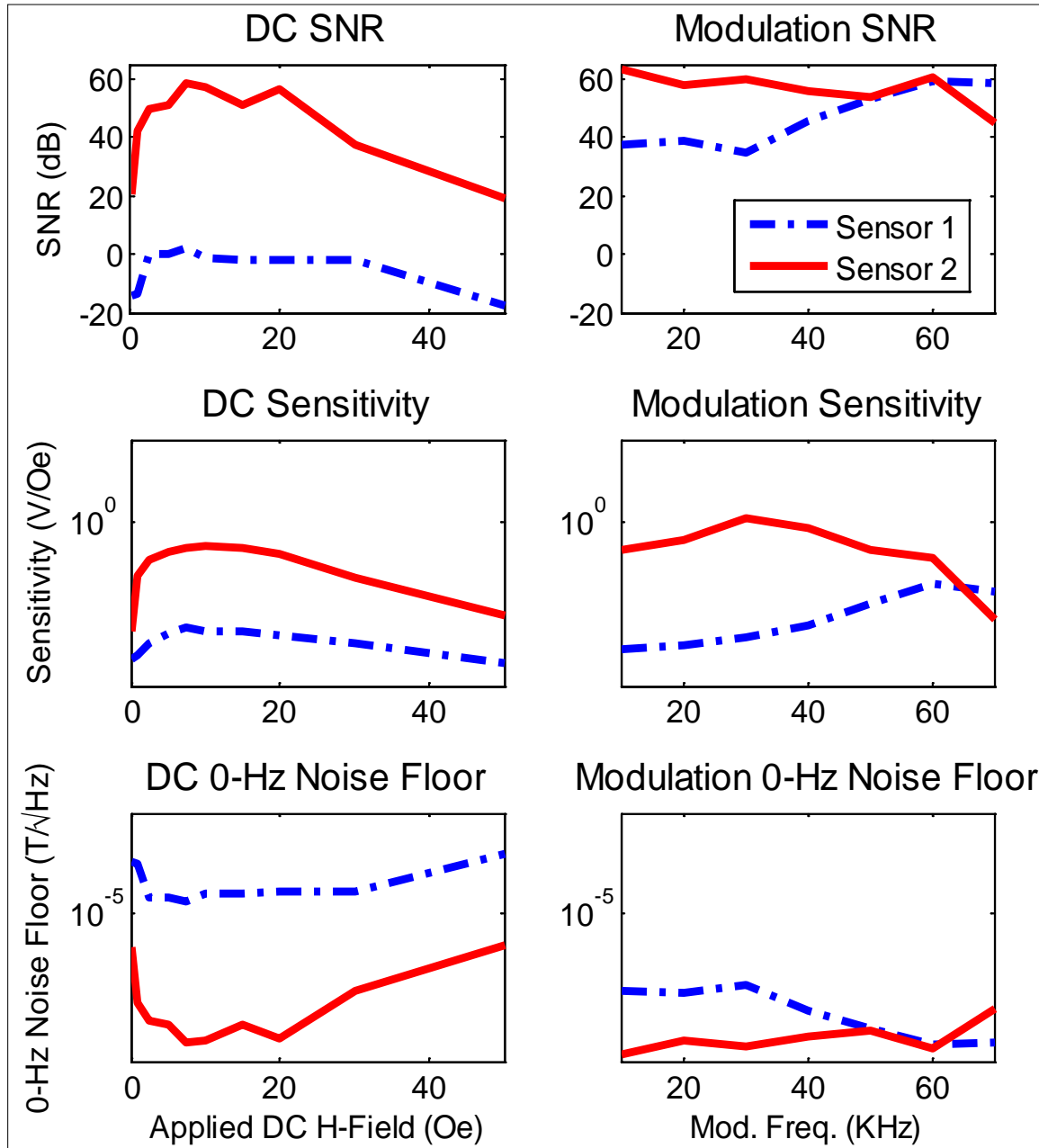


Figure 218. SNR, Sensitivity, and 0-Hz noise floor of Northeastern's ME sensor (Sensor 1) and VT's sensor (Sensor 2) using the DC biasing method (left column) and the modulation sensing technique (right column).

The data presented below in Table 49 compares the peak values of SNR, sensitivity and 0-Hz noise floor of both sensors in both sensing configurations. The modulated sensing technique exhibits impressive improvements to Sensor 1 and moderate improvements to Sensor 2.

Table 49. Comparison of DC biasing method with modulated sensing technique for both magnetoelectric heterostructural magnetic field sensors.

Peak Parameter	DC Biasing Method	Modulated Sensing Technique	Mod. Sensing Technique Improvement
Sensor 1 SNR	1.858 dB	59.29 dB	+ 57.43 dB
Sensor 1 Sensitivity	2.713×10^{-3} V/Oe	3.154×10^{-2} V/Oe	11.62 x
Sensor 1 0-Hz Noise Floor	1.632×10^{-5} T/ $\sqrt{\text{Hz}}$	2.194×10^{-8} T/ $\sqrt{\text{Hz}}$	743.85 x
Sensor 2 SNR	58.8 dB	63.18 dB	+ 4.38 dB
Sensor 2 Sensitivity	2.583×10^{-1} V/Oe	1.273 V/Oe	4.93 x
Sensor 2 0-Hz Noise Floor	2.404×10^{-8} T/ $\sqrt{\text{Hz}}$	1.401×10^{-8} T/ $\sqrt{\text{Hz}}$	1.72 x

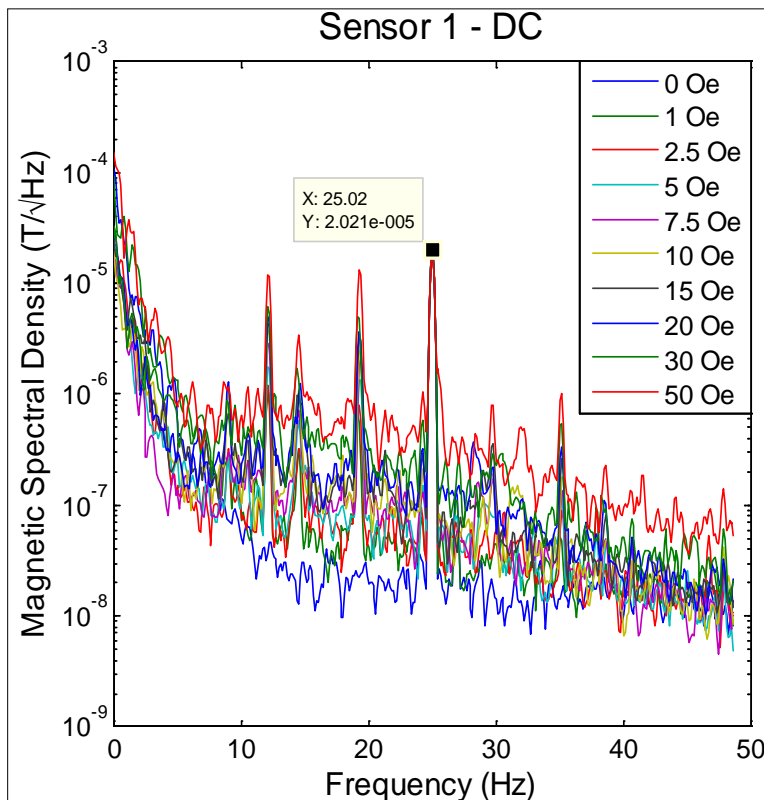


Figure 219. MSD measurements of Sensor 1 for the DC biasing method.

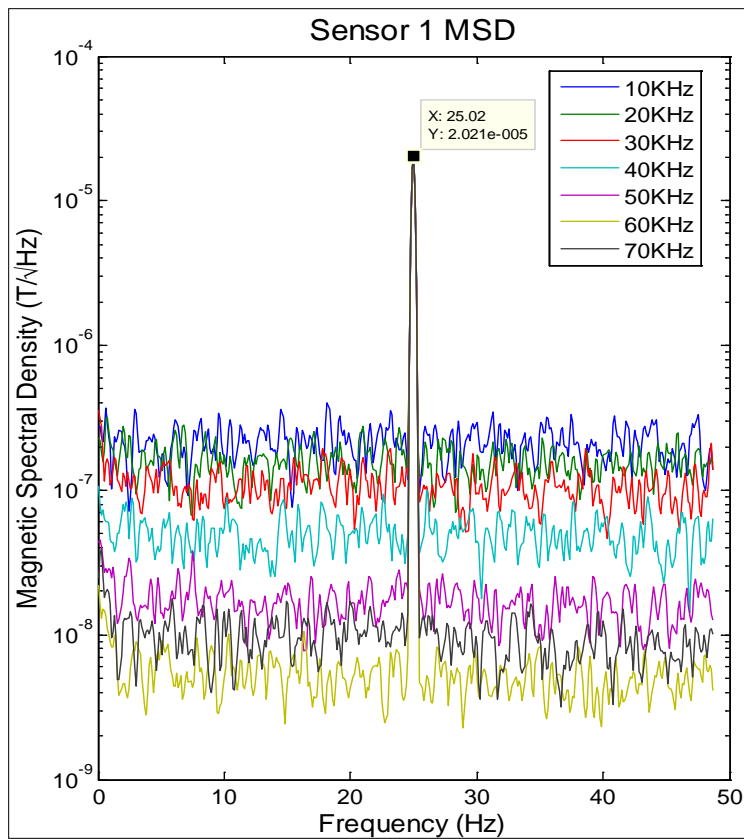


Figure 220. MSD measurements of Sensor 1 for the modulated sensing technique.

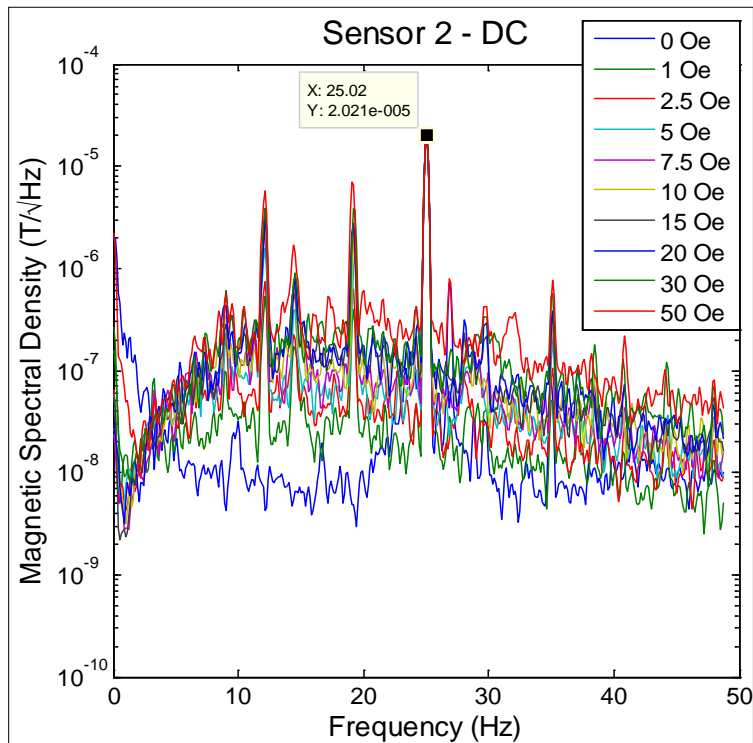


Figure 221. MSD measurements of Sensor 2 for the DC biasing method.

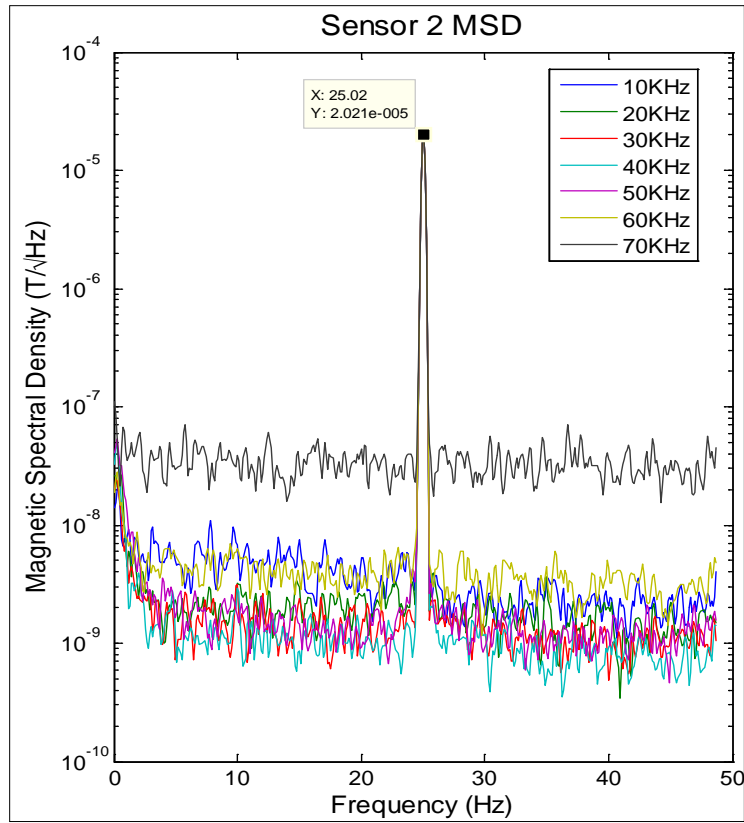


Figure 222. MSD measurements of Sensor 2 for the modulated sensing technique.

In summary, it is shown through a comparison of peak parameter values captured using the DC biasing method and the modulation sensing technique that the modulation sensing technique exhibits SNR, sensitivity, and 0-Hz noise floor enhancement for both Sensor 1 and Sensor 2. It is also observed that the degree of enhancement provided by the modulation sensing technique is non-uniform between sensors. This is believed to occur due to Sensor 2, which is Virginia Tech's highly sensitive magnetoelectric element, exhibiting a noise floor much lower than that of the detection instruments.

When examining the magnetic spectral density plots and comparing them to the DC MSD plots, it is clearly observed that the modulation sensing technique exhibits a superior ability to reject environmental and spurious noise at frequencies above the 0-Hz point. This ability shows that the modulation sensing technique may be utilized to not only provide peak value improvement in SNR, sensitivity and 0-Hz noise floor, but may also be used to reject environmental noise components.

The modulation sensing technique demonstrates the ability to improve the characteristics of a magnetoelectric sensing element conventionally used in a DC biasing scheme.

In the updated following section, we report significant improvements in the measurements captured using an improved modulation sensing technique. The goal of these experiments was to see if any improvement in noise floor could be achieved if the amplitude of the test and modulation H-fields were reduced. In addition, measurements were taken inside of an earth-

grounded dual-walled Gauss chamber to reduce the effects of environmental electric and magnetic noise. A small dual-nesting Helmholtz coil was characterized to generate small-amplitude test and modulation magnetic fields on the order of 100 nT and 1000 nT, respectively. This crucial step ensured dynamic range compatibility with the instruments and relieved the dynamic range limiting effects that caused higher noise floor values in previous HUMS reports. We are pleased to report up to a 40x increase in 0-Hz noise floor values and, when compared to the conventional DC biasing method, the modulation sensing technique exhibits up to 3-orders-of-magnitude improvement in 0-Hz noise floor, while simultaneously enhancing SNR and sensitivity. As previously demonstrated, the modulation technique continues to offer superior spurious noise mitigating than the conventional DC biasing method.

Virginia Tech has generously provided an updated highly sensitive Metglas/poled-PZT/Metglas laminated composite ME sensor, herein referred to as VTn, which was used in these measurements. In Figure 223, VTn is positioned next to a Metglas/PZT/Metglass laminated composite ME sensor provided by Carmine Carosella, which was also retested under the improved modulation sensing conditions, and a dime for size reference.

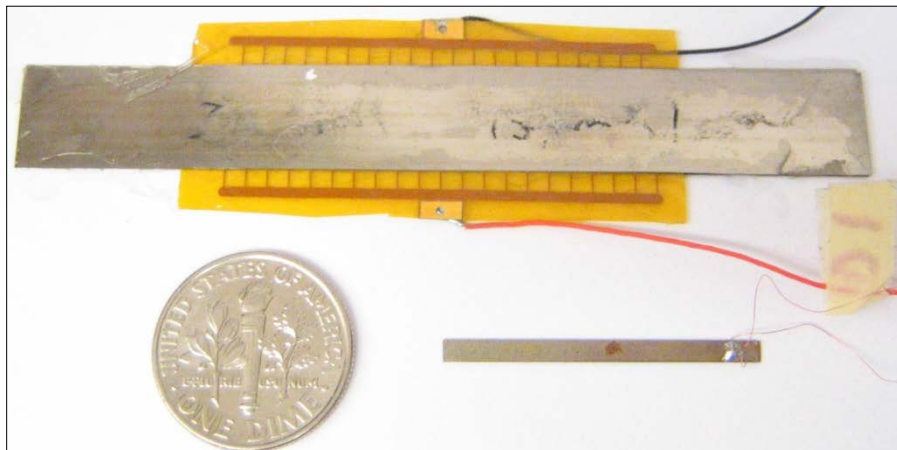


Figure 223. VTn sensor (Top) provided by Virginia Tech and NU sensor (lower right) provided by Carmine Carosella.

Three sensors, NU, VTn, and VTo (the previous highly sensitivity ME sensor provided by Virginia Tech), were retested using both the conventional DC biasing method and modulation sensing technique for an applied test magnetic field of 0.001 Oe (100 nanoTesla) at 25 Hz. The optimal DC biasing conditions for each sensor was found to be approximately 7.5 Oe. For the modulated sensing technique, a 0.01 Oe on-resonance modulation field was applied. The magnetic spectral density plots for each sensor are shown in Figure 224.

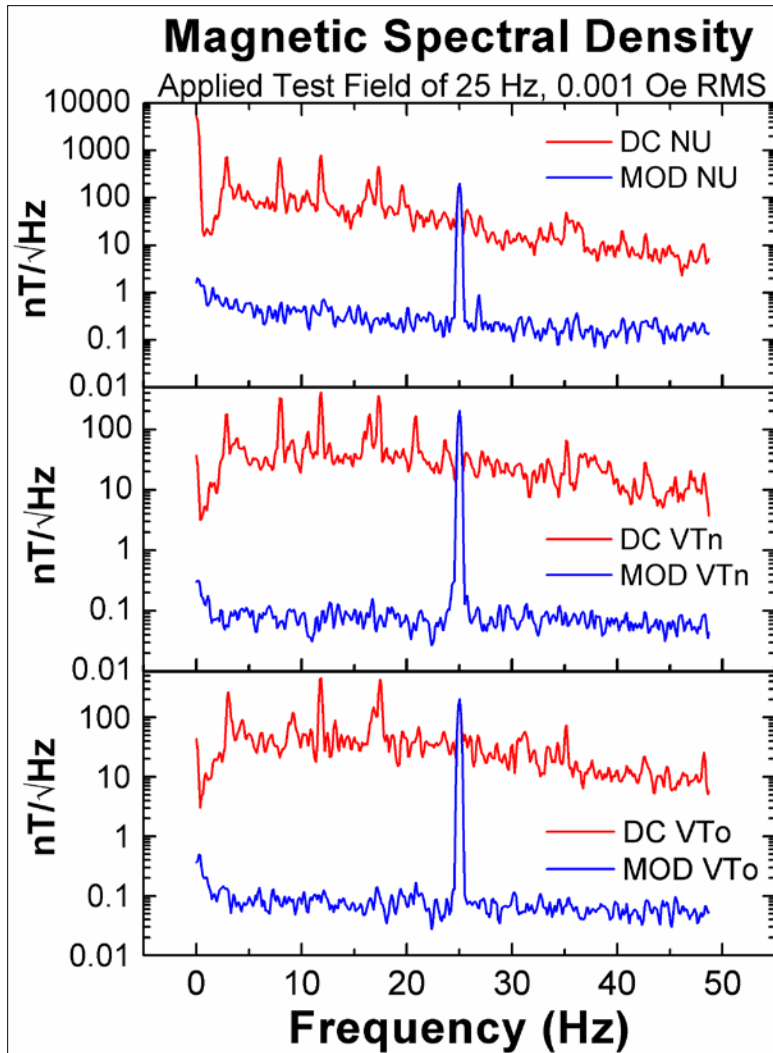


Figure 224. Magnetic spectral density plots of NU (upper), VTn (middle), and VTo (lower) compare the conventional DC biasing method (red) response with the modulated sensing technique (blue) response for a 25 Hz 0.001 Oe RMS test H-field.

Figure 224 clearly demonstrates the ability of the modulation sensing technique to reduce the 0-Hz noise floor in addition to reducing the spurious noise and noise floor throughout the spectrum. Modulation technique measurements were taken using on-resonance stimulation frequencies. To enable a resonance mode, a 61.46 KHz H-field was applied to NU sensor, a 33.30 KHz H-field was applied to VTo sensor and a 29.80 KHz H-field was applied to VTn sensor. The modulation fields were held constant at amplitude of 0.01 Oe RMS. Table 50 shows the SNR, sensitivity and noise floor associated with each sensor type for both DC and modulated sensing schemes.

Table 50. Comparison of magnetic field sensitivity and noise floor.

<u>Sensor & Configuration</u>	<u>0-Hz SNR (dB)</u>	<u>25-Hz Sensitivity (V/Oe)</u>	<u>0-Hz Noise Floor (nT/$\sqrt{\text{Hz}}$)</u>
DC NU	-28.4	0.0055	5300
MOD NU	41.9	0.0123	1.6
DC VTn	14.7	1.1	37.0
MOD VTn	59.7	3.1	0.30
DC VTo	13.3	0.708	44.0
MOD VTo	55.0	3.7	0.36

The results reported continue to demonstrate the benefits of utilizing a modulation sensing technique instead of the conventional DC biasing method. In addition, through the application of small test field and modulation field amplitudes, a further reduction in noise floor measurements has been achieved. Due to the similarities of the magnetic spectral density plots between sensors in Figure 224, it is plausible that the noise floor of the experimental test setup may still be limited by the detection electronics and not fully represent the noise floor of the sensors.

G.3.2. Magnetic Spectral Density Response Comparison

Simultaneously, we have investigated the 1-Hz noise floor values of both DC biasing method and modulated sensing techniques for four magnetoelectric sensors, including the recently developed PZT tube sensor. A comparison of magnetic spectral density response, sensitivity and signal-to-noise ratio for each sensor is also provided. This study demonstrates that the modulation technique has the ability to provide a lower noise floor than the conventional DC biasing method and holds no preference on sensor construction type.

The same experimental test setups were used as described in the previous section. Measurements were made using a dual-walled Gauss chamber tied to earth ground. Two sets of Helmholtz coils were used to generate a 0.001Oe (100nT) test field at 25Hz and to provide either DC magnetic biasing at 10 Oe or an AC modulation magnetic field at 0.1 Oe (10 μ T). Power spectral density measurements, consisting of 500 averaged sweeps, were captured for each sensor from ~1Hz to ~50Hz. The following sensors were used in this testing and are shown in Figure 225:

- CC Sensor: Metglas/PZT/Metglas laminated composite. (Held with green tweezers)
- VT Old Sensor: Virginia Tech's 1st Metglas/poled-PZT/Metglas laminated composite.
- VT New Sensor: Virginia Tech's 2nd Metglas/poled-PZT/Metglas laminated composite.
- PZT Tube Sensor: Galfenol wire/PZT tube composite.

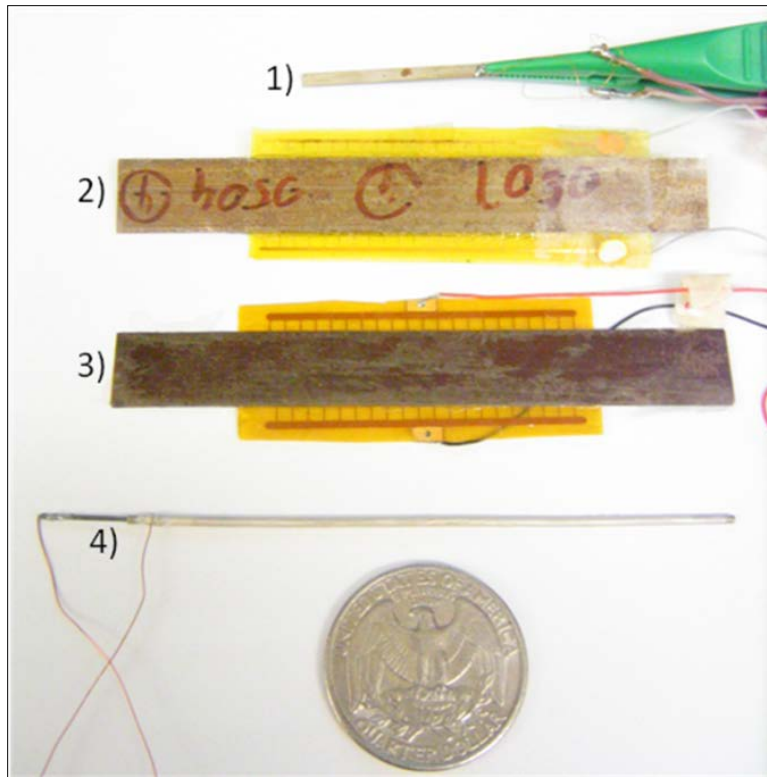


Figure 225. 1) CC Sensor. 2) VT Old Sensor. 3) VT New Sensor. 4) PZT Tube Sensor.

Two power spectral density measurements were taken for each sensor under both DC biased and modulation sensing configurations. The PSD measurements, in $\text{Vrms}/\sqrt{\text{Hz}}$, were converted to magnetic spectral density in $\text{T}/\sqrt{\text{Hz}}$. The 25Hz, 0.001 Oe (100nT) test field has been marked and provides a point of reference for surrounding noise levels. Figures 226, 227, 228 and 229, demonstrate the reduction in overall noise floor associated with using the modulation sensing technique for CC, VT Old, VT New, and PZT Tube sensors, respectively.

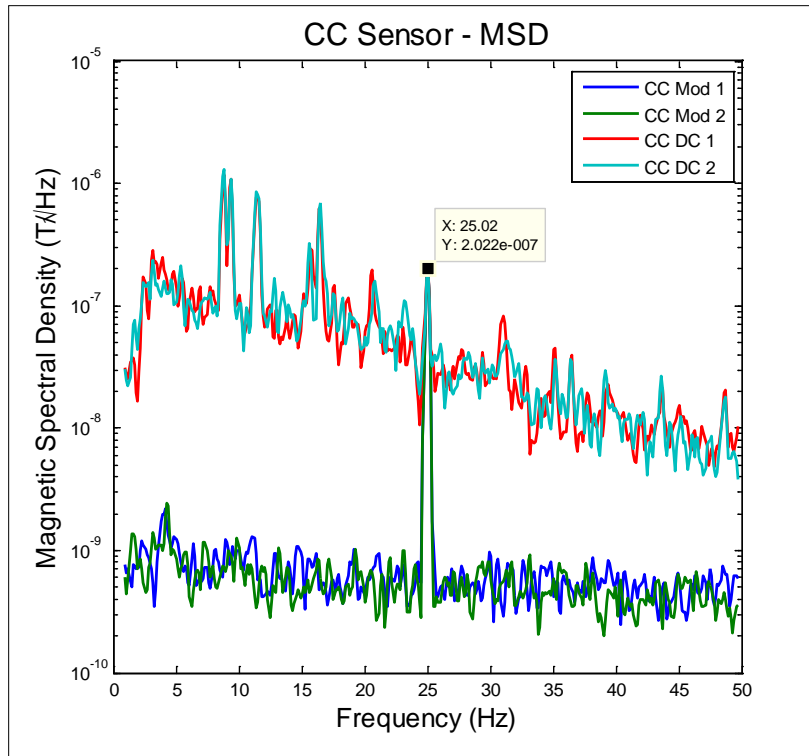


Figure 226. Magnetic spectral density comparison of DC vs. modulation technique for CC sensor.

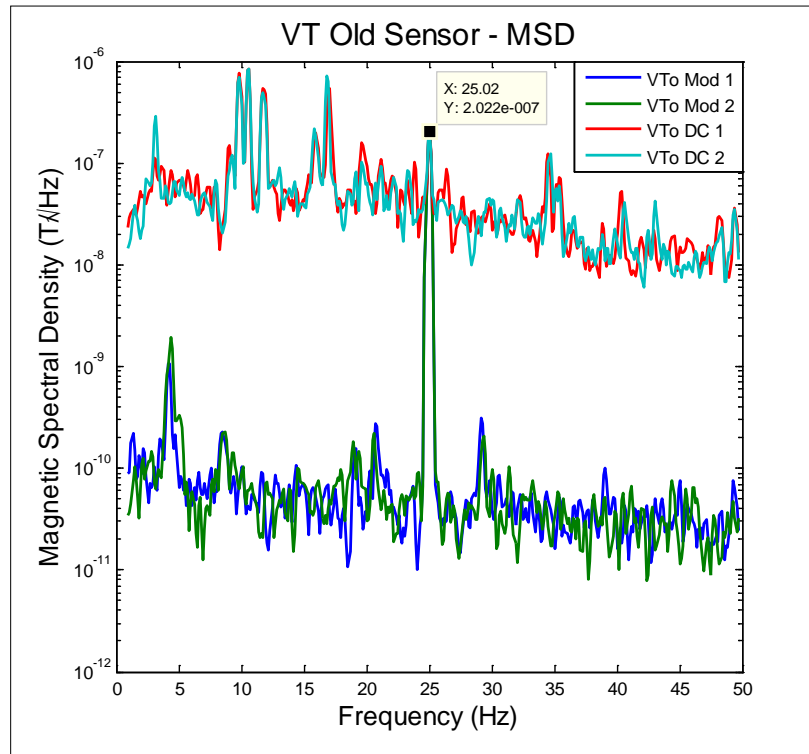


Figure 227. Magnetic spectral density comparison of DC vs. modulation technique for VT old.

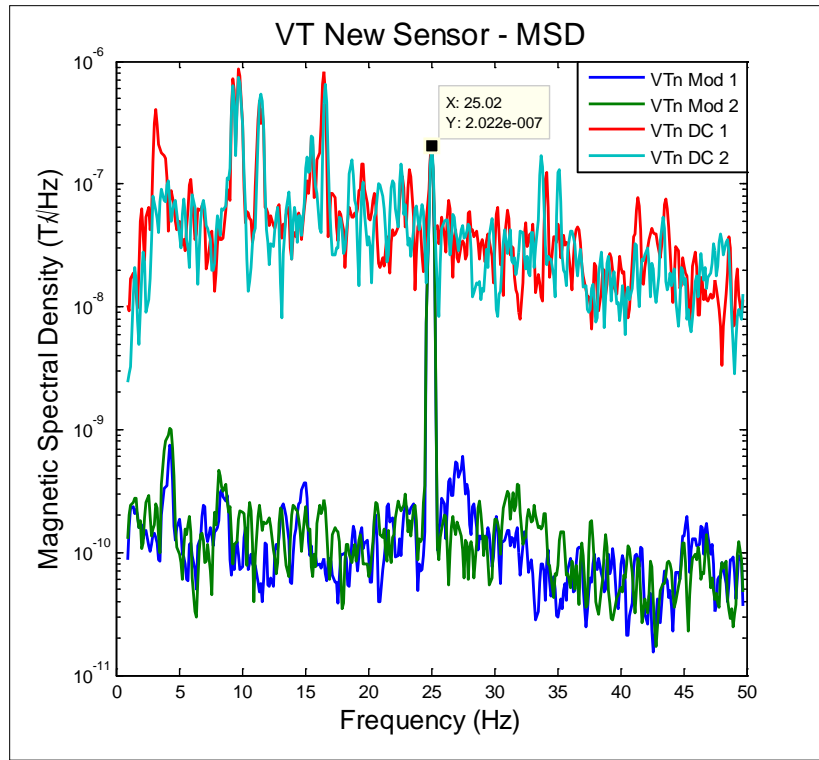


Figure 228. Magnetic spectral density comparison of DC vs. modulation technique for VT new.

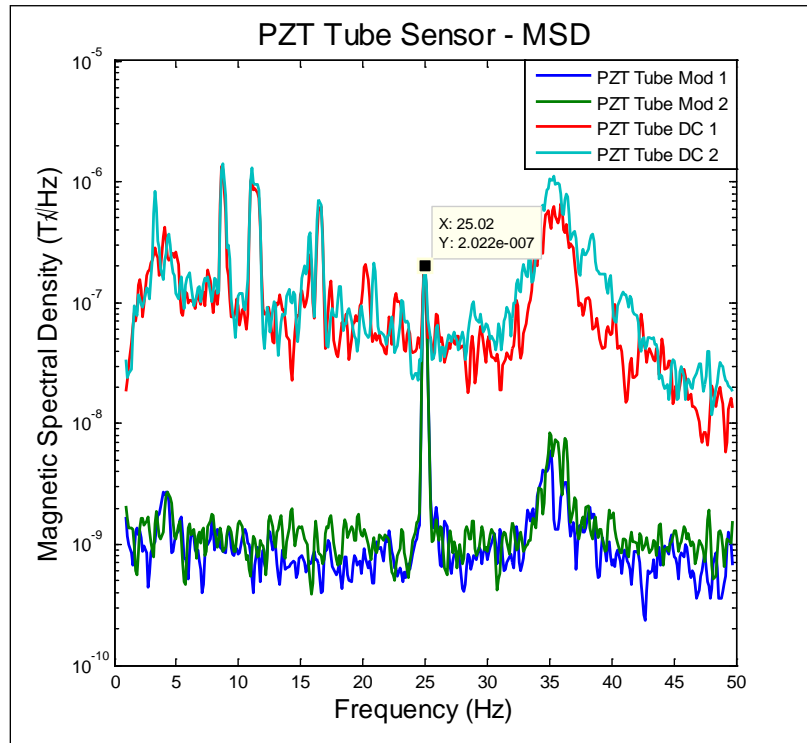


Figure 229. Magnetic spectral density comparison of DC vs. modulation technique for PZT tube.

Two MSD curves are shown per condition to demonstrate repeatability where each successive curve was captured approximately 10 minutes later. Several strong persistent environmental noise peaks can be seen in the DC biased configurations at approximately 4, 9, 11, 16, and 39 Hz. These noise peaks are shown to be attenuated when using the modulation sensing technique. Values of 1-Hz SNR, sensitivity, and 1-Hz noise floor, taken from each pair of curves exhibiting lowest 1-Hz noise floor are listed in the Table 51.

Table 51. Comparison of magnetic field sensitivity and noise floor.

<u>Sensor & Configuration</u>	<u>1-Hz SNR (dB)</u>	<u>25-Hz Sensitivity (Vrms/Oe)</u>	<u>1-Hz Noise Floor (nT/$\sqrt{\text{Hz}}$)</u>
DC CC	16.2	0.0029	30.2
MOD CC	50.5	0.0517	0.61
DC VTo	22.8	0.468	14.6
MOD VTo	75.5	0.345	0.034
DC VTn	38.3	0.288	2.45
MOD VTn	67.4	2.09	0.087
DC PZT Tube	20.9	0.0056	18.3
MOD PZT Tube	41.5	0.0094	1.7

The results reported once again prove that the modulated sensing technique significantly increases the 1-Hz signal-to-noise ratio. It is important to note that in this investigation the modulation field frequency was tuned to generate high SNR instead of maximum sensitivity. In comparing the DC Vto with MOD VTo sensitivity values, of 0.468 Vrms/Oe and 0.345 Vrms/Oe, respectively, a decrease in sensitivity is shown when using the modulated sensing technique. In past studies, the modulation field was tuned to stimulate a resonance mode in the sensor which resulted in much greater sensitivity values associated with the modulation technique. However, it was noticed that not all sensors exhibit peak sensitivity and peak SNR at the same modulation frequency.

We are pleased to report that a magnetic noise floor of 34pT/ $\sqrt{\text{Hz}}$ was measured using the modulation technique in conjunction with Virginia Tech's original donated sensor. This figure of merit represents the lowest 1-Hz noise floor value our lab has measured for the HUMS project.

G.3.3. On-resonance vs. off-resonance modulation.

We investigated the on- vs. off-resonance characteristics of four magnetoelectric sensors using the modulated sensing configuration. This investigation was spurred by the behavior observed when using the newly-developed PZT tube sensors in conjunction with the modulated sensing technique. It was reported that peak signal-to-noise ratio (SNR) and peak sensitivity did not occur at the same modulation frequency for the PZT tube sensors. Prior HUMS reports utilized the modulation configuration with CC sensor and both VT sensors at a single, sensor-specific,

on-resonance modulation frequency to provide peak sensitivity, with peak SNR occurring at that same modulation frequency. We investigated the cause of these differences in performance using the following sensor elements:

- CC Sensor: A Metglas/PZT/Metglas laminated composite.
- VT Old Sensor: Virginia Tech's 1st Metglas/poled-PZT/Metglas laminated composite.
- VT New Sensor: Virginia Tech's 2nd Metglas/poled-PZT/Metglas composite.
- PZT FN Tube Sensor: 5cm Iron-Nickel wire/PZT tube composite.

Note that the term “on-resonance” refers to the condition where peak sensitivity is generated due to electro-magneto-mechanical resonance.

The modulation sensing technique setup was configured to apply a 25 Hz, 0.001 Oe (100nT) test H-field and a 0.1 Oe (10 μ T) modulation field at varying frequencies to the DUT using dual nesting Helmholtz coils positioned inside a dual-walled Gauss chamber. Power spectral density measurements, consisting of 500 averaged sweeps, were captured for each sensor from ~1Hz to ~50Hz. A block diagram of the experimental test setup is shown below in Figure 230.

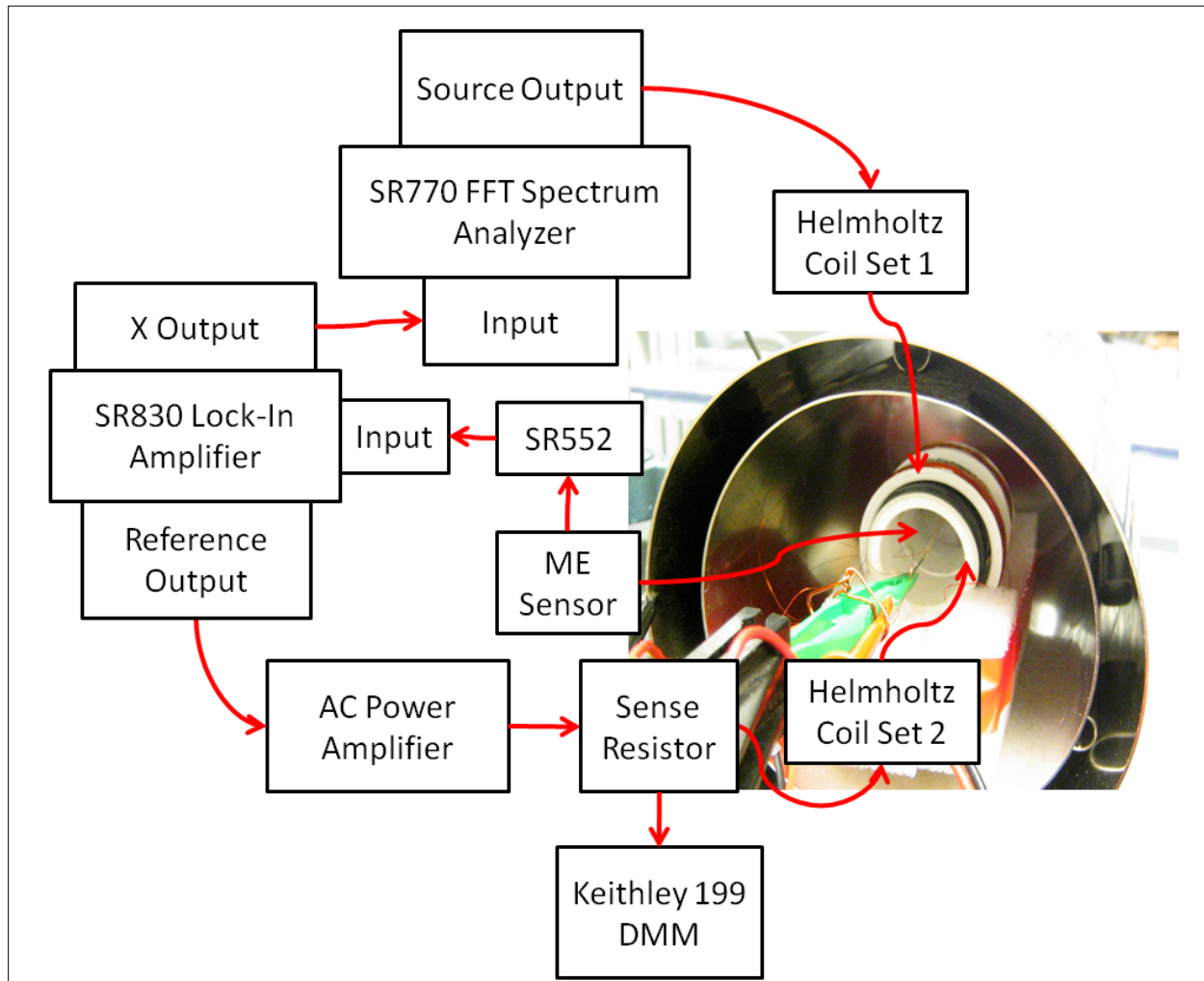


Figure 230. Experimental test setup.

Each sensor was modulated at three different frequencies; the on-resonance frequency which produces peak sensitivity, 1 KHz below resonance, and 1 KHz above resonance. A table listing device sensitivity and SNR at each frequency is shown below in Table 52. On-resonance measurements are italicized.

Table 52. Comparison of sensitivity, SNR and noise floor with respect to modulation frequency for several ME sensors.

<u>Sensor & Mod Frequency</u>	<u>25-Hz Sensitivity (Vrms/Oe)</u>	<u>1-Hz SNR (dB)</u>	<u>1-Hz Noise Floor (nT/√Hz)</u>
CC 60 KHz	0.0069	44.98	1.14
CC 59 KHz	0.0056	40.94	1.81
CC 61 KHz	0.0049	35.34	3.46
VTo 33 KHz	0.9758	64.03	0.127
Vto 32 KHz	0.7696	68.27	0.078
Vto 34 KHz	0.8121	64.05	0.127
VTn 30 KHz	1.9108	61.55	0.169
VTn 29 KHz	1.1068	58.91	0.229
VTn 31 KHz	1.7709	67.37	0.087
PZT FN 36 KHz	0.0024	25.91	10.24
PZT FN 35 KHz	0.0019	32.30	4.90
PZT FN 37 KHz	0.0007675	17.37	27.35

These results indicate that sensors VTo, VTn, and PZT FN have lower 1-Hz noise floor values, corresponding to higher SNR values, when stimulated with an off-resonance modulation field. The 5cm PZT FN tube sensor exhibits the largest improvement factor in noise floor of 2.09 x while suffering only a 1.26 x reduction in sensitivity. It is probable that this behavior went unnoticed previously due to the small change in noise floor seen with CC, VTo, and VTn sensors. Magnetic spectral response of the 5cm PZT FN tube sensor, shown in Figure 231, clearly demonstrates the improvement in noise floor achieved through off-resonance modulation.

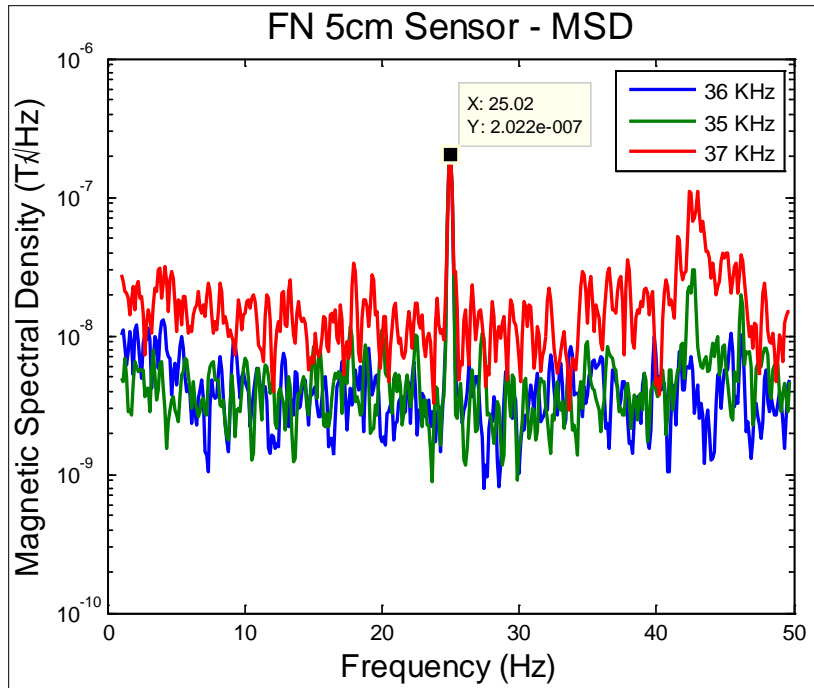


Figure 231. Magnetic spectral density plots of 5cm PZT FN tube sensor for modulation frequencies of 36 KHz, 35 KHz, and 37 KHz.

The presented trends observed in comparing on- vs. off-resonance modulation are still under investigation.

G.3.4. PZT Tube sensor sensitivity and noise floor measurements.

In mid-July 2011, two PZT tube sensors were sent to SAIC in France for characterization of sensitivity and noise floor using the conventional DC biased method. We currently believe that high environmental noise due to Northeastern University's urban environment is limiting noise floor measurements.

Noise floor measurements of two PZT tube sensors; WB21 and WBFN, sent to SAIC in France have been completed and returned to us. These measurements are reported in the format they were sent to us, shown in Figure 232 and Figure 233. *Their results confirm our suspicions that measurements taken at Northeastern University are limited by the high magnetic noise floor of the urban environment. It is noticed that the results from SAIC presents obviously 1-2 orders of magnitude in noise floor lower than those captured at NEU for both of the PZT tube sensors.* In addition, preliminary tests at SAIC have indicated that the sensitivity of the PZT tube sensor is 1-2 orders of magnitude higher than the data derived from NEU, which was reported previously.

Northeastern University sensor noise characterization

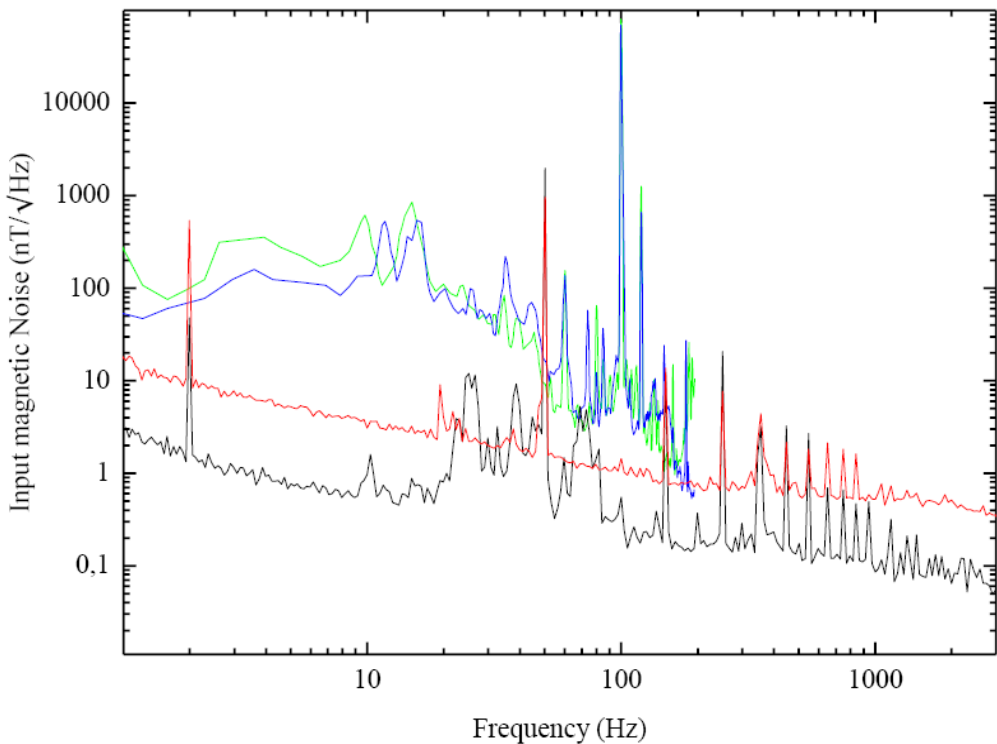


Figure 232. Magnetic noise of WBFN 8cm sensor captured at Northeastern (blue) and at SAIC (black) and of the WB21 7.5cm sensor captured at Northeastern (green) and at SAIC (red). Shown with log scale x axis.

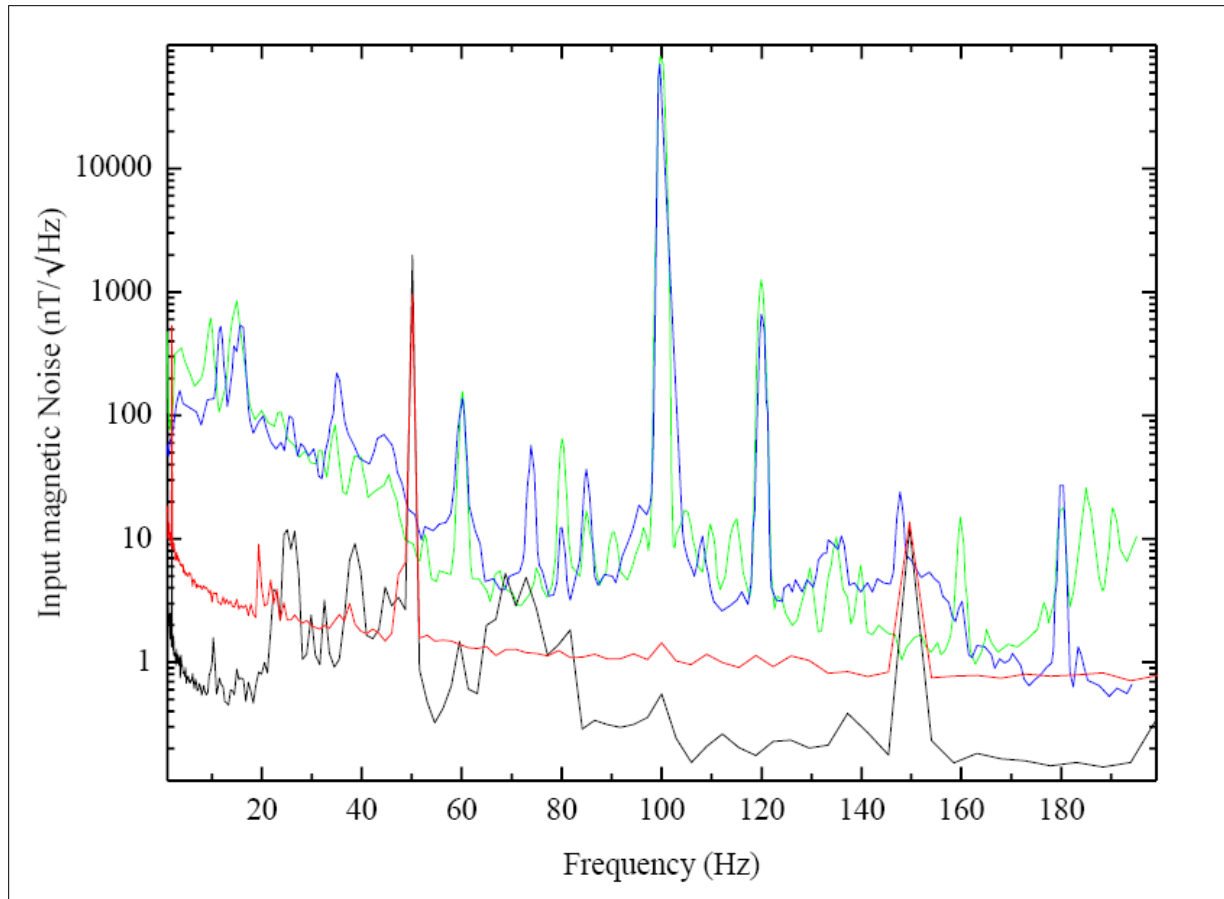


Figure 233. Magnetic noise of WBFN 8cm sensor captured at Northeastern (blue) and at SAIC (black) and of the WB21 7.5cm sensor captured at Northeastern (green) and at SAIC (red).

Shown with linear scale x axis.

G.3.5. PZT/FN (Iron/Nickel) ME Tube Sensors.

We have investigated reducing the frequency of the applied test field from 25 Hz to 10 Hz, which is lowest magnetic field frequency able to be calibrated to with the current experimental setup. The goal of reducing the frequency of the test H-field to 10 Hz is to characterize the PZT tube sensors at near-1Hz frequencies as required by the goal of the DARPA HUMS project. Two nearly-identical 5cm ME tube sensors consisting of a PZT tube and FN (Iron-Nickel) wire were tested. One sensor (named FN 1) was fabricated approximately 2 months apart, while FN 2 sensor was made recently. But both sensors were simultaneously polarized under identical conditions prior to testing.

The conventional DC biasing configuration was used for this investigation to apply H-bias fields from 0- 30 Oe in the following intervals; 0, 1, 2.5, 5, 7.5, 10, 15, 20, and 30 Oe. Power spectral density data was captured for each sensor under each H-bias field and used to calculate sensitivity, signal-to-noise ratio (SNR), noise floor, and magnetic spectral density, shown in Figure 234, Figure 235, Figure 236, and Figure 237, respectively.

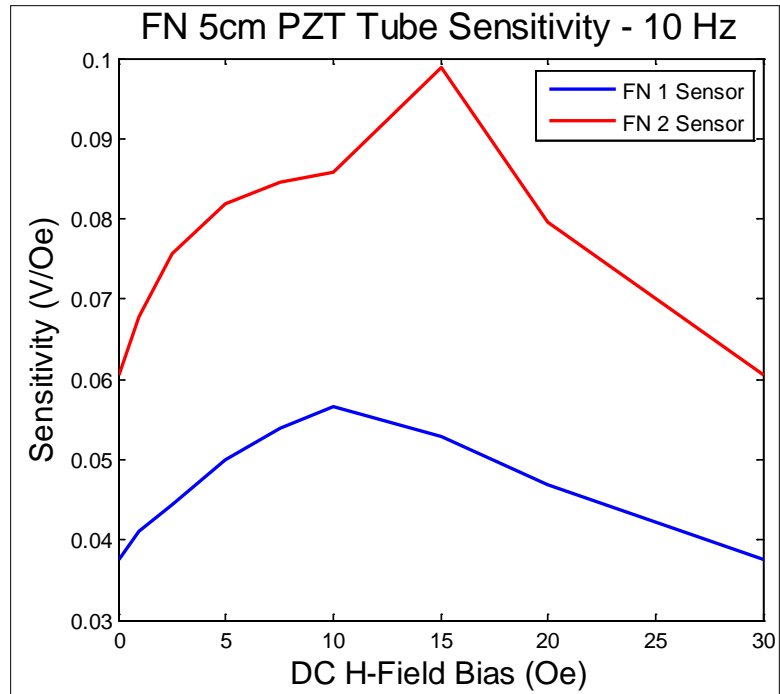


Figure 234. 10 Hz sensitivity of two 5cm PZT/FN magnetoelectric tube sensors.

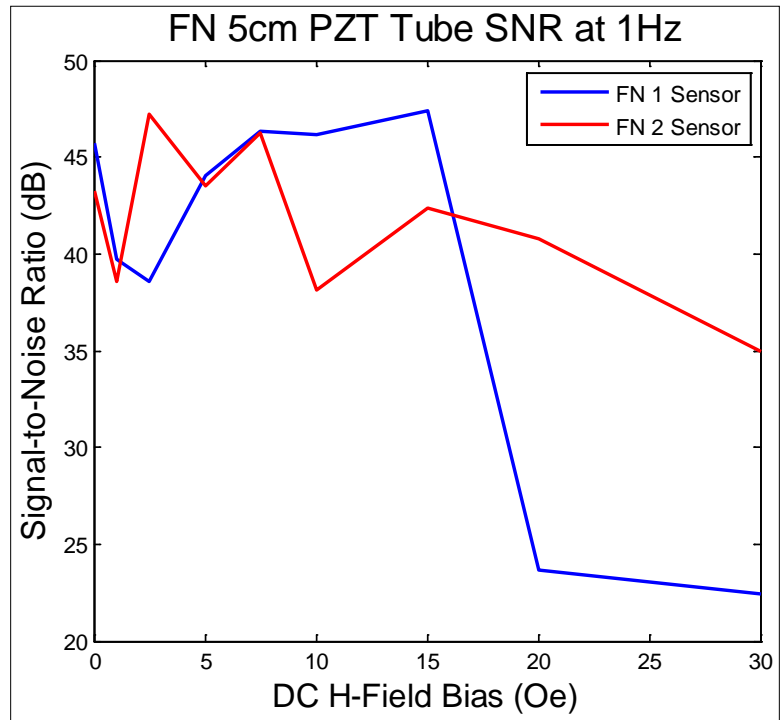


Figure 235. 10 Hz sensitivity of two 5cm PZT/FN magnetoelectric tube sensors.

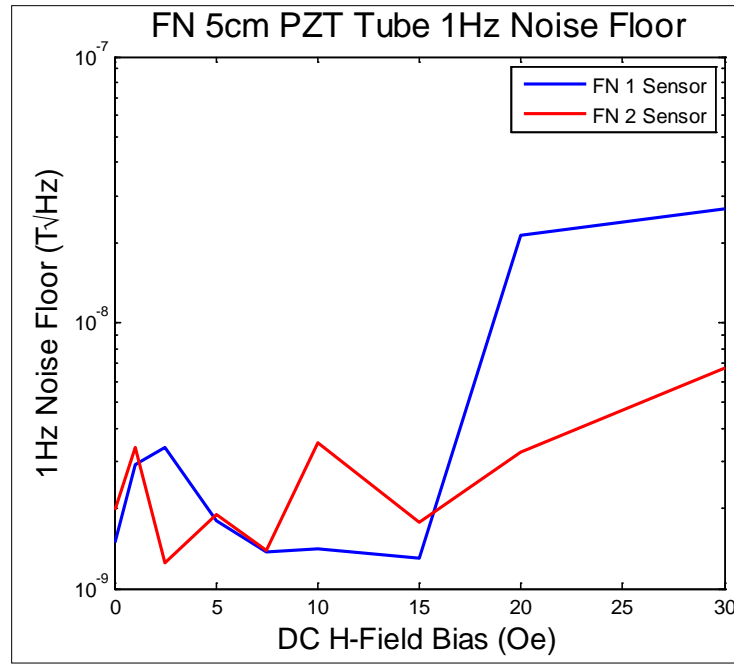


Figure 236.10 Hz sensitivity of two 5cm PZT/FN magnetoelectric tube sensors.

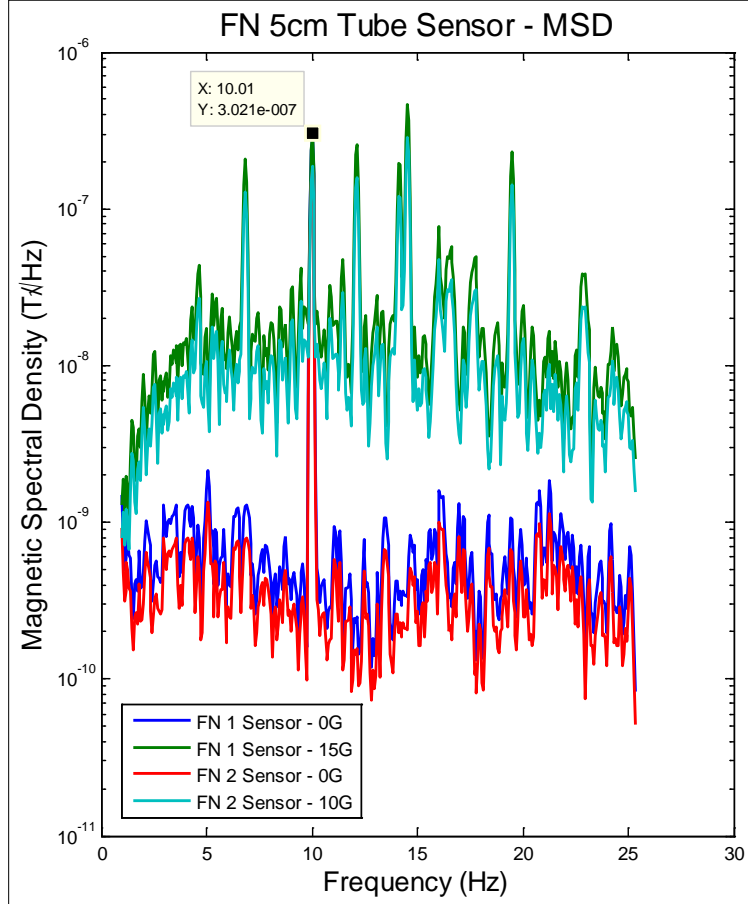


Figure 237.10 Hz sensitivity of two 5cm PZT/FN magnetoelectric tube sensors.

Both sensors are observed to have similar magnetic spectral density response characteristics in which the noise floor >5Hz is shown to increase approximately 1.5 orders of magnitude. These results also show similar values of SNR and noise floor between both 5cm FN ME tube sensors but show an approximate 1.6x increase in sensitivity for FN 2 sensor. FN 2 sensor was fabricated approximately 2 months after FN 1 sensor. There appear to be aging effects associated with these sensors. It is known that humidity severely degrades the sensitivity of their sensors by increasing the conductivity of the PZT, therefore increasing leakage current, which reduces the magnitude of a voltage response to a magnetic field. A future investigation will test these aging effects by first addressing the effects of humidity on the magnetoelectric tube sensors.

G.3.6. Galfenol-based PZT tube sensors.

We have also focused on DC testing and fabrication of GaFe wire-based PZT tube sensors. The GaFe magnetostriction wires used in have high magnetization and magnetostrictive coefficient, as well as especially have a diameter of less than 0.4-0.6 mm. The wires are not yet commercially available. For the Fe83Ga17 wires having $<1\ 0\ 0>$ crystallographic texture, an enhanced magnetostrictive coefficient can be achieved by magnetic field annealing of the wires can present high magnetostriction coefficient, 150-180 ppm, while subjected to an annealing at 500-1000 °C in a magnetic field (100-1000 Oe) and in air. Figure 238 (a) presents magnetic hysteresis loop, indicating 15,000 G of saturation magnetization. A saturation magnetostriction field is around 300 Oe, see Figure 238 (b).

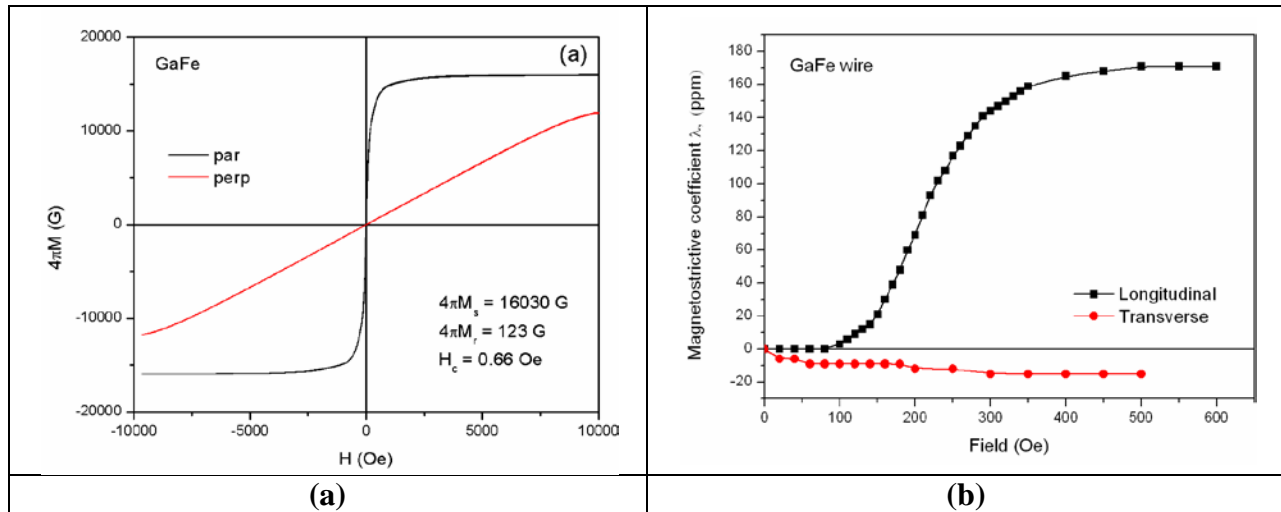


Figure 238. (a) Magnetic hysteresis loops and (b) magnetostriction measurements of GaFe wires used in this patented invention.

Parallel and perpendicular magnetizations stand for an applied magnetic field parallel and perpendicular to an axial direction of the wire. Longitudinal and transverse magnetostriction coefficients represent strains parallel and transverse to an applied magnetic field, respectively

G.3.6.1. Comparison in sensitivity for 1D-tube sensor

The tube sensor consisting of PZT tube and GaFe wire for 5 cm length was tested in 100 Hz signal and amplitude of 1 Oe in either free-standing or bending mode. The bending mode is

subject to a fixed end of the sensor, while another end retains free. It produces electro-mechanical resonance (EMR) while applied an alternative field, which is assumed to enhance magnetoelectric coupling effect. The DC bias field dependence of sensitivity is depicted in Figure 239. It clearly indicates an increase of 15% in sensitivity for the bending mode, especially when a DC bias field is higher than 15 Oe.

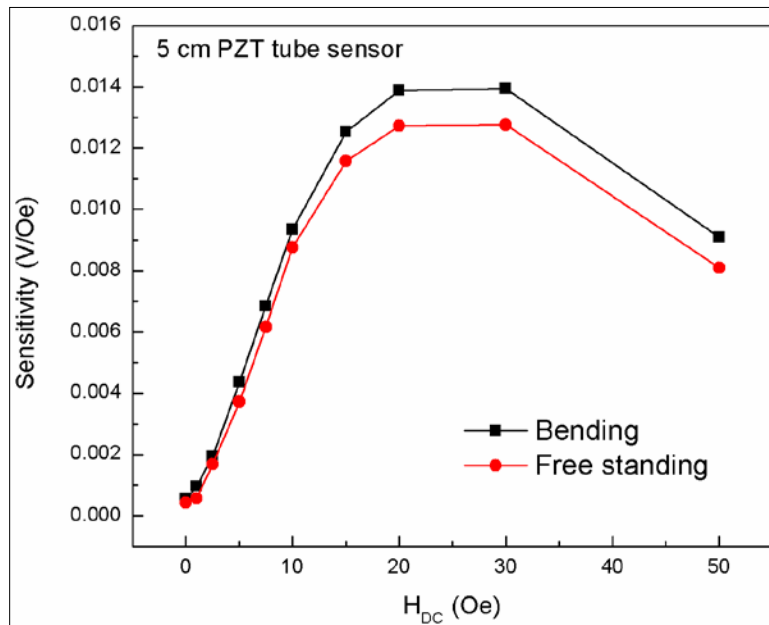


Figure 239. A Bias field dependence of sensitivity for 1D GaFe/PZT sensor with bending and free standing mode. ($f=100$ Hz, $H_{ac}=1$ Oe)

Note that this result leads to all of the following tests for the 1D-MF sensors based on a bending mode.

G.3.6.2. Length dependence of sensitivity for 1D-tube sensor

Figure 240 and Figure 241 present an effect of length on sensitivity for a 1D- ME sensor consisting of PZT tube and GaFe wire. Note that increasing length enhances significantly sensitivity, especially for a DC biased field > 10 Oe. The relation between biased field and sensitivity is determined by piezomagnetic coefficient, i.e $d\lambda/dH$. It is noticed that sensitivity almost saturates as a bias field is above 15 Oe for the 7.5-cm length sensor, whereas the others still increase with bias field.

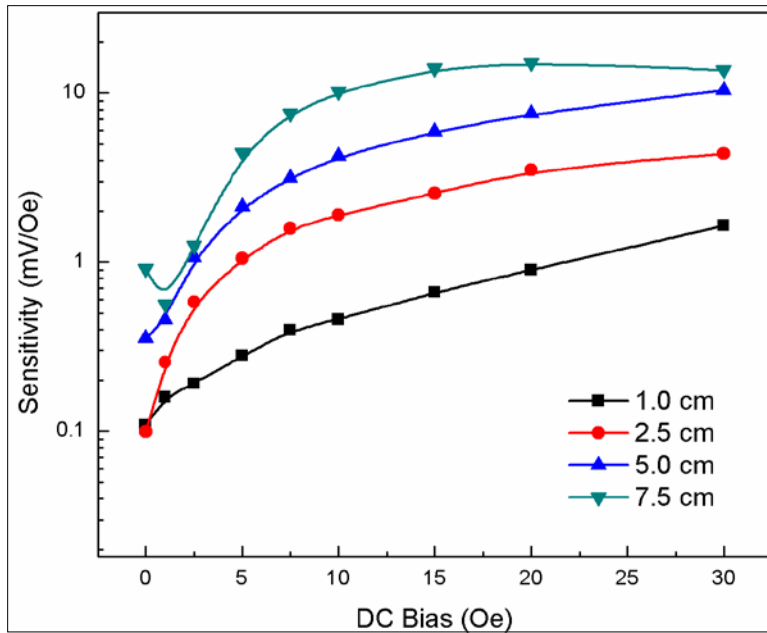


Figure 240. Bias field dependence of sensitivity for 1D GaFe/PZT sensor with different PZT tube lengths ($H_{DC}=0, 10$ and 20 Oe). ($f=100$ Hz, $H_{ac}=1$ Oe)

On the other hand, sensitivity is proportional to a sensor length at any bias fields. It is understandable that the relation between sensitivity and length is considered to relate electromechanical resonance frequency. In fact, the trend of sensitivity with sensor length is available for other 1D MF sensors as well, such as piezoelectric PZT, BTO tube etc, and magnetostriction wires, such as, FeNi etc.

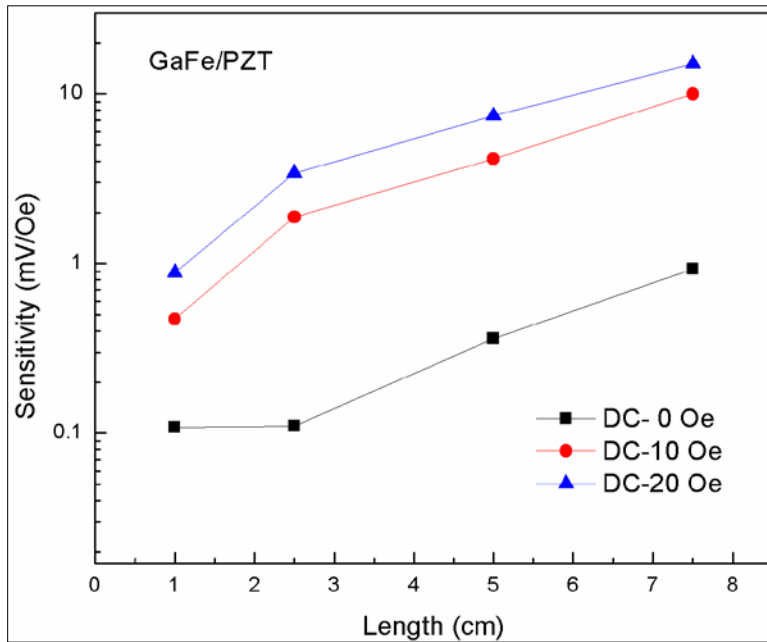


Figure 241. PZT tube length dependence of sensitivity for 1D GaFe/PZT sensor with different bias fields ($H_{DC}=0, 10$ and 20 Oe). ($f=100$ Hz, $H_{ac}=1$ Oe).

G.3.7. Thin film PZT/Metglas composites

G.3.7.1. Experiment

Metglas® substrates was buffered with Pt or Au layers to form a seed layer for the epitaxial growth of PZT films. Pt and Au facilitate epitaxy because they possess crystal structures and lattice parameters similar to PZT. The seed layers, deposited using DC magnetron sputter deposition, had (111) orientation and thicknesses of 80-150 nm. PLD was employed to deposit PZT at a temperature of 650 °C under varying oxygen pressures. The laser was of the KrF gas with $\lambda=248\text{nm}$ type with an average output power of 400 mJ/cm². Two pieces of Metglas® substrates, buffered with Pt or Au, were mounted on the substrate holder for each deposition cycle. The deposition chamber was evacuated and backfilled with oxygen prior to deposition. Effect of oxygen pressure on the growth was investigated for deposition time of 3.5 hours under 100 mTorr, 150 mTorr and 200 mTorr, respectively. By using a profilometer, the thicknesses of the samples were determined to be 2.1 to 2.4 μm . The crystal structure was characterized by XRD indicating a single phase PZT structure existed. All of diffraction peaks were indexed to a highly textured single-phase perovskite having a lattice parameter consistent with PZT. SEM was utilized to capture surface images of the PZT films. Chemical compositions were also determined by Energy-dispersive X-ray spectroscopy (EDX), yielding the ratio of Pb: Zr: Ti, (1~1.15):0.52: (0.44~0.48). The ferroelectric properties were measured by polarization hysteresis measurement driven by a triangular waveform of frequency 10 kHz. The piezoelectric coefficient d_{33} was measured by using Veeco SPI 3100 piezoelectric force microscopy (PFM).

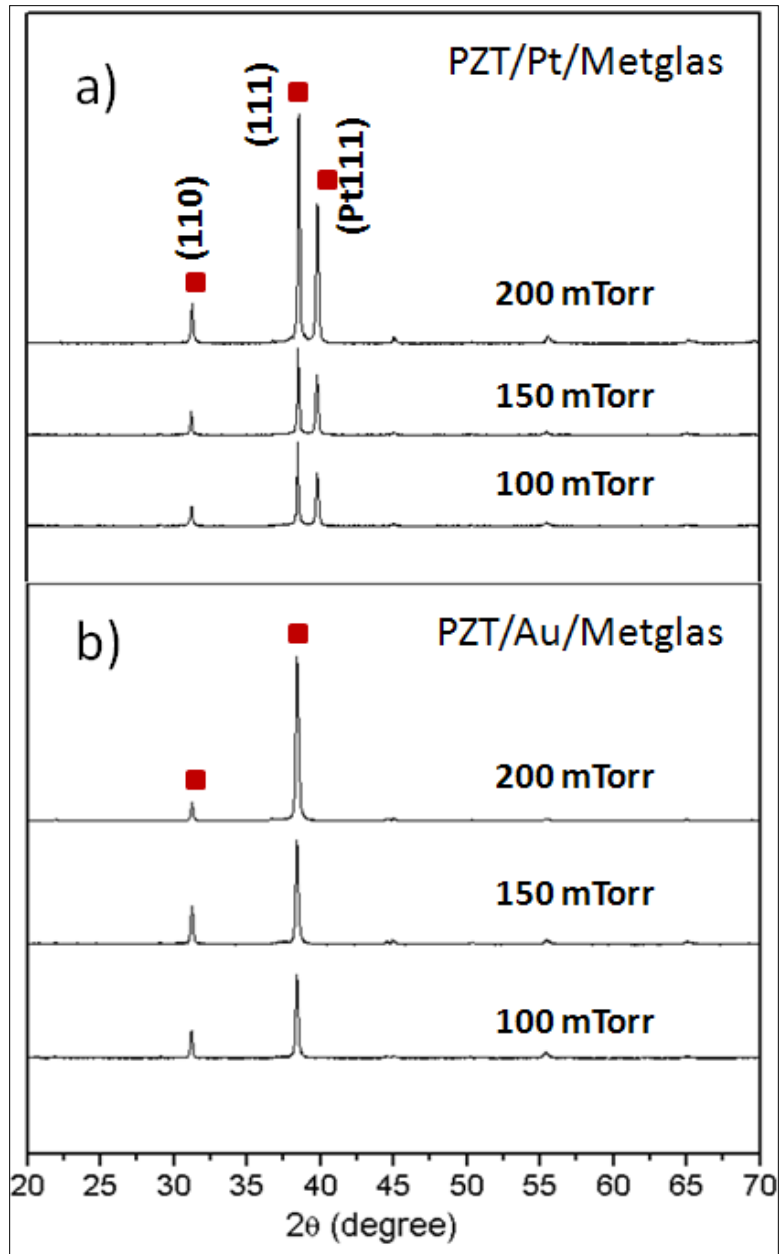


Figure 242. XRD pattern of PZT thin film on Pt (a) and Au (b) buffer layer

G.3.7.2. Result and discussion

XRD spectra for the PZT films deposited on Matglas® substrates with either Pt or Au as a buffer layer were collected by a Rigaku Ultima III x-ray diffractometer using Cu K α radiation in a q-2 θ geometry at room temperature. The XRD patterns obtained for the Pt buffered samples are presented in Figure 242 (a) for different oxygen pressure depositions. It is noticed that the PZT films remain as a pure phase structure as the oxygen pressure changes from 100 to 200 mTorr. The peaks at 31.2° and 38.3° correspond to (110) and (111) planes of the PZT film, respectively. It is clear that (111) plane is dominant. The (111) plane of Pt or Au buffer layer should be at $2\theta=39.5^\circ$ and 38.1° , respectively. But it is invisible for Au buffered films because the Au (111) peak overlapped the PZT (111) peak, as shown in Figure 242 (b). At an oxygen pressure of 100

to 200 mTorr, the PZT crystal film is strongly orientated along the $<111>$ direction as determined by the templating by the Pt or Au (111) oriented buffer layers. With the variation of oxygen pressure, either Pt or Au buffered PZT film presents similar trends in growth, i.e. the PZT films are of (111) preferably orientation that is manipulated by the (111)-oriented Pt or Au buffer layer. It builds up a solid foundation for an enhancement of the ferroelectric and piezoelectric performance.

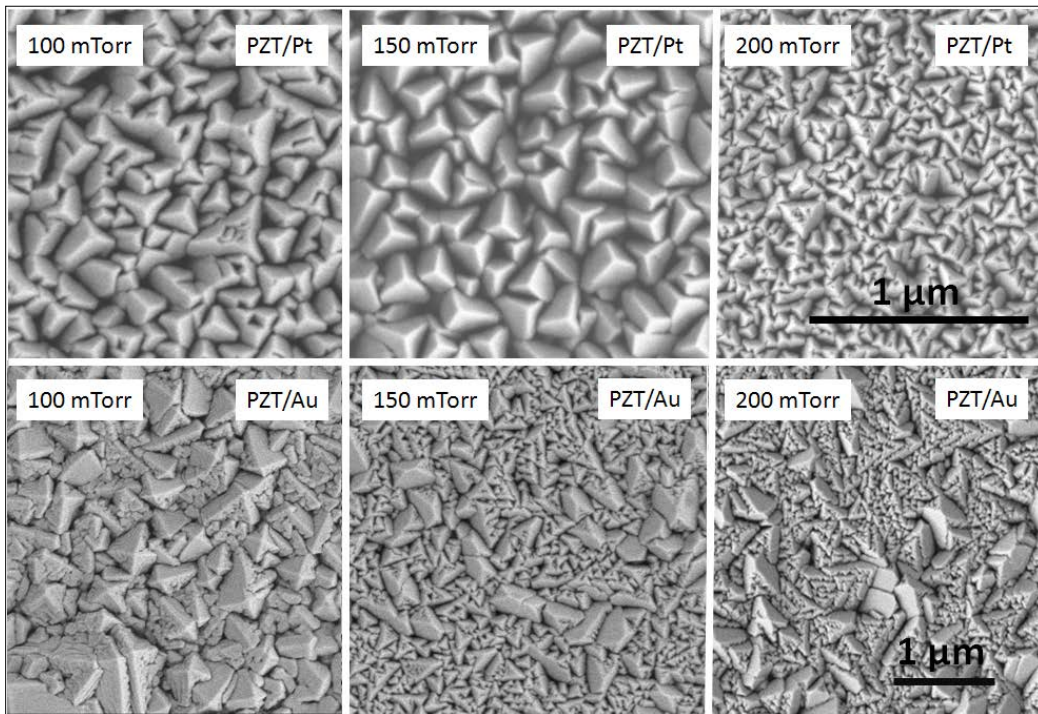


Figure 243. SEM images of Pt or Au buffered PZT thin films under different oxygen pressures

The surface morphology of PZT films on Metglas® substrates were observed by scanning electron microscopy (SEM), as shown in Figure 243 (a). The SEM images represent the PZT films deposited at 650 °C and under 100 mTorr, 150 mTorr, and 200 mTorr O₂ pressure with Pt or Au buffer layer, respectively. The SEM images of the PZT films with a Pt buffer layer resulted in very uniform grain growth with triangle-shaped grains, reflecting strong (111) orientation. However, Au buffered films showed somewhat an inhomogeneous and non-uniform distribution of the grains, as shown in Figure 243 (b). Some of the grains for the Au buffered PZT thin film look like octahedral shaped agglomerations containing triangle-shaped fine grains. It implies that the growth of PZT crystal is incomplete, which is quite different from the growth on the Pt buffer layers. The difference in morphology between Au and Pt buffered PZT films may arise from different lattice mismatches and/or roughness of the buffer layer. Note, that the lattice constant of Pt, Au and PZT crystal is 3.920, 4.080 and 4.040 Å, respectively. Clearly, the lattice mismatch between (111) Au and (111) PZT crystallographic structure is much smaller, ~1%, whereas the lattice mismatch between (111) Pt and (111) PZT film is about 3%. Bragg equation and Miller indices were used to calculate lattice constant a for both Pt and Au buffered. The PZT was considered to a be a tetragonal structure, and lattice constant a and c are listed in Table 53.

Table 53. Comparison of PZT lattice constant between Pt and Au buffered samples by using XRD analysis

O₂ Pressure (mTorr)	Lattice constant (Å) of PZT with Pt buffer layer			Lattice constant (Å) of PZT with Au buffer layer		
	a	c	c/a	a	c	c/a
100	4.0509	4.0787	1.0069	4.0540	4.0580	1.0010
150	4.0472	4.0909	1.0108	4.0483	4.0877	1.0097
200	4.0444	4.2665	1.0549	4.0460	4.2953	1.0616

It was found the PZT deposited on Au buffered layer had a larger lattice constant *a* than that deposited on Pt buffered. That is, the lattice constant of PZT buffered with Au is closer to the Au lattice constant (4.08Å). As the pressure rises, the c/a ratio increases gradually for both Pt and Au buffered PZT films, indicating a slight change in PZT crystal from cubic to tetragonal symmetry. A small lattice mismatch is responsible for continuous and rapid growth of the PZT crystal structure. Note that by reducing the oxygen pressure from 200 to 100 mTorr, either Pt or Au buffered PZT thin film tends to form the microstructure with fine grains. Actually, as the pressure is reduced, the surface mobility increases, creating larger grains.

In our experiment, the pressure was the variable while considering other parameters as constants. When the pressure is reduced, the free mean path is increased, resulting in the reduction of thermalizing collisions of particles during a deposition process. With fewer thermalizing collisions the adatom mobilities remain high, resulting in larger grains and thicker films (i.e. deposition rates).ⁱ At the same time, we noticed that the PZT films with Au layer are thicker than those buffered with Pt by 5 to 10%. i.e. At 150 mTorr of O₂ pressure, the thickness of the PZT film with a Pt buffer layer is around 2.3 μm, 9.52% thicker than the film with the thickness of 2.1 μm with Au buffered at the same pressure. It is easier for the atoms to combine into island on the substrate so as to form larger grains. The grain sizes of PZT thin film with Pt layer were determined as a function of pressure by the SEM images, as depicted in Figure 243 (b). For the Pt buffered films, the grains are uniformly arranged. So an average grain size is derived from the SEM images, indicating an inverse relationship between deposition pressure and grain size. It follows the theoretical prediction as described above. As for those grains distributed on Au buffered layers, they are grouped as large grains and small grains separately. Therefore, it is clear to see from the SEM images that both Pt and Au buffered PZT films show similar behavior in response to the changes in deposition pressure, that is, the grain size increases as the oxygen pressure decreases.

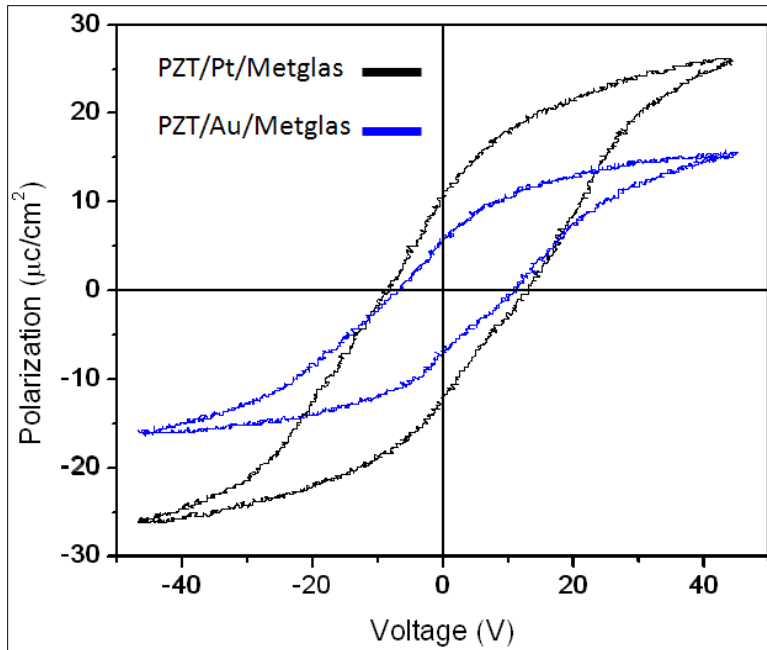


Figure 244. Ferroelectric measurements for PZT thin films on an Metglas substrate with a Au or Pt buffer layer.

More importantly, ferroelectric measurements of the PZT films were performed, i.e. piezoelectric constant d_{33} and polarization hysteresis loop. Figure 244 is a representative ferroelectric hysteresis loop with an applied voltage of 50 volts for both Pt and Au buffered PZT samples grown at 650°C under 150 mTorr oxygen pressure. The PZT films were previously sputtered with a 150 nm thick gold top electrodes with mask grid size of 20 μm by 20 μm . Gold wire with 25 μm in radius were bonded to the top electrodes. The PZT film was polarized in the out-of-plane direction. For Pt buffered sample, it is found that the saturation polarization and a remnant polarization are $P_s \approx 27 \text{ mC/cm}^2$, and $P_r \approx 10 \text{ mC/cm}^2$, respectively. While the Au sputtered PZT film has $P_s \approx 16 \text{ mC/cm}^2$ and $P_r \approx 6 \text{ mC/cm}^2$. Obviously, Pt buffered PZT films show higher polarization than that of Au buffered films, which resulted from the uniform and continuous growth of films with fine grains on a Pt buffered substrate. Nevertheless, those values for both of the films are comparable to other PZT films previously reported. It is worth noting that the piezoelectric properties depend sensitively upon grain size and film thickness. An increase of coercive field was observed with decreasing thickness of the ferroelectric film.⁴ Since the Pt buffered PZT film has a slow deposition rate, compared to the Au buffered one, so it leads to a thinner PZT layer, corresponding to a high coercive field. It is assumed that the microstructure with fine grains in the Pt buffered PZT films may offer large permittivity due to high grain boundary capacitance, consequently resulting in a high saturation polarization, as displayed in Figure 244. Also, from the previous SEM images, it is clear that the PZT thin film with an Au layer reveals non-uniform surface so as to generate an extra leakage current which may reduce the ferroelectric polarization.

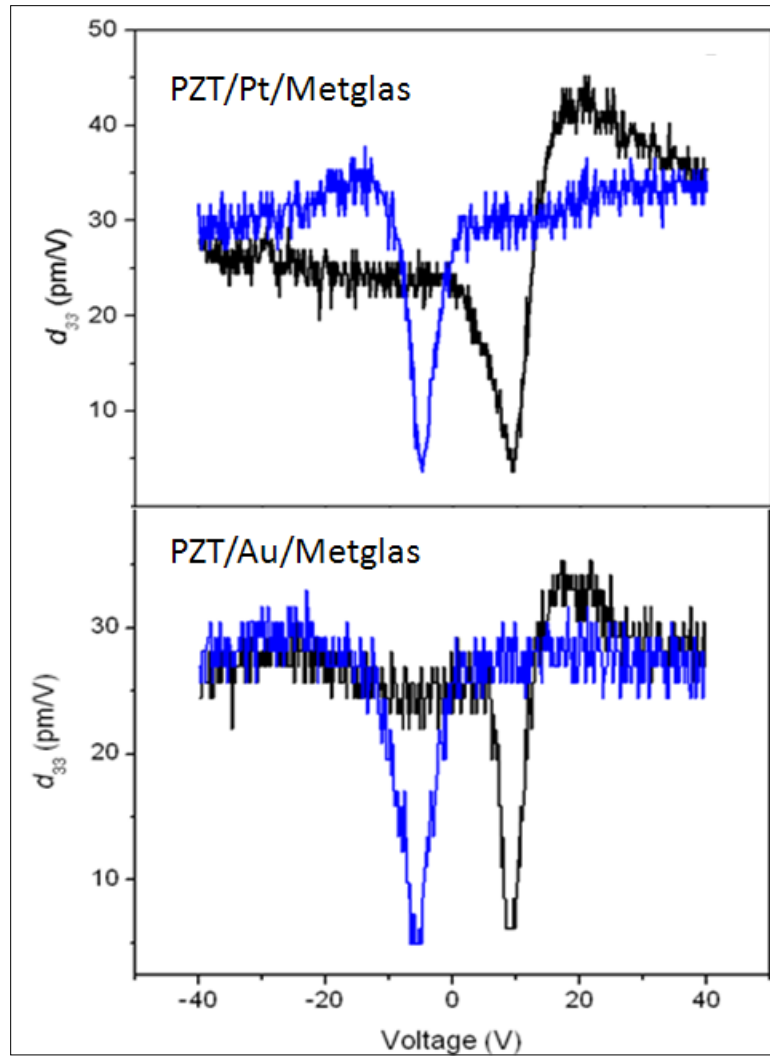


Figure 245. Piezoelectric coefficient d_{33} measurements for the PZT thin film on a Metglas substrate with a Pt or Au buffer layer.

Finally, the piezoelectric constant d_{33} was measured as a function of applied voltage, as shown in Figure 245. The curve from Pt buffered layer presents a more symmetric butterfly shaped loop and a higher d_{33} value, than those of Au buffered PZT films. . The measurement indicates a maximum value of $d_{33} \sim 46$ pm/V of the Pt buffered sample, and 35 pm/V of the Au buffered one. The $d_{33} \sim 46$ pm/V of the Pt buffered sample is 53% higher than the reported piezoelectric constant d_{33} of BTO deposited on Metglas® substrate. Such a high d_{33} may benefit from three factors: (1) the uniformity of the structure provides a better strain transfer, (2) the PZT film is of high quality in crystallography, and (3) Metglas® might provide smaller strain inside PZT film than Si substrates.

H. Alan Edelstein, Army Research Lab

H.3.1. Modeling and Experimental Results on Flux concentrators

We have modeled the design of the magnetic flux concentrators needed to enhance the field at the position of the ME sensors using the finite element code ANSYS Maxwell. Our ME sensors used Metglas 2605 for the magnetostrictive layers. Even though it does not have a large magnetostrictive coefficient ($\lambda_s \sim 20-27$), this material was chosen because of its high permeability. Materials with high permeability have the ability to concentrate magnetic flux and, thus, increase the field at the position of the sensor. Figure 246 shows our modeling results for a material with the same dimensions as the sensor (e.g. 8 x 1 x 0.075 cm) as function of the relative permeability (μ_r) of the material. The field enhancement is calculated by applying a constant field of 1000 nT across the entire region and normalizing the integrated flux over the volume of the sensor to a non-permeable μ_r of 1. If $\mu_r = 10,000$, one sees that the Metglas itself already provides a considerable enhancement at the position of the ME sensor. Our goal was to increase this enhancement without changing the size of the sensor. Accordingly, we considered how the enhancement is further augmented by adding different lengths of highly permeable flux concentrators to each side of the sensor, as seen in Figure 247 (a). Based on recent literature, we used a permeability of 30,000 for both the Metglas in the sensor and the mu metal in the additional flux concentrators.

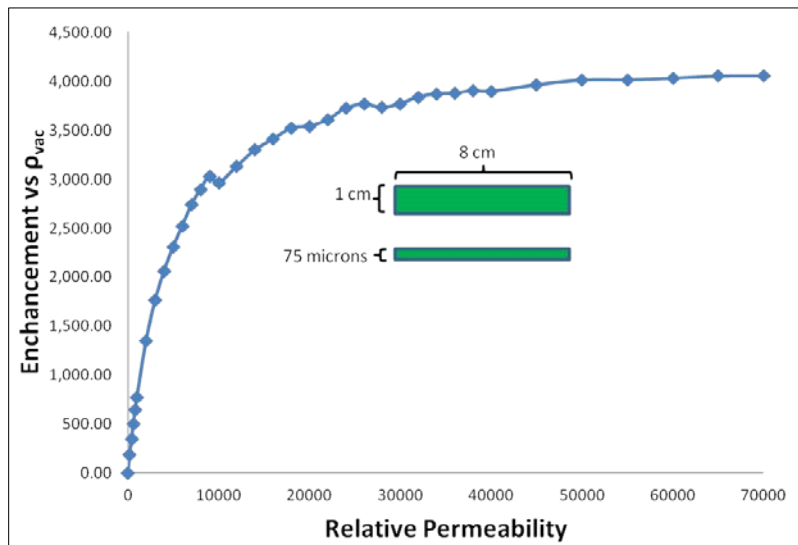


Figure 246. Enhancement as a function of the relative permeability of the magnetostrictive material in ME sensors.

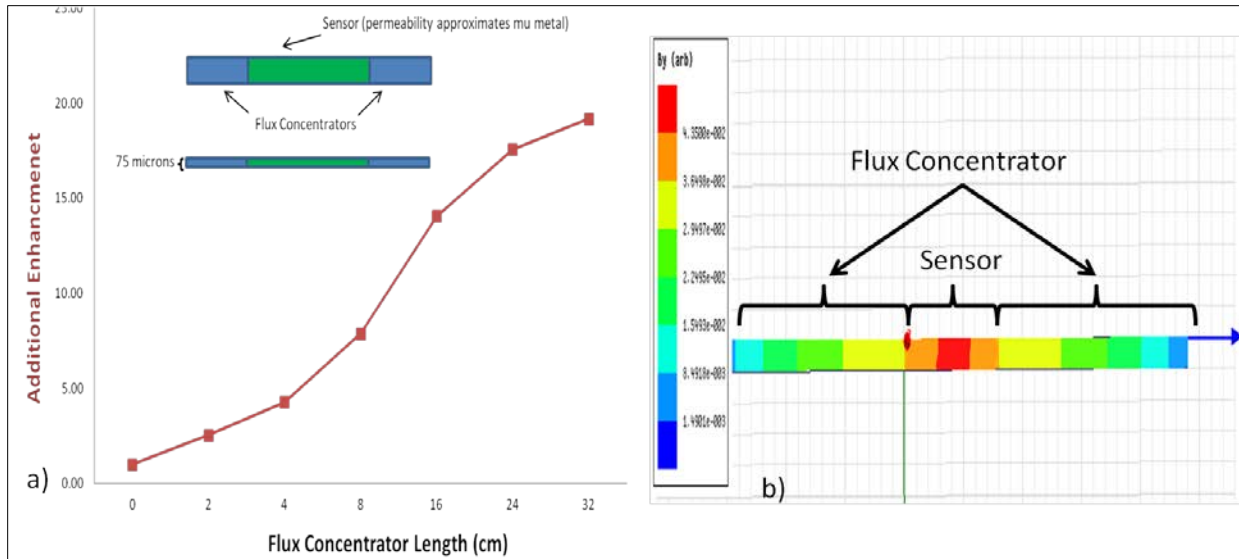


Figure 247. (a) Additional enhancement achieved by including flux concentrators symmetrically place around the sensor as a function of the length of each flux concentrators. (b) The magnitude of the field as a function the longitudinal position along the length of the sensor.

The nonlinear enhancement along the length of the sensor is a result of magnetic flux lines being both drawn into and escaping the sensor/flux concentration system. As a result, the flux concentration has a maximum in the middle of the system where the sensor is located, as shown in Figure 247 (b). Increasing the length of the additional flux concentrators broadens and increase the magnitude of the maximum. When the additional flux concentrators are 100 cm long, the enhancement is within 90% of its maximum value along the 8 cm length of the sensor. Initially, we did not consider overlap between the sensor and the additional flux concentrators that were on each side of the ME sensor, but later we modeled the optimal overlap and vertical gap enhancement for the two additional flux concentrators. We could either lay the Metglas or the PZT side of the sensor on these flux concentrators, with respective vertical gaps of either ~ 0 mm or ~ 0.300 mm. As seen in Figure 248 (a), the enhancement from facing the Metglas side on the concentrators was nearly double that of the PZT. Therefore, the Metglas was placed downward and with as little overlap as possible while still supporting the sensor.

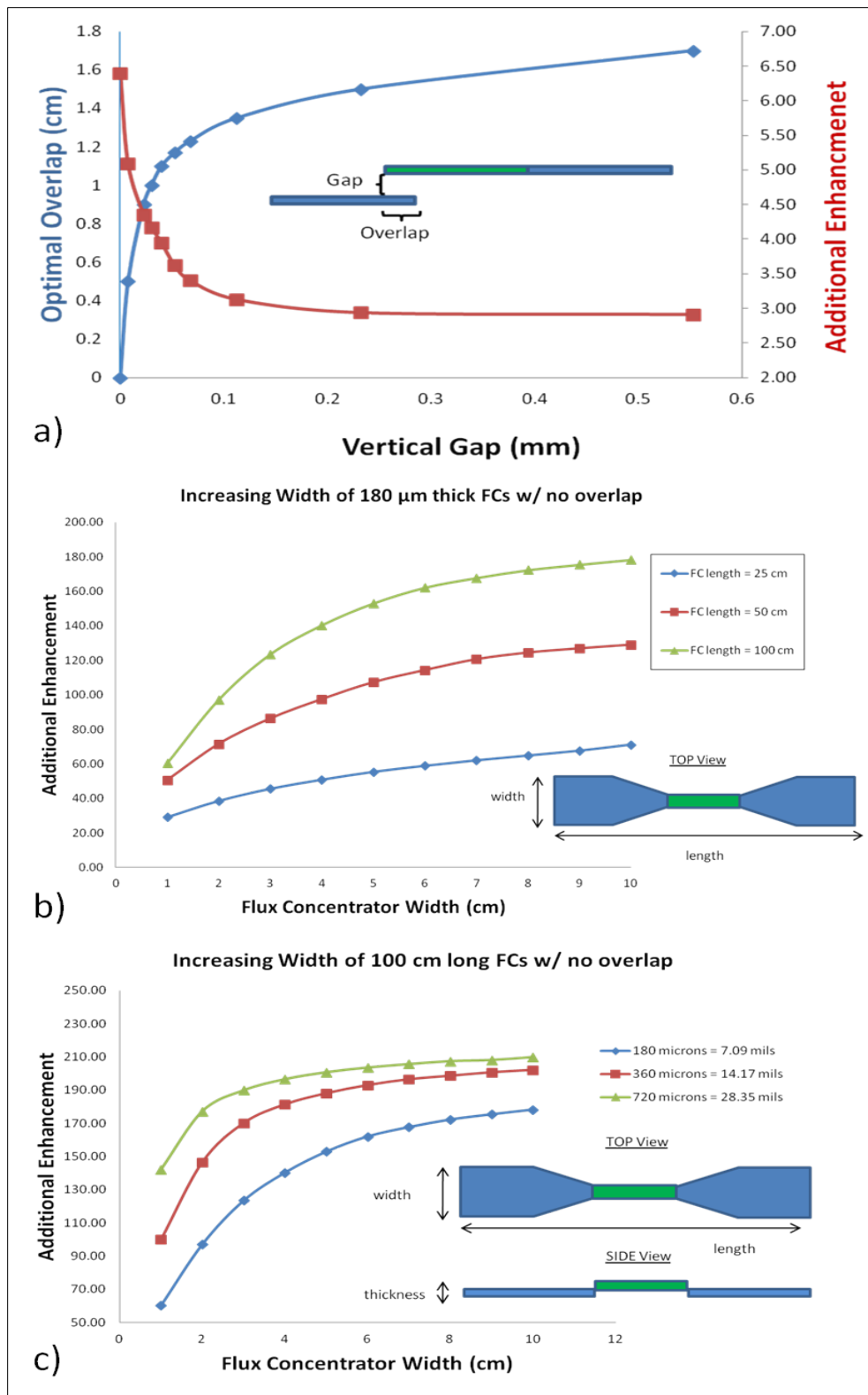


Figure 248. (a) Additional enhancement as a function of overlap and vertical gap between the sensor and flux concentrators of similar dimensions. Additional enhancement from tapered flux concentrators as a function of (b) width/length and (c) width/thickness.

Tapered flux concentrators were modeled to further increase the enhancement. Figure 248 (b) shows the calculated enhancement as a function of the maximum width of each concentrator was varied at several lengths. The optimal enhancement occurs at a flux concentrator lengths greater than 100 cm and at widths greater than 10 cm. The added benefit of the longer length, as mentioned previously, was a more uniform flux throughout the sensor. The enhancement as a function of the width at several thicknesses and with a length of 100 cm for each concentrator is plotted in Figure 248 (c). At a width of 10 cm, there was no significant benefit from increasing the thickness of the concentrators above 360 μ m.

Using the modeling information in designing the flux concentration system, we tested a variety of configurations and magnetically soft materials at low fields. The optimal configuration is a combination of inner and outer flux concentrators shown in Figure 249 (a). The sensor itself bridged a set of rectangular ‘inner flux concentrators’ of dimensions 15.2 cm x 1 cm x 0.0625 cm. Both the sensor and part of the inner flux concentrators were placed within a solenoid for magnetic DC biasing of the sensor. The inner flux concentrators in turn overlapped a set of larger, tapered ‘outer flux concentrators’ with lengths of ~1.5 m, maximum widths of 10 cm, and thicknesses of 0.0350 cm. Conetic AA mu metal was found to work best for both the inner and outer flux concentrators. The type of enhancement we were able to attain with this system is shown in Figure 249 (b). The sensor itself has a normalized power spectral density (PSD) enhancement of 1 at the optimal DC bias. The enhancement in the power spectral density increases to about 115 at the optimal bias in the flux concentration system, indicating a flux enhancement of more than an order of magnitude. More details on the experimental results are presented in the field test section of this report.

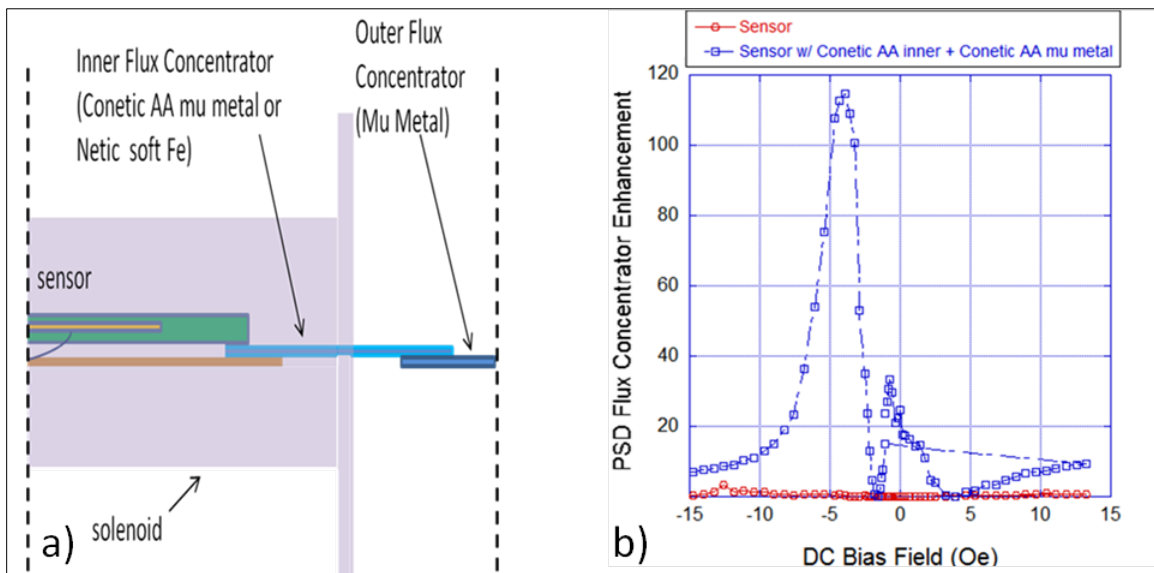


Figure 249. (a) Optimal sensor setup with solenoid for magnetic DC bias and flux concentrators for enhancement of the measurement field. (b) The PSD enhancement with DC bias using Conetic AA mu metal as both the inner and outer flux concentrators.

H.3.2. Modulating the field with Rotations

One goal of our program was to improve performance by increase the performance of ME sensor by increasing the operating frequency by modulating the magnetic field. Our first method for modulating the magnetic field was to use flux concentrators placed on a disc that was driven to rotate by an air turbine. A picture of the device is shown in Figure 250. As seen in Figure 251 the method was successful in increasing the operating frequency. Modulation frequencies of 100 Hz were achieved using flux concentrators on a rotating disc, but unfortunately acoustic vibrations increased the background noise. Another method of field modulation is discussed in section 5 of this summary.

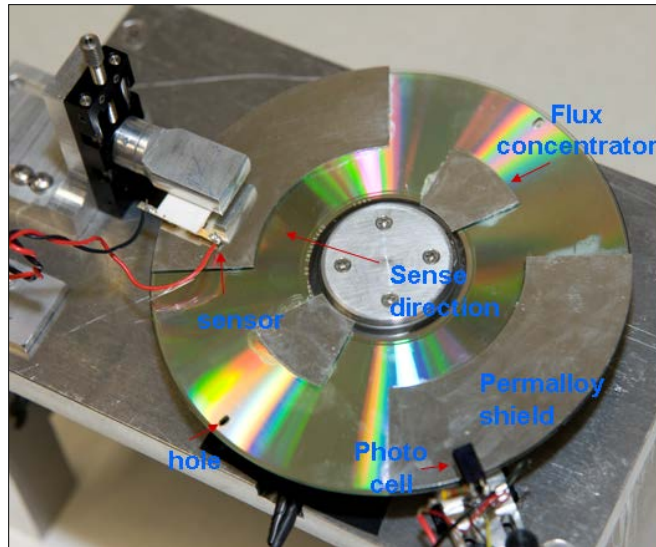


Figure 250. Rotating flux concentrator system

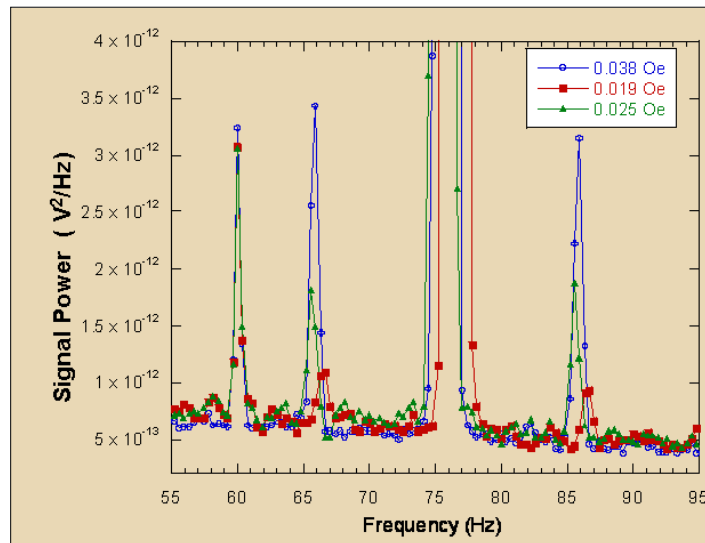


Figure 251. Power spectrum showing the 10 Hz sidebands from a modulating field created by a rotating disc containing flux concentrators.

H.3.3. Shifting the resonant frequency of magnetoelectric sensors

Consider the situation depicted in Figure 252 (a). We are using the bending mode in our experiments on the asymmetric ME sensor with the suspended weight. As the cantilever sensor bends, because of its inertia, the suspended weight does not move appreciably. Nevertheless, the suspended weight provides an additional restoring torque. This additional restoring torque τ_{ar} is given by

$$\tau_{ar} \cong mgd\left(1 + \frac{l_s}{l}\right) \quad (267)$$

where mg is the weight, d is the deflection of the free end of the sensor from the vertical direction, l_s is the length of the sensor, and l is the length of the wire. Based on Equation 267, one sees that there are two ways to change this additional restoring torque. One can vary either the tensile force through the weight mg or the length of the wire l transferring this force. We have investigated both methods and found that either one can be used to increase the resonant frequency of asymmetric ME sensors.

In the experiments, the ME sensors were clamped at one end and oriented with their longitudinal axis in a vertical orientation. An aluminum clip was used to attach a 34 gauge copper wire and a suspended weight from the free end of the cantilever. The length of the wire was varied from 4 to 20 cm long. The largest weight employed was 4 N. A set of Helmholtz coils, powered by an Agilent 33220A signal generator, applied a sinusoidal, time varying field along the longitudinal axis of the sensor. The ME sensors used for these experiments were self-biased, asymmetric, cantilever ME sensors that were 6 cm x 1 cm x 0.5 cm laminates consisting of three layers of 25- μm Metglas/200- μm Ni/300- μm PZT, all mechanically coupled with epoxy. Electrical leads were silver-epoxied to the PZT, which was poled transverse to the length of the laminate in an L-T configuration. The Ni provided the necessary field to bias each ME sensor. Recent investigations of asymmetric sensors in which the ferromagnetic layer is composed of two phases with different magnetization, the so-called functionally graded composites, show ME effects without an external magnetic bias field. Such ME sensors containing functionally graded ferromagnetic layers are denoted as self-biased sensors.

Figure 252 (b) shows an increase in f_r as one increases the in-plane tensile forces applied to the free end of the cantilever by adding weights to an attached wire of length 10.2 cm. The shift in resonance frequency is consistent with previous studies on cantilevers with axial loads. The mechanical quality factor Q did not appreciably change for the range of forces in this study. Therefore, one observes, as expected for a larger restoring torque, that as the tensile force is increased above 2 N the ME response is reduced, i.e., the amplitude of the peaks decreases. An interesting, unexpected result is that for small forces near 0.5 N, the amplitude of the resonance peak increases with increasing tensile force. This result was observed for two similar asymmetric ME sensors. The increase in amplitude is likely due to the Villari effect induced by the added tensile force on the magnetic properties of the Metglas and/or Ni. The change in f_r and the amplitude of the signal at resonance as a function of the in-plane tensile force from the suspended weight is shown in Figure 253. As seen in Figure 254 increasing the resonant frequency does not decrease the sensitivity of the sensor.

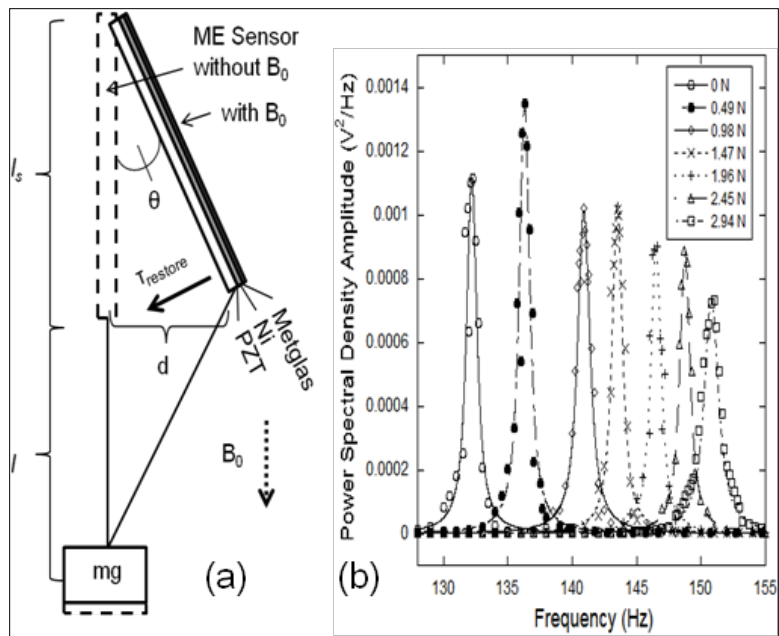


Figure 252. (a) Diagram of the setup in which θ is the small angle away from the vertical direction. (b) Resonance peaks of sensor in an oscillating field of 0.0162 Oe with different in-plane tensile forces.

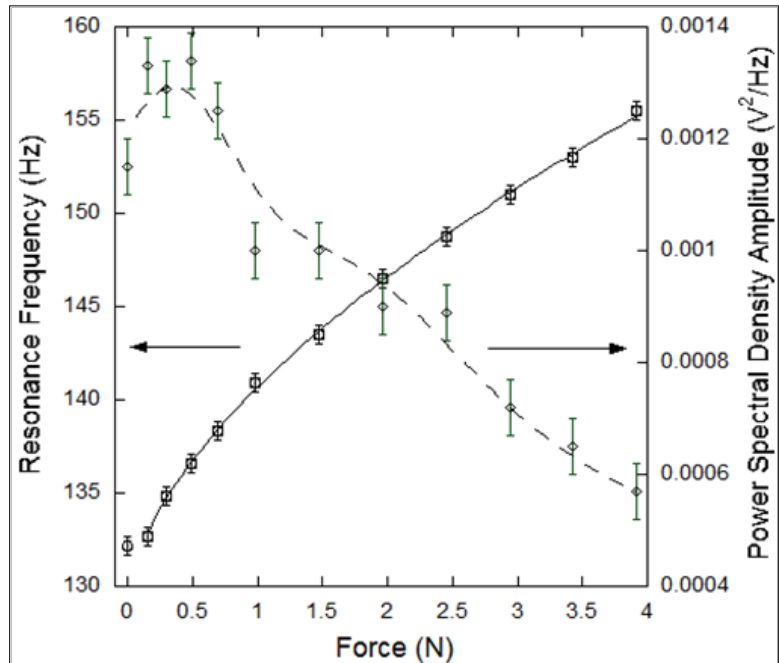


Figure 253. The change in resonance frequency and peak amplitude in the power spectrum at this frequency measured in an AC field of 0.0162 Oe as a function of the in-plane tensile force.

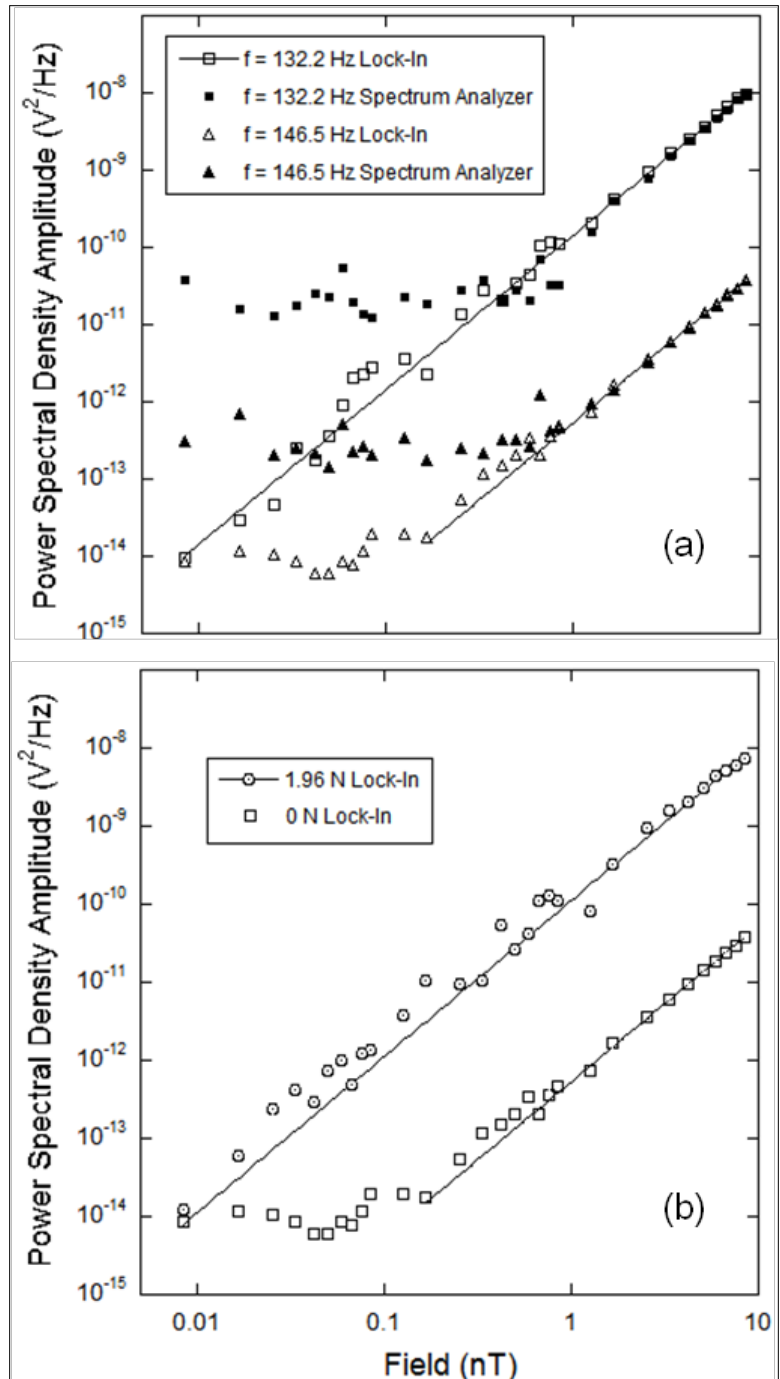


Figure 254. (a) Signal vs. applied field at and above the unshifted resonant frequency of 132.2 Hz. (b) Signal vs. applied field at the shifted resonant frequency $f_r = 146.5 \text{ Hz}$ and at the unshifted $f_r = 132.2 \text{ Hz}$ in the presence of a 1.96 N tensile force.

The unfilled (filled) symbols denote the points from the spectrum analyzer with (without) using the lock-in amplifier.

H.3.4. Increasing the sensitivity of magnetoelectric sensors by field modulation

We have found that by using the non-linearity of magnetostrictive materials we can increase the operating frequency of magnetic sensors and increase their sensitivity. For itinerant systems, the magnetostrictive response is given by

$$\frac{\Delta V}{V} = \frac{V\kappa}{2D\mu_B^2} \frac{\partial \ln D}{\partial \ln V} M^2 \quad (268)$$

where V , κ , D , and M are the volume, the isothermal compressibility, the electronic density of states at the Fermi energy, and the magnetization density, respectively. We assume that M is proportional to the field H and take

$$H(t) = H_s \sin \omega_s t + H_m \sin \omega_m t, \quad H_s \ll H_m \quad (269)$$

where H_s , H_m , ω_s , and ω_m are the magnetic signal amplitude to be measured, the magnetic modulation amplitude, signal frequency, and modulation frequency, respectively. Substituting Equation (269) into Equation (268), one finds that there is a term in the magnetostrictive response of the form $H_s H_m \sin \omega_s t \sin \omega_m t$. The transfer of this strain to the piezoelectric layer(s) creates sidebands in the ME output at $\omega_m \pm \omega_s$ with amplitudes proportional to $H_s H_m$.

We applied AC magnetic modulation fields in the measurement direction of both symmetric and asymmetric ME sensors. The symmetric sensor consisted of a layer of longitudinally poled lead zirconate titanate (PZT) core sandwiched between 6 layers of Metglas (Vitrovac 7600F, Vitrovac Inc. Hanau, German) of length 8 cm and width 1 cm. The PZT core is a planar bundle of 5 PZT fibers, with dimensions of 40 x 2 x 0.2mm. The asymmetric sensor, which had dimension 6 cm x 1 cm x 0.5 cm and consisted of three layers of 25-μm Metglas/200-μm nickel/300-μm PZT, all mechanically coupled with epoxy and fixed at one end in a cantilever configuration. The Ni provided a field to self-bias the ME sensor. Helmholtz coils, powered by an Agilent 33220A signal generator was used to apply the signal field H_s along the longitudinal axis of the sensor. Solenoid coils applied both the DC and the modulation field H_m . The signal was detected using a charge coupled amplifier, PCB Piezotronics Model 441A101, and then filtered in a SR640 low-pass filter with no gain before being sent either to a spectrum analyzer that uses a LabVIEW VI program or to a SR830 DSP Lock-In Amplifier. No magnetic, electric, and thermal shielding was employed.

The output power spectrum of the symmetric sensor at two different modulation frequencies f_m is shown in Figure 255. In both cases, H_m was 0.72 Oe and H_s was 0.0162 Oe at 1.019 Hz. The three main peaks in each spectrum correspond to f_m and the sidebands $f_m +/- f_s$. The 28.9 kHz f_m was chosen so that the $f_m - f_s$ sideband matched the longitudinal resonant frequency of the sensor. In this case, all three peaks were enhanced by approximately two orders of magnitude by the increased sensitivity near the resonant frequency.

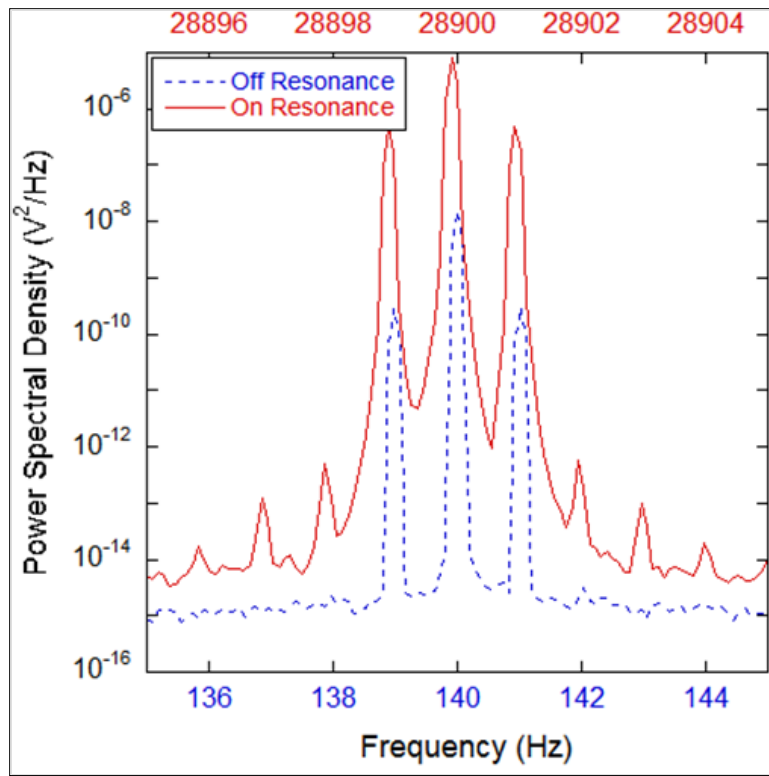


Figure 255. Power spectra from the symmetric sensor detecting a 1.019 Hz, 0.0162 Oe field while modulating the sensor with a 0.72 Oe field either off resonance at 140 Hz (dashed curve) or on resonance at 28.9 kHz (solid curve, top x-scale).

In Figure 256, both the direct output with an optimal DC bias of 6.9 Oe and the demodulated output from a 0.47 Oe H_m at 28.9 kHz are plotted as a function of H_s at 1.019 Hz. When H_m was applied, no DC bias was employed. The modulation technique increases the field detectivity of the symmetric sensor by a factor of 10. We were able to detect $4 \text{ pT}/\sqrt{\text{Hz}}$ at 1 Hz in a magnetically unshielded environment.

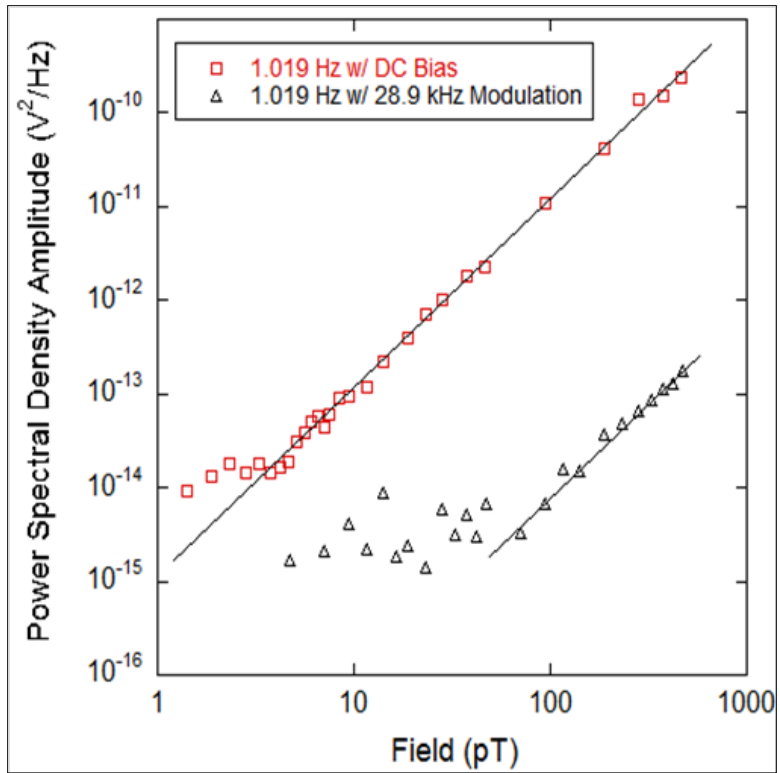


Figure 256. Comparison of the direct signal (squares) and the demodulated sideband signal (triangles) from the symmetric ME sensor at resonance as a function of signal field.

H.3.5. Field Test Results

We have used a two-tier approach with inner and outer flux concentrators to introduce flux concentration into the system, as seen in Figure 257 (d). The sensor itself bridges an ‘inner flux concentrator’ of dimensions 15.2 cm x 1 cm x 0.0625 cm. The ‘inner flux concentrator’ overlapped a larger tapered ‘outer flux concentrator’ with a length ~1.5 m, width of 10 cm, and thickness of 0.0350 cm.

Inner: Conetic AA (annealed mu metal) or Netic (soft Fe) Outer: Non-Annealed Mu Metal

In the initial study, two different inner flux concentrators were used, Conetic AA mu metal and Netic (i.e. soft Fe). The Netic was included over concerns of saturation from the DC biasing field. Since the outer flux concentrators would be farther from the biasing solenoid and thus less likely to saturate, Conetic AA mu metal was used for the outer flux concentrator. These materials were cut using a wire EDM to eliminate reduced permeability associated with shearing stress. Since the larger flux concentrators were being fabricated during initial testing, mu metal obtained from our local stockroom was substituted for the Conetic AA mu metal. The mu metal outer flux concentrator had a length of 1.5 m, a width of 75%, and a thickness 50% of the modeled outer flux concentrator. The fact that it was not optimally annealed had the effect of reducing its permeability by a factor of 2. Nevertheless, as seen in Figure 257 (a) and 257 (b), we were able to enhance the signal by a factor of 5 with this combination of the Conetic AA mu and the stockroom mu metal. The optimum DC bias must be established as one changes the experimental conditions. The factors that must be considered in optimizing the DC bias are the concentration of the Earth’s field (which itself acts as a DC bias), the concentration of the

solenoid field, and the varying permeability of the concentrators with field.

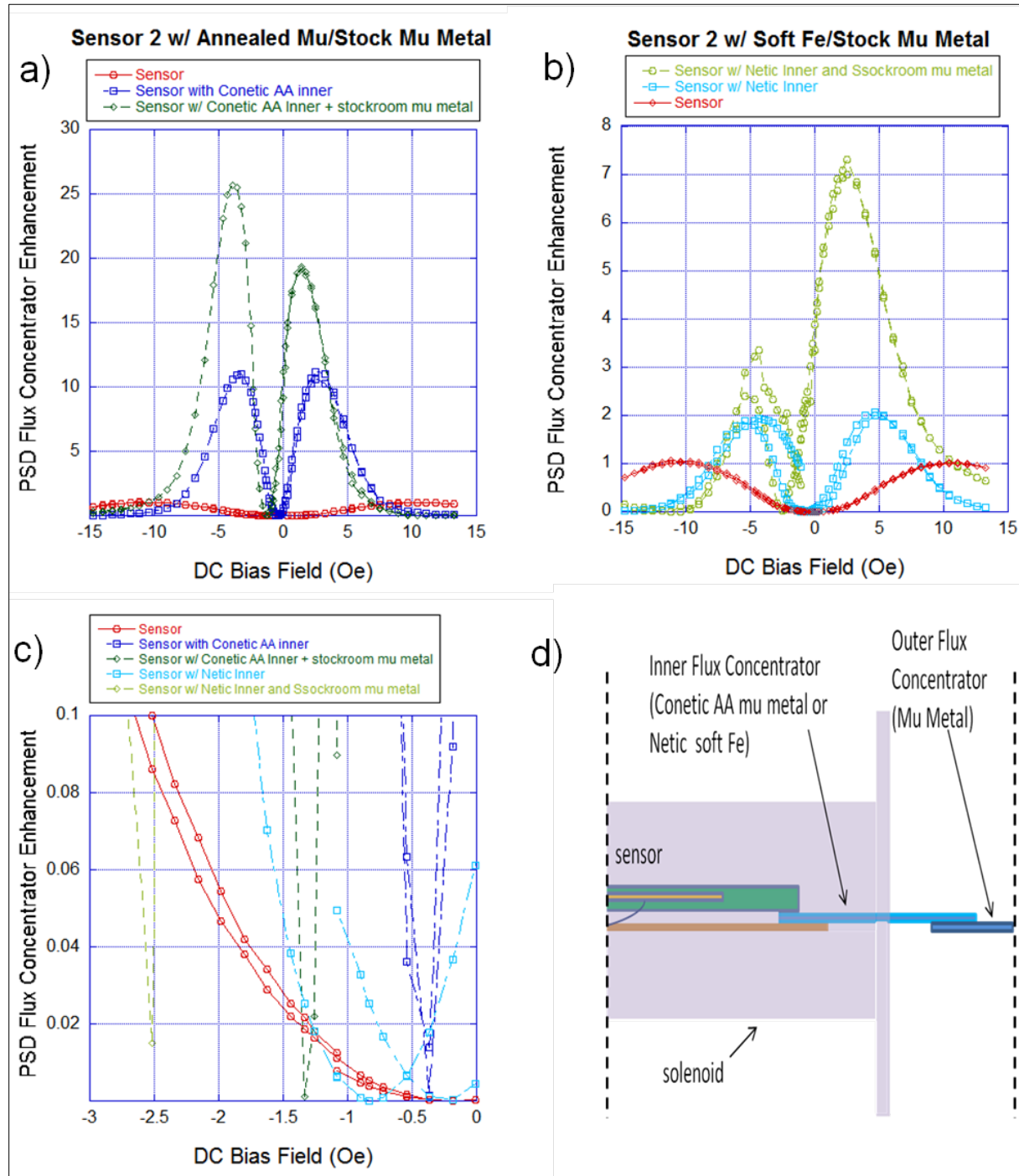


Figure 257. The PSD enhancement with DC bias from stockroom mu metal flux concentrators

These include a) inner Conetic AA mu metal and b) Netic (soft Fe) metal. Enhancements of up to 25 and 7 are possible with the respective Conetic AA mu metal and soft Fe. c) Enlarge view of Figs a) and b). The offset in the sensor at -0.186 Oe without flux concentrators roughly

corresponds to the field needed to balance the Earth's field in the sense direction. The offset field increases with the different flux concentrators. d) schematic of the experimental situation with two sets of flux concentrators.

Inner: Conetic B (annealed 50 Ni/50 Fe permalloy) Outer: None

Conetic AA, a brand of annealed mu metal, has an extremely high relative permeability of the thousands that has the potential to provide a very high flux concentration. We have been using this for the inner flux concentrator. However, there is concern that the 10 Oe biasing field from the coil has the potential to saturate the mu metal, which has a saturation induction of about 0.8 Tesla. If one is close to saturation, the enhancement would be lower than modeled. To address these concerns, we tried replacing the mu metal with annealed Conetic B, a brand of 50/50 Ni/Fe permalloy. While its permeability is somewhat lower than the mu metal, the increased Fe percentage boosts its saturation induction to ~1.5 Tesla, nearly double that of the mu metal. The power spectrum density (PSD) sensor enhancement with Conetic B and Conetic AA as the inner flux concentrator can be seen, respectively, in Figure 258 (a) and 258 (b) for an external signal of 260 nT field at 10Hz. Using Conetic B resulted in an enhancement under an order of magnitude as compared to the Conetic AA that gave an enhancement greater than an order of magnitude. This would suggest that no improvement is gained from replacing the mu metal in the inner flux concentrator with 50/50 Ni/Fe permalloy. Interestingly, the PSD enhancement vs. bias field for the Conetic B was shifted towards more negative bias fields as contrasted with the Conetic AA inner flux concentrator.

Inner: Conetic AA or Conetic B Outer: Conetic AA

As mentioned in the previous report, we replaced the stockroom mu metal we were using as the outer flux concentrator with Conetic AA perfection-annealed mu metal. The Conetic had a higher permeability than the mu metal, a similar length (~1.5 m), a 33% larger width, and a 100% larger thickness. To reduce stress effects, the Conetic AA was precision cut using wire EDM to eliminate reduced permeability associated with shearing stress. The PSD enhancement for an inner flux concentrator of either Conetic B permalloy or similar Conetic AA mu metal are shown in Figure 258 (a) and Figure 258 (b). The enhancement to Conetic B was approximately a factor of 5 while that to Conetic AA was 5.5. When compared to the stockroom mu metal enhancement of 2.5 for Conetic AA in Figure 254 (b), the new Conetic AA mu metal doubles the enhancement while at the same time making the bias curve more symmetric. This result indicates that the Conetic AA outer flux concentrator not only has a higher intrinsic permeability than the stockroom mu metal, but it is also less hysteretic. There is a shift in the bias curve towards a more negative field value (i.e. greater enhancement of the earth's field) that also supports the increased enhancement of the Conetic AA outer flux concentrator. The bias curve for Conetic B inner/Conetic AA outer flux concentrator is shifted towards more positive values as compared to simply the Conetic B alone. Thus, the optimal configuration for our setup consisted of both the inner and outer sensors containing ConeticAA.

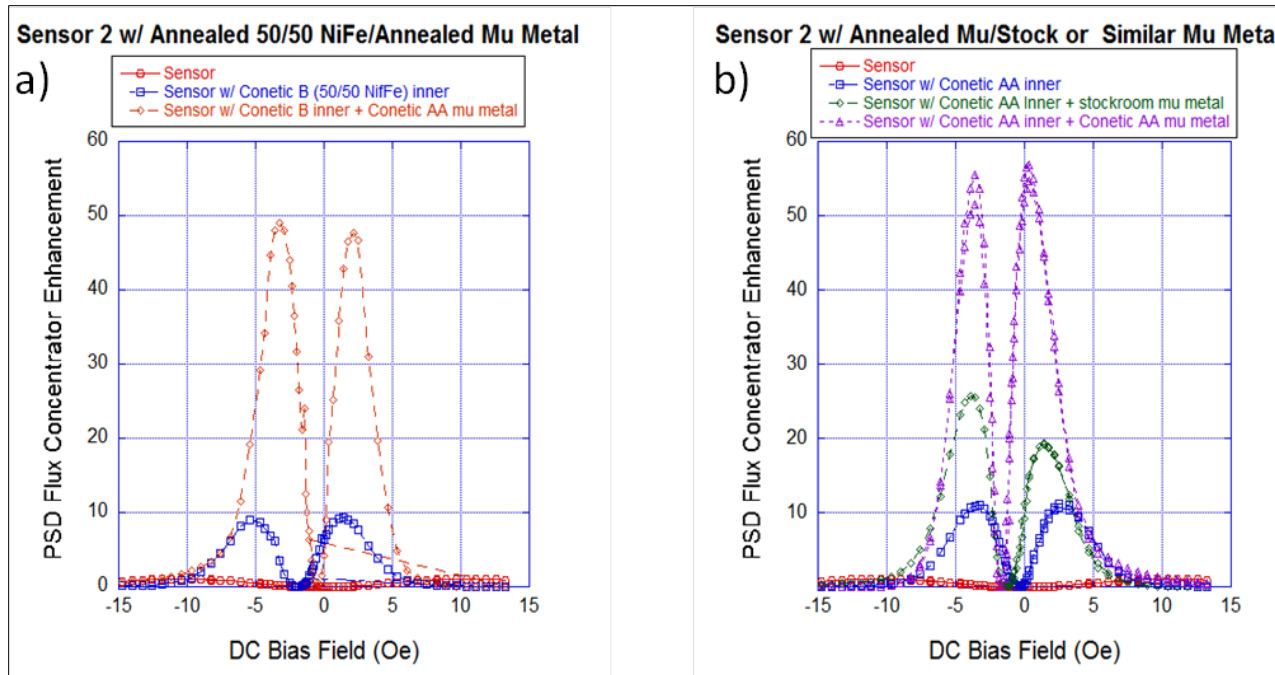


Figure 258. The PSD enhancement with DC bias and mu metal outer flux concentrators

These are with inner flux concentrators of a) inner Conetic B permalloy or b) Conetic AA mu metal. Enhancements in the PSD of up to 50 or 55 are possible with the respective Conetic B or Conetic AA metal.

Measurement Field Optimization for Flux Concentration:

Even though we have reached significant enhancement with the flux concentrators, our modeling suggested we should have been able to achieve even larger values. Scans of B vs H made using our alternating gradient magnetometer indicate that the permeability of the flux concentrators was lower than expected (e.g. $\mu_r < 10,000$). Another possible problem was our initial signal field geometry (See Figure 259). We found that when our source was 3 ft away from the nearest sensor, the signal field was non-uniform over the length of the system. To make the field more uniform across the setup, the solenoid source was moved progressively farther away from the setup until, at ~24 ft seen in Figure 259, the field strength only varied by 10 % over a length equal to the length of the flux concentrators. To produce this more constant field (10-20 nT) at this distance without requiring huge coils, strips of mu metal were placed inside the source solenoid to enhance the flux of the signal field. When measured by a coil magnetometer, the measurement field was sinusoidal, indicating little hysteresis in the mu metal strips. In this unique case, flux concentration was used to both generate and detect a field. As shown in Figure 259 (b), the PSD enhancement with Conetic AA as the inner and outer flux concentrators was doubled from 55 to 110. This increase in flux concentration by more than an order of magnitude in sensors on the scale of centimeters is quite significant and opens the door for enhancement of a wide class of magnetic sensors.

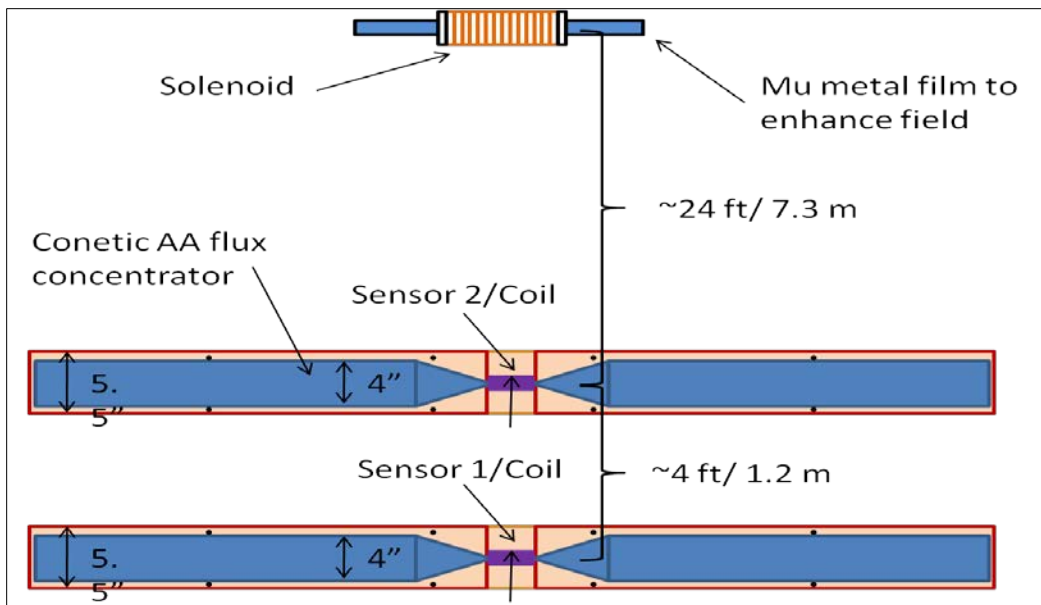


Figure 259. Setup to achieve a signal field within 10% across each sensor/flux concentrator setup in the direction of the long axis of the sensor.

The source was moved 8x farther than it had initially been (i.e. 3 ft from Sensor 2) to do this. The signal field was boosted with the incorporation of mu metal into the solenoid.

H.3.6. Conclusions and Recommendations

Our investigations have led to several important results. For example, we found that one can tune the resonant frequency of ME sensors to make them operate at a frequency where they have the signal is higher or the noise lower. Our measurements show that field modulation can shift the operating frequency of ME and greatly increase their sensitivity. Flux concentrators also enhance the performance of ME sensors, but it is difficult to take full advantage of the potential increase in the enhancement because of the size of the sensors and the trade off used in choosing the magnetostrictive material. If the size of the sensors could be decreased without paying too large a cost in sensitivity, then flux concentrators could play a larger role in enhancing the performance of ME sensors. Second, our ME sensors and many other ME sensors were designed for use without additional flux concentration. As a result, the high permeability of Metglas made it a good choice even though it has a low magnetostrictive response ($\lambda_s \sim 20-27$) compared to other materials, such as Terfenol-D ($\lambda_s > 1000$). Using flux concentrators decreases the need for using high permeable materials in the sensor. Thus, better performance might be obtained by using a material with a lower permeability and a higher magnetostrictive response. In comparison with current magnetic sensors, ME sensors are much more sensitive than similarly priced sensors. For this reason ME sensors should be serious candidates for many military and commercial applications.

I. Edmund Nowak, University of Delaware

I.3.1. Noise Statistics of Magnetoelectric Laminate Composite Sensors

Earlier work showed that the noise in these sensors had negligible magnetic contribution and the $1/f$ spectrum was principally due to thermal dielectric polarization noise in the piezoelectric material. Figure 260 shows an example of a ME sensor's response for different biasing fields. The response to a 20 nT excitation field is largest at zero field (point A) and smallest near 13 G (point B).

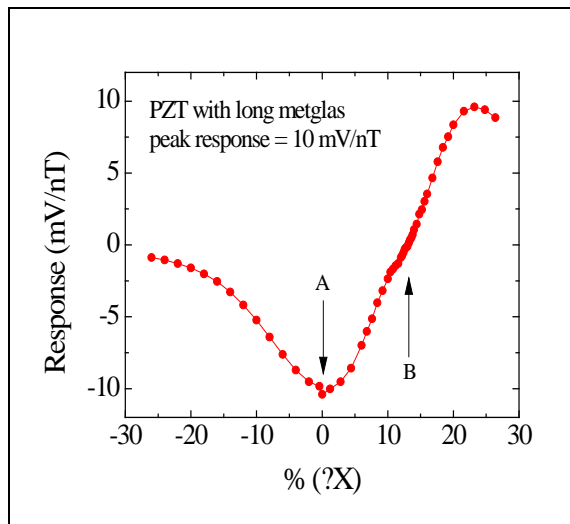


Figure 260. The response of the PZT with long metglas sensor to a 20 Hz, 20 nT excitation field.

The corresponding noise power spectra are shown in Figure 261. If (thermal) magnetization noise in the Metglas layer is more significant than one would expect a larger noise power at maximum response. It can be seen in Figure 261 that the noise spectra are essentially identical, indicating that principal contribution to the noise is not magnetic.

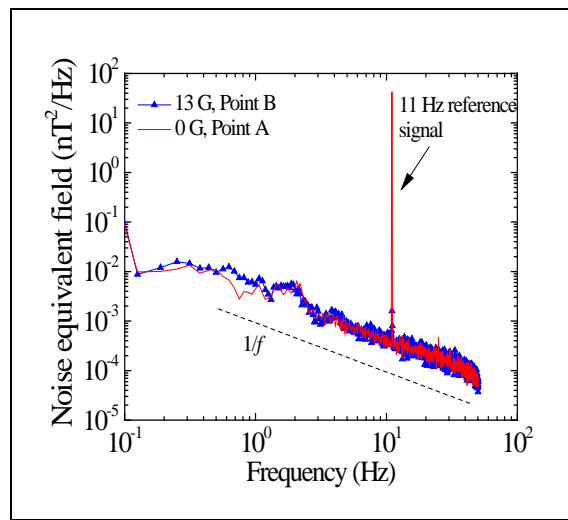


Figure 261. The noise equivalent magnetic field spectra of the PZT with long Metglas sensor at the point of maximum magnetic field response (point A in Figure 260).

The spectrum at point B was also normalized to the maximum field response to illustrate that the output voltage noise is the same at points A and B.

Having established that the magnetostrictive material is not a significant contributor to the low frequency $1/f$ noise in these sensors, we turned our attention to analyzing the statistics of the time-dependent noise power fluctuations in the frequency range where the noise power had a $1/f$ dependence. In this region the noise is principally due to dielectric polarization fluctuation from the piezoelectric material. The statistical properties of the noise are important for two reasons. One reason is that small-signal recovery is often based on assumptions that the noise power fluctuations are Gaussian in nature. Establishing where the noise is Gaussian is required when selecting and/or developing algorithms for discriminating signals from ‘true’ background noise. The second reason is that noise statistics can be used to further guide materials development and improvement.

The statistical tools we applied to the study of noise power fluctuations included: probability distributions, covariance matrix, and ‘second-spectra’ techniques. The latter is sometimes referred to as the noise of the noise. Together, these properties of the noise signal can be used to distinguish between different models that predict identical power spectra. For example, the frequency dependence of the fluctuations in noise power can be used to distinguish between systems involving interacting fluctuates and those involving the superposition of a fixed set of independent two-state systems (TSS).

The non-Gaussian properties of the noise were determined by recording consecutively measured power spectra, subdividing the spectra in to octaves, and then constructing time records of the octave noise power fluctuations. To reduce the amount of numbers to be dealt with and the fractional uncertainty associated with sampling a random signal, each spectrum is summed into 7 octaves, O_i with $i = 1, 2 \dots 7$. This process is repeated 1024 times to generate the time series of the octave powers. The power spectra of these octaves were then computed and are dubbed the ‘second spectra’. Figure 262 shows that octave numbers 2, 3 and 4 correspond to that region of the spectra having a $1/f$ dependence (due to polarization noise in the dielectric).

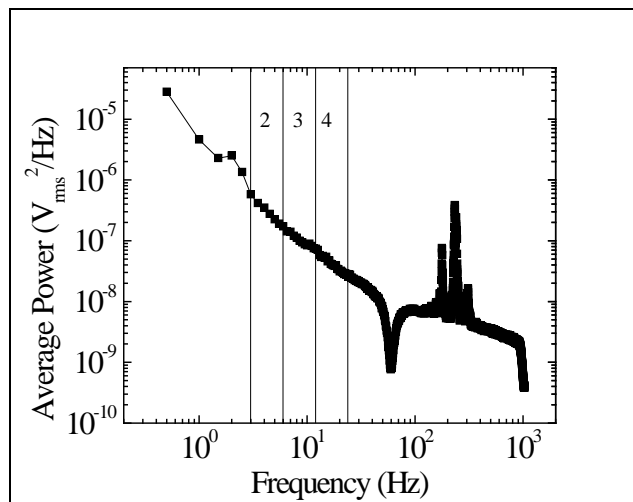


Figure 262. Time average noise power spectrum of an ME long Metglas sensor and the octave frequency bands used for studying statistical properties of the noise.

Octaves 2, 3, and 4 correspond to center frequencies 4.8, 9, and 19 Hz, respectively.

Figure 263 shows the octave time series for these three octaves. Notice that there are spikes in the octave noise power at certain times and that these spikes are often correlated across all three octaves. A test chamber incorporating acoustic, magnetic, and vibration shielding was used to mitigate extrinsic laboratory and environmental background noise during these measurements.

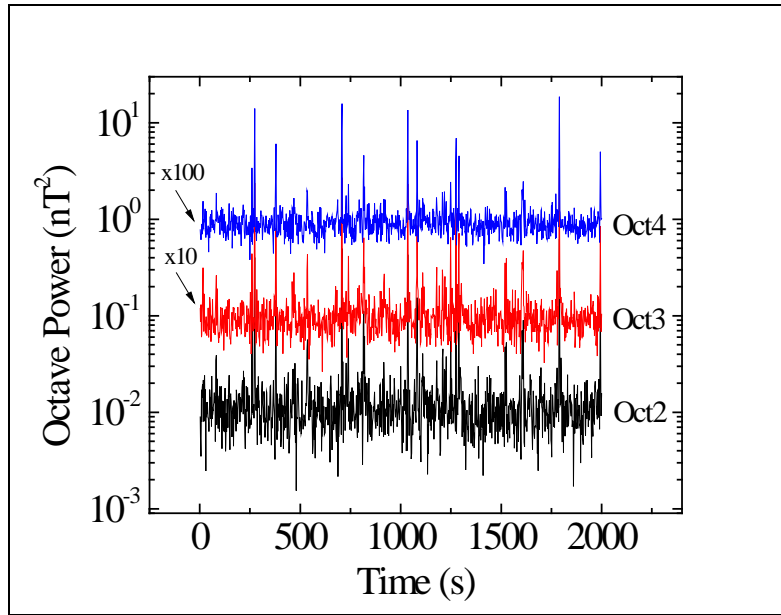


Figure 263. Representative octave time series for the ME long Metglas sensor. Octave 3 and 4 are offset for clarity.

Each octave is the sum of N_i frequency bins and each bin is the sum of the squares of a real and imaginary random variable corresponding to the Fourier components of the noise signal. The For random independent variables one expects that the octave noise power fluctuations to follow a Chi-square distribution with $2N$ degrees of freedom and having a probability density function given by:

$$f(x, k) = \frac{1}{2^{k/2} \Gamma(k/2)} x^{k/2-1} \exp^{-x/2} \quad (268)$$

The resulting probability distribution is

$$P\left(\frac{2ON}{\bar{O}}\right) = \left(\frac{N}{\bar{O}}\right)^N \frac{\bar{O}^{N-1}}{\Gamma(N)} \exp^{-ON/\bar{O}} \quad (269)$$

Where \bar{O} is the time average octave power and Γ is the gamma function.

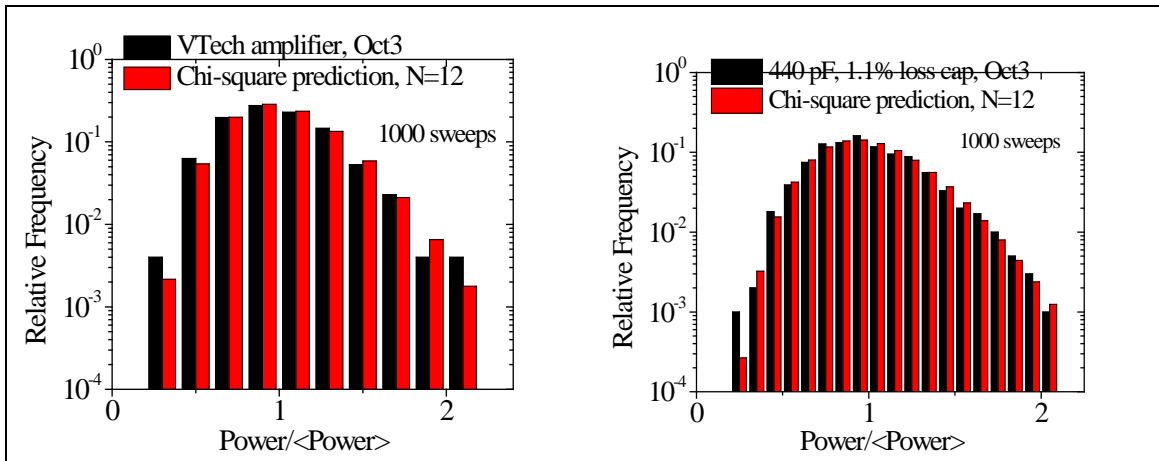


Figure 264. Measured and predicted octave noise power distributions.

The prediction is based on the Chi-square distribution. Both panels show agreement with the prediction. Left panel is the voltage noise of the charge amplifier with open circuit inputs, and the right panel is the noise when a 440 pF low loss capacitor is connected across the inputs.

Figure 264 illustrates that Gaussian noise (distributions in quantitative agreement with the Chi-square distribution) is observed from the output of the charge amplifier. Similarly, Gaussian noise is found when a 440 pF is connected across the input of the charge amplifier to simulate the capacitance of the PZT transducer. However, the measured distributions differ markedly from the Chi-square distribution when a ME sensor or a PZT fiber is connected to the charge amplifier. Figure 265 shows an example of each case. Notice that the frequency of smaller and, in particular, larger noise power events is significantly higher than the Chi-square prediction. This is a signature of non-Gaussian noise. Non-Gaussian noise was also found when the ME sensor was saturated using a large DC biasing field. The fact that non-Gaussian noise is observed in a PZT fiber device corroborates that the magnetostrictive Metglas material does not play a significant role in limiting the performance of current generation ME sensors, rather it is the piezoelectric material.

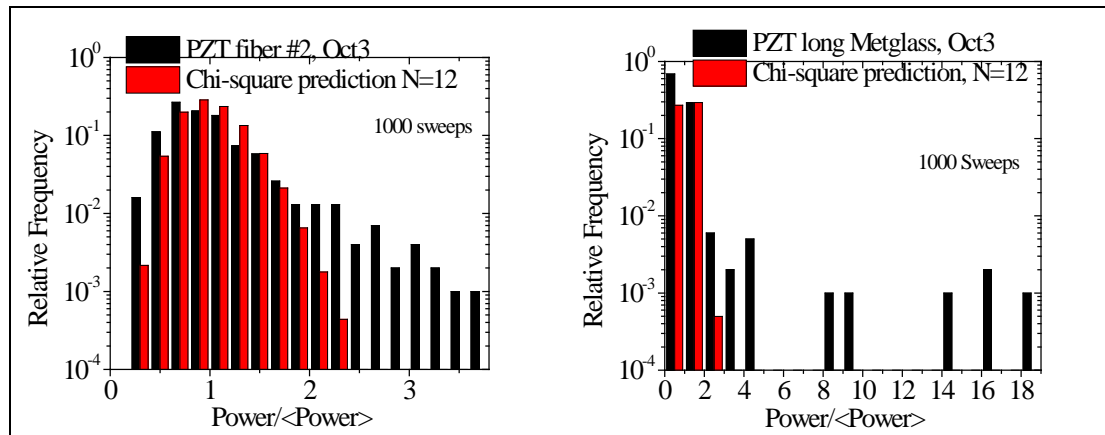


Figure 265. Measured and predicted octave noise power distributions for a PZT device and the long Metglas ME sensor device. Significant deviations from the Chi-square distribution are evident.

These higher moments of the octave noise power fluctuations can be quantified using the covariance matrix. Essentially, the covariance matrix quantifies the extent to which the fluctuations are non-Gaussian and its diagonal and off-diagonal elements are defined as:

$$CM_{ii} = \frac{\langle \delta O_i^2 \rangle}{\sum_k \langle P_k \rangle^2} \quad \text{and} \quad CM_{ij} = \frac{\langle \delta O_i \delta O_j \rangle}{[\langle \delta O_i^2 \rangle \langle \delta O_j^2 \rangle]^{1/2}}, \quad (270)$$

Where P_k is the noise power in frequency bin k of octave i and the brackets denote time averages. In this form, Gaussian noise will have diagonal elements equal to 1.0. The off-diagonal elements are of limited value as the other octaves (e.g., 5, 6, and 7) tend to be corrupted with extrinsic noise such as harmonics of 60 Hz.

Table 54 below show the diagonal elements (for octave 2, 3 and 4) of the covariance matrix for a number of devices. These elements were determined from 1000 individual spectral measurements and have an uncertainty of ± 0.03 . As expected, the Virginia Tech charge amplifier with and without the 440 pF low-loss capacitor shows diagonal elements very close to 1.0, that is, Gaussian noise. All the other devices, some with and others without magnetostrictive material, show elements in excess of 1.0 and in some cases significantly greater than 1. We conclude that the dielectric polarization fluctuations in the piezoelectric material are non-Gaussian.

Table 54. The diagonal elements of the covariance matrix are shown for octaves 2, 3, and 4.

			near saturation, $dV/dB \approx 0$		
			Oct 2	Oct 3	Oct 4
Vtech amp	Oct 2	0.993	2.363	2.027	2.573
	Oct 3	0.956	1.217	1.38	1.774
440 pF	Oct 4	0.949	2.377	1.907	1.874
		1.023	2.652	1.944	1.92
PZT fiber #2	Oct 2	2.948	1.496	1.451	1.636
	Oct 3	3.93	2.034	2.37	2.071
PZT ME sensor	Oct 4	3.4			
		1.59	1.257	1.083	
Long Metglas	Oct 2	1.303	1.48	1.22	1.58
	Oct 3	1.111	2.38	2.68	2.41
Metglas	Oct 4	1.05	14.97	21.12	20.34
		13.43	27.82	29.64	25.05

A value of 1.0 indicates Gaussian noise. For some devices, there are multiple row entries highlighting a time-dependence of the values. The Virginia Tech amplifier,, with and without a 440 pF capacitor connected to its inputs, showed stationary (time-independent) Gaussian noise. The other devices showed non-Gaussian behavior, some with considerable variation over the course of an hour or more. The rightmost column shows data for devices in which the magnetostrictive Metglas layer was magnetically saturated. The uncertainty in all reported values is ± 0.03 .

A row in Table 54 lists the diagonal elements of the covariance matrix. Some devices have more than one row. These additional rows correspond to repeating the measurement either immediately after the preceding one or some time (e.g., hours) later. The amplifier and capacitor show Gaussian noise at all time, ie., the noise is stationary. However, for all the other devices the extent to which the noise is non-Gaussian varies with time in a non-trivial manner. For example consider the Long Metglas device is the rightmost column. The first measurement showed very strong non-Gaussian characteristics and then later it was still non-Gaussian but to a lesser extent.

The time variation of the octave noise power time series can be studies by examining its frequency dependence or equivalently its power spectra. The power spectrum of the octave noise power time series is referred to as the ‘second spectrum’. The second spectrum, $S_2(f_2, f_1)$, is given by

$$S_{2,i}(f_2, f_1) \equiv \frac{F[O_i(t, f_1)]F[O_i(t, f_1)]^*}{\langle O_i(t, f_1) \rangle^2} \quad (271)$$

where F denotes the Fourier transform, f_1 is the center frequency of the octave i , and f_2 is frequency of the second spectrum. For purely Gaussian noise the second spectrum is frequency independent (white) and a magnitude determined by the variance in octave power and the length of the octave time series record.

Figure 266 shows the second spectra for octave 2, 3, and 4 on a PZT ME sensor. Also shown is the expected Gaussian noise background expected for octave 4. The second spectra are well above the Gaussian background and exhibit a frequency-dependent spectrum. This data immediately eliminates models for the dielectric noise that are based on a superposition of independent fluctuators. The fluctuators can be thought of microscopic dipole moments or domains whose polarization direction is changing in response to thermal excitations. More plausible models would involve interacting dipoles that modulate each other’s reconfiguration kinetics or a small number of unusually large fluctuators.

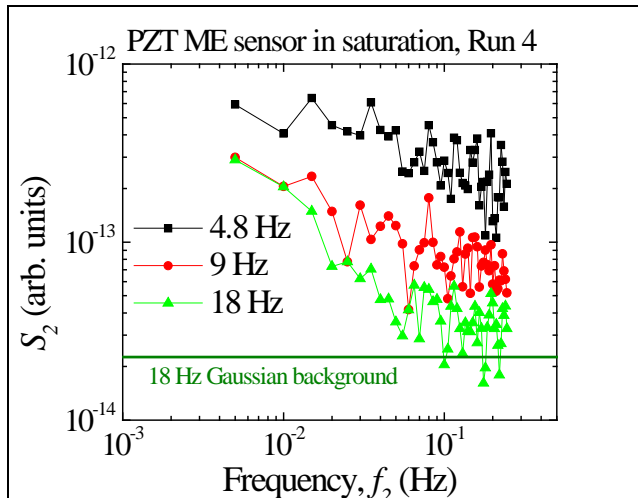


Figure 266. Second spectra for octaves 2, 3, and 4 that were computed from the corresponding octave time series.

The horizontal line represents the predicted Gaussian white noise second spectrum for the fourth octave.

We have also measured the second spectra of the PZT ME sensor over the course of a day. Figure 267 shows several runs for the third octave that were spread out over several hours. It is evident that the second spectra are not stationary, both the magnitude and spectral slope change with time.

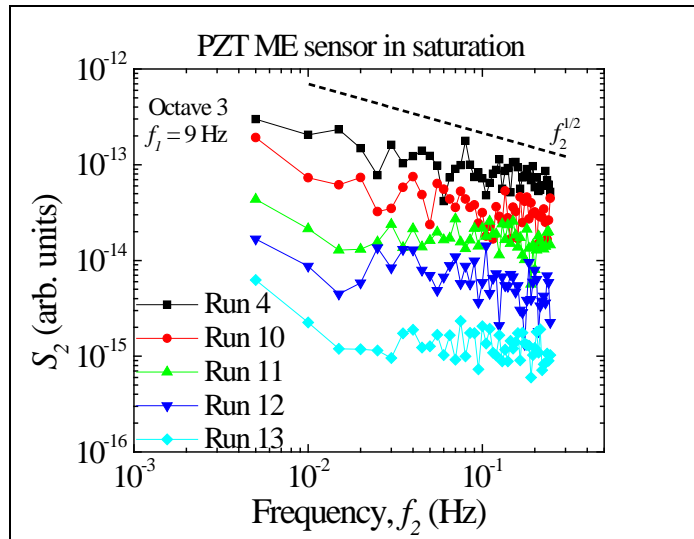


Figure 267. Several second spectra for a given device that were measure successively in time.

Both the magnitude and spectral slope change with time.

Figure 268 shows that the time variations in the second spectra (parameterized by its variance) are much larger than that of the mean noise power of the ‘first spectrum’. In other words, the time variations in the octave noise powers are not directly correlated to the average noise power in the octave.

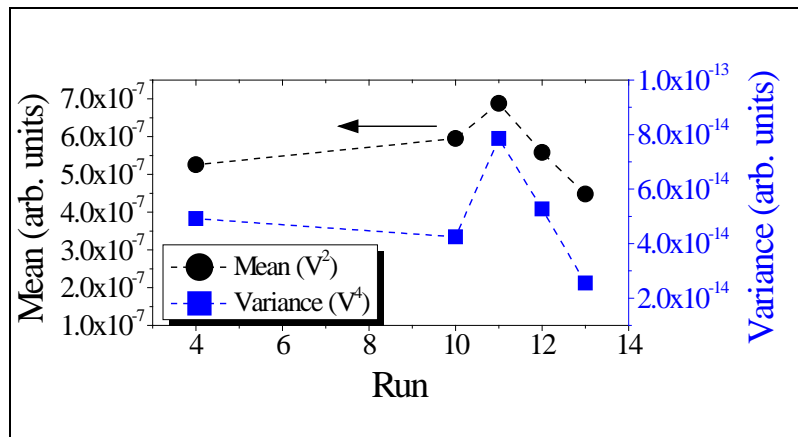


Figure 268. Plots the variation from successive runs of the mean (average) octave noise power and its variance.

The variance shows larger time dependence.

In conclusion, we have shown that non-Gaussian behavior exists in macroscopic ME devices. This is surprising in that by the central limit theorem one expects macroscopic devices to show purely Gaussian noise. Devices consisting of only piezoelectric fiber and ME devices incorporating a laminate composite of piezoelectric and magnetostrictive materials both showed non-Gaussian noise that was time dependent and having a non-trivial second power spectrum $S_2(f_2) \propto 1/f_2^\alpha$, with $\alpha < 1$. We infer that the source of these non-Gaussian fluctuations must be related to complicated interactions between microscopic dipoles or domains that lead to cooperative relaxation effects (such as glassy behavior or aging phenomena), or that this noise comes from a small number of large fluctuating entities possibly indicating the influence of inhomogeneity in the piezoelectric material. Non-Gaussian noise is also observed under magnetic saturation conditions and in a PZT fiber device indicating that the non-Gaussian noise is not of magnetic origin. We conclude that the PZT component of ME devices is the principal source of the $1/f$ noise. The non-Gaussian $1/f$ noise is due to material losses that can be intrinsic to the PZT material, dependent on the interfaces between the electrodes and the PZT material, and possibly arising from the mounting fixture. Extrinsic factors contributing to losses and noise may be operative in composite/laminates, such as the epoxy used to bind the various layers together. Detection of very small signals will require discriminating between a ‘real’ signal and a non-Gaussian noise event.

4. Conclusions

Virginia Tech HUMS program has made important progress with regards to their Phase I goals of lowering noise. Virginia Tech has achieved noise floors of about $1\text{pT}/\sqrt{\text{Hz}}$ at $f=1\text{Hz}$ in passive sensors operated at room temperature that consisted of magnetostrictive Metglas layers bonded to piezoelectric PMN-PT single crystal fiber ones. We note that this was done without incorporating signal modulation, flux concentration, or signal condition/analysis: which offer the opportunity to lower the noise floor by an order of magnitude further. These noise floors were benchmarked by our international team members at the University of Caen. Furthermore, Passive Sensors has developed 3x3 arrays of ME sensors, also achieving noise floors on the order of $1\text{pT}/\sqrt{\text{Hz}}$ at $f=1\text{Hz}$. Working together Virginia Tech and University of Caen have developed gradiometers with high common mode rejection efficiencies, enabling real world applications. Issues that remained unresolved included an internal supply of grain oriented PMN-PT fibers, and incorporation of the signal/flux modulation methodologies. Overall the investigations have clearly identified Metglas/PMN-PT tri-layer laminates as the superior technology.

5. References

- 1 M. Bichurin, V. Petrov, and G. Srinivasan, Phys. Rev. B 68, 054402 (2003).
- 2 S. X. Dong, J. F. Li, and D. Viehland, Appl. Phys. Lett. 85, 5305 (2004).
- 3 Y. J. Wang, S. W. Or, H. L. W. Chan, X. Y. Zhao, and H. S. Luo, J. Appl. Phys. 103, 124511 (2008).
- 4 C. W. Nan, M. I. Bichurin, S. X. Dong, D. Viehland, and G. Srinivasan, J. Appl. Phys. 103, 031101 (2008).
- 5 F. Wang, L. Luo, D. Zhou, X. Zhao, and H. Luo, Appl. Phys. Lett. 90, 212903 (2007).
- 6 D. Zhou, F. Wang, L. Luo, J. Chen, W. Ge, X. Zhao, and H. Luo, Journal of Physics D-Applied Physics 41 (2008).
- 7 S. Dong, J. Zhai, F. Bai, J. F. Li, and D. Viehland, Appl. Phys. Lett. 87, 062502 (2005).
- 8 D. Hasanyan, Y. J. Wang, J. Q. Gao, M. H. Li, J. F. Li, and D. Viehland, Sbumitted (2012).
- 9 Y. J. Wang, D. Gray, D. Berry, J. Q. Gao, M. H. Li, J. F. Li, and Viehland.D., Adv. Mater. 23, 4111 (2011).
- 10 L. Luo, D. Zhou, Y. Tang, Y. Jia, H. Xu, and H. Luo, Appl. Phys. Lett. 90 (2007).
- 11 Z. P. Xing, J. Y. Zhai, J. Q. Gao, J. F. Li, and D. Viehland, IEEE Electron Device Lett. 30, 445 (2009).
- 12 R. A. Thisted, *Elements of Statistical Computing*. (Chapman and Hall., 1988).
- 13 J. Kim, Thesis, Virginia Polytechnic Institute and State University, 1997.
- 14 Y. Shen, J. Gao, L. Shen, D. Gray, J. Li, P. Finkel, and D. Viehland, Sensors and Actuators A: Physical (2011).
- 15 A. Barzilai, T. VanZandt, and T. Kenny, Review of Scientific Instruments 69 (1998).
- 16 S. dong, J-F. Li, D. Viehland, IEEE Trans. on Ultrasonics, Ferroelectrics and Frequency Control, Vol. 50, N°10, October 2003
- 17 S. Dong, J.Y. Zhai, Chinese Science Bulletin, July 2008, Vol. 53, N°14, pp. 2113-2123
- 18 Ondes élastiques dans les solides, Tome 1 (Propagation libre et guidée) & Tome 2 (Génération, interaction acousto-optique, applications), Daniel Royer, Masson, Paris (1999)
- 19 Ondes élastiques dans les solides, Tome 1 (Propagation libre et guidée) & Tome 2 (Génération, interaction acousto-optique, applications), Daniel Royer, Masson, Paris (1999)
- 20 F. Yang, Y. M. Wen, P. Li, M. Zheng, L. Bian, Sensors and actuators A 141 (2008), pp. 129-135

APPENDIX
List of Publications and Presentations
Based in Whole or in Part on Results from the Current Program

Publications:

- [1] J. Gao, J. Das, Z. Xing, J. Li, D. Viehland, Comparison of noise floor and sensitivity for different magnetoelectric laminates, Journal of Applied Physics, 108 (2010).
- [2] J. Gao, D. Gray, Y. Shen, J. Li, D. Viehland, Enhanced dc magnetic field sensitivity by improved flux concentration in magnetoelectric laminates, Applied Physics Letters, 99 (2011).
- [3] J. Gao, L. Shen, Y. Wang, D. Gray, J. Li, D. Viehland, Enhanced sensitivity to direct current magnetic field changes in Metglas/Pb(Mg(1/3)Nb(2/3))O(3)-PbTiO(3) laminates, Journal of Applied Physics, 109 (2011).
- [4] J. Gao, Y. Shen, Y. Wang, P. Finkel, J. Li, D. Viehland, Magnetoelectric Bending-Mode Structure Based on Metglas/Pb(Zr,Ti)O-3 Fiber Laminates, Ieee Transactions on Ultrasonics Ferroelectrics and Frequency Control, 58 (2011) 1545-1549.
- [5] J. Gao, J. Zhai, Y. Shen, L. Shen, D. Gray, J. Li, P. Finkel, D. Viehland, Differential-Mode Vibrational Noise Cancellation Structure for Metglas/Pb(Zr,Ti)O-3 Fiber Magnetoelectric Laminates, Ieee Transactions on Ultrasonics Ferroelectrics and Frequency Control, 58 (2011) 1541-1544.
- [6] D. Hasanyan, Y.J. Wang, J.Q. Gao, M.H. Li, J.F. Li, D. Viehland, Modeling of dynamic behavior of ferromagnetic-ferroelectric-substrate multilayer composites: Longitudinal and bending modes, Physical Review B, submitted, (2012)
- [7] Hasanyan D, J. Gao, Y. Wang, R. Viswan, M. Li, Y. Shen, J. Li, D. Viehland
Theoretical and experimental investigation of magnetoelectric effect for bending-tension coupled modes in magnetostrictive-piezoelectric layered composites (Journal of Applied Physics, submmited)
- [8] Hasanyan D, Y. Wang, J. Gao, M. Li, Y. Shen, J. Li, D. Viehland EFFECTIVE PROPERTIES AND MAGNETO-ELECTRIC COEFFICIENTS OF THERMO- MAGNETO-ELECTRO-ELASTIC MULTILAYER COMPOSITES: NONPERFECT CONNECTIVITY BETWEEN LAYERS (Sensors and Actuators A: Physical, submitted)
- [9] M. Li, D. Berry, J. Das, D. Gray, J. Li, D. Viehland, Enhanced Sensitivity and Reduced Noise Floor in Magnetoelectric Lamine Sensors by an Improved Lamination Process, Journal of the American Ceramic Society, 94 (2011) 3738-3741.
- [10] M. Li, Y. Wang, J. Gao, D. Gray, J. Li, D. Viehland, Dependence of magnetic field sensitivity of a magnetoelectric laminate sensor pair on separation distance: Effect of mutual inductance, Journal of Applied Physics, 111 (2012).
- [11] M. Li, Y. Wang, D. Hasanyan, J. Li, D. Viehland, Giant converse magnetoelectric effect in multi-push-pull mode Metglas/Pb(Zr,Ti)O-3/Metglas laminates, Applied Physics Letters, 100 (2012).
- [12] L. Shen, M. Li, J. Gao, Y. Shen, J.F. Li, D. Viehland, X. Zhuang, M.L.C. Sing, C. Cordier, S. Saez, C. Dolabdjian, Magnetoelectric nonlinearity in magnetoelectric laminate sensors, Journal of Applied Physics, 110 (2011).

- [13] Y. Shen, J. Gao, L. Shen, D. Gray, J. Li, P. Finkel, D. Viehland, X. Zhuang, S. Saez, C. Dolabdjian, Analysis of the environmental magnetic noise rejection by using two simple magnetoelectric sensors, Sensors and Actuators a-Physical, 171 (2011) 63-68.
- [14] Y. Shen, J. Gao, Y. Wang, J. Li, D. Viehland, Thermal stability of magnetoelectric sensors, Applied Physics Letters, 100 (2012).
- [15] Y. Wang, J. Gao, M. Li, D. Hasanyan, Y. Shen, J. Li, D. Viehland, H. Luo, Ultralow equivalent magnetic noise in a magnetoelectric Metglas/Mn-doped Pb(Mg_{1/3}Nb_{2/3})O₃-PbTiO₃ heterostructure, Applied Physics Letters, (2012) Accepted.
- [16] Y. Wang, J. Gao, M. Li, Y. Shen, D. Hasanyan, R. Viswan, P. Finkel, J. Li, D. Viehland, A Hybrid Differentiated Magnetoelectric Sensor: Internal Noise Reduction and External Noise Cancellation, Advanced Materials, (2012) Submitted.
- [17] Y. Wang, D. Gray, D. Berry, J. Gao, J. Li, D. Viehland, H. Luo, Equivalent magnetic noise in magnetoelectric Metglas/Pb(Mg_{1/3}Nb_{2/3})O₃-PbTiO₃ laminate composites, Physica Status Solidi-Rapid Research Letters, 5 (2011) 232-234.
- [18] Y. Wang, D. Gray, D. Berry, J. Gao, M. Li, J. Li, D. Viehland, An Extremely Low Equivalent Magnetic Noise Magnetoelectric Sensor, Advanced Materials, 23 (2011) 4111.
- [19] Y. Wang, D. Gray, D. Berry, J. Li, D. Viehland, Self-amplified magnetoelectric properties in a dumbbell-shaped magnetostrictive/piezoelectric composite, Ieee Transactions on Ultrasonics Ferroelectrics and Frequency Control, 59 (2012) 859-862.
- [20] Y. Wang, D. Gray, D. Berry, M. Li, J. Gao, J. Li, D. Viehland, Influence of interfacial bonding condition on magnetoelectric properties in piezofiber/Metglas heterostructures, Journal of Alloys and Compounds, 513 (2012) 242-244.
- [21] Y. Wang, D. Gray, J. Gao, D. Berry, M. Li, J. Li, D. Viehland, H. Luo, Improvement of magnetoelectric properties in Metglas/Pb(Mg_{1/3}Nb_{2/3})O₃-PbTiO₃ laminates by poling optimization, Journal of Alloys and Compounds, 519 (2012) 1-3.
- [22] Y. Wang, D. Hasanyan, J. Li, D. Viehland, H. Luo, Shear-mode magnetostrictive/piezoelectric composite with an enhanced magnetoelectric coefficient, Applied Physics Letters, 100 (2012) 202903.
- [23] Y. Wang, D. Hasanyan, M. Li, J. Gao, J. Li, D. Viehland, H. Luo, Theoretical model for geometry-dependent magnetoelectric effect in magnetostrictive/piezoelectric composites, Journal of Applied Physics, 111 (2012) 124513-124518.
- [24] Y. Wang, D. Hasanyan, M. Li, J. Gao, R. Viswan, J. Li, D. Viehland, Electric-field tuning of magnetoelectric properties in Metglas/piezofiber composites, physica status solidi (RRL) - Rapid Research Letters, (2012) 265-267.
- [25] Y. Wang, D. Hasanyan, M. Li, J. Gao, R. Viswan, J. Li, D. Viehland, Magnetic field dependence of the effective permittivity in multiferroic composites, physica status solidi (a)-applications and materials science, (2012) Accepted.
- [26] Y. Wang, M. Li, D. Hasanyan, J. Gao, J. Li, D. Viehland, Geometry-induced magnetoelectric effect enhancement and noise floor reduction in Metglas/piezofiber sensors, Applied Physics Letters, in press (2012).
- [27] Y. Wang, D. Hasanyan, M. Li, J. Gao, J. Li, D. Viehland, Equivalent magnetic noise in multi-push-pull configuration magnetoelectric composites: model and experiment, Ieee Transactions on Ultrasonics Ferroelectrics and Frequency Control, Minior revision (2012).

- [28] Hasanyan D, Y. Wang, J. Gao, M. Li, Y. Shen, J. Li, D. Viehland, Modeling of resonant magneto-electric effect in a magnetostrictive and piezoelectric laminate composite structure coupled by a bonding material (Phys. Rev. B, submmited);
- [29] X.Zhuang, M. Lam Chok Sing, C. Cordier, S. Saez, C.Dolabdjian, J. Das, J. Gao, J.Li, D.Viehland, Analysis of noise in Magneto-Electric thin layer composites used as magnetic sensor. IEEE Sensors Journal, 11(10), 2183-2188(2011)
- [30] X.Zhuang, M. Lam Chok Sing, C. Cordier, S. Saez, C.Dolabdjian, L.Shen, J.Li, M.Li, D.Viehland, Efficiency of applied axial field modulation technique on ME sensor input magnetic noise rejection. IEEE Sensors Journal, 11(10), 2266-2272(2011)
- [31] X.Zhuang, C.Cordier, S.Saez, M.LamChok Sing, C.Dolabdjian, J. Gao, J.Li, D.Viehland, Theoretical analysis of the intrinsic magnetic noise spectral density of magnetostricitve piezoelectric laminated composite. Appl. Phys Letters, 109, 124512(2011)
- [32] X.Zhuang, M.LamChok Sing, C.Cordier, S.Saez, C.Dolabdjian, , J.F.Li, D.Viehland, S.K.Mandal, G.Sreenivasulu, G.Srinivasan, Investigation on the magnetic noise of stacked Magnetostrictive-Piezoelectric laminated composites, Sensors Letters, x(x), xxx-xxx(2012)
- [33] X.Zhuang, M.LamChok Sing, C.Cordier, S.Saez, C.Dolabdjian, J.F.Li, D.Viehland Expected Equivalent Magnetic Noise Spectral Density of Magnetoelectric Composites as Magnetic sensors: From Theory to Experiments, MRS Online Proceedings Library, Volume 1398, January 2012, pp mrsf11-1398-q01-02, doi: 10.1557/opl.2012.767, Published online by Cambridge University Press 23 Apr 2012
- [34] X.Zhuang, M.LamChok Sing, C.Dolabdjian, Investigation of the near-carrier noise for a strain-driven ME laminates by using cross-correlation techniques, EMSA'12 Conference, 1 - 4 July, Prague (2012)
- [35] Yongke Yan, Kyung-Hoon Cho, Deepam Maurya, Amit Kumar, Sergei V. Kalinin, Armen Khachaturyan and Shashank Priya, “<001> Textured PZT-Based Piezoelectric Ceramics Exhibiting Giant Energy Density”, Nature Materials (under review).
- [36] Yongke Yan, Yuan Zhou, and Shashank Priya, “Giant Magnetoelectric Response in Co-fired Textured Magnetoelectric Composite: A Step Closer to Commercial Realization” Advanced Materials (under review).
- [37] Yongke Yan, Yu.U. Wang, and Shashank Priya, “Electromechanical Behavior of [001]-Textured Pb(Mg_{1/3}Nb_{2/3})O₃-PbTiO₃ Ceramics”, Applied Physics Letters, 100, 192905 (2012).
- [38] Yongke Yan, Ashok Kumar, Margarita Correa, Kyung-Hoon Cho, R.S. Katiyar, and Shashank Priya, “Phase Transition and Temperature Stability of Piezoelectric Properties in Mn-modified Pb(Mg_{1/3}Nb_{2/3})O₃-PbZrO₃-PbTiO₃ Ceramics”, Applied Physics Letters, 100, 152902 (2012).
- [39] Yongke Yan, Kyung-Hoon Cho, and Shashank Priya, “Piezoelectric Properties and Temperature Stability of Mn-doped Pb(Mg_{1/3}Nb_{2/3})-PbZrO₃-PbTiO₃ Textured Ceramics”, Applied Physics Letters, 100, 132908 (2012).
- [40] Yongke Yan, Kyung-Hoon. Cho, Shashank. Priya, “Role of Secondary Phase in High Power Piezoelectric PMN-PZT Ceramics,” Journal of the American Ceramic Society, 94 [12] 4138–4141 (2011).
- [41] Su Chul Yang, Kyung-Hoon Cho, Chee-Sung Park, and Shashank Priya, “Self-biased Converse Magnetoelectric Effect,” Applied Physics Letters, 99, 202904(2011).

- [42] Kyung-Hoon. Cho, Shashank Priya, “Direct and Converse Effect in Magnetoelectric Laminate Composites,” *Applied Physics Letters*, **98**, 232904 (2011).
- [43] Yongke Yan, Kyung-Hoon. Cho, Shashank Priya, “Identification and Effect of Secondary Phase in MnO₂-doped 0.8Pb(Zr_{0.52}Ti_{0.48})O₃-0.2Pb(Zn_{1/3}Nb_{2/3})O₃ Piezoelectric Ceramics,” *Journal of the American Ceramic Society*, **94**[11], 3953 (2011).
- [44] Yongke Yan, Kyung-Hoon. Cho, Shashank Priya, “Templated Grain Growth of <001>-Textured 0.675Pb(Mg_{1/3}Nb_{2/3})O₃-0.325PbTiO₃ Piezoelectric Ceramics for Magnetic Field Sensors,” *Journal of the American Ceramic Society*, **94**[6], 1784 (2011).
- [45] Chee-Sung Park, Dragan Avirovik, Scott Bressers, and Shashank Priya, “Low-frequency nanotesla sensitivity in Metglas/piezoelectric/carbon fiber/piezoelectric composites with active tip mass”, *Applied Physics Letters*, **98**, 062904 (2011).
- [46] Kyung-Hoon Cho, Shashank Priya, “Synthesis of ferroelectric PZT fibers using sol-gel technique”, *Materials Letters*, **65**, 775–779, (2011).
- [47] Kyung-Hoon Cho, Chee-Sung Park, and Shashank Priya, “Effect of intensive and extensive loss factors on the dynamic response of magnetoelectric laminates”, *Applied Physics Letters*, **97**, 182902 (2010).
- [48] Chee-Sung Park, Kyung-Hoon Cho, Mustafa Ali Arat, Jeff Evey, and Shashank Priya, “High magnetic field sensitivity in Pb(Zr,Ti)O₃–Pb(Mg_{1/3}Nb_{2/3})O₃ single crystal/Terfenol-D/Metglas magnetoelectric laminate composites”, *Journal of Applied Physics*, **107**, 094109 (2010).
- [49] S. K. Mandal, G. Sreenivasulu, V. M. Petrov, S. Bandekar, and G. Srinivasan, “Functionally graded piezomagnetic and piezoelectric bilayers for magnetic field sensors: Magnetoelectric interactions at low frequencies and at bending modes,” *Ceramic Transactions* **226**, 223 (2011).
- [50] L. Y. Fetisov, N. S. Perov, Y. K. Fetisov, G. Srinivasan, and V. M. Petrov “ Resonance magnetoelectric interactions in an asymmetric ferromagnetic-ferroelectric layered structure,”, *J. Appl. Phys.* **109**, 053908 (2011).
- [51] G. Sreenivasulu, S. K. Mandal, V. M. Petrov, A. Mukundan, S. Rengesh, and G. Srinivasan, “Bending resonance in a magnetostrictive-piezoelectric bilayer and magnetoelectric interactions,” *Integ. Ferroelec.* **126**, 87 (2011).
- [52] G. Lawes and G. Srinivasan, “Introduction to magnetoelectric coupling and multiferroic films,” *J. Phys.D: Appl. Phys.* **44**, 243001 (2011).
- [53] S. K. Mandal, G. Sreenivasulu, V. M. Petrov, and G. Srinivasan “Magnetization graded multiferroic composites and magnetoelectric effects at zero bias,”, *Phys. Rev. B* **84**, 014432 (2011).
- [54] J. R. Petire, J. Fine, S. Mandal, G. Sreenivasulu, G. Srinivasan, and A. S. Edelstein “Enhanced sensitivity of magnetoelectric sensors by tuning the resonant frequency,”, *Appl. Phys. Lett.* **99**, 043504 (2011).
- [55] D. A. Filippov, T. A. Galkina, V. M. Laletin, and G. Srinivasan “Inverse magnetoelectric effect in disk shaped samples of ferrite piezoelectric composites,”, *Phys. Solid State* **53**, 1737 (2011).
- [56] Y. K. Fetisov, D. V. Chashin, A. G. Segalla, and G. Srinivasan “Resonance magnetoelectric effects in a piezoelectric bimorph,”, *J. Appl. Phys.* **110**, 066101 (2011).

- [57] G. Sreenivasulu, S. K. Mandal, S. Bandekar, V. M. Petrov, and G. Srinivasan, “Low-frequency and resonance magnetoelectric effects in piezoelectric and functionally stepped ferromagnetic layered composites,” *Phys. Rev. B*. **84**, 144426 (2011)
- [58] J.Petrie, D. Viehland, D. Gray, S. Mandal, G. SreenivasuluG. Srinivasan, and Alan S. Edelstein, “Enhancing the Sensitivity of Magnetoelectric Sensors by Increasing the Operating Frequency,” *J. Appl. Phys.* **110**, 124506 (2011).
- [59] G. Sreenivasulu, U. Laletin, V. M. Petrov, V. V. Petrov, and G. Srinivasan, “A Permendur-Piezoelectric Multiferroic Composite for Low-Noise Ultrasensitive Magnetic Field Sensors,” *J. Appl. Phys.* **100**, 173506 (2012).
- [60] G. Sreenivasulu, L. Y. Fetisov, Y. K. Fetisov, and G. Srinivasan, “Piezoelectric single crystal langatate and ferromagnetic composites: Studies on low-frequency and resonance magnetoelectric effects,” *Appl. Phys. Lett.* **100**, 052901 (2012).

Presentations:

- [1] Yaojin Wang, Menghui Li, Junqi Gao, Jiefang Li and Dwight Viehland, Equivalent magnetic noise in magnetoelectric laminate sensors, 2011 MRS Fall Conference, Boston, Nov 28, 2011
- [2] Ying Shen, Junqi Gao, Jiefang Li, Dwight Viehland, Keith McLaughlin, Greg Beall, AC Magnetic Dipole Localization by Magnetoelectric Sensor, 2011 MRS Fall Conference, Boston, Nov 28, 2011
- [3] Investigation on the magnetic noise of stacked Magnetostrictive-Piezoelectric laminated composites, X.Zhuang, M.LamChok Sing, C.Cordier, S.Saez, C.Dolabdjian, J.F.Li, D.Viehland, S.K.Mandal, G.Sreenivasulu, G.Srinivasan, Sensors Letters, x(x), xxx-xxx(2012)
- [4] C.Dolabdjian, Intrinsic or Equivalent magnetic noise of magnetic sensors. Problematic and analysis exemplified with Magneto(Elasto)electric and Giant Magneto-Impedance sensor developments., , SFB 855 Spring Meeting, Wednesday 7 to Friday 9, March 2012 - Prof. Quandt, Kiel University, Kiel, 2012
- [5] X.Zhuang, M.LamChok Sing, C.Cordier, S.Saez, C.Dolabdjian, J.F.Li, D.Viehland, From Magneto-Elasto-Electric device to ultra-low noise magnetic sensor, , CIMTEC 2012, 10-14 June 2012, Montecatini(Italie)

LIST OF ACRONYMS, ABBREVIATIONS, AND SYMBOLS

<u>Acronym</u>	<u>Description</u>
ME	Magnetoelectric
PZT	Pb(ZrxTi1-x)O3
PMN-PT	Pb(Mg1/3Nb2/3)O3-PbTiO3
PMN-PZT	Pb(Mg1/3Nb2/3)O3- PbZrO3-PbTiO3
Metglas	Fe74.4Co21.6Si0.5B3.3Mn0.1C0.1
L-L	Longitudinal-longitudinal
L-T	Longitudinal-transverse
M-P-P	Multi-push-pull
Symbol	Description
ϵ_r	Dielectric constant
$\tan\delta$	Dielectric loss
k_{33}	Electromechanical coupling factor
d_{33}	Piezoelectric coefficient
α_E	Magnetoelectric coefficient
α_V	Magnetoelectric voltage coefficient
α_Q	Magnetoelectric charge coefficient
H_{dc}	DC magnetic bias field
H_{ac}	AC magnetic bias field
k	Boltzmann's constant ($1.38 \times 10^{-23} \text{ J/K}$)
T	Temperature in Kelvin
C	Capacitance of a sensor
Rdc	DC resistance of a sensor